CARDIOMYOCYTE MICRODOMAINS: AN EMERGING CONCEPT OF LOCAL REGULATION AND REMODELING

EDITED BY: Alexey V. Glukhov, Di Lang, Sarah Calaghan and Julia Gorelik
PUBLISHED IN: Frontiers in Physiology

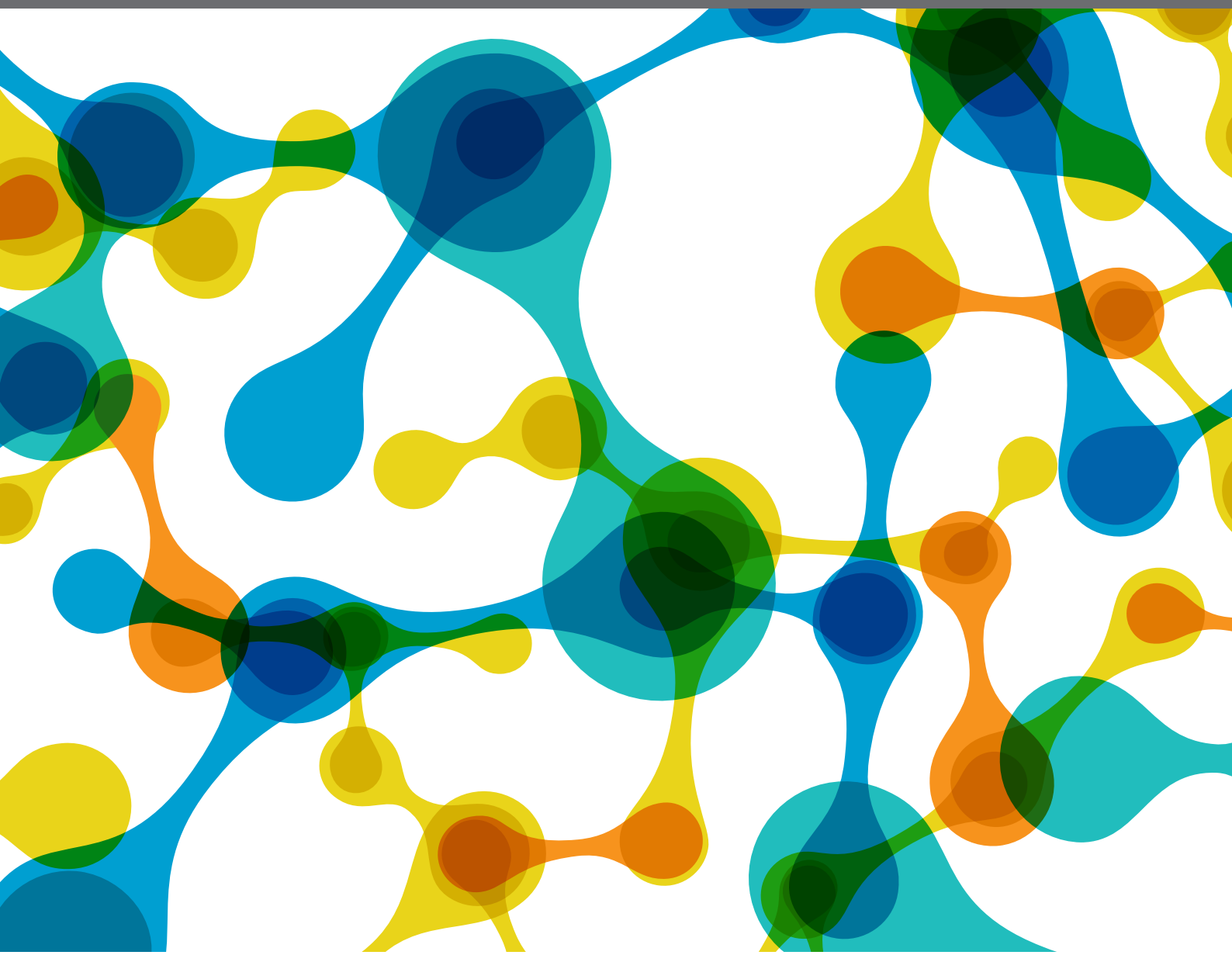

frontiers Research Topics

frontiers

ISSN 1664-8714
ISBN 978-2-88963-836-9
DOI 10.3389/978-2-88963-836-9

About Frontiers

Frontiers is more than just an open-access publisher of scholarly articles: it is a pioneering approach to the world of academia, radically improving the way scholarly research is managed. The grand vision of Frontiers is a world where all people have an equal opportunity to seek, share and generate knowledge. Frontiers provides immediate and permanent online open access to all its publications, but this alone is not enough to realize our grand goals.

Frontiers Journal Series

The Frontiers Journal Series is a multi-tier and interdisciplinary set of open-access, online journals, promising a paradigm shift from the current review, selection and dissemination processes in academic publishing. All Frontiers journals are driven by researchers for researchers; therefore, they constitute a service to the scholarly community. At the same time, the Frontiers Journal Series operates on a revolutionary invention, the tiered publishing system, initially addressing specific communities of scholars, and gradually climbing up to broader public understanding, thus serving the interests of the lay society, too.

Dedication to Quality

Each Frontiers article is a landmark of the highest quality, thanks to genuinely collaborative interactions between authors and review editors, who include some of the world's best academicians. Research must be certified by peers before entering a stream of knowledge that may eventually reach the public - and shape society; therefore, Frontiers only applies the most rigorous and unbiased reviews.
Frontiers revolutionizes research publishing by freely delivering the most outstanding research, evaluated with no bias from both the academic and social point of view. By applying the most advanced information technologies, Frontiers is catapulting scholarly publishing into a new generation.

What are Frontiers Research Topics?

Frontiers Research Topics are very popular trademarks of the Frontiers Journals Series: they are collections of at least ten articles, all centered on a particular subject. With their unique mix of varied contributions from Original Research to Review Articles, Frontiers Research Topics unify the most influential researchers, the latest key findings and historical advances in a hot research area! Find out more on how to host your own Frontiers Research Topic or contribute to one as an author by contacting the Frontiers Editorial Office: researchtopics@frontiersin.org

CARDIOMYOCYTE MICRODOMAINS: AN EMERGING CONCEPT OF LOCAL REGULATION AND REMODELING

Topic Editors:
Alexey V. Glukhov, University of Wisconsin-Madison, United States
Di Lang, University of Wisconsin-Madison, United States
Sarah Calaghan, University of Leeds, United Kingdom
Julia Gorelik, Imperial College London, United Kingdom

Citation: Glukhov, A. V., Lang, D., Calaghan, S., Gorelik, J., eds. (2020). Cardiomyocyte Microdomains: An Emerging Concept of Local Regulation and Remodeling. Lausanne: Frontiers Media SA. doi: 10.3389/978-2-88963-836-9

Table of Contents

frontiers in Physiology

EDITORIAL
published: 26 May 2020
doi: 10.3389/fphys.2020.00512

Editorial: Cardiomyocyte Microdomains: An Emerging Concept of Local Regulation and Remodeling

Di Lang[1], *Sarah C. Calaghan*[2], *Julia Gorelik*[3] *and Alexey V. Glukhov*[1]*

[1] Department of Medicine, University of Wisconsin-Madison School of Medicine and Public Health, Madison, WI, United States, [2] School of Biomedical Sciences, University of Leeds, Leeds, United Kingdom, [3] Myocardial Function, National Heart and Lung Institute, Imperial College London, London, United Kingdom

Keywords: microdomain, cardiomyocte, caveolae, t-tubule, L-type Ca channel, intercalated disc, Na channel

Editorial on the Research Topic

Cardiomyocyte Microdomains: An Emerging Concept of Local Regulation and Remodeling

Technological advances facilitate scientific breakthroughs that lead to leaps in our understanding of human physiology and pathophysiology. We are beginning to recognize the key roles of cardiomyocyte microdomains in essential aspects of many cellular processes and their importance as a mechanistic driver of life-threatening arrhythmias and cardiac dysfunction in a range of pathologies. This concept opens new avenues to understand heart disease from a more systematic and dynamic perspective and benefits clinical treatment strategies, as summarized in the current Research Topic.

Emerging evidence demonstrates that in cardiomyocytes discrete clusters of ion channels, regulatory receptors and various signaling molecules are present throughout the sarcolemma, where they form an interacting network and work together as a part of different macromolecular signaling complexes. It has been recognized that compartmentalized distribution of proteins impacts their function and regulation by various neurohormonal pathways, either via a direct interaction with G-protein coupled receptors or by means of second messengers. In the cardiac myocyte, this enables the specificity, reproducibility, and accuracy of the neurohormonal modulation of numerous cellular processes, including membrane excitability and excitation-contraction coupling (ECC) (reviewed in Radwanski et al.), hormone secretion, gene expression, and the immune response during cellular stress (Chen G. et al.). A series of reviews, perspectives, and original research articles in this Research Topic presents the latest advances on microdomain-specific distribution, functioning, regulation, and remodeling of: ion channels, including L-type Ca^{2+} channels (LTCCs) (Wright et al.), transient receptor potential canonical (TRPC) channels (Wen et al.), potassium inward rectifier channels (Vaidyanathan et al.), sodium channels (Chen X. et al.), regulatory proteins and second messengers (Loucks et al.), mitochondria (Zhou et al.), the inflammasome (Chen G. et al.), fibrosis (Shao et al.). Taken together, these give novel insight into the contribution of microdomains to cellular signaling and cardiac pathology.

The most studied aspect is, probably, a compartmentalized distribution of LTCCs, their functional coupling with sarcoplasmic reticulum Ca^{2+}-induced Ca^{2+} release channels, ryanodine receptors (RyRs), and their regulation by β-adrenergic receptors (βARs) (as reviewed in Jones et al.) A recent study by Sanchez-Alonso and colleagues demonstrated that disruption of T-tubule structures in heart failure leads to the redistribution of functional LTCCs from their canonical location in T-tubules to the crest of the sarcolemma, where their open probability is dramatically increased via Ca^{2+}-calmodulin kinase II (CaMKII)-mediated phosphorylation. This subsequently elevates the whole-cell L-type Ca^{2+} current ($I_{Ca,L}$) window

Edited and reviewed by:
Ruben Coronel,
University of Amsterdam, Netherlands

***Correspondence:**
Alexey V. Glukhov
aglukhov@medicine.wisc.edu

Specialty section:
This article was submitted to Cardiac Electrophysiology, a section of the journal Frontiers in Physiology

Received: *17 April 2020*
Accepted: *27 April 2020*
Published: *26 May 2020*

Citation:
Lang D, Calaghan SC, Gorelik J and Glukhov AV (2020) Editorial: Cardiomyocyte Microdomains: An Emerging Concept of Local Regulation and Remodeling. Front. Physiol. 11:512. doi: 10.3389/fphys.2020.00512

current and results in the development of arrhythmogenic early afterdepolarizations (Sanchez-Alonso et al., 2016). A similar mechanism could be also involved in pathological remodeling in cardiac hypotrophy as reviewed in Tanaka et al.

Importantly, redistributed LTCCs are no longer co-localized with RyRs and thus do not contribute to ECC. These findings indicate that the same protein could behave differently when located in distinct subcellular compartments. This could explain the low therapeutic efficiency and high incidence of side-effects of conventional therapies focused on the targeting of activity of certain proteins. For example, conventional calcium channel blockers are generally felt to be contraindicated in heart failure because of their negatively inotropic effects via inhibiting both peak and window $I_{Ca,L}$. Such adverse effects may relate to non-specific targeting of LTCCs. It therefore indicates a need for the development of targeted therapies which take into account a microdomain-specific localization of affected proteins as well as their surrounding molecular partners to achieve the localized effects.

The redistribution of LTCCs in heart failure impairs LTCC-RyR functional coupling leading to both electrical and contractile abnormalities (see review by Jones et al.). It is also accompanied by the disruption of an associated macromolecular signaling complex which includes, besides LTCCs, β_2ARs, protein kinase A, phosphodiesterase 4, and adenylyl cyclase 5/6, resulting in a blunted response of diseased myocardium to sympathetic stimulation. Using novel Forster Resonance Energy Transfer (FRET)-based biosensors for live cell imaging (the most recent methodological advances of FRET biosensors are reviewed by Dikolayev et al.) as well as sophisticated biochemical, electrophysiological and optical (Jayasinghe et al.) techniques, several groups have shown a disruption of β_2AR-mediated cyclic adenosine monophosphate (cAMP) signaling in failing ventricular myocytes. From a confined, local increase in healthy myocytes under β_2AR stimulation, cAMP becomes diffuse throughout the cytosol in failing myocytes (Nikolaev et al., 2010). It subsequently leads to abnormal phosphorylation of contractile proteins and loss of the cardioprotective effect of β_2ARs which contributes to the heart failure phenotype.

Loss of compartmentalized cAMP signaling has been linked to disruption of caveolae and downregulation of caveolar scaffolding protein caveolin-3 (Calaghan et al., 2008; Wright et al., 2014). A crucial role of caveolin-3 in controlling cAMP signaling microdomains has been recently demonstrated in ventricular myocytes (see a computational study by Loucks et al.), as well as in atrial and sinoatrial node myocytes which lack a developed T-tubule system (reviewed in Lang and Glukhov). In atrial myocytes, caveolin-3 participates in the formation of specialized "axial couplons" that are composed of voluminous axial tubules with extensive junctions to the sarcoplasmic reticulum including clusters of highly phosphorylated RyRs (Brandenburg et al., 2016). This increases the frequency of spontaneous Ca^{2+} releases from RyRs when compared with ventricular myocytes (Glukhov et al., 2015) but facilitates the synchronization of the subcellular Ca^{2+} release and thus contraction in atrial myocytes (Brandenburg et al.). Similar clusters of highly phosphorylated RyRs have been also identified in sinoatrial node pacemaker cells where they are responsible for the generation of spontaneous local Ca^{2+} releases, a critical part of the Ca^{2+} component of the coupled-clock pacemaker system (reviewed in Vinogradova et al.).

Finally, caveolae structures have been described as membrane mechanosensors and linked to the activation of mechano-sensitive, swelling-activated chloride channels $I_{Cl,swell}$ (Egorov et al., 2019). Stretch-dependent regulation of membrane microdomains has been proposed to play an important role in the mechano-electrical feedback in the heart regulating pre-loading dependent cardiomyocyte shortening (Kozera et al., 2009), LTCC and β_2AR signaling microdomains (Wright et al.) and also could be involved in stress-induced membrane damage (Nikouee et al.) and associated inflammation (Chen G. et al.).

CONCLUSIONS AND FUTURE DIRECTIONS

All these studies pave the road to expand our knowledge of cardiac physiology from the new perspective of microdomain compartments which will advance clinical treatment strategies in the future. In most cases, a poor efficacy of current therapeutics can be ascribed to incomplete understanding of electrophysiological, cellular and molecular mechanisms that underlie certain heart diseases. The conventional description of cardiac pathologies, in terms of dysfunction of one or several proteins often described via changes in their expression or function, further compounds the poor efficacy of available therapies. These limitations contribute to the non-specific action of cardiac medications on other organs and tissues, and even throughout different regions of the heart. This leads to common side-effects of conventional therapies and, in the worse cases, increases morbidity and mortality in a long-term perspective.

This view was changed by consideration of post-translational modification of proteins. Various post-translational modifications, including phosphorylation, glycosylation, nitrosylation, and lipidation, have been shown to dramatically modify protein activity, critically contributing to pathological cell signaling. Recent methodological advances have made it possible to visualize localization, regulation and interaction of single proteins at nanoscale resolution allowing study of the clustering of functional ion channels, receptors, and various second messengers as well as their coupling within specific cellular microdomains. This extends the classical concept of cardiac remodeling and adds a new dimension to cardiovascular disease, namely microdomain-targeted protein remodeling, which could be a development platform for more sophisticated therapeutic approaches based on the subcellular distribution of their targets.

AUTHOR CONTRIBUTIONS

AG and DL wrote the editorial. SC and JG provided comments and edits.

FUNDING

This work was supported by NIH R01 HL141214-01, R01 HL139738-01A1, and AHA 16SDG29120011 to AG, AHA Fellowship 17POST33370089 to DL, British Heart Foundation project grants to SC (PG/15/42/31563 and PG/17/84/33372), and British Heart Foundation grants to JG (RG/17/13/33173 and PG/17/3/32722).

REFERENCES

Brandenburg, S., Kohl, T., Williams, G. S., Gusev, K., Wagner, E., Rog-Zielinska, E. A., et al. (2016). Axial tubule junctions control rapid calcium signaling in atria. *J. Clin. Invest.* 126, 3999–4015. doi: 10.1172/JCI88241

Calaghan, S., Kozera, L., and White, E. (2008). Compartmentalisation of cAMP-dependent signalling by caveolae in the adult cardiac myocyte. *J. Mol. Cell. Cardiol.* 45, 88–92. doi: 10.1016/j.yjmcc.2008.04.004

Egorov, Y. V., Lang, D., Tyan, L., Turner, D., Lim, E., Piro, Z. D., et al. (2019). Caveolae-mediated activation of mechanosensitive chloride channels in pulmonary veins triggers atrial arrhythmogenesis. *J. Am. Heart Assoc.* 8:e012748. doi: 10.1161/JAHA.119.012748

Glukhov, A. V., Balycheva, M., Sanchez-Alonso, J. L., Ilkan, Z., Alvarez-Laviada, A., Bhogal, N., et al. (2015). Direct evidence for microdomain-specific localization and remodeling of functional L-type calcium channels in rat and human atrial myocytes. *Circulation* 132, 2372–2384. doi: 10.1161/CIRCULATIONAHA.115.018131

Kozera, L., White, E., and Calaghan, S. (2009). Caveolae act as membrane reserves which limit mechanosensitive I(Cl,swell) channel activation during swelling in the rat ventricular myocyte. *PLoS ONE* 4:e8312. doi: 10.1371/journal.pone.0008312

Nikolaev, V. O., Moshkov, A., Lyon, A. R., Miragoli, M., Novak, P., Paur, H., et al. (2010). Beta2-adrenergic receptor redistribution in heart failure changes cAMP compartmentation. *Science* 327, 1653–1657. doi: 10.1126/science.1185988

Sanchez-Alonso, J. L., Bhargava, A., O'Hara, T., Glukhov, A. V., Schobesberger, S., Bhogal, N., et al. (2016). Microdomain-specific modulation of L-type calcium channels leads to triggered ventricular arrhythmia in heart failure. *Circ. Res.* 119, 944–955. doi: 10.1161/CIRCRESAHA.116.308698

Wright, P. T., Nikolaev, V. O., O'Hara, T., Diakonov, I., Bhargava, A., Tokar, S., et al. (2014). Caveolin-3 regulates compartmentation of cardiomyocyte beta2-adrenergic receptor-mediated cAMP signaling. *J. Mol. Cell Cardiol.* 67, 38–48. doi: 10.1016/j.yjmcc.2013.12.003

Conflict of Interest: The authors declare that the research was conducted in the absence of any commercial or financial relationships that could be construed as a potential conflict of interest.

frontiers in Physiology

REVIEW
published: 15 June 2018
doi: 10.3389/fphys.2018.00755

ER–Mitochondria Microdomains in Cardiac Ischemia–Reperfusion Injury: A Fresh Perspective

Hao Zhou[1,2], Shuyi Wang[2], Shunying Hu[1], Yundai Chen[1]* and Jun Ren[2,3]**

[1] Chinese People's Liberation Army General Hospital, People's Liberation Army Medical School, Beijing, China, [2] Center for Cardiovascular Research and Alternative Medicine, University of Wyoming College of Health Sciences, Laramie, WY, United States, [3] Department of Cardiology, Zhong Shan Hospital, Fudan University, Shanghai, China

The mitochondrial and endoplasmic reticulum (ER) homeostasis is pivotal to the maintenance of an array of physiological processes. The physical contact and association between ER and mitochondria, known as the ER–mitochondria microdomains or mitochondria-associated ER membrane (MAM), temporally and spatially regulates the mitochondria/ER structure and function. More evidence suggests a role for MAMs in energy production, cellular contraction and mobility, and normal extracellular signal transmission. In pathological states, such as cardiac ischemia–reperfusion (I/R injury), this ER–mitochondria microdomains may act to participate in the cellular redox imbalance, ER stress, mitochondrial injury, energy deletion, and programmed cell death. From a therapeutic perspective, a better understanding of the cellular and molecular mechanisms of the pathogenic ER–mitochondria contact should help to identify potential therapeutic target for cardiac I/R injury and other cardiovascular diseases and also pave the road to new treatment modalities pertinent for the treatment of reperfusion damage in clinical practice. This review will mainly focus on the possible signaling pathways involved in the regulation of the ER–mitochondria contact. In particular, we will summarize the downstream signaling modalities influenced by ER–mitochondria microdomains, for example, mitochondrial fission, mitophagy, calcium balance, oxidative stress, and programmed cell death in details.

Keywords: ER–mitochondria microdomains, ischemia/reperfusion injury, mitochondrial fission, mitophagy, oxidative stress, calcium signaling, cell death

OPEN ACCESS

Edited by:
Di Lang,
University of Wisconsin–Madison, United States

Reviewed by:
Coert J. Zuurbier,
Academic Medical Center (AMC), Netherlands
Claudia Penna,
Università degli Studi di Torino, Italy

****Correspondence:***
Hao Zhou
zhouhao301@outlook.com
Yundai Chen
yundaic@163.com
Jun Ren
jren@uwyo.edu

Specialty section:
This article was submitted to Cardiac Electrophysiology, a section of the journal Frontiers in Physiology

Received: *06 April 2018*
Accepted: *29 May 2018*
Published: *15 June 2018*

Citation:
Zhou H, Wang S, Hu S, Chen Y and Ren J (2018) ER–Mitochondria Microdomains in Cardiac Ischemia–Reperfusion Injury: A Fresh Perspective. Front. Physiol. 9:755. doi: 10.3389/fphys.2018.00755

INTRODUCTION

Myocardial infarction (MI) is one of the leading causes of mortality worldwide due to acute occlusion of coronary arteries. Although revascularization treatment has offered proven protective efficacy for patients with MI, it also yields undesired ischemia–reperfusion (I/R) injury following the restoration of epicardial blood flow (Nunez-Gomez et al., 2017; Zhou et al., 2018b). A number of scenarios have been postulated for I/R injury, including oxidative stress, calcium imbalance, mitochondrial damage, excessive inflammation response, endoplasmic reticulum (ER) stress, and programmed cell death (Du et al., 2017; Garcia-Nino et al., 2017; Harisseh et al., 2017; Jahandiez et al., 2017). These culprit factors unfortunately lead to a secondary damage to the heart and thus compromise the clinical benefits from revascularization therapy (Merjaneh et al., 2017; Rienks et al., 2017). Notably, mitochondrial damage and ER stress have been well recognized as major

upstream factors governing the progression of cardiac I/R injury. Thereby, the structural and functional association between mitochondria and ER has emerged as an area of intensive research that has evolved rapidly over the last decade (Pihan et al., 2017).

The existence of physical links between ER and mitochondria have been suggested based on co-sedimentation of ER particles with mitochondria and electron microscopic observations of close associations between mitochondria and ER vesicles (Shore and Tata, 1977; Meier et al., 1981; Mannella et al., 1998). ER–mitochondrial microdomains [termed as the mitochondria-associated membranes (MAMs)] are purportedly comprised of a variety of proteins including, but not limited to, (i) the inositol 1,4,5-trisphosphate receptors (IP3R) on the ER and voltage-dependent anion-selective channel protein (VDAC) located on the mitochondria, through GRP75, which play a role in calcium signaling; (ii) the mitofusin 2 (Mfn2) located in the ER and other molecular chaperones such as mitofusin 1 (Mfn1) and FUNDC1 in the mitochondria, that play a role in tethering and modulating mitochondrial dynamics; (iii) the ER stress sensor PERK that initiates signaling in response to ER stress; and (iv) many more others including ryanodine receptor Ca^{2+} channel (RyR) (Chen et al., 2012), AMF-R (Wang et al., 2000), Miro1 (Fransson et al., 2003), BAP31 (Iwasawa et al., 2011), Fis1 (Wang et al., 2011; **Figures 1A,B**).

Structural and functional interactions of mitochondria with the ER have been demonstrated for rat hearts (Ruiz-Meana et al., 2010; Fernandez-Sanz et al., 2014; Gomez et al., 2016) and the distance between the ER and the outer mitochondrial membrane (OMM) is originally estimated to be approximately 100 nm (Soltys and Gupta, 1992; Mannella et al., 1994). However, a more recent study using electron tomography demonstrated that the minimum distance is much less, 10 nm at the smooth ER and 25 nm at the rough ER (Csordas et al., 2006). The physical cooperation between the ER and mitochondria offers pivotal roles in several aspects of cellular functions, including Ca^{2+} signaling, lipid transport, energy metabolism, and cellular survival (Honrath et al., 2018). However, in response to stress response, especially cardiac I/R injury, ER–mitochondria contact converts mitochondria and ER from ATP providers and protein factories that energize the cell to agents of cell death, respectively. Here, this mini-review is intended to summarize the current contemporary understanding with regards to the casual role of ER–mitochondrial microdomains in the onset and development of myocardial I/R injury.

MITOCHONDRIAL FISSION

Although commonly depicted as shuttle-shaped structures, mitochondria form a highly dynamic network within cardiomyocyte where they constantly undergo the fission and fusion processes (Lopez-Crisosto et al., 2017; Wang et al., 2017). The mitochondrial fission could be apparently noted in cardiac I/R injury (Gao et al., 2016; Cowan et al., 2017; Maneechote et al., 2017; Nan et al., 2017; Zhou et al., 2018e), and the aim of mitochondrial fission is to generate more daughter mitochondria that meet the cardiomyocyte demand in ischemic stage and/or in reperfusion phase. Under physiological conditions, moderate mitochondrial fission allows the dissemination of various metabolites and macromolecules throughout the entire compartment (Westermann, 2012). At the same time, mitochondrial fission is required for the removal of damaged and inactive organelles by way of autophagy (Twig et al., 2008a,b). When the bioenergetic state becomes critical, for example under nutrient deprivation (Sauvanet et al., 2010; Toyama et al., 2016), exercise (Coronado et al., 2018), or exposure to certain forms of stress (Theurey and Rieusset, 2017), fission is turned on to optimize mitochondrial function. However, excessive mitochondrial fission has been suggested as a primary causative factor in the pathogenesis of myocardial reperfusion injury based on succinct studies from independent laboratories (Ong et al., 2010; Sharp et al., 2014) including ourselves (Zhou et al., 2017a, 2018c,f; Jin et al., 2018). At the molecular levels, mitochondrial fission is exclusively governed by dynamin-related 1 (Drp1) and its adaptors such as mitochondrial fission factor (Mff) and mitochondrial fission 1 protein (Fis1) which help Drp1 tightly dock on mitochondria and then assist Drp1 to form the contractile ring around mitochondria (Garcia-Nino et al., 2017; Hong et al., 2017; Zhou et al., 2017c). Interestingly, recent research has depicted that ER–mitochondria microdomain closely wraps around the mitochondria and initiates a mitochondrial constriction at the contact sites before Drp1 is recruited to trigger mitochondrial fission (Friedman et al., 2011). Besides, Drp1 is also found to assemble on mitochondria preferentially at sites of the ER–mitochondria contact (Westermann, 2011), suggesting that ER–mitochondria microdomain may play an active role in the early stages of mitochondrial fission via defining the division sites. Thereby, these effects may aggravate the cardiac I/R injury through Drp1 recruitment and constriction. Besides, earlier work by Korobova et al. (2013) also observed a similar action for the ER–mitochondria microdomain on mitochondrial division, suggesting that repression of ER–mitochondria communication may provide more benefits for cardiac I/R injury via disrupting mitochondrial fission. Notably, Korobova et al. (2013) further pointed out that the ER-bound protein inverted formin 2 (INF2) predominantly controls mitochondrial fission possibly by forming a constrictions ring prior to translocation of Drp1 onto the mitochondrial membrane. More importantly, INF2 interacts with the calcium-binding protein calmodulin, which empowers the ER–mitochondria microdomain to shape the local calcium homeostasis (Wales et al., 2016). This regulatory mechanism amplifies the intracellular calcium delivery from ER to mitochondria, ensuring the success of mitochondrial fission, which would need sufficient Ca^{2+} to complete the organelle contraction. Following studies further confirm that INF2 also enhances actin polymerization on the ER (Gurel et al., 2015; Chakrabarti et al., 2018), which facilitates mitochondrial division through actin-dependent mitochondrial contractile.

Interestingly, the actin polymerization mediated by INF2 could in turn increases the ER–mitochondria contact area, as assessed by electron microscopy (Steffen and Koehler, 2018). These observations propose a positive feedback between ER–mitochondria microdomain and mitochondrial fission;

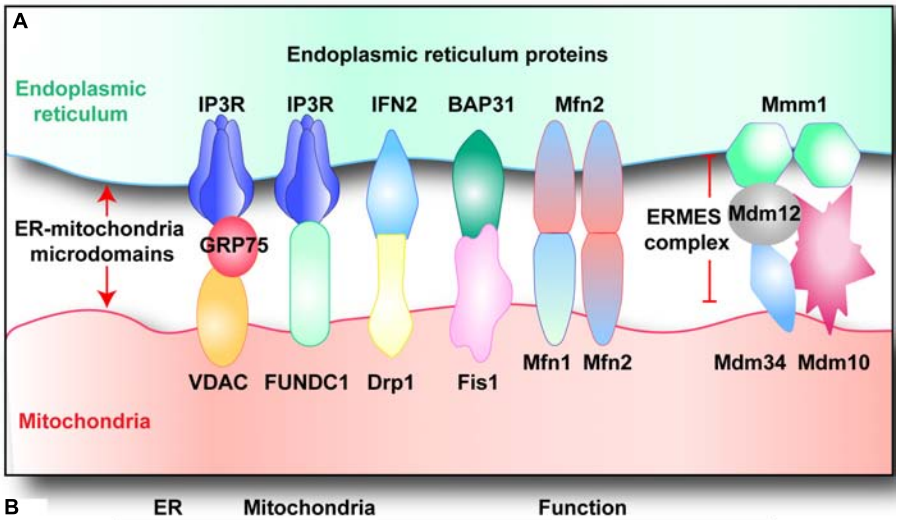

B

ER	Mitochondria	Function
Mfn2	Mfn1/2	Mitochondrial fission/mitophagy
BAP31	Fis1	Mitochondria to ER apoptotic regulation
IP3R	VDAC	Calcium signaling
IP3R	FUNDC1	Calcium signaling
IFN2	Drp1	Mitochondrial fission

FIGURE 1 | (A,B) Endoplasmic reticulum–mitochondria microdomains complexes. Multiple structures that tether mitochondria with ER have been described. Voltage-dependent anion channel (VDAC) and inositol 1,4,5-trisphosphate receptor (IP3R) interacts via GRP75, regulating calcium balance between mitochondria and ER. Similarly, IP3R also cooperates with FUN14 domain-containing protein 1 (FUNDC1), modifying mitochondrial calcium homeostasis. B-cell receptor associated protein 31 (BAP31) binds to mitochondrial fission 1 protein (Fis1), regulating cellular apoptosis. Inverted formin-2 (INF2) interacts with dynamin-related protein 1 (Drp1), handling mitochondrial fission. ER-located mitofusin 2 (Mfn2) interacts with mitochondrial Mfn1/Mfn2, controlling mitochondrial fission and mitophagy. Besides, the ER–mitochondria encounter structure (ERMES) complex is composed of: the OMM proteins Mdm10 and Mdm34, the ER protein Mmm1, and the cytosolic protein Mdm12.

ER–mitochondria microdomain first establishes the potential contractile site for mitochondria fission via INF2, which in turn further narrows the distance between ER and mitochondria, leading to a progressive amplification of fission signals. Based on this, we question whether the distance between ER and mitochondria may serve as an early hallmark for the extent of mitochondrial fission and cardiac I/R injury. More work is needed to verify this hypothesis. Besides, another study notes a reduction in mitochondrial diameter at sites in which the ER is almost completely wrapped around the mitochondrial membrane (from ∼210 nm for uncircumscribed mitochondria to ∼140 nm for circumscribed mitochondria) (Friedman et al., 2011; Kang et al., 2017). In other words, the area of ER–mitochondria microdomain is positively correlated with the extent mitochondrial fission.

Besides, other components of ER–mitochondria microdomain are also reported to engage in mitochondrial division. Knockdown of mitochondrial calcium uniporter (MCU) interrupted mitochondrial fission, and Chakrabarti et al. (2018) noted a 2.5-fold decrease in the fission event in cells lacking MCU. Subsequent studies have identified the casual relationship between MCU activation and cardiac I/R injury. Using myocardial reperfusion model, inhibition of MCU via genetic ablation or pharmacological inhibition sustains myocardial contractile function (Kwong et al., 2015), alleviates necroptosis and apoptosis levels by 30 and 50%, respectively (Oropeza-Almazan et al., 2017). In addition, inhibition of MCU represses caspase-3/-7/-8/-9 activation (Oropeza-Almazan et al., 2017), interrupts calcium imbalance (Seidlmayer et al., 2015), maintains mitochondria oxygen consumption rates (Rasmussen et al., 2015), preserves mitochondrial potential (Rasmussen et al., 2015), reduces cellular ROS generation (Rasmussen et al., 2015), and blocks the opening of mitochondrial permeability transition pore (mPTP) (Luongo et al., 2015). These findings have highlighted that the activity of MCU in ER–mitochondria microdomain is highly responsible for mitochondrial anomalies and cardiomyocyte injury induced by I/R injury, and support the concept of MCU inhibition as a potential therapeutic strategy.

Besides, mitochondrial fission may also be regulated by mitofusins expressed within the ER–mitochondria microdomain. Structurally, Mfn1 and Mfn2 both localize predominantly on the OMM, whereas the latter also expresses on ER and ER–mitochondria microdomain (Koshiba et al., 2004). Genetic ablation of Mfn1 or Mfn2 results in embryonic lethality, suggesting essential developmental roles for both isoforms (Chen et al., 2003, 2007). Mechanistically, the expression of ER-located Mfn2 is crucial for tethering the ER to the mitochondria and thus stabilizing ER–mitochondria microdomain formation via tight interaction with mitochondrial Mfn1 and forming the Mfn1–Mfn2 heteromultimer (de Brito and Scorrano, 2008).

Recent studies have found that Mfn2 deletion attenuates cardiac cell death in response to I/R injury and the potential to undergo calcium-dependent mitochondrial permeability transition (Papanicolaou et al., 2011). This observation is further confirmed by a report that adult murine heart deficient in both Mfn1 and Mfn2 is protected against acute cardiac I/R injury (Hall et al., 2016), a finding which is associated with defects in mitochondrial fission and reduced mitochondrial calcium overload, suggesting that mitofusins, regulated by ER–mitochondria microdomain, is of importance to promote the progression of cardiac I/R injury. Taken together, owing to the direct contact of ER and mitochondria, the ER–mitochondria microdomain are easy to cope with mitochondrial fission via pleiotropic molecular mechanisms on the one hand, and that they have ideally "guard" roles to prevent cardiac I/R injury on the other hand. Accordingly, it seems likely that inhibition of the key site in ER–mitochondria microdomain may prove as an effective pharmacological intervention for reducing the severity of cardiac I/R damage via interrupting lethal mitochondrial fission.

MITOPHAGY

Mitophagy, a kind of mitochondrial autophagy, sweeps the damaged mitochondria and provides the nutrients necessary to preserve cell viability via timely removal of poor-structured mitochondria with the assistance of lysosome (Goiran et al., 2018; Lindqvist et al., 2018). Recent reports suggested that autophagosome membrane may be derived primarily from the ER (Molino et al., 2017; Song et al., 2018). This notion is also confirmed by an observation that pre-autophagosome/autophagosome marker ATG14 re-localizes to the ER–mitochondria contact site after starvation (Hamasaki et al., 2013). This means ATG14, an indispensable factor for mitophagy activation, is actually regulated by ER–mitochondria microdomain. Interestingly, in the cardiac myocardial infraction or coronary artery disease model, ATG14 is required for the angiogenesis via Becn1–Vps34–ATG14 complex (Lu et al., 2016), which is a novel agent for treatment of acute ischemia-mediated myocardial injury via handling revascularization. This observation is further verified by Liu et al. (2017) using cardiomyocyte hypoxia-reoxygenation (HR) model. These investigators found that ATG14 unfortunately decreases in response to HR stimulus as a result of elevated microRNA-130a, and reintroduction of ATG14 via inhibition of microRNA-130a attenuates HR-mediated cardiomyocyte apoptosis. Taken together, these pieces of evidence have pointed out that ATG14 cooperates with ER–mitochondria microdomain to ensure mitophagy activation which provides pro-survival signals for the damaged hearts.

Besides, other studies further revealed that the pro-autophagic proteins BECN1/Beclin1 are both found to re-localize at ER–mitochondria microdomain, where they enhance the ER–mitochondria interaction along with increased mitophagy activity (Gelmetti et al., 2017). Ample evidence has depicted a protective function of Beclin1 on cardiac I/R injury. In particular, Beclin1 expression is downregulated after reperfusion injury (Dai et al., 2017), although it is significantly upregulated by ischemia preconditioning (Xie et al., 2018). Restoration of Beclin1 attenuates HR-mediated cardiomyocyte death (Ma et al., 2012). At the molecular levels, Beclin1 activation is involved in stress protein degradation (Fuhrmann and Brune, 2017), ROS clearance (Sun et al., 2017), inflammation repression (Chi et al., 2018), and eNOS-dependent vasodilation restoration (Zhang J.X. et al., 2018). Overall, the above information comprehensively validated the permissive role for Beclin1 in cardiac I/R injury, which acts as an upstream mediator for mitophagy via cooperation with ER–mitochondria microdomain.

Notably, a recent study from Gautier et al. (2016) has provided some new insights into the interactive mechanism for mitophagy and ER–mitochondria microdomain. In patients with Parkinson's disease or Parkin-knockout mice, ER and mitochondria seem to be in closer proximity, followed by excessive calcium flux to the cytosol partly owing to the enhanced ER-to-mitochondria Ca^{2+} transfers. This finding has indicated that loss of mitophagy receptor fosters ER to move too close to the mitochondria, which unexpectedly contributes to the calcium leakage into cytoplasm and subsequent neurodegeneration. These data highlight that mitophagy is highly manipulated by ER–mitochondria microdomain on the one hand, and it also in turn corrects the excessive ER–mitochondria contact in a Parkin-dependent manner which could be considered as a negative feedback response to ensure the moderate ER–mitochondria communication. However, the negative feedback reaction has not been identified in cardiac I/R injury and thus more works are required to provide several evidences for this.

In spite of the extensive research which has been carried out over the past decades to figure out the molecular feature of mitophagy in cardiac I/R injury, the precise action of mitophagy in acute cardiomyocyte damage still remains elusive (Zhou et al., 2018b). Interestingly, the upstream regulatory mechanism for mitophagy is well-documented. There are three adaptors identified as the mitophagy inducer including Parkin, BCL2/adenovirus E1B 19 kDa protein-interacting protein 3 (Bnip3), and FUN14 domain containing 1 (FUNDC1). Interestingly, those adaptors could signal distinct mitophagic response for cardiomyocytes fate in I/R injury ranging from survival to death based on recent studies. Briefly, Binp3-mediated mitophagy is harmful for reperfused heart through turning on mitochondrial death (Jin et al., 2018). Similarly, the Parkin-dependent mitophagy also promoted mitophagy activity which unfortunately consumes most mitochondria, leading to the energy depletion and cell death (Zhou et al., 2017d). Interestingly, FUNDC1-related mitophagy is primarily activated by ischemic preconditioning and confers the protection against reperfusion injury (Zhou et al., 2017b,e, 2018f). Our finding is also supported by several in-depth studies in different disease models such as fatty liver disease and cancer (Chen et al., 2017; Li et al., 2018; Shi et al., 2018; Zhou et al., 2018a).

Recently, a delicate work from Wu et al. (2017) demonstrated that FUNDC1 could bind to IP3Rs to form the ER–mitochondria microdomain, which modulates ER–mitochondria Ca^{2+} exchange, mitochondrial fission, and mitophagy. Genetic ablation of FUNDC1 downregulates

the levels of IP3R, disrupts ER–mitochondria microdomain contact, and worsens cardiac function in cardiac I/R model. This work has identified, for the first time, the FUNDC1, a mitophagy-related protein, as an integral component of ER–mitochondria microdomain, redefining the paradigm between ER–mitochondria microdomain and mitophagy regulation. Notably, mitofusins, the indispensable elements for ER–mitochondria microdomain as our mentioned above, have recently been suggested in the recycling of mitochondria content during starvation-induced autophagy (Marchi et al., 2014; Tubbs and Rieusset, 2017). Disruption of ER–mitochondria microdomain by Mfn2 deletion inhibits mitophagy and thus increases the vulnerability of heart to I/R challenge (Zhao et al., 2012) due to extensive accumulation of autophagosomes. This observation is also subsequently supported by other studies that Mfn2 is required for protective mitophagy activation and cardioprotection in the setting of I/R injury (Campos et al., 2016). At the molecular levels, Mfn2 tethers the mitochondrial outer membrane to the ER, and this effect facilitates the transfer of phosphatidylserine from the ER to mitochondria, which in turn, is required for phosphatidylethanolamine production employed in autophagosome membrane formation (Hailey et al., 2010). Notably, these data indicate that ER–mitochondria microdomain-located Mfn2 has the ability to activate protective mitophagy which sends the pro-survival signals for reperfused heart. Accordingly, several researchers suggest that activation of Mfn2-dependent mitophagy would provide more benefits for cardiomyocyte under I/R stress (Zhang W. et al., 2018).

However, this conclusion seems to oppose to the observations that Mfn2 deletion attenuates cardiac cell death in response to I/R injury via modifying mitochondrial fission, as we summarized above. To explain the plausibly inconsistent results, several key points need to be emphasized. One is that the fatal fission activated by ER–mitochondria microdomain is heavily relying on the formation of Mfn1–Mfn2 heteromultimer; the former expressed on ER and the latter located on mitochondria. However, the protective mitophagy modified by ER–mitochondria microdomain is only dependent on Mfn2 rather than the Mfn1–Mfn2 heteromultimer. Considering that pro-apoptotic fission is excessively activated, whereas pro-survival mitophagy is mostly inhibited at the stage of I/R injury, we ask whether increased mitochondrial fission "over-consumes" Mfn2 via establishing links between Mfn1 and Mfn2 heteromultimer, leading to the failure of deficient Mfn2 to trigger mitophagy. Last but not the least, the functional role of Mfn2 in mitophagy activation is to help the phospholipid transfer from ER to mitochondria, promoting the formation of autophagosome membrane. However, due to the Mfn1–Mfn2 interaction, decreased Mfn2 monomer in ER–mitochondria microdomain is by no means capable of initiating mitophagy. Collectively, although ER–mitochondria microdomain-located Mfn2 could activate the protective mitophagy to enhance the heart resistance to I/R injury, it is unfortunately employed by mitochondrial fission, leading to the increased mitochondrial fission and decreased mitophagy. This information may lay the foundation to help us understand the paradoxical role of Mfn2 in cardiac I/R injury. Nonetheless, further work to illustrate the potential pleiotropic effects of Mfn2 on I/R injury via balancing fission and mitophagy are required to obtain more comprehensive picture of ER–mitochondria microdomain in cardiomyocyte fate under acute reperfusion stress.

CELLULAR CALCIUM BALANCE

The enzymes involved in the tricarboxylic acid (TCA) cycle and the mitochondrial respiratory complex are critically dependent on the moderate rise in mitochondrial Ca^{2+} levels to maintain cellular bioenergetics and meet the cell demand via ATP generation (Boone et al., 2017; Fuhrmann and Brune, 2017; Torres-Estay et al., 2017). Subsequently, with the assistance of mitochondria-produced ATP, ER rapidly releases Ca^{2+} into cytoplasm where Ca^{2+} interacts with troponin and ensures the cardiomyocyte beating and myocardial contraction (Eisner et al., 2017; Merjaneh et al., 2017; Mughal et al., 2018). Notably, excessive mitochondrial Ca^{2+} uptake leads to mitochondrial dysfunction and initiation of a cascade of pro-apoptotic events. The checkpoint for this phenomena lies on the ER–mitochondria microdomain (Dreser et al., 2017). The calcium handling proteins, RyRs (excitable cells) and IP3Rs (non-excitable cells) on the ER, as well as VDAC and MCU on the outer and inner mitochondrial membranes (Ligeza et al., 2017), respectively, have been shown to reside in close proximity at this interface of ER–mitochondria microdomain where they function to help the facile transfer of Ca^{2+} from the ER to mitochondria. Mechanistically, a high microdomain Ca^{2+} levels may be shaped after IP3Rs opening and the microdomain Ca^{2+} is largely buffered by mitochondria via MCU. Besides, a recent study also demonstrates that VDAC1 is structurally and physically linked to the type-1 IP3R through the molecular chaperone Grp75 (Szabadkai et al., 2006) and facilitates the Ca^{2+} communication between mitochondria and ER. Notably, those two Ca^{2+}-exchange mechanisms regulated by ER–mitochondria microdomain are also noted in cardiac I/R injury. First, it is generally believed that Ca^{2+} should flow easily through VDAC channels because VDAC shows only a weak selectivity for small monovalent ions (Colombini, 1980; Hodge and Colombini, 1997). Per recent findings, acute myocardial reperfusion injury promotes VDAC phosphorylation (Schwertz et al., 2007) and this process is mainly regulated by glycogen synthase kinase (GSK)-3 or Akt (Das et al., 2008). Inhibition of VDAC phosphorylation by GSK-3 inhibitors is beneficial for reperfused heats (Das et al., 2008). At the molecular levels, two mechanisms involved in this; one is that dephosphorylation of VDAC by GSK-3 inhibition alters channel conductance directly, and the other is that GSK-3 inhibitors increase Bcl-2 binding to VDAC affecting the OMM transport. Besides, cardiac IR injury also enhances the activity of VDAC via promoting protein tyrosine nitration in VDAC (Yang et al., 2012).

Other new Ca^{2+} regulators located in ER–mitochondria microdomain have been reported. For example, GSK-3β could specifically interact with IP3Rs in ER–mitochondria microdomain, and subsequently increases the transfer of Ca^{2+} from ER to mitochondria, as well as sensitivity of cardiomyocytes to IR-caused apoptosis (Gomez et al., 2016). Additionally,

mitochondrial chaperone cyclophilin D (CypD), a composition of mPTP, also cooperates with the VDAC1/Grp75/IP3R1 complex in cardiomyocyte (Paillard et al., 2013), enhancing ER Ca^{2+} efflux into mitochondria. The mitochondrial Ca^{2+} overload triggers excessive mPTP opening and thus initiates mitochondria-dependent cellular death in reperfusion-treated cardiomyocytes (Paillard et al., 2013). Conversely, a recent report suggested that mPTP opening modulates mitochondrial Ca^{2+} balance (Andrienko et al., 2016). This notion was initially confirmed by an earlier study that mPTP inhibitor, CsA, prevents mitochondrial Ca^{2+} efflux in adult rat ventricular cardiomyocytes (Andrienko et al., 2016), thereby postulating that mPTP may mediate mitochondrial calcium homeostasis. Altogether, the above information collectively suggest that moderate mitochondrial Ca^{2+} elevation governed by ER–mitochondria microdomain benefits cell energy metabolism and, however, uncontrolled mitochondrial Ca^{2+} accumulation, driven by ER–mitochondria microdomain in response to cardiac I/R injury, is detrimental to cardiomyocyte viability. Thus, preservation of mitochondrial Ca^{2+} balance via downregulating Ca^{2+}-handling molecules in ER–mitochondria microdomain is an essential step to prevent the propagation of dangerous reperfusion signals.

Apart from mitochondrial calcium imbalance, cellular calcium overload also has the deleterious consequences on reperfused heart, which is highly handled with ER–mitochondria contact. The sarco-ER Ca^{2+} transport ATPase (SERCA), an ATP-driven protein, inversely transports Ca^{2+} back to the SR. However, in previous studies (Zhang Y. et al., 2016; Cui et al., 2018), the activity and expression of SERCA are statistically decreased in answer to cardiac I/R injury. The decreased SERCA is closely associated with cytoplasm calcium overload which obligates cardiomyocyte to mitochondria-dependent programmed death and finally amplifies reperfusion injury to heart either via triggering SR–Ca^{2+}–XO–mitochondrial ROS axis (Zhu H. et al., 2018) or activating Ca^{2+}–ROS–Drp1–mitochondrial fission pathways (Cui et al., 2018). Following study from Raturi et al. (2016) identified thioredoxin-related transmembrane protein 1 (TMX1) as a novel SERCA-inhibiting protein at ER–mitochondrial microdomains; inhibition of TMX1 may reduce the susceptibility of heart to I/R injury. Interestingly, the TMX1–SERCA complex formation could be enhanced by mitochondria-produced ROS (Krols et al., 2016). That is to say, mitochondria ROS may tighten up TMX1–SERCA interaction within ER–mitochondrial microdomains, effectively inhibiting SERCA activity. In traditional concept, mitochondria are the downstream effectors of ER via uptake of Ca^{2+} in ER–mitochondrial microdomains. However, their findings have established a new interactive mechanism in ER–mitochondria; damaged mitochondria could send a positive feedback to ER via ROS–TMX1–SERCA axis, further disrupting ER–calcium homeostasis and aggravating Ca^{2+} overload-mediated cell damage. However, no study is available to verify the feedback response between ER and mitochondria in cardiac I/R injury, and accordingly, further investigation is required to confirm this in acute cardiac damage model.

OXIDATIVE STRESS

In response to reperfusion therapy, the restored blood rapidly re-introduces the fresh oxygen to the ischemic heart. Unfortunately, abundant oxygen would evoke a burst of reactive oxygen species (ROS) via multiple mechanisms reported by numerous studies (Zhou et al., 2015; Zhang Y. et al., 2016; Liu D. et al., 2017; Zong et al., 2017; Nuntaphum et al., 2018), leading to the cardiomyocyte oxidative stress. Cellular ROS is mainly produced by mitochondria when the electrons cannot be tightly coupled by the mitochondrial respiratory complex I and III (Hernansanz-Agustin et al., 2017; Miranda-Vizuete and Veal, 2017; Niaudet et al., 2017). However, other mechanisms have also been put forward to participate in this process, especially ER–mitochondrial microdomain. First, ER–mitochondrial microdomain could directly produce ROS via Ero1 (Gilady et al., 2010) and p66Shc (Lebiedzinska et al., 2009). Ero1, a key controller of oxidative folding and ER redox homeostasis, is enriched in ER–mitochondrial microdomain. Higher expression of Ero1 is closely associated with increased ROS production (Anelli et al., 2012). p66Shc (a 66-kDa isoform of the growth factor adapter Shc), a cytosolic adaptor protein related to ROS generation, could be detected in the ER–mitochondrial microdomain fraction (Patergnani et al., 2011). Careful examination from Lebiedzinska et al. (2009) revealed that the levels of p66Shc in the ER–mitochondrial microdomain is age-dependent and corresponds well to the mitochondrial ROS production. These data raise the possibility of a direct role for ER–mitochondrial microdomain in ROS outburst, which may be implicated in the cardiac I/R-mediated oxidative stress. Besides, in the repair stage of I/R injury or in the early phase of heart failure, the mitochondrial calcium overload mediated through the leaky RyRs increases the ROS production via NAD(P)H (Pacher et al., 2000). More importantly, the excessive superoxide in turn oxidizes the RyRs, thereby exacerbating mitochondrial calcium overload and ROS generation (Blackburn et al., 2017; Tomczyk et al., 2017). In consequence, this viscous cycle of Ca^{2+} leakage, mitochondrial calcium overload, and ROS outburst completely paralyzes cardiac contractility and obligates cardiomyocytes to apoptosis in the context of I/R injury (Gadicherla et al., 2017; Yang et al., 2017). Consistent with the above observations, following investigation further confirms that the ER-localized NADPH oxidase Yno1 is definitely required for cellular ROS accumulation in yeast (Leadsham et al., 2013). These pieces of information indicate that ER–mitochondrial microdomain-mediated ROS eruption is universal in many kinds of species.

More recently, in-depth study argue that ER–mitochondrial interface actually hosts a dynamic ROS nanodomain (Booth et al., 2016). At the molecular levels, ER–mitochondrial Ca^{2+} communication stimulates ROS mobilization from mitochondria to microdomain. It is the microdomain ROS transients rather than mitochondrial ROS overproduction sensitizes ER Ca^{2+} release to amplify Ca^{2+} oscillations (Booth et al., 2016). This piece of evidence fully updates our concept regarding microdomain ROS and verifies the existence of microdomain ROS for the first time. The difference between microdomain

ROS- and mitochondrial ROS-triggered calcium imbalance is that the former requires lower concentration of ROS to oxidize ER–calcium channel. That is to say, the microdomain ROS may spatially and temporally confines or amplifies the mitochondrial superoxide anion production, which should be considered as the ROS switch and source. However, the detailed functional role of microdomain ROS is incompletely understood and little is known its function in the development and progression of cardiac I/R injury. Starting from these observations, further work is needed to explore the influence and mechanisms of microdomain ROS in cardiac I/R injury.

APOPTOSIS AND NECROPTOSIS

The importance of cell death following IR injury is demonstrated in *in vivo* rodent model. Notably, prolonged periods of myocardial ischemia are related to an increase in the rate of apoptosis, whereas, paradoxically, reperfusion leads to an enhancement in necroptosis. There is more supportive evidence from our recent findings and other published data that most of cellular death could be blocked through inhibiting necrosis (or necroptosis), whereas only very marginal of reperfusion-induced cell death is attributable to apoptosis (Hochhauser et al., 2003; McCully et al., 2004; Yang et al., 2012; Zhang T. et al., 2016). Therefore, relieving cell death via preventing apoptosis and necrosis is vital to reduce I/R injury and improve the therapeutic efficiency of revascularization treatment. Many researchers have attempted to demonstrate the causal role of ER–mitochondrial microdomain in modifying I/R-mediated cell death. First, it is well documented that the sensitivity of cardiomyocyte to death (regardless of apoptosis and necroptosis) is fine-tuned by cellular calcium concentration (Mofid et al., 2017; Zhu et al., 2017; Pan et al., 2018) which drastically is affected by the ER–mitochondrial microdomain. Based on previous studies (Zhou et al., 2018d; Zhu H. et al., 2018), IP3R expression is upregulated in response to I/R stress, leading to the calcium overload in mitochondria. Subsequently, the calcium overload would activate necroptotic signaling in reperfused hearts via CaMKII–mPTP (Zhang T. et al., 2016) or XO–ROS–mPTP (Zhu P. et al., 2018) pathway. However, some other researchers argued that Ripk3-related cardiomyocyte necroptosis in I/R injury is not mediated through mPTP opening. They reported that suppression of autophagic flux contributes to cardiomyocyte death by activation of necroptotic pathways (Ogasawara et al., 2017). Actually, necroptosis is a kind of cell death program due to ATP depletion. Both mPTP opening and autophagic inhibition may interrupt the ATP supply, therefore exacerbating the reperfusion-mediated necroptosis. More recently, we provided partial evidence to confirm that ER-located IP3R is actually managed by Ripk3; genetic ablation of Ripk3 abrogates reperfusion-induced IP3R upregulation and ER stress (Zhu P. et al., 2018). These findings acknowledged the necessity of ER–mitochondrial microdomain in the excitation of Ripk3-induced necroptosis in cardiac I/R injury. However, we cannot exclude the protein interaction between Ripk3 and IP3R. If Ripk3 has the ability to directly integrate with IP3R, a new composition of ER–mitochondrial microdomain would be established, which means that the strategies to regulate the balance of Ripk3 and ER–mitochondrial microdomain could be a therapeutic target to cardiac I/R injury.

Besides, the downstream executive event of necroptosis is Ripk3-activated mPTP opening, which mediates the swelling and rupture of the organelle and cell due to the energy production disorder (Alghanem et al., 2017; Rossello et al., 2017; Rossello and Yellon, 2017). According to previous finding (Jahandiez et al., 2017; Zhou et al., 2017d), VDAC, one of the components of ER–mitochondrial microdomain, undergoes polymerization and resultantly promotes the hexokinase 2 liberation from mitochondria into cytoplasm. Hexokinase 2 is the endogenous inhibitor of mPTP opening and dissociation of hexokinase 2 from mitochondria has been shown to regulate, at least in part, cardiac I/R injury and mitochondrial integrity (Smeele et al., 2011; Pasdois et al., 2012; Nederlof et al., 2016).

Notably, other factors have also been reported to be involved in mitochondria-dependent cell death. Mitochondrial cardiolipin is a kind of phospholipid that predominantly embed in the inner mitochondrial membrane. The role of cardiolipin in the prevention of mitochondrial apoptosis and cardiac I/R injury is a well-established factor via repressing cyt-c liberation from mitochondria into cytoplasm (Brown et al., 2013; Shen et al., 2015; Ackermann et al., 2017). The cardiolipin downregulation and peroxidation would weaken the binding affinity of cyt-c to inner mitochondrial membrane and promote cyt-c leakage into cytoplasm (Zazueta et al., 2007; Zhang et al., 2010;

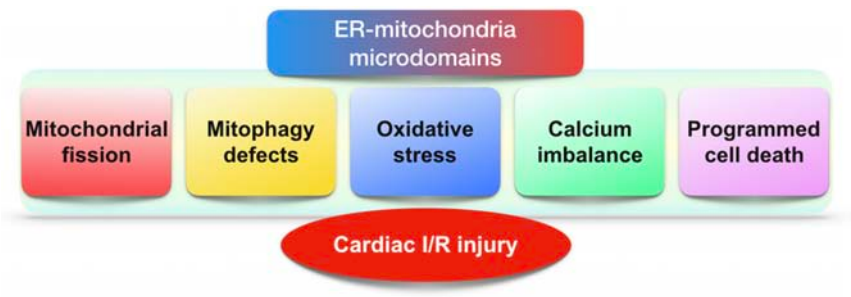

FIGURE 2 | The role of ER–mitochondria microdomains in cardiac I/R injury. In the setting of cardiac I/R injury, excessive mitochondrial fission, defective mitophagy, oxidative stress, calcium dyshomeostasis, and programmed cell death are modulated by ER–mitochondria microdomains.

Le Cras et al., 2017). Notably, although cardiolipin is synthesized by ER (Fleischer et al., 1967), the transfer of primarily phospholipids from the ER to mitochondria has been thought to be mediated via ER–mitochondrial microdomain (Gaigg et al., 1995). At the molecular levels, ER-mitochondrial encounter structure (ERMES) (Kornmann, 2013) is responsible for the cardiolipin exchange between mitochondria and ER. Structurally, ERMES is composed of mitochondrial distribution and morphology 10 (Mdm10), Mdm12, Mdm34, mitochondrial morphology 1 (Mmm1), and the regulatory subunit GTPase EF-hand protein of mitochondria (Gem1) (Klinkenberg et al., 2013). Functionally, ERMES possesses a synaptotagmin-like mitochondrial lipid-binding (SMP) domain that harbors an elongated hydrophobic groove in which different lipids can bind and possibly be transported (Kopec et al., 2010). Outside of cardiolipin transmission, ERMES also governs cardiolipin peroxidation via monitoring mitochondrial DNA (mtDNA) replication. Because the mitochondrial respiratory complex is encoded by mtDNA, the destruction of mtDNA inevitably suppresses the transcription and activity of mitochondrial respiratory complex. The decreased complex activity fails to capture free electron, finally evoking ROS outburst and subsequent cardiolipin peroxidation. In a word, the dysfunction of mtDNA copy is closely associated with cardiolipin oxidation. Interestingly, ER-resident protein Mmm1, one element of ERMES complex, structurally coimmunoprecipitates with Mgm101, a DNA-binding protein of the nucleoid, in chemically cross-linked mitochondrial extracts (Mbantenkhu et al., 2013; Pevala et al., 2016). This information proposes that a complex situated at the ER–mitochondrial microdomain has the ability to manage mitochondrial genome integrity and thus influence cardiolipin oxidation which facilitates the cyt-c liberation from mitochondria into cytoplasm under cardiac I/R injury. Interestingly, despite the established functional relationship between ER–mitochondrial microdomain and mtDNA over 10 years, little attempt is made to figure out whether microdomain-mediated mtDNA damage is one of the pathogenic factors for I/R injury.

CONCLUDING REMARKS

This review shows clearly that ER–mitochondria microdomain plays important roles in regulating cardiac I/R injury (**Figure 2**). The pathological interaction between ER and mitochondria promotes the malignant mitochondrial fission and inhibits the protective mitophagy. Thus, the ER regulates mitochondrial dynamics, and alterations in mitochondrial morphology uniquely reflect cell health. Interestingly, mitochondria are not only the downstream effector of microdomain; it also sends negative and/or positive feedback response to ER via microdomain. Accordingly, microdomain help ER and mitochondria shape the regulatory loop between them. Besides, ER and mitochondria also reciprocally transmit danger signals such as calcium overload and oxidative stress through microdomain which conveys organelle-extrinsic stress signals to promote cardiomyocyte death. Notably, little evidence is available for the precise role of ER–mitochondria microdomain in regulating I/R-initiated inflammation although NLRP3 infiammasome was found activated by ER–mitochondria microdomain (Zhou et al., 2011). Similarly, the relationship between ER–mitochondria microdomain and the cardioprotective signaling pathways including reperfusion injury salvage kinase (RISK) axis and survivor activating factor enhancement (SAFE) cascade has not adequately established, and therefore, more studies are required. Overall, in response to cardiac I/R injury, the ER–mitochondria microdomain represents a platform to modify the extracellular signal determining the degree of cellular insult. Based on this, therapies to influence the homeostasis of ER–mitochondria microdomain would be a therapeutic target to cardiac reperfusion stress in the clinical practice.

AUTHOR CONTRIBUTIONS

HZ, SW, SH, YC, and JR contributed to conception, drafted the manuscript, critically revised the manuscript, gave final approval, and agree to be accountable for all aspects of work ensuring integrity and accuracy.

FUNDING

This study was supported by grants from the National Natural Science Foundation of China (No. 81770237). The funders had no role in the study design, decision to publish, or preparation of the manuscript.

REFERENCES

Ackermann, M., Kim, Y. O., Wagner, W. L., Schuppan, D., Valenzuela, C. D., Mentzer, S. J., et al. (2017). Effects of nintedanib on the microvascular architecture in a lung fibrosis model. *Angiogenesis* 20, 359–372. doi: 10.1007/s10456-017-9543-z

Alghanem, A. F., Wilkinson, E. L., Emmett, M. S., Aljasir, M. A., Holmes, K., Rothermel, B. A., et al. (2017). RCAN1.4 regulates VEGFR-2 internalisation, cell polarity and migration in human microvascular endothelial cells. *Angiogenesis* 20, 341–358. doi: 10.1007/s10456-017-9542-0

Andrienko, T., Pasdois, P., Rossbach, A., and Halestrap, A. P. (2016). Real-time fluorescence measurements of ROS and [Ca^{2+}] in ischemic / reperfused rat hearts: detectable increases occur only after mitochondrial pore opening and are attenuated by ischemic preconditioning. *PLoS One* 11:e0167300. doi: 10.1371/journal.pone.0167300

Anelli, T., Bergamelli, L., Margittai, E., Rimessi, A., Fagioli, C., Malgaroli, A., et al. (2012). Ero1alpha regulates Ca^{2+} fluxes at the endoplasmic reticulum-mitochondria interface (MAM). *Antioxid. Redox Signal.* 16, 1077–1087. doi: 10.1089/ars.2011.4004

Blackburn, N. J. R., Vulesevic, B., McNeill, B., Cimenci, C. E., Ahmadi, A., Gonzalez-Gomez, M., et al. (2017). Methylglyoxal-derived advanced glycation end products contribute to negative cardiac remodeling and dysfunction post-myocardial infarction. *Basic Res. Cardiol.* 112:57. doi: 10.1007/s00395-017-0646-x

Boone, C. H. T., Grove, R. A., Adamcova, D., Seravalli, J., and Adamec, J. (2017). Oxidative stress, metabolomics profiling, and mechanism of local anesthetic

induced cell death in yeast. *Redox Biol.* 12, 139–149. doi: 10.1016/j.redox.2017.01.025

Booth, D. M., Enyedi, B., Geiszt, M., Varnai, P., and Hajnoczky, G. (2016). Redox nanodomains are induced by and control calcium signaling at the ER-mitochondrial interface. *Mol. Cell* 63, 240–248. doi: 10.1016/j.molcel.2016.05.040

Brown, D. A., Sabbah, H. N., and Shaikh, S. R. (2013). Mitochondrial inner membrane lipids and proteins as targets for decreasing cardiac ischemia/reperfusion injury. *Pharmacol. Ther.* 140, 258–266. doi: 10.1016/j.pharmthera.2013.07.005

Campos, J. C., Bozi, L. H., Bechara, L. R., Lima, V. M., and Ferreira, J. C. (2016). Mitochondrial quality control in cardiac diseases. *Front. Physiol.* 7:479. doi: 10.3389/fphys.2016.00479

Chakrabarti, R., Ji, W. K., Stan, R. V., de Juan Sanz, J., Ryan, T. A., and Higgs, H. N. (2018). INF2-mediated actin polymerization at the ER stimulates mitochondrial calcium uptake, inner membrane constriction, and division. *J. Cell Biol.* 217, 251–268. doi: 10.1083/jcb.201709111

Chen, H., Detmer, S. A., Ewald, A. J., Griffin, E. E., Fraser, S. E., and Chan, D. C. (2003). Mitofusins Mfn1 and Mfn2 coordinately regulate mitochondrial fusion and are essential for embryonic development. *J. Cell Biol.* 160, 189–200. doi: 10.1083/jcb.200211046

Chen, H., McCaffery, J. M., and Chan, D. C. (2007). Mitochondrial fusion protects against neurodegeneration in the cerebellum. *Cell* 130, 548–562. doi: 10.1016/j.cell.2007.06.026

Chen, Y., Csordas, G., Jowdy, C., Schneider, T. G., Csordas, N., Wang, W., et al. (2012). Mitofusin 2-containing mitochondrial-reticular microdomains direct rapid cardiomyocyte bioenergetic responses via interorganelle Ca^{2+} crosstalk. *Circ. Res.* 111, 863–875. doi: 10.1161/CIRCRESAHA.112.266585

Chen, Z., Siraj, S., Liu, L., and Chen, Q. (2017). MARCH5-FUNDC1 axis fine-tunes hypoxia-induced mitophagy. *Autophagy* 13, 1244–1245. doi: 10.1080/15548627.2017.1310789

Chi, J., Wang, L., Zhang, X., Fu, Y., Liu, Y., Chen, W., et al. (2018). Cyclosporin A induces autophagy in cardiac fibroblasts through the NRP-2/WDFY-1 axis. *Biochimie* 148, 55–62. doi: 10.1016/j.biochi.2018.02.017

Colombini, M. (1980). Structure and mode of action of a voltage dependent anion-selective channel (VDAC) located in the outer mitochondrial membrane. *Ann. N. Y. Acad. Sci.* 341, 552–563. doi: 10.1111/j.1749-6632.1980.tb47198.x

Coronado, M., Fajardo, G., Nguyen, K., Zhao, M., Kooiker, K., Jung, G., et al. (2018). Physiological mitochondrial fragmentation is a normal cardiac adaptation to increased energy demand. *Circ. Res.* 122, 282–295. doi: 10.1161/CIRCRESAHA.117.310725

Cowan, D. B., Yao, R., Thedsanamoorthy, J. K., Zurakowski, D., Del Nido, P. J., and McCully, J. D. (2017). Transit and integration of extracellular mitochondria in human heart cells. *Sci. Rep.* 7:17450. doi: 10.1038/s41598-017-17813-0

Csordas, G., Renken, C., Varnai, P., Walter, L., Weaver, D., Buttle, K. F., et al. (2006). Structural and functional features and significance of the physical linkage between ER and mitochondria. *J. Cell Biol.* 174, 915–921. doi: 10.1083/jcb.200604016

Cui, J., Li, Z., Zhuang, S., Qi, S., Li, L., Zhou, J., et al. (2018). Melatonin alleviates inflammation-induced apoptosis in human umbilical vein endothelial cells via suppression of Ca^{2+}-XO-ROS-Drp1-mitochondrial fission axis by activation of AMPK/SERCA2a pathway. *Cell Stress Chaperones* 23, 281–293. doi: 10.1007/s12192-017-0841-6

Dai, S., Xu, Q., Liu, S., Yu, B., Liu, J., and Tang, J. (2017). Role of autophagy and its signaling pathways in ischemia/reperfusion injury. *Am. J. Transl. Res.* 9, 4470–4480.

Das, S., Wong, R., Rajapakse, N., Murphy, E., and Steenbergen, C. (2008). Glycogen synthase kinase 3 inhibition slows mitochondrial adenine nucleotide transport and regulates voltage-dependent anion channel phosphorylation. *Circ. Res.* 103, 983–991. doi: 10.1161/CIRCRESAHA.108.178970

de Brito, O. M., and Scorrano, L. (2008). Mitofusin 2 tethers endoplasmic reticulum to mitochondria. *Nature* 456, 605–610. doi: 10.1038/nature07534

Dreser, A., Vollrath, J. T., Sechi, A., Johann, S., Roos, A., Yamoah, A., et al. (2017). The ALS-linked E102Q mutation in Sigma receptor-1 leads to ER stress-mediated defects in protein homeostasis and dysregulation of RNA-binding proteins. *Cell Death Differ.* 24, 1655–1671. doi: 10.1038/cdd.2017.88

Du, G. Q., Shao, Z. B., Wu, J., Yin, W. J., Li, S. H., Wu, J., et al. (2017). Targeted myocardial delivery of GDF11 gene rejuvenates the aged mouse heart and enhances myocardial regeneration after ischemia-reperfusion injury. *Basic Res. Cardiol.* 112:7. doi: 10.1007/s00395-016-0593-y

Eisner, D. A., Caldwell, J. L., Kistamas, K., and Trafford, A. W. (2017). Calcium and excitation-contraction coupling in the heart. *Circ. Res.* 121, 181–195. doi: 10.1161/CIRCRESAHA.117.310230

Fernandez-Sanz, C., Ruiz-Meana, M., Miro-Casas, E., Nunez, E., Castellano, J., Loureiro, M., et al. (2014). Defective sarcoplasmic reticulum-mitochondria calcium exchange in aged mouse myocardium. *Cell Death Dis.* 5:e1573. doi: 10.1038/cddis.2014.526

Fleischer, S., Rouser, G., Fleischer, B., Casu, A., and Kritchevsky, G. (1967). Lipid composition of mitochondria from bovine heart, liver, and kidney. *J. Lipid Res.* 8, 170–180.

Fransson, A., Ruusala, A., and Aspenstrom, P. (2003). Atypical Rho GTPases have roles in mitochondrial homeostasis and apoptosis. *J. Biol. Chem.* 278, 6495–6502. doi: 10.1074/jbc.M208609200

Friedman, J. R., Lackner, L. L., West, M., DiBenedetto, J. R., Nunnari, J., and Voeltz, G. K. (2011). ER tubules mark sites of mitochondrial division. *Science* 334, 358–362. doi: 10.1126/science.1207385

Fuhrmann, D. C., and Brune, B. (2017). Mitochondrial composition and function under the control of hypoxia. *Redox Biol.* 12, 208–215. doi: 10.1016/j.redox.2017.02.012

Gadicherla, A. K., Wang, N., Bulic, M., Agullo-Pascual, E., Lissoni, A., De Smet, M., et al. (2017). Mitochondrial Cx43 hemichannels contribute to mitochondrial calcium entry and cell death in the heart. *Basic Res. Cardiol.* 112:27. doi: 10.1007/s00395-017-0618-1

Gaigg, B., Simbeni, R., Hrastnik, C., Paltauf, F., and Daum, G. (1995). Characterization of a microsomal subfraction associated with mitochondria of the yeast, *Saccharomyces cerevisiae*. Involvement in synthesis and import of phospholipids into mitochondria. *Biochim. Biophys. Acta* 1234, 214–220. doi: 10.1016/0005-2736(94)00287-Y

Gao, D., Yang, J., Wu, Y., Wang, Q., Wang, Q., Lai, E. Y., et al. (2016). Targeting dynamin 2 as a novel pathway to inhibit cardiomyocyte apoptosis following oxidative stress. *Cell. Physiol. Biochem.* 39, 2121–2134. doi: 10.1159/000447908

Garcia-Nino, W. R., Correa, F., Rodriguez-Barrena, J. I., Leon-Contreras, J. C., Buelna-Chontal, M., Soria-Castro, E., et al. (2017). Cardioprotective kinase signaling to subsarcolemmal and interfibrillar mitochondria is mediated by caveolar structures. *Basic Res. Cardiol.* 112:15. doi: 10.1007/s00395-017-0607-4

Gautier, C. A., Erpapazoglou, Z., Mouton-Liger, F., Muriel, M. P., Cormier, F., Bigou, S., et al. (2016). The endoplasmic reticulum-mitochondria interface is perturbed in PARK2 knockout mice and patients with PARK2 mutations. *Hum. Mol. Genet.* 25, 2972–2984. doi: 10.1093/hmg/ddw148

Gelmetti, V., De Rosa, P., Torosantucci, L., Marini, E. S., Romagnoli, A., Di Rienzo, M., et al. (2017). PINK1 and BECN1 relocalize at mitochondria-associated membranes during mitophagy and promote ER-mitochondria tethering and autophagosome formation. *Autophagy* 13, 654–669. doi: 10.1080/15548627.2016.1277309

Gilady, S. Y., Bui, M., Lynes, E. M., Benson, M. D., Watts, R., Vance, J. E., et al. (2010). Ero1alpha requires oxidizing and normoxic conditions to localize to the mitochondria-associated membrane (MAM). *Cell Stress Chaperones* 15, 619–629. doi: 10.1007/s12192-010-0174-1

Goiran, T., Duplan, E., Rouland, L., El Manaa, W., Lauritzen, I., Dunys, J., et al. (2018). Nuclear p53-mediated repression of autophagy involves PINK1 transcriptional down-regulation. *Cell Death Differ.* 25, 873–884. doi: 10.1038/s41418-017-0016-0

Gomez, L., Thiebaut, P. A., Paillard, M., Ducreux, S., Abrial, M., Crola Da Silva, C., et al. (2016). The SR/ER-mitochondria calcium crosstalk is regulated by GSK3beta during reperfusion injury. *Cell Death Differ.* 23, 313–322. doi: 10.1038/cdd.2015.101

Gurel, P. S., Mu, A., Guo, B., Shu, R., Mierke, D. F., and Higgs, H. N. (2015). Assembly and turnover of short actin filaments by the formin INF2 and profilin. *J. Biol. Chem.* 290, 22494–22506. doi: 10.1074/jbc.M115.670166

Hailey, D. W., Rambold, A. S., Satpute-Krishnan, P., Mitra, K., Sougrat, R., Kim, P. K., et al. (2010). Mitochondria supply membranes for autophagosome biogenesis during starvation. *Cell* 141, 656–667. doi: 10.1016/j.cell.2010.04.009

Hall, A. R., Burke, N., Dongworth, R. K., Kalkhoran, S. B., Dyson, A., Vicencio, J. M., et al. (2016). Hearts deficient in both Mfn1 and Mfn2 are protected against acute myocardial infarction. *Cell Death Dis.* 7:e2238. doi: 10.1038/cddis.2016.139

Hamasaki, M., Furuta, N., Matsuda, A., Nezu, A., Yamamoto, A., Fujita, N., et al. (2013). Autophagosomes form at ER-mitochondria contact sites. *Nature* 495, 389–393. doi: 10.1038/nature11910

Harisseh, R., Pillot, B., Gharib, A., Augeul, L., Gallo-Bona, N., Ferrera, R., et al. (2017). Unacylated ghrelin analog prevents myocardial reperfusion injury independently of permeability transition pore. *Basic Res. Cardiol.* 112:4. doi: 10.1007/s00395-016-0595-9

Hernansanz-Agustin, P., Ramos, E., Navarro, E., Parada, E., Sanchez-Lopez, N., Pelaez-Aguado, L., et al. (2017). Mitochondrial complex I deactivation is related to superoxide production in acute hypoxia. *Redox Biol.* 12, 1040–1051. doi: 10.1016/j.redox.2017.04.025

Hochhauser, E., Kivity, S., Offen, D., Maulik, N., Otani, H., Barhum, Y., et al. (2003). Bax ablation protects against myocardial ischemia-reperfusion injury in transgenic mice. *Am. J. Physiol. Heart Circ. Physiol.* 284, H2351–H2359. doi: 10.1152/ajpheart.00783.2002

Hodge, T., and Colombini, M. (1997). Regulation of metabolite flux through voltage-gating of VDAC channels. *J. Membr. Biol.* 157, 271–279. doi: 10.1007/s002329900235

Hong, H., Tao, T., Chen, S., Liang, C., Qiu, Y., Zhou, Y., et al. (2017). MicroRNA-143 promotes cardiac ischemia-mediated mitochondrial impairment by the inhibition of protein kinase Cepsilon. *Basic Res. Cardiol.* 112:60. doi: 10.1007/s00395-017-0649-7

Honrath, B., Culmsee, C., and Dolga, A. M. (2018). One protein, different cell fate: the differential outcome of depleting GRP75 during oxidative stress in neurons. *Cell Death Dis.* 9:32. doi: 10.1038/s41419-017-0148-7

Iwasawa, R., Mahul-Mellier, A. L., Datler, C., Pazarentzos, E., and Grimm, S. (2011). Fis1 and Bap31 bridge the mitochondria-ER interface to establish a platform for apoptosis induction. *EMBO J.* 30, 556–568. doi: 10.1038/emboj.2010.346

Jahandiez, V., Cour, M., Bochaton, T., Abrial, M., Loufouat, J., Gharib, A., et al. (2017). Fast therapeutic hypothermia prevents post-cardiac arrest syndrome through cyclophilin D-mediated mitochondrial permeability transition inhibition. *Basic Res. Cardiol.* 112:35. doi: 10.1007/s00395-017-0624-3

Jin, Q., Li, R., Hu, N., Xin, T., Zhu, P., Hu, S., et al. (2018). DUSP1 alleviates cardiac ischemia/reperfusion injury by suppressing the Mff-required mitochondrial fission and Bnip3-related mitophagy via the JNK pathways. *Redox Biol.* 14, 576–587. doi: 10.1016/j.redox.2017.11.004

Kang, P. T., Chen, C. L., Lin, P., Chilian, W. M., and Chen, Y. R. (2017). Impairment of pH gradient and membrane potential mediates redox dysfunction in the mitochondria of the post-ischemic heart. *Basic Res. Cardiol.* 112:36. doi: 10.1007/s00395-017-0626-1

Klinkenberg, J., Sardina, G., de Lange, H. C., and Brandt, L. (2013). Numerical study of laminar-turbulent transition in particle-laden channel flow. *Phys. Rev. E Stat. Nonlin. Soft Matter Phys.* 87:043011. doi: 10.1103/PhysRevE.87.043011

Kopec, K. O., Alva, V., and Lupas, A. N. (2010). Homology of SMP domains to the TULIP superfamily of lipid-binding proteins provides a structural basis for lipid exchange between ER and mitochondria. *Bioinformatics* 26, 1927–1931. doi: 10.1093/bioinformatics/btq326

Kornmann, B. (2013). The molecular hug between the ER and the mitochondria. *Curr. Opin. Cell Biol.* 25, 443–448. doi: 10.1016/j.ceb.2013.02.010

Korobova, F., Ramabhadran, V., and Higgs, H. N. (2013). An actin-dependent step in mitochondrial fission mediated by the ER-associated formin INF2. *Science* 339, 464–467. doi: 10.1126/science.1228360

Koshiba, T., Detmer, S. A., Kaiser, J. T., Chen, H., McCaffery, J. M., and Chan, D. C. (2004). Structural basis of mitochondrial tethering by mitofusin complexes. *Science* 305, 858–862. doi: 10.1126/science.1099793

Krols, M., Bultynck, G., and Janssens, S. (2016). ER-Mitochondria contact sites: a new regulator of cellular calcium flux comes into play. *J. Cell Biol.* 214, 367–370. doi: 10.1083/jcb.201607124

Kwong, J. Q., Lu, X., Correll, R. N., Schwanekamp, J. A., Vagnozzi, R. J., Sargent, M. A., et al. (2015). The mitochondrial calcium uniporter selectively matches metabolic output to acute contractile stress in the heart. *Cell Rep.* 12, 15–22. doi: 10.1016/j.celrep.2015.06.002

Le Cras, T. D., Mobberley-Schuman, P. S., Broering, M., Fei, L., Trenor, C. C. III, and Adams, D. M. (2017). Angiopoietins as serum biomarkers for lymphatic anomalies. *Angiogenesis* 20, 163–173. doi: 10.1007/s10456-016-9537-2

Leadsham, J. E., Sanders, G., Giannaki, S., Bastow, E. L., Hutton, R., Naeimi, W. R., et al. (2013). Loss of cytochrome c oxidase promotes RAS-dependent ROS production from the ER resident NADPH oxidase. Yno1p, in yeast. *Cell Metab.* 18, 279–286. doi: 10.1016/j.cmet.2013.07.005

Lebiedzinska, M., Duszynski, J., Rizzuto, R., Pinton, P., and Wieckowski, M. R. (2009). Age-related changes in levels of p66Shc and serine 36-phosphorylated p66Shc in organs and mouse tissues. *Arch. Biochem. Biophys.* 486, 73–80. doi: 10.1016/j.abb.2009.03.007

Li, Y., Liu, Z., Zhang, Y., Zhao, Q., Wang, X., Lu, P., et al. (2018). PEDF protects cardiomyocytes by promoting FUNDC1-mediated mitophagy via PEDF-R under hypoxic condition. *Int. J. Mol. Med.* 41, 3394–3404. doi: 10.3892/ijmm.2018.3536

Ligeza, J., Marona, P., Gach, N., Lipert, B., Miekus, K., Wilk, W., et al. (2017). MCPIP1 contributes to clear cell renal cell carcinomas development. *Angiogenesis* 20, 325–340. doi: 10.1007/s10456-017-9540-2

Lindqvist, L. M., Frank, D., McArthur, K., Dite, T. A., Lazarou, M., Oakhill, J. S., et al. (2018). Autophagy induced during apoptosis degrades mitochondria and inhibits type I interferon secretion. *Cell Death Differ.* 25, 782–794. doi: 10.1038/s41418-017-0017-z

Liu, D., Zeng, X., Li, X., Mehta, J. L., and Wang, X. (2017). Role of NLRP3 inflammasome in the pathogenesis of cardiovascular diseases. *Basic Res. Cardiol.* 113:5. doi: 10.1007/s00395-017-0663-9

Liu, H., Huan, L., Yin, J., Qin, M., Zhang, Z., Zhang, Z., et al. (2017). Role of microRNA-130a in myocardial hypoxia/reoxygenation injury. *Exp. Ther. Med.* 13, 759–765. doi: 10.3892/etm.2016.3984

Lopez-Crisosto, C., Pennanen, C., Vasquez-Trincado, C., Morales, P. E., Bravo-Sagua, R., Quest, A. F. G., et al. (2017). Sarcoplasmic reticulum-mitochondria communication in cardiovascular pathophysiology. *Nat. Rev. Cardiol.* 14, 342–360. doi: 10.1038/nrcardio.2017.23

Lu, Q., Yao, Y., Hu, Z., Hu, C., Song, Q., Ye, J., et al. (2016). Angiogenic factor AGGF1 activates autophagy with an essential role in therapeutic angiogenesis for heart disease. *PLoS Biol.* 14:e1002529. doi: 10.1371/journal.pbio.1002529

Luongo, T. S., Lambert, J. P., Yuan, A., Zhang, X., Gross, P., Song, J., et al. (2015). The mitochondrial calcium uniporter matches energetic supply with cardiac workload during stress and modulates permeability transition. *Cell Rep.* 12, 23–34. doi: 10.1016/j.celrep.2015.06.017

Ma, X., Liu, H., Foyil, S. R., Godar, R. J., Weinheimer, C. J., Hill, J. A., et al. (2012). Impaired autophagosome clearance contributes to cardiomyocyte death in ischemia/reperfusion injury. *Circulation* 125, 3170–3181. doi: 10.1161/CIRCULATIONAHA.111.041814

Maneechote, C., Palee, S., Chattipakorn, S. C., and Chattipakorn, N. (2017). Roles of mitochondrial dynamics modulators in cardiac ischaemia/reperfusion injury. *J. Cell Mol. Med.* 21, 2643–2653. doi: 10.1111/jcmm.13330

Mannella, C. A., Buttle, K., Rath, B. K., and Marko, M. (1998). Electron microscopic tomography of rat-liver mitochondria and their interaction with the endoplasmic reticulum. *Biofactors* 8, 225–228. doi: 10.1002/biof.5520080309

Mannella, C. A., Marko, M., Penczek, P., Barnard, D., and Frank, J. (1994). The internal compartmentation of rat-liver mitochondria: tomographic study using the high-voltage transmission electron microscope. *Microsc. Res. Tech.* 27, 278–283. doi: 10.1002/jemt.1070270403

Marchi, S., Patergnani, S., and Pinton, P. (2014). The endoplasmic reticulum-mitochondria connection: one touch, multiple functions. *Biochim. Biophys. Acta* 1837, 461–469. doi: 10.1016/j.bbabio.2013.10.015

Mbantenkhu, M., Wierzbicki, S., Wang, X., Guo, S., Wilkens, S., and Chen, X. J. (2013). A short carboxyl-terminal tail is required for single-stranded DNA binding, higher-order structural organization, and stability of the mitochondrial single-stranded annealing protein Mgm101. *Mol. Biol. Cell* 24, 1507–1518. doi: 10.1091/mbc.E13-01-0006

McCully, J. D., Wakiyama, H., Hsieh, Y. J., Jones, M., and Levitsky, S. (2004). Differential contribution of necrosis and apoptosis in myocardial ischemia-reperfusion injury. *Am. J. Physiol. Heart Circ. Physiol.* 286, H1923–H1935. doi: 10.1152/ajpheart.00935.2003

Meier, P. J., Spycher, M. A., and Meyer, U. A. (1981). Isolation and characterization of rough endoplasmic reticulum associated with mitochondria from normal rat liver. *Biochim. Biophys. Acta* 646, 283–297. doi: 10.1016/0005-2736(81)90335-7

Merjaneh, M., Langlois, A., Larochelle, S., Cloutier, C. B., Ricard-Blum, S., and Moulin, V. J. (2017). Pro-angiogenic capacities of microvesicles produced by skin wound myofibroblasts. *Angiogenesis* 20, 385–398. doi: 10.1007/s10456-017-9554-9

Miranda-Vizuete, A., and Veal, E. A. (2017). *Caenorhabditis elegans* as a model for understanding ROS function in physiology and disease. *Redox Biol.* 11, 708–714. doi: 10.1016/j.redox.2016.12.020

Mofid, A., Newman, N. S., Lee, P. J., Abbasi, C., Matkar, P. N., Rudenko, D., et al. (2017). Cardiac overexpression of S100A6 attenuates cardiomyocyte apoptosis and reduces infarct size after myocardial ischemia-reperfusion. *J. Am. Heart Assoc.* 6:e004738. doi: 10.1161/JAHA.116.004738

Molino, D., Nascimbeni, A. C., Giordano, F., Codogno, P., and Morel, E. (2017). ER-driven membrane contact sites: evolutionary conserved machineries for stress response and autophagy regulation? *Commun. Integr. Biol.* 10:e1401699. doi: 10.1080/19420889.2017.1401699

Mughal, W., Martens, M., Field, J., Chapman, D., Huang, J., Rattan, S., et al. (2018). Myocardin regulates mitochondrial calcium homeostasis and prevents permeability transition. *Cell Death Differ.* doi: 10.1038/s41418-018-0073-z [Epub ahead of print].

Nan, J., Zhu, W., Rahman, M. S., Liu, M., Li, D., Su, S., et al. (2017). Molecular regulation of mitochondrial dynamics in cardiac disease. *Biochim. Biophys. Acta* 1864, 1260–1273. doi: 10.1016/j.bbamcr.2017.03.006

Nederlof, R., Gurel-Gurevin, E., Eerbeek, O., Xie, C., Deijs, G. S., Konkel, M., et al. (2016). Reducing mitochondrial bound hexokinase II mediates transition from non-injurious into injurious ischemia/reperfusion of the intact heart. *J. Physiol. Biochem.* 73, 323–333. doi: 10.1007/s13105-017-0555-3

Niaudet, C., Bonnaud, S., Guillonneau, M., Gouard, S., Gaugler, M. H., Dutoit, S., et al. (2017). Plasma membrane reorganization links acid sphingomyelinase/ceramide to p38 MAPK pathways in endothelial cells apoptosis. *Cell. Signal.* 33, 10–21. doi: 10.1016/j.cellsig.2017.02.001

Nunez-Gomez, E., Pericacho, M., Ollauri-Ibanez, C., Bernabeu, C., and Lopez-Novoa, J. M. (2017). The role of endoglin in post-ischemic revascularization. *Angiogenesis* 20, 1–24. doi: 10.1007/s10456-016-9535-4

Nuntaphum, W., Pongkan, W., Wongjaikam, S., Thummasorn, S., Tanajak, P., Khamseekaew, J., et al. (2018). Vagus nerve stimulation exerts cardioprotection against myocardial ischemia/reperfusion injury predominantly through its efferent vagal fibers. *Basic Res. Cardiol.* 113:22. doi: 10.1007/s00395-018-0683-0

Ogasawara, M., Yano, T., Tanno, M., Abe, K., Ishikawa, S., Miki, T., et al. (2017). Suppression of autophagic flux contributes to cardiomyocyte death by activation of necroptotic pathways. *J. Mol. Cell Cardiol.* 108, 203–213. doi: 10.1016/j.yjmcc.2017.06.008

Ong, S. B., Subrayan, S., Lim, S. Y., Yellon, D. M., Davidson, S. M., and Hausenloy, D. J. (2010). Inhibiting mitochondrial fission protects the heart against ischemia/reperfusion injury. *Circulation* 121, 2012–2022. doi: 10.1161/CIRCULATIONAHA.109.906610

Oropeza-Almazan, Y., Vazquez-Garza, E., Chapoy-Villanueva, H., Torre-Amione, G., and Garcia-Rivas, G. (2017). Small interfering RNA targeting mitochondrial calcium uniporter improves cardiomyocyte cell viability in hypoxia/reoxygenation injury by reducing calcium overload. *Oxid. Med. Cell. Longev.* 2017:5750897. doi: 10.1155/2017/5750897

Pacher, P., Csordas, P., Schneider, T., and Hajnoczky, G. (2000). Quantification of calcium signal transmission from sarco-endoplasmic reticulum to the mitochondria. *J. Physiol.* 529(Pt 3), 553–564. doi: 10.1111/j.1469-7793.2000.00553.x

Paillard, M., Tubbs, E., Thiebaut, P. A., Gomez, L., Fauconnier, J., Da Silva, C. C., et al. (2013). Depressing mitochondria-reticulum interactions protects cardiomyocytes from lethal hypoxia-reoxygenation injury. *Circulation* 128, 1555–1565. doi: 10.1161/CIRCULATIONAHA.113.001225

Pan, W., Yang, Z., Cheng, J., Qian, C., and Wang, Y. (2018). Contractile heterogeneity in ventricular myocardium. *J. Cell. Physiol.* 233, 6273–6279. doi: 10.1002/jcp.26512

Papanicolaou, K. N., Khairallah, R. J., Ngoh, G. A., Chikando, A., Luptak, I., O'Shea, K. M., et al. (2011). Mitofusin-2 maintains mitochondrial structure and contributes to stress-induced permeability transition in cardiac myocytes. *Mol. Cell. Biol.* 31, 1309–1328. doi: 10.1128/MCB.00911-10

Pasdois, P., Parker, J. E., and Halestrap, A. P. (2012). Extent of mitochondrial hexokinase II dissociation during ischemia correlates with mitochondrial cytochrome c release, reactive oxygen species production, and infarct size on reperfusion. *J. Am. Heart Assoc.* 2:e005645. doi: 10.1161/JAHA.112.005645

Patergnani, S., Suski, J. M., Agnoletto, C., Bononi, A., Bonora, M., De Marchi, E., et al. (2011). Calcium signaling around mitochondria associated membranes (MAMs). *Cell Commun. Signal.* 9:19. doi: 10.1186/1478-811X-9-19

Pevala, V., Truban, D., Bauer, J. A., Kostan, J., Kunova, N., Bellova, J., et al. (2016). The structure and DNA-binding properties of Mgm101 from a yeast with a linear mitochondrial genome. *Nucleic Acids Res.* 44, 2227–2239. doi: 10.1093/nar/gkv1529

Pihan, P., Carreras-Sureda, A., and Hetz, C. (2017). BCL-2 family: integrating stress responses at the ER to control cell demise. *Cell Death Differ.* 24, 1478–1487. doi: 10.1038/cdd.2017.82

Rasmussen, T. P., Wu, Y., Joiner, M. L., Koval, O. M., Wilson, N. R., Luczak, E. D., et al. (2015). Inhibition of MCU forces extramitochondrial adaptations governing physiological and pathological stress responses in heart. *Proc. Natl. Acad. Sci. U.S.A.* 112, 9129–9134. doi: 10.1073/pnas.1504705112

Raturi, A., Gutierrez, T., Ortiz-Sandoval, C., Ruangkittisakul, A., Herrera-Cruz, M. S., Rockley, J. P., et al. (2016). TMX1 determines cancer cell metabolism as a thiol-based modulator of ER-mitochondria Ca^{2+} flux. *J. Cell Biol.* 214, 433–444. doi: 10.1083/jcb.201512077

Rienks, M., Carai, P., Bitsch, N., Schellings, M., Vanhaverbeke, M., Verjans, J., et al. (2017). Sema3A promotes the resolution of cardiac inflammation after myocardial infarction. *Basic Res. Cardiol.* 112:42. doi: 10.1007/s00395-017-0630-5

Rossello, X., Riquelme, J. A., He, Z., Taferner, S., Vanhaesebroeck, B., Davidson, S. M., et al. (2017). The role of PI3Kalpha isoform in cardioprotection. *Basic Res. Cardiol.* 112:66. doi: 10.1007/s00395-017-0657-7

Rossello, X., and Yellon, D. M. (2017). The RISK pathway and beyond. *Basic Res. Cardiol.* 113:2. doi: 10.1007/s00395-017-0662-x

Ruiz-Meana, M., Fernandez-Sanz, C., and Garcia-Dorado, D. (2010). The SR-mitochondria interaction: a new player in cardiac pathophysiology. *Cardiovasc. Res.* 88, 30–39. doi: 10.1093/cvr/cvq225

Sauvanet, C., Duvezin-Caubet, S., di Rago, J. P., and Rojo, M. (2010). Energetic requirements and bioenergetic modulation of mitochondrial morphology and dynamics. *Semin. Cell Dev. Biol.* 21, 558–565. doi: 10.1016/j.semcdb.2009.12.006

Schwertz, H., Carter, J. M., Abdudureheman, M., Russ, M., Buerke, U., Schlitt, A., et al. (2007). Myocardial ischemia/reperfusion causes VDAC phosphorylation which is reduced by cardioprotection with a p38 MAP kinase inhibitor. *Proteomics* 7, 4579–4588. doi: 10.1002/pmic.200700734

Seidlmayer, L. K., Juettner, V. V., Kettlewell, S., Pavlov, E. V., Blatter, L. A., and Dedkova, E. N. (2015). Distinct mPTP activation mechanisms in ischaemia-reperfusion: contributions of Ca^{2+}, ROS, pH, and inorganic polyphosphate. *Cardiovasc. Res.* 106, 237–248. doi: 10.1093/cvr/cvv097

Sharp, W. W., Fang, Y. H., Han, M., Zhang, H. J., Hong, Z., Banathy, A., et al. (2014). Dynamin-related protein 1 (Drp1)-mediated diastolic dysfunction in myocardial ischemia-reperfusion injury: therapeutic benefits of Drp1 inhibition to reduce mitochondrial fission. *FASEB J.* 28, 316–326. doi: 10.1096/fj.12-226225

Shen, Z., Ye, C., McCain, K., and Greenberg, M. L. (2015). The role of cardiolipin in cardiovascular health. *Biomed Res. Int.* 2015:891707. doi: 10.1155/2015/891707

Shi, C., Cai, Y., Li, Y., Li, Y., Hu, N., Ma, S., et al. (2018). Yap promotes hepatocellular carcinoma metastasis and mobilization via governing cofilin/F-actin/lamellipodium axis by regulation of JNK/Bnip3/SERCA/CaMKII pathways. *Redox Biol.* 14, 59–71. doi: 10.1016/j.redox.2017.08.013

Shore, G. C., and Tata, J. R. (1977). Two fractions of rough endoplasmic reticulum from rat liver. I. Recovery of rapidly sedimenting endoplasmic reticulum in association with mitochondria. *J. Cell Biol.* 72, 714–725. doi: 10.1083/jcb.72.3.714

Smeele, K. M., Southworth, R., Wu, R., Xie, C., Nederlof, R., Warley, A., et al. (2011). Disruption of hexokinase II-mitochondrial binding blocks ischemic preconditioning and causes rapid cardiac necrosis. *Circ. Res.* 108, 1165–1169. doi: 10.1161/CIRCRESAHA.111.244962

Soltys, B. J., and Gupta, R. S. (1992). Interrelationships of endoplasmic reticulum, mitochondria, intermediate filaments, and microtubules–a quadruple fluorescence labeling study. *Biochem. Cell Biol.* 70, 1174–1186. doi: 10.1139/o92-163

Song, S., Tan, J., Miao, Y., and Zhang, Q. (2018). Crosstalk of ER stress-mediated autophagy and ER-phagy: involvement of UPR and the core autophagy machinery. *J. Cell. Physiol.* 233, 3867–3874. doi: 10.1002/jcp.26137

Steffen, J., and Koehler, C. M. (2018). ER-mitochondria contacts: actin dynamics at the ER control mitochondrial fission via calcium release. *J. Cell Biol.* 217, 15–17. doi: 10.1083/jcb.201711075

Sun, Y., Li, Q., Zhang, J., Chen, Z., He, Q., Liu, X., et al. (2017). Autophagy regulatory molecule, TMEM74, interacts with BIK and inhibits BIK-induced apoptosis. *Cell. Signal.* 36, 34–41. doi: 10.1016/j.cellsig.2017.04.005

Szabadkai, G., Bianchi, K., Varnai, P., De Stefani, D., Wieckowski, M. R., Cavagna, D., et al. (2006). Chaperone-mediated coupling of endoplasmic reticulum and mitochondrial Ca^{2+} channels. *J. Cell Biol.* 175, 901–911. doi: 10.1083/jcb.200608073

Theurey, P., and Rieusset, J. (2017). Mitochondria-associated membranes response to nutrient availability and role in metabolic diseases. *Trends Endocrinol. Metab.* 28, 32–45. doi: 10.1016/j.tem.2016.09.002

Tomczyk, M., Kraszewska, I., Szade, K., Bukowska-Strakova, K., Meloni, M., Jozkowicz, A., et al. (2017). Splenic Ly6C(hi) monocytes contribute to adverse late post-ischemic left ventricular remodeling in heme oxygenase-1 deficient mice. *Basic Res. Cardiol.* 112:39. doi: 10.1007/s00395-017-0629-y

Torres-Estay, V., Carreno, D. V., Fuenzalida, P., Watts, A., San Francisco, I. F., Montecinos, V. P., et al. (2017). Androgens modulate male-derived endothelial cell homeostasis using androgen receptor-dependent and receptor-independent mechanisms. *Angiogenesis* 20, 25–38. doi: 10.1007/s10456-016-9525-6

Toyama, E. Q., Herzig, S., Courchet, J., Lewis, T. L. Jr., Losón, O. C., Hellberg, K., et al. (2016). Metabolism. AMP-activated protein kinase mediates mitochondrial fission in response to energy stress. *Science* 351, 275–281. doi: 10.1126/science.aab4138

Tubbs, E., and Rieusset, J. (2017). Metabolic signaling functions of ER-mitochondria contact sites: role in metabolic diseases. *J. Mol. Endocrinol.* 58, R87–R106. doi: 10.1530/JME-16-0189

Twig, G., Elorza, A., Molina, A. J., Mohamed, H., Wikstrom, J. D., Walzer, G., et al. (2008a). Fission and selective fusion govern mitochondrial segregation and elimination by autophagy. *EMBO J.* 27, 433–446. doi: 10.1038/sj.emboj.7601963

Twig, G., Hyde, B., and Shirihai, O. S. (2008b). Mitochondrial fusion, fission and autophagy as a quality control axis: the bioenergetic view. *Biochim. Biophys. Acta* 1777, 1092–1097. doi: 10.1016/j.bbabio.2008.05.001

Wales, P., Schuberth, C. E., Aufschnaiter, R., Fels, J., Garcia-Aguilar, I., Janning, A., et al. (2016). Calcium-mediated actin reset (CaAR) mediates acute cell adaptations. *eLife* 5:e19850. doi: 10.7554/eLife.19850

Wang, B., Nguyen, M., Chang, N. C., and Shore, G. C. (2011). Fis1, Bap31 and the kiss of death between mitochondria and endoplasmic reticulum. *EMBO J.* 30, 451–452. doi: 10.1038/emboj.2010.352

Wang, H. J., Guay, G., Pogan, L., Sauve, R., and Nabi, I. R. (2000). Calcium regulates the association between mitochondria and a smooth subdomain of the endoplasmic reticulum. *J. Cell Biol.* 150, 1489–1498. doi: 10.1083/jcb.150.6.1489

Wang, K., Gan, T. Y., Li, N., Liu, C. Y., Zhou, L. Y., Gao, J. N., et al. (2017). Circular RNA mediates cardiomyocyte death via miRNA-dependent upregulation of MTP18 expression. *Cell Death Differ.* 24, 1111–1120. doi: 10.1038/cdd.2017.61

Westermann, B. (2011). Organelle dynamics: ER embraces mitochondria for fission. *Curr. Biol.* 21, R922–R924. doi: 10.1016/j.cub.2011.10.010

Westermann, B. (2012). Bioenergetic role of mitochondrial fusion and fission. *Biochim. Biophys. Acta* 1817, 1833–1838. doi: 10.1016/j.bbabio.2012.02.033

Wu, S., Lu, Q., Wang, Q., Ding, Y., Ma, Z., Mao, X., et al. (2017). Binding of FUN14 domain containing 1 with inositol 1,4,5-trisphosphate receptor in mitochondria-associated endoplasmic reticulum membranes maintains mitochondrial dynamics and function in hearts in vivo. *Circulation* 136, 2248–2266. doi: 10.1161/CIRCULATIONAHA.117.030235

Xie, Y., Jiang, D., Xiao, J., Fu, C., Zhang, Z., Ye, Z., et al. (2018). Ischemic preconditioning attenuates ischemia/reperfusion-induced kidney injury by activating autophagy via the SGK1 signaling pathway. *Cell Death Dis.* 9:338. doi: 10.1038/s41419-018-0358-7

Yang, G., Zhang, X., Weng, X., Liang, P., Dai, X., Zeng, S., et al. (2017). SUV39H1 mediated SIRT1 trans-repression contributes to cardiac ischemia-reperfusion injury. *Basic Res. Cardiol.* 112:22. doi: 10.1007/s00395-017-0608-3

Yang, M., Camara, A. K., Wakim, B. T., Zhou, Y., Gadicherla, A. K., Kwok, W. M., et al. (2012). Tyrosine nitration of voltage-dependent anion channels in cardiac ischemia-reperfusion: reduction by peroxynitrite scavenging. *Biochim. Biophys. Acta* 1817, 2049–2059. doi: 10.1016/j.bbabio.2012.06.004

Zazueta, C., Franco, M., Correa, F., Garcia, N., Santamaria, J., Martinez-Abundis, E., et al. (2007). Hypothyroidism provides resistance to kidney mitochondria against the injury induced by renal ischemia-reperfusion. *Life Sci.* 80, 1252–1258. doi: 10.1016/j.lfs.2006.12.023

Zhang, G. X., Kimura, S., Murao, K., Obata, K., Matsuyoshi, H., and Takaki, M. (2010). Inhibition of cytochrome c release by 10-N-nonyl acridine orange, a cardiolipin-specific dye, during myocardial ischemia-reperfusion in the rat. *Am. J. Physiol. Heart Circ. Physiol.* 298, H433–H439. doi: 10.1152/ajpheart.00938.2009

Zhang, J. X., Qu, X. L., Chu, P., Xie, D. J., Zhu, L. L., Chao, Y. L., et al. (2018). Low shear stress induces vascular eNOS uncoupling via autophagy-mediated eNOS phosphorylation. *Biochim. Biophys. Acta* 1865, 709–720. doi: 10.1016/j.bbamcr.2018.02.005

Zhang, T., Zhang, Y., Cui, M., Jin, L., Wang, Y., Lv, F., et al. (2016). CaMKII is a RIP3 substrate mediating ischemia- and oxidative stress-induced myocardial necroptosis. *Nat. Med.* 22, 175–182. doi: 10.1038/nm.4017

Zhang, W., Chen, C., Wang, J., Liu, L., He, Y., and Chen, Q. (2018). Mitophagy in cardiomyocytes and in platelets: a major mechanism of cardioprotection against ischemia/reperfusion injury. *Physiology* 33, 86–98. doi: 10.1152/physiol.00030.2017

Zhang, Y., Zhou, H., Wu, W., Shi, C., Hu, S., Yin, T., et al. (2016). Liraglutide protects cardiac microvascular endothelial cells against hypoxia/reoxygenation injury through the suppression of the SR-Ca^{2+}-XO-ROS axis via activation of the GLP-1R/PI3K/Akt/survivin pathways. *Free Radic. Biol. Med.* 95, 278–292. doi: 10.1016/j.freeradbiomed.2016.03.035

Zhao, T., Huang, X., Han, L., Wang, X., Cheng, H., Zhao, Y., et al. (2012). Central role of mitofusin 2 in autophagosome-lysosome fusion in cardiomyocytes. *J. Biol. Chem.* 287, 23615–23625. doi: 10.1074/jbc.M112.379164

Zhou, H., Du, W., Li, Y., Shi, C., Hu, N., Ma, S., et al. (2018a). Effects of melatonin on fatty liver disease: the role of NR4A1/DNA-PKcs/p53 pathway, mitochondrial fission, and mitophagy. *J. Pineal Res.* 64:e12450. doi: 10.1111/jpi.12450

Zhou, H., Ma, Q., Zhu, P., Ren, J., Reiter, R. J., and Chen, Y. (2018b). Protective role of melatonin in cardiac ischemia-reperfusion injury: from pathogenesis to targeted therapy. *J. Pineal Res.* 64:e12471. doi: 10.1111/jpi.12471

Zhou, H., Shi, C., Hu, S., Zhu, H., Ren, J., and Chen, Y. (2018c). BI1 is associated with microvascular protection in cardiac ischemia reperfusion injury via repressing Syk-Nox2-Drp1-mitochondrial fission pathways. *Angiogenesis* doi: 10.1007/s10456-018-9611-z [Epub ahead of print].

Zhou, H., Wang, J., Zhu, P., Hu, S., and Ren, J. (2018d). Ripk3 regulates cardiac microvascular reperfusion injury: the role of IP3R-dependent calcium overload, XO-mediated oxidative stress and F-action/filopodia-based cellular migration. *Cell. Signal.* 45, 12–22. doi: 10.1016/j.cellsig.2018.01.020

Zhou, H., Wang, J., Zhu, P., Zhu, H., Toan, S., Hu, S., et al. (2018e). NR4A1 aggravates the cardiac microvascular ischemia reperfusion injury through suppressing FUNDC1-mediated mitophagy and promoting Mff-required mitochondrial fission by CK2alpha. *Basic Res. Cardiol.* 113:23. doi: 10.1007/s00395-018-0682-1

Zhou, H., Zhu, P., Wang, J., Zhu, H., Ren, J., and Chen, Y. (2018f). Pathogenesis of cardiac ischemia reperfusion injury is associated with CK2alpha-disturbed mitochondrial homeostasis via suppression of FUNDC1-related mitophagy. *Cell Death Differ.* doi: 10.1038/s41418-018-0086-7 [Epub ahead of print].

Zhou, H., Hu, S., Jin, Q., Shi, C., Zhang, Y., Zhu, P., et al. (2017a). Mff-dependent mitochondrial fission contributes to the pathogenesis of cardiac microvasculature ischemia/reperfusion injury via induction of mROS-mediated cardiolipin oxidation and HK2/VDAC1 disassociation-involved mPTP opening. *J. Am. Heart Assoc.* 6:e005328. doi: 10.1161/JAHA.116.005328

Zhou, H., Li, D., Shi, C., Xin, T., Yang, J., Zhou, Y., et al. (2015). Effects of Exendin-4 on bone marrow mesenchymal stem cell proliferation, migration and apoptosis in vitro. *Sci. Rep.* 5:12898. doi: 10.1038/srep12898

Zhou, H., Li, D., Zhu, P., Hu, S., Hu, N., Ma, S., et al. (2017b). Melatonin suppresses platelet activation and function against cardiac ischemia/reperfusion injury via PPARgamma/FUNDC1/mitophagy pathways. *J. Pineal Res.* 63:e12438. doi: 10.1111/jpi.12438

Zhou, H., Wang, S., Zhu, P., Hu, S., Chen, Y., and Ren, J. (2017c). Empagliflozin rescues diabetic myocardial microvascular injury via AMPK-mediated inhibition of mitochondrial fission. *Redox Biol.* 15, 335–346. doi: 10.1016/j.redox.2017.12.019

Zhou, H., Zhang, Y., Hu, S., Shi, C., Zhu, P., Ma, Q., et al. (2017d). Melatonin protects cardiac microvasculature against ischemia/reperfusion injury via suppression of mitochondrial fission-VDAC1-HK2-mPTP-mitophagy axis. *J. Pineal Res.* 63:e12413. doi: 10.1111/jpi.12413

Zhou, H., Zhu, P., Guo, J., Hu, N., Wang, S., Li, D., et al. (2017e). Ripk3 induces mitochondrial apoptosis via inhibition of FUNDC1 mitophagy in cardiac IR injury. *Redox Biol.* 13, 498–507. doi: 10.1016/j.redox.2017.07.007

Zhou, R., Yazdi, A. S., Menu, P., and Tschopp, J. (2011). A role for mitochondria in NLRP3 inflammasome activation. *Nature* 469, 221–225. doi: 10.1038/nature09663

Zhu, H., Jin, Q., Li, Y., Ma, Q., Wang, J., Li, D., et al. (2018). Melatonin protected cardiac microvascular endothelial cells against oxidative stress injury via suppression of IP3R-[Ca^{2+}]c/VDAC-[Ca^{2+}]m axis by activation of MAPK/ERK signaling pathway. *Cell Stress Chaperones* 23, 101–113. doi: 10.1007/s12192-017-0827-4

Zhu, P., Hu, S., Jin, Q., Li, D., Tian, F., Toan, S., et al. (2018). Ripk3 promotes ER stress-induced necroptosis in cardiac IR injury: a mechanism involving calcium overload/XO/ROS/mPTP pathway. *Redox Biol.* 16, 157–168. doi: 10.1016/j.redox.2018.02.019

Zhu, S., Xu, T., Luo, Y., Zhang, Y., Xuan, H., Ma, Y., et al. (2017). Luteolin enhances sarcoplasmic reticulum Ca^{2+}-ATPase activity through p38 MAPK signaling thus improving rat cardiac function after ischemia/reperfusion. *Cell. Physiol. Biochem.* 41, 999–1010. doi: 10.1159/000460837

Zong, C., Qin, D., Yu, C., Gao, P., Chen, J., Lu, S., et al. (2017). The stress-response molecule NR4A1 resists ROS-induced pancreatic beta-cells apoptosis via WT1. *Cell. Signal.* 35, 129–139. doi: 10.1016/j.cellsig.2017.03.012

Conflict of Interest Statement: The authors declare that the research was conducted in the absence of any commercial or financial relationships that could be construed as a potential conflict of interest.

frontiers in Physiology

ORIGINAL RESEARCH
published: 13 July 2018
doi: 10.3389/fphys.2018.00899

Eplerenone Reverses Cardiac Fibrosis via the Suppression of Tregs by Inhibition of Kv1.3 Channel

Pei-Pei Shao[1†], Chang-Jiang Liu[1†], Qi Xu[2], Bo Zhang[3], Shao-Hua Li[1], Yang Wu[1], Zhan Sun[4] and Lu-Feng Cheng[1]*

[1] Department of Pharmacology, School of Pharmacy, Xinjiang Medical University, Ürümqi, China, [2] Department of Immunology, School of Pre-clinical Medicine, Xinjiang Medical University, Ürümqi, China, [3] Key Laboratory of Xinjiang Phytomedicine Resource and Utilization, Ministry of Education, Shihezi University, Shihezi, China, [4] Center of Functional Experiment, School of Pre-clinical Medicine, Xinjiang Medical University, Ürümqi, China

Background: Fibroblast proliferation is a critical feature during heart failure development. Previous studies reported regulatory T-lymphocytes (Tregs)' protective role against myocardial fibrosis. However, notably, Tregs also secrete fibrogenic cytokine TGF-β when activated. This study aimed to clarify the intriguing link between Tregs and fibrosis, the role of Tregs Kv1.3 potassium channel (regulating T-lymphocytes activation) in the fibrosis process, and how selective aldosterone receptor antagonist Eplerenone affects Tregs and fibrosis through its action on Kv1.3 channel.

Methods and Results: After co-incubation with Tregs, cardiac fibroblast proliferation (CCK-8 assay) and levels of collagen I, III, and Matrix metalloproteinase2 (ELISA) significantly elevated. Cell viability assays, Kv1.3 channel mRNA (RT-qPCR), and protein expression (In-Cell Western Blotting) revealed Tregs were activated/proliferated when co-cultured with fibroblasts. Treg intracellular TGF-β level increased by 5.8-fold, far more than that of intracellular IL-10, extracellular TGF-β and IL-10 (ELISA). And 30 μM eplerenone suppressed Tregs proliferation by 82.77% and furthermore, suppressed intracellular TGF-β level to a significantly greater extent than that of intracellular IL-10, extracellular TGF-β and IL-10. Moreover, the Kv1.3 current (whole-cell patch clamp) of Tregs in congestive heart failure patients and rats (induced by coronary artery ligation and exhaustive exercise) elevated by >4-fold than that of healthy volunteers and control rats, whereas 30 μM eplerenone suppressed the current by >60% in control Tregs. In addition, docking calculations (AutoDock software 4.0 suite) showed eplerenone has higher H-bond energy with Kv1.3 channel than other selective blockers.

Conclusion: Immuno-regulation in the late stage of CHF activates Tregs proliferation via the upregulation of Kv1.3 channels, which promotes cardiac fibrosis by primarily secreting TGF-β. Taken together, eplerenone's high affinity to Kv1.3 channel enables it to antagonize the Kv1.3 channels directly to suppress Tregs proliferation, which in turn may play an immuno-regulatory role during CHF.

Keywords: eplerenone, cardiac fibrosis, $CD4^+CD25^+$ Treg lymphocytes, Kv1.3 channel, TGF-β

OPEN ACCESS

Edited by:
Di Lang,
University of Wisconsin–Madison, United States

Reviewed by:
Núria Comes,
University of Barcelona, Spain
Wayne Rodney Giles,
University of Calgary, Canada

****Correspondence:***
Lu-Feng Cheng
lfcheng@xjmu.edu.cn

[†] These authors have contributed equally to this work.

Specialty section:
This article was submitted to Cardiac Electrophysiology, a section of the journal Frontiers in Physiology

Received: *16 April 2018*
Accepted: *21 June 2018*
Published: *13 July 2018*

Citation:
Shao P-P, Liu C-J, Xu Q, Zhang B, Li S-H, Wu Y, Sun Z and Cheng L-F (2018) Eplerenone Reverses Cardiac Fibrosis via the Suppression of Tregs by Inhibition of Kv1.3 Channel. Front. Physiol. 9:899. doi: 10.3389/fphys.2018.00899

INTRODUCTION

Eplerenone, a highly selective aldosterone receptor antagonist used to treat heart failure, is known to reduce all-cause mortality and sudden cardiac death when used in combination with angiotensin converting enzyme inhibitors and β-blockers (Seferovic et al., 2015; Heggermont et al., 2016; Ponikowski et al., 2016).

The role of inflammation in the development of cardiovascular diseases has been investigated extensively (Borthwick et al., 2013; Prabhu and Frangogiannis, 2016). Local myocardial injury and cardiomyocyte necrosis, i.e., ischemia, atherosclerosis, and myocardial infarction (MI) trigger intense inflammatory responses. However, dysregulated chronic inflammatory response may result in pathological wound repair, accumulation of permanent fibrotic scar tissue at the site of injury, failure of the tissue to regain normal function, and lead to myocardial fibrosis eventually.

A variety of immune cells and cytokines have been reported to play a direct or indirect role in the pathogenesis of myocardial fibrosis. Th17 cells play a vital role in the development of autoimmune disease and anaphylactic reactions, while $CD4^+CD25^+$ regulatory T lymphocytes (Treg cells) have anti-inflammatory activity and maintain immune homeostasis by secreting anti-inflammatory cytokines, i.e., interleukin (IL)-10 and transforming growth factor (TGF)-β. Therefore, the balance between Th17 and Treg cells is vital to the development/prevention of inflammation and autoimmune diseases (Sun et al., 2017).

Several studies have shown that Tregs are inversely correlated to cardiovascular diseases (Tang et al., 2010; Hofmann and Frantz, 2013; Frieler and Mortensen, 2015). Accordingly, Tregs have been established as a valuable prognostic marker and a therapeutic target in the treatment of heart failure (Meng X. et al., 2016). However, the exact role of Tregs in organ fibrosis under inflammatory conditions remains controversial. Some hypothesized that immune-suppressing Tregs play a profibrotic role, and suppression of TGF-β can alleviate fibrosis of the heart, liver, and kidneys (Wei, 2011). In the contrary, Cao et al. (2013) suggested that intravenous Tregs can reverse myocardial fibrosis mediated by the secretion of IL-10. A number of *in vivo* studies have shown that the suppression of TGF-β can alleviate fibrosis of the heart, liver, and kidneys in various animal species (Borthwick et al., 2013; Meng X.M. et al., 2016). The voltage-gated Kv1.3 channel, a T lymphocyte-specific ion channel, is involved in the differentiation and activation of T lymphocytes, and has been validated as a therapeutic target for the treatment of diversified autoimmune diseases (Gilhar et al., 2016; Wang et al., 2016; Chandy and Norton, 2017). Many studies proposed that Kv1.3 channels affect proliferation through K^+ efflux and membrane hyperpolarization, which promotes Ca^{2+} influx to activate Ca^{2+}-dependent transcriptional factors (Wang and Xiang, 2013; Orban et al., 2014; Perez-Garcia et al., 2018).

This study was to investigate the involvement of Tregs in the development of cardiac fibrosis as well as to determine whether eplerenone influences the activation and/or proliferation of Tregs in the treatment of congestive heart failure (CHF).

MATERIALS AND METHODS

Reagents

Fetal bovine serum (FBS) and RPMI1640 were purchased from Thermo Fisher Scientific (Waltham, MA, United States), HISTOPAQUE®-1077/1083 from Sigma-Aldrich (St. Louis, MO, United States), and the primary mouse anti-rat KCNA3 and β-actin antibodies from Abcam (Cambridge, MA, United States). (PerCP-CyTM5.5) Mouse Anti-Human CD3, (FITC) Mouse Anti-Human CD4, (APC) Mouse Anti-Human CD183 and (PE) Mouse Anti-Human CD196; (FITC) Mouse Anti-Human CD4, (APC) Mouse Anti-Human CD25 and (PE) Mouse Anti-Human CD127 for flow cytometry measurement of Th17 and Tregs were purchased from Becton Dickinson (Franklin lake, NJ, United States). IRDye®800CW goat anti-mouse antibody was purchased from LI-COR Biosciences (Fullerton, CA, United States), and Biotin-conjugated mouse anti-rat CD4 as well as PE-conjugated mouse anti-rat CD25 were purchased from Becton Dickinson (Franklin Lake, NJ, United States). Biotin-conjugated mouse anti-human CD4, PE-conjugated mouse anti-human CD25 Multisort MicroBeads, LS columns and MiniMACS™ separator were purchased from Miltenyi Biotec (Bergisch Gladbach, Germany). SYBR™ Select Master Mix and Trizol were purchased from Life Technologies (Waltham, MA, United States). RevertAid First Strand cDNA Synthesis Kit was purchased from Thermo scientific (925 West 1800 South Logan, United States). Kv1.3, KCa3.1, CRAC gene sequences were purchased by Quintarabio (Ürümqi, Xinjiang, China). The CCK-8 Kit was purchased from Bosterbio (Pleasanton, CA, United States). ELISA assays for Collagen I, Collagen III and Matrix metalloproteinase2 (MMP2), brain natriuretic peptide (BNP), IL-1β, IL-6, IL-17, IFN-γ, and TNF-α were purchased from CUSABIO Biotech (Wuhan, Hubei, China), while those for TGF-β, and IL-10 as well as the Masson Stain Kit were purchased from Jiancheng Bioengineering Institute (Nanjing, Jiangsu, China). Psora-4 and eplerenone were purchased from Sigma-Aldrich (St. Louis, MO, United States).

CHF Patients Inclusion/Exclusion Statements

Twenty-five patients with chronic heart failure (CHF) aged 30–80 years old were collected from Department of Heart Failure, the First Affiliated Hospital of Xinjiang Medical University from January 2016 to May 2017. The experiment was approved by the Ethics Committee of the First Affiliated Hospital. The clinical general data were collected. Cardiac function was measured by echocardiography to evaluate left ventricular systolic/diastolic function, and the immuno-factors were determined by flow cytometry and/or ELISA. 15 healthy volunteers aged 30–55 years old were screened from the Health Examination Center of the First Affiliated Hospital as the control group.

CHF patients inclusion criteria: (1) voluntary informed participation with no limitation of gender; (2) according to the diagnostic criteria, the cardiac function was at NYHA grade III–IV; (3) left ventricular ejection fraction (LVEF) $\leq$ 40%; (4) 3000 $\leq$ Brain Natriuretic Peptide (BNP) $\leq$ 5000.

Exclusion criteria: (1) acute or chronic infection; (2) autoimmune diseases; rheumatic diseases with rheumatic activity within 3 months; recent use of drugs affecting immune response (e.g., corticosteroids); (3) acute cardiovascular diseases and organic heart diseases within 3 months, e.g., acute pulmonary edema, acute left ventricular dysfunction, unstable angina pectoris, acute myocardial infarction as well; (4) others: e.g., abnormal thyroid function; obvious hepatic and renal dysfunction; malignant tumor; pregnancy.

Animal Ethics

Male Sprague–Dawley rats were purchased from the Animal Experimental Center (Xinjiang Medical University). All rats weighed between 180 and 220 g at the time of the experiments. All procedures involving animals were performed under an NIH Guidelines approved protocol in accordance with the Institutional Animal Care and Use Committee (approved by AAALAC in England) at the First Affiliated Hospital of Xinjiang Medical University. Rats were anesthetized with a 2% isoflurane gas mixture of oxygen inhalation for 3–5 min using a Matrix VIP3000 Isoflurane Vaporizer (Matrix, New York, United States) during coronary artery ligation (CAL) surgery, echocardiographic and hemodynamic detection, and blood and major organs were isolated for further detection and sample preparation. The fully anesthesia was confirmed with no reflex response to foot clamp. Neonatal rats were euthanized via cervical dislocation, and hearts were isolated for cardiac fibroblasts enrichment. All surgeries and follow-up analyses complied with blind principle.

Establishment of a Rat Model of CHF

Congestive heart failure was initiated with coronary artery ligation on rats according to Ren et al. (2017). Briefly, after being anesthetized, the left coronary artery was ligated with a 7-0 suture near the initiation of coronary artery (the point between left auricle inferior margin and pulmonary conus). The myocardial infarction was confirmed with a pale surface color and S-T segment elevation by electrocardiographic (ECG) monitoring. To further establish the CHF model, 30-min-per-day exhausted swimming was implemented on every surgery rats sustaining for 15 days. 10–12 weeks later after coronary ligation, when the indexes of B-ultrasound reached the following criteria (Ponikowski et al., 2016): left ventricular ejection fraction (LVEF) <50% and/or a 40% suppressant in the maximum systolic velocity of left ventricular pressure (LV + dp/dt_{max}), the following-up experiments would be performed.

Isolation of $CD4^+CD25^+$ Tregs

$CD4^+CD25^+$ Tregs from human peripheral blood were isolated in accordance with the manufacturer's instructions. Briefly, mononuclear cells precipitation was separated by HISTOPAQUE®-1077 human lymphocytes separation medium and centrifugation (1600 rpm, 20 min, 4°C). $CD4^+$ T cells were then isolated by negative selection using Biotin-Antibody Cocktail with Multisort MicroBeads and Anti-Biotin MicroBeads (Miltenyi Biotec, GER) at 4°C, passing through the LS separate column around the MiniMACS separator, releasing and terminating by Multisort Release and Stop Reagents sequentially at 4°C. $CD4^+$ T cells were enriched and $CD4^+CD25^+$ T cells were further screened for positive expression of CD25 using CD25 MicroBeads II human with MicroBeads and MiniMACS separator. The purity of isolated $CD4^+CD25^+$ Tregs was greater than 95%, and incubated with 10% FBS (Gibco, United States) media at 37°C in a 5% CO_2 incubator.

The single cell suspensions from spleen of Sprague–Dawley rat were prepared by passing the sheared tissue through a 200-mesh stainless steel strainer (Sigma-Aldrich, St. Louis, MO, United States), and following the manufacturer's instructions, mononuclear cells precipitation was separated by HISTOPAQUE®-1083 rat lymphocytes separation medium and centrifugation (1600 rpm, 20 min, 4°C). $CD4^+$ T cells were then isolated by positive selection using Biotin-Mouse Anti-Rat with Multisort MicroBeads and Anti-Biotin MicroBeads (Miltenyi Biotec, GER) at 4°C, passing through the LS separate column around the MiniMACS separator, releasing and terminating by Multisort Release and Stop Reagents sequentially at 4°C. $CD4^+$ T cells were enriched and $CD4^+CD25^+$ T cells were further screened for positive expression of CD25 using PE-Mouse Anti-Rat CD25 with MicroBeads and MiniMACS separator. The purity of isolated $CD4^+CD25^+$Tregs was greater than 95%, and incubated with 10% FBS (Gibco, United States) media at 37°C in a 5% CO_2 incubator.

Primary Culture of Cardiac Fibroblasts of Rats

Cardiac fibroblasts (CFs) were isolated from hearts of neonatal (3-day-old) rats by digestion and differential adhesion, as described previously (Barry et al., 2013). Briefly, the heart was removed, chopped into tiny pieces, and digested in phosphate-buffered saline (PBS) solution containing 0.25% trypsin on a shaking platform (30 rpm) at 4°C overnight. The digested tissue was then treated with 0.1% collagenase II for 8–10 min with 3–4 times at 37°C. The digestion was discontinued along with 10% FBS. After centrifugation (1300 rpm, 5 min, 20°C), the resulting supernatant was discarded and the precipitated cells were re-suspended and seeded in 50 mL flasks before being cultured for 90 min at 37°C in an incubator (1st differential adhesion) and then 40 min (the 2nd differential adhesion). Bromodeoxyuridine (BrdU: 0.1 mM) was then added to terminate the growth of the remaining fibroblasts. Cells (5×10^5 per well) were planted into plates with media containing 10 g/L FCS, 1 g/L double antibody, 1 g/L glutamate, and 1 g/L non-essential amino acid was replaced every 48 h. The cells were purified to obtain the primary fibroblasts, and 3–4 generations were collected for subsequent experiments.

Co-culture of Cardiac Fibroblasts and Tregs *in Vitro*

The treatment protocol included the following groups: CFs, Tregs, CFs + EPL, Tregs + EPL, CFs + Tregs, and CFs + Tregs + EPL. Fibroblasts were planted into 96-well plates

with 10^4 cells/hole at 37°C in a 5% CO_2 incubator for 48 h. When an adhesion rate of 80.0 ± 5.0% was achieved, the fibroblasts were incubated with PBS for 12 h. In the meantime, the Tregs were treated in the same way. Next, the fibroblasts and Tregs were mixed and treated with eplerenone in RPMI 1640 containing 1 g/L double antibody for 48 h. The Tregs were replaced with fresh ones after 24 h due to the viability being reduced by this time.

Since cardiac fibroblasts are passaged cells while Tregs are not, for different *in vitro* experiments, fibroblasts were extracted from same batch of newborn rats ($n = 10$) and Tregs from different batches of adult rats.

Flow Cytometric Analysis of Th17 and Treg Cells

Two hundred microliter anticoagulant total blood mixed with 5 μL (PerCP-CyTM5.5) Mouse Anti-Human CD3, (FITC) Mouse Anti-Human CD4, (APC) Mouse Anti-Human CD183 and (PE) Mouse Anti-Human CD196 for Th17 cells or with 5 μL (FITC) Mouse Anti-Human CD4, (APC) Mouse Anti-Human CD25 and (PE) Mouse Anti-Human CD127 for Treg cells were reacted away from light for 30 min, followed by adding lytic erythrocyte, centrifuging (1000 rpm, 5 min, 20°C) and washing cells for three times. Lastly 300 μL buffer solution was fully mixed the cells for flow cytometer measurement.

Echocardiography

Echocardiography was performed with an ultrasound instrument (HP 5500, United States) on day 70 post-surgery. After being anesthetized, the anatomical data of the rat heart were obtained by averaging results from three consecutive heart beats. On day 4 after ultrasound assessment, rats underwent right carotid artery catheterization into the left ventricle and using a biological experimental system (Powerlab, Australian); hemodynamic indexes were recorded after steady state was achieved.

Assessment of Cardiac Fibrosis by Masson-Trichrome Staining

A horizontal section of left ventricle stained with Masson-trichrome was examined to evaluate the infarct size (cardiac fibrosis). Mice with infarct size less than 25% of total area of left ventricle were excluded.

Cell Viability Assay

The CCK-8 Kit was employed to analyze cell proliferation rates. Due to the non-adherent nature of the Tregs, the cells were re-suspended by gentle pipetting up and down to ensure that both cell types were accurately represented. Tregs were collected after 24 and 48 h, washed, and seeded into 96-well plates for subsequent analysis. Both cell types were incubated for an additional 2 h at 37°C. CCK-8 (10 μL) was added to each well and the volume in each well was made up to 200 μL with PBS. Absorbance (OD value) was detected at a double-wavelength of 450 nm and 610 nm using a microplate reader (Thermo Multiskan Spectrum, Waltham, MA, United States).

Analysis of Kv1.3 Channel on Tregs Using the Whole-Cell Patch-Clamp Technique

Tregs were "floated off" in the working chambers of culture plates for 10 min before being washed and then studied within 20–90 min after plating in the whole-cell patch clamp technique with an EPC-10^+ HEKA amplifier (Germany). Patch pipettes were pulled from micropipette raw glass (OD 1.5 mm × ID 0.84 mm, Vital Sense Scientific Instrument, China) to resistances of ∼5 MΩ when submerged in the bath solution. The pipette solution contained 150.0 mM KCl, 1.0 mM $CaCl_2$, 1.0 mM $MgCl_2$, 10.0 mM HEPES, and 10.0 mM K_2EGTA (pH 7.20, adjusted with KOH). The perfusing solution contained 150.0 mM NaCl, 4.5 mM KCl, 1.0 mM $CaCl_2$, 1.0 mM $MgCl_2$, and 10.0 mM HEPES (pH 7.35, adjusted by NaOH), and Kv1.3 currents were elicited with voltage ramps from −80 to +40 mV of 300-ms duration applied every 30 s, as described previously (Zhao et al., 2014; Zhang et al., 2016). Fast and slow capacitances were compensated before every recording. Cell capacitance and access resistance were continuously monitored during recordings. Kv1.3 current densities were determined by the cell capacitance.

mRNA Expression of Ion Channels in Tregs by RT-qPCR

Total RNA was extracted from the Tregs harvested from every treatment group, after which reverse transcription was immediately carried out as described in the manufacturer's instructions. PCR amplification was performed using the Green Master Mix Kit (Life Technologies, Waltham, MA, United States), and the reagents, prepared on ice, consisted of the following: 6.4 μL H_2O, 10 μL SYBR, 0.8 μL each primer (forward and reverse), and 2.0 μL sample. The PCR steps were as follows: 50.0°C for 2 min; 95.0°C for 2 min; 95.0°C for 15 s with 40 loops; 60°C for 15 s; and 95°C for 15 s. Primer sequences are shown in **Table 1**.

In-Cell Western Blotting Assay of Kv1.3 Channel on Tregs

A Tregs suspension was seeded into 96-well plates with a "U"-type black wall and the cells were fixed with 4% paraformaldehyde. Cells were then sealed with TBS sealing liquid (prepared with 0.5% defatted milk powder) for an hour before being incubated with 50 μL KCNA3 primary antibody (diluted

TABLE 1 | Gene sequences of ion channels.

Gene	Gene ID	Upstream (5′–3′)	Downstream (5′–3′)
G3PD	GAPDH	GGCAGCCTGTTGGAA AAGAA	GGCAGCCTGTTGG AAAAGAA
Kv1.3	KCNA3	GGCAGCCTGTTGGAA AAGAA	GGCAGCCTGTTGG AAAAGAA
KCa3.1	KCNN4	ACTGGAGTCATGGG TGTCTG	ATGAGACTCCTTCC TGCGAG
CRAC	CRACR2A	TCTCCGTTGAAGAAG ACCCC	GGCAGCCTGTTGG AAAAGAA

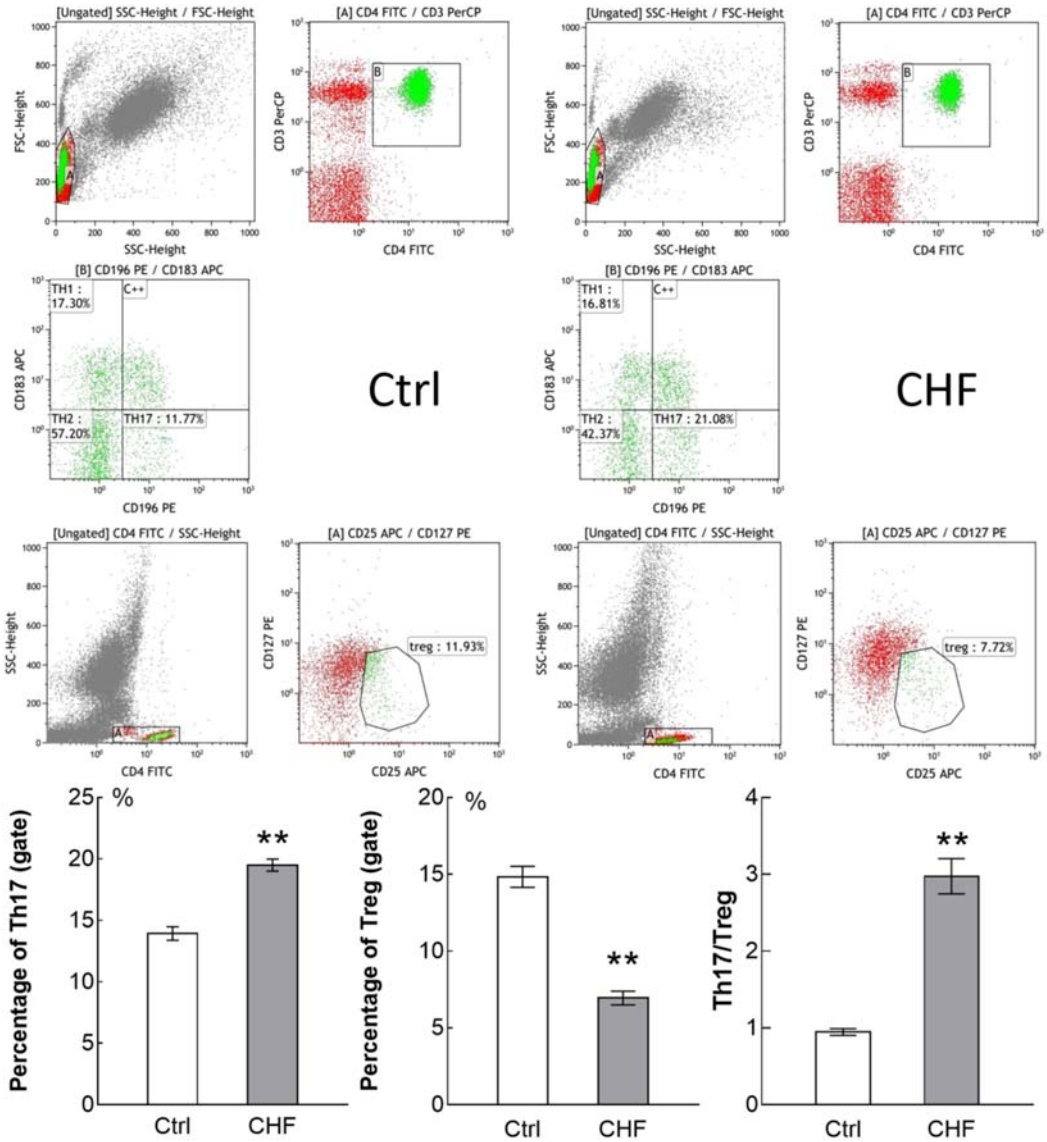

FIGURE 1 | Flow cytometry assay showed the percentage of Th17 cells and Treg cells in CHF patients (25 cases) compared to control subjects (15 cases). The original flow cytometry plots of the two groups is displayed above, and histogram comparison of Th17, Treg cells and the ratio of Th17/Treg is displayed below. Th17 cells in CHF group was significantly higher than in control group (**$P < 0.01$), while Treg cells in the CHF group was significantly lower than in control group (**$P < 0.01$); thereby the ratio of Th17/Treg in the CHF group was significantly higher than that in the control group (by ∼3-fold, **$P < 0.01$).

in 0.25 g/L defatted milk powder; 1:800) on a shaking platform (30 rpm) overnight at 4°C. After an hour of incubation with secondary antibody the following day, the resulting signals were detected using an Odyssey (LI-COR Biosciences, Fullerton, CA, United States) scanner with the following conditions: double channels of 700 and 800 nm, medium scanning quality, 169 μm dpi, 3.0 mm focal length, and level 5 of brightness.

Measurement of BNP and Inflammatory Cytokine Levels by ELISA

Levels of BNP and inflammatory cytokines in the plasma were measured using commercially available ELISA Kits according to the manufacturer's instructions. Data were analyzed using a microplate reader (Bio-Rad Coda, United States).

Measurement of Extracellular and Intracellular TGF-β and IL-10 Levels in Tregs by ELISA

After 48 h of culture, post-centrifugal supernatant fluid was collected from each treatment group as extracellular fluid. The precipitated Tregs were subjected to repeated freezing and melting cycles to release the cell contents (intracellular fluid). The TGF-β and IL-10 levels in the extracellular and intracellular fluid samples were detected by ELISA Kits in accordance with the

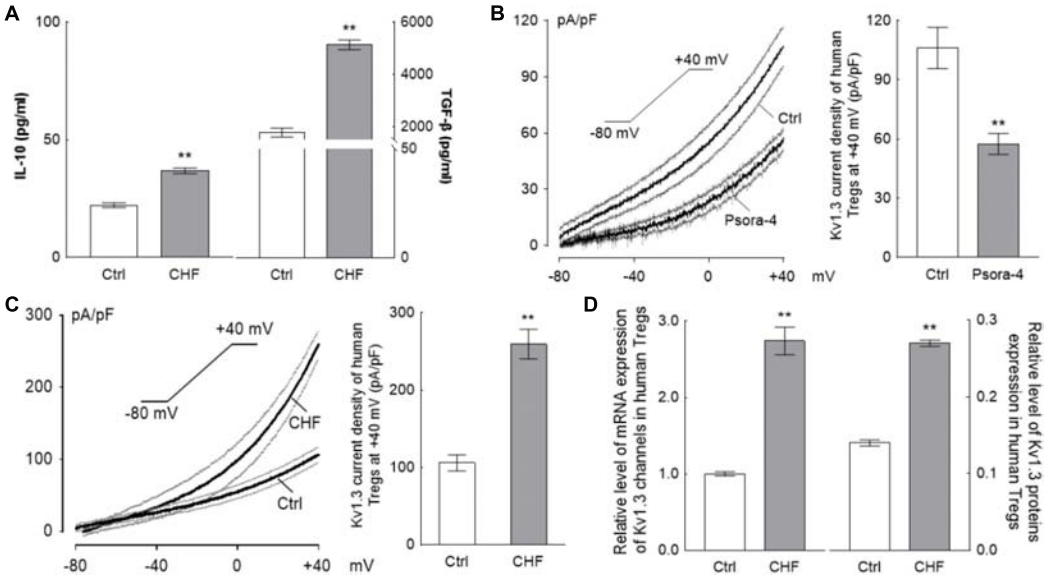

FIGURE 2 | The changing of Tregs activation for CHF patients. **(A)** The histograms differences of serum IL-10 and TGF-β between the CHF patients and the control persons by ELISA assay. Levels of both IL-10 and TGF-β were elevated significantly in the CHF group compared to the blank control group, nevertheless, the elevation of IL-10 (65.9%) was far less than that of TGF-β (2.9-fold) (**$P < 0.01$, $n = 30$ vs. 30). **(B)** The Kv1.3 channels on the Tregs membrane were identified by perfusion with 3 nM Psora-4 (a specific Kv1.3 channels inhibitor) under voltage ramp from –80 mV to +40 mV of 300 ms duration ($n = 15$, the black traces are averaged dots of all the recording cells and the gray lines are standard error dots of them); the histogram on the right of B is the Kv1.3 current density at +40 mV spot. **(C)** Recording at same protocol on the Treg cells of CHF patients, the elevation of the current density (~2.5-fold of the healthy volunteers, $n = 22$ vs. 20, **$P < 0.01$) was obtained at +40 mV of voltage clamp. **(D)** Relative level of mRNA and protein expressions of Kv1.3 channels of Tregs of the CHF patients were also elevated significantly compared to the control ($n = 10$ vs. 3 for mRNA and $n = 6$ vs. 6 for protein, **$P < 0.01$). All the above graphs elucidated that during the CHF states, Tregs were activated and secreted cytokines, i.e., IL-10 and TGF-β, though the proliferation of Tregs was suppressed significantly (according to the results of **Figure 1**).

Kit instructions. Data were analyzed using a microplate reader (Thermo Multiskan Spectrum, United States).

Expression of ECM-Associated Proteins by ELISA

After the CFs, CFs + Tregs, and CFs + Tregs + EPL cell groups were incubated for 48 h at 37°C in a 5% CO_2 incubator, the culture medium was collected from each culture and assessed for secretion of Collagen I, Collagen III, and MMP-2 using ELISA method. Results were analyzed using a microplate reader (Bio-Rad Coda, United States).

Structure Preparation and Molecular Docking

Atomic coordinates for the human renal potassium channel Kv1.3 structure, with accession number PDB ID: 4BGC (Bhuyan and Seal, 2015), were used. Initial atomic coordinates for all ligands were obtained from PubChem[1]. The molecular interactions between the Kv1.3 and the three ligands were computed using AutoDock 4.0 suite (Molecular Graphics Laboratory, La Jolla, CA, United States).

Docking calculations were carried out on the protein models. Essential hydrogen atoms, kollman charges, and solvation parameters were added with the aid of AutoDock tools.

[1]https://pubchem.ncbi.nlm.nih.gov/

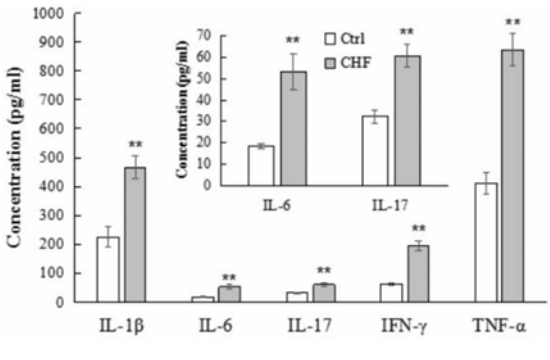

FIGURE 3 | The histograms comparison of plasma levels of the inflammatory cytokines including IL-1β, IL-6, IL-17, IFN-γ, and TNF-α of control vs. CHF rats (determined by ELISA). All the inflammatory cytokines levels in CHF group were significantly higher than that in the control group ($n = 12$, **$P < 0.01$). The inner histogram comparison graph of IL-6 and IL-17 levels is zoomed in from the bigger one since their levels were relatively lower than other three cytokines.

Affinity maps were calculated using probes corresponding to all possible atomic types present in the full set of ligands. Atom types were assigned by AutoDock Tools. Affinity maps of 86 × 72 × 110 A grid points and 0.375 A spacing were generated using the Autogrid program. AutoDock parameter set and distance-dependent dielectric functions were used in the

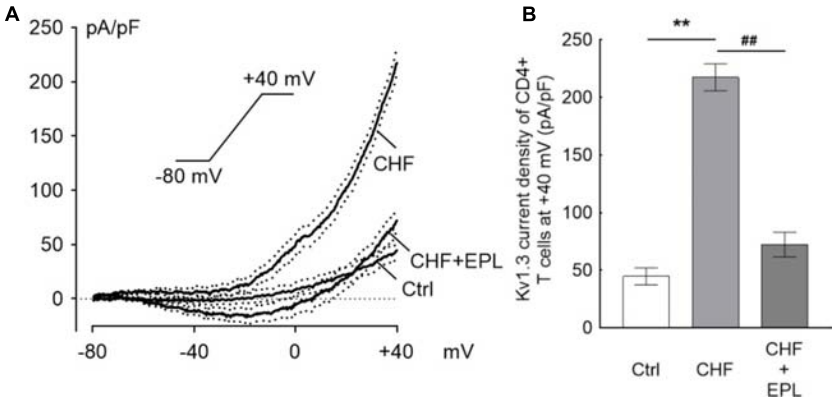

FIGURE 4 | Eplerenone suppresses the Kv1.3 current, which is elevated in the CHF model. The ramp line was elicited with whole-cell patch clamp mode. The ramp protocol stimulation is sustaining from –80 mV to +40 mV of 300 ms duration applied every 30 s. **(A)** The original current density trace elicited from Tregs of the CHF rats was significantly higher than that of Tregs from the control rats (n = 10 cells for each group); 30 μM eplerenone (EPL) markedly suppressed the ramp line of the Kv1.3 current density in the CHF model rats (the black traces are averaged dots of the current density and the dotted lines are standard error bars). **(B)** At +40 mV in particular, the current density was ∼5-fold higher in the CHF rats than in the control rats ($^{**}P < 0.01$); the suppression of the current density by EPL was calculated as ∼67% comparing to the CHF rats ($^{\#\#}P < 0.01$).

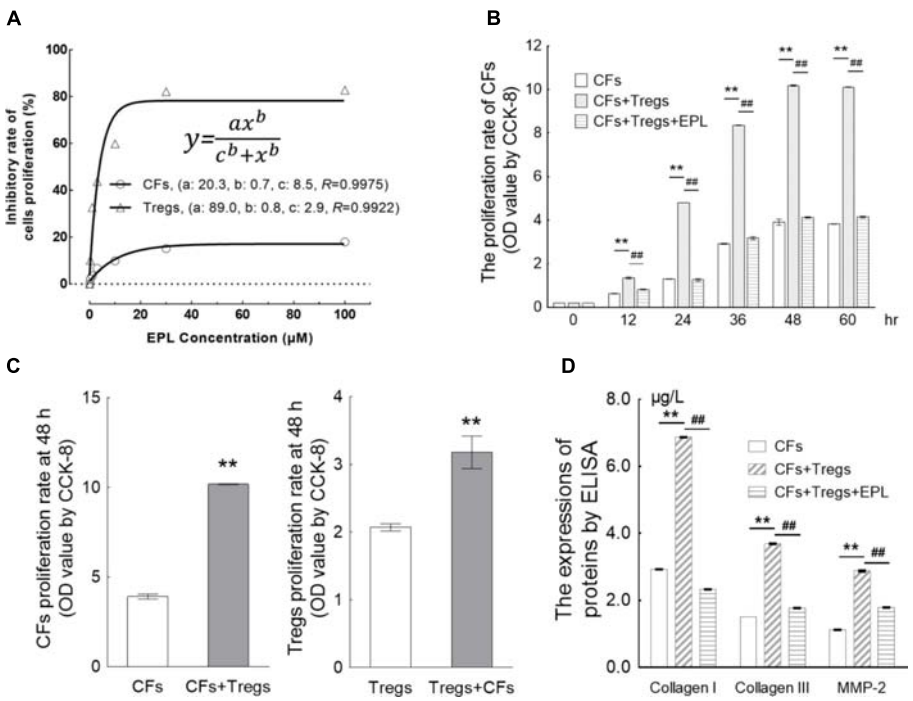

FIGURE 5 | Eplerenone suppresses the proliferation of CFs induced by co-incubation with Tregs. **(A)** After 48-h treatment of Tregs and CFs with eplerenone at 0.1, 0.3, 1, 3, 10, 30, and 100 μM, cell viability (by CCK-8 assay, n = 8) of both cell types was inhibited in a concentration-dependent manner in accordance with the Hill equation: $y = \frac{ax^b}{c^b+x^b}$. The IC_{50}s for Tregs and CFs were calculated as 2.9 and 8.5 μM, respectively. 30 μM eplerenone suppressed cell viability by 82.77 and 17.94% in Tregs and CFs, respectively, after which the viabilities stabilized. Accordingly, 30 μM was chosen as the eplerenone dose for subsequent experiments. **(B)** Tregs induced the proliferation of CFs in a time-dependent manner (CFs + Tregs vs. CFs, n = 8, $^{**}P < 0.01$ every 12 h). The percentage of proliferation in the CFs + Tregs group was ∼2.6-fold higher than that in the CFs group at 48 h (maximum proliferation was achieved with Tregs induction). 30 μM eplerenone suppressed the augmented proliferation rate at every time point ($^{\#\#}P < 0.01$), even down to the levels of CF proliferation in the absence of Tregs. **(C)** After 48 h of co-culture, proliferation of the CFs + Tregs cultures was significantly higher than that of the single cultures: OD values of CFs vs. CFs + Tregs were 3.91 ± 0.14 vs. 10.18 ± 0.03, while those of Tregs vs. Tregs + CFs were 2.07 ± 0.15 vs. 3.18 ± 0.68 (n = 8, both $^{**}P < 0.01$). **(D)** After 48-h of CFs + Tregs co-culture, the expression levels of collagen I, collagen III, and MMP-2 (by ELISA assay) were elevated by 2.34-, 2.46-, and 2.57-fold relative to the levels in the CFs cultured alone (CFs + Tregs vs. CFs, n = 8, $^{**}P < 0.01$), whereas they were suppressed to 33.92, 47.97, and 62.15% of these elevated levels by 30 μM eplerenone treatment (CFs + Tregs + EPL vs. CFs + Tregs, n = 8, $^{\#\#}P < 0.01$).

TABLE 2 | The proliferation of CFs over the time curve stimulated by Tregs in co-incubation by CCK-8 assay ($\bar{x} \pm s$, $n = 8$).

	OD value					
	0 h	**12 h**	**24 h**	**36 h**	**48 h**	**60 h**
CFs	0.19 ± 0.00	0.63 ± 0.01	1.30 ± 0.01	2.92 ± 0.02	3.91 ± 0.14	3.83 ± 0.01
CFs + Tregs	0.19 ± 0.00	1.35 ± 0.04**	4.81 ± 0.00**	8.36 ± 0.01**	10.18 ± 0.03**	10.11 ± 0.01**
CFs + Tregs + EPL	0.19 ± 0.00	0.82 ± 0.02##	1.26 ± 0.06##	3.18 ± 0.07##	4.13 ± 0.03##	4.15 ± 0.04##

***P < 0.01 for CFs + Tregs vs. CFs, ##P < 0.01 for CFs + Tregs + EPL vs. CFs + Tregs.*

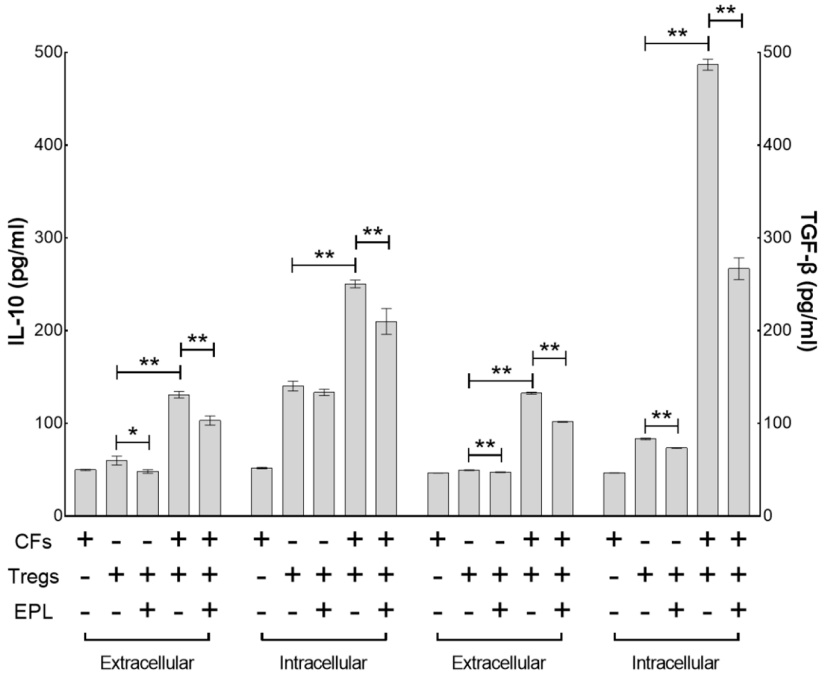

FIGURE 6 | Eplerenone primarily antagonizes the augmentation of intracellular TGF-β in Tregs co-cultured with CFs. ELISA assay demonstrates that co-culture of CFs with Tregs elevated the intracellular cytokines to a significantly higher degree than it did the extracellular cytokines after 48 h (Tregs + CFs vs. Tregs, $n = 8$, $P < 0.01$). Of the intracellular cytokines, TGF-β secretion (5.8-fold from 83.21 ± 0.82 to 486.85 ± 5.95) was elevated to a greater extent than IL-10 secretion (1.8-fold from 140.24 ± 5.30 to 250.42 ± 4.17), whereas there was no significant difference between the degree of elevation for the extracellular cytokines (2.7-fold from 49.54 ± 0.33 to 132.52 ± 1.08 for TGF-β and 2.2-fold from 59.98 ± 4.78 to 130.82 ± 3.54 for IL-10). Treatment with 30 μM eplerenone was shown to suppress intracellular TGF-β levels (45.2% suppression from 486.85 ± 5.95 to 266.80 ± 11.76) to a greater extent than intracellular IL-10 levels (16.2% suppression 250.42 ± 4.17 to 209.91 ± 14.01), whereas the extent of suppression of the extracellular cytokines levels by eplerenone did not differ significantly (23.3% suppression from 132.52 ± 1.08 to 101.60 ± 0.41 for TGF-β and 21.2% suppression from 130.82 ± 3.54 to 103.02 ± 4.99 for IL-10) (*$P < 0.05$, **$P < 0.01$).

calculation of the Van der Waals and the electrostatic terms, respectively. Docking simulations were performed using the Lamarckian genetic algorithm (LGA). The docking parameters set to perform each docking experiments was derived from 10 different runs. The best run coordinates of the compounds with enzyme were visualized and analyzed through AutoDock Tools for analysis of their mode of interaction with binding site residues.

Statistical Analysis

ELISA response standard curve equations were obtained using Curve Expert 1.3 software (Biological Software, MN, United States Re seller), and patch clamp data were exported by Igor Pro 5.05A software (WaveMetrics Inc., Lake Oswego, OR, United States). Except for patch-clamp data (presented as mean ± SE), all data are presented as mean ± SD. One-way ANOVA and subsequent Student's *t*-test (SPSS 22.0 statistical software, Chicago, IL, United States) were used to analyze comparative data, where differences with $P < 0.05$ indicated statistical significance.

RESULTS

Immune System Alterations in CHF Patients

Th17/Treg Ratio in CHF Patients

Flowcytometry assay showed the quantity of Th17 cells in CHF patients was significantly higher than that in healthy people (19.50 ± 1.81 vs. 13.94 ± 1.55%, $n = 25$ vs. 15, **$P < 0.01$), while

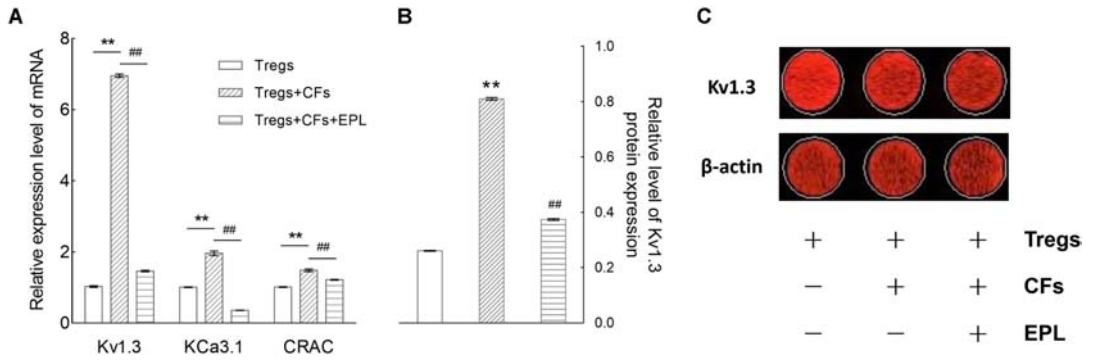

FIGURE 7 | Eplerenone antagonizes the augmentation of mRNA and protein expression of Kv1.3 channel (and/or other channels) by Tregs co-cultured with CFs. **(A)** After 48 h of co-culture, the mRNA expression levels (by RT-qPCR) of Kv1.3, KCa3.1, and CRAC (Ca^{2+} release-activated Ca^{2+}) channels were enhanced by 6.76-, 1.94-, and 1.46- fold, respectively (Tregs + CFs vs. Tregs, $n = 8$, $^{**}P < 0.01$), whereas treatment with 30 μM eplerenone suppressed these levels by 78.98, 81.68, and 17.93%, respectively (Tregs + CFs + EPL vs. Tregs + CFs, $n = 8$, $^{\#\#}P < 0.01$). Accordingly, the protein expression of Kv1.3 channels were detected shown in **(B)**. The relative levels of Kv1.3 channel protein expression in the Tregs + CFs group were increased by 2.11-fold relative to the Tregs group ($n = 8$, $^{**}P < 0.01$), and 30 μM eplerenone suppressed these elevated protein expression levels by 52.85% (Tregs + CFs + EPL vs. Tregs + CFs, $n = 8$, $^{\#\#}P < 0.01$). **(C)** Original images of Kv1.3 channel protein detecting by In-Cell Western Blotting.

TABLE 3 | The scores of docking and the residues.

	Binding Energy	H Bonds	Other residues
Eplerenone	−7.25	ARG119	PRO124; ILE125; ASP126
PAP-1	−4.98		ARG83; ARG88; TYR87; PHE134; LEU77; GLN136
Psora-4	−4.31		VAL121

the quantity of Treg cells in the CHF was significantly lower than that in the control (6.95 ± 1.65 vs. 14.85 ± 1.92%, $^{**}P < 0.01$) (**Figure 1**). Thereby the Th17/Treg ratio of the CHF patients was significantly higher than that of the healthy people (2.97 ± 0.86 vs. 0.95 ± 0.12, $^{**}P < 0.01$).

Plasma IL-10 and TGF-β in CHF Patients

ELISA assays showed IL-10 and TGF-β level in CHF patients plasma were both significantly elevated compared to the normal control ($^{**}P < 0.01$) (IL-10: 36.84 ± 5.42 vs. 22.21 ± 3.26 pg/mL, $n = 30$; TGF-β: 5131.25 ± 829.65 vs. 1775.83 ± 541.16 pg/mL, $n = 30$) (**Figure 2A**). Noteworthily, the elevation of IL-10 was significantly lower than the elevation of TGF-β ($^{**}P < 0.01$).

Kv1.3 Current of Treg Cell Is Elevated in the CHF Patients

By whole-cell patch clamp, treatment with 3 nM Psora-4, a Kv1.3 channel-sensitive inhibitor, was shown to suppress the *I–V* curve significantly with the ramp recording; at +40 mV. The current density was (106.11 ± 10.47) pA/pF at average for the control vs. (35.6 ± 3.51) pA/pF for the Psora-4 perfusion ($n = 15$, $^{**}P < 0.01$) (**Figure 2B**), indicating that the monitored line was indeed the Kv1.3 current.

The average Kv1.3 current density curve elicited from Tregs of CHF patients was significantly higher than that of Tregs from the normal control. At +40 mV in particular, the current density in the CHF patients was ∼2.4-fold higher than in the control group (259.57 ± 19.07 vs. 107.09 ± 9.74 pA/pF, $n = 22$ vs. 20, $^{**}P < 0.01$) (**Figure 2C**). The capacitance levels in control and CHF rat Treg cells were similar (1.11 ± 0.02 vs. 1.14 ± 0.01 pF in CHF vs. control, $P > 0.05$, not shown in the figure).

The relative expressions of mRNA and protein of Kv1.3 channels also risen remarkably in CHF patients compared to normal control (mRNA: 2.74 ± 0.57 vs. 1.00 ± 0.06, $n = 10$ vs. 6, $^{**}P < 0.01$; protein: 0.27 ± 0.01 vs. 0.14 ± 0.01, $n = 6$ vs. 6, $^{**}P < 0.01$) (**Figure 2D**).

Immune System Alterations in CHF Model Rats

Plasma Levels of Inflammatory Factors Are Significantly Elevated in CHF

The plasma levels of IL-1β, IL-6, IL-17, IFN-γ, and TNF-α in the CHF group were obviously higher than that in the control group ($n = 12$, $^{**}P < 0.01$), as determined by ELISA (**Figure 3**).

Eplerenone Suppresses the Kv1.3 Current, Which Is Elevated in the CHF Model

The original average Kv1.3 current density trace elicited from Tregs of the CHF rats was significantly higher than that of control rats, and 30 μM EPL furthermore markedly suppressed the ramp trace of the Kv1.3 current density in the CHF model rats ($n = 10$) (**Figure 4A**). At +40 mV in particular, the current density was ∼5-fold higher in the CHF rats than that in the control rats (44.63 ± 7.43 vs. 217.34 ± 11.74 pA/pF in control vs. CHF, $^{**}P < 0.01$); the suppression of the current density by EPL was calculated as ∼67% (72.13 ± 10.73 pA/pF, $n = 10$, $^{\#\#}P < 0.01$) (**Figure 4B**). The average capacitance value of Treg cells in the three groups were similar (1.38 ± 0.19, 1.23 ± 0.13, and 1.21 ± 0.12 pF in control, CHF and CHF + EPL, $n = 10$, $P > 0.05$, not shown in the figure).

Co-incubation of CFs With Tregs

Inhibition of Tregs and CF Proliferation by Eplerenone

After 48-h treatment of Tregs and CFs with eplerenone at 0.1, 0.3, 1, 3, 10, 30, and 100 μM ($n = 8$) (**Figure 5A**), cell viability of both cell types was inhibited in a concentration-dependent manner in accordance with the Hill equation: $y = \frac{ax^b}{c^b+x^b}$. The IC_{50}s for Tregs and CFs were calculated as 2.9 and 8.5 μM, respectively. At concentration of 30 μM, eplerenone suppressed cell viability by 82.77 and 17.94% in Tregs and CFs, respectively, after which the viabilities stabilized. Accordingly, 30 μM was chosen as the eplerenone dose for subsequent experiments.

Eplerenone Suppresses the Proliferation of CFs Stimulated by Co-incubation With Tregs

Tregs were shown to induce the proliferation of CFs in a time-dependent manner (CFs + Tregs vs. CFs, $n = 8$, $P < 0.001$ every 12 h) (**Table 2** and **Figure 5B**). The rate of proliferation in the CFs + Tregs group was ∼2.6-fold higher than that in the CFs group at 48 h (maximum proliferation was achieved with Tregs induction). Treatment with 30 μM eplerenone was shown to suppress the augmented proliferation rate at every time point ($n = 8$, $P < 0.001$), even down to the levels of CF proliferation in the absence of Tregs. After 48 h of co-culture, proliferation of the CFs + Tregs cultures was significantly higher than that of the single cultures: OD values of CFs vs. CFs + Tregs were 3.91 ± 0.14 vs. 10.18 ± 0.03, while those of Tregs vs. Tregs + CFs were 2.07 ± 0.15 vs. 3.18 ± 0.68 ($n = 8$, both $P < 0.001$) (**Figure 5C**).

Eplerenone Suppresses ECM Secretion From CFs Co-incubated With Tregs

Collagen I, collagen III, and MMP-2 are typical extracellular matrix (ECM) factors in the CF cultures, and were thus used to further evaluate CF proliferation. After 48h of CFs + Tregs

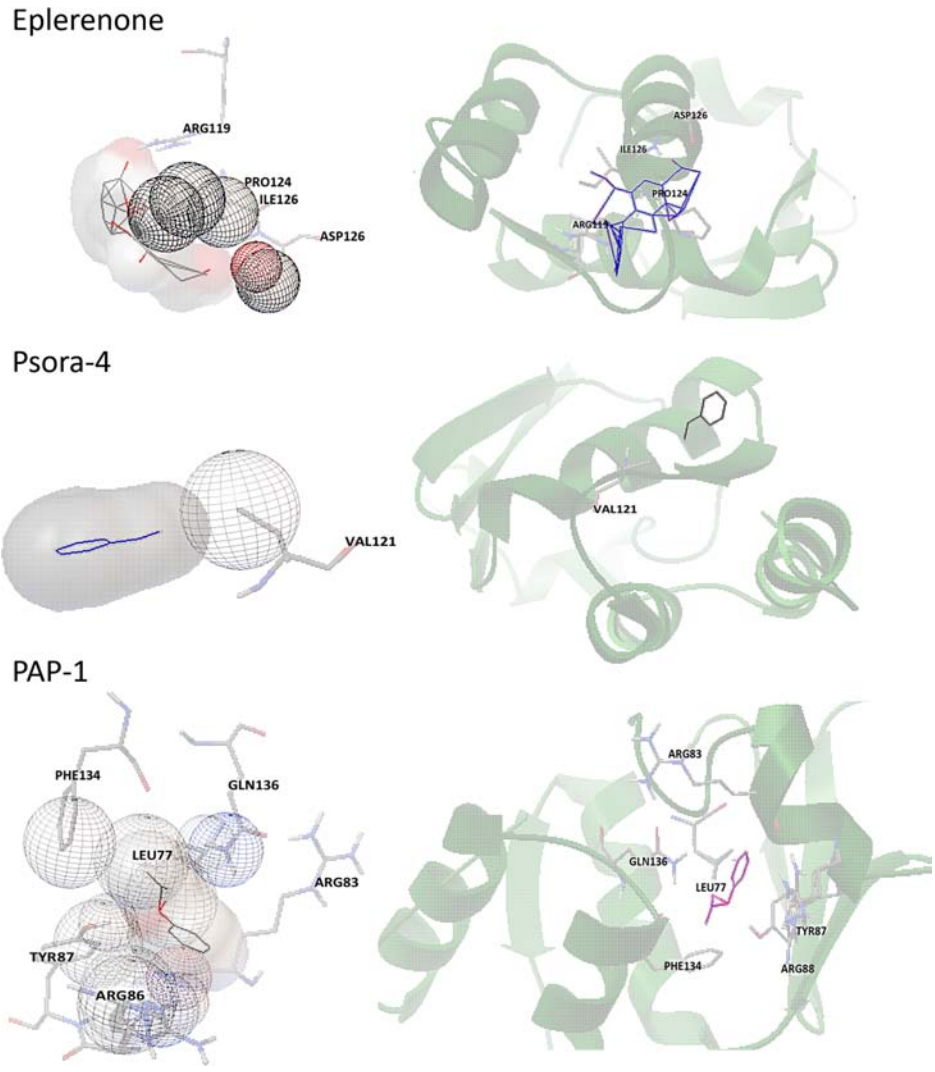

FIGURE 8 | Stereo view of important residues in Kv1.3. Protein is shown in transparent cartoon, ligands and important residues in sticks.

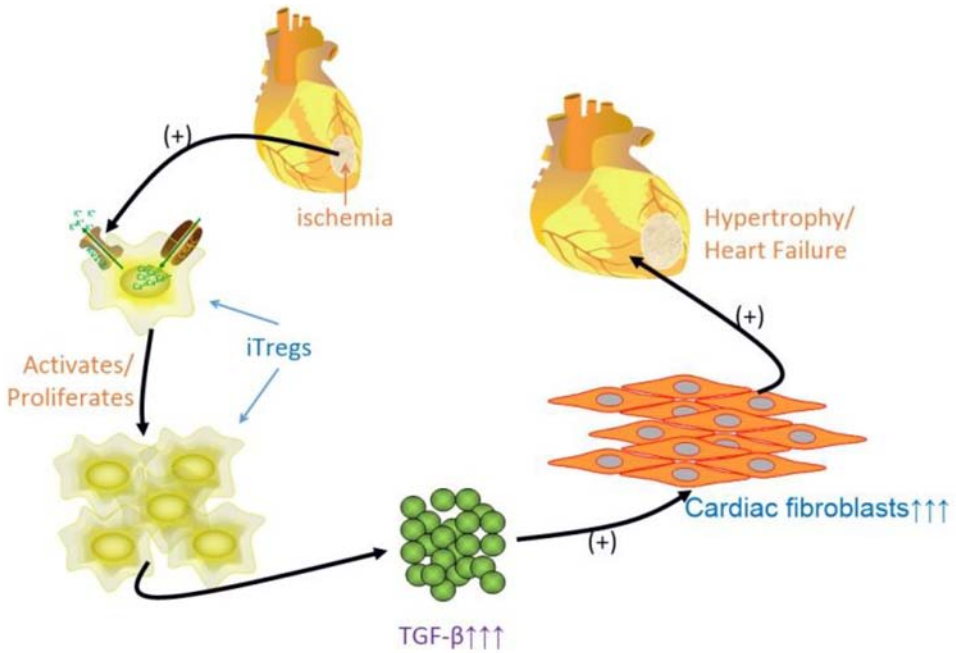

FIGURE 9 | Schematic graph of the idea of the article. Some inflammatory states of heart disease, i.e., ischemia, atherosclerosis, myocardial infarction, late stage of CHF, and etc., activate immuno-response, induced regulatory T lymphocytes (iTregs) is activated/proliferated by activating Kv1.3 channels to assist Ca^{2+} influx, and releasing much more TGF-β (less IL-10 relatively), which multiplies cardiac fibroblasts leading to cardiac fibrosis to process the hypertrophy, even to heart failure.

co-culture, the expression levels of collagen I, collagen III, and MMP-2 were elevated by 2.34-, 2.46-, and 2.57-fold relative to the levels in the CFs cultured alone (CFs + Tregs vs. CFs, $n = 8$, $P < 0.001$), whereas they were suppressed to 33.92, 47.97, and 62.15% of these elevated levels by 30 μM eplerenone treatment (CFs + Tregs + EPL vs. CFs + Tregs, $n = 8$, $P < 0.001$) (**Figure 5D**).

Eplerenone Primarily Antagonizes the Augmentation of Intracellular TGF-β in Tregs Co-cultured With CFs

Tregs primarily secrete TGF-β and IL-10 upon activation and/or proliferation. Co-culture of CFs with Tregs elevated the intracellular cytokines to a significantly higher degree than it did the extracellular cytokines after 48 h (Tregs + CFs vs. Tregs, $n = 8$, $P < 0.01$) (**Figure 6**). Of the intracellular cytokines, TGF-β secretion (5.8-fold from 83.21 ± 0.82 to 486.85 ± 5.95) was elevated to a greater extent than IL-10 secretion (1.8-fold from 140.24 ± 5.30 to 250.42 ± 4.17), whereas there was no significant difference between the degree of elevation for the extracellular cytokines (2.7-fold from 49.54 ± 0.33 to 132.52 ± 1.08 for TGF-β and 2.2-fold from 59.98 ± 4.78 to 130.82 ± 3.54 for IL-10). Treatment with 30 μM eplerenone was shown to suppress intracellular TGF-β levels (45.2% suppression from 486.85 ± 5.95 to 266.80 ± 11.76) to a greater extent than intracellular IL-10 levels (16.2% suppression 250.42 ± 4.17 to 209.91 ± 14.01), whereas the extent of suppression of the extracellular cytokines levels by eplerenone did not differ significantly (23.3% suppression from 132.52 ± 1.08 to 101.60 ± 0.41 for TGF-β and 21.2% suppression from 130.82 ± 3.54 to 103.02 ± 4.99 for IL-10).

Eplerenone Antagonizes the Augmentation of Kv1.3, KCa3.1, and CRAC Channel mRNA Expression by Tregs Co-cultured With CFs

After 48 h of co-culture, the mRNA expression levels of Kv1.3, KCa3.1, and CRAC (Ca^{2+} release-activated Ca^{2+}) channels were elevated by 6.76-, 1.94-, and 1.46-fold, respectively (Tregs + CFs vs. Tregs, $n = 8$, $P < 0.01$), whereas treatment with 30 μM eplerenone suppressed these levels by 78.98, 81.68, and 17.93%, respectively (Tregs + CFs + EPL vs. Tregs + CFs, $n = 8$, $P < 0.01$) (**Figure 7A**).

Eplerenone Antagonizes the Augmentation of Kv1.3 Channel Protein Expression by Tregs Co-cultured With CFs

The relative levels of Kv1.3 channel protein expression in the Tregs + CFs group were elevated by 2.11-fold relative to the Tregs group ($n = 8$, $P < 0.01$), and 30 μM eplerenone suppressed these elevated protein expression levels by 53.85% (Tregs + CFs + EPL vs. Tregs + CFs, $n = 8$, $P < 0.01$) (**Figures 7B,C**).

Eplerenone Has High Affinity With Kv1.3 Channels Protein

Comparing to the known selective Kv1.3 channels blockers (PAP-1 and Psora-4), the binding energy between Eplerenone and Kv1.3 channels is higher. Though with less binding site, the H bonds makes the binding more stabilized (**Table 3** and **Figure 8**).

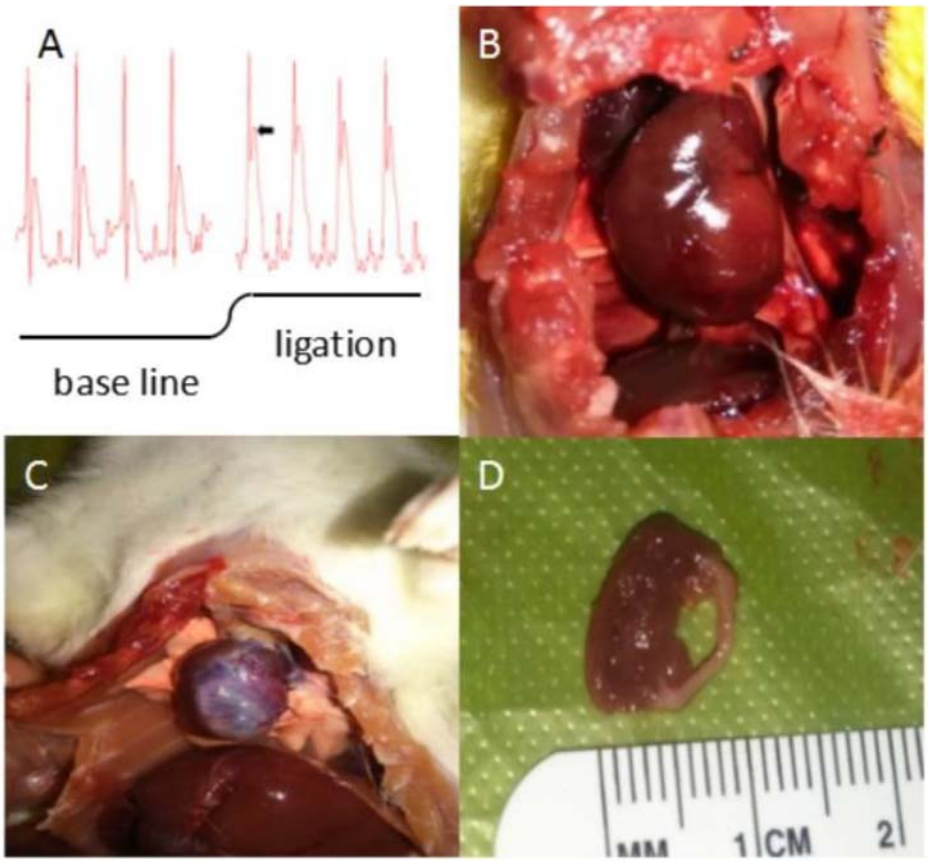

FIGURE 10 | Physical features of rat hearts after coronary artery ligation (CAL). **(A)** Classic significant S-T segment elevation (ΔS-T segment > 0.1 mV is the criteria for myocardial infarction) by ECG appeared immediately when the left anterior descending coronary artery was ligated. **(B)** Ischemic pale-turning at the local precordia was visible to the unaided eye after a few minutes of CAL. **(C)** After 10 weeks, the rat hearts exhibited different degrees of fibrosis. Large-scale cardiac fibrosis of praecordia was distinctly observed, even spreading to apex of the heart and the whole heart shrunk to smaller. **(D)** Dissection of the hearts into cross-sections revealed that the ventricular wall of the left heart was thinning, and myocardial tissue was replaced by fibrosis.

DISCUSSION

Extensive evidence demonstrates that immune activation and inflammation are the important pathophysiological mechanisms involved in heart failure. Neurohormonal activation is considered an important factor in causing inflammation and development of heart failure. It is well known that aldosterone can cause alterations in the cardiovascular system, such as fibrosis, cardiac remodeling and hypertrophy. Recently, many clinical trials confirmed that aldosterone is an independent pro-inflammatory factor in key organs (Gilbert and Brown, 2010; Brown, 2013) and activates the immune system by producing inflammatory mediators in the heart, endothelium, fibroblasts, and circulating cells (Kasal and Schiffrin, 2012) to promote the progress of heart failure.

T helper lymphocytes (Th) is the main effector cell type that mediates immune response, and a Th17/Treg imbalance is the manifestation of a series of inflammatory responses. Tregs make a difference in regulating the immune response. It was shown that the quantity of Th17 cell is elevated in the total blood of patients with CHF, whereas the quantity of Treg cell is reduced (Li et al., 2010); however, another clinical trial demonstrated that Th17 cells in total blood don't grow in patients with heart failure (Zhu et al., 2012), possibly due to a decay in Tregs and an increase in Th17/Treg ratio (Friedel and Todd, 1988). Therefore, the function of Treg cells in heart failure may be more significant than previously thought. A few studies and reviews reported that Tregs are the target in the protection of myocardial and vascular organ damage and remodeling process (Gilbert and Brown, 2010; Brown, 2013; Ramos et al., 2016). It's also has been hinted that intravenous Tregs can reverse myocardial fibrosis mediated by the secretion of IL-10 (Cao et al., 2013). In this study, patients with CHF showed markedly imbalance of Th17/Tregs ratio with significantly higher Th17 cells and lower Treg cells compared to the healthy volunteers. Furthermore, although the serum level of both IL-10 and TGF-β elevated significantly, the elevation of TGF-β was higher than that of IL-10. As we know, TGF-β is primarily secreted from Tregs but IL-10 is not. Therefore, our results suggest the proliferation of Tregs might not parallel the activation of Tregs.

In the context of the signaling pathway of T cell activation, it is acknowledged that Kv1.3 channels maintain the resting potential

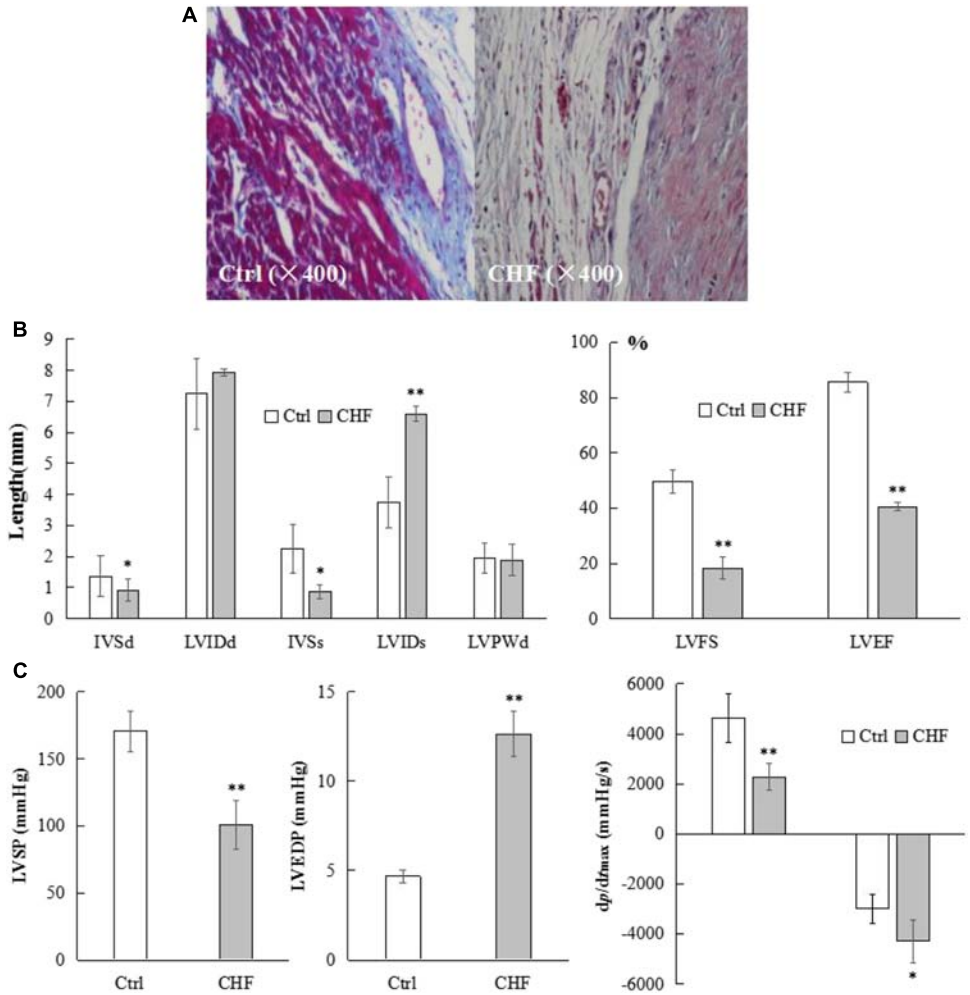

FIGURE 11 | Microscopic morphological, general structural and functional alterations in the heart of CHF model rats. **(A)** Microscopic view (400×) of representative myocytes in control and CHF by Masson staining (n = 10). Most myocytes in the control exhibited relatively clean and neatly ordered muscular stripes (red dyed) with less collagen fibers (blue dyed) and nuclei, whereas the CHF myocytes exhibited more messy, unordered, cord-like collagen fibers instead of stripes, where some collagen fibers were found to be wrapped together in masses, forming flakes. In the CHF rats, very few complete muscular fibers were identified under high magnification. **(B)** The histograms comparison of cardiac structure parameters in control and CHF rats (n = 25) measured by Doppler ultrasound. The IVSd and IVSs in the CHF group were thinner than those in the control group (*$P < 0.05$), while the LVIDs was significantly thicker in the CHF group than in the control group (**$P < 0.01$). The LVIDd did not differ between the two groups. The LVFS and LVEF values were lower in the rats with CHF than in the control rats (**$P < 0.01$). **(C)** The histograms comparison of hemodynamic parameters in control and CHF rats (n = 17) by right carotid artery catheterization into the left ventricle. LVSP, $+dp/dt_{max}$ and $-dp/dt_{max}$ in CHF group rats decreased significantly (*$P < 0.05$, **$P < 0.01$), whereas LVEDP in CHF group rats increased significantly (**$P < 0.01$), compared with the control group rats.

of T lymphocytes and enable T cells to be activated. When T lymphocytes are activated under inflammatory conditions, the KCa3.1 channels drive membrane potential downward to hyperpolarization, thereby promoting CRAC channels open to facilitate Ca^{2+} influx, and the resulting Ca^{2+} elevation initiates the transcription of various cytokines via calcium-dependent protein kinase to promote efficient immunity. The motility of Kv1.3 channels can be used as a marker of functional viability of T cells (Lopez-Sendon, 2013) and a therapeutic target in the prevention of immune diseases. Hence, the function of Kv1.3 channels on Tregs was detected by whole-cell patch clamp technique to evaluate the activation of Tregs. The Kv1.3 channel current density in the CHF patients was significantly higher than the healthy people. And the same increasing tendencies were found in the mRNA and protein expressions of Kv1.3 channels.

In this study, coronary artery ligation was used to establish a myocardial infarction model and animals were further subjected to exhausted swimming to accelerate CHF development. The model inclusion rate was ∼50%. Cardiac function and structure were assessed by catheterization, ultrasound, Masson staining, and BNP level measurements, all of which confirmed that the inclusive CHF model was consistent with the expected clinical indicators (see **Appendix**).

In the CHF model established in this study, IL-1β, 6, 17, IFN-γ, and TNF-α levels were all elevated, as expected. IL-1β, IFN-γ, and TNF-α are involved in almost all inflammatory processes. IL-6 participates in autoimmune diseases such as hepatitis and multiple sclerosis, the secretion of which could be induced by TNF-α. IL-17, only secreted by Th17 cells, acts as a unique inflammatory factor in chronic inflammatory diseases. In the present model of CHF, all the key cytokines were shown to highly express. The 10-week CHF model rats likely still sustained the inflammatory status, and elevation of both IL-6 and IL-17 may therefore have facilitated the differentiation of $CD4^+$ T lymphocytes to Th17 cells.

In the CHF model rats of this study, the Kv1.3 current density of Tregs was ∼5-fold higher than that of Tregs in the control rats. Consistent with the corresponding *in vitro* results of patients, it seems that Tregs were also activated in the CHF model, and 30 μM eplerenone could suppressed the current density in CHF model rats by ∼66.8%, which surprised us that a selective aldosterone inhibitor might directly inhibit Kv1.3 channels function since the suppressant alteration occurred within short period of time (∼15 min). In addition, docking calculation confirmed eplerenone has a higher affinity even than the selective Kv1.3 channel blockers, which suggests a direct action of eplerenone on Kv1.3 channel. To further confirm it with direct evidence, we need an appropriate cell line which possesses more Kv1.3 channels but without aldosterone receptors. Unfortunately, no such cell line was found until now.

To explain whether Tregs induce cardiac fibrosis or reverse cardiac fibrosis, we conducted the co-incubation of Tregs and cardiac fibroblasts. The features of two cells are different, Tregs are suspension cells, while cardiac fibroblasts are adherent cells, so after co-incubation the two cells could be easier to separate and be accurately detected with relative indicators. The discussion as following:

In the CFs and Tregs co-culture system used in this study, the proliferation rates of both cell types were significantly induced by each other; however, CF proliferation was induced by Tregs to a greater extent than Tregs by CF (160.6% vs. 53.4% proliferation rates). After 48 h of co-culture of CFs with Tregs, extracellular TGF-β levels were shown to elevate to a greater extent than that of IL-10, and the fold change of intracellular TGF-β augmentation (5.8) was significantly higher than that of IL-10 (1.8). Therefore, the proliferation of CFs induced by Tregs is assumed to be predominantly caused by TGF-β secretion.

Although TGF-β and IL-10 secretion was little suppressed by eplerenone treatment in Tregs cultured alone, intracellular TGF-β (45.2% diminished) and lesser degree of intracellular IL-10 (16.2% diminished) secretion was significantly suppressed by eplerenone treatment in Tregs co-incubated with CFs. The degree of suppression of extracellular TGF-β (23.3% diminished) was comparative to that of extracellular IL-10 (21.2% diminished). The proposed mechanism for the observed suppression is that eplerenone antagonizes adoptive Tregs (proliferated Tregs by autocrine secretion) rather than natural ones through inhibition of Kv1.3 channels, which potentially act as markers or targets of activation and/or proliferation of adoptive Tregs.

In the 48 h co-culture system described here, the expression of Treg channels were all elevated, furthermore, the Kv1.3 channels were most significantly elevated (almost sevenfold for mRNA and threefold for protein alterations).

The effect of eplerenone on the proliferation of CFs and Tregs indicated a dose-dependent inhibition. At 30 μM, eplerenone markedly suppressed Tregs proliferation; significantly down-regulated the augmented secretion of ECMs from CFs induced by co-incubation of Tregs.

CONCLUSION

Late-stage CHF is characterized by constant activation of the immune system, in which adoptive Tregs (induced Tregs, iTregs) are activated and/or induced to proliferate by Kv1.3 channel activation, subsequently through autocrine secretion or paracrine secretion of predominantly TGF-β and to a much lesser extent IL-10 to stimulate cardiac fibroblast proliferation (cardiac fibrosis), thereby facilitating the progression to heart failure (**Figure 9**). The anti-inflammatory effect of eplerenone on the CHF process may occur via antagonization of Kv1.3 channels in Tregs, suppression of Tregs activation/proliferation. Therefore, eplerenone could play an alleviation role to cardiac fibrosis during the development of CHF.

ETHICS STATEMENT

This study was carried out in accordance with the recommendations of Measures for the Ethical Review of Biomedical Research Involving Human Subjects, China National Standardization Administration Committee. The protocol was approved by the Ethics Committee of First Affiliated Hospital of Xinjiang Medical University. All subjects gave written informed consent in accordance with the Declaration of Helsinki. This study was carried out in accordance with the recommendations of Laboratory Animals—Guideline of Welfare and Ethics, China National Standardization Administration Committee. The protocol was approved by the Ethics Committee of First Affiliated Hospital of Xinjiang Medical University.

AUTHOR CONTRIBUTIONS

All persons who have made substantial contributions to the work reported in the manuscript. The listed authors agree to be accountable for all aspects of the work in ensuring that questions related to the accuracy or integrity of any part of the work are appropriately investigated and resolved. And individual contributes to the manuscript cover as follows: L-FC, QX, and BZ conception or design of the work. P-PS, C-JL, BZ, S-HL and YW data collection. L-FC, QX, and BZ data analysis and interpretation. L-FC drafted the article. QX, BZ, and ZS critical revision of the article. P-PS, C-JL, QX, BZ, S-HL, YW, ZS, and L-FC final approval of the version to be published.

FUNDING

This research was supported by National Natural Science Foundation of China, Project No. 81360491 (L-FC), Title: Immunoregulatory mechanisms of Aldosterone receptor antagonists on Th17/Treg balance based on T lymphocytes Kv1.3 channels during chronic heart failure, 2014/01-2017/12, ¥0.49 million.

ACKNOWLEDGMENTS

The authors thank for the support of the lab tutors in Central Lab Platform of 2011 Collaborative Innovation Building, in the 5th-floor Sharing Platform of the First Affiliated Hospital's Science and Technology Building in Xinjiang Medical University and in Key Laboratory of Xinjiang Phytomedicine Resource and Utilization of Ministry of Education in Shihezi University.

REFERENCES

Barry, S. P., Ounzain, S., McCormick, J., Scarabelli, T. M., Chen-Scarabelli, C., Saravolatz, L. I., et al. (2013). Enhanced IL-17 signalling following myocardial ischaemia/reperfusion injury. *Int. J. Cardiol.* 163, 326–334. doi: 10.1016/j.ijcard.2011.08.849

Bhuyan, R., and Seal, A. (2015). Molecular dynamics of Kv1.3 ion channel and structural basis of its inhibition by scorpion toxin-OSK1 derivatives. *Biophys. Chem.* 203–204, 1–11. doi: 10.1016/j.bpc.2015.04.004

Borthwick, L. A., Wynn, T. A., and Fisher, A. J. (2013). Cytokine mediated tissue fibrosis. *Biochim. Biophys. Acta* 1832, 1049–1060. doi: 10.1016/j.bbadis.2012.09.014

Brown, N. J. (2013). Contribution of aldosterone to cardiovascular and renal inflammation and fibrosis. *Nat. Rev. Nephrol.* 9, 459–469. doi: 10.1038/nrneph.2013.110

Cao, Y., Xu, W., and Xiong, S. (2013). Adoptive transfer of regulatory T cells protects against Coxsackievirus B3-induced cardiac fibrosis. *PLoS One* 8:e74955. doi: 10.1371/journal.pone.0074955

Chandy, K. G., and Norton, R. S. (2017). Peptide blockers of Kv1.3 channels in T cells as therapeutics for autoimmune disease. *Curr. Opin. Chem. Biol.* 38, 97–107. doi: 10.1016/j.cbpa.2017.02.015

Friedel, H. A., and Todd, P. A. (1988). Nabumetone. A preliminary review of its pharmacodynamic and pharmacokinetic properties, and therapeutic efficacy in rheumatic diseases. *Drugs* 35, 504–524.

Frieler, R. A., and Mortensen, R. M. (2015). Immune cell and other noncardiomyocyte regulation of cardiac hypertrophy and remodeling. *Circulation* 131, 1019–1030. doi: 10.1161/circulationaha.114.008788

Gilbert, K. C., and Brown, N. J. (2010). Aldosterone and inflammation. *Curr. Opin. Endocrinol. Diabetes Obes.* 17, 199–204.

Gilhar, A., Schrum, A. G., Etzioni, A., Waldmann, H., and Paus, R. (2016). Alopecia areata: animal models illuminate autoimmune pathogenesis and novel immunotherapeutic strategies. *Autoimmun. Rev.* 15, 726–735. doi: 10.1016/j.autrev.2016.03.008

Heggermont, W. A., Goethals, M., Dierckx, R., Verstreken, S., Bartunek, J., and Vanderheyden, M. (2016). Should MRAs be at the front row in heart failure? A plea for the early use of mineralocorticoid receptor antagonists in medical therapy for heart failure based on clinical experience. *Heart Fail. Rev.* 21, 699–701. doi: 10.1007/s10741-016-9583-2

Hofmann, U., and Frantz, S. (2013). How can we cure a heart "in flame"? A translational view on inflammation in heart failure. *Basic Res. Cardiol.* 108:356. doi: 10.1007/s00395-013-0356-y

Kasal, D. A., and Schiffrin, E. L. (2012). Angiotensin II, aldosterone, and anti-inflammatory lymphocytes: interplay and therapeutic opportunities. *Int. J. Hypertens.* 2012:829786. doi: 10.1155/2012/829786

Li, N., Bian, H., Zhang, J., Li, X., Ji, X., and Zhang, Y. (2010). The Th17/Treg imbalance exists in patients with heart failure with normal ejection fraction and heart failure with reduced ejection fraction. *Clin. Chim. Acta* 411, 1963–1968. doi: 10.1016/j.cca.2010.08.013

Lopez-Sendon, J. (2013). To BNP or not to BNP. *Eur. Heart J.* 34, 2498–2500. doi: 10.1093/eurheartj/eht262

Meng, X., Yang, J., Dong, M., Zhang, K., Tu, E., Gao, Q., et al. (2016). Regulatory T cells in cardiovascular diseases. *Nat. Rev. Cardiol.* 13, 167–79. doi: 10.1038/nrcardio.2015.169

Meng, X. M., Nikolic-Paterson, D. J., and Lan, H. Y. (2016). TGF-beta: the master regulator of fibrosis. *Nat. Rev. Nephrol.* 12, 325–338. doi: 10.1038/nrneph.2016.48

Orban, C., Bajnok, A., Vasarhelyi, B., Tulassay, T., and Toldi, G. (2014). Different calcium influx characteristics upon Kv1.3 and IKCa1 potassium channel inhibition in T helper subsets. *Cytometry A* 85, 636–641. doi: 10.1002/cyto.a.22479

Ponikowski, P., Voors, A. A., Anker, S. D., Bueno, H., Cleland, J. G.,Coats, A. J., et al. (2016). ESC guidelines for the diagnosis and treatment of acute and chronic heart failure: the task force for the diagnosis and treatment of acute and chronic heart failure of the European society of cardiology (ESC). Developed with the special contribution of the heart failure association (HFA) of the ESC. *Eur. J. Heart Fail.* 18, 891–975.

Prabhu, S. D., and Frangogiannis, N. G. (2016). The biological basis for cardiac repair after myocardial infarction: from inflammation to fibrosis. *Circ. Res.* 119, 91–112. doi: 10.1161/circresaha.116.303577

Perez-Garcia, M. T., Cidad, P., and Lopez-Lopez, J. R. (2018). The secret life of ion channels: Kv1.3 potassium channels and proliferation. *Am. J. Physiol. Cell Physiol.* 314, C27–C42. doi: 10.1152/ajpcell.00136.2017

Ramos, G., Hofmann, U., and Frantz, S. (2016). Myocardial fibrosis seen through the lenses of T-cell biology. *J. Mol. Cell. Cardiol.* 92, 41–45. doi: 10.1016/j.yjmcc.2016.01.018

Ren, X., Zhang, F., Zhao, M., Zhao, Z., Sun, S., Fraidenburg, D. R., et al. (2017). Angiotensin-(1-7) in paraventricular nucleus contributes to the enhanced cardiac sympathetic afferent reflex and sympathetic activity in chronic heart failure rats. *Cell. Physiol. Biochem.* 42, 2523–2539. doi: 10.1159/000480214

Seferovic, P. M., Pelliccia, F., Zivkovic, I., Ristic, A., Lalic, N., Seferovic, J., et al. (2015). Mineralocorticoid receptor antagonists, a class beyond spironolactone–focus on the special pharmacologic properties of eplerenone. *Int. J. Cardiol.* 200, 3–7. doi: 10.1016/j.ijcard.2015.02.096

Sun, L., Fu, J., and Zhou, Y. (2017). Metabolism controls the balance of Th17/T-regulatory cells. *Front. Immunol.* 8:1632. doi: 10.3389/fimmu.2017.01632

Tang, T. T., Ding, Y. J., Liao, Y. H., Yu, X., Xiao, H., Xie, J. J., et al. (2010). Defective circulating CD4CD25+Foxp3+CD127(low) regulatory T-cells in patients with chronic heart failure. *Cell. Physiol. Biochem.* 25, 451–458. doi: 10.1159/000303050

Wang, J., and Xiang, M. (2013). Targeting potassium channels Kv1.3 and KC a 3.1: routes to selective immunomodulators in autoimmune disorder treatment? *Pharmacotherapy* 33, 515–528. doi: 10.1002/phar.1236

Wang, R. E., Wang, Y., Zhang, Y., Gabrelow, C., Zhang, Y., Chi, V., et al. (2016). Rational design of a Kv1.3 channel-blocking antibody as a selective immunosuppressant. *Proc. Natl. Acad. Sci. U.S.A.* 113, 11501–11506. doi: 10.1073/pnas.1612803113

Wei, L. (2011). Immunological aspect of cardiac remodeling: T lymphocyte subsets in inflammation-mediated cardiac fibrosis. *Exp. Mol. Pathol.* 90, 74–78. doi: 10.1016/j.yexmp.2010.10.004

Zhang, Q., Gou, F., Zhang, Y., He, Y., He, J., Peng, L., et al. (2016). Potassium channel changes of peripheral blood T-lymphocytes from kazakh hypertensive patients in Northwest China and the inhibition effect towards potassium channels by telmisartan. *Kardiol. Pol.* 74, 476–488. doi: 10.5603/KP.a2015.0210

Zhao, N., Dong, Q., Fu, X. X., Du, L. L., Cheng, X., Du, Y. M., et al. (2014). Acacetin blocks kv1.3 channels and inhibits human T cell activation. *Cell. Physiol. Biochem.* 34, 1359–1372. doi: 10.1159/000366343

Zhu, Z. F., Li, J. J., Liu, J., Tang, T. T., Ding, Y. J., Liao, Y. H., et al. (2012). Circulating Th17 cells are not elevated in patients with chronic heart failure. *Scand. Cardiovasc. J.* 46, 295–300. doi: 10.3109/14017431.2012.699096

Conflict of Interest Statement: The authors declare that the research was conducted in the absence of any commercial or financial relationships that could be construed as a potential conflict of interest.

APPENDIX

Rat Model of CHF: Confirmation

Physical Features of Rat Hearts After Coronary Artery Ligation

Following successful ligation of the left anterior descending coronary artery in rats, ischemic S-T segment elevation was determined by ECG, ischemic pale-turning at the local precordia was visible to the unaided eye, and a decreased heart rate and a weak heartbeat were observed. After 10 weeks, the rat hearts exhibited different degrees of fibrosis. Dissection of the hearts into cross-sections revealed that the ventricular wall of the left heart was thinning, and myocardial tissue was replaced by fibrosis (**Figure 10**).

Microscopic Morphological Examination of Hearts in CHF Status

Approximately 30% of the rats established for CHF model died, where death occurred mainly during the 1st day after ligation (∼5% died during swimming). Microscopic assessment ($n = 10$) of cardiac myocytes by Masson staining and the use of different magnifications revealed that most myocytes in the control animals exhibited relatively clean and neatly ordered muscular stripes (red dyed) with less collagen fibers (blue dyed) and nuclei, whereas the CHF myocytes exhibited more messy, unordered, cord-like collagen fibers instead of stripes, where some collagen fibers were found to be wrapped together in masses, forming flakes. In the CHF rats, very few complete muscular fibers were identified under high magnification (**Figure 11A**).

Cardiac Structure Parameters in CHF Measured by Doppler Ultrasound

The IVSd and IVSs in the CHF group were thinner than those in the control group ($n = 25$, $^{*}P < 0.05$), while the LVIDs was significantly thicker in the CHF group than in the control group ($n = 25$, $^{**}P < 0.01$). The LVIDd did not differ between the two groups ($n = 25$). The LVFS and LVEF values were lower in the rats with CHF than in the control rats ($n = 25$, $^{**}P < 0.01$) (**Figure 11B**).

Hemodynamic Parameters During Heart Failure by Right Carotid Artery Catheterization Into the Left Ventricle

Compared with the corresponding parameters in the control group, the left ventricular systolic pressure (LVSP) and the maximum rate of rise/drop of left ventricular pressure ($\pm dp/dt_{max}$) in the rats with CHF decreased ($n = 17$, $^{*}P < 0.05$, $^{**}P < 0.01$), whereas the left ventricular end-dilating pressure (LVEDP) increased ($n = 17$, $^{**}P < 0.01$). There was no statistically significant difference in heart rates between the control and CHF rats ($n = 17$, 367.42 ± 18.64 vs. 372.19 ± 16.73) (**Figure 11C**).

Plasma BNP Levels Were Significantly Elevated in CHF Rats

Plasma BNP levels in the control and CHF groups were 378.54 ± 13.72 and 572.63 ± 21.86 ng/mL, respectively, demonstrating a significant increase ($n = 19$, $^{**}P < 0.01$) 6 weeks after the ligation of the coronary artery.

frontiers in Physiology

MINI REVIEW
published: 07 August 2018
doi: 10.3389/fphys.2018.01081

Caveolae-Specific CaMKII Signaling in the Regulation of Voltage-Dependent Calcium Channel and Cardiac Hypertrophy

*Shota Tanaka, Yasushi Fujio and Hiroyuki Nakayama**

Laboratory of Clinical Science and Biomedicine, Graduate School of Pharmaceutical Sciences, Osaka University, Osaka, Japan

Cardiac hypertrophy is a major risk for the progression of heart failure; however, the underlying molecular mechanisms contributing to this process remain elusive. The caveolae microdomain plays pivotal roles in various cellular processes such as lipid homeostasis, signal transduction, and endocytosis, and also serves as a signaling platform. Although the caveolae microdomain has been postulated to have a major contribution to the development of cardiac pathologies, including cardiac hypertrophy, recent evidence has placed this role into question. Lack of direct evidence and appropriate methods for determining activation of caveolae-specific signaling has thus far limited the ability to obtain a definite answer to the question. In this review, we focus on the potential physiological and pathological roles of the multifunctional kinase Ca^{2+}/calmodulin-dependent kinase II and voltage-dependent L-type calcium channel in the caveolae, toward gaining a better understanding of the contribution of caveolae-based signaling in cardiac hypertrophy.

Keywords: caveolae, caveolin, CaMKII, L-type calcium channel, cardiac hypertrophy

OPEN ACCESS

Edited by:
Alexey V. Glukhov, University of Wisconsin System, United States

Reviewed by:
Di Lang, University of Wisconsin-Madison, United States
Jonathan Jaseth Hernandez, University of Michigan, United States

***Correspondence:**
Hiroyuki Nakayama
nakayama@phs.osaka-u.ac.jp

Specialty section:
This article was submitted to Cardiac Electrophysiology, a section of the journal Frontiers in Physiology

Received: *30 April 2018*
Accepted: *19 July 2018*
Published: *07 August 2018*

Citation:
Tanaka S, Fujio Y and Nakayama H (2018) Caveolae-Specific CaMKII Signaling in the Regulation of Voltage-Dependent Calcium Channel and Cardiac Hypertrophy. Front. Physiol. 9:1081. doi: 10.3389/fphys.2018.01081

INTRODUCTION

Caveolae are unique flask-like membrane invaginations of 50–80 nm in diameter, which are enriched in cholesterol and sphingolipids (Shaul and Anderson, 1998; Parton and Simons, 2007). Currently, caveolae are considered to be involved in various cellular functions such as lipid homeostasis, signal transduction, endocytosis, and transcytosis (Cheng and Nichols, 2016). The structure of caveolae is supported by two major component proteins: caveolins and cavins (Rothberg et al., 1992; Hill et al., 2008). Owing to their specific lipid composition, caveolae are highly concentrated in multiple signaling molecules, including receptors, kinases, and ion channels. Those include endothelial nitric oxide synthase (Garcia-Cardena et al., 1997), insulin (Nystrom et al., 1999), epidermal growth factor (Couet et al., 1997b), transforming growth factor-beta (Strippoli et al., 2015), P2X7 receptor (Gangadharan et al., 2015), and G-protein coupling signaling molecules (Insel et al., 2005). Thus, the caveolae are considered to function as a signaling platform to facilitate efficient and specific cellular responses against stress (Razani et al., 2002; Cohen et al., 2004; Harvey and Calaghan, 2012). However, determination of the specific physiological properties of caveolae signaling has been challenging due to the lack of efficient tools for direct visualization of kinase activation inside the caveolae. Understanding these signaling mechanisms

of the caveolae can help to gain insight into their role in pathological mechanisms, particularly with regard to the contribution of cardiac hypertrophy, which remains controversial. Here, we review recent evidence on the signaling pathways and related molecules in the caveolae microdomain and their relation to cardiac pathogenesis, with a particular focus on Ca^{2+}/calmodulin-dependent kinase II (CaMKII) and voltage-dependent L-type calcium channel (LTCC). This review can help to highlight targets of research focus and specific questions to tackle toward gaining a better understanding of the molecular mechanisms linking caveolae signaling and heart health, toward establishing new therapeutic strategies.

CAVEOLAE MICRODOMAIN AND SIGNAL TRANSDUCTION

There are two types of structural proteins in caveolae: caveolins and cavins. Caveolin is comprised of three isoforms, caveolin-1, caveolin-2, and caveolin-3 (Rothberg et al., 1992; Scherer et al., 1996; Tang et al., 1996), with specific cellular distributions. For instance, caveolin-1 is dominantly expressed in endothelial cells, whereas caveolin-3 shows abundant expression in skeletal muscle cells and cardiomyocytes (Tang et al., 1996). These isoforms contain a common peptide sequence constituted by eight amino acids localized in the N-terminal cytosolic oligomerization domain (Tang et al., 1996). As a monomer, caveolin is comprised of three domains, oligomerization domain localized in N-terminus, caveolin scaffolding domain (CSD), and intramembrane domain in C-terminal part of the protein. Caveolin is inserted into the plasma membrane through intramembrane domain and CSD. Caveolin monomers assemble and form a oligomer, and contribute to caveolae formation (Sonnino and Prinetti, 2009). The CSD directly binds to a putative corresponding caveolin binding domain (CBD) identified in a number of signaling effectors localized in caveolae (Song et al., 1996; Nystrom et al., 1999; Kirkham et al., 2008; Taira et al., 2011). Couet et al. (1997a) identified a peptide sequence "RNVPPIFNDVYWIAF" as a CBD, which strongly binds to the CSD of caveolin 1 or caveolin 3. Currently, the physiological implication of the binding between CSD and CBD remains controversial (Collins et al., 2012). However, it is considered that CBD-fused protein binds to caveolin and demonstrates a specific localization in caveolae (Makarewich et al., 2012). Caveolin deficiency in a genetically engineered mouse model results in loss of the caveolae structure, indicating that caveolin is indispensable for the formation of caveolae (Park et al., 2002). Cavin contains four isoforms comprised of cavin-1 or polymerase I transcript factor (PTRF) (Hill et al., 2008), cavin-2 or serum deprivation protein response (SDPR) (Hansen et al., 2009), cavin-3 or SDR-related gene product that binds to C kinase (SRBC) (McMahon et al., 2009), and cavin-4 or muscle-related coiled-coiled protein (MURC) (Bastiani et al., 2009). Similar to caveolins, the cavin protein family shows a specific cellular distribution, and cavin-4 is thought to be a muscle-specific isoform. Cavin-1 is required for caveolae assembly and regulates the functions of caveolae by determining the localization of activated receptors (Li et al., 2014; Moon et al., 2014). In contrast, cavin-4 is dispensable for caveolae formation in cardiomyocytes, whereas it facilitates ERK1/2 recruitment to the caveolae and supports effective α1-andrenic receptor (AR) signaling activation in the development of cardiomyocyte hypertrophy (Ogata et al., 2014).

MICRODOMAIN SIGNALING AND CARDIAC HYPERTROPHY

Cardiac hypertrophy is one of the predominant risks of heart failure (Lloyd-Jones et al., 2002). The development of cardiac hypertrophy is governed by multiple intracellular protein signaling cascades from the plasma membrane to nuclei (Heineke and Molkentin, 2006). Subcellular compartmentalization is considered to allow signaling-related proteins to carry out multiple biological functions using a relatively small number of membrane receptors. However, the precise contribution of microdomain signaling in cardiomyocyte hypertrophy remains elusive. Horikawa et al. (2011) reported that caveolin-3 overexpression in the mouse heart attenuates cardiac hypertrophy via upregulation of natriuretic peptide, suggesting the involvement of caveolin-dependent signaling in the development of myocyte hypertrophy. Balijepalli et al. (2006) reported that ARs and a component of the LTCC exist in caveolae microdomains. Ca^{2+}-dependent signaling molecules such as calcineurin and CaMKII play vital roles in the development of cardiac hypertrophy, and activation of these molecules is associated with LTCC activity (Anderson et al., 2011; Chen et al., 2011). Makarewich et al. (2012) further demonstrated that caveolae-targeted inhibition of the LTCC mediates the attenuation of calcineurin activation induced by pacing stimulation without affecting Ca^{2+} influxes and transient in whole cells (Makarewich et al., 2012). To inhibit Ca^{2+} influxes in caveolae, they generated a fusion protein comprised of the caveolin-binding domain and Rem protein, which specifically inhibits LTCC activity. They found that caveolae-localized LTCCs are not involved in excitation-contraction coupling or the regulation of Ca^{2+}, which governs contractility in isolated cardiomyocytes. However, the same group failed to demonstrate similar effects in the mouse heart in which pressure-overload was applied to a genetically engineered model expressing the fused Rem protein with the caveolin-binding domain (Correll et al., 2017). These results indicated that caveolae-related calcineurin/NFAT signaling alone is not sufficient for the development of cardiac hypertrophy.

CaMKII IN THE HEART

CaMKII is a serine-threonine (Ser/Thr) kinase that is activated in a Ca^{2+}/calmodulin-dependent manner. The activation of CaMKII is also regulated by autophosphorylation (Hudmon and Schulman, 2002), oxidation (Erickson et al., 2011), and glycosylation (Erickson et al., 2013). CaMKII phosphorylates a vast number of substrates such as ion channels, calcium handling

proteins, and transcription factors (Anderson et al., 2011). Activation of CaMKII in the heart has been observed in both experimental models of cardiac hypertrophy and dysfunction as well as in patients suffering from heart failure (Zhang et al., 2003; Sossalla et al., 2010). Genetic ablation of dominant CaMKII isoforms in the heart attenuates cardiac hypertrophy or the transition to cardiac dysfunction after pressure overload (Zhang et al., 2003; Backs et al., 2009; Ling et al., 2009). Thus, CaMKII is considered to play a pivotal role in the development of cardiac hypertrophy and in the transition from the adaptive responses to heart failure (Swaminathan et al., 2012). In addition, the location of CaMKII activation is critical for its biological effects (Mishra et al., 2011). Two isoforms of CaMKII, CaMKIIδ, and CaMKIIγ, are mainly expressed in the heart, and the splicing isoform CaMKIIδ shows a unique subcellular localization. Such differential localization of CaMKII activation has been demonstrated to lead to a distinct intracellular function and cardiac phenotype (Zhang et al., 2002, 2003). Moreover, the cardiac overexpression of the cytosolic CaMKIIδ_C isoform in mice impairs excitation-contraction coupling (Zhang et al., 2003), whereas activation of the nuclear isoform CaMKIIδ_B mediates hypertrophic gene induction (Zhang et al., 2002). Further, the mitochondrial inhibition of CaMKII was shown to attenuate necrotic cell death (Joiner et al., 2012). Collectively, these findings indicate that the subcellular localization of CaMKII determines its biological effect based on the availability of substrate molecules, and is closely related to cardiac pathogenesis (Mishra et al., 2011). However, the specific biological role of CaMKII in the caveolae microdomain remains to be elucidated. In particular, deciphering its role in the membrane, as central platform for signal transduction, is required to gain a better understanding of its contribution to cardiac hypertrophy.

ASSESSMENT OF CaMKII ACTIVATION IN THE CAVEOLAE MICRODOMAIN USING A PHOSPHOR-PEPTIDE TAG

One of the major obstacles in determining the precise pathophysiological role of CaMKII in the caveolae microdomain is the lack of efficient and simple methodology to assess microdomain-specific activation of the kinase. Conventionally, the activation of a kinase is determined biochemically by detecting the phosphorylation of its specific substrate using a radioisotope or fluorescence from a whole cell lysate. However, these methods are not suitable for the assessment of microdomain-specific signaling, since fraction preparation is complicated and time-consuming. Alternatively, the detection of phosphorylation using a phosphor-specific antibody is a simple, useful, and reliable method. The detection of mitogen-activated protein kinases (MAPKs) such as ERK and p38 MAPK is a representative example of the application of phosphor-specific antibodies for assessing signaling pathway activation.

We recently developed a novel tool to examine the caveolae-specific activation of CaMKII using a fusion protein comprising 22 amino acids of the cytosolic domain of phospholamban (PLN) fused to caveolin-3 (**Figure 1**) (Tonegawa et al., 2017). PLN is a 52-amino acid phospho-protein anchoring the membrane

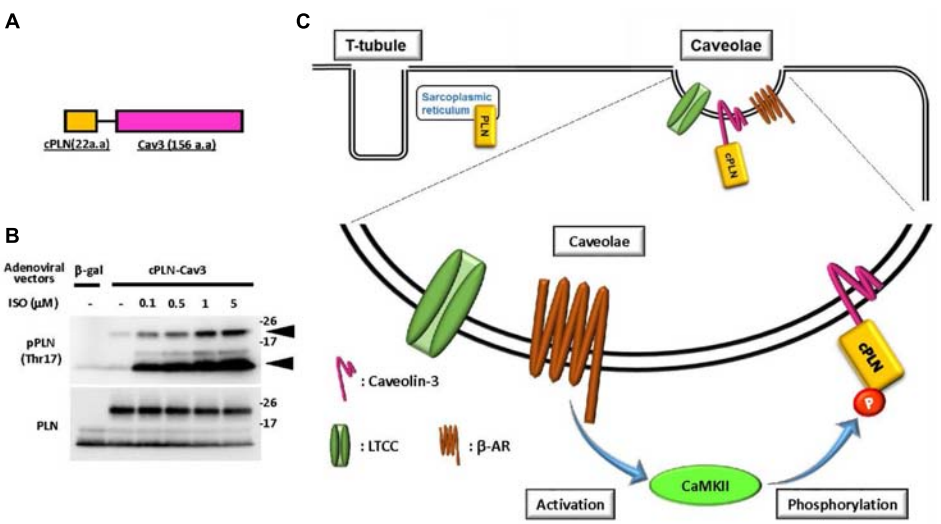

FIGURE 1 | Caveolae-specific CaMKII activation was detectable using phosphor-peptide tags. **(A)** Schematic diagram of a fusion protein comprised of the cytosolic domain of phospholamban (cPLN) and caveolin-3 (Cav3). **(B)** Phosphorylation at threonine 17 of the cytosolic domain of phospholamban in the fusion protein and endogenous phospholamban. The fusion protein comprised of cPLN and caveolin-3 (cPLN-Cav3) was expressed by adenoviral gene transfer in neonatal rat cardiomyocytes (NRCMs). After 15 min of β-adrenergic stimulation with isoproterenol (ISO) at the indicated concentration, cells were harvested and their protein extracts were prepared. The phosphorylation of phospholamban at threonine 17 (Thr17), the CaMKII-specific phosphorylation site, was assessed using a phospho-specific antibody for Thr17 of PLN, and its level was enhanced in a dose-dependent manner in both cPLN-Cav3 (upper arrow) and endogenous PLN (lower arrow). The membrane was re-probed using an anti-PLN antibody. **(C)** Schema of the proposed method for caveolae-specific CaMKII activation using a fusion protein and phospho-specific antibody. CaMKII activation induced by β-adrenergic stimulation provokes phosphorylation of cPLN-Cav3, which is localized in caveolae.

of the sarcoplasmic reticulum, which is comprised of a flexible cytosolic domain and an intramembrane domain (Tonegawa et al., 2017). The cytosolic domain of PLN contains two distinct phosphorylation sites: Ser16, which is mainly phosphorylated by cAMP-dependent kinase (PKA), and Thr17, which is specifically phosphorylated by CaMKII (Simmerman et al., 1986; Wegener et al., 1989; Hagemann and Xiao, 2002). Notably, each phosphorylation is detectable using the corresponding phospho-specific antibody, and the phosphorylation state is considered to represent activation of the corresponding kinases in the cytosol (Drago and Colyer, 1994). Therefore, we took advantage of these properties of PLN to develop a novel tool for determining the caveolae-specific activation of CaMKII. Indeed, phosphorylation of Thr17 in tagged cPLN localized in the caveolae was successfully detected using the phospho-specific antibody. Moreover, the phosphorylation level was enhanced by caveolae-specific activation or was suppressed by the caveolae-specific inhibition of CaMKII, indicating the reliability of this method (Tonegawa et al., 2017).

LTCC AND CARDIAC HYPERTROPHY

The LTCC is a multi-protein complex composed of a pore-forming α-subunit and accessory subunits, including β-subunit proteins (Catterall, 2000). The β-subunits play important roles in regulation of channel activity as well as in channel membrane trafficking via interaction with the I-II intracellular loop of α-subunits (Catterall, 2000). Among the multiple splice variants of β-subunits, β2a is the dominant isoform in the heart. The LTCC serves as the primary source of Ca^{2+} influx for inducing contractions by triggering Ca^{2+}-induced Ca^{2+} release (Bers, 2008). However, enhanced Ca^{2+} influxes caused by the targeted expression of the cardiac α1 or β2a subunit mediates or enhances cardiac hypertrophy (Muth et al., 2001; Chen et al., 2011). In addition, increased Ca^{2+} influxes caused by overexpression of the β2a subunit in feline cardiomyocytes or in the mouse heart driven by adenoviral expression or transgenesis induced pronounced myocardial Ca^{2+} overload that resulted in myocyte death (Chen et al., 2005; Nakayama et al., 2007). Therefore, functional sequestration of the LTCC subpopulation could be an important strategy to regulate cardiac pathogenesis. The LTCC has been shown to localize not only in the T-tubules but also in the plasma membrane microdomains such as the caveolae, and its localization is assumed to contribute to the distinct biological roles of the channel (Balijepalli et al., 2006; Best and Kamp, 2012; Shaw and Colecraft, 2013).

CaMKII AND LTCC IN THE CAVEOLAE MICRODOMAIN MEDIATE CARDIAC HYPERTROPHY

Besides cardiomyocytes, several reports suggested the involvement of CaMK in caveolae-related biological effects, such as 1α,25(OH)2D3-dependent signaling or P2X3 receptor-mediated Ca^{2+} influx (Chen et al., 2014; Doroudi et al., 2015). In cardiomyocytes, voltage-gated LTCC complex is a well-known substrate of CaMKII (Buraei and Yang, 2010). Phosphorylation of the β2 subunit by PKA or CaMKII has been proposed as an activation mechanism of LTCC mediated by extracellular stimuli (Bunemann et al., 1999; Koval et al., 2010). Several studies have also shown that the CaMKII- and PKA-mediated phosphorylation of the α1C subunit of LTCC facilitates its activity (Buraei and Yang, 2010; Weiss et al., 2013). However, the physiological importance of phosphorylation of the β2 subunit remains controversial. Mutant mice with a truncated β2 subunit lacking the phosphorylatable domain failed to show alteration of LTCC activity under physiological conditions (Brandmayr et al., 2012). By contrast, overexpression of a mutated β2 subunit resistant to CaMKII binding (L493A) and phosphorylation (T498A) resulted in attenuation of the cell death induced by delayed rapid-pacing (Koval et al., 2010). Therefore, upregulation of β2 subunit phosphorylation is thought to play a role in cardiac pathogenesis. In support of this hypothesis, increased expression of the LTCC β2a subunit and enhanced CaMKII activation are frequently observed in cases of human heart failure (Hullin et al., 2007; Anderson et al., 2011). Thus, sustained, excessive CaMKII activation is considered to be an upstream signaling event for increased LTCC opening probability, which is involved in excitation-contraction coupling dysfunction, myocardial hypertrophy, heart failure, and lethal arrhythmia (Wu et al., 1999; Rokita and Anderson, 2012; Zhu et al., 2016). However, whether the increased β2 subunit is phosphorylated by CaMKII and the subcellular location in which this critical event occurs remained unclear. Using our phospho-specific antibody, we demonstrated that the LTCC β2 subunit is phosphorylated by CaMKII in the caveolae to further induce CaMKII activation, possibly by increased Ca^{2+} influxes through the channel (**Figure 2**, Tonegawa et al., 2017). This suggested the possibility of a positive feedback loop between the β2 subunit and CaMKII that specifically occurs in the caveolae microdomain. This activation mechanism would contribute to the promotion of cardiac hypertrophy caused by chronic α1 adrenergic stimulation *in vivo*, since overexpression of the non-phosphorylated mutant of the β2a subunit failed to display enhancement of cardiac hypertrophy (Tonegawa et al., 2017). However, further investigation is required to clarify the direct link between caveolae-specific CaMKII signaling and cardiac hypertrophy *in vivo*, using genetically engineered mouse models such as caveolae-specific expression of constitutive active CaMKII (activation) or a CaMKII-specific inhibitory peptide (inhibition).

CONCLUSION AND PROSPECTS

We have here summarized the current knowledge on the effects of caveolae-specific signal activation in relation to the pathogenesis of cardiac hypertrophy. The related molecules such as CaMKII and LTCC have multiple cellular functions that seem to depend on the corresponding subcellular localization of the molecules, including intracellular organelles and microdomains. Thus,

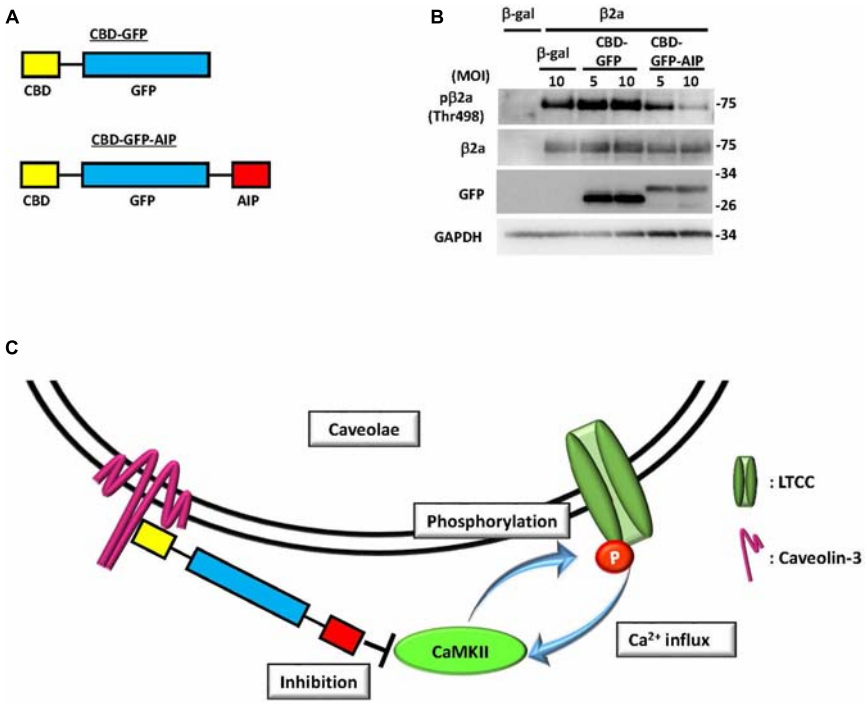

FIGURE 2 | Inhibition of CaMKII specifically in caveolae abolished phosphorylation of the β2a subunit of the L-type calcium channel. **(A)** Schematic diagram of a fusion protein comprised of green fluorescent protein (GFP) tagged with caveolae-binding domain (CBD) and autocamtide-2-related inhibitory peptide (AIP), a CaMKII-specific inhibitory molecule. **(B)** Phosphorylation of the β2a subunit of the L-type calcium channel at threonine 498, a CaMKII phosphorylation site, in NRCMs expressing the β2a subunit or β-galactosidase (β-gal) as a control by adenoviral gene transfer. The additional adenoviral expression of a fusion protein, either CBD-GFP or CBD-GFP-AIP, was induced, and phosphorylation or expression levels were assessed by immunoblot analysis using the indicated antibodies. Phosphorylation of the overexpressed β2a subunit was substantially attenuated by CBD-GFP-AIP expression, indicating that phosphorylation of this protein occurs exclusively in caveolae. **(C)** Schema of the proposed mechanism based on immunoblot analysis. Phosphorylation of the β2a subunit by CaMKII induces a Ca^{2+} influx, which in turn elicits CaMKII activation to develop a positive feedback loop between the two molecules in the caveolae microdomain of NRCMs. Expression of CBD-GFP-AIP, which binds to caveolin-3, inhibits caveolae-specific CaMKII activation to terminate the positive feedback loop and abolish phosphorylation of the β2a subunit. MOI: multiplicity of infection. These figures were prepared with minor modifications from Tonegawa et al. (2017).

regulation of location-dependent signal activation is a potential therapeutic target for heart failure. For instance, inhibition of the specific population of CaMKII or LTCC, those which are involved in the development of cardiac hypertrophy or induction of cell death, could potentially improve the prognosis of patients with heart failure without disturbance of excitation-contraction coupling. However, several questions remain to be answered regarding the role of microdomain-specific signaling in the development of cardiac hypertrophy and heart failure. First, the contribution of other microdomains such as lipid rafts (Dodelet-Devillers et al., 2009) or couplons (Chopra and Knollmann, 2013) needs to be determined, which requires the development of novel and simple tools to assess these microdomain signals. Second, the physiological relevance of the regulation of these microdomain-specific signaling pathways should be determined *in vivo*. Third, the methodology for assessing signals other than CaMKII needs to be developed. Finally, the role of the specific activation of these signals in subcellular organelles such as the mitochondrion should be determined. Methods based on a phosphorylatable peptide-tag have great potential to help tackle these questions. Taken together, the evidence accumulated to date indicates that selective inhibition of target molecules involved in caveolae-specific signaling based on their subcellular location could be a promising therapeutic tool to treat cardiac hypertrophy and heart failure in the future.

AUTHOR CONTRIBUTIONS

ST and HN wrote the manuscript. YF checked and approved the manuscript.

FUNDING

This work was partially supported by MEXT/JSPS KAKENHI (Grant No. 17K09576) and Smoking Research Foundation to HN. This research was also supported by AMED under Grant No. 17am0101084j0001.

ACKNOWLEDGMENTS

We thank Chiharu Tottori for the excellent secretarial work.

REFERENCES

Anderson, M. E., Brown, J. H., and Bers, D. M. (2011). CaMKII in myocardial hypertrophy and heart failure. *J. Mol. Cell Cardiol.* 51, 468–473. doi: 10.1016/j.yjmcc.2011.01.012

Backs, J., Backs, T., Neef, S., Kreusser, M. M., Lehmann, L. H., Patrick, D. M., et al. (2009). The delta isoform of CaM kinase II is required for pathological cardiac hypertrophy and remodeling after pressure overload. *Proc. Natl. Acad. Sci. U.S.A.* 106, 2342–2347. doi: 10.1073/pnas.0813013106

Balijepalli, R. C., Foell, J. D., Hall, D. D., Hell, J. W., and Kamp, T. J. (2006). Localization of cardiac L-type Ca(2+) channels to a caveolar macromolecular signaling complex is required for beta(2)-adrenergic regulation. *Proc. Natl. Acad. Sci. U.S.A.* 103, 7500–7505. doi: 10.1073/pnas.0503465103

Bastiani, M., Liu, L., Hill, M. M., Jedrychowski, M. P., Nixon, S. J., Lo, H. P., et al. (2009). MURC/Cavin-4 and cavin family members form tissue-specific caveolar complexes. *J. Cell Biol.* 185, 1259–1273. doi: 10.1083/jcb.200903053

Bers, D. M. (2008). Calcium cycling and signaling in cardiac myocytes. *Annu. Rev. Physiol.* 70, 23–49. doi: 10.1146/annurev.physiol.70.113006.100455

Best, J. M., and Kamp, T. J. (2012). Different subcellular populations of L-type Ca2+ channels exhibit unique regulation and functional roles in cardiomyocytes. *J. Mol. Cell Cardiol.* 52, 376–387. doi: 10.1016/j.yjmcc.2011.08.014

Brandmayr, J., Poomvanicha, M., Domes, K., Ding, J., Blaich, A., Wegener, J. W., et al. (2012). Deletion of the C-terminal phosphorylation sites in the cardiac beta-subunit does not affect the basic beta-adrenergic response of the heart and the Ca(v)1.2 channel. *J. Biol. Chem.* 287, 22584–22592. doi: 10.1074/jbc.M112.366484

Bunemann, M., Gerhardstein, B. L., Gao, T., and Hosey, M. M. (1999). Functional regulation of L-type calcium channels via protein kinase A-mediated phosphorylation of the beta(2) subunit. *J. Biol. Chem.* 274, 33851–33854. doi: 10.1074/jbc.274.48.33851

Buraei, Z., and Yang, J. (2010). The ss subunit of voltage-gated Ca2+ channels. *Physiol. Rev.* 90, 1461–1506. doi: 10.1152/physrev.00057.2009

Catterall, W. A. (2000). Structure and regulation of voltage-gated Ca2+ channels. *Annu. Rev. Cell Dev. Biol.* 16, 521–555. doi: 10.1146/annurev.cellbio.16.1.521

Chen, X., Nakayama, H., Zhang, X., Ai, X., Harris, D. M., Tang, M., et al. (2011). Calcium influx through Cav1.2 is a proximal signal for pathological cardiomyocyte hypertrophy. *J. Mol. Cell. Cardiol.* 50, 460–470. doi: 10.1016/j.yjmcc.2010.11.012

Chen, X., Zhang, X., Kubo, H., Harris, D. M., Mills, G. D., Moyer, J., et al. (2005). Ca2+ influx-induced sarcoplasmic reticulum Ca2+ overload causes mitochondrial-dependent apoptosis in ventricular myocytes. *Circ. Res.* 97, 1009–1017. doi: 10.1161/01.RES.0000189270.72915.D1

Chen, X. Q., Zhu, J. X., Wang, Y., Zhang, X., and Bao, L. (2014). CaMKIIalpha and caveolin-1 cooperate to drive ATP-induced membrane delivery of the P2X3 receptor. *J. Mol. Cell. Biol.* 6, 140–153. doi: 10.1093/jmcb/mju011

Cheng, J. P. X., and Nichols, B. J. (2016). Caveolae: one function or many? *Trends Cell Biol.* 26, 177–189. doi: 10.1016/j.tcb.2015.10.010

Chopra, N., and Knollmann, B. C. (2013). Triadin regulates cardiac muscle couplon structure and microdomain Ca^{2+} signalling: a path towards ventricular arrhythmias. *Cardiovasc. Res.* 98, 187–191. doi: 10.1093/cvr/cvt023

Cohen, A. W., Hnasko, R., Schubert, W., and Lisanti, M. P. (2004). Role of caveolae and caveolins in health and disease. *Physiol. Rev.* 84, 1341–1379. doi: 10.1152/physrev.00046.2003

Collins, B. M., Davis, M. J., Hancock, J. F., and Parton, R. G. (2012). Structure-based reassessment of the caveolin signaling model: do caveolae regulate signaling through caveolin-protein interactions? *Dev. Cell* 23, 11–20. doi: 10.1016/j.devcel.2012.06.012

Correll, R. N., Makarewich, C. A., Zhang, H., Zhang, C., Sargent, M. A., York, A. J., et al. (2017). Caveolae-localized L-type Ca2+ channels do not contribute to function or hypertrophic signalling in the mouse heart. *Cardiovasc. Res.* 113, 749–759. doi: 10.1093/cvr/cvx046

Couet, J., Li, S., Okamoto, T., Ikezu, T., and Lisanti, M. P. (1997a). Identification of peptide and protein ligands for the caveolin-scaffolding domain. Implications for the interaction of caveolin with caveolae-associated proteins. *J. Biol. Chem.* 272, 6525–6533.

Couet, J., Sargiacomo, M., and Lisanti, M. P. (1997b). Interaction of a receptor tyrosine kinase, EGF-R, with caveolins. Caveolin binding negatively regulates tyrosine and serine/threonine kinase activities. *J. Biol. Chem.* 272, 30429–30438.

Dodelet-Devillers, A., Cayrol, R., van Horssen, J., Haqqani, A. S., de Vries, H. E., Engelhardt, B., et al. (2009). Functions of lipid raft membrane microdomains at the blood-brain barrier. *J. Mol. Med.* 87, 765–774. doi: 10.1007/s00109-009-0488-6

Doroudi, M., Plaisance, M. C., Boyan, B. D., and Schwartz, Z. (2015). Membrane actions of 1alpha,25(OH)2D3 are mediated by Ca(2+)/calmodulin-dependent protein kinase II in bone and cartilage cells. *J. Steroid Biochem. Mol. Biol.* 145, 65–74. doi: 10.1016/j.jsbmb.2014.09.019

Drago, G. A., and Colyer, J. (1994). Discrimination between two sites of phosphorylation on adjacent amino acids by phosphorylation site-specific antibodies to phospholamban. *J. Biol. Chem.* 269, 25073–25077.

Erickson, J. R., He, B. J., Grumbach, I. M., and Anderson, M. E. (2011). CaMKII in the cardiovascular system: sensing redox states. *Physiol. Rev.* 91, 889–915. doi: 10.1152/physrev.00018.2010

Erickson, J. R., Pereira, L., Wang, L., Han, G., Ferguson, A., Dao, K., et al. (2013). Diabetic hyperglycaemia activates CaMKII and arrhythmias by O-linked glycosylation. *Nature* 502, 372–376. doi: 10.1038/nature12537

Gangadharan, V., Nohe, A., Caplan, J., Czymmek, K., and Duncan, R. L. (2015). Caveolin-1 regulates P2X7 receptor signaling in osteoblasts. *Am. J. Physiol. Cell Physiol.* 308, C41–C50. doi: 10.1152/ajpcell.00037.2014

Garcia-Cardena, G., Martasek, P., Masters, B. S., Skidd, P. M., Couet, J., Li, S., et al. (1997). Dissecting the interaction between nitric oxide synthase (NOS) and caveolin. Functional significance of the nos caveolin binding domain *in vivo*. *J. Biol. Chem.* 272, 25437–25440. doi: 10.1074/jbc.272.41.25437

Hagemann, D., and Xiao, R. P. (2002). Dual site phospholamban phosphorylation and its physiological relevance in the heart. *Trends Cardiovasc. Med.* 12, 51–56. doi: 10.1016/S1050-1738(01)00145-1

Hansen, C. G., Bright, N. A., Howard, G., and Nichols, B. J. (2009). SDPR induces membrane curvature and functions in the formation of caveolae. *Nat. Cell Biol.* 11, 807–814. doi: 10.1038/ncb1887

Harvey, R. D., and Calaghan, S. C. (2012). Caveolae create local signalling domains through their distinct protein content, lipid profile and morphology. *J. Mol. Cell Cardiol.* 52, 366–375. doi: 10.1016/j.yjmcc.2011.07.007

Heineke, J., and Molkentin, J. D. (2006). Regulation of cardiac hypertrophy by intracellular signalling pathways. *Nat. Rev. Mol. Cell Biol.* 7, 589–600. doi: 10.1038/nrm1983

Hill, M. M., Bastiani, M., Luetterforst, R., Kirkham, M., Kirkham, A., Nixon, S. J., et al. (2008). PTRF-Cavin, a conserved cytoplasmic protein required for caveola formation and function. *Cell* 132, 113–124. doi: 10.1016/j.cell.2007.11.042

Horikawa, Y. T., Panneerselvam, M., Kawaraguchi, Y., Tsutsumi, Y. M., Ali, S. S., Balijepalli, R. C., et al. (2011). Cardiac-specific overexpression of caveolin-3 attenuates cardiac hypertrophy and increases natriuretic peptide expression and signaling. *J. Am. Coll. Cardiol.* 57, 2273–2283. doi: 10.1016/j.jacc.2010.12.032

Hudmon, A., and Schulman, H. (2002). Neuronal CA2+/calmodulin-dependent protein kinase II: the role of structure and autoregulation in cellular function. *Annu. Rev. Biochem.* 71, 473–510. doi: 10.1146/annurev.biochem.71.110601.135410

Hullin, R., Matthes, J., von Vietinghoff, S., Bodi, I., Rubio, M., D'Souza, K., et al. (2007). Increased expression of the auxiliary beta(2)-subunit of ventricular L-type Ca^{2+} channels leads to single-channel activity characteristic of heart failure. *PLoS One* 2:e292. doi: 10.1371/journal.pone.0000292

Insel, P. A., Head, B. P., Ostrom, R. S., Patel, H. H., Swaney, J. S., Tang, C. M., et al. (2005). Caveolae and lipid rafts: g protein-coupled receptor signaling microdomains in cardiac myocytes. *Ann. N. Y. Acad. Sci.* 1047, 166–172. doi: 10.1196/annals.1341.015

Joiner, M. L., Koval, O. M., Li, J., He, B. J., Allamargot, C., Gao, Z., et al. (2012). CaMKII determines mitochondrial stress responses in heart. *Nature* 491, 269–273. doi: 10.1038/nature11444

Kirkham, M., Nixon, S. J., Howes, M. T., Abi-Rached, L., Wakeham, D. E., Hanzal-Bayer, M., et al. (2008). Evolutionary analysis and molecular dissection of caveola biogenesis. *J. Cell Sci.* 121, 2075–2086. doi: 10.1242/jcs.024588

Koval, O. M., Guan, X., Wu, Y., Joiner, M. L., Gao, Z., Chen, B., et al. (2010). CaV1.2 beta-subunit coordinates CaMKII-triggered cardiomyocyte death and afterdepolarizations. *Proc. Natl. Acad. Sci. U.S.A.* 107, 4996–5000. doi: 10.1073/pnas.0913760107

Li, Q., Bai, L., Liu, N., Wang, M., Liu, J. P., Liu, P., et al. (2014). Increased polymerase I and transcript release factor (Cavin-1) expression attenuates platelet-derived growth factor receptor signalling in senescent human fibroblasts. *Clin. Exp. Pharmacol. Physiol.* 41, 169–173. doi: 10.1111/1440-1681.12202

Ling, H., Zhang, T., Pereira, L., Means, C. K., Cheng, H., Gu, Y., et al. (2009). Requirement for Ca2+/calmodulin-dependent kinase II in the transition from pressure overload-induced cardiac hypertrophy to heart failure in mice. *J. Clin. Invest.* 119, 1230–1240. doi: 10.1172/JCI38022

Lloyd-Jones, D. M., Larson, M. G., Leip, E. P., Beiser, A., D'Agostino, R. B., Kannel, W. B., et al. (2002). Lifetime risk for developing congestive heart failure: the framingham heart study. *Circulation* 106, 3068–3072. doi: 10.1161/01.CIR.0000039105.49749.6F

Makarewich, C. A., Correll, R. N., Gao, H., Zhang, H., Yang, B., Berretta, R. M., et al. (2012). A caveolae-targeted L-type Ca(2)+ channel antagonist inhibits hypertrophic signaling without reducing cardiac contractility. *Circ. Res.* 110, 669–674. doi: 10.1161/CIRCRESAHA.111.264028

McMahon, K. A., Zajicek, H., Li, W. P., Peyton, M. J., Minna, J. D., Hernandez, V. J., et al. (2009). SRBC/cavin-3 is a caveolin adapter protein that regulates caveolae function. *EMBO J.* 28, 1001–1015. doi: 10.1038/emboj.2009.46

Mishra, S., Gray, C. B., Miyamoto, S., Bers, D. M., and Brown, J. H. (2011). Location matters: clarifying the concept of nuclear and cytosolic CaMKII subtypes. *Circ. Res.* 109, 1354–1362. doi: 10.1161/CIRCRESAHA.111.248401

Moon, H., Lee, C. S., Inder, K. L., Sharma, S., Choi, E., Black, D. M., et al. (2014). PTRF/cavin-1 neutralizes non-caveolar caveolin-1 microdomains in prostate cancer. *Oncogene* 33, 3561–3570. doi: 10.1038/onc.2013.315

Muth, J. N., Bodi, I., Lewis, W., Varadi, G., and Schwartz, A. (2001). A Ca(2+)-dependent transgenic model of cardiac hypertrophy: a role for protein kinase calpha. *Circulation* 103, 140–147. doi: 10.1161/01.CIR.103.1.140

Nakayama, H., Chen, X., Baines, C. P., Klevitsky, R., Zhang, X., Zhang, H., et al. (2007). Ca2+- and mitochondrial-dependent cardiomyocyte necrosis as a primary mediator of heart failure. *J. Clin. Invest.* 117, 2431–2444. doi: 10.1172/JCI31060

Nystrom, F. H., Chen, H., Cong, L. N., Li, Y., and Quon, M. J. (1999). Caveolin-1 interacts with the insulin receptor and can differentially modulate insulin signaling in transfected Cos-7 cells and rat adipose cells. *Mol. Endocrinol.* 13, 2013–2024. doi: 10.1210/mend.13.12.0392

Ogata, T., Naito, D., Nakanishi, N., Hayashi, Y. K., Taniguchi, T., Miyagawa, K., et al. (2014). MURC/Cavin-4 facilitates recruitment of ERK to caveolae and concentric cardiac hypertrophy induced by alpha1-adrenergic receptors. *Proc. Natl. Acad. Sci. U.S.A.* 111, 3811–3816. doi: 10.1073/pnas.1315359111

Park, D. S., Woodman, S. E., Schubert, W., Cohen, A. W., Frank, P. G., Chandra, M., et al. (2002). Caveolin-1/3 double-knockout mice are viable, but lack both muscle and non-muscle caveolae, and develop a severe cardiomyopathic phenotype. *Am. J. Pathol.* 160, 2207–2217. doi: 10.1016/S0002-9440(10)61168-6

Parton, R. G., and Simons, K. (2007). The multiple faces of caveolae. *Nat. Rev. Mol. Cell Biol.* 8, 185–194. doi: 10.1038/nrm2122

Razani, B., Woodman, S. E., and Lisanti, M. P. (2002). Caveolae: from cell biology to animal physiology. *Pharmacol. Rev.* 54, 431–467. doi: 10.1124/pr.54.3.431

Rokita, A. G., and Anderson, M. E. (2012). New therapeutic targets in cardiology: arrhythmias and Ca2+/calmodulin-dependent kinase II (CaMKII). *Circulation* 126, 2125–2139. doi: 10.1161/CIRCULATIONAHA.112.124990

Rothberg, K. G., Heuser, J. E., Donzell, W. C., Ying, Y. S., Glenney, J. R., and Anderson, R. G. (1992). Caveolin, a protein component of caveolae membrane coats. *Cell* 68, 673–682. doi: 10.1016/0092-8674(92)90143-Z

Scherer, P. E., Okamoto, T., Chun, M., Nishimoto, I., Lodish, H. F., and Lisanti, M. P. (1996). Identification, sequence, and expression of caveolin-2 defines a caveolin gene family. *Proc. Natl. Acad. Sci. U.S.A.* 93, 131–135. doi: 10.1073/pnas.93.1.131

Shaul, P. W., and Anderson, R. G. (1998). Role of plasmalemmal caveolae in signal transduction. *Am. J. Physiol.* 275, L843–L851. doi: 10.1152/ajplung.1998.275.5.L843

Shaw, R. M., and Colecraft, H. M. (2013). L-type calcium channel targeting and local signalling in cardiac myocytes. *Cardiovasc. Res.* 98, 177–186. doi: 10.1093/cvr/cvt021

Simmerman, H. K., Collins, J. H., Theibert, J. L., Wegener, A. D., and Jones, L. R. (1986). Sequence analysis of phospholamban. Identification of phosphorylation sites and two major structural domains. *J. Biol. Chem.* 261, 13333–13341.

Song, K. S., Li, S., Okamoto, T., Quilliam, L. A., Sargiacomo, M., and Lisanti, M. P. (1996). Co-purification and direct interaction of Ras with caveolin, an integral membrane protein of caveolae microdomains. Detergent-free purification of caveolae microdomains. *J. Biol. Chem.* 271, 9690–9697. doi: 10.1074/jbc.271.16.9690

Sonnino, S., and Prinetti, A. (2009). Sphingolipids and membrane environments for caveolin. *FEBS Lett.* 583, 597–606. doi: 10.1016/j.febslet.2009.01.007

Sossalla, S., Fluschnik, N., Schotola, H., Ort, K. R., Neef, S., Schulte, T., et al. (2010). Inhibition of elevated Ca2+/calmodulin-dependent protein kinase II improves contractility in human failing myocardium. *Circ. Res.* 107, 1150–1161. doi: 10.1161/CIRCRESAHA.110.220418

Strippoli, R., Loureiro, J., Moreno, V., Benedicto, I., Perez Lozano, M. L., Barreiro, O., et al. (2015). Caveolin-1 deficiency induces a MEK-ERK1/2-Snail-1-dependent epithelial-mesenchymal transition and fibrosis during peritoneal dialysis. *EMBO Mol. Med.* 7, 102–123. doi: 10.15252/emmm.201404127

Swaminathan, P. D., Purohit, A., Hund, T. J., and Anderson, M. E. (2012). Calmodulin-dependent protein kinase II: linking heart failure and arrhythmias. *Circ. Res.* 110, 1661–1677. doi: 10.1161/CIRCRESAHA.111.243956

Taira, J., Sugishima, M., Kida, Y., Oda, E., Noguchi, M., and Higashimoto, Y. (2011). Caveolin-1 is a competitive inhibitor of heme oxygenase-1 (HO-1) with heme: identification of a minimum sequence in caveolin-1 for binding to HO-1. *Biochemistry* 50, 6824–6831. doi: 10.1021/bi200601t

Tang, Z., Scherer, P. E., Okamoto, T., Song, K., Chu, C., Kohtz, D. S., et al. (1996). Molecular cloning of caveolin-3, a novel member of the caveolin gene family expressed predominantly in muscle. *J. Biol. Chem.* 271, 2255–2261. doi: 10.1074/jbc.271.4.2255

Tonegawa, K., Otsuka, W., Kumagai, S., Matsunami, S., Hayamizu, N., Tanaka, S., et al. (2017). Caveolae-specific activation loop between CaMKII and L-type Ca(2+) channel aggravates cardiac hypertrophy in alpha1-adrenergic stimulation. *Am. J. Physiol. Heart Circ. Physiol.* 312, H501–H514. doi: 10.1152/ajpheart.00601.2016

Wegener, A. D., Simmerman, H. K., Lindemann, J. P., and Jones, L. R. (1989). Phospholamban phosphorylation in intact ventricles. Phosphorylation of serine 16 and threonine 17 in response to beta-adrenergic stimulation. *J. Biol. Chem.* 264, 11468–11474.

Weiss, S., Oz, S., Benmocha, A., and Dascal, N. (2013). Regulation of cardiac L-type Ca(2)(+) channel CaV1.2 via the beta-adrenergic-cAMP-protein kinase a pathway: old dogmas, advances, and new uncertainties. *Circ. Res.* 113, 617–631. doi: 10.1161/CIRCRESAHA.113.301781

Wu, Y., MacMillan, L. B., McNeill, R. B., Colbran, R. J., and Anderson, M. E. (1999). CaM kinase augments cardiac L-type Ca2+ current: a cellular mechanism for long Q-T arrhythmias. *Am. J. Physiol.* 276, H2168–H2178. doi: 10.1152/ajpheart.1999.276.6.H2168

Zhang, T., Johnson, E. N., Gu, Y., Morissette, M. R., Sah, V. P., Gigena, M. S., et al. (2002). The cardiac-specific nuclear delta(B) isoform of Ca2+/calmodulin-dependent protein kinase II induces hypertrophy and dilated cardiomyopathy associated with increased protein phosphatase 2A activity. *J. Biol. Chem.* 277, 1261–1267. doi: 10.1074/jbc.M108525200

Zhang, T., Maier, L. S., Dalton, N. D., Miyamoto, S., Ross, J. Jr., Bers, D. M., et al. (2003). The deltaC isoform of CaMKII is activated in cardiac hypertrophy and induces dilated cardiomyopathy and heart failure. *Circ. Res.* 92, 912–919. doi: 10.1161/01.RES.0000069686.31472.C5

Zhu, W., Tsang, S., Browe, D. M., Woo, A. Y., Huang, Y., Xu, C., et al. (2016). Interaction of beta1-adrenoceptor with RAGE mediates cardiomyopathy via CaMKII signaling. *JCI Insight* 1:e84969. doi: 10.1172/jci.insight.84969

Conflict of Interest Statement: The authors declare that the research was conducted in the absence of any commercial or financial relationships that could be construed as a potential conflict of interest.

frontiers in Physiology

MINI REVIEW
published: 13 August 2018
doi: 10.3389/fphys.2018.01115

Cardiomyocyte Inflammasome Signaling in Cardiomyopathies and Atrial Fibrillation: Mechanisms and Potential Therapeutic Implications

*Gong Chen[1], Mihail G. Chelu[2,3], Dobromir Dobrev[4] and Na Li[1,5,6]**

[1] Section of Cardiovascular Research, Department of Medicine, Baylor College of Medicine, Houston, TX, United States, [2] Comprehensive Arrhythmia Research and Management Center, School of Medicine, University of Utah, Salt Lake City, UT, United States, [3] Cardiovascular Medicine Division, Section of Cardiac Electrophysiology, School of Medicine, University of Utah, Salt Lake City, UT, United States, [4] Institute of Pharmacology, West German Heart and Vascular Center, University Duisburg-Essen, Essen, Germany, [5] Cardiovascular Research Institute, Baylor College of Medicine, Houston, TX, United States, [6] Department of Molecular Physiology and Biophysics, Baylor College of Medicine, Houston, TX, United States

Inflammasomes are high molecular weight protein complexes in the cytosol of immune and other cells that play a critical role in the innate immune system in response to cellular stress. NLRP3 inflammasome, the best-understood inflammasome, is known to mediate the maturation (activation) of caspase-1 from pro-caspase-1, causing the maturation and release of cytokines (e.g., interleukin-1β) and potentially leading to a form of inflammatory programmed cell death called pyroptosis. Previous work has shown that the NLRP3 components are expressed in cardiomyocytes and cardiac fibroblasts and recent studies have identified the NLRP3 inflammasome as a key nodal point in the pathogenesis of cardiomyopathies and atrial fibrillation, which may create an opportunity for the development of new therapeutic agents. Here we review the recent evidence for a role of NLRP3 inflammasome in the cardiomyocytes and discuss its potential role in the evolution of cardiac remodeling and arrhythmias and new opportunities created by these very recent developments.

Keywords: NLRP3 inflammasome, innate immune system, cardiomyocytes, cardiac fibroblasts, cardiomyopathy, atrial fibrillation

OPEN ACCESS

Edited by:
Di Lang,
University of Wisconsin-Madison, United States

Reviewed by:
Marina Cerrone,
New York University, United States
Masafumi Takahashi,
Jichi Medical University, Japan

***Correspondence:**
Na Li
nal@bcm.edu

Specialty section:
This article was submitted to Cardiac Electrophysiology, a section of the journal Frontiers in Physiology

Received: *17 May 2018*
Accepted: *25 July 2018*
Published: *13 August 2018*

Citation:
Chen G, Chelu MG, Dobrev D and Li N (2018) Cardiomyocyte Inflammasome Signaling in Cardiomyopathies and Atrial Fibrillation: Mechanisms and Potential Therapeutic Implications. Front. Physiol. 9:1115. doi: 10.3389/fphys.2018.01115

THE INNATE IMMUNE SYSTEM, INFLAMMATION AND INFLAMMASOME SIGNALING

Inflammation is a vital biological process involving an acute response to infection and tissue damage aiming to prevent harmful influence to the host (Medzhitov, 2008; Buckley et al., 2013). The mammalian innate immune system plays an important role in recognizing foreign pathogen- or damage-associated molecular patterns (PAMPs and DAMPs, respectively) and defending the host against infection or injury caused by other pathological organisms (Matzinger, 1994).

Inflammasome acts as an intracellular innate immune sensor (Martinon et al., 2002). The inflammasome is a multi-protein signaling platform that generally involves 3 proteins: (1) a NOD-like receptor (NLR), (2) an adaptor protein like apoptosis-associated speck-like protein containing a CARD (ASC), and (3) a cysteine protease such as caspase-1 or caspase-5 (Kanneganti, 2015).

NLRs are a class of pattern recognition receptors (PRRs) that act as a sensor for the inflammasome. At least 22 different NLR proteins have been identified in humans and 34 in mouse (Ting et al., 2008). Most NLRs consist of a tripartite structure that includes: (1) a N-terminal caspase-recruitment domain (CARD) or pyrin domain that mediates downstream protein-protein assembly, (2) a centrally located nucleotide-binding-and-oligomerization domain that facilitates self-oligomerization, and (3) a C-terminal leucine-rich repeats (LRRs) that are thought to be involved in stimuli sensing (Martinon et al., 2002). To date, the best investigated and validated inflammasome type is the "NACHT, LRR and PYD domain containing protein 3" (NLRP3) inflammasome (He et al., 2016). Upon recognizing a series of inflammation-inducing stimuli (e.g., PAMPs and DAMPs), NLRP3 inflammasomes in the innate immune cells activate caspase-1 (Casp-1) which promotes the production of proinflammatory cytokines (IL-1β and pro-IL-18) and may lead to cell death known as pyroptosis (Schroder and Tschopp, 2010; Davis et al., 2011). The activation of the NLRP3 inflammasome requires two primary signals (**Figure 1**): (1) a priming step in which the toll-like receptor (TLR)-nuclear factor-κB (NFκB) signaling pathway promotes the transcription of NLRP3 and precursor ILs (pro-IL1β or pro-IL-18); and (2) a triggering step in which a series of stimuli (K^+ efflux, increase in cytosolic Ca^{2+}, generation of reactive oxygen species [ROS], mitochondrial dysfunction, and lysosomal rupture) (He et al., 2016) can facilitate the assembly of the NLRP3 inflammasome components by recruiting precursor-caspase-1 (pro-Casp-1) into the complex via the adaptor protein ASC. This promotes the autocleavage of pro-Casp-1 to Casp-1 containing the active p20/p10 heterodimer proteins (Wilson et al., 1994). Alternatively, NLRP3 inflammasome may also activate caspase-11 or human orthologues caspase-4/caspase-5 (casp-4/5), which is also known as "non-canonical" NLRP3 inflammasome pathway (Kanneganti, 2015). Activated Casp-1 holoenzyme further cleaves pro-IL-1β and pro-IL-18 to form their respective mature forms (Li et al., 1995; Gu et al., 1997). Mature IL-1β is a potent proinflammatory mediator in many immune reactions, including the recruitment of innate immune cells to the site of infection and modulation of adaptive immune cells, whereas mature IL-18 is important for the production of interferon-γ and potentiation of cytotoxic activity of natural killer and T cells (Dinarello, 2009).

In addition, active Casp-1 may promote pyroptosis, which is characterized by increased membrane permeability with extracellular release of pro-inflammatory signaling molecules and cell swelling and eventually cell membrane rupture (Fink et al., 2008; Toldo and Abbate, 2018). Oligomerization of N-terminal fragments resulting from the cleavage of gasdermin D by Casp-1 lead to formation of membrane pores, which are permeable for mature IL-1β, IL-18, and active Casp-1 (Liu et al., 2016). Furthermore, cleavage of several proteins involved in the Krebs cycle by Casp-1 leads to a significant decrease in cell energy production which results in cell swelling and rupture (Shao et al., 2007).

NLRP3 INFLAMMASOME SIGNALING IN THE HEART

Cardiomyocytes (CMs) make up approximately 75% of normal adult myocardial tissue (Camelliti et al., 2005). Although non-cardiomyocytes occupy a relatively small fraction of myocardial volume, they are essential for normal cardiac function by providing extracellular matrix (ECM), intercellular communication, and vascular supply needed for efficient function and survival of CMs (Travers et al., 2016). The NLRP3 inflammasome components have been identified in both CMs and cardiac fibroblasts (CFs), which are the two most abundant cell populations in the mammalian heart (Baudino et al., 2006). An augmented function of NLRP3 inflammasome has been proposed to play a role in multiple human diseases, such as auto-inflammatory disease (Hoffman and Wanderer, 2010), diabetes (Vandanmagsar et al., 2011), atherosclerosis (Duewell et al., 2010; Baldrighi et al., 2017), and ischemic cardiomyopathy (Kawaguchi et al., 2011; Mezzaroma et al., 2011; Sandanger et al., 2013; Liu et al., 2014; Toldo et al., 2016). The innate immune system functions as the primary cardiac defense against pathogens and tissue damage (Askevold et al., 2014). Myocardial infarction is the most common cause of cardiac injury (Jennings et al., 1990), resulting from coronary atherosclerosis-mediated plaque rupture and involving acute loss of CMs. Necrotic cardiac cells can trigger inflammatory cascades to get rid of dead cell debris in the infarcted area (Pfeffer and Braunwald, 1990; Opie et al., 2006). Conversely, cell death can also release intracellular components, which further stimulate innate immune mechanisms to facilitate the inflammatory responses. Endogenous ligands released after injury can be recognized as danger signals by cell surface receptors, thereby activating cellular inflammatory signaling (Beg, 2002). TLR-mediated pathways can trigger post-infarction inflammatory responses by activating toll-like receptor (TLR)-nuclear factor-kB (NFκB) and related signaling (Lawrence, 2009). Chemokines recruit inflammatory leukocytes to the infarcted area, and cytokines promote leukocyte-endothelial cell adhesions. Moreover, transforming growth factor-β (TGF-β) and interleukin-10 (IL-10) can promote cardiac repair by suppressing inflammation, enhancing fibroblast-to-myofibroblast transition, and promoting ECM deposition (Kaur et al., 2009; Frangogiannis, 2014). Compared to the well-established canonical function of the NLRP3 inflammasome in the innate immune cells, the putative role of the NLRP3 inflammasome in non-immune cells including cardiac cells is poorly defined. NLRP3 and other important components of the inflammasome may not be constitutively expressed in healthy mouse and human heart but expression is induced in leukocytes, endothelial cells, CFs in the granulation tissue and CMs in the infarct border zones in a mouse model of acute MI (Yin et al., 2009; Mezzaroma et al., 2011). NLRP3, IL-1β, and IL-18 mRNA levels were shown to be increased in both left ventricle CMs and CFs in a post-MI mouse model (Sandanger et al., 2013). ASC is constitutively expressed in mouse CMs and CFs (Kawaguchi et al., 2011). The entire signaling cascade appears to be operative in CFs: NLRP3 inflammasome activation by DAMP molecule

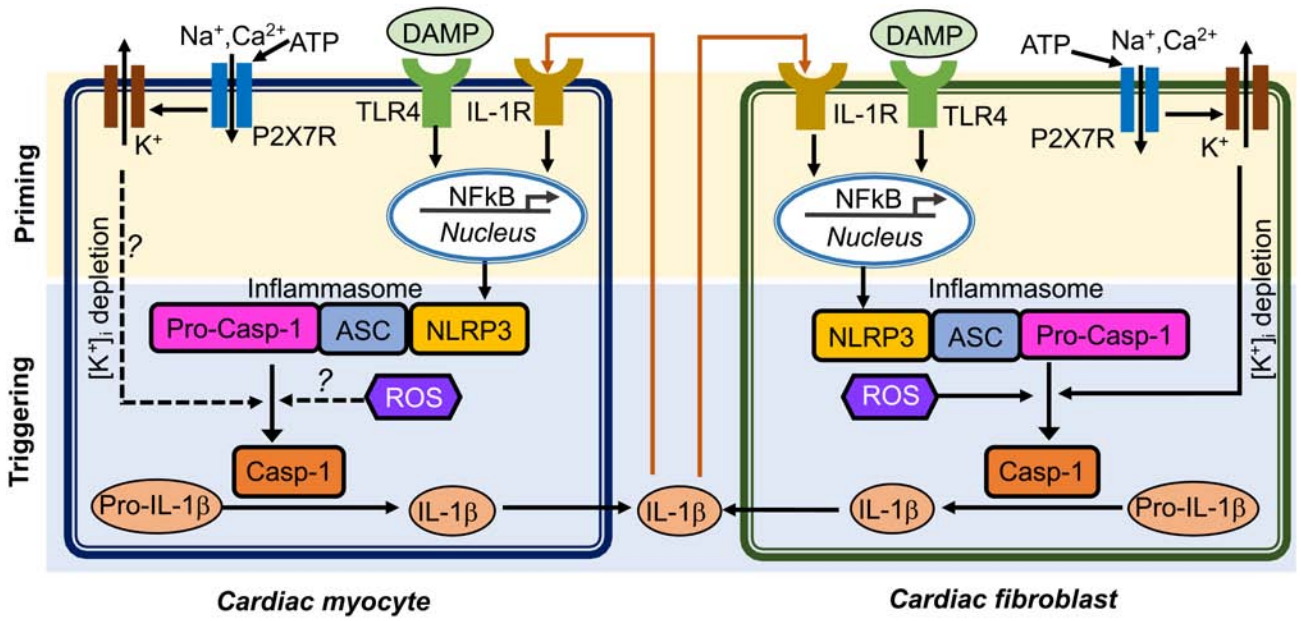

FIGURE 1 | Putative mechanisms of NLRP3 inflammasome activation in cardiomyocytes and cardiac fibroblasts. Question marks indicated the mechanisms that need to be investigated. ASC, apoptosis-associated speck-like protein containing a CARD; ATP, adenosine triphosphate; Casp-1, caspase-1; DAMP, damage-associate molecular pattern; IL-1β, interleukin-1β; IL-1R, interleukin-1 receptor; NFκB, nuclear factor kappa-light-chain-enhancer of activated B cells; NLRP3, NACHT, LRR and PYD domain containing protein 3; ROS, reactive oxidative species; pro-Casp-1, precursor Caspase-1; P2X7R, P2X7 receptor; TLR4, toll-like receptor 4.

ATP, TLR ligand specific activation in a NFκB dependent manner, assembly of the NLRP3/ASC inflammasome, and activation of Casp-1 (Kawaguchi et al., 2011; Sandanger et al., 2013). ASC was highly expressed in the inflammatory infiltrate cells and weakly expressed in CMs and the interstitial cells obtained from patients who had died after an acute myocardial infarction (Kawaguchi et al., 2011). **Figure 1** illustrates the putative mechanisms potentially underlying the activation of the NLRP3 inflammasome and the postulated interaction patterns between CMs and CFs through complex autocrine and paracrine mechanisms (**Figure 1**). In this review, we will focus on the very recently established role of the NLRP3 inflammasome in cardiac cells and its potential involvement in cardiac diseases, such as cardiomyopathies and atrial fibrillation (AF).

ROLE OF NLRP3 INFLAMMASOME IN CARDIOMYOPATHIES

Cardiomyopathies are cardiac diseases that severely impact patient morbidity and mortality (Wexler et al., 2009). They can be induced by myocardial injury that is often accompanied by transient or persistent local inflammatory responses. This type of inflammation is deemed as sterile inflammation due to the lack of a microbial pathogen. A number of studies have illustrated a central role of NLRP3 inflammasome in murine models of ischemic and non-ischemic cardiomyopathies (Mezzaroma et al., 2011; Bracey et al., 2013; Liu et al., 2014; Toldo et al., 2016; Valle Raleigh et al., 2017). NLRP3 inflammasome can be activated by several signals generated during the initial ischemia-induced myocardial injury: dsDNA, RNA, and ATP released from dying cells. DAMPs including dsDNA and RNA can activate the TLR-NFkB signaling pathway and promote the "priming" of NLRP3 and pro-IL1β. On the other hand, ATP can activate P2X purinoceptor 7 (P2X7R) in CMs thereby enhancing the K^+ efflux and subsequently facilitating the assembly of NLRP3 inflammasome complex, which promotes the autocatalytic activation of Casp-1. The mature Casp-1 further perpetuates myocardial remodeling via two established mechanisms. On one hand, mature Casp-1 can increase the production of IL-1β and IL-18 by cleaving their precursor proteins into the mature forms. An increased release of IL-1β and IL-18 will spread and amplify the local inflammation and promote fibrosis, a major factor contributing to the structural remodeling of myocardium (Nguyen et al., 2017). On the other hand, mature Casp-1 cleaves gasdermin-D (GSDMD), another crucial component of the NLRP3 inflammasome, resulting in the formation of the N-terminal proteolytic fragment of GSDMD (GSDMD-Nt), which can promote inflammatory cell death known as "pyroptosis" (He et al., 2015; Shi et al., 2015), further deteriorating the function of the remaining myocardium. Moreover, GSDMD-Nt is not only a potential executor of pyroptosis, but is also a requirement for the release of IL-1β, because genetic deletion of GSDMD precluding the GSDMD membrane pore formation eliminates the ability of the cells to release IL-1β (He et al., 2015; Sborgi et al., 2016). Although it is unclear which degree of NLRP3 inflammasome

activation is associated with pyroptosis induction, Mezzaroma et al. (2011) has demonstrated that the Casp-1-mediated cell death is restricted to the granulation tissue and CMs located to the infarct border zone following acute myocardium infarction.

The NLRP3 inflammasome might also be implicated in the pathogenesis of non-ischemic cardiomyopathy. Bracey et al. have shown that the development of cardiac hypertrophy, apoptosis and ventricular dilatation in the cardiac-specific calcineurin transgenic mice (CN-Tg) (Bracey et al., 2013) is associated with increased protein levels of NLRP3 in cardiac tissue and IL-1β in serum, which suggest that both the "priming" and "triggering" steps are activated during the development of heart failure with reduced ejection fraction (HFrEF). Most importantly, administration of IL-1 receptor antagonist (IL-1-ra) prevented the progressive reduction of cardiac contractility, reduced infiltration of inflammatory cells in the myocardium, and decreased apoptosis in CN-Tg mice.

The pathogenesis of diabetic cardiomyopathy has also been linked to the activation of NLRP3 inflammasome (Shaw et al., 2010). Diabetic cardiomyopathy often manifests as heart failure with preserved ejection fraction (HFpEF), and is a consequence of increased ventricular wall stiffness leading to left ventricular diastolic dysfunction. It is well established that hyperglycemia increases the production of ROS, which is a known trigger for the assembly of the NLRP3 inflammasome complex. Glucose itself has also been reported to be an effective activator of the NLRP3 inflammasome (Shi et al., 2015; Zu et al., 2015). In a type-2 diabetic rat model induced by high fat diet and low dose streptozotocin, the expression of NLRP3, ASC, Casp-1, and IL-1β was increased in the heart. Genetic inhibition of Nlrp3 by a small interfering RNA *in vivo* improved left ventricular diastolic function in these diabetic rats (Luo et al., 2014), which was attributed to a reduction in cell death, an improvement of myofilament and mitochondria structures, and a reduction in cardiac fibrosis. Thus there is accumulating evidence pointing to a critical role of NLRP3 inflammasome activation in ischemic and non-ischemic cardiomyopathy.

ROLE OF NLRP3 INFLAMMASOME IN AF

AF is the most frequent clinical arrhythmia which is associated with an increased risk of stroke and worsening heart failure (Andrade et al., 2014; Freeman et al., 2017). The development of AF often involves ectopic triggers acting on an arrhythmogenic substrate to initiate AF-maintaining reentry (Heijman et al., 2014). The current therapeutic approaches are moderately effective perhaps because of critical gaps in current knowledge about arrhythmia mechanisms and important translational challenges of available therapeutic concepts (Heijman et al., 2016, 2018).

An enhanced inflammatory response is frequently associated with AF development (Aviles et al., 2003; Harada et al., 2015) and increased levels of circulating IL-1β and IL-18 positively correlated with progression from paroxysmal AF (pAF) to long-lasting persistent AF (perAF), along with left atrial dilatation (an independent risk factor of AF) in AF patients (Luan et al., 2010; Gungor et al., 2013). We recently showed that the activity of the NLRP3 inflammasome is increased in CMs from patients with pAF and perAF (Yao et al., 2018). In atrial CMs from pAF patients, protein levels of active Casp-1-p20 were significantly increased, despite the unchanged protein levels of NLRP3 and pro-Casp-1, likely reflecting the fact that the increase in NLRP3 inflammasome activity in pAF might be due to an increased "triggering" (enhanced assembly), rather than "priming" (increased gene transcription) processes. In contrast, atrial CMs from perAF patients showed not only higher protein levels of Casp-1-p20, but also an upregulation of NLRP3, ASC, and pro-Casp-1 proteins, indicating that both "priming" and "triggering" processes contribute to the activation of the NLRP3 inflammasome in CMs of these patients. To the best of our knowledge this study is the first to show that the NLRP3 inflammasome is expressed and upregulated in non-immune cardiac cells (CMs) from pAF and perAF patients and that its activity in human CMs correlates with the progression of AF to more persistent forms.

To determine whether CM-restricted activation of the NLRP3 inflammasome plays a causative role in AF pathogenesis, a CM-specific knockin mouse model expressing a gain-of-function mutation of NLRP3 ($NLRP3^{A350V}$) mimicking the constitutive NLRP3 activation seen in CMs from AF patients, was established by crossing a previously established conditional allele (Brydges et al., 2009) to the CM-specific Cre transgenic mouse ($Myh6^{Cre}$:$Nlrp3^{A350V/+}$, CM-KI). In this CM-KI mouse model, total protein levels of NLRP3, ASC and pro-Casp-1 remained unchanged, whereas Casp-1-p20 protein levels were increased, recapitulating the changes we observed in pAF patients. Electrophysiological studies have demonstrated that the constitutive activation of NLRP3 inflammasome in CMs only increased the AF susceptibility by producing both ectopic (triggered) activity and reentry-promoting electrical remodeling in CM-KI mice (Yao et al., 2018). Moreover, the enhanced AF susceptibility was associated with abnormal diastolic sarcoplasmic reticulum (SR) Ca^{2+} releases due to increased protein levels of ryanodine receptor type-2 (RyR2), which might represent the molecular correlates of ectopic activity as reflected by the higher incidence of premature atrial contractions. In addition, the atrial effective refractory period (AERP) was abbreviated most likely because of an enhanced function of the ultra-rapid delayed-rectifier K^+-current (Kv1.5) in CMs. Genetic inhibition of Nlrp3 in CM-KI mice using the adeno-associated virus type 9 (AAV9)-mediated gene transfer of a short-hairpin RNA (shRNA), reduced the incidence of inducible AF episodes. Thus, this study clearly validated the causal relationship between the CM-specific NLRP3 inflammasome activation and the susceptibility to AF (Yao et al., 2018). **Figure 2** summarizes the putative molecular mechanisms associated with AF development due to the activation of the NLRP3 inflammasome in CMs only. Since NLRP3 inflammasomes exist also in CFs and CFs play an important role in atrial fibrosis, a well-recognized substrate for AF maintenance, future studies should address

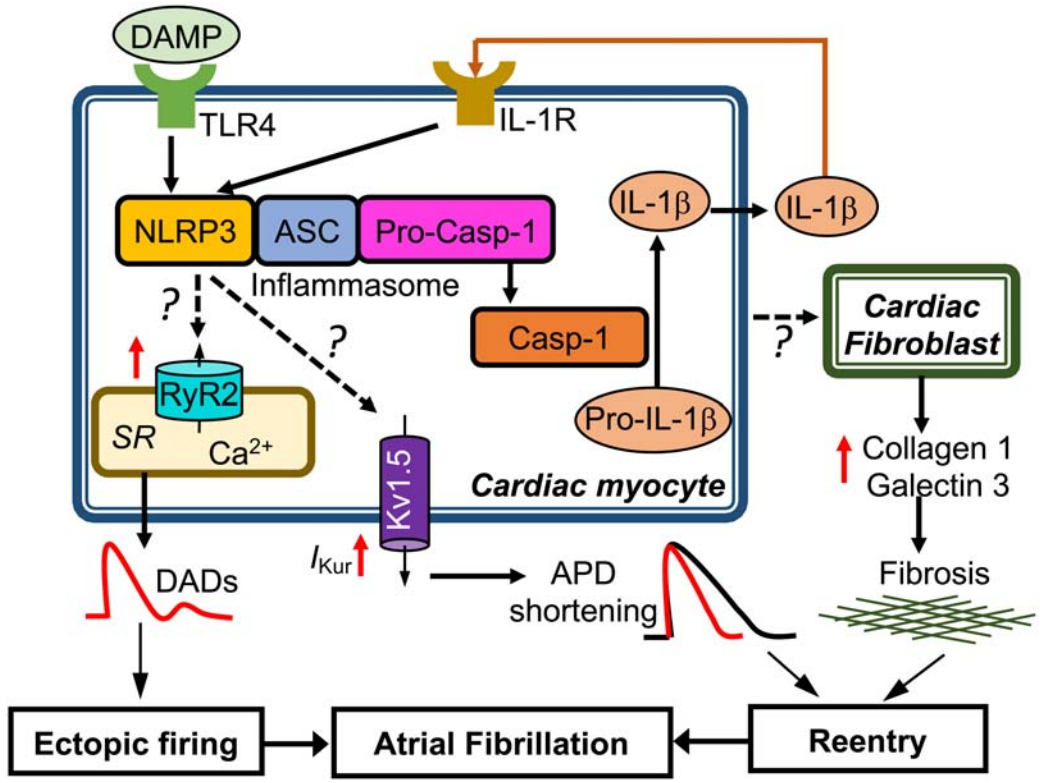

FIGURE 2 | Putative molecular mechanisms underlying the development of atrial fibrillation due to constitutive activation of NLRP3 inflammasome in mouse cardiac myocytes only. Question marks indicated the mechanisms that need to be investigated. APD, action potential duration; DADs, delayed afterdepolarizations; I_{Kur}, ultra-rapid delayed rectifier potassium current; SR, sarcoplasmic reticulum.

the potential role of the CF NLRP3 inflammasome for AF pathophysiology.

TARGETING OF THE NLRP3 INFLAMMASOME AS A THERAPEUTIC OPTION

Based on available experimental evidence, targeting the NLRP3 inflammasome-signaling pathway may represent a unique therapeutic opportunity for patients with cardiomyopathy and/or AF. Most of the agents described below have been tested only pre-clinically in animal models and their potential translation into clinical practice will require prospective clinical trials in the suitable patient populations. The multiple players involved in the NLRP3 inflammasome signaling cascade offer a variety of viable options for therapeutic exploitation. Targeting the upstream regulators of NLRP3 inflammasome function, selective inhibition of different members of NLRP3 inflammasome complex, interruption of the complex preventing maturation of Casp-1, and selective blockade of the downstream effectors (mature caspase-1 and IL-1β) of NLRP3-inflammasome activation, may all be viable therapeutic interventions. An inhibition of the upstream regulators could be achieved by inhibition of K^+ efflux with the antidiabetic drug glyburide (Haque et al., 2016) or the application of a ROS-scavenger (Liu et al., 2014). The inhibition of individual NLRP3 inflammasome members could be accomplished by genetic silencing of Nlrp3, ASC, or pro-Casp-1 using specific shRNAs (Dai et al., 2011; Yao et al., 2018) or CRISP/Cas9-mediated non-homologous end joining (NHEJ) (Zhang et al., 2014) via the AAV-mediated gene transfer system. Disruption of inter–domain interaction between NLRP3 and ASC can be achieved using the MCC950 compound (Coll et al., 2015). The blockade of IL-1β functions is currently the most advanced strategy with two agents being clinically available: the IL-1 receptor antagonist anakinra (Mitroulis et al., 2010) and the neutralizing IL-1β antibody canakinumab (Jesus and Goldbach-Mansky, 2014; Ridker et al., 2017). Moreover, several Casp-1 inhibitors (e.g., Ac-WEHD-Cho and Ac-YVAD-cho) are currently under development for patients with auto-inflammatory diseases (Howley and Fearnhead, 2008; MacKenzie et al., 2010). Interestingly, the recently completed large-scale clinical trial "The Canakinumab Anti-inflammatory Thrombosis Outcomes Study" (CANTOS) showed that selective targeting of the IL-1β pathway can significantly reduce the rate of recurrent cardiovascular events including myocardial infarction, and that this effect was independent of lipid levels lowering (Ridker et al., 2017). This study provides a promise that targeting of the NLRP3-inflammasome could potentially be a viable therapeutic option

for cardiomyopathies, AF, and perhaps other cardiovascular diseases including heart failure. Prospective randomized clinical trials including suitable clinical patient populations are needed to prove and validate the therapeutic potential of NLRP3 inflammasome inhibition for the management of cardiovascular diseases.

AUTHOR CONTRIBUTIONS

NL designed the study. GC organized the database. GC and MC wrote sections of the manuscript. DD and NL revised the manuscript critically for important intellectual content. All authors contributed to the manuscript revision, read, and approved the submitted version.

FUNDING

This work was supported by the National Institutes of Health (R56-HL131649 to NL, R01-HL136389 to NL, and DD, R01-HL131517 to DD), the American Heart Association (14SDG20080008 to NL), the German Research Foundation DFG (Do 769/4-1 to DD), and DZHK (German Center for Cardiovascular Research to DD).

REFERENCES

Andrade, J., Khairy, P., Dobrev, D., and Nattel, S. (2014). The clinical profile and pathophysiology of atrial fibrillation: relationships among clinical features, epidemiology, and mechanisms. *Circ. Res.* 114, 1453–1468. doi: 10.1161/CIRCRESAHA.114.303211

Askevold, E. T., Gullestad, L., Dahl, C. P., Yndestad, A., Ueland, T., and Aukrust, P. (2014). Interleukin-6 signaling, soluble glycoprotein 130, and inflammation in heart failure. *Curr. Heart Fail. Rep.* 11, 146–155. doi: 10.1007/s11897-014-0185-9

Aviles, R. J., Martin, D. O., Apperson-Hansen, C., Houghtaling, P. L., Rautaharju, P., Kronmal, R. A., et al. (2003). Inflammation as a risk factor for atrial fibrillation. *Circulation* 108, 3006–3010. doi: 10.1161/01.CIR.0000103131.70301.4F

Baldrighi, M., Mallat, Z., and Li, X. (2017). NLRP3 inflammasome pathways in atherosclerosis. *Atherosclerosis* 267, 127–138. doi: 10.1016/j.atherosclerosis.2017.10.027

Baudino, T. A., Carver, W., Giles, W., and Borg, T. K. (2006). Cardiac fibroblasts: friend or foe? *Am. J. Physiol. Heart Circ. Physiol.* 291, H1015–H1026. doi: 10.1152/ajpheart.00023.2006

Beg, A. A. (2002). Endogenous ligands of Toll-like receptors: implications for regulating inflammatory and immune responses. *Trends Immunol.* 23, 509–512. doi: 10.1016/S1471-4906(02)02317-7

Bracey, N. A., Beck, P. L., Muruve, D. A., Hirota, S. A., Guo, J., Jabagi, H., et al. (2013). The Nlrp3 inflammasome promotes myocardial dysfunction in structural cardiomyopathy through interleukin-1β. *Exp. Physiol.* 98, 462–473. doi: 10.1113/expphysiol.2012.068338

Brydges, S. D., Mueller, J. L., McGeough, M. D., Pena, C. A., Misaghi, A., Gandhi, C., et al. (2009). Inflammasome-mediated disease animal models reveal roles for innate but not adaptive immunity. *Immunity* 30, 875–887. doi: 10.1016/j.immuni.2009.05.005

Buckley, C. D., Gilroy, D. W., Serhan, C. N., Stockinger, B., and Tak, P. P. (2013). The resolution of inflammation. *Nat. Rev. Immunol.* 13, 59–66. doi: 10.1038/nri3362

Camelliti, P. L., Borg, T. K., and Kohl, P. (2005). Structural and functional characterisation of cardiac fibroblasts. *Cardiovasc. Res.* 1, 40–51. doi: 10.1016/j.cardiores.2004.08.020

Coll, R. C., Robertson, A. A., Chae, J. J., Higgins, S. C., Muñoz-Planillo, R., Inserra, M. C., et al. (2015). A small-molecule inhibitor of the NLRP3 inflammasome for the treatment of inflammatory diseases. *Nat. Med.* 21, 248–255. doi: 10.1038/nm.3806

Dai, X., Sayama, K., Tohyama, M., Shirakata, Y., Hanakawa, Y., Tokumaru, S., et al. (2011). Mite allergen is a danger signal for the skin via activation of inflammasome in keratinocytes. *J. Allergy Clin. Immunol.* 127, 806–814. doi: 10.1016/j.jaci.2010.12.006

Davis, B. K., Wen, H., and Ting, J. P. (2011). The inflammasome NLRs in immunity, inflammation, and associated diseases. *Annu. Rev. Immunol.* 29, 707–735. doi: 10.1146/annurev-immunol-031210-101405

Dinarello, C. A. (2009). Immunological and inflammatory functions of the interleukin-1 family. *Annu. Rev. Immunol.* 27, 519–550. doi: 10.1146/annurev.immunol.021908.132612

Duewell, P., Kono, H., Rayner, K. J., Sirois, C. M., Vladimer, G., Bauernfeind, F. G., et al. (2010). NLRP3 inflammasomes are required for atherogenesis and activated by cholesterol crystals. *Nature* 464, 1357–1361. doi: 10.1038/nature08938

Fink, S. L., Bergsbaken, T., and Cookson, B. T. (2008). Anthrax lethal toxin and *Salmonella* elicit the common cell death pathway of caspase-1-dependent pyroptosis via distinct mechanisms. *Proc. Natl. Acad. Sci. U.S.A.* 105, 4312–4317. doi: 10.1073/pnas.0707370105

Frangogiannis, N. G. (2014). Targeting the transforming growth factor (TGF)-β cascade in the remodeling heart: benefits and perils. *J. Mol. Cell. Cardiol.* 76, 169–171. doi: 10.1016/j.yjmcc.2014.09.001

Freeman, J. V., Wang, Y., Akar, J., Desai, N., and Krumholz, H. (2017). National trends in atrial fibrillation hospitalization, readmission, and mortality for medicare beneficiaries, 1999-2013. *Circulation* 135, 1227–1239. doi: 10.1161/CIRCULATIONAHA.116.022388

Gu, Y., Kuida, K., Tsutsui, H., Ku, G., Hsiao, K., Fleming, M. A., et al. (1997). Activation of interferon-gamma inducing factor mediated by interleukin-1beta converting enzyme. *Science* 275, 206–209. doi: 10.1126/science.275.5297.206

Gungor, B., Ekmekci, A., Arman, A., Ozcan, K. S., Ucer, E., Alper, A. T., et al. (2013). Assessment of interleukin-1 gene cluster polymorphisms in lone atrial fibrillation: new insight into the role of inflammation in atrial fibrillation. *Pacing Clin. Electrophysiol.* 36, 1220–1227. doi: 10.1111/pace.12182

Haque, S., Lan, X., Wen, H., Lederman, R., Chawla, A., Attia, M., et al. (2016). HIV promotes nlrp3 inflammasome complex activation in murine hiv-associated nephropathy. *Am. J. Pathol.* 186, 347–358. doi: 10.1016/j.ajpath.2015.10.002

Harada, M., Van Wagoner, D. R., and Nattel, S. (2015). Role of inflammation in atrial fibrillation pathophysiology and management. *Circ. J.* 79, 495–502. doi: 10.1253/circj.CJ-15-0138

He, W. T., Wan, H., Hu, L., Chen, P., Wang, X., Huang, Z., et al. (2015). Gasdermin D is an executor of pyroptosis and required for interleukin-1beta secretion. *Cell Res.* 25, 1285–1298. doi: 10.1038/cr.2015.139

He, Y., Hara, H., and Núñez, G. (2016). Mechanism and regulation of nlrp3 inflammasome activation. *Trends Biochem. Sci.* 41, 1012–1021. doi: 10.1016/j.tibs.2016.09.002

Heijman, J., Algalarrondo, V., Voigt, N., Melka, J., Wehrens, X. H., Dobrev, D., et al. (2016). The value of basic research insights into atrial fibrillation mechanisms as a guide to therapeutic innovation: a critical analysis. *Cardiovasc. Res.* 109, 467–479. doi: 10.1093/cvr/cvv275

Heijman, J., Guichard, J. B., Dobrev, D., and Nattel, S. (2018). Translational challenges in atrial fibrillation. *Circ. Res.* 122, 752–773. doi: 10.1161/CIRCRESAHA.117.311081

Heijman, J., Voigt, N., Nattel, S., and Dobrev, D. (2014). Cellular and molecular electrophysiology of atrial fibrillation initiation, maintenance, and progression. *Circ. Res.* 114, 1483–1499. doi: 10.1161/CIRCRESAHA.114.302226

Hoffman, H. M., and Wanderer, A. A. (2010). Inflammasome and IL-1β-mediated disorders. *Curr. Allergy Asthma Rep.* 10, 229–235. doi: 10.1007/s11882-010-0109-z

Howley, B., and Fearnhead, H. O. (2008). Caspases as therapeutic targets. *J. Cell. Mol. Med.* 12, 1502–1516. doi: 10.1111/j.1582-4934.2008.00292.x

Jennings, R. B., Murry, C. E., Steenbergen, C. Jr., and Reimer, K. A. (1990). Development of cell injury in sustained acute ischemia. *Circulation* 82, II2–II12.

Jesus, A. A., and Goldbach-Mansky, R. (2014). IL-1 blockade in autoinflammatory syndromes. *Annu. Rev. Med.* 65, 223–244. doi: 10.1146/annurev-med-061512-150641

Kanneganti, T. D. (2015). The inflammasome: firing up innate immunity. *Immunol. Rev. Immunol. Rev.* 265, 1–5. doi: 10.1111/imr.12297

Kaur, K., Dhingra, S., Slezak, J., Sharma, A. K., Bajaj, A., and Singal, P. K. (2009). Biology of TNFα and IL-10, and their imbalance in heart failure. *Heart Fail. Rev.* 14, 113–123. doi: 10.1007/s10741-008-9104-z

Kawaguchi, M., Takahashi, M., Hata, T., Kashima, Y., Usui, F., Morimoto, H., et al. (2011). Inflammasome activation of cardiac fibroblasts is essential for myocardial ischemia/reperfusion injury. *Circulation* 123, 594–604. doi: 10.1161/CIRCULATIONAHA.110.982777

Lawrence, T. (2009). The nuclear factor NF-kappaB pathway in inflammation. *Cold Spring Harb. Perspect. Biol.* 1:a001651. doi: 10.1101/cshperspect.a001651

Li, P., Allen, H., Banerjee, S., Franklin, S., Herzog, L., Johnston, C., et al. (1995). Mice deficient in il-1-beta-converting enzyme are defective in production of mature il-1-beta and resistant to endotoxic-shock. *Cell* 80, 401–411. doi: 10.1016/0092-8674(95)90490-5

Liu, X., Zhang, Z., Ruan, J., Pan, Y., Magupalli, V. G., Wu, H., et al. (2016). Inflammasome-activated gasdermin D causes pyroptosis by forming membrane pores. *Nature* 535, 153–158. doi: 10.1038/nature18629

Liu, Y., Lian, K., Zhang, L., Wang, R., Yi, F., Gao, C., et al. (2014). TXNIP mediates NLRP3 inflammasome activation in cardiac microvascular endothelial cells as a novel mechanism in myocardial ischemia/reperfusion injury. *Basic Res. Cardiol.* 109:415. doi: 10.1007/s00395-014-0415-z

Luan, Y., Li, S., Yu, B., Zhu, S., Li, S., Li, N., et al. (2010). Interleukin-18 among atrial fibrillation patients in the absence of structural heart disease. *Europace* 12, 1713–1718. doi: 10.1093/europace/euq321

Luo, B., Li, B., Wang, W., Liu, X., Xia, Y., Zhang, C., et al. (2014). NLRP3 gene silencing ameliorates diabetic cardiomyopathy in a type 2 diabetes rat model. *PLoS One* 9:e104771. doi: 10.1371/journal.pone.0104771

MacKenzie, S. H., Schipper, J. L., and Clark, A. C. (2010). The potential for caspases in drug discovery. *Curr. Opin. Drug Discov. Devel.* 13, 568–576.

Martinon, F., Burns, K., and Tschopp, J. (2002). The inflammasome: a molecular platform triggering activation of inflammatory caspases and processing of proIL-beta. *Mol. Cell.* 10, 417–426. doi: 10.1016/S1097-2765(02)00599-3

Matzinger, P. (1994). Tolerance, danger, and the extended family. *Annu. Rev. Immunol.* 12, 991–1045. doi: 10.1146/annurev.iy.12.040194.005015

Medzhitov, R. (2008). Origin and physiological roles of inflammation. *Nature* 454, 428–435. doi: 10.1038/nature07201

Mezzaroma, E., Toldo, S., Farkas, D., Seropian, I. M., Van Tassell, B. W., Salloum, F. N., et al. (2011). The inflammasome promotes adverse cardiac remodeling following acute myocardial infarction in the mouse. *Proc. Natl. Acad. Sci. U.S.A.* 108, 19725–19730. doi: 10.1073/pnas.1108586108

Mitroulis, I., Skendros, P., and Ritis, K. (2010). Targeting IL-1beta in disease; the expanding role of NLRP3 inflammasome. *Eur. J. Intern. Med.* 21, 157–163. doi: 10.1016/j.ejim.2010.03.005

Nguyen, M. N., Kiriazis, H., Gao, X. M., and Du, X. J. (2017). Cardiac Fibrosis and Arrhythmogenesis. *Compr. Physiol.* 7, 1009–1049. doi: 10.1002/cphy.c160046

Opie, L. H., Commerford, P. J., Gersh, B. J., and Pfeffer, M. A. (2006). Controversies in ventricular remodelling. *Lancet* 367, 356–367. doi: 10.1016/S0140-6736(06)68074-4

Pfeffer, M. A., and Braunwald, E. (1990). Ventricular remodeling after myocardial infarction. Experimental observations and clinical implications. *Circulation* 81, 1161–1172. doi: 10.1161/01.CIR.81.4.1161

Ridker, P. M., Everett, B. M., Thuren, T., MacFadyen, J. G., Chang, W. H., Ballantyne, C., et al. (2017). Antiinflammatory therapy with canakinumab for atherosclerotic disease. *N. Engl. J. Med.* 377, 1119–1131. doi: 10.1056/NEJMoa1707914

Sandanger, O., Ranheim, T., Vinge, L. E., Bliksoen, M., Alfsnes, K., Finsen, A. V., et al. (2013). The NLRP3 inflammasome is up-regulated in cardiac fibroblasts and mediates myocardial ischaemia-reperfusion injury. *Cardiovasc. Res.* 99, 164–174. doi: 10.1093/cvr/cvt091

Sborgi, L., Ruhl, S., Mulvihill, E., Pipercevic, J., Heilig, R., Stahlberg, H., et al. (2016). GSDMD membrane pore formation constitutes the mechanism of pyroptotic cell death. *EMBO J.* 35, 1766–1778. doi: 10.15252/embj.201694696

Schroder, K., and Tschopp, J. (2010). The inflammasomes. *Cell* 140, 821–832. doi: 10.1016/j.cell.2010.01.040

Shao, W., Yeretssian, G., Doiron, K., Hussain, S. N., and Saleh, M. (2007). The caspase-1 digestome identifies the glycolysis pathway as a target during infection and septic shock. *J. Biol. Chem.* 282, 36321–36329. doi: 10.1074/jbc.M708182200

Shaw, J. E., Sicree, R. A., and Zimmet, P. Z. (2010). Global estimates of the prevalence of diabetes for 2010 and 2030. *Diabetes Res. Clin. Pract.* 87, 4–14. doi: 10.1016/j.diabres.2009.10.007

Shi, J., Zhao, Y., Wang, K., Shi, X., Wang, Y., Huang, H., et al. (2015). Cleavage of GSDMD by inflammatory caspases determines pyroptotic cell death. *Nature* 526, 660–665. doi: 10.1038/nature15514

Ting, J. P., Lovering, R. C., Alnemri, E. S., Bertin, J., Boss, J. M., Davis, B. K., et al. (2008). The NLR gene family: a standard nomenclature. *Immunity* 28, 285–287. doi: 10.1016/j.immuni.2008.02.005

Toldo, S., and Abbate, A. (2018). The NLRP3 inflammasome in acute myocardial infarction. *Nat. Rev. Cardiol.* 15, 203–214. doi: 10.1038/nrcardio.2017.161

Toldo, S., Marchetti, C., Mauro, A. G., Chojnacki, J., Mezzaroma, E., Carbone, S., et al. (2016). Inhibition of the NLRP3 inflammasome limits the inflammatory injury following myocardial ischemia-reperfusion in the mouse. *Int. J. Cardiol.* 209, 215–220. doi: 10.1016/j.ijcard.2016.02.043

Travers, J. G., Kamal, F. A., Robbins, J., Yutzey, K. E., and Blaxall, B. C. (2016). Cardiac fibrosis: the fibroblast awakens. *Circ. Res.* 118, 1021–1040. doi: 10.1161/CIRCRESAHA.115.306565

Valle Raleigh, J., Mauro, A. G., Devarakonda, T., Marchetti, C., He, J., Kim, E., et al. (2017). Reperfusion therapy with recombinant human relaxin-2 (Serelaxin) attenuates myocardial infarct size and NLRP3 inflammasome following ischemia/reperfusion injury via eNOS-dependent mechanism. *Cardiovasc. Res.* 113, 609–619. doi: 10.1093/cvr/cvw246

Vandanmagsar, B., Youm, Y. H., Ravussin, A., Galgani, J. E., Stadler, K., Mynatt, R. L., et al. (2011). The NLRP3 inflammasome instigates obesity-induced inflammation and insulin resistance. *Nat. Med.* 17, 179–188. doi: 10.1038/nm.2279

Wexler, R. K., Elton, T., Pleister, A., and Feldman, D. (2009). Cardiomyopathy: an overview. *Am. Fam. Physician* 79, 778–784.

Wilson, K. P., Black, J. A., Thomson, J. A., Kim, E. E., Griffith, J. P., Navia, M. A., et al. (1994). Structure and mechanism of interleukin-1 beta converting enzyme. *Nature* 28, 270–275. doi: 10.1038/370270a0

Yao, C., Veleva, T., Scott, L., Cao, S., Li, L., Chen, G., et al. (2018). Enhanced cardiomyocyte nlrp3 inflammasome signaling promotes atrial fibrillation. *Circulation* doi: 10.1161/CIRCULATIONAHA.118.035202 [Epub ahead of print].

Yin, Y., Yan, Y., Jiang, X., Mai, J., Chen, N. C., Wang, H., et al. (2009). Inflammasomes are differentially expressed in cardiovascular and other tissues. *Int. J. Immunopathol. Pharmacol.* 22, 311–322. doi: 10.1177/039463200902200208

Zhang, F., Wen, Y., and Guo, X. (2014). CRISPR/Cas9 for genome editing: progress, implications and challenges. *Hum. Mol. Genet.* 23, R40–R46. doi: 10.1093/hmg/ddu125

Zu, Y., Wan, L. J., Cui, S. Y., Gong, Y. P., and Li, C. L. (2015). The mitochondrial Na+/Ca2+ exchanger may reduce high glucose-induced oxidative stress and nucleotide-binding oligomerization domain receptor 3 inflammasome activation in endothelial cells. *J. Geriatr. Cardiol.* 12, 270–278.

Conflict of Interest Statement: The authors declare that the research was conducted in the absence of any commercial or financial relationships that could be construed as a potential conflict of interest.

frontiers in Physiology

REVIEW
published: 04 September 2018
doi: 10.3389/fphys.2018.01228

Cardiac Arrhythmias as Manifestations of Nanopathies: An Emerging View

Przemysław B. Radwański[1,2,3,4], Christopher N. Johnson[2,5], Sándor Györke[1,2,3] and Rengasayee Veeraraghavan[1,2,3,6]**

[1] Bob and Corinne Frick Center for Heart Failure and Arrhythmia, The Ohio State University Wexner Medical Center, Columbus, OH, United States, [2] Dorothy M. Davis Heart and Lung Research Institute, College of Medicine, The Ohio State University Wexner Medical Center, Columbus, OH, United States, [3] Department of Physiology and Cell Biology, College of Medicine, The Ohio State University, Columbus, OH, United States, [4] Division of Pharmacy Practice and Science, College of Pharmacy, The Ohio State University, Columbus, OH, United States, [5] Vanderbilt Center for Arrhythmia Research and Therapeutics, Nashville, TN, United States, [6] Department of Biomedical Engineering, The Ohio State University, Columbus, OH, United States

OPEN ACCESS

Edited by:
Alexey V. Glukhov, University of Wisconsin System, United States

Reviewed by:
Yohannes Castro Shiferaw, California State University, Northridge, United States
Wayne Rodney Giles, University of Calgary, Canada
Rob Gourdie, Medical University of South Carolina, United States

***Correspondence:**
Przemysław B. Radwański
Przemyslaw.Radwanski@osumc.edu
Rengasayee Veeraraghavan
Veeraraghavan.12@osu.edu; Saiv@vt.edu

Specialty section:
This article was submitted to Cardiac Electrophysiology, a section of the journal Frontiers in Physiology

Received: *01 June 2018*
Accepted: *14 August 2018*
Published: *04 September 2018*

Citation:
Radwański PB, Johnson CN, Györke S and Veeraraghavan R (2018) Cardiac Arrhythmias as Manifestations of Nanopathies: An Emerging View. Front. Physiol. 9:1228. doi: 10.3389/fphys.2018.01228

A nanodomain is a collection of proteins localized within a specialized, nanoscale structural environment, which can serve as the functional unit of macroscopic physiologic processes. We are beginning to recognize the key roles of cardiomyocyte nanodomains in essential processes of cardiac physiology such as electrical impulse propagation and excitation–contraction coupling (ECC). There is growing appreciation of nanodomain dysfunction, i.e., nanopathy, as a mechanistic driver of life-threatening arrhythmias in a variety of pathologies. Here, we offer an overview of current research on the role of nanodomains in cardiac physiology with particular emphasis on: (1) sodium channel-rich nanodomains within the intercalated disk that participate in cell-to-cell electrical coupling and (2) dyadic nanodomains located along transverse tubules that participate in ECC. The beat to beat function of cardiomyocytes involves three phases: the action potential, the calcium transient, and mechanical contraction/relaxation. In all these phases, cell-wide function results from the aggregation of the stochastic function of individual proteins. While it has long been known that proteins that exist in close proximity influence each other's function, it is increasingly appreciated that there exist nanoscale structures that act as functional units of cardiac biophysical phenomena. Termed nanodomains, these structures are collections of proteins, localized within specialized nanoscale structural environments. The nano-environments enable the generation of localized electrical and/or chemical gradients, thereby conferring unique functional properties to these units. Thus, the function of a nanodomain is determined by its protein constituents as well as their local structural environment, adding an additional layer of complexity to cardiac biology and biophysics. However, with the emergence of experimental techniques that allow direct investigation of structure and function at the nanoscale, our understanding of cardiac physiology and pathophysiology at these scales is rapidly advancing. Here, we will discuss the structure and functions of multiple cardiomyocyte nanodomains, and novel strategies that target them for the treatment of cardiac arrhythmias.

Keywords: nanopathies, arrhythmias, cardiac, sodium channels, sodium calcium exchanger, RyR2

THE NANO-MACHINERY OF CARDIAC ELECTRICAL EXCITATION

For over a century, it has been recognized that cardiac myocytes come into close contact at the intercalated disk (ID), where adjacent cells are only nanometers apart. By the mid-20th century, gap junctions (GJs) were identified as specialized structures within the ID, which afford electrochemical coupling between cells (Sjostrand and Andersson, 1954; Barr et al., 1965). The closest apposition between neighboring myocytes occurs within these GJs, with as little as 2 nm separating the cells. Despite this, GJs themselves do not constitute a functional nanodomain – they afford direct cytosolic continuity between coupled cells, and since neither cytosolic compartment is a restricted environment, the effects unique to nanoscale compartments do not come into play. Thus, cardiac conduction, the cell-to-cell spread of electrical excitation through the heart, was thought a relatively simple process with cardiac voltage-gated sodium (Na^+) channels ($Na_V1.5$) affording excitability, and GJs providing cell-to-cell electrical coupling (Kleber and Rudy, 2004).

This electrotonic view of cardiac conduction allowed the formalism of cable theory to be applied to cardiac conduction, and adequately explained experimental observations for several decades (Kleber and Rudy, 2004). However, findings have accumulated, that are not well-explained by this model. Transgenic mice with reduced Cx43 expression displayed significant conduction slowing in some studies (Guerrero et al., 1997; Eloff et al., 2001; Gutstein et al., 2001), but not in others (Morley et al., 1999; Vaidya et al., 2001; Thomas et al., 2003; Beauchamp et al., 2004; Danik et al., 2004; van Rijen et al., 2004; Stein et al., 2009). Likewise, GJ remodeling and reduced Cx43 expression correlated with arrhythmogenic conduction slowing in one pacing-induced canine heart failure model (Poelzing et al., 2004), but preceded it in another (Akar et al., 2007). Another discrepant finding stemmed from investigations of the electrophysiological impact of cardiac interstitial edema (fluid accumulation in the extracellular space): per the electrotonic model, an increase interstitial volume would lower extracellular resistance, and consequently, increase conduction velocity (Spach et al., 2004; Plonsey and Barr, 2007). However, experimental measurements in guinea pig ventricles revealed conduction slowing during to interstitial edema (Veeraraghavan et al., 2012, 2015, 2016) and edema was linked to reversible conduction block in patients undergoing ablation for the treatment of atrial fibrillation (AF) (Arujuna et al., 2012). These findings prompted speculation that non-electrotonic mechanisms of intercellular communication may play a role in the heart.

Theoretical studies had long raised the possibility of an alternate mode of intercellular coupling (Pertsov and Medvinskii, 1976; Sperelakis and Mann, 1977; Kucera et al., 2002; Sperelakis and McConnell, 2002; Copene and Keener, 2008; Mori et al., 2008). Dubbed ephaptic coupling, this mechanism envisions cells communicating via local extracellular electrochemical transients (ion accumulation/depletion). The aforementioned models suggest that a cardiac ephapse (a functional nanodomain capable of supporting ephaptic coupling) would require $Na_V1.5$-rich membranes from neighboring cells, separated by a very narrow extracellular cleft ($\leq$30 nm) (Veeraraghavan et al., 2014a,b). Whereas channels located at the lateral sarcolemma would face a large bulk of extracellular fluid with a practically inexhaustible supply of ions, channels facing narrow extracellular clefts would have a limited supply of ions. In the latter case, ion channel activity could mount local extracellular electrochemical transients, in turn altering the local transmembrane potential. In this context, early results demonstrating that $Na_V1.5$ channels are enriched at the ID (Maier et al., 2004; Petitprez et al., 2011) prompted speculation that functional nanodomains capable of supporting ephaptic coupling, i.e., ephapses, may exist within the ID. Until recently, the 250–350 nm resolution limit imposed on confocal microscopy by diffraction had precluded precise localization of $Na_V1.5$ within the ID. However, this restriction was removed by the advent of super-resolution microscopy techniques with resolutions extending down to 20 nm. Work conducted by the Gourdie (Rhett et al., 2012; Veeraraghavan et al., 2013, 2015; Veeraraghavan and Gourdie, 2016) and Delmar (Agullo-Pascual et al., 2013, 2014; Leo-Macias et al., 2016) labs using super-resolution techniques identified $Na_V1.5$ enrichment within specific regions of the ID (**Figure 1**). One subpopulation of ID-localized $Na_V1.5$ was located at the perinexus, a specialized nanodomain located at the periphery of Cx43 GJs (Rhett et al., 2011; Rhett and Gourdie, 2012). A second localized to N-cadherin-rich plicate regions of the ID, where mechanical junctions are concentrated. Electron microscopy studies revealed disparate ultrastructural properties at these sites: within the perinexus, adjacent cell membranes were no more than 10–15 nm apart (Veeraraghavan et al., 2015), whereas at N-cadherin-rich mechanical junctions, intermembrane spacing was as high as 60–75 nm (Leo-Macias et al., 2015, 2016). The latter significantly exceeds the theoretically derived $\leq$ 30 nm intermembrane spacing limit for ephaptic coupling; however, the properties of the perinexus may enable it to function as an ephapse.

Providing functional support for the ephaptic coupling hypothesis, the Poelzing and Gourdie groups demonstrated that acute interstitial edema selectively disrupted perinexal ultrastructure without altering other ID sites, and precipitated arrhythmogenic conduction slowing (Veeraraghavan et al., 2012, 2015, 2016). Additionally, perinexal disruption increased the dependence of conduction on GJ coupling and vice versa, suggesting that both modes of intercellular coupling operate in tandem (Veeraraghavan et al., 2012). Notably, in a setting of perinexal disruption, inhibition of channels enriched at perinexal sites – $Na_V1.5$, and inward-rectifier potassium channels ($K_{ir}2.1$) – resulted in anisotropic changes in conduction velocity, preferentially affecting transverse conduction (Veeraraghavan et al., 2015, 2016). In contrast, modulating ionic currents under normal conditions does not produce direction-specific impact. Keener and colleagues demonstrated that these experimental results could be predicted by a computational model incorporating both ephaptic and electrotonic coupling, but not by a purely electrotonic model (Lin and Keener, 2010, 2014; Veeraraghavan et al., 2015, 2016). Recently, Hichri and colleagues provided experimental and *in silico* evidence that the behavior of ID-localized $Na_V1.5$ is modulated by their clustering,

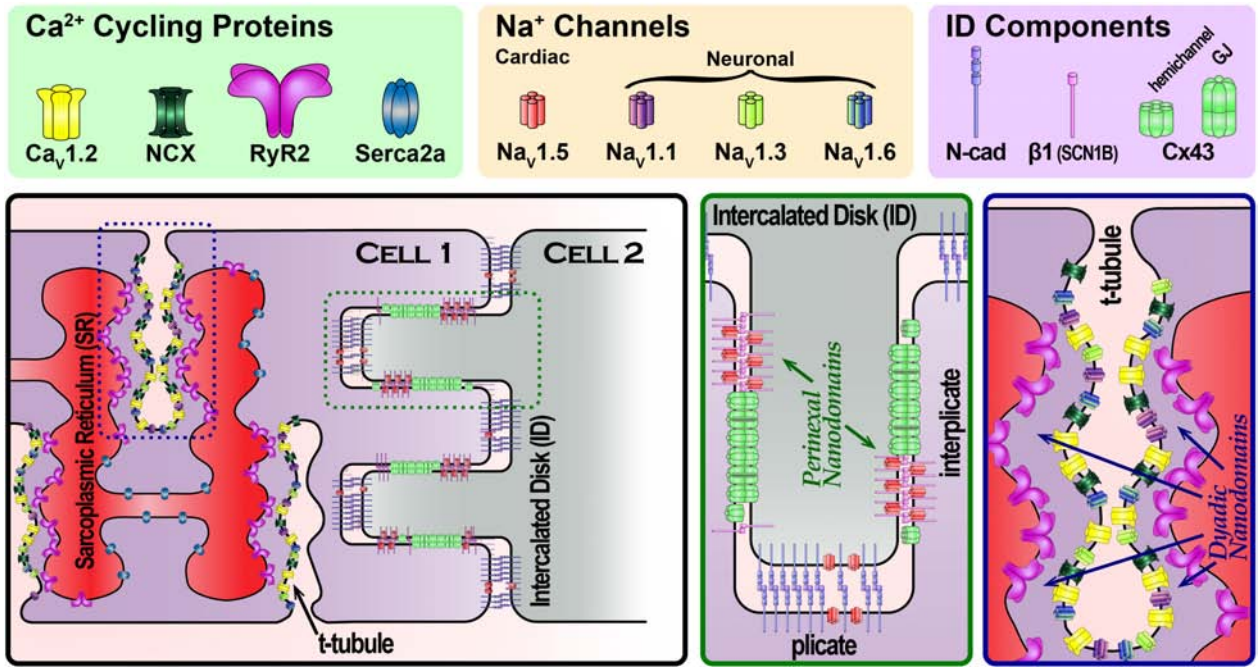

FIGURE 1 | Schematic cartoon depicting the organization of Na^+ channels in different parts of the cardiac myocyte, highlighting Na^+ channel-rich nanodomains within the intercalated disk (green dashed box) and t-tubules (blue dashed box). Zoomed in views of these nanodomains are provided in the green and blue boxed panels.

location within the ID (relative to the bulk interstitium), and the trans-alignment of these clusters (Hichri et al., 2017). In sum, these results illustrate macroscopic physiologic phenomena driven by the behavior of functional nanodomains, which can only be understood through knowledge of structure–function relationships at the nanodomain level.

In the larger context, the results highlighting the perinexus as a functional nanodomain involved in cardiac cell-to-cell communication pose the question: is the ID home to other functional nanodomains? The likelihood is high, given that the ID contains other sites enriched with $Na_V1.5$ (Milstein et al., 2012; Veeraraghavan et al., 2015; Leo-Macias et al., 2016) and $K_{ir}2.1$ (Milstein et al., 2012; Veeraraghavan et al., 2016; Ponce-Balbuena et al., 2018) as well as other ion channel species such as ATP-sensitive K^+ channels ($K_{ir}6.2$) (Hong et al., 2012). Notably, extracellular sodium has been shown to strongly modulate $K_{ir}2.1$ function (Ishihara, 2018), hinting at the potential for complex interrelationships between ion channel species within ID nanodomains. Thus, ID-localized ion channels clearly merit further investigation, with particular emphasis on their protein neighbors and local structural environment, both within the cell and without. In this regard, available observations on the composition and subcellular location of $Na_V1.5$-containing macromolecular complexes hint at significant complexity. $Na_V1.5$ has been demonstrated to associate with ankyrin-G (Makara et al., 2014), SAP97 (Petitprez et al., 2011; Gillet et al., 2015), $K_{ir}2.1$ and Kir2.2 (Milstein et al., 2012; Matamoros et al., 2016; Ponce-Balbuena et al., 2018), syntrophin and dystrophin (Petitprez et al., 2011), and CASK (Eichel et al., 2016). Both ankyrin-G and SAP97 preferentially associate with ID-localized $Na_V1.5$. However, loss of ankyrin-G reduced functional $Na_V1.5$ expression (Makara et al., 2014) whereas loss of SAP97 did not (Gillet et al., 2015). Similarly, $Na_V1.5$ at the lateral sarcolemma associates with syntrophin, dystrophin, and CASK. Loss of dystrophin reduced $Na_V1.5$ functional expression at this location (Petitprez et al., 2011). Conversely, loss of CASK increased $Na_V1.5$ surface expression at the lateral sarcolemma (Eichel et al., 2016). These intriguing findings suggest that we have much to learn about the organization and regulation of sodium channel-rich nanodomains, and the functional implications thereof.

Pathophysiology

Pathological alterations in $Na_V1.5$ function are a well-established cause of cardiac arrhythmias (Veerman et al., 2015; Sottas and Abriel, 2016). Likewise, GJ remodeling is widely recognized as a feature of multiple cardiac pathologies (Jongsma and Wilders, 2000; Stroemlund et al., 2015), and implicated as a contributor to arrhythmogenesis (De Vuyst et al., 2011; Ongstad et al., 2013). While the arrhythmogenic impacts of functional loss of I_{Na} and GJ coupling have long been subjects of intense inquiry, we are only beginning to recognize the effects of nanoscale organization of $Na_V1.5$ and Cx43, various scaffolding proteins associated with them, and changes in their ultrastructural environment. An interesting development in this context is the growing appreciation of the non-channel functions of Cx43 and their role in pathophysiology (Agullo-Pascual and Delmar, 2012). Knockdown of Cx43 in mice was

associated with concomitant reductions in $Na_V1.5$ expression, and I_{Na} density (Jansen et al., 2012) but not with alterations in adherens junctions or desmosomes (Gutstein et al., 2003). Proximity ligation assays indicate that the association between Cx43, and $Na_V1.5$ is concentrated within the perinexus (Rhett et al., 2012). This raises the possibility that the aforementioned loss of I_{Na} function may result from the loss of Cx43 to scaffold $Na_V1.5$ within perinexal nanodomains, and thereby, preferentially impact these sites. Thus, nanopathy may underlie arrhythmias in the wide array of cardiac pathologies where Cx43 is remodeled (Akar et al., 2007; Desplantez et al., 2007; Dhein et al., 2011; Chkourko et al., 2012). Along similar lines, missense mutations in the desmosomal protein plakophilin-2 were demonstrated to reduce N-cadherin-associated $Na_V1.5$ density at the ID, reduce I_{Na}, and result in a Brugada syndrome phenotype (Cerrone et al., 2014). Taken together, these results underscore the clinical relevance of understanding the molecular organization of functional nanodomains, and the specific role of nanopathy in disease.

In addition to direct alterations of $Na_V1.5$ and/or its molecular partners, nanopathy could also result from pathological changes in nanodomain ultrastructure. In this context, the previously discussed effects of interstitial edema on the perinexal nanodomain take on interesting implications given the wide array of pathologies that are associated with both cardiac edema and arrhythmias (Mehlhorn et al., 1996, 2001; Boyle et al., 2007; Fernandez-Jimenez et al., 2015; Migliore et al., 2015). Additionally, in long QT syndrome type 3 (LQT3; a disorder stemming from pathological gain of $Na_V1.5$ function), the Poelzing group recently demonstrated that transient depletion of extracellular Na^+ within perinexal nanodomains may mitigate risk of premature beats, and that perinexal widening may unmask the latent arrhythmia risk (Greer-Short et al., 2017). More recently, they have demonstrated that wider perinexi associated with the occurrence of AF in human patients (Raisch et al., 2018). While these are early days yet, these results collectively support the view that ultrastructural alterations within $Na_V1.5$-rich nanodomains may be a key determinant of arrhythmia risk, and therefore, a potential target for antiarrhythmic therapy.

THE NANO-MACHINERY OF CARDIAC EXCITATION-CONTRACTION COUPLING

Our understanding of excitation–contraction coupling (ECC) has followed a similar trajectory to the one outlined for the electrical excitation. Early studies first identified invaginations in the membrane called transverse (T)-tubules (Lindner, 1957) and demonstrated that an activating current localized to those domains prompts contraction (Huxley and Taylor, 1955, 1958). Subsequent work demonstrated that Ca^{2+} entry through the sarcolemma, via L-type Ca^{2+} channels (LTCC), results in calcium-induced calcium release from the sarcoplasmic reticulum (SR) via ryanodine receptor channels (RyR2) to couple electrical excitation with mechanical contraction (Fabiato and Fabiato, 1977). Examination of the structural underpinnings of cardiac ECC led to the identification of a restricted space dubbed the "fuzzy" dyadic space (Lederer et al., 1990) where the sarcolemma and the terminal cisternae of the SR are separated by only ∼12 nm (Forbes and Sperelakis, 1983) (**Figure 1**). These results led to the realization that local protein function and electrochemical fluxes within nanodomains govern ECC rather than bulk effects across larger scales. Indeed, both systolic and diastolic Ca^{2+} concentrations in the dyadic cleft have been found to exceed that of the bulk cytosol (Despa et al., 2014; Popescu et al., 2016), and differences in Na^+ concentrations have been reported as well (Despa and Bers, 2003).

An early clue to the complexity of the dyadic nanodomain function came with the demonstration by Leblanc and Hume that Na^+ influx may regulate Ca^{2+} release (Leblanc and Hume, 1990). Specifically, they provided evidence that Na^+ influx during the action potential upstroke was linked with Ca^{2+} cycling through the action of the Na^+–Ca^{2+} exchanger (NCX). Interestingly, a component of I_{Na} persists during the plateau phases, dubbed late I_{Na}, and is tetrodotoxin (TTX) – sensitive (Conforti et al., 1993). Further investigation along these intriguing lines by the Bridge and Goldhaber groups suggested the involvement of neuronal Na^+ channel (nNa_V) isoforms (Torres et al., 2010). This findings are consistent with aforementioned structural results: (1) $Na_V1.5$ localizes to the ID and the lateral sarcolemma and (2) nNa_Vs localize to t-tubules (Dhar Malhotra et al., 2001; Maier et al., 2002, 2004; Westenbroek et al., 2013; Radwański et al., 2015) (**Figure 1**). Indeed, up to 50% of the late I_{Na} in canine cardiac myocytes has been reported to be TTX-sensitive (Biet et al., 2012). These results raised the possibility that nNa_Vs, and NCX may constitute essential components of dyadic nanodomains along with LTCCs and RYR2. Since then, multiple groups have provided evidence for co-compartmentation of Na^+ and Ca^{2+} handling proteins within dyadic nanodomains (Scriven et al., 2000; Jayasinghe et al., 2009). In recent years, evidence has mounted that the high gain system of cardiac Ca^{2+} cycling is tightly regulated by nNa_Vs, and NCX localized within the cleft (Radwański and Poelzing, 2011; Radwański et al., 2013, 2015, 2016; Veeraraghavan et al., 2017). However, the molecular stoichiometry of Na^+/Ca^{2+} handling machinery (NCX, RyR, Na_Vs) and inter-species differences remain to be elucidated.

An additional layer of complexity in dyadic nanodomain function derives from its structure. It encompasses three spatial compartments – the extracellular space within the t-tubule, the cytosolic subspace, and the terminal cisternae of the junctional SR. In contrast, Na^+ channel-rich nanodomains at the ID only consist of two compartments, extracellular and intracellular. While much of the inquiry into dyadic nanodomain function has focused on dynamics within the cytosolic subspace, emerging evidence is drawing attention to the complexity of the t-tubular network. Electron microscopy has revealed microfolds along t-tubules (Lavorato et al., 2015), thought to be generated by the action of the protein Bridging integrator 1 (BIN1) (Hong et al., 2014; Fu and Hong, 2016). Experimental observations also suggest that diffusion within t-tubules is significantly slowed in comparison to bulk interstitial space (Blatter and Niggli, 1998; Shepherd and McDonough, 1998; Pasek et al., 2006; Swift et al., 2006). The Lopatin group recently demonstrated that the presence of expansions and

constrictions along t-tubules, the result of microfolds, likely accounts for this slow diffusion (Uchida and Lopatin, 2018). This slowed diffusion within t-tubules enables the development of local electrochemical transients within t-tubular nanodomains, paralleling ID nanodomains. This phenomenon has important consequences for cardiac electrophysiology as well as ECC. Likewise local dynamics in luminal Ca^{2+} within the junctional SR would strongly modulate dyadic nanodomain behavior (particularly RYR2 gating) and merit further investigation (Gyorke et al., 2017). While there has been much progress in understanding dyadic nanodomains as the structural and functional units of cardiac ECC, further investigation is needed to understand how structure–function relationships at the nanoscale determine physiology at cellular, tissue, and organ levels.

Pathophysiology

Dysregulated Ca^{2+} cycling is widely recognized as the cause of arrhythmias in multiple pathological states. Aberrant Ca^{2+} release from the SR can be prompted by SR Ca^{2+} overload, RyR2 dysfunction, or mistimed Ca^{2+} entry across the sarcolemma. This in turn can activate NCX, depolarizing the membrane, and prompting premature beats that can trigger arrhythmias (Berlin et al., 1989; Venetucci et al., 2008). Intriguingly, a recent report suggests that aberrant cytosolic Ca^{2+} levels may also produce arrhythmogenic conditions by facilitating untimely Na_V re-opening (Johnson et al., 2018). Overall, the behavior of individual Na^+ and Ca^{2+} -cycling proteins is fairly well-characterized, yet the interplay between Na^+ and Ca^{2+} within dyadic nanodomains is very much the subject of active inquiry.

Modeling studies suggest that enhanced late Na^+ entry into dyadic nanodomains can prompt reversal of NCX, resulting in Ca^{2+} entry into the subspace, and thereby, contribute to arrhythmogenic aberrance Ca^{2+} release (Armoundas et al., 2003; Radwański and Poelzing, 2011). Late I_{Na} carried by nNa_Vs has been implicated in inherited arrhythmia disorders such as catecholaminergic polymorphic ventricular tachycardia (CPVT) (Radwański et al., 2015, 2016). Specifically, Ca^{2+}/calmodulin – dependent kinase II (CaMKII) -dependent enhancement of nNa_V activity during β-adrenergic stimulation contributes to diastolic Ca^{2+} release and consequent arrhythmias *in vivo* via an NCX-mediated mechanism. Additionally, this pro-arrhythmic mechanism was consistent regardless of whether the CPVT resulted from "leaky" RyRs or from SR Ca^{2+} overload. In the broader context, these results point to pathological overload of cytosolic Na^+ and Ca^{2+} being inextricably linked, particularly within the dyadic subspace.

Consistent with this hypothesis, aberrant Ca^{2+} release is the principal mechanism of arrhythmogenesis in disorders characterized by pathological gain of Na^+ channel function. Multiple studies have linked pathological enhancement of nNa_V function with arrhythmogenic diastolic Ca^{2+} release. These include mice lacking the Na^+ channel auxiliary subunit β1 (SCN1B) which exhibit enhanced $Na_V1.3$ expression (Lin et al., 2014), a rat pilocarpine-induced status epilepticus model where $Na_V1.1$ expression is elevated (Biet et al., 2015), and a murine model of epileptic encephalopathy resulting from a gain of function mutation in $Na_V1.6$ (Frasier et al., 2016). While these cases involve direct enhancement of Na^+ entry into the dyadic nanodomain via nNa_Vs, LQT3 is characterized by gain of $Na_V1.5$ function, resulting in global Na^+ overload throughout the myocyte. Nonetheless, recent evidence indicates that Na^+ entry into the dyadic subspace via nNa_Vs is still a key element of arrhythmogenesis in LQT3 (Koleske et al., 2018). Paralleling the aforementioned results in inherited arrhythmic syndromes, are studies implicating pathological enhancement of late I_{Na} in arrhythmias in acquired forms of ECC dysfunction such as heart failure (Valdivia et al., 2005; Undrovinas and Maltsev, 2008; Undrovinas et al., 2010; Sossalla and Maier, 2012; Antzelevitch et al., 2014; Makielski, 2016). Specifically, augmentation of Na^+ influx via $Na_V1.1$ (Mishra et al., 2014) as well as of NCX function (Pogwizd and Bers, 2002) in failing hearts have been shown to contribute to arrhythmias.

Given that late I_{Na} is central to aberrant Ca^{2+} cycling and arrhythmogenesis in multiple pathologies, it should come as no surprise that late I_{Na} inhibition by drugs such as ranolazine has demonstrated efficacy as an antiarrhythmic therapy (Burashnikov, 2017). However, emerging research suggests that selective targeting of nNa_V-mediated Na^+ entry into dyadic nanodomains may hold even greater promise (Radwański et al., 2015, 2016; Koleske et al., 2018). Additional impetus for pursuing this strategy comes from the dire negative consequences resulting from the off-target effects of non-isoform-selective Na^+ channel inhibition: although non-selective I_{Na} inhibition suppressed triggered activity following myocardial infarction (The Cardiac Arrhythmia Pilot Study, 1986), the concomitant reduction in excitability precipitated reentrant arrhythmias, thereby increasing mortality (Echt et al., 1991; Starmer et al., 1991). Selective inhibition of nNa_V would reduce Na^+ entry into dyadic nanodomains, thereby ameliorating triggered arrhythmia incidence, without any attendant adverse impact on excitability. Indeed, selective inhibition of nNa_Vs, and of $Na_V1.6$ in particular, whether using TTX analogs or a clinically relevant drug, riluzole, has been demonstrated to effectively suppress arrhythmias in murine models of CPVT (Radwański et al., 2015, 2016) and LQT3 (Radwański et al., 2013; Koleske et al., 2018).

Based on this logic, and available evidence, we posit the following requirements for arrhythmogenesis in pathologies directly driven by Ca^{2+} cycling defects (i.e., CPVT), and those arising from QT prolongation: (1) abnormal RyR2 function, whether genetic or acquired, (2) increased dyadic subspace Ca^{2+} levels, and (3) augmentation of nanodomain Na^+ entry via nNa_Vs (Radwański et al., 2010, 2016; Cheng et al., 2011; Radwański and Poelzing, 2011; Terentyev et al., 2014). Any individual factor in the absence of the other two is unlikely to cause arrhythmia. For instance, genetic defects in the RyR2 complex alone are insufficient to induce triggered activity (Rios and Györke, 2009; Radwański et al., 2016); augmentation of Na^+ entry via nNa_V, and SR Ca^{2+} load, secondary to β-adrenergic receptor stimulation, is necessary for arrhythmogenesis (Radwański et al., 2016). On the other hand, LQT may promote CaMKII activity, which in turn modifies the components of the dyadic nanodomain (Terentyev et al., 2014; Viatchenko-Karpinski et al., 2014; Radwański et al., 2016). Given

that augmentation of nNa_V-mediated Na^+ influx into dyadic nanodomains is a common element of both arrhythmogenic processes, it follows that late I_{Na} inhibition should prove antiarrhythmic in a broad range of pathologies including CPVT (Radwański et al., 2015, 2016), LQT3 (Koleske et al., 2018), LQT type 7 (Andersen-Tawil Syndrome; resulting from loss of repolarization reserve) (Radwański et al., 2013; Janson et al., 2014), and LQT type 8 (Timothy syndrome; resulting from pathological gain of LTCC function) (Gao et al., 2013).

While Na_V isoform-selectivity is one focus in developing novel antiarrhythmic drugs, we note that the pharmacological mode of action (i.e., use-dependence vs. tonic block) will also determine therapeutic success. Use-dependent Na_V inhibitors can effectively ameliorate triggered arrhythmias (The Cardiac Arrhythmia Pilot Study, 1986). However, under conditions such as elevated heart rates, they can suppress excitability and thereby, exacerbate conduction slowing. This, in turn, precipitates reentrant arrhythmias and increases mortality (Echt et al., 1991; Starmer et al., 1991). In contrast, tonic Na_V inhibitors function independently of heart rate, thereby avoiding this adverse effect. Therefore, we postulate that tonic blockade may hold greater potential for delivering efficacy with safety. Intriguingly, a recent report by Buyan et al. (2018) provides clues to fundamental properties (inhibitor protonation state determines binding site) that may lead to development of novel Na_V blockers with tailored modes of action. This highlights the need for mechanistically-driven drug development research grounded in understanding of atomic level Na_V structure.

As with ID nanodomains, the behavior of dyadic nanodomains is determined not only by the function of their Na^+/Ca^{2+} cycling protein constituents but also by their local ultrastructure. An example of this is found in failing hearts where β-adrenergic stimulation fails to effectively enhance ECC, despite augmented nNa_V and NCX function (Viatchenko-Karpinski et al., 2005). This is likely a result of t-tubules being severely disrupted in failing hearts (Li et al., 2015), compromising cell-wide coordination of individual nanodomains. In addition, the remaining t-tubules in these hearts contain abnormal dyadic nanodomains consisting of nNa_Vs, NCX, and hypersensitized RyRs which are prone to arrhythmogenic aberrant Ca^{2+} release (Belevych et al., 2012). Additionally, loss of BIN1 has been linked to compromised LTCC trafficking as well as loss of t-tubule microfolds in heart failure (Caldwell et al., 2014; Hong et al., 2014; Laury-Kleintop et al., 2015). Both experimental and modeling studies suggest that the latter effect could compromise the previously discussed slowing of diffusion within t-tubules, thereby dysregulating electrophysiology and ECC. Indeed, the Sachse and Bridge groups have demonstrated that the arrhythmia burden in failing hearts is reduced secondary to restoration of the t-tubule network following cardiac resynchronization therapy (Sachse et al., 2012; Lichter et al., 2014; Li et al., 2015). Thus, available evidence points to dyadic nanodomains as promising targets for the prevention of arrhythmias resulting from aberrant Ca^{2+} cycling.

CONCLUSION

Current research, propelled by emerging technologies capable of assessing structure/function at the nanoscale, suggests that nanodomains located at the ID and the t-tubule may respectively constitute the functional units of cardiac electrical excitation and ECC. Thus, we are beginning to appreciate nanodomain dysfunction, i.e., nanopathy, as a key mechanistic driver of cardiac disease and arrhythmogenesis. It follows therefore that antiarrhythmic treatments should be designed to correct underlying nanopathies, and indeed, such therapies currently under investigation show a great deal of promise. In the broader context, the emerging understanding of how nanoscale biophysics and biochemistry determine cardiovascular physiology and pathophysiology across protein, cell, tissue, and organ scales may represent a paradigm shift on par with the advent of molecular biology. It should drive multiple avenues of scientific and medical research including (1) new diagnostic approaches that can non-invasively interrogate functional nanodomains within patients, (2) new methods to assess nanodomain alterations during autopsies, and (3) new therapeutic approaches designed to restore nanodomain structure/function.

AUTHOR CONTRIBUTIONS

RV, CNJ, SG, and PR drafted the work or revised it critically for important intellectual content.

FUNDING

This work was supported by American Heart Association (Grant No. 16SDG29870007 to RV) and NIH (Grant Nos. R01-HL074045, R01-HL063043, and R01-HL138579 to SG; R00-HL127299 to PR).

REFERENCES

Agullo-Pascual, E., and Delmar, M. (2012). The noncanonical functions of Cx43 in the heart. *J. Membr. Biol.* 245, 477–482. doi: 10.1007/s00232-012-9466-y

Agullo-Pascual, E., Lin, X., Leo-Macias, A., Zhang, M., Liang, F. X., Li, Z., et al. (2014). Super-resolution imaging reveals that loss of the C-terminus of connexin43 limits microtubule plus-end capture and NaV1.5 localization at the intercalated disc. *Cardiovasc. Res.* 104, 371–381. doi: 10.1093/cvr/cvu195

Agullo-Pascual, E., Lin, X., Pfenniger, A., Lubkemeier, I., Willecke, K., Rothenberg, E., et al. (2013). A novel noncanonical role of cx43 in the heart: ensuring the arrival of nav1.5 to the intercalated disk. *Heart Rhythm.* 10:1742. doi: 10.1016/j.hrthm.2013.09.016

Akar, F. G., Nass, R. D., Hahn, S., Cingolani, E., Shah, M., Hesketh, G. G., et al. (2007). Dynamic changes in conduction velocity and gap junction properties during development of pacing-induced heart failure. *Am. J. Physiol. Heart Circ. Physiol.* 293, H1223–H1230. doi: 10.1152/ajpheart.00079.2007

Antzelevitch, C., Nesterenko, V., Shryock, J. C., Rajamani, S., Song, Y., and Belardinelli, L. (2014). The role of late I Na in development of cardiac arrhythmias. *Handb. Exp. Pharmacol.* 221, 137–168. doi: 10.1007/978-3-642-41588-3_7

Armoundas, A. A., Hobai, I. A., Tomaselli, G. F., Winslow, R. L., and O'Rourke, B. (2003). Role of sodium-calcium exchanger in modulating the action potential of ventricular myocytes from normal and failing hearts. *Circ. Res.* 93, 46–53. doi: 10.1161/01.RES.0000080932.98903.D8

Arujuna, A., Karim, R., Caulfield, D., Knowles, B., Rhode, K., Schaeffter, T., et al. (2012). Acute pulmonary vein isolation is achieved by a combination of reversible and irreversible atrial injury after catheter ablation: evidence from magnetic resonance imaging. *Circ. Arrhythm. Electrophysiol.* 5, 691–700. doi: 10.1161/CIRCEP.111.966523

Barr, L., Dewey, M. M., and Berger, W. (1965). Propagation of action potentials and the structure of the nexus in cardiac muscle. *J. Gen. Physiol.* 48, 797–823. doi: 10.1085/jgp.48.5.797

Beauchamp, P., Choby, C., Desplantez, T., de Peyer, K., Green, K., Yamada, K. A., et al. (2004). Electrical propagation in synthetic ventricular myocyte strands from germline connexin43 knockout mice. *Circ. Res.* 95, 170–178. doi: 10.1161/01.RES.0000134923.05174.2f

Belevych, A. E., Terentyev, D., Terentyeva, R., Ho, H. T., Gyorke, I., Bonilla, I. M., et al. (2012). Shortened Ca2+ signaling refractoriness underlies cellular arrhythmogenesis in a postinfarction model of sudden cardiac death. *Circ. Res.* 110, 569–577. doi: 10.1161/CIRCRESAHA.111.260455

Berlin, J. R., Cannell, M. B., and Lederer, W. J. (1989). Cellular origins of the transient inward current in cardiac myocytes. Role of fluctuations and waves of elevated intracellular calcium. *Circ. Res.* 65, 115–126. doi: 10.1161/01.RES.65.1.115

Biet, M., Barajas-Martinez, H., Ton, A. T., Delabre, J. F., Morin, N., and Dumaine, R. (2012). About half of the late sodium current in cardiac myocytes from dog ventricle is due to non-cardiac-type Na(+) channels. *J. Mol. Cell Cardiol.* 53, 593–598. doi: 10.1016/j.yjmcc.2012.06.012

Biet, M., Morin, N., Lessard-Beaudoin, M., Graham, R. K., Duss, S., Gagne, J., et al. (2015). Prolongation of action potential duration and QT interval during epilepsy linked to increased contribution of neuronal sodium channels to cardiac late Na+ current: potential mechanism for sudden death in epilepsy. *Circ. Arrhythm. Electrophysiol.* 8, 912–920. doi: 10.1161/CIRCEP.114.002693

Blatter, L. A., and Niggli, E. (1998). Confocal near-membrane detection of calcium in cardiac myocytes. *Cell Calcium* 23, 269–279. doi: 10.1016/S0143-4160(98)90023-9

Boyle, A., Maurer, M. S., and Sobotka, P. A. (2007). Myocellular and interstitial edema and circulating volume expansion as a cause of morbidity and mortality in heart failure. *J. Card. Fail.* 13, 133–136. doi: 10.1016/j.cardfail.2006.10.015

Burashnikov, A. (2017). Late INa inhibition as an antiarrhythmic strategy. *J. Cardiovasc. Pharmacol.* 70, 159–167. doi: 10.1097/FJC.0000000000000510

Buyan, A., Sun, D., and Corry, B. (2018). Protonation state of inhibitors determines interaction sites within voltage-gated sodium channels. *Proc. Natl. Acad. Sci. U.S.A.* 115, E3135–E3144. doi: 10.1073/pnas.1714131115

Caldwell, J. L., Smith, C. E., Taylor, R. F., Kitmitto, A., Eisner, D. A., Dibb, K. M., et al. (2014). Dependence of cardiac transverse tubules on the BAR domain protein amphiphysin II (BIN-1). *Circ. Res.* 115, 986–996. doi: 10.1161/CIRCRESAHA.116.303448

Cerrone, M., Lin, X., Zhang, M., Agullo-Pascual, E., Pfenniger, A., Chkourko Gusky, H., et al. (2014). Missense mutations in plakophilin-2 cause sodium current deficit and associate with a Brugada syndrome phenotype. *Circulation* 129, 1092–1103. doi: 10.1161/CIRCULATIONAHA.113.003077

Cheng, E. P., Yuan, C., Navedo, M. F., Dixon, R. E., Nieves-Cintron, M., Scott, J. D., et al. (2011). Restoration of normal L-type Ca2+ channel function during timothy syndrome by ablation of an anchoring protein. *Circ. Res.* 109, 255–261. doi: 10.1161/CIRCRESAHA.111.248252

Chkourko, H. S., Guerrero-Serna, G., Lin, X., Darwish, N., Pohlmann, J. R., Cook, K. E., et al. (2012). Remodeling of mechanical junctions and of microtubule-associated proteins accompany cardiac connexin43 lateralization. *Heart Rhythm.* 9, 1133.e6–1140.e6. doi: 10.1016/j.hrthm.2012.03.003

Conforti, L., Tohse, N., and Sperelakis, N. (1993). Tetrodotoxin-sensitive sodium current in rat fetal ventricular myocytes–contribution to the plateau phase of action potential. *J. Mol. Cell Cardiol.* 25, 159–173. doi: 10.1006/jmcc.1993.1019

Copene, E. D., and Keener, J. P. (2008). Ephaptic coupling of cardiac cells through the junctional electric potential. *J. Math. Biol.* 57, 265–284. doi: 10.1007/s00285-008-0157-3

Danik, S. B., Liu, F., Zhang, J., Suk, H. J., Morley, G. E., Fishman, G. I., et al. (2004). Modulation of cardiac gap junction expression and arrhythmic susceptibility. *Circ. Res.* 95, 1035–1041. doi: 10.1161/01.RES.0000148664.33695.2a

De Vuyst, E., Boengler, K., Antoons, G., Sipido, K. R., Schulz, R., and Leybaert, L. (2011). Pharmacological modulation of connexin-formed channels in cardiac pathophysiology. *Br. J. Pharmacol.* 163, 469–483. doi: 10.1111/j.1476-5381.2011.01244.x

Despa, S., and Bers, D. M. (2003). Na/K pump current and [Na](i) in rabbit ventricular myocytes: local [Na](i) depletion and Na buffering. *Biophys. J.* 84, 4157–4166. doi: 10.1016/S0006-3495(03)75140-6

Despa, S., Shui, B., Bossuyt, J., Lang, D., Kotlikoff, M. I., and Bers, D. M. (2014). Junctional cleft [Ca(2)(+)]i measurements using novel cleft-targeted Ca(2)(+) sensors. *Circ. Res.* 115, 339–347. doi: 10.1161/CIRCRESAHA.115.303582

Desplantez, T., Dupont, E., Severs, N., and Weingart, R. (2007). Gap junction channels and cardiac impulse propagation. *J. Membr. Biol.* 218, 13–28. doi: 10.1007/s00232-007-9046-8

Dhar Malhotra, J., Chen, C., Rivolta, I., Abriel, H., Malhotra, R., Mattei, L. N., et al. (2001). Characterization of sodium channel alpha- and beta-subunits in rat and mouse cardiac myocytes. *Circulation* 103, 1303–1310. doi: 10.1161/01.CIR.103.9.1303

Dhein, S., Rothe, S., Busch, A., Rojas Gomez, D. M., Boldt, A., Reutemann, A., et al. (2011). Effects of metoprolol therapy on cardiac gap junction remodelling and conduction in human chronic atrial fibrillation. *Br. J. Pharmacol.* 164, 607–616. doi: 10.1111/j.1476-5381.2011.01460.x

Echt, D. S., Liebson, P. R., Mitchell, L. B., Peters, R. W., Obias-Manno, D., Barker, A. H., et al. (1991). Mortality and morbidity in patients receiving encainide, flecainide, or placebo, the cardiac arrhythmia suppression trial. *N. Engl. J. Med.* 324, 781–788. doi: 10.1056/NEJM199103213241201

Eichel, C. A., Beuriot, A., Chevalier, M. Y., Rougier, J. S., Louault, F., Dilanian, G., et al. (2016). Lateral membrane-specific MAGUK CASK down-regulates NaV1.5 channel in cardiac myocytes. *Circ. Res.* 119, 544–556. doi: 10.1161/CIRCRESAHA.116.309254

Eloff, B. C., Lerner, D. L., Yamada, K. A., Schuessler, R. B., Saffitz, J. E., and Rosenbaum, D. S. (2001). High resolution optical mapping reveals conduction slowing in connexin43 deficient mice. *Cardiovasc. Res.* 51, 681–690. doi: 10.1016/S0008-6363(01)00341-8

Fabiato, A., and Fabiato, F. (1977). Calcium release from the sarcoplasmic reticulum. *Circ. Res.* 40, 119–129. doi: 10.1161/01.RES.40.2.119

Fernandez-Jimenez, R., Sanchez-Gonzalez, J., Aguero, J., Garcia-Prieto, J., Lopez-Martin, G. J., Garcia-Ruiz, J. M., et al. (2015). Myocardial edema after ischemia/reperfusion is not stable and follows a bimodal pattern: imaging and histological tissue characterization. *J. Am. Coll. Cardiol.* 65, 315–323. doi: 10.1016/j.jacc.2014.11.004

Forbes, M. S., and Sperelakis, N. (1983). The membrane systems and cytoskeletal elements of mammalian myocardial cells. *Cell Muscle Motil.* 3, 89–155. doi: 10.1007/978-1-4615-9296-9_5

Frasier, C. R., Wagnon, J. L., Bao, Y. O., McVeigh, L. G., Lopez-Santiago, L. F., Meisler, M. H., et al. (2016). Cardiac arrhythmia in a mouse model of sodium channel SCN8A epileptic encephalopathy. *Proc. Natl. Acad. Sci. U.S.A.* doi: 10.1073/pnas.1612746113 [Epub ahead of print].

Fu, Y., and Hong, T. (2016). BIN1 regulates dynamic t-tubule membrane. *Biochim. Biophys. Acta* 1863(7Pt B), 1839–1847. doi: 10.1016/j.bbamcr.2015.11.004

Gao, Y., Xue, X., Hu, D., Liu, W., Yuan, Y., Sun, H., et al. (2013). Inhibition of late sodium current by mexiletine: a novel pharmotherapeutical approach in timothy syndrome. *Circ. Arrhythm. Electrophysiol.* 6, 614–622. doi: 10.1161/CIRCEP.113.000092

Gillet, L., Rougier, J. S., Shy, D., Sonntag, S., Mougenot, N., Essers, M., et al. (2015). Cardiac-specific ablation of synapse-associated protein SAP97 in mice decreases potassium currents but not sodium current. *Heart Rhythm.* 12, 181–192. doi: 10.1016/j.hrthm.2014.09.057

Greer-Short, A., George, S. A., Poelzing, S., and Weinberg, S. H. (2017). Revealing the concealed nature of long-QT type 3 syndrome. *Circ. Arrhythm. Electrophysiol.* 10:e004400. doi: 10.1161/CIRCEP.116.004400

Guerrero, P. A., Schuessler, R. B., Davis, L. M., Beyer, E. C., Johnson, C. M., Yamada, K. A., et al. (1997). Slow ventricular conduction in mice heterozygous

for a connexin43 null mutation. *J. Clin. Invest.* 99, 1991–1998. doi: 10.1172/JCI119367

Gutstein, D. E., Liu, F. Y., Meyers, M. B., Choo, A., and Fishman, G. I. (2003). The organization of adherens junctions and desmosomes at the cardiac intercalated disc is independent of gap junctions. *J. Cell Sci.* 116(Pt 5), 875–885. doi: 10.1242/jcs.00258

Gutstein, D. E., Morley, G. E., Tamaddon, H., Vaidya, D., Schneider, M. D., Chen, J., et al. (2001). Conduction slowing and sudden arrhythmic death in mice with cardiac-restricted inactivation of connexin43. *Circ. Res.* 88, 333–339. doi: 10.1161/01.RES.88.3.333

Gyorke, S., Belevych, A. E., Liu, B., Kubasov, I. V., Carnes, C. A., and Radwański, P. B. (2017). The role of luminal Ca regulation in Ca signaling refractoriness and cardiac arrhythmogenesis. *J. Gen. Physiol.* 149, 877–888. doi: 10.1085/jgp.201711808

Hichri, E., Abriel, H., and Kucera, J. P. (2017). Distribution of cardiac sodium channels in clusters potentiates ephaptic interactions in the intercalated disc. *J. Physiol.* 596, 563–589. doi: 10.1113/JP275351

Hong, M., Bao, L., Kefaloyianni, E., Agullo-Pascual, E., Chkourko, H., Foster, M., et al. (2012). Heterogeneity of ATP-sensitive K+ channels in cardiac myocytes: enrichment at the intercalated disk. *J. Biol. Chem.* 287, 41258–41267. doi: 10.1074/jbc.M112.412122

Hong, T., Yang, H., Zhang, S. S., Cho, H. C., Kalashnikova, M., Sun, B., et al. (2014). Cardiac BIN1 folds T-tubule membrane, controlling ion flux and limiting arrhythmia. *Nat. Med.* 20, 624–632. doi: 10.1038/nm.3543

Huxley, A. F., and Taylor, R. E. (1955). Function of Krause's membrane. *Nature* 176:1068. doi: 10.1038/1761068a0

Huxley, A. F., and Taylor, R. E. (1958). Local activation of striated muscle fibres. *J. Physiol.* 144, 426–441. doi: 10.1113/jphysiol.1958.sp006111

Ishihara, K. (2018). External K(+) dependence of strong inward rectifier K(+) channel conductance is caused not by K(+) but by competitive pore blockade by external Na. *J. Gen. Physiol.* 150, 977–989. doi: 10.1085/jgp.201711936

Jansen, J. A., Noorman, M., Musa, H., Stein, M., de Jong, S., van der Nagel, R., et al. (2012). Reduced heterogeneous expression of Cx43 results in decreased Nav1.5 expression and reduced sodium current that accounts for arrhythmia vulnerability in conditional Cx43 knockout mice. *Heart Rhythm.* 9, 600–607. doi: 10.1016/j.hrthm.2011.11.025

Janson, C. M., Poelzing, S., and Shah, M. J. (2014). Combined inhibition of Na(+) and Ca(2)(+) channels: a novel paradigm for the treatment of incessant ventricular arrhythmias in Andersen-Tawil syndrome. *Heart Rhythm.* 11, 318–320. doi: 10.1016/j.hrthm.2013.11.003

Jayasinghe, I. D., Cannell, M. B., and Soeller, C. (2009). Organization of ryanodine receptors, transverse tubules, and sodium-calcium exchanger in rat myocytes. *Biophys. J.* 97, 2664–2673. doi: 10.1016/j.bpj.2009.08.036

Johnson, C. N., Potet, F., Thompson, M. K., Kroncke, B. M., Glazer, A. M., Voehler, M. W., et al. (2018). A mechanism of calmodulin modulation of the human cardiac sodium channel. *Structure* 26, 683.e3–694.e3. doi: 10.1016/j.str.2018.03.005

Jongsma, H. J., and Wilders, R. (2000). Gap junctions in cardiovascular disease. *Circ. Res.* 86, 1193–1197. doi: 10.1161/01.RES.86.12.1193

Kleber, A. G., and Rudy, Y. (2004). Basic mechanisms of cardiac impulse propagation and associated arrhythmias. *Physiol. Rev.* 84, 431–488. doi: 10.1152/physrev.00025.2003

Koleske, M., Bonilla, I., Thomas, J., Zaman, N., Baine, S., Knollmann, B. C., et al. (2018). Tetrodotoxin-sensitive Navs contribute to early and delayed afterdepolarizations in long QT arrhythmia models. *J. Gen. Physiol.* 150, 991–1002. doi: 10.1085/jgp.201711909

Kucera, J. P., Rohr, S., and Rudy, Y. (2002). Localization of sodium channels in intercalated disks modulates cardiac conduction. *Circ. Res.* 91, 1176–1182. doi: 10.1161/01.RES.0000046237.54156.0A

Laury-Kleintop, L. D., Mulgrew, J. R., Heletz, I., Nedelcoviciu, R. A., Chang, M. Y., Harris, D. M., et al. (2015). Cardiac-specific disruption of Bin1 in mice enables a model of stress- and age-associated dilated cardiomyopathy. *J. Cell Biochem.* 116, 2541–2551. doi: 10.1002/jcb.25198

Lavorato, M., Huang, T. Q., Iyer, V. R., Perni, S., Meissner, G., and Franzini-Armstrong, C. (2015). Dyad content is reduced in cardiac myocytes of mice with impaired calmodulin regulation of RyR2. *J. Muscle Res. Cell Motil.* 36, 205–214. doi: 10.1007/s10974-015-9405-5

Leblanc, N., and Hume, J. R. (1990). Sodium current-induced release of calcium from cardiac sarcoplasmic reticulum. *Science* 248, 372–376. doi: 10.1126/science.2158146

Lederer, W. J., Niggli, E., and Hadley, R. W. (1990). Sodium-calcium exchange in excitable cells: fuzzy space. *Science* 248:283. doi: 10.1126/science.2326638

Leo-Macias, A., Agullo-Pascual, E., Sanchez-Alonso, J. L., Keegan, S., Lin, X., Arcos, T., et al. (2016). Nanoscale visualization of functional adhesion/excitability nodes at the intercalated disc. *Nat. Commun.* 7:10342. doi: 10.1038/ncomms10342

Leo-Macias, A., Liang, F. X., and Delmar, M. (2015). Ultrastructure of the intercellular space in adult murine ventricle revealed by quantitative tomographic electron microscopy. *Cardiovasc. Res.* 107, 442–452. doi: 10.1093/cvr/cvv182

Li, H., Lichter, J. G., Seidel, T., Tomaselli, G. F., Bridge, J. H., and Sachse, F. B. (2015). Cardiac resynchronization therapy reduces subcellular heterogeneity of ryanodine receptors, T-Tubules, and Ca2+ sparks produced by dyssynchronous heart failure. *Circ. Heart Fail.* 8, 1105–1114. doi: 10.1161/CIRCHEARTFAILURE.115.002352

Lichter, J. G., Carruth, E., Mitchell, C., Barth, A. S., Aiba, T., Kass, D. A., et al. (2014). Remodeling of the sarcomeric cytoskeleton in cardiac ventricular myocytes during heart failure and after cardiac resynchronization therapy. *J. Mol. Cell Cardiol.* 72, 186–195. doi: 10.1016/j.yjmcc.2014.03.012

Lin, J., and Keener, J. P. (2010). Modeling electrical activity of myocardial cells incorporating the effects of ephaptic coupling. *Proc. Natl. Acad. Sci. U.S.A.* 107, 20935–20940. doi: 10.1073/pnas.1010154107

Lin, J., and Keener, J. P. (2014). Microdomain effects on transverse cardiac propagation. *Biophys. J.* 106, 925–931. doi: 10.1016/j.bpj.2013.11.1117

Lin, X., O'Malley, H., Chen, C., Auerbach, D., Foster, M., Shekhar, A., et al. (2014). Scn1b deletion leads to increased tetrodotoxin-sensitive sodium current, altered intracellular calcium homeostasis and arrhythmias in murine hearts. *J Physiol.* 593, 1389–1407. doi: 10.1113/jphysiol.2014.277699

Lindner, E. (1957). [Submicroscopic morphology of the cardiac muscle]. *Z. Zellforsch. Mikrosk. Anat.* 45, 702–746.

Maier, S. K., Westenbroek, R. E., McCormick, K. A., Curtis, R., Scheuer, T., and Catterall, W. A. (2004). Distinct subcellular localization of different sodium channel alpha and beta subunits in single ventricular myocytes from mouse heart. *Circulation* 109, 1421–1427. doi: 10.1161/01.CIR.0000121421.61896.24

Maier, S. K., Westenbroek, R. E., Schenkman, K. A., Feigl, E. O., Scheuer, T., and Catterall, W. A. (2002). An unexpected role for brain-type sodium channels in coupling of cell surface depolarization to contraction in the heart. *Proc. Natl. Acad. Sci. U.S.A.* 99, 4073–4078. doi: 10.1073/pnas.261705699

Makara, M. A., Curran, J., Little, S. C., Musa, H., Polina, I., Smith, S. A., et al. (2014). Ankyrin-G coordinates intercalated disc signaling platform to regulate cardiac excitability in vivo. *Circ. Res.* 115, 929–938. doi: 10.1161/CIRCRESAHA.115.305154

Makielski, J. C. (2016). Late sodium current: a mechanism for angina, heart failure, and arrhythmia. *Trends Cardiovasc. Med.* 26, 115–122. doi: 10.1016/j.tcm.2015.05.006

Matamoros, M., Perez-Hernandez, M., Guerrero-Serna, G., Amoros, I., Barana, A., Nunez, M., et al. (2016). Nav1.5 N-terminal domain binding to alpha1-syntrophin increases membrane density of human Kir2.1, Kir2.2 and Nav1.5 channels. *Cardiovasc. Res.* 110, 279–290. doi: 10.1093/cvr/cvw009

Mehlhorn, U., Davis, K. L., Laine, G. A., Geissler, H. J., and Allen, S. J. (1996). Myocardial fluid balance in acute hypertension. *Microcirculation* 3, 371–378. doi: 10.3109/10739689609148309

Mehlhorn, U., Geissler, H. J., Laine, G. A., and Allen, S. J. (2001). Myocardial fluid balance. *Eur. J. Cardiothorac. Surg.* 20, 1220–1230. doi: 10.1016/S1010-7940(01)01031-4

Migliore, F., Zorzi, A., Perazzolo Marra, M., Iliceto, S., and Corrado, D. (2015). Myocardial edema as a substrate of electrocardiographic abnormalities and life-threatening arrhythmias in reversible ventricular dysfunction of takotsubo cardiomyopathy: imaging evidence, presumed mechanisms, and implications for therapy. *Heart Rhythm.* 12, 1867–1877. doi: 10.1016/j.hrthm.2015.04.041

Milstein, M. L., Musa, H., Balbuena, D. P., Anumonwo, J. M., Auerbach, D. S., Furspan, P. B., et al. (2012). Dynamic reciprocity of sodium and potassium channel expression in a macromolecular complex controls cardiac excitability and arrhythmia. *Proc. Natl. Acad. Sci. U.S.A.* 109, E2134–E2143. doi: 10.1073/pnas.1109370109

Mishra, S., Reznikov, V., Maltsev, V. A., Undrovinas, N. A., Sabbah, H. N., and Undrovinas, A. (2014). Contribution of sodium channel neuronal isoform Nav1.1 to late sodium current in ventricular myocytes from failing hearts. *J. Physiol.* 593, 1409–1427. doi: 10.1113/jphysiol.2014.278259

Mori, Y., Fishman, G. I., and Peskin, C. S. (2008). Ephaptic conduction in a cardiac strand model with 3D electrodiffusion. *Proc. Natl. Acad. Sci. U.S.A.* 105, 6463–6468. doi: 10.1073/pnas.0801089105

Morley, G. E., Vaidya, D., Samie, F. H., Lo, C., Delmar, M., and Jalife, J. (1999). Characterization of conduction in the ventricles of normal and heterozygous Cx43 knockout mice using optical mapping. *J. Cardiovasc. Electrophysiol.* 10, 1361–1375. doi: 10.1111/j.1540-8167.1999.tb00192.x

Ongstad, E. L., O'Quinn, M. P., Ghatnekar, G. S., Yost, M. J., and Gourdie, R. G. (2013). A connexin43 mimetic peptide promotes regenerative healing and improves mechanical properties in skin and heart. *Adv. Wound Care (New Rochelle)* 2, 55–62. doi: 10.1089/wound.2011.0341

Pasek, M., Simurda, J., and Christe, G. (2006). The functional role of cardiac T-tubules explored in a model of rat ventricular myocytes. *Philos. Trans. A Math Phys. Eng. Sci.* 364, 1187–1206. doi: 10.1098/rsta.2006.1764

Pertsov, A. M., and Medvinskii, A. B. (1976). [Electric coupling in cells without highly permeable cell contacts]. *Biofizika* 21, 698–670.

Petitprez, S., Zmoos, A. F., Ogrodnik, J., Balse, E., Raad, N., El-Haou, S., et al. (2011). SAP97 and dystrophin macromolecular complexes determine two pools of cardiac sodium channels Nav1.5 in cardiomyocytes. *Circ. Res.* 108, 294–304. doi: 10.1161/CIRCRESAHA.110.228312

Plonsey, R., and Barr, R. C. (2007). *Bioelectricity: A Quantitative Approach*. Berlin: Springer.

Poelzing, S., Akar, F. G., Baron, E., and Rosenbaum, D. S. (2004). Heterogeneous connexin43 expression produces electrophysiological heterogeneities across ventricular wall. *Am. J. Physiol. Heart Circ. Physiol.* 286, H2001–H2009. doi: 10.1152/ajpheart.00987.2003

Pogwizd, S. M., and Bers, D. M. (2002). Na/Ca exchange in heart failure: contractile dysfunction and arrhythmogenesis. *Ann. N. Y. Acad. Sci.* 976, 454–465. doi: 10.1111/j.1749-6632.2002.tb04775.x

Ponce-Balbuena, D., Guerrero-Serna, G., Valdivia, C. R., Caballero, R., Diez-Guerra, F. J., Jimenez-Vazquez, E. N., et al. (2018). Cardiac Kir2.1 and NaV1.5 channels traffic together to the sarcolemma to control excitability. *Circ Res.* 122, 1501–1516. doi: 10.1161/CIRCRESAHA.117.311872

Popescu, I., Galice, S., Mohler, P. J., and Despa, S. (2016). Elevated local [Ca^{2+}] and CaMKII promote spontaneous Ca^{2+} release in ankyrin-B-deficient hearts. *Cardiovasc. Res.* 111, 287–294. doi: 10.1093/cvr/cvw093

Radwański, P. B., Brunello, L., Veeraraghavan, R., Ho, H. T., Lou, Q., Makara, M. A., et al. (2015). Neuronal Na^{+} channel blockade suppresses arrhythmogenic diastolic Ca^{2+} release. *Cardiovasc. Res.* 106, 143–152. doi: 10.1093/cvr/cvu262

Radwański, P. B., Greer-Short, A., and Poelzing, S. (2013). Inhibition of Na(+) channels ameliorates arrhythmias in a drug-induced model of Andersen-Tawil syndrome. *Heart Rhythm.* 10, 255–263. doi: 10.1016/j.hrthm.2012.10.005

Radwański, P. B., Ho, H.-T., Veeraraghavan, R., Brunello, L., Liu, B., Belevych, A. E., et al. (2016). Neuronal Na+ channels are integral components of pro-arrhythmic Na+/Ca2+ signaling nanodomain that promotes cardiac arrhythmias during β-adrenergic stimulation. *JACC Basic Transl. Sci.* 1, 251–266. doi: 10.1016/j.jacbts.2016.04.004

Radwański, P. B., and Poelzing, S. (2011). NCX is an important determinant for premature ventricular activity in a drug-induced model of Andersen-Tawil syndrome. *Cardiovasc. Res.* 92, 57–66. doi: 10.1093/cvr/cvr180

Radwański, P. B., Veeraraghavan, R., and Poelzing, S. (2010). Cytosolic calcium accumulation and delayed repolarization associated with ventricular arrhythmias in a guinea pig model of Andersen-Tawil syndrome. *Heart Rhythm.* 7, 1428–1435. doi: 10.1016/j.hrthm.2010.03.044

Raisch, T. B., Yanoff, M. S., Larsen, T. R., Farooqui, M. A., King, D. A., Veeraraghavan, R., et al. (2018). Intercalated disc extracellular nanodomain expansion in patients with atrial fibrillation. *Front. Physiol.* 9:398. doi: 10.3389/fphys.2018.00398

Rhett, J. M., and Gourdie, R. G. (2012). The perinexus: a new feature of Cx43 gap junction organization. *Heart Rhythm.* 9, 619–623. doi: 10.1016/j.hrthm.2011.10.003

Rhett, J. M., Jourdan, J., and Gourdie, R. G. (2011). Connexin 43 connexon to gap junction transition is regulated by zonula occludens-1. *Mol. Biol. Cell* 22, 1516–1528. doi: 10.1091/mbc.e10-06-0548

Rhett, J. M., Ongstad, E. L., Jourdan, J., and Gourdie, R. G. (2012). Cx43 associates with Na(v)1.5 in the cardiomyocyte perinexus. *J. Membr. Biol.* 245, 411–422. doi: 10.1007/s00232-012-9465-z

Rios, E., and Györke, S. (2009) Calsequestrin, triadin and more: the molecules that modulate calcium release in cardiac and skeletal muscle. *J. Physiol.* 587, 3069–3070. doi: 10.1113/jphysiol.2009.175083

Sachse, F. B., Torres, N. S., Savio-Galimberti, E., Aiba, T., Kass, D. A., Tomaselli, G. F., et al. (2012). Subcellular structures and function of myocytes impaired during heart failure are restored by cardiac resynchronization therapy. *Circ. Res.* 110, 588–597. doi: 10.1161/CIRCRESAHA.111.257428

Scriven, D. R., Dan, P., and Moore, E. D. (2000). Distribution of proteins implicated in excitation-contraction coupling in rat ventricular myocytes. *Biophys. J.* 79, 2682–2691. doi: 10.1016/S0006-3495(00)76506-4

Shepherd, N., and McDonough, H. B. (1998). Ionic diffusion in transverse tubules of cardiac ventricular myocytes. *Am. J. Physiol.* 275(3 Pt 2), H852–H860. doi: 10.1152/ajpheart.1998.275.3.H852

Sjostrand, F. S., and Andersson, E. (1954). Electron microscopy of the intercalated discs of cardiac muscle tissue. *Experientia* 10, 369–370. doi: 10.1007/BF02160542

Sossalla, S., and Maier, L. S. (2012). Role of ranolazine in angina, heart failure, arrhythmias, and diabetes. *Pharmacol. Ther.* 133, 311–323. doi: 10.1016/j.pharmthera.2011.11.003

Sottas, V., and Abriel, H. (2016). Negative-dominance phenomenon with genetic variants of the cardiac sodium channel Nav1.5. *Biochim. Biophys. Acta* 1863(7 Pt B), 1791–1798. doi: 10.1016/j.bbamcr.2016.02.013

Spach, M. S., Heidlage, J. F., Barr, R. C., and Dolber, P. C. (2004). Cell size and communication: role in structural and electrical development and remodeling of the heart. *Heart Rhythm.* 1, 500–515. doi: 10.1016/j.hrthm.2004.06.010

Sperelakis, N., and Mann, J. E. J. (1977). Evaluation of electric field changes in the cleft between excitable cells. *J. Theor. Biol.* 64, 71–96. doi: 10.1016/0022-5193(77)90114-X

Sperelakis, N., and McConnell, K. (2002). Electric field interactions between closely abutting excitable cells. *IEEE Eng. Med. Biol. Mag.* 21, 77–89. doi: 10.1109/51.993199

Starmer, C. F., Lastra, A. A., Nesterenko, V. V., and Grant, A. O. (1991). Proarrhythmic response to sodium channel blockade, theoretical model and numerical experiments. *Circulation* 84, 1364–1377. doi: 10.1161/01.CIR.84.3.1364

Stein, M., van Veen, T. A., Remme, C. A., Boulaksil, M., Noorman, M., van Stuijvenberg, L., et al. (2009). Combined reduction of intercellular coupling and membrane excitability differentially affects transverse and longitudinal cardiac conduction. *Cardiovasc. Res.* 83, 52–60. doi: 10.1093/cvr/cvp124

Stroemlund, L. W., Jensen, C. F., Qvortrup, K., Delmar, M., and Nielsen, M. S. (2015). Gap junctions – Guards of excitability. *Biochem. Soc. Trans.* 43, 508–512. doi: 10.1042/BST20150059

Swift, F., Stromme, T. A., Amundsen, B., Sejersted, O. M., and Sjaastad, I. (2006). Slow diffusion of K^{+} in the T tubules of rat cardiomyocytes. *J. Appl. Physiol.* 101, 1170–1176. doi: 10.1152/japplphysiol.00297.2006

Terentyev, D., Rees, C. M., Li, W., Cooper, L. L., Jindal, H. K., Peng, X., et al. (2014). Hyperphosphorylation of RyRs underlies triggered activity in transgenic rabbit model of LQT2 syndrome. *Circ. Res.* 115, 919–928. doi: 10.1161/CIRCRESAHA.115.305146

The Cardiac Arrhythmia Pilot Study (1986). The CAPS investigators. *Am. J. Cardiol.* 57, 91–95.

Thomas, S. P., Kucera, J. P., Bircher-Lehmann, L., Rudy, Y., Saffitz, J. E., and Kleber, A. G. (2003). Impulse propagation in synthetic strands of neonatal cardiac myocytes with genetically reduced levels of connexin43. *Circ. Res.* 92, 1209–1216. doi: 10.1161/01.RES.0000074916.41221.EA

Torres, N. S., Larbig, R., Rock, A., Goldhaber, J. I., and Bridge, J. H. (2010). Na+ currents are required for efficient excitation-contraction coupling in rabbit ventricular myocytes: a possible contribution of neuronal Na+ channels. *J. Physiol.* 588(Pt 21), 4249–4260. doi: 10.1113/jphysiol.2010.194688

Uchida, K., and Lopatin, A. N. (2018). Diffusional and electrical properties of T-tubules are governed by their constrictions and dilations. *Biophys. J.* 114, 437–449. doi: 10.1016/j.bpj.2017.11.3742

Undrovinas, A., and Maltsev, V. A. (2008). Late sodium current is a new therapeutic target to improve contractility and rhythm in failing heart. *Cardiovasc. Hematol. Agents Med. Chem.* 6, 348–359. doi: 10.2174/187152508785909447

Undrovinas, N. A., Maltsev, V. A., Belardinelli, L., Sabbah, H. N., and Undrovinas, A. (2010). Late sodium current contributes to diastolic cell Ca2+ accumulation in chronic heart failure. *J. Physiol. Sci.* 60, 245–257. doi: 10.1007/s12576-010-0092-0

Vaidya, D., Tamaddon, H. S., Lo, C. W., Taffet, S. M., Delmar, M., Morley, G. E., et al. (2001). Null mutation of connexin43 causes slow propagation of ventricular activation in the late stages of mouse embryonic development. *Circ. Res.* 88, 1196–1202. doi: 10.1161/hh1101.091107

Valdivia, C. R., Chu, W. W., Pu, J., Foell, J. D., Haworth, R. A., Wolff, M. R., et al. (2005). Increased late sodium current in myocytes from a canine heart failure model and from failing human heart. *J. Mol. Cell Cardiol.* 38, 475–483. doi: 10.1016/j.yjmcc.2004.12.012

van Rijen, H. V., Eckardt, D., Degen, J., Theis, M., Ott, T., Willecke, K., et al. (2004). Slow conduction and enhanced anisotropy increase the propensity for ventricular tachyarrhythmias in adult mice with induced deletion of connexin43. *Circulation* 109, 1048–1055. doi: 10.1161/01.CIR.0000117402.70689.75

Veeraraghavan, R., and Gourdie, R. (2016). Stochastic optical reconstruction microscopy-based relative localization analysis (STORM-RLA) for quantitative nanoscale assessment of spatial protein organization. *Mol. Biol. Cell.* 27, 3583–3590. doi: 10.1091/mbc.E16-02-0125

Veeraraghavan, R., Gourdie, R., and Poelzing, S. (2014a). Mechanisms of cardiac conduction: a history of revisions. *Am. J. Physiol. Heart Circ. Physiol.* 306, H619–H627. doi: 10.1152/ajpheart.00760.2013

Veeraraghavan, R., Poelzing, S., and Gourdie, R. G. (2014b). Intercellular electrical communication in the heart: a new, active role for the intercalated Disk. *Cell Commun. Adhes.* 21, 161–167. doi: 10.3109/15419061.2014.905932

Veeraraghavan, R., Gyorke, S., and Radwański, P. B. (2017). Neuronal sodium channels: emerging components of the nano-machinery of cardiac calcium cycling. *J. Physiol.* 595, 3823–3834. doi: 10.1113/JP273058

Veeraraghavan, R., Larsen, A. P., Torres, N. S., Grunnet, M., and Poelzing, S. (2013). Potassium channel activators differentially modulate the effect of sodium channel blockade on cardiac conduction. *Acta Physiol. (Oxf.)* 207, 280–289. doi: 10.1111/j.1748-1716.2012.02481.x

Veeraraghavan, R., Lin, J., Hoeker, G. S., Keener, J. P., Gourdie, R. G., and Poelzing, S. (2015). Sodium channels in the Cx43 gap junction perinexus may constitute a cardiac ephapse: an experimental and modeling study. *Pflugers Arch.* 467, 2093–2105. doi: 10.1007/s00424-014-1675-z

Veeraraghavan, R., Lin, J., Keener, J. P., Gourdie, R., and Poelzing, S. (2016). Potassium channels in the Cx43 gap junction perinexus modulate ephaptic coupling: an experimental and modeling study. *Pflugers. Arch.* 468, 1651–1661. doi: 10.1007/s00424-016-1861-2

Veeraraghavan, R., Salama, M. E., and Poelzing, S. (2012). Interstitial volume modulates the conduction velocity- gap junction relationship. *Am. J. Physiol. Heart Circ. Physiol.* 302, H278–H286. doi: 10.1152/ajpheart.00868.2011

Veerman, C. C., Wilde, A. A., and Lodder, E. M. (2015). The cardiac sodium channel gene SCN5A and its gene product NaV1.5: role in physiology and pathophysiology. *Gene* 573, 177–187. doi: 10.1016/j.gene.2015.08.062

Venetucci, L. A., Trafford, A. W., O'Neill, S. C., and Eisner, D. A. (2008). The sarcoplasmic reticulum and arrhythmogenic calcium release. *Cardiovasc. Res.* 77, 285–292. doi: 10.1093/cvr/cvm009

Viatchenko-Karpinski, S., Kornyeyev, D., El-Bizri, N., Budas, G., Fan, P., Jiang, Z., et al. (2014). Intracellular Na+ overload causes oxidation of CaMKII and leads to Ca2+ mishandling in isolated ventricular myocytes. *J. Mol. Cell Cardiol.* 76, 247–256. doi: 10.1016/j.yjmcc.2014.09.009

Viatchenko-Karpinski, S., Terentyev, D., Jenkins, L. A., Lutherer, L. O., and Gyorke, S. (2005). Synergistic interactions between Ca2+ entries through L-type Ca2+ channels and Na+-Ca2+ exchanger in normal and failing rat heart. *J. Physiol.* 567(Pt 2), 493–504. doi: 10.1113/jphysiol.2005.091280

Westenbroek, R. E., Bischoff, S., Fu, Y., Maier, S. K., Catterall, W. A., and Scheuer, T. (2013). Localization of sodium channel subtypes in mouse ventricular myocytes using quantitative immunocytochemistry. *J. Mol. Cell Cardiol.* 64, 69–78. doi: 10.1016/j.yjmcc.2013.08.004

Conflict of Interest Statement: The authors declare that the research was conducted in the absence of any commercial or financial relationships that could be construed as a potential conflict of interest.

frontiers in Physiology

ORIGINAL RESEARCH
published: 05 September 2018
doi: 10.3389/fphys.2018.01230

Key Role of the Membrane Trafficking of Nav1.5 Channel Protein in Antidepressant-Induced Brugada Syndrome

Xi Chen[1,2†], Chao Zhu[2†], Hao Zhou[2†], Yu Zhang[2], Zhongqi Cai[2], Honglin Wu[3], Xiaomeng Ren[2], Lei Gao[2], Jiancheng Zhang[3] and Yang Li[2]**

[1] Department of Geriatrics, The First Affiliated Hospital of Chongqing Medical University, Chongqing, China, [2] Department of Cardiology, Chinese People's Liberation Army General Hospital, Beijing, China, [3] Department of Cardiology, Provincial Clinical Medicine College of Fujian Medical University, Fuzhou, China

OPEN ACCESS

Edited by:
Di Lang,
University of Wisconsin-Madison, United States

Reviewed by:
Ravi Vaidyanathan,
University of Wisconsin-Madison, United States
Rob Gourdie,
Medical University of South Carolina, United States

***Correspondence:**
Jiancheng Zhang
fjzhangjiancheng@yahoo.com.cn
Yang Li
liyangbsh@163.com

† These authors have contributed equally to this work

Specialty section:
This article was submitted to Cardiac Electrophysiology, a section of the journal Frontiers in Physiology

Received: *18 April 2018*
Accepted: *15 August 2018*
Published: *05 September 2018*

Citation:
Chen X, Zhu C, Zhou H, Zhang Y, Cai Z, Wu H, Ren X, Gao L, Zhang J and Li Y (2018) Key Role of the Membrane Trafficking of Nav1.5 Channel Protein in Antidepressant-Induced Brugada Syndrome. Front. Physiol. 9:1230. doi: 10.3389/fphys.2018.01230

Anti-depressant treatment has been found to be associated with the development of Brugada syndrome (BrS) through poorly defined mechanisms. Herein, this study aimed to explore the molecular basis for amitriptyline-induced BrS. The effects of long-term treatments of amitriptyline on Nav1.5 were investigated using neonatal rat ventricular myocytes. The electrophysiological properties, expression and distribution of Nav1.5 were studied using the patch clamp, Western blot and confocal laser microscopy assays. Interactions between Nav1.5 and its interacting proteins, including ankyrin-G and dystrophin, were evaluated by co-immunoprecipitation. A larger decrease in the peak I_{Na} occurred after long-term treatments to amitriptyline (56.64%) than after acute exposure to amitriptyline (28%). Slow recovery from inactivation of Nav1.5 was observed after acute or long-term treatments to amitriptyline. The expression of Nav1.5 on the cell membrane showed a larger decrease by long-term treatments to amitriptyline than by acute exposure to amitriptyline. After long-term treatments to amitriptyline, we observed reduced Nav1.5 proteins on the cell membrane and the disrupted co-localization of Nav1.5 and ankyrin-G or dystrophin. Co-immunoprecipitation experiments further testified that the combination of Nav1.5 and ankyrin-G or dystrophin was severely weakened after long-term treatments to amitriptyline, implying the failed interaction between Nav1.5 and ankyrin-G or dystrophin. Our data suggest that the long-term effect of amitriptyline serves as an important contribution to BrS induced by amitriptyline. The mechanisms of BrS induced by amitriptyline were related to Nav1.5 trafficking and could be explained by the disrupted interaction of ankyrin-G, dystrophin and Nav1.5.

Keywords: Brugada syndrome, antidepressant, Nav1.5, long-term effect, trafficking, interacting proteins

INTRODUCTION

Brugada syndrome (BrS) is an inherited arrhythmia disease diagnosed by the ECG findings of ST-segment elevation in the right precordial lead, without identifiable structural abnormalities (Priori et al., 2013). The prevalence of BrS in Southeast Asians is estimated to be 0.1%, much higher than in other ethnicities (Ng et al., 2012). In the Chinese population, its prevalence was demonstrated

to be 3.3% in a recent epidemiological study (Juang et al., 2015). Despite the low prevalence, BrS is strongly associated with the increased risk of ventricular fibrillation and sudden cardiac death (SCD) (Murakoshi and Aonuma, 2013).

Intensive research has emphasized the concern that antidepressants increase the risk of BrS. Overall, more than 16 antidepressants have been identified to be associated with BrS and related SCD[1]. Among the cases of cyclic antidepressant application, the prevalence of a Brugada electrocardiographic pattern was reported to be 15.3% (Goldgran-Toledano et al., 2002). It should be noted that amitriptyline and nortriptyline use was associated with 2.5-fold and 4.5-fold increases, respectively, in the risk of SCD (Ray et al., 2004; Bardai et al., 2013). These facts underlie the importance of revealing the mechanisms of antidepressant-induced BrS that remain poorly understood.

Previous studies on antidepressant-induced BrS mainly focused on the altered gating properties of the alpha subunit of the voltage-gated Nav1.5 cardiac sodium channel, such as a decreased peak current and delayed recovery from inactivation (Minoura et al., 2012). However, the Brugada ECG pattern or symptomatic BrS in antidepressant users often occurred after the long-term use of these drugs (Chow et al., 2005; Kofune et al., 2013). Thus, the gating property changes of Nav1.5 may not well explain these clinical manifestations. Since a recent study discovered a 15-fold increase in I_{Na-L} by chronic exposure to dofetilide but not by acute exposure to dofetilide (Yang et al., 2014), increasing attention has been given to the long-term treatments effect of drugs. Therefore, we speculate that apart from the acute effect, the long-term treatments of antidepressants may better explain the induction of BrS in antidepressant users.

To fulfill the physiological function, the Nav1.5 channel should be delivered from the endoplasmic reticulum to the Golgi apparatus and finally to specific subdomains of the plasma membrane, namely, the process of trafficking (Herfst et al., 2004). Sodium channel-interacting proteins such as ankyrin-G and dystrophin were proven to be essential to maintain the precise process of Nav1.5 trafficking. Trafficking of Nav1.5 to the cell membrane could be disrupted in ankyrin-G-knockout myocytes, and ventricular arrhythmia was observed in ankyrin-G-knockout mice (Makara et al., 2014). Deficiency of dystrophin could account for an almost 30% decrease in the sodium current (Gavillet et al., 2006). Thus, this study tests the hypothesis that antidepressants may have a long-term blockade effect on Nav1.5, which may be due to the fault of Nav1.5 trafficking to the cell membrane, with the regulation of the sodium channel-interacting proteins ankyrin-G and dystrophin.

MATERIALS AND METHODS

Neonatal Rat Cardiomyocyte Isolation

Twenty-four-hour-old neonatal Sprague–Dawley rats were purchased from the animal center of SiBeiFu in Beijing, China. The protocol of the study was approved by the animal ethics committee of the Chinese People's Liberation Army General Hospital in accordance with NIH guidelines. We used a modified method according to previous reports (Kadota et al., 2017; Wu et al., 2017). Isolated ventricles of the hearts from the rats were placed in cold phosphate-buffered saline (PBS) (HyClone, United States). Next, the ventricles were minced and digested in a protease solution (0.025% type 2 collagenase/0.08% pancreatin, Gibco, United States) at 37°C. Fetal bovine serum (FBS) (Gibco, United States) was used to terminate the digestion. Digestion was repeated 8–10 times, for 2∼5 min each. The cells in the supernatant were collected by centrifugation at 1500 rpm for 10 min. The collected cells were then cultured in Dulbecco's modified Eagle's medium (DMEM) (HyClone, United States) supplemented with 5% FBS (Gibco, United States) and 1% streptomycin (100 mg/ml)/penicillin (100 U/ml) (Gibco, United States). After incubation for 2 h, ventricular myocytes were separated from cardiac fibroblasts (CFs). Cells in the supernatant were subsequently plated in cell culture dishes at 37°C with 5% CO_2. The culture medium was supplemented with 30 μg/ml of bromodeoxyuridine (Sigma, United States) to prevent CF growth.

For the acute effect of the drugs, the cells were directly superfused with drugs for 5 min, and the I_{Na} of the cells was recorded. For the long-term effect of the drugs, with coincubation of the drugs for 24 h, the I_{Na} of the cells was recorded. The drugs used were amitriptyline (1.0 μM), clomipramine (1.0 μM), nortriptyline (1.0 μM), and desipramine (1.0 μM) (Sigma, United States).

Patch Clamp

All whole-cell recordings were obtained at room temperature, utilizing an Axon Multiclamp 700B Amplifier (Molecular Devices, United States). Signal acquisition was completed using a digidata 1440A acquisition interface (Molecular Devices, United States) controlled by pCLAMP programs (version 10.2). Isolated neonatal rat ventricular myocytes were incubated for 24 h before the incubation solution was replaced by an extracellular solution for the patch experiment. The extracellular solution contained the following: 116 mM of NaCl, 20 mM of TEA-Cl, 3 mM of KCl, 1 mM of $CaCl_2$, 1 mM of $MgCl_2.6H_2O$, 10 mM of HEPES, 10 mM of glucose, 0.1 mM of $CdCl_2$, and 4 mM of choline chloride, with the pH adjusted to 7.3 with NaOH. The pipette solution contained the following: 5 mM of NaCl, 135 mM of CsCl, 10 mM of EGTA, 5 mM of Na_2ATP, 5 mM of $MgCl_2.6H_2O$, and 5 mM of HEPES, with the pH adjusted to 7.2 with NaOH. The pipette resistance ranged from 2 to 3 MΩ and was maintained to record I_{Na}. The series resistance was compensated by 90∼95%, and slow capacitance was compensated by 85∼90% to minimize the voltage clamp errors.

To determine the voltage dependence of the peak I_{Na}, cells were held at −120 mV, and 300-ms voltage steps were applied from −90 to +40 mV by 10-mV increments. The peak I_{Na} was then divided by the membrane capacitance to analyze the peak current density. To determine the voltage dependence of activation, normalized I_{Na} was plotted as voltage-dependent activation curves fitted to the Boltzmann distribution. To determine the voltage-dependent inactivation, I_{Na} was elicited

[1] www.brugadadrugs.org

by application of 1000-ms conditioning pulses from −150 mV to 0 mV, followed by a 30-ms test pulse to −35 mV. Voltage-dependent inactivation curves were fitted to the Boltzmann distribution. To determine the recovery from inactivation, paired test pulses to −35 mV were applied, each for 30 ms, with increasing intervals of 40 ms to a maximum of 740 ms between the paired pulses and a holding potential of −120 mV. The time-dependent recovery curves were fitted to exponential functions. For analysis of the intermediate-state inactivation, pre-pulses to −20 mV with increasing intervals ranging from 1 to 3200 ms were applied, followed by a 50-ms test pulse to −20 mV. For analysis of the closed-state inactivation, pre-pulses to −100 mV with increasing intervals ranging from 1 to 500 ms were applied, followed by a 50-ms pulse to −20 mV.

Confocal Imaging

As described previously (Casini et al., 2010), cells were rinsed with cold PBS twice and then were fixed with 4% polyformaldehyde for 15 min at 4°C. After rinsing with cold PBS again, the cells were incubated in PBS solution containing 10% normal goat serum, 1% bovine serum albumin (BSA) and 0.1% TritonX-100 to block non-specific sites. Primary antibodies or secondary antibodies were diluted in a PBS solution containing 3% normal goat serum and 1% BSA. Cells were incubated with primary antibodies at 4°C overnight and then were incubated with secondary antibody at room temperature for 2 h. The antibodies used in the present study were as follows: mouse-anti-ankyrin-G (Santa Cruz, United States), mouse-anti-dystrophin (Sigma, United States), rabbit-anti-Nav1.5 (Alomone Labs), goat-anti-rabbit RBITC and goat-anti-mouse FITC. Finally, the samples were examined using a Leica TCS-SP2 digital scanning confocal microscope.

Western Blotting

This method was described previously (Zhang et al., 2015; Chen et al., 2016). Briefly, the collected neonatal ventricular myocytes were rinsed with cold PBS and were lysed in RIPA (Radio Immuno Precipitation Assay) buffer (Sigma, United States) containing proteinase inhibitor to prepare the cell lysates. The lysates were then centrifuged at 700 *g* at 4°C for 10 min. The supernatants were collected for an additional centrifugation (10,000 *g*, 4°C for 10 min). The plasma membrane protein extraction kit (Biovision, United States) was used for total membrane protein extraction. The protein concentration was measured using the BCA (bicinchoninic acid) protein assay kit (Sigma, United States). The proteins were separated by electrophoresis on SDS-polyacrylamide gels, transferred to nitrocellulose membranes and incubated with primary antibodies against Nav1.5, ankyrin-G and dystrophin at 4°C overnight. After rinsing, the blots were incubated with the appropriate horseradish peroxidase-conjugated secondary antibody at 24°C for 1 h. Chemiluminescence detection was performed with substrate reagents by a CCD camera. Densitometric analysis was performed with Bandscan 5.0 software. For quantification, the protein expression levels were normalized to the GAPDH levels and against controls. Each experiment was repeated at least three times.

Co-immunoprecipitation

Cells were lysed in RIPA buffer (Sigma, United States) supplemented with proteinase inhibitor. After rotating at 4°C for 30 min, the homogenates were centrifuged at 16000 rpm at 4°C for 20 min. The supernatants were incubated with the primary antibody at 4°C for 2 h. Next, the immune complexes were incubated with protein A/G beads at 4°C overnight. After centrifugation, the supernatants were discarded, and the immunoprecipitates were rinsed for Western blotting. Each experiment was repeated at least three times.

Statistical Analysis

Off-line leak correction was performed on all of the amplitude data. The data are presented as mean values ± SD., with n representing the number of cells analyzed. pCLAMP version 10.2 (Axon Instruments) and Origin (Microcal Software) were used for the data analysis. P-values < 0.05 were considered significant, and statistical analyses between the experimental groups were performed using Student's t-test. One-way analysis of variance (ANOVA) was used when comparing multiple groups, and the significance between any two groups was evaluated by ANOVA followed by the Student–Newman–Keuls (S–N–K) *post hoc* test. The SPSS computer program (version 17.0) was used for the analyses. SSA curves were fitted using a Boltzmann distribution as follows: $G_{(t)}/G_{max} = 1/(1 \times \mathrm{Exp}[(V_m - V_{1/2})/k]$. The conductance value was computed using the following equation: $G = I_{max}/(V_m - E_{Na})$, where G is the conductance, G_{max} is the maximum conductance value, I_{max} represents the peak test pulse current, V_m represents the test pulse voltage, and E_{Na} represents the measured equilibrium potential for sodium. The SSIs were fitted using the Boltzmann equation, $I_{(t)}/I_{max} = [1 \times \mathrm{Exp}(-(V_m - V_{1/2})/k)]$, to determine the membrane potential for half-maximal inactivation ($V_{1/2}$) and the slope factor k. $I_{(t)}$ represents the test pulse potentials, I_{max} represents the peak test pulse current, and V_m is the test pulse/pre-pulse potential. Recovery from inactivation was assessed using the double-pulse protocol shown in the inset and fitted using a single-exponential function $I_{(\Delta t)}/I_{max} = A\mathrm{Exp}(\Delta t/\tau)$, where the values for A refer to the amplitudes, and those for τ refer to the time constants. I refers to the current, and t refers to time. All the data were fitted using a nonlinear least-squares minimization method.

RESULTS

Acute and Long-Term Effects of Amitriptyline on I_{Na}

I_{Na} was elicited by the protocols shown in **Figure 1A**. Representative I_{Na} before and after treatments with amitriptyline are shown in **Figure 1B** (acute effect) and **Figure 1E** (long-term effect). After acute treatments with amitriptyline, the I_{Na} densities were decreased, and at −35 mV of the test potential, the peak I_{Na} densities were reduced from −279.9 ± 24.9 pA/pF to −201.5 ± 26.3 pA/pF ($P < 0.001$, $n = 6$) (**Figures 1C,D**). With coincubation with amitriptyline for 24 h, the I_{Na} densities were decreased. At −35 mV of the test potential, the peak

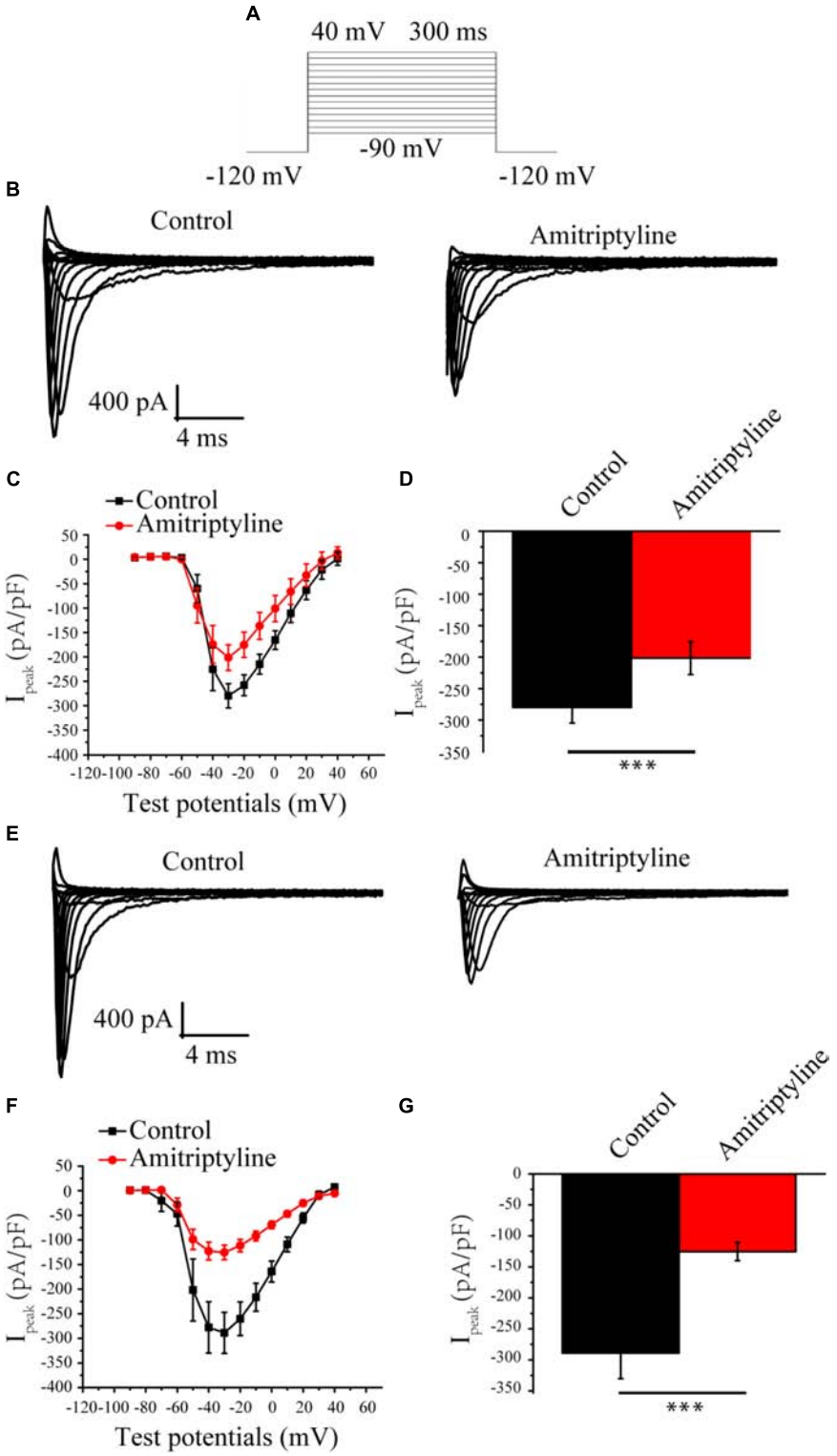

FIGURE 1 | Effect of amitriptyline on Nav1.5 currents. **(A)** Protocols for I_{Na} eliciting. **(B)** Representative I_{Na} in control cells and in cells with acute treatments of amitriptyline. **(C)** *I-V* curves for control cells and cells with acute treatments of amitriptyline. **(D)** Analysis of peak I_{Na} densities for the acute effect of amitriptyline. **(E)** Representative I_{Na} in control cells and cells with long-term treatments of amitriptyline. **(F)** *I-V* curves for control cells and cells with long-term treatments of amitriptyline. **(G)** Analysis of peak I_{Na} densities for the long-term effect of amitriptyline. ***$P < 0.001$.

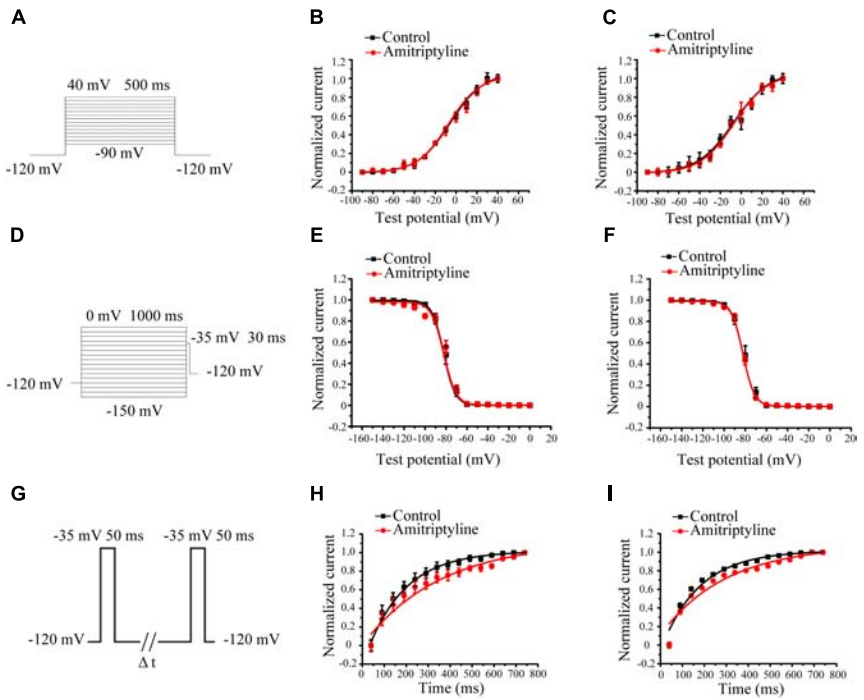

FIGURE 2 | Effect of amitriptyline on the gating properties of Nav1.5 currents. **(A)** Protocols for steady-state activation (SSA) recording. **(B)** SSA curves for the acute effect of amitriptyline. **(C)** SSA cures for the long-term effect of amitriptyline. **(D)** Protocols for steady-state inactivation (SSI) recording. **(E)** SSI curves for the acute effect of amitriptyline. **(F)** SSI curves for the long-term effect of amitriptyline. **(G)** Protocols for recovery from inactivation (RFI) recording. **(H)** RFI curves for the acute effect of amitriptyline. **(I)** RFI curves for the long-term effect of amitriptyline.

I_{Na} densities were decreased from -288.8 ± 41.5 pA/pF to -125.2 ± 14.8 pA/pF ($P < 0.001$, $n = 15$, **Figures 1F,G**). An obvious decrease in I_{Na} induced by amitriptyline (both acute and long-term treatments) was observed at test potentials ranging from -40 mV to -10 mV. It is interesting that the reduction of I_{Na} with the coincubation of amitriptyline for 24 h was twice that of the directly superfused with drug for 5 min. At the test potential of -35 mV, the peak I_{Na} was decreased by 28.2 and 56.6% due to acute and long-term treatments with amitriptyline, respectively (**Figures 1D,F**). The results suggested a stronger effect on I_{Na} induced by the long-term effect of amitriptyline.

Effect of Amitriptyline on the Gating Properties of I_{Na}

Steady-state activation (SSA) of I_{Na} was evaluated by a protocol shown in **Figure 2A**. After acute treatments with amitriptyline, $V_{1/2}$ did not shift significantly, and k did not change significantly. After long-term treatments with amitriptyline, there was no significant shift of $V_{1/2}$ and k (**Figures 2B,C**).

Steady-state inactivation (SSI) was evaluated by a protocol shown in **Figure 2D**. The SSI processes of I_{Na} was not significantly changed with acute and long-term treatments of amitriptyline. Compared with controls, $V_{1/2}$ or k were not markedly different either directly superfused or with coincubation for 24 h with amitriptyline (**Figures 2E,F**).

Recovery from inactivation (RFI) was evaluated by a protocol shown in **Figure 2G**. The recovery time constants from the inactivation of I_{Na} were affected by amitriptyline. The acute effect of amitriptyline caused significant prolongation of the recovery time constants (from 120.8 ± 6.2 ms to 244.7 ± 16.1 ms, $P < 0.01$, $n = 6$). Similarly, the long-term effect of amitriptyline also showed a prolongation of the recovery time constant from 120.7 ± 9.2 ms to 206.9 ± 11.2 ms ($P < 0.01$, $n = 15$, **Figures 2H,I**).

Effect of Amitriptyline on Intermediate-State Inactivation and Closed-State Inactivation of I_{Na}

Intermediate-state inactivation and closed-state inactivation were evaluated by protocols shown in **Figures 3A,B**. Neither the acute effect of amitriptyline nor the long-term effect of amitriptyline had an obvious impact on the intermediate-state inactivation of Nav1.5 currents (**Figures 3C,D**). However, the acute effect of amitriptyline and long-term effect of amitriptyline prolonged the time constants of the closed-state inactivation to a similar extent (**Figures 3E,F**).

Cellular Membrane Expression and Distribution of the Nav1.5 Channel Protein After Long-Term Treatments With Amitriptyline

Compared with the controls, both the acute effect of amitriptyline and long-term effect of amitriptyline caused significantly less

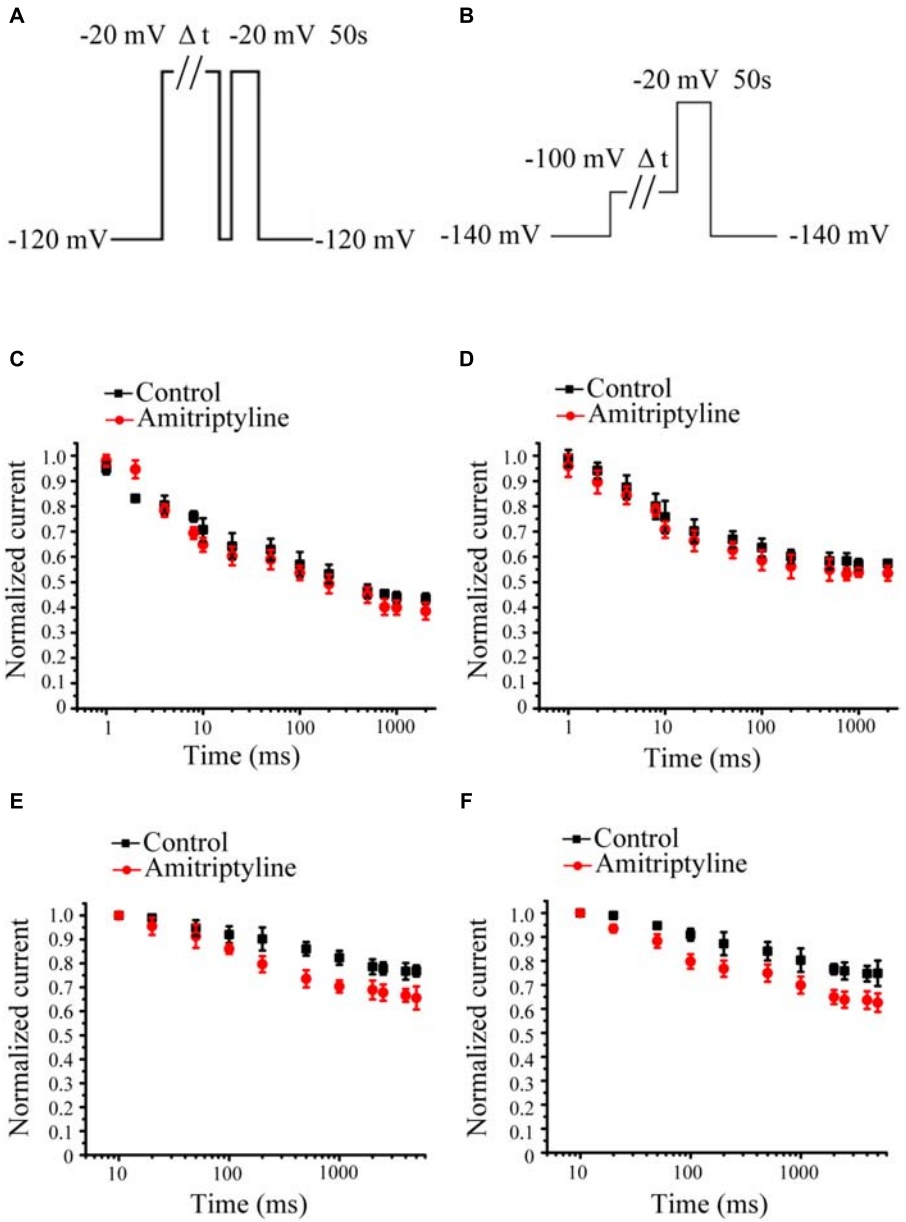

FIGURE 3 | Effect of amitriptyline on intermediate-state inactivation (ISI) and closed-state inactivation (CSI) of Nav1.5 currents. **(A)** Protocols for ISI recording. **(B)** Protocols for CSI recording. **(C)** ISI curves for the acute effect of amitriptyline. **(D)** ISI cures for the long-term effect of amitriptyline. **(E)** CSI curves for the acute effect of amitriptyline. **(F)** CSI cures for the long-term effect of amitriptyline.

Nav1.5 protein expressed on the cell membrane (1.00 ± 0.07 vs. 0.75 ± 0.07 vs. 0.54 ± 0.09, $P < 0.05$, $n = 3$). However, the Nav1.5 protein on the cell membrane was decreased more after long-term treatments with amitriptyline (0.54 ± 0.09) than after acute treatments with amitriptyline (0.75 ± 0.07, $P < 0.05$, $n = 3$) (**Figure 4A**). We did not observe significant reduction of cytosolic Nav1.5 protein compared with controls, after either acute or long-term treatments with amitriptyline (1.03 ± 0.07 vs. 0.96 ± 0.05 vs. 0.90 ± 0.05, $P > 0.05$, $n = 3$). Immunostaining experiments showed that the red signal intensity, which represented Nav1.5 protein, was distributed both in the cytoplasm and on the cell membrane. Nav1.5 on the cell membrane was observed clearly before long-term treatments with amitriptyline and was reduced markedly after long-term treatments with amitriptyline. The results suggested that the long-term effect of amitriptyline caused the retention of Nav1.5 protein within the cell.

In addition, in cells without treatments of amitriptyline, we observed that Nav1.5 protein was localized together with ankyrin-G (**Figure 4B**) and dystrophin (**Figure 4C**) on the cell membrane. However, after long-term treatments with amitriptyline, the co-localization of Nav1.5 with ankyrin-G or dystrophin could not

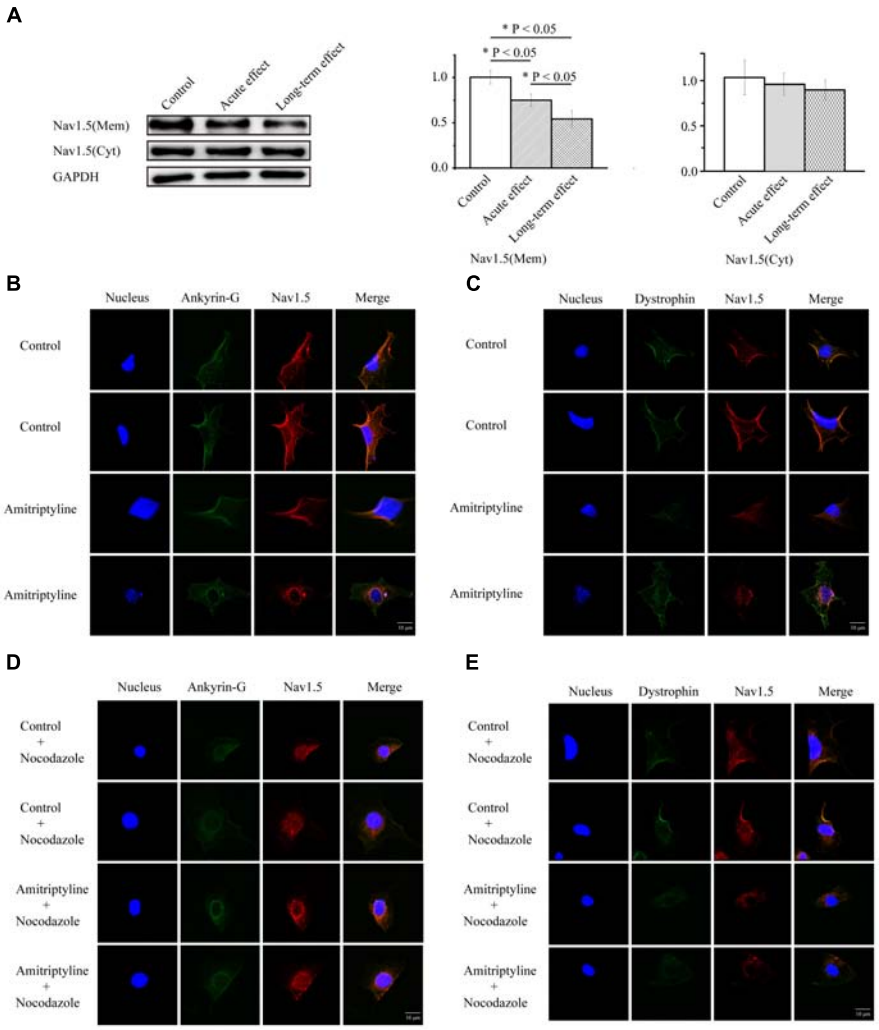

FIGURE 4 | Long-term effect of amitriptyline on protein expression and distribution of Nav1.5. **(A)** Protein expression of Nav1.5 in control cells, cells with acute treatments of amitriptyline and cells with long-term treatments with amitriptyline. **(B)** Representative confocal images of Nav1.5 (red) and ankyrin-G (green) without or with long-term treatments with amitriptyline. **(C)** Representative confocal images of Nav1.5 (red) and dystrophin (green) without or with long-term treatments with amitriptyline. **(D)** Representative confocal images of Nav1.5 and ankyrin-G with nocodazole treatments. **(E)** Representative confocal images of Nav1.5 and dystrophin with nocodazole treatments. The blue signal indicates the nucleus. Scale bar: 10 μm. $^*P < 0.05$.

be clearly observed. To further investigate whether trafficking dysfunction was related to the long-term effect of amitriptyline, we pre-treated all cells with nocodazole. Next, we observed similar a distribution of Nav1.5, ankyrin-G and dystrophin between the groups with or without long-term treatments with amitriptyline (**Figures 4D,E**).

Disrupted Interaction of Ankyrin-G, Dystrophin and Nav1.5 After Long-Term Treatments With Amitriptyline

Co-immunoprecipitation experiments were used to test the Nav1.5-ankyrin-G interaction and Nav1.5-dystrophin interaction. Anti-Nav1.5 antibody was used to analyze the immuno-complex. Nav1.5 protein could be precipitated by anti-ankyrin-G antibody and anti-dystrophin antibody before exposure to amitriptyline. However, the Nav1.5 protein bands could hardly be observed in the immuno-complex precipitated either by the anti-ankyrin-G antibody (**Figure 5A**) or anti-dystrophin antibody (**Figure 5B**) after 24 h of incubation with amitriptyline. These results suggested that the interaction between Nav1.5 and ankyrin-G or dystrophin could be weakened by the long-term effect of amitriptyline.

Effect of Several Other Antidepressants on I_{Na}

To determine whether the above long-term effects are specific to amitriptyline, we examined the effects of several other antidepressants on the sodium current. The results showed that clomipramine showed similar response characteristics as amitriptyline regarding I_{Na}. A larger decline in the peak I_{Na}

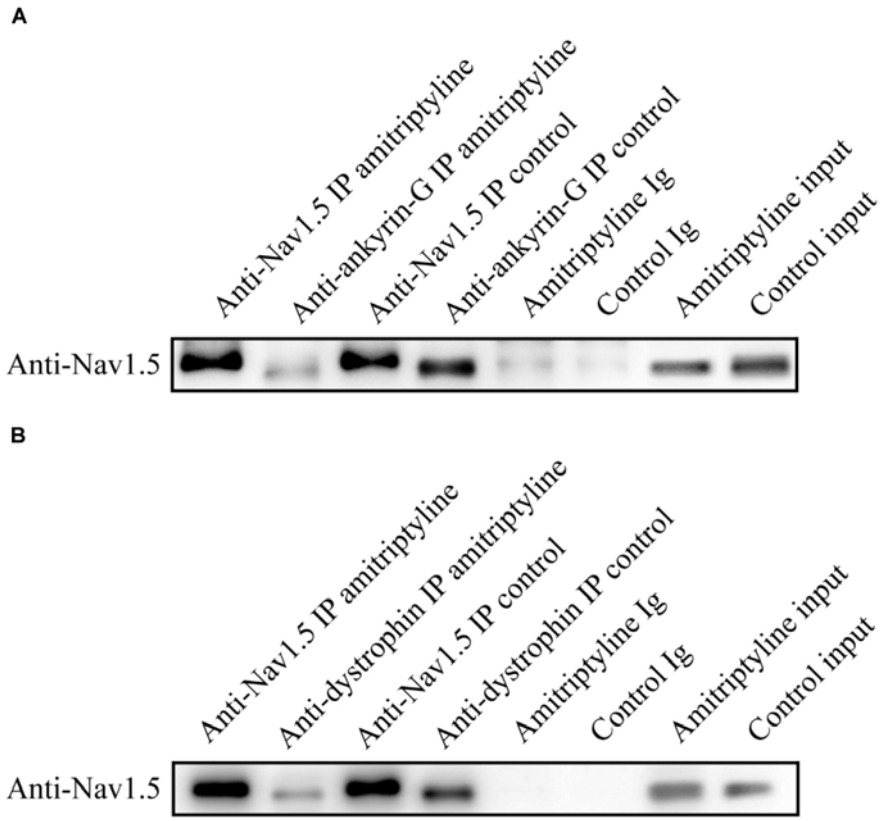

FIGURE 5 | Long-term effect of amitriptyline on the Nav1.5-ankyrin-G interaction and Nav1.5-dystrophin interaction. **(A)** With the anti-ankyrin-G antibody, Nav1.5 was detectable without long-term treatments with amitriptyline but was not clearly observed after long-term treatments with amitriptyline. **(B)** With anti-dystrophin antibody, Nav1.5 was detectable without long-term treatments with amitriptyline but was not clearly observed after the long-term treatments with amitriptyline. Input: Western blotting of total protein lysates.

was shown to be induced more by long-term treatments with clomipramine (32.0%) than by acute treatments (23.6%). However, the results observed with the other two antidepressants were not always consistent with those with amitriptyline. The acute effect of nortriptyline caused a 20.9% decrease in I_{Na}, and the long-term effect caused a 19.3% decrease. I_{Na} was not significantly changed by both acute or long-term treatments with desipramine (**Figure 6**).

DISCUSSION

Amitriptyline has been widely used and associated with BrS, whereas the mechanisms remain poorly understood. To the best of our knowledge, the present study confirmed for the first time that the long-term effect might be an important contribution to BrS induced by amitriptyline. The underlying mechanisms involved the impairment of Nav1.5 trafficking, which could be regulated by the Nav1.5-ankyrin-G interaction and Nav1.5-dystrophin interaction.

The concentrations of antidepressants used in this study are near therapeutic plasma concentration used in the clinic. Actually, in patients receiving daily doses of 75–300 mg of amitriptyline, plasma steady-state concentrations range from 0.3 to 0.9 μM (Pancrazio et al., 1998). The concentration of 1 μM nortriptyline exposed to ventricular myocytes is equivalent to serum levels in patients during chronic use of 150 mg nortriptyline (Bardai et al., 2013). In the present study, we used the same concentration of amitriptyline as previous studies to explore the electrophysiological and molecular biological changes of cardiac sodium cannels induced by amitriptyline (Nau et al., 2000).

The present study demonstrated that the long-term blockade effect of amitriptyline on Nav1.5 was stronger than the acute blockade effect. Similar to our previous study, the rescue effect of alpha-allocryptopine on the SCN5A-T353I current was observed only by coincubation with alpha-allocryptopine for 24 h but not by direct perfusion of alpha-allocryptopine (Zhang et al., 2015). There were also other studies illustrating similar results for the long-term effects of drugs. Dofetilide showed a strong capacity to increase the late sodium current only through exposure for 48 h (Chen et al., 2016). Desipramine imposed an acute effect, a short-term effect or a long-term effect according to the different exposure times on hERG channels (Staudacher et al., 2011). Thus, a stronger long-term effect other than the acute effect of amitriptyline turned out to be an important contribution to

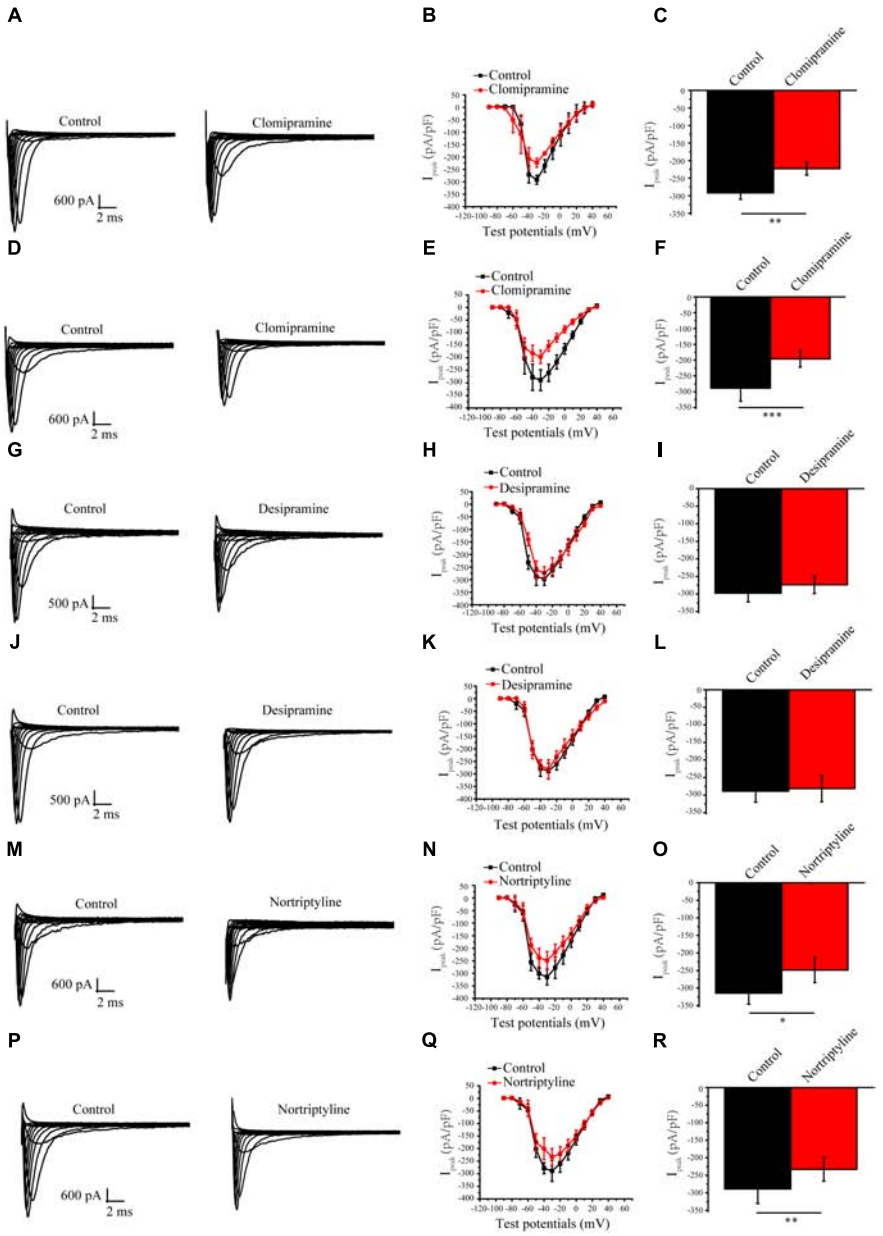

FIGURE 6 | Effect of other antidepressants on Nav1.5 currents. **(A)** Representative I_{Na} current traces recorded from cells under control conditions and acute clomipramine treatments of **(B,C)** *I-V* curves and analysis of the peak I_{Na} densities for the acute effect of clomipramine. **(D)** Representative I_{Na} current traces recorded from cells with long-term treatments of clomipramine. **(E,F)** *I-V* curves and peak I_{Na} densities of cells with long-term treatmentsn of clomipramine. **(G–I)** Representative I_{Na} in cells with acute desipramine treatments. **(J–L)** Representative I_{Na} in cells with long-term treatments of desipramine. **(M–R)** Representative I_{Na} in cells with acute and long-term treatments of nortriptyline. $^*P < 0.05$, $^{**}P < 0.01$.

the occurrence of BrS and a better explanation for the clinical manifestations.

Consistent with previous reports (Wang et al., 2004; Donovan et al., 2011; Liang et al., 2014), the slow recovery from the inactivated state was the main gating property alteration demonstrated in the present study. The cause might involve the high affinity of amitriptyline for inactivated-state sodium channels (Nau et al., 2000). However, no shift of the SSI curves induced by amitriptyline was detected in the present study, a finding that was in contrast to the previous findings that SSI curves were shifted to the negative direction by the application of amitriptyline (Minoura et al., 2012). Such inconsistency may result from different protocols and cell sources. The neonatal rat ventricular myocytes used in this study were expected to share more electrophysiological characteristics with human myocytes than cells transfected with cardiac sodium channels. Despite the similar changes in the gating properties imposed by acute and long-term effects of amitriptyline, the long-term effect of

amitriptyline caused a much larger decline in the peak sodium current. Thus, the altered gating properties may not fully explain this phenomenon, indicating other underlying mechanisms.

In the present study, we found a decreased expression and distribution of Nav1.5 protein on the cell membrane, as well as the retention of Nav1.5 protein within cells after long-term treatments with amitriptyline. With the application of nocodazole, an inhibitor for channel trafficking (Zhang et al., 2014), the impact of amitriptyline was almost covered. Such a close relationship between long-term drug incubation and its effect on channel trafficking implied in this study has been revealed previously. As stated previously, desipramine could exert different impacts on hERG channels such as gating property changes and trafficking dysfunction, depending on the exposure time to the drug (Staudacher et al., 2011). Our previous study also found that after coincubation with cells for 24 h, alpha-allocryptopine had the capacity to rescue trafficking dysfunction of SCN5A-T353I (Zhang et al., 2015). As deduced from these findings, the novel mechanism responsible for the long-term blockade effect of amitriptyline on Nav1.5 was the impairment of Nav1.5 trafficking.

Furthermore, we observed less co-localization and weaker binding between Nav1.5 and ankyrin-G or dystrophin after the long-term treatments with amitriptyline, indicating the disrupted Nav1.5-ankyrin-G interaction and Nav1.5-dystrophin interaction induced by amitriptyline. Actually, a conserved ankyrin-binding motif was detected in Nav1.5 protein (Garrido et al., 2003; Lemaillet et al., 2003). The loss of ankyrin-G could cause a decrease in the sodium current and Nav1.5 surface expression without affecting channel gating properties, owing to the requirements of ankyrin-G for Nav1.5 trafficking (Lowe et al., 2008). Interestingly, the binding site between Nav1.5 and ankyrin-G was confirmed to be somewhere near E1053 (Mohler et al., 2004), while the binding site between Nav1.5 and amitriptyline was proven to be a structure formed by Y1767 and F1760 (Nau et al., 2000). Although there is a long distance between these two binding sites on the primary sequence, the spatial proximity may exist to provide the necessary conditions for amitriptyline to impair the interaction between Nav1.5 and ankyrin-G. On the other hand, we discovered that the long-term effect of amitriptyline could destroy the Nav1.5-dystrophin interaction. It should be noted that dystrophin was functionally related to the cardiac sodium channels located on the lateral membrane and was responsible for the sodium current originating from those channels (Gavillet et al., 2006). Although we could not distinguish intercalated disks from the lateral membrane on neonatal rat ventricular myocytes, these results did suggest that the Nav1.5 channels located on both intercalated disks and the lateral membrane might be involved in the mechanisms of amitriptyline-induced BrS.

In line with the findings on amitriptyline, we found that clomipramine also showed a stronger blockade effect on Nav1.5 by long-term application than by acute application. Inconsistently, nortriptyline showed similar blockade effects on Nav1.5 with long-term or acute application, whereas desipramine failed to block Nav1.5 by either long-term or acute application. Although different antidepressants may have different capacities in the blockade of Nav1.5, the long-term effect of drugs should be considered seriously in further studies referring to drug-induced BrS.

We acknowledge the limitations in the present study. The adult rat myocytes should be a better choice to observe the specific location of Nav1.5 on intercalated disks and the lateral membrane. However, considering the difficulty regarding the long-term culture of adult rat myocytes, we used neonatal rat myocytes instead, without observation of the intercalated disk and lateral membrane. In addition, the impacts of other antidepressants (including clomipramine, nortriptyline, and desipramine) on the expression and distribution of the Nav1.5 protein were not studied in the present study but deserve further research. More importantly, evidence is accumulating that Nav1.5 channels were part of the sodium channel macromolecular complexes and trafficking of Nav1.5 proteins were regulated by many Nav1.5-interacting proteins, such as SAP97, MOG1, Plakophilin-2, beta subunits (Shao et al., 2009; Abriel et al., 2015). In the present study, we only chose two typical Nav1.5 proteins for experiments. Ankyrin-G mainly regulates the Nav1.5 proteins on intercalated disk membrane and dystrophin regulates the Nav1.5 proteins on lateral membranes, respectively. However, the function of Nav1.5 depends on the complicated cooperation among multiple Nav1.5-interacting proteins. Apart from above Nav1.5-interacting proteins, the Kir2.x channels have also been proved to function within the macromolecular complexes. Nav1.5/Kir2.x reciprocal modulation has been elucidated previously through a critical domain of Nav1.5, which increases the sodium and potassium currents (Matamoros et al., 2016). If the critical domain could be influenced by amitriptyline, currents of both Nav1.5 and Kir2.x would decrease, which could give rise to Brs. Meanwhile, Nav1.5 and Kir2.x interact with common partners including ankyrin-G and dystrophin (Willis et al., 2015). Thus Kir2.x and other interacting proteins may as well paly important roles in antidepressant-induced BrS, which could be further explored in the future. Still, the present findings demonstrated for the first time that the long-term effect should be considered important in BrS induced by amitriptyline. Impaired Nav1.5 trafficking, regulated by Nav1.5-ankyrin-G and Nav1.5-dystrophin interaction, was suggested to be the mechanism related to such a long-term effect. The present study may provide a new clue for the further investigation on BrS and experimental basis for rational clinical drug use in the future.

AUTHOR CONTRIBUTIONS

XC carried out experiments and wrote the manuscript. CZ and HZ assisted with the Western blot experiments. YZ and ZC assisted with data analysis. HW and XR assisted with path clamp experiments. LG assisted to write the manuscript. JZ assisted to design experiments. YL designed experiments.

FUNDING

This work was supported by the National Natural Science Foundation of China (Grant Nos. 81671731 and 81470542).

REFERENCES

Abriel, H., Rougier, J. S., and Jalife, J. (2015). Ion channel macromolecular complexes in cardiomyocytes: roles in sudden cardiac death. *Circ. Res.* 116, 1971–1988. doi: 10.1161/CIRCRESAHA.116.305017

Bardai, A., Amin, A. S., Blom, M. T., Bezzina, C. R., Berdowski, J., Langendijk, P. N., et al. (2013). Sudden cardiac arrest associated with use of a non-cardiac drug that reduces cardiac excitability: evidence from bench, bedside and community. *Eur. Heart J.* 34, 1506–1516. doi: 10.1093/eurheartj/eht054

Casini, S., Tan, H. L., Demirayak, I., Remme, C. A., Amin, A. S., Scicluna, B. P., et al. (2010). Tubulin polymerization modifies cardiac sodium channel expression and gating. *Cardiovasc. Res.* 85, 691–700. doi: 10.1093/cvr/cvp352

Chen, X., Zhang, Y., Xu, B., Cai, Z., Wang, L., Tian, J., et al. (2016). The mitochondrial calcium uniporter is involved in mitochondrial calcium cycle dysfunction: underlying mechanism of hypertension associated with mitochondrial tRNA(Ile) A4263G mutation. *Int. J. Biochem. Cell Biol.* 78, 307–314. doi: 10.1016/j.biocel.2016.07.018

Chow, B. J., Gollob, M., and Birnie, D. (2005). Brugada syndrome precipitated by a tricyclic antidepressant. *Heart* 91:651. doi: 10.1136/hrt.2004.049593

Donovan, B. T., Bakshi, T., Galbraith, S. E., Nixon, C. J., Payne, L. A., and Martens, S. F. (2011). Utility of frozen cell lines in medium throughput electrophysiology screening of hERG and NaV1.5 blockade. *J. Pharmacol. Toxicol. Methods* 64, 269–276. doi: 10.1016/j.vascn.2011.09.002

Garrido, J. J., Giraud, P., Carlier, E., Fernandes, F., Moussif, A., Fache, M. P., et al. (2003). Targeting motif involved in sodium channel clustering at the axonal initial segment. *Science* 300, 2091–2094. doi: 10.1126/science.1085167

Gavillet, B., Rougier, J. S., Domenighetti, A. A., Behar, R., Boixel, C., Ruchat, P., et al. (2006). Cardiac sodium channel Nav1.5 is regulated by a multiprotein complex composed of syntrophins and dystrophin. *Circ. Res.* 99, 407–414. doi: 10.1161/01.RES.0000237466.13252.5e

Goldgran-Toledano, D., Sideris, G., and Kevorkian, J. P. (2002). Overdose of cyclic antidepressants and the Brugada syndrome. *N. Engl. J. Med.* 346, 1591–1592. doi: 10.1056/NEJM200205163462020

Herfst, L. J., Rook, M. B., and Jongsma, H. J. (2004). Trafficking and functional expression of cardiac Na+ channels. *J. Mol. Cell. Cardiol.* 36, 185–193. doi: 10.1016/j.yjmcc.2003.11.014

Juang, J. M., Chen, C. Y., Chen, Y. H., Wu, I. C., Hsu, C. C., Chen, L. N., et al. (2015). Prevalence and prognosis of Brugada electrocardiogram patterns in an elderly han chinese population: a nation-wide community-based study (HALST cohort). *Europace* 17(Suppl. 2), ii54–ii62. doi: 10.1093/europace/euv141

Kadota, S., Pabon, L., Reinecke, H., and Murry, C. E. (2017). In vivo maturation of human induced pluripotent stem cell-derived cardiomyocytes in neonatal and adult rat hearts. *Stem Cell Rep.* 8, 278–289. doi: 10.1016/j.stemcr.2016.10.009

Kofune, M., Kofune, T., Ohkubo, K., and Watanabe, I. (2013). Electrocardiographic changes upon tricyclic antidepressant administration mimicking Brugada syndrome. *Intern. Med.* 52:1427. doi: 10.2169/internalmedicine.52.0016

Lemaillet, G., Walker, B., and Lambert, S. (2003). Identification of a conserved ankyrin-binding motif in the family of sodium channel alpha subunits. *J. Biol. Chem.* 278, 27333–27339. doi: 10.1074/jbc.M303327200

Liang, J., Liu, X., Pan, M., Dai, W., Dong, Z., Wang, X., et al. (2014). Blockade of Nav1.8 currents in nociceptive trigeminal neurons contributes to anti-trigeminovascular nociceptive effect of amitriptyline. *Neuromolecular Med.* 16, 308–321. doi: 10.1007/s12017-013-8282-6

Lowe, J. S., Palygin, O., Bhasin, N., Hund, T. J., Boyden, P. A., Shibata, E., et al. (2008). Voltage-gated Nav channel targeting in the heart requires an ankyrin-G dependent cellular pathway. *J. Cell. Biol.* 180, 173–186. doi: 10.1083/jcb.200710107

Makara, M. A., Curran, J., Little, S. C., Musa, H., Polina, I., Smith, S. A., et al. (2014). Ankyrin-G coordinates intercalated disc signaling platform to regulate cardiac excitability in vivo. *Circ. Res.* 115, 929–938. doi: 10.1161/CIRCRESAHA.115.305154

Matamoros, M., Pérez-Hernández, M., Guerrero-Serna, G., Amorós, I., Barana, A., Núñez, M., et al. (2016). Nav1.5 N-terminal domain binding to α1-syntrophin increases membrane density of human Kir2.1, Kir2.2 and Nav1.5 channels. *Cardiovasc. Res.* 110, 279–290. doi: 10.1093/cvr/cvw009

Minoura, Y., Di Diego, J. M., Barajas-Martinez, H., Zygmunt, A. C., Hu, D., Sicouri, S., et al. (2012). Ionic and cellular mechanisms underlying the development of acquired Brugada syndrome in patients treated with antidepressants. *J. Cardiovasc. Electrophysiol.* 23, 423–432. doi: 10.1111/j.1540-8167.2011.02196.x

Mohler, P. J., Rivolta, I., Napolitano, C., LeMaillet, G., Lambert, S., Priori, S. G., et al. (2004). Nav1.5 E1053K mutation causing Brugada syndrome blocks binding to ankyrin-G and expression of Nav1.5 on the surface of cardiomyocytes. *Proc. Natl. Acad. Sci. U.S.A.* 101, 17533–17538. doi: 10.1073/pnas.0403711101

Murakoshi, N., and Aonuma, K. (2013). Epidemiology of arrhythmias and sudden cardiac death in Asia. *Circ. J.* 77, 2419–2431. doi: 10.1253/circj.CJ-13-1129

Nau, C., Seaver, M., Wang, S. Y., and Wang, G. K. (2000). Block of human heart hH1 sodium channels by amitriptyline. *J. Pharmacol. Exp. Ther.* 292, 1015–1023.

Ng, C. T., Ong, H. Y., Cheok, C., Chua, T. S., and Ching, C. K. (2012). Prevalence of electrocardiographic abnormalities in an unselected young male multi-ethnic South-East Asian population undergoing pre-participation cardiovascular screening: results of the Singapore armed forces electrocardiogram and echocardiogram screening protocol. *Europace* 14, 1018–1024. doi: 10.1093/europace/eur424

Pancrazio, J. J., Kamatchi, G. L., Roscoe, A. K., and Lynch, C. III (1998). Inhibition of neuronal Na+ channels by antidepressant drugs. *J. Pharmacol. Exp. Ther.* 284, 208–214.

Priori, S. G., Wilde, A. A., Horie, M., Cho, Y., Behr, E. R., Berul, C., et al. (2013). HRS/EHRA/APHRS expert consensus statement on the diagnosis and management of patients with inherited primary arrhythmia syndromes: document endorsed by HRS, EHRA and APHRS in May 2013 and by ACCF, AHA, PACES and AEPC in June 2013. *Heart Rhythm* 10, 1932–1963. doi: 10.1016/j.hrthm.2013.05.014

Ray, W. A., Meredith, S., Thapa, P. B., Hall, K., and Murray, K. T. (2004). Cyclic antidepressants and the risk of sudden cardiac death. *Clin. Pharmacol. Ther.* 75, 234–241. doi: 10.1016/j.clpt.2003.09.019

Shao, D., Okuse, K., and Djamgoz, M. B. (2009). Protein-protein interactions involving voltage-gated sodium channels: post-translational regulation, intracellular trafficking and functional expression. *Int. J. Biochem. Cell Biol.* 41, 1471–1481. doi: 10.1016/j.biocel.2009.01.016

Staudacher, I., Wang, L., Wan, X., Obers, S., Wenzel, W., Tristram, F., et al. (2011). HERG K^+ channel-associated cardiac effects of the antidepressant drug desipramine. *Naunyn Schmiedebergs Arch. Pharmacol.* 383, 119–139. doi: 10.1007/s00210-010-0583-9

Wang, G. K., Russell, C., and Wang, S. Y. (2004). State-dependent block of voltage-gated Na+ channels by amitriptyline via the local anesthetic receptor and its implication for neuropathic pain. *Pain* 110, 166–174. doi: 10.1016/j.pain.2004.03.018

Willis, B. C., Ponce-Balbuena, D., and Jalife, J. (2015). Protein assemblies of sodium and inward rectifier potassium channels control cardiac excitability and arrhythmogenesis. *Am. J. Physiol. Heart Circ. Physiol.* 308, H1463–H1473. doi: 10.1152/ajpheart.00176.2015

Wu, L., Li, H., Li, X., Chen, Y., Zhang, Q., Cheng, Z., et al. (2017). Peptidomic analysis of cultured cardiomyocytes exposed to acute ischemic-hypoxia. *Cell. Physiol. Biochem.* 41, 358–368. doi: 10.1159/000456282

Yang, T., Chun, Y. W., Stroud, D. M., Mosley, J. D., Knollmann, B. C., Hong, C., et al. (2014). Screening for acute IKr block is insufficient to detect torsades de pointes liability: role of late sodium current. *Circulation* 130, 224–234. doi: 10.1161/CIRCULATIONAHA.113.007765

Zhang, C., Chen, B., Guo, A., Zhu, Y., Miller, J. D., Gao, S., et al. (2014). Microtubule-mediated defects in junctophilin-2 trafficking contribute to myocyte transverse-tubule remodeling and Ca^{2+} handling dysfunction in heart

failure. *Circulation* 129, 1742–1750. doi: 10.1161/CIRCULATIONAHA.113.008452

Zhang, J., Chen, Y., Yang, J., Xu, B., Wen, Y., Xiang, G., et al. (2015). Electrophysiological and trafficking defects of the SCN5A T353I mutation in Brugada syndrome are rescued by alpha-allocryptopine. *Eur. J. Pharmacol.* 746, 333–343. doi: 10.1016/j.ejphar.2014.09.028

Conflict of Interest Statement: The authors declare that the research was conducted in the absence of any commercial or financial relationships that could be construed as a potential conflict of interest.

The reviewer RV and handling Editor declared their shared affiliation at the time of the review.

frontiers in Physiology

ORIGINAL RESEARCH
published: 19 September 2018
doi: 10.3389/fphys.2018.01302

Partial Mechanical Unloading of the Heart Disrupts L-Type Calcium Channel and Beta-Adrenoceptor Signaling Microdomains

*Peter T. Wright[1], Jose L. Sanchez-Alonso[1], Carla Lucarelli[1,2], Anita Alvarez-Laviada[1], Claire E. Poulet[1], Sean O. Bello[1], Giuseppe Faggian[2], Cesare M. Terracciano[1] and Julia Gorelik[1]**

[1] Myocardial Function, National Heart and Lung Institute, Imperial College London, Imperial Centre for Translational and Experimental Medicine, Hammersmith Hospital, London, United Kingdom, [2] Department of Cardiac Surgery, School of Medicine, University of Verona, Verona, Italy

OPEN ACCESS

Edited by:
Gaetano Santulli,
Columbia University, United States

Reviewed by:
Jin O-Uchi,
University of Minnesota Twin Cities, United States
Carlo Gaetano,
IRCCS Istituti Clinici Scientifici Maugeri (ICS Maugeri), Italy
Elisabetta Cerbai,
Università degli Studi di Firenze, Italy

***Correspondence:**
Julia Gorelik
j.gorelik@imperial.ac.uk

Specialty section:
This article was submitted to Cardiac Electrophysiology, a section of the journal Frontiers in Physiology

Received: 22 June 2018
Accepted: 29 August 2018
Published: 19 September 2018

Citation:
Wright PT, Sanchez-Alonso JL, Lucarelli C, Alvarez-Laviada A, Poulet CE, Bello SO, Faggian G, Terracciano CM and Gorelik J (2018) Partial Mechanical Unloading of the Heart Disrupts L-Type Calcium Channel and Beta-Adrenoceptor Signaling Microdomains. Front. Physiol. 9:1302. doi: 10.3389/fphys.2018.01302

Introduction: We investigated the effect of partial mechanical unloading (PMU) of the heart on the physiology of calcium and beta-adrenoceptor-cAMP (βAR-cAMP) microdomains. Previous studies have investigated PMU using a model of heterotopic-heart and lung transplantation (HTHAL). These studies have demonstrated that PMU disrupts the structure of cardiomyocytes and calcium handling. We sought to understand these processes by studying L-Type Calcium Channel (LTCC) activity and sub-type-specific βAR-cAMP signaling within cardiomyocyte membrane microdomains.

Method: We utilized an 8-week model of HTHAL, whereby the hearts of syngeneic Lewis rats were transplanted into the abdomens of randomly assigned cage mates. A pronounced atrophy was observed in hearts after HTHAL. Cardiomyocytes were isolated via enzymatic perfusion. We utilized Förster Resonance Energy Transfer (FRET) based cAMP-biosensors and scanning ion conductance microscopy (SICM) based methodologies to study localization of LTCC and βAR-cAMP signaling.

Results: β_2AR-cAMP responses measured by FRET in the cardiomyocyte cytosol were reduced by PMU (loaded 28.51 ± 7.18% vs. unloaded 10.84 ± 3.27% N,n 4/10-13 mean ± SEM $*p < 0.05$). There was no effect of PMU on β_2AR-cAMP signaling in RII_Protein Kinase A domains. β_1AR-cAMP was unaffected by PMU in either microdomain. Consistent with this SICM/FRET analysis demonstrated that β_2AR-cAMP was specifically reduced in t-tubules (TTs) after PMU (loaded TT 0.721 ± 0.106% vs. loaded crest 0.104 ± 0.062%, unloaded TT 0.112 ± 0.072% vs. unloaded crest 0.219 ± 0.084% N,n 5/6-9 mean ± SEM $**p < 0.01$, $***p < 0.001$ vs. loaded TT). By comparison β_1AR-cAMP responses in either TT or sarcolemmal crests were unaffected by the PMU. LTCC occurrence and open probability (P_o) were reduced by PMU (loaded TT P_o 0.073 ± 0.011% vs. loaded crest P_o 0.027 ± 0.006% N,n 5/18-26 mean ± SEM $*p < 0.05$) (unloaded TT 0.0350 ± 0.003% vs. unloaded crest P_o 0.025 N,n 5/20-30 mean ± SEM NS $^{\#}p < 0.05$ unloaded vs. loaded TT). We discovered that PMU had reduced the association between Caveolin-3, Junctophilin-2, and Cav1.2.

Discussion: PMU suppresses' β_2AR-cAMP and LTCC activity. When activated, the signaling of β_2AR-cAMP and LTCC become more far-reaching after PMU. We suggest that a situation of 'suppression/decompartmentation' is elicited by the loss of refined cardiomyocyte structure following PMU. As PMU is a component of modern device therapy for heart failure this study has clinical ramifications and raises important questions for regenerative medicine.

Keywords: cAMP, beta-adrenergic, excitation-contraction, calcium, microdomains, cardiac, t-tubules, unloading

INTRODUCTION

Mechanical load is a key factor in the control of cardiomyocyte structure and subsequently controls cellular physiology (Ibrahim et al., 2013b). The cardiomyocyte is invaginated at regular intervals by transverse (t)-tubules which allow the formation of dyadic couplings between LTCC and the ryanodine receptors of the intracellular sarcoplasmic reticulum. These structures are integrally important to the control of intracellular calcium (Sanchez-Alonso et al., 2016) and secondary messengers such as cAMP (Nikolaev et al., 2010). They contribute to the faithful control of cardiomyocyte excitation contraction-coupling via the careful compartmentation of intracellular signaling processes. The PMU of healthy hearts disrupts some aspects of TT function (Ibrahim et al., 2012a). It is proposed that the transverse-axial tubules system (TATS) exists in dynamic equilibrium whereby both under and overloading scenarios can distort the system (Terracciano et al., 2009; Ibrahim et al., 2010, 2012a). The unloading of previously overloaded failing hearts can normalize cellular structure and subsequently cellular function (Ibrahim et al., 2012b). The potentially pathological effects of PMU are clinically important due to the common deployment of LVADs as therapy for heart failure (Holmberg et al., 2017). Although, LVADs are of crucial importance as a 'bridge to transplant,' the explant rate remains low (Drakos et al., 2012). It would therefore be useful to explore the subtleties of 'ineffective' unloading of cardiomyocytes with a view to better understanding how to tune therapies to provide the correct regenerative environment.

Previously, Ibrahim et al. (2012a) studied PMU of healthy hearts with a HTHAL model using an 8-week period of unloading. They compared this against control hearts and those of animals which had received trans-aortic constriction (hypertrophy). Isolated cardiomyocytes from healthy hearts which had received PMU were atrophied, had aberrant cytoarchitecture and calcium handling. The morphology of the calcium transient was altered (lower amplitude and longer times to peak and relaxation) in comparison to control. Importantly, like the model of overload, the cells had an increased frequency of calcium sparks and altered spark morphology. These changes were attributed to the loss of normal TATS organization. However, the localized signaling functions of molecules such as the LTCCs and β-adrenergic receptors (βARs) which are fundamental to excitation-contraction processes within the cells, were not investigated in detail in these studies.

We sought to examine the role of unloading in organizing molecular activity at the level of the cell membrane. We employed an animal model of partial myocardial mechanical unloading by performing HTHALs (Ibrahim et al., 2013a). We enzymatically isolated cells from healthy hearts and hearts after 8 weeks of unloading. The cells' structural parameters were studied with confocal and SICM. The localized signaling of LTCCs was studied with a modified SICM technique which allows the selective patching of specific membrane sub-domains such as TT openings or sarcolemmal crests (Bhargava et al., 2013). βAR function was assessed by monitoring sub-cellular cAMP responses using FRET-based biosensors (Nikolaev et al., 2004; Di Benedetto et al., 2008; Wright et al., 2018). These biosensors were delivered to either the cell cytosol or membrane regions using specific molecular tags. This allowed us to monitor the function of β_1AR and β_2AR sub-types within different sub-cellular microdomains. The localization of β_2AR-cAMP activity was studied using a further modification of SICM, which combines SICM and FRET techniques (Nikolaev et al., 2010). This allows the study of cAMP activity in specific regions of the cell by permitting the acquisition of cellular membrane topography and localized application of agonist via the SICM probe. Any cAMP responses evoked by the local treatment can be measured concurrently using FRET biosensors. Using this technique, we discovered a suppression of β_2AR-cAMP but not of β_1AR-cAMP signaling. LTCCs signaling was suppressed by unloading, but this was dynamic and occurred without the removal of specific 'activatable' LTCC capacity from the cell.

MATERIALS AND METHODS

Animals and Ethics Statement

Approval for this work was obtained from the Animal Welfare and Ethics Review Board (AWERB) of Imperial College London. This study was carried out in accordance with United Kingdom Home Office guidelines (ASPA 1986 and EU directive 2010/83) and conformed to all protocols of Imperial College London. All procedures were carried out on male, syngeneic, Lewis rats (150–250 g) obtained from Charles River Laboratories (Margate,

Abbreviations: $\beta_{(1,2)}$AR, beta-adrenergic receptor subtype 1 or 2; BAYK, BAYK8644; cAMP, cyclic adenosine monophosphate; CaMKII, calcium-calmodulin kinase 2; Cav1.2, sub-unit of L-type calcium channel; Cav-3, caveolin-3; cEPAC2, cytosolic epac2 localized cAMP sensor; CGP, CGP20712A; Epac, exchange protein activated by cAMP; FRET, Förster resonance energy transfer; HTHAL, heterotopic heart and lung transplant; ISO, isoprenaline; ICI, ICI118, 551; JPH-2, junctophilin-2; LTCC, L-type calcium channel; LVAD, left ventricular assist device; NKH, NKH477; PKA, protein kinase A; PMU, partial mechanical unloading; P_o, open probability of LTCC; RII_epac, PKA RII based cAMP sensor; SICM, scanning ion conductance microscopy; TATS, transverse axial tubule system; TT, t-tubule.

United Kingdom). Animals were kept at 25°C in ventilated cages and fed standard chow. Animals were randomly assigned to be either donors or recipients. Recipient animals received 'healthy' heart and lung grafts from the first group. Following 8 weeks of maintenance, and upon sacrifice, cells isolated from implanted (heterotopic) hearts are defined as **Unloaded** and cells from the animal's thoracic (orthotopic) heart are defined as age-matched **Loaded** control.

Heterotopic Heart and Lung Transplant

A more detailed description of this surgery has been published previously (Ibrahim et al., 2013a). Briefly, the recipient animal was prepared (hair removed and skin sterilized) and an incision was made in the abdomen. The mesentery and bowel were carefully removed and wrapped in damp, sterile swabbing material. The IVC and aorta were revealed and undermined. They were manipulated with 2-0 suture and clamped. A 2–3 mm incision was made in the aorta. The heart and lung block was removed from storage solution and carefully wrapped in swab, soaked in cold cardioplegia, which was refreshed periodically throughout the operation. The tissue block was maneuvered toward the abdominal cavity, an 8-0 prolene suture was passed through the aorta at the 5 o'clock position outside-in. The suture was then passed through the aortic incision at the 7 o'clock position – the anastomosis then continued clockwise–counter-clockwise, respectively, until it was sealed at the 8 o'clock position on the aorta with three surgeons' knots. Following careful removal of the swabbing protecting the heart and orientation of the tissue, the clamps were removed to allow the perfusion of the heart, as well as the restoration of circulation to the limbs distal to the anastomosis. Hemostasis was provided around the anastomosis site until bleeding ceased. The beating rate and strength of contraction of the implanted heart was assessed. Once the graft activity was deemed optimal the gut was returned and carefully orientated within the abdominal cavity. The abdominal musculature was closed with 5-0 vicryl suture in a continuous pattern. The animal's skin was closed with 4-0 vicryl sutures using a continuous sub-cuticular suture pattern. Carprofen was provided (1.25 mg, s.c.) for analgesia and enrofloxacin (2.5 mg, s.c.) as an antibiotic. Fluid was also given (2 ml saline s.c.). Animals were allowed to recover for about 45 min in a heated chamber, before being transferred individually to standard cages. Operated animals received carprofen and enrofloxacin s.c at 24 and 48 h post-operation and soft food. They were returned to normal chow after ∼72 h.

Unloaded Heart Harvest

After 8 weeks the recipient animals were anesthetized with isoflurane. The abdomen was incised and bowel manipulated to reveal the implanted heart. The aorta and IVC were manipulated and clamped. The heart and lung block were extracted and placed in ice cold Krebs solution. The diaphragm and thorax were incised and opened to allow the removal of the loaded heart. The heart and lung block were excised and placed in ice-cold Krebs.

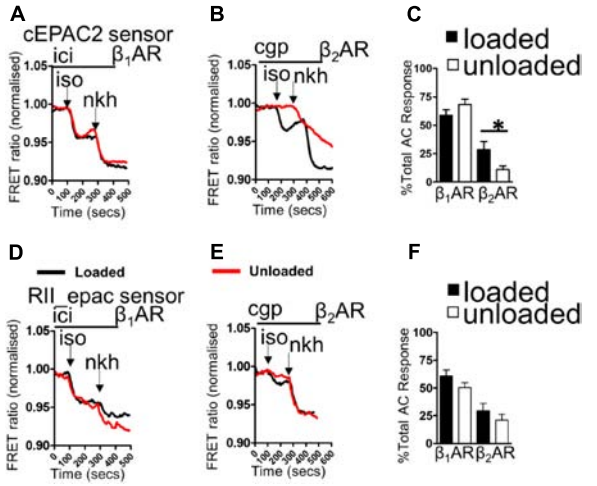

FIGURE 1 | (A) Illustrative traces showing β_1AR-cAMP (ICI+ISO) and full AC-cAMP (NKH) responses measured by FRET microscopy using the cEPAC2 sensor in loaded and unloaded cells. **(B)** Illustrative traces showing β_2AR-cAMP (CGP+ISO) and full AC-cAMP (NKH) responses measured by FRET microscopy using the cEPAC2 sensor in loaded and unloaded cells. **(C)** Graph presenting mean β_1AR-cAMP and β_2AR-cAMP responses as a function of total AC responses for loaded and unloaded cells. cEPAC2 sensor, β_1AR-cAMP (loaded 58.78 ± 4.82% vs. unloaded 68.12 ± 4.85% N,n 5/10-13 mean ± SEM, NS). cEPAC2, β_2AR-cAMP (loaded 28.51 ± 7.18% vs. unloaded 10.84 ± 3.27% N,n 4/10-13 mean ± SEM $^*p < 0.05$). **(D)** Illustrative traces showing β_1AR-cAMP (ICI+ISO) and full AC-cAMP (NKH) responses measured by FRET microscopy using the RII_epac sensor in loaded and unloaded cells. **(E)** Illustrative traces showing β_2AR-cAMP (CGP+ISO) and full AC-cAMP (NKH) responses measured by FRET microscopy using the RII_epac sensor in loaded and unloaded cells. **(F)** Graph presenting mean β_1AR-cAMP and β_2AR-cAMP responses as a function of total AC responses for loaded and unloaded cells. RII_epac sensor, β_1AR-cAMP (loaded 60.64 ± 5.45 vs. unloaded 50.21 ± 4.44 N,n 4/5-6 mean ± SEM, NS). RII_epac, β_2AR-cAMP (loaded 29.47 ± 6.55% vs. unloaded 21.02 ± 5.14% N,n 4/6-8 mean ± SEM NS).

Cell Isolation

Both loaded and unloaded hearts were retrogradely perfused with Krebs-Henseleit solution (37°C, 95% O_2, 5% CO_2 1 mM Ca^{2+}) using a Langendorff perfusion apparatus. After beating was properly established the heart was arrested by perfusion with a low calcium buffer for 5 min. The heart was then perfused with a mixture of collagenase:hyaluronidase (1 mg/ml:0.6 mg/ml) for 10 min. After this period, the heart was cut down, the atria and right ventricle were removed. The ventricle was then disrupted and the mixture shaken mechanically in collagenase/hyaluronidase solution (35°C). After 30 min this yielded single isolated cardiomyocytes. These mixtures were centrifuged 1,000 rpm 2 min. Cell pellets were re-suspended in buffer not containing enzymes.

Förster Resonance Energy Transfer (FRET) Microscopy

Isolated cardiomyocytes were centrifuged, re-suspended in M199 and around 5,000 plated on individual laminin coated 25 mm coverslips. After attachment they were washed with new M199

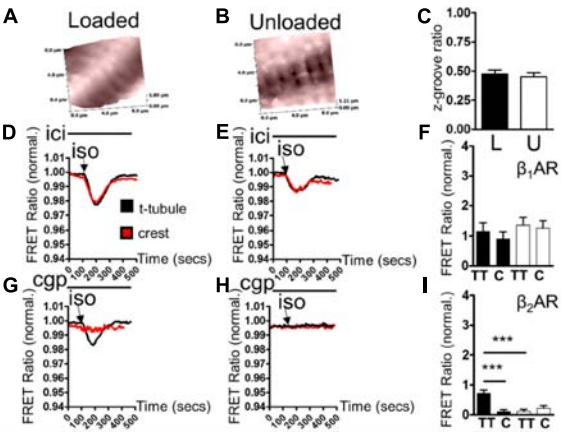

FIGURE 2 | (A) Illustrative topographical image of a loaded control cardiomyocyte membrane acquired with SICM. **(B)** Illustrative topographical image of an unloaded control cardiomyocyte membrane acquired with SICM. **(C)** Graph comparing the z-groove ratios of loaded and unloaded cells (loaded 0.473 ± 0.035 vs. unloaded 0.451 ± 0.035 N,n 5/(36-40) mean ± SEM NS). **(D)** Illustrative traces showing β_1AR-cAMP (ICI+ISO) responses elicited in t-tubule or crest regions by combination SICM/FRET microscopy using the cEPAC2 sensor in a loaded cell. **(E)** Illustrative traces showing β_1AR-cAMP (ICI+ISO) responses elicited in t-tubule or crest regions by combination SICM/FRET microscopy using the cEPAC2 sensor in an unloaded cell. **(F)** Graph comparing β_1AR-cAMP responses evoked in t-tubule (TT) or crest (C) regions by SICM/FRET in loaded and unloaded cells (loaded t-tubule 1.155 ± 0.27% vs. loaded crest 0.903 ± 0.24%, unloaded t-tubule 1.356 ± 0.25% vs. unloaded crest 1.259 ± 0.232% N,n 5/6-9 mean ± SEM NS). **(G)** Illustrative traces showing β_2AR-cAMP (CGP+ISO) responses elicited in t-tubule or crest regions by combination SICM/FRET microscopy using the cEPAC2 sensor in a loaded cell. **(H)** Illustrative traces showing β_2AR-cAMP (CGP+ISO) responses elicited in t-tubule or crest regions by combination SICM/FRET microscopy using the cEPAC2 sensor in an unloaded cell. **(I)** Graph comparing β_2AR-cAMP responses evoked in t-tubule (TT) or crest (C) regions by SICM/FRET in loaded and unloaded cells (loaded t-tubule 0.721 ± 0.106% vs. loaded crest 0.104 ± 0.062%, unloaded t-tubule 0.112 ± 0.072% vs. unloaded crest 0.219 ± 0.084% N,n 5/6-9 mean ± SEM $^{**}p < 0.01$, $^{***}p < 0.001$ vs. loaded t-tubule).

and cultured for 48 h in M199 in the presence of adenovirus encoding the RII_Epac or cEPAC2 cAMP sensors (Di Benedetto et al., 2008; Nikolaev et al., 2010; MacDougall et al., 2012). FRET experiments were conducted with ORCA-4.0 CCD camera's using DualView or QuadView beamsplitters. Both FRET construct consist of CFP and YFP complexed with an exchange protein activated by cAMP (epac)-derived cAMP binding domain. In the case of the RII_Epac sensor the construct also contains the regulatory II subunit of PKA, as a result this sensor aligns to the cardiomyocyte sarcomere in conjunction with A-kinase anchoring proteins. Binding of cAMP to this sensor indicates the penetration of cAMP into PKA domains, whereas cEPAC2 indicates cytosolic responses. After baseline FRET measurements in the presence of 100 nM CGP20712A (to block β_1AR) or 50 nM ICI118, 551 (to block β_2AR) cells were perfused with 100 nM isoprenaline to stimulate β_1AR or β_2AR. Following this phase NKH477 (5 μM) was perfused onto the cells to fully stimulate adenylate cyclase and allow the correction of β_2AR-cAMP responses to maximal cAMP responses.

Scanning Ion Conductance Microscopy

Scanning ion conductance microscopy is a scanning probe microscopy technique based upon the ability to reconstruct topographical images of surfaces on the basis of changes in conductance at the tip of a nanopipette. The physical basis of this technique has been explained in exhaustive detail previously (Novak et al., 2009). Briefly, the sample in this case the cell, is rastered underneath a scanning pipette and a high-resolution image of the cell is constructed. Once this image has been acquired the tip of the pipette can be localized to very specific positions on the cell surface.

Super Resolution (Smart) Patch Clamp

This technique has been explained in detail elsewhere. Following the acquisition of a topographical image of the cell with SICM an area of interest is selected. The pipette is moved to a neutral area of the dish and clipped to give the patch-clamp resistance. It is then moved back to the original area of interest and the pipette is fused with the membrane patch and calcium channel recordings made as described in the references above. A sub-population of cells were treated with the non-specific calcium channel activator BAYK8644 (Tocris Biosciences, United States).

SICM/FRET

This technique has also been employed and described in more detail elsewhere. Following the acquisition of cell topography, as TT or sarcolemmal crest region was targeted and ISO was applied via electrophoresis. FRET response is measured as described above (Nikolaev et al., 2010; Wright et al., 2014).

Whole-Cell Patch Clamp Recordings

L-type calcium currents (ICa, L) were recorded using the whole-cell patch-clamp configuration with the external recording solution of the following composition (in mmol/L): 140 NaCl, 6 KCl, 10 glucose, 10 HEPES, 1.5 $MgCl_2$, 1 $CaCl_2$, pH 7.4 with 1M NaOH. An internal pipette solution contained (in mmol/L): 100 Cs-methanesulfonate, 40 CsCl, 10 HEPES, 5 EGTA, 5 Mg-ATP free acid, 0.75 $MgCl_2$, pH 7.2 with CsOH. Patch pipettes had mean resistances of 3.5–5 MΩ. Currents were recorded using an Axopatch-1D amplifier connected to a Digidata 1322A acquisition system (Axon Instruments, Foster City, CA, USA). The bath was connected to the ground via a reference electrode containing Ag–AgCl pellet. Data were low-pass filtered at 2 kHz using the Bessel filter of the amplifier and sampled at 2 kHz. All recordings were performed at room temperature (22–24°C). ICa, L channel activity was recorded during 200 ms from a holding potential of −40 mV to test potentials ranging from −40 to +60 mV, with pulses applied every 2 s in 5 mV increments. Current amplitude at 0 mV was taken as a peak current and divided by a capacitance value for each cell (current density, pA/pF).

Measurement of Cav3, T-Cap and Junctophilin-2 Density and Regularity and Proximity Ligation Assay

Isolated cells were plated on 13 mm coverslips, fixed with methanol (−20°C) and kept in PBS at 4°C. Proximity

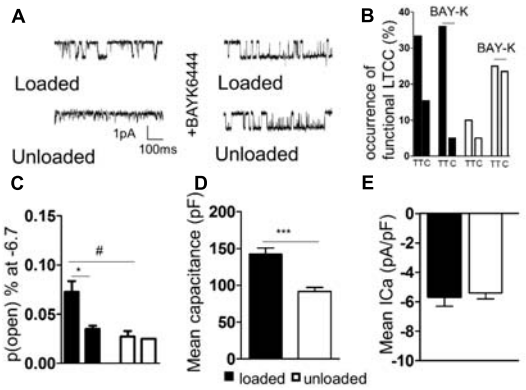

FIGURE 3 | (A) Illustrative traces of LTCC activity recorded in 'cell-attached' mode from loaded and unloaded cells. **(B)** Graph comparing the occurrence functional LTCC's within different cellular microdomains of loaded or unloaded cells. A sub-population of loaded and unloaded cells were treated with the non-specific LTCC agonist BAYK8644. **(C)** Graph comparing the open probability of LTCC's within different cellular microdomains of loaded or unloaded cells (loaded t-tubule 0.073 ± 0.011% vs. loaded crest 0.027 ± 0.006% N,n 5/18-26 mean ± SEM $^{*}p < 0.05$) (unloaded t-tubule 0.0350 ± 0.003% vs. unloaded crest 0.025 N,n 5/20-30 mean ± SEM NS). $^{\#}p < 0.05$ vs. loaded t-tubule. **(D)** Graph comparing the mean capacitance of loaded and unloaded cardiomyocytes (loaded 142.1 ± 8.65 pF vs. unloaded 91.67 ± 5.40 pF N,n 5/11-15 mean ± SEM $^{***}p < 0.001$). **(E)** Graph comparing the mean I_{Ca} of loaded and unloaded cardiomyocytes (loaded -5.67 ± 0.64 pA/pF vs. unloaded –4.62 ± 0.46 pA/pF N,n 5/11-14 mean ± SEM NS).

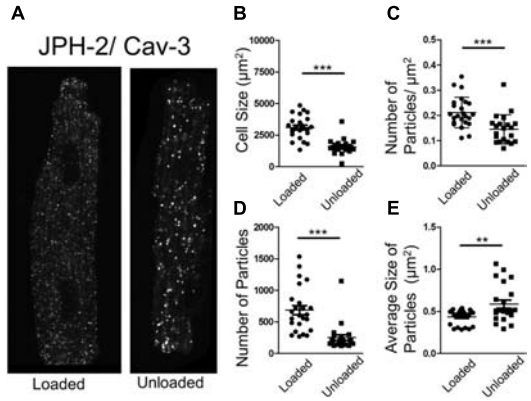

FIGURE 4 | (A) PLA image demonstrating the association of JPH-2 and Cav-3 in loaded and unloaded cells. **(B)** Graph comparing the size of loaded and unloaded cells (loaded 3104 ± 186.1 μm^2 vs. unloaded 1561 ± 128.9 μm^2 N,n 3/22-24 mean ± SEM $^{***}p < 0.001$). **(C)** Graph comparing the number of particles/μm^2 in loaded and unloaded cells (loaded 0.212 ± 0.012 particles/μm^2 vs. 0.145 ± 0.013 particles/μm^2 N,n 3/21-24 mean ± SEM $^{***}p < 0.001$). **(D)** Graph comparing the number of particles in loaded and unloaded cells (loaded 685.9 ± 73.33 vs. unloaded 250.3 ± 46.01 N,n 3/21-24 mean ± SEM $^{***}p < 0.001$). **(E)** Graph comparing the average size of particles in loaded and unloaded cells (loaded 0.435 ± 0.019 μm^2 vs. unloaded 0.587 ± 0.048 μm^2 N,n 3/21-24 mean ± SEM $^{**}p < 0.01$).

ligation assay was performed with the Duolink (inSitu) kit (Sigma-Aldrich, United Kingdom) using anti-Goat, anti-Rabbit or anti-Mouse reagents as required with Duolink 'green' detection reagents (Sigma-Aldrich, United Kingdom), as per the manufacturers instructions. Primary antibodies for JPH-2 (Goat polyclonal, Santa Cruz, sc - 51313), caveolin-3 (Cav3, mouse monoclonal 610421) and Cav1.2 (Alomone, Rabbit polyclonal). Cell imaging was performed with 60x oil immersion Zeiss lens, using inverted confocal laser scanning microscope (A Zeiss LSM-780), with argon laser beam at specific wavelengths for the secondary antibodies (Alexa Fluor Cav3 546 nm). Protein density and respective regularity of distribution were obtained with the same method used for TTs analysis described in more detail elsewhere (Wright et al., 2018). PLA analysis was performed by automatically thresholding cell images in ImageJ (Image J Corp, United States) and utilizing default plugins to measure area covered by particles, size of particles, number of particles and number of particles per μm.

di-8ANNEPPS Staining of Freshly Isolated Cardiomyocytes

After staining freshly isolated cells with di-8ANNEPPS image stacks were obtained with a Zeiss LSM710 confocal microscope as previously described (Schobesberger et al., 2017). A 40 × 5 μm area was selected and binarized. Density and power of regularity were analyzed as per our laboratories protocols. Density was defined as the percentage of black pixels. Power of regularity was calculated using a bespoke MATLAB code by plotting a waveform of the binarized image of the cell and the Fast-Fourier transform was used to plot a representative curve of the frequency of di8ANNEPPS stained ultrastructure. The strength of the peak at ∼0.5 micron indicated the regularity of di8ANEPPS staining and therefore TT structure.

Statistical Analysis

Where unrelated two populations were analyzed statistical difference was determined using an unpaired (two-tailed) Students' *T*-test. Where more than two unrelated populations were analyzed, a one-way ANOVA with a Bonferroni post-test (*post hoc*) was used. This was performed by using Graph-Pad 4.0 software. In the figure legends, N refers to the number of preparations, *n* refers to the number of measurements.

RESULTS

Partial Mechanical Unloading Differentially Distorts βAR-cAMP Microdomains

Loaded and unloaded cells were transfected with cEPAC2 or RII_epac sensors and cultured for 48 h. β_1AR-cAMP and β_2AR-cAMP were then assessed as a function of the total cAMP response. Unloading did not affect the β_1AR-cAMP response or the overall cellular cAMP response in the cell cytosol (**Figures 1A,C**). Unloading reduced the β_2AR-cAMP responses within the cell cytosol (**Figures 1B,C**). Withdrawal of mechanical load reduced the amount of cAMP penetrating cellular RII_PKA domains but this difference did not reach statistical significance (**Figures 1D,F**). No difference was observed in total RII domain

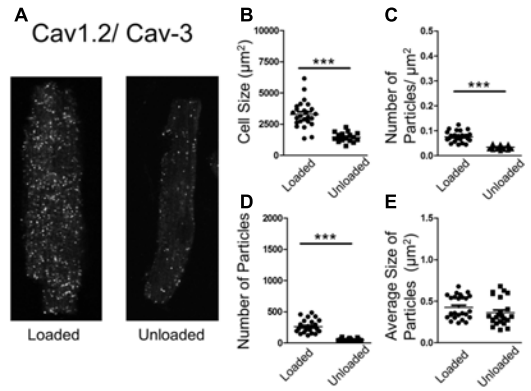

FIGURE 5 | (A) PLA image demonstrating the association of Cav1.2 and Cav-3 in loaded and unloaded cells. **(B)** Graph comparing the size of loaded and unloaded cells (loaded 3271 ± 212.4 μm^2 vs. unloaded 1444 ± 92.03 μm^2 N,n 3/17-25 mean ± SEM ***$p < 0.001$). **(C)** Graph comparing the number of particles/μm^2 in loaded and unloaded cells (loaded 0.076 ± 0.0042 particles/μm^2 vs. unloaded 0.034 ± 0.0016 particles/μm^2 N,n 3/23-25 mean ± SEM ***$p < 0.001$). **(D)** Graph comparing the number of particles in loaded and unloaded cells (loaded 261.9 ± 20.61 vs. unloaded 50.52 ± 3.70 N,n 3/23-25 mean ± SEM ***$p < 0.001$). **(E)** Graph comparing the average size of particles in loaded and unloaded cells (loaded 0.425 ± 0.028 μm^2 vs. unloaded 0.361 ± 0.03 μm^2 3/23-25 N,n mean ± SEM NS).

cAMP responses. Specific stimulation of β_2AR-cAMP elicited a slightly higher response in RII_PKA domains, in control cells. However, similar to experiments studying β_1AR-cAMP this effect was also not statistically significant (**Figures 1E,F**). In summary, unloading only significantly reduced the cytosolic β_2AR-cAMP response.

Partial Mechanical Unloading Selectively Reduces β_2AR-cAMP Microdomain Responses

Scanning ion conductance microscopy scans showed similar degrees of sarcolemmal organization in loaded and unloaded cardiomyocytes (**Figures 2A,B**) (freshly isolated in preparation for LTCC experiments). Z-groove ratios were calculated for multiple scans and the relative degrees of cell membrane organization were analyzed. Mean Z-groove ratios were no different for the loaded and unloaded cell groups (**Figure 2C**). As a result it can be reported that PMU does not produce its effect on cytosolic β_2AR-cAMP responses by reducing the organization of the cellular sarcolemma. In control, loaded cells (cultured for 48 h) β_1AR-cAMP responses were elicited in both tubule and crest domains after application of ISO in the presence of ICI (β_2AR blockade). This is consistent with previous studies of this particular sensor (**Figure 2D**). Unloading did not appear to alter β_1AR-cAMP responses in tubule or crest domains (**Figure 2E**). Analysis revealed no statistical difference between β_1AR-cAMP responses from the TT or crest regions of loaded or unloaded cardiomyocytes (**Figure 2F**). Consistent with previous work, application of ISO in the presence of CGP (β_1AR blockade) only elicited β_2AR-cAMP responses on t-tubular surfaces (**Figure 2G**). Mechanical unloading significantly reduced the β_2AR-cAMP response on cellular t-tubular structures (**Figures 2H,I**), which is consistent with the effect of unloading on the 'whole-cell' stimulation of β_2AR-cAMP responses measured with the cEPAC2 sensor. Cell crests yielded very little β_2AR-cAMP response in the control condition and the unloaded cells were no different (**Figures 2G,I**).

Partial Mechanical Unloading 'Silences' L-Type Calcium Channel (LTCC) Activity

TT LTCC activity was faithfully recorded from freshly isolated loaded cardiomyocytes (**Figure 3A**). In comparison, LTCC activity was suppressed in unloaded cardiomyocytes (**Figure 3A**). The occurrence of LTCC channels, the number of channels recorded vs. successful patches, was higher in TT membranes of loaded cells than cell crests (**Figure 3B** and **Supplementary Figure S1A**). In comparison a far lower occurrence of LTCCs was observed in the TT membrane and cell crests of unloaded cells. The difference between TT and crest domains observed in loaded controls was lost after unloading. The specific LTCC channel activator BAY-K was employed to assess whether the channels had been lost or whether their activity was being suppressed. LTCC activity was recorded in TT domains in both conditions (**Figure 3A**). BAY-K treated loaded cells showed the same occurrence of LTCCs as observed in untreated cells. In comparison BAY-K treatment revealed a large amount of LTCCs in both the TT and crest domains of unloaded cells (**Figure 3B**). The suggestion is that LTCCs are silenced by unloading and that this treatment removes the restriction of the channels to TT domains. The biophysical characteristics of LTCCs are also altered by unloading. In loaded cells the probability of a calcium channel being open is greater in the TT domain than in the crest (**Figure 3C** and **Supplementary Figure S1B**). In unloaded cells the open probability is also decreased, alongside the occurrence. To assess whether these alterations were as a result of gross changes in calcium handling, we assessed 'whole-cell' calcium current. We discovered that unloaded cells had a lower capacitance in comparison to loaded cells, which is due to their smaller size (**Figure 3D**). Whole-cell calcium current was no different between loaded and unloaded cells following correction for capacitance (**Figure 3E**). This suggests that differences in LTCC function are directly attributable to the activity of the channels within the membrane microdomain.

Partial Mechanical Unloading Alters the Association of Structural Proteins Crucial for LTCC Function

In an attempt to understand the suppression of LTCC activity, we performed proximity ligation assays (PLA) on loaded and unloaded cells, which were isolated and fixed. PLA quantifies the association of peptides by measuring fluorescence produced by antibody constructs using confocal microscopy. The size and number of fluorescent particles were assessed. We utilized this method to explore the association of JPH-2 and Cav-3, two proteins crucial for the control of sub-cellular LTCC signaling

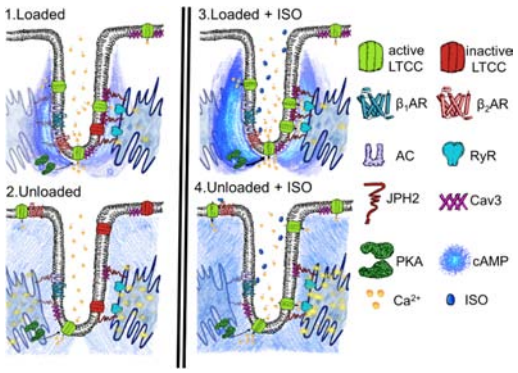

FIGURE 6 | Schematic demonstrating the speculated state of a t-tubular microdomain in loaded or unloaded scenarios with or without isoprenaline stimulation. (1) Loaded cell. LTCC are generally active within the tubule owning to some constitutive cAMP production and consequent PKA activity, scaffolded by Cav-3 and JPH-2. Calcium spark activity at the sarcoplasmic reticulum is nominal. (2) Unloaded cell. LTCC are generally inactive as there is a loss of coherent confinement of cAMP and PKA activity to the t-tubular microdomain. This is due to the mechanosensitivity of the association between Cav1.2, Cav-3, and JPH-2 and the loss of t-tubules. Even though there is a smaller amount of LTCC activity spark activity increases as orphaned RyR no longer receive effective control and thus experience a gain of function. (3) Loaded cell stimulated with ISO. After stimulation β2AR increase cAMP levels in the cytoplasm of the sarcomeric dyad and this activates a sub-population of PKA which activates almost all LTCC. Spark activity remains nominal as effective measures to control LTCC and RYR phosphorylation and the degradation of cAMP remain effective due to scaffolding by the cellular microdomain. (4) Unloaded cell stimulated with ISO. Despite a reduction in the amount of cAMP response initiated by β_2AR in the cytosol, signals still reach RII_PKA domains, due to the loss of efficient cAMP compartmentation. This stimulates further aberrant spark activity due to the relatively uncontrolled calcium influx in the cell and EC mediator hyperphosphorylation following the loss of normal structure within the sarcomeric dyad following unloading.

microdomains. We also assessed the association between Cav-3 and the $Ca_v1.2$ sub-unit of the LTCC itself. Unloading reduced the size of cardiomyocytes and reduced the density and regularity of Cav-3 staining (**Supplementary Figures S2A–D**). The staining of cells with di-8-ANNEPPS also reveals the effect of PMU on cell area and aspect ratio, as well as cellular ultrastructure. PMU causes the loss of TT regularity but not TT density (**Supplementary Figures S3A–F**). The JPH-2/Cav-3 PLA demonstrated that the cell size was reduced by unloading (**Figures 4A,B**). The number of particles per micron and total number of particles were decreased by the partial withdrawal of mechanical load (**Figures 4C,D**). This suggested that after unloading the degree of association between these two structural proteins was lower and less organized. Interestingly, the size of particles increased suggesting that where these associations occur there is an agglomeration of the peptides (**Figure 4E**). The $Ca_v1.2$/Cav-3 PLA demonstrated once again that cell size was reduced by unloading (**Figures 5A,B**). The number of particles by area and total number was also decreased following unloading (**Figures 5C,D**). Unlike the JPH-2/Cav-3 PLA there was no increase in particle size (**Figure 5E**). This suggested that the association between $Ca_v1.2$/Cav-3 was simply reduced following unloading.

DISCUSSION

Partial mechanical unloading profoundly reduces cardiomyocyte size and modulates the structure and organization of TATS (Ibrahim et al., 2010, 2012a). It has been demonstrated to increase the frequency and persistence of calcium 'sparks.' Spark activity is speculated to be elicited by ryanodine receptors and the loss of organization of the sarcomeric dyad following the withdrawal of load. We sought to assess the effect of PMU on the physiology of LTCC's and βARs. The physiology of βAR-cAMP was altered in a sub-type and microdomain specific way. PMU did not reduce the amplitude of β_1AR-cAMP responses elicited by whole-cell perfusion and measured in the cell cytosol or RII-PKA domains. PMU reduced the amplitude of β_2AR-cAMP responses in the cytosol but not in the RII-PKA domains. This is an intriguing finding, as previous papers (MacDougall et al., 2012; Wright et al., 2018) which have employed these two sensors have demonstrated that β_2AR is a compartmentalized receptor in healthy cardiomyocytes, which will produce cAMP responses in the cell cytosol but not in the RII_PKA domains. The data we present suggest that the production of β_2AR-cAMP is load-sensitive and may involve the loss of receptor subunits. In the situation of PMU-induced atrophy this is potentially superimposed on a cell which has lost structural integrity via the loss of important components of the cAMP compartmentation machinery such as TTs. As a result we are not observing the increase of absolute β_2AR-cAMP capacity, in fact we witness its reduction, and this is concomitant with increased persistence and subsequent enhancement of its efficacy due to the PMU-induced loss of cAMP compartmentation. We only employed a saturating level of stimulation for β_1AR but prior reports (Agarwal et al., 2011) have demonstrated that at sub-maximal levels β_1AR may act in a compartmentalized fashion. As a result, the effects of PMU may also affect β_1AR-cAMP in different scenarios. We posit that the primary factor in the lack of an effect of PMU on β_1AR activity may be a combination of its relative lack of 'compartmentation' by important subcellular structures such as TTs. Therefore their loss after PMU has less of an effect on this receptor. Equally, the supra-maximal stimulation afforded by our selected dose of isoprenaline may mean the effects of PMU on β_1AR-cAMP have eluded us in this case.

The effects of PMU on membrane microdomains were investigated by stimulating β_1AR or β_2AR-cAMP responses via local application of agonist and measuring responses evoked in the cardiomyocyte cytosol. β_1AR-cAMP responses in t-tubular or sarcolemmal crest regions were unaffected by PMU. This is concordant with our findings using whole-cell perfusion of agonist. β_2AR-cAMP responses were of greater amplitude in t-tubular regions than on cardiomyocyte crests. This is comparable with previous reports (Nikolaev et al., 2010; Wright et al., 2014). PMU appeared to suppress the β_2AR-cAMP responses in t-tubular domains. β_2AR-cAMP responses in crest regions were unaltered, but were of such a low amplitude in control cells that an effect could not be seen. This is consistent with our measurements made after perfusing the whole cell with agonist. This may suggest that the effect in whole-cell measurements is purely due to the loss of t-tubular

β_2AR-cAMP responses. The effects of PMU on β_2AR-cAMP responses occurred without an obvious loss of total cAMP production capacity within the cells. Mechanical load could therefore be an essential stimulus for the production of organized t-tubular networks which are capable of conducting normal compartmentalized β_2AR-cAMP responses. Mechanical load may be a prerequisite to allow the cells to produce β_2AR-cAMP responses which are faithfully produced in the TT and restricted from the RII_PKA domains. This phenomena would appear to be less significant for β_1AR-cAMP responses. However, as suggested the relatively liberal control of this receptor may belie more significant effects at sub-maximal levels. The effects of the singular load-dependent 'suppression/decompartmentation' behavior observed for β_2AR-cAMP responses are unclear for the β_1AR.

Like β_2AR-cAMP activity, LTCC seem to be confined to t-tubular microdomains. Greater numbers of LTCC were observed in TTs in normally loaded cardiomyocytes. These channels had a higher open probability, suggesting a larger more active population of LTCC in the loaded cardiomyocyte tubule in comparison to crest domains. This is consistent with our previous work (Sanchez-Alonso et al., 2016). Interestingly, following PMU, LTCC seemed to almost disappear from the TTs of cardiomyocytes. LTCC activity was also significantly reduced. This was demonstrated to be due to a 'silencing' of LTCC following PMU, as well as the loss of confinement of LTCC to the TT domains. Experiments performed in the presence of BAYK show the silencing effect of PMU. Simply adding this agent activated LTCCs in both TTs and crest domains. This once again raises the suggestion that the activation and maintenance of compartmentation pathways of molecular signaling processes within cardiomyocyte microdomains are load-dependent.

We observed that the organization and association of proteins which are usually involved in the compartmentation of calcium and cAMP in cardiomyocytes was lost following PMU (Chen et al., 2013; Wong et al., 2013). We also specifically observed the agglomeration of JPH-2 and Cav-3 following PMU, alongside the loss of normal association of $Ca_v1.2$ subunit of LTCC with Cav-3. JPH-2 has been reported to be essential for the normal formation of TTs (Chen et al., 2013), which in turn control both calcium handling and cAMP. Caveolae are the site of a sub-population of LTCC (Chen et al., 2013). LTCC activation is achieved by the selective phosphorylation of the channel by PKA or CaMKII, depending on the specific compartment involved (Sanchez-Alonso et al., 2016). We also observe the loss of regularity within the TAT network following PMU which is concordant with previous work in our laboratory (Ibrahim et al., 2012a). These findings suggest that mechanical load is responsible for the collection, distribution and organization of the cell membrane and structural proteins which are then able to form and arrange sub-cellular signaling microdomains. This is apparently achieved by the association and sequestration of receptors, channels and other signaling molecules. Loss of this stimulus as well as causing the atrophy of the cell, causes the loss of faithful signaling organization. This could potentially be a passive process.

Hypertrophy is stimulated by the increased demands placed upon the myocardial tissue, so-called overload, which causes two separate phases of cell behavior. The myocardium exhibits marked structural and functional plasticity, this property is largely due to the modulation of individual cardiomyocytes (Frisk et al., 2016; Watson et al., 2016). Initially, the cell grows and copes with the increased demand and 'compensates.' This is followed by an energetic crisis where the biomechanical properties of the cardiomyocytes are stretched to a point beyond which neither adequate functional capacity or maintenance can be sustained. This is referred to as decompensation and leads to myocardial failure. During these phases, the TATS is progressively altered. Atrophy most likely represents the converse of hypertrophy. It has been reported that the integrity of the TAT network is disrupted by the degree and timescales of mechanical unloading (Ibrahim et al., 2012a). As a result it can be posited that as the demand for myocardial function is withdrawn by unloading, the cardiomyocytes adapt by reducing their structural and organizational complexity, which are energetically expensive to sustain. The result is a passive rather than active loss of cardiac structure. This nonetheless results in a pathological loss of cardiac fitness and capacity. We suggest that unloading causes a situation like the one presented in our schematic in **Figure 6**. We suggest that the loss of TT organization removes the innate activity of molecules such as LTCC. The disorganization of TTs and structural proteins seems to result in the increased malignancy of calcium spark activity, as previously reported, (Ibrahim et al., 2012a) despite this loss of LTCC activity. We suggest this may be the effect of the loss of coherent molecular organization. It also reduces the capacity of β_2AR to signal once stimulated with isoprenaline, the necessity of effective localization of the molecules to produce normative function suggests this effect is in someways similar to the effect on LTCC. Finally, the loss of normal activity in the cytosol but continuing stimulation of RII_PKA domains by β_2AR after activation is further indicative of a loss of molecular control leading to a scenario in which one receives 'more bang for the buck' after excitation due to mechanosensitive decompartmentation.

The role of βAR in the pathophysiology is well characterized but somewhat poorly understood. It is known that chronic βAR stimulation is cardiotoxic and pro-arrhythmic (Engelhardt et al., 1999; Nguyen et al., 2015; Lucia et al., 2018). In settings of heart failure the sympathetic nervous system is upregulated in an effort to produce greater cardiac inotropy, the long term effects of this as described above are deleterious and this gives rise the paradoxical efficacy of 'beta-blockers' in maintaining patients with cardiac pathology (Baker et al., 2011). This aspect presents an equally complex picture as β_1AR is desensitized and β_2AR is uncoupled from inotropic Gs/cAMP pathways in failing hearts (Paur et al., 2012). Some beta-blockers are suggested to be effective via the Gi-coupled β_2AR, once again paradoxically rescuing the heart by making it perform less well (Wisler et al., 2007). In our atrophic model, we see a loss of action/gain of function phenotype which is qualitatively different to hypertrophic or failing hearts. However, we also posit deleterious effects of this pathology on βAR function and a reduction of cardiac functional capacity in atrophic situations

as a result of the effects of PMU on membrane structure and organization.

In this study, we employed unloaded cardiomyocytes. Unfortunately, this model system has some limitations. The removal of the cells from their normal configuration in integrated myofibers is somewhat unnatural. It removes them from the normal neurohormonal milieu which they generally experience. Perhaps, more importantly for this study it also removes them from the 'force' environment they usually experience. The cells are under cyclic stress and strain throughout the entire life-cycle of the animal and we then study them in a very quiescent state. In some experiments we also employ culture methodology to allow the transduction of FRET reporters it is well known that culture disrupts cellular homeostasis and the TT environment in particular (Pavlović et al., 2010). However, the justification for using isolated cardiomyocytes is that many of the techniques employed within this study are not possible in isolated tissue slices or integrated *ex vivo* preparations. Imaging studies are made complicated by non-specific binding in integrated tissues. Equally, the measurement of cAMP and LTCC activity within cellular microdomains is also currently prohibited in tissue due to the difficulties presented by factors such as the thickness of integrated tissue. Finally, transduction of FRET reporters into isolated cells is also currently a necessity due to practicalities of infecting tissue in, for example, a slice based modality. We also lack transgenic rats expressing FRET sensors, which would be appropriate for this study. A study could be attempted in which the animals could be infected with AAV-9 vectors expressing FRET constructs of interest. This would allow FRET studies to be completed on the day of sacrifice, avoiding cells culture but the necessity for cell isolation would remain.

Mechanical support via ventricular assist devices represents an increasingly common therapy for heart failure. It has functioned as a 'bridge to transplant' for many years. Current research is geared toward repurposing mechanical support as a 'bridge to recovery.' The latter project requires mechanical unloading to provide curative relief to a heart which is theoretically capable of regenerating its normal function. Bridge to recovery is defined by the number of successful explants of LVADs following the recovery of cardiac function. The rate of explant is around 6% and is usually reliant on heart failure to be in its earliest stages, where minimal cytoarchitectural changes have occurred within the myocytes (Seidel et al., 2017). The exact interplay of the adult hearts lack of intrinsic regenerative capacity and the pathological effects of atrophy is unclear here but must be considered. Indeed, some clinicians are actively pursuing removal of LVADs and some groups are investigating 'weaning' protocols (Formica et al., 2010; Selzman et al., 2015). Currently, 'turn-down' protocols are employed to assess the heart's ability to cope on its own with or without adjuvant medical therapy prior to the decision to explant an LVAD. Hemodynamic studies are utilized during 'turn-down' to provide this assurance to physicians. The rationale of 'weaning' as part of therapy would be to allow the heart to receive enough support to provide sufficient cardiac output and adequate support to regenerate. But this 'turn-down' would also appear to offer a training program/stimulus to the damaged myocardium, providing the stimulus to prevent atrophic losses and rebuild essential structures within the cardiomyocytes. In this study, we present data showing the pathological effects of mild withdrawal of load. It would appear that myocardial βAR-cAMP and calcium handling are exquisitely load-sensitive. This should be considered during the provision of mechanical unloading therapy where functional recovery is desired.

DATA AVAILABILITY STATEMENT

The raw data supporting the conclusions of this manuscript will be made available by the authors, without undue reservation, to any qualified researcher.

AUTHOR CONTRIBUTIONS

PW conceived research question, conducted experiments, and authored manuscript. JS-A, CL, CP, and AA-L conducted experiments and performed data analysis. SB conducted experiments. GF, CT, and JG contributed resources and conceived research question.

FUNDING

This study was supported by British Heart Foundation RG/17/13/33173 (JG), PG/14/23/30723 (CT and SB) and Medical Research Council (United Kingdom) MR/L006855/1 (JG and PW).

ACKNOWLEDGMENTS

We would like to thank Prof. Manuela Zaccolo for her gift of the RII_epac FRET construct and Prof. Viacheslav Nikolaev for his gift of the cEPAC2 construct. We also would like to thank Pete O'Gara for his assistance with cell isolation.

SUPPLEMENTARY MATERIAL

The Supplementary Material for this article can be found online at: https://www.frontiersin.org/articles/10.3389/fphys.2018.01302/full#supplementary-material

FIGURE S1 | (A) Table comparing number of LTCC units vs. number of successful patches (those containing LTCCs). These values are used to calculate the relative occurrence of LTCCs in different cellular microdomains (freshly isolated cells). **(B)** Table comparing the number of LTCC units acquired vs. total number of successful patches: units (patches). These data should be assessed alongside data regarding open probability (freshly isolated cells).

FIGURE S2 | (A) Example image showing a loaded cardiomyocyte with Cav3 immunostaining (freshly isolated cells). **(B)** Example image showing an unloaded cardiomyocyte with Cav3 immunostaining (freshly isolated cells). **(C)** Graph comparing the density of Cav-3 immunostaining in loaded and unloaded cells (loaded 36.52 ± 1.02% vs. unloaded 33.54 ± 0.77% N,n 3/22-27 mean ± SEM $*p < 0.05$) (freshly isolated cells). **(D)** Graph comparing the regularity of Cav-3 staining in loaded and unloaded cells (loaded $1.64 \times 10^8 \pm 1.67 \times 10^7$ vs. unloaded $0.85 \times 10^8 \pm 1.04 \times 10^7$ N,n 3/22-27 mean ± SEM $***p < 0.001$) (freshly isolated cells).

FIGURE S3 | (A) Example image showing a loaded cardiomyocyte stained with di8ANNEPPS (freshly isolated cells). **(B)** Example image showing an unloaded cardiomyocyte stained with di8ANNEPPS (freshly isolated cells). **(C)** Graph comparing the density of di8ANNEPPS staining in loaded and unloaded cardiomyocytes (freshly isolated cells). **(D)** Graph comparing the regularity of di8ANNEPPS staining in loaded and unloaded cardiomyocytes (freshly isolated cells). **(E)** Graph comparing the ratio of cell length vs. width in loaded and unloaded cardiomyocytes (freshly isolated cells). **(F)** Graph comparing the cell area of loaded and unloaded cardiomyocytes (freshly isolated cells).

REFERENCES

Agarwal, S. R., MacDougall, D. A., Tyser, R., Pugh, S. D., Calaghan, S. C., and Harvey, R. D. (2011). Effects of cholesterol depletion on compartmentalized cAMP responses in adult cardiac myocytes. *J. Mol. Cell. Cardiol.* 50, 500–509. doi: 10.1016/j.yjmcc.2010.11.015

Baker, J. G., Hill, S. J., and Summers, R. J. (2011). Evolution of β-blockers: from anti-anginal drugs to ligand-directed signalling. *Trends Pharmacol. Sci.* 32, 227–234. doi: 10.1016/j.tips.2011.02.010

Bhargava, A., Lin, X., Novak, P., Mehta, K., Korchev, Y., Delmar, M., et al. (2013). Super-resolution scanning patch clamp reveals clustering of functional ion channels in adult ventricular myocyte. *Circ. Res.* 112, 1112–1120. doi: 10.1161/CIRCRESAHA.111.300445

Chen, B., Guo, A., Zhang, C., Chen, R., Zhu, Y., Hong, J., et al. (2013). Critical roles of junctophilin-2 in T-tubule and excitation–contraction coupling maturation during postnatal development. *Cardiovasc. Res.* 100, 54–62. doi: 10.1093/cvr/cvt180

Di Benedetto, G., Zoccarato, A., Lissandron, V., Terrin, A., Li, X., Houslay, M. D., et al. (2008). Protein kinase A type I and type II define distinct intracellular signaling compartments. *Circ. Res.* 103, 836–844. doi: 10.1161/CIRCRESAHA.108.174813

Drakos, S. G., Kfoury, A. G., Stehlik, J., Selzman, C. H., Reid, B. B., Terrovitis, J. V., et al. (2012). Bridge to recovery: understanding the disconnect between clinical and biological outcomes. *Circulation* 126, 230–241. doi: 10.1161/CIRCULATIONAHA.111.040261

Engelhardt, S., Hein, L., Wiesmann, F., and Lohse, M. J. (1999). Progressive hypertrophy and heart failure in beta1-adrenergic receptor transgenic mice. *Proc. Natl. Acad. Sci. U.S.A.* 96, 7059–7064. doi: 10.1073/pnas.96.12.7059

Formica, P., Murthy, S., Edwards, P., Goldstein, D., and Maybaum, S. (2010). A structured 3-step approach to evaluate cardiac recovery with continuous flow circulatory support. *J. Hear. Lung Transplant.* 29, 1440–1442. doi: 10.1016/j.healun.2010.07.008

Frisk, M., Ruud, M., Espe, E. K. S., Aronsen, J. M., Røe, ÅT., Zhang, L., et al. (2016). Elevated ventricular wall stress disrupts cardiomyocyte t-tubule structure and calcium homeostasis. *Cardiovasc. Res.* 112, 443–451. doi: 10.1093/cvr/cvw111

Holmberg, E., Ahn, H., and Peterzén, B. (2017). More than 20 years' experience of left ventricular assist device implantation at a non-transplant centre. *Scand. Cardiovasc. J.* 51, 293–298. doi: 10.1080/14017431.2017.1388536

Ibrahim, M., Al, M. A., Navaratnarajah, M., Siedlecka, U., Soppa, G. K., Moshkov, A., et al. (2010). Prolonged mechanical unloading affects cardiomyocyte excitation-contraction coupling, transverse-tubule structure, and the cell surface. *FASEB J.* 24, 3321–3329. doi: 10.1096/fj.10-156638

Ibrahim, M., Kukadia, P., Siedlecka, U., Cartledge, J. E., Navaratnarajah, M., Tokar, S., et al. (2012a). Cardiomyocyte Ca^{2+} handling and structure is regulated by degree and duration of mechanical load variation. *J. Cell. Mol. Med.* 16, 2910–2918. doi: 10.1111/j.1582-4934.2012.01611.x

Ibrahim, M., Navaratnarajah, M., Siedlecka, U., Rao, C., Dias, P., Moshkov, A. V., et al. (2012b). Mechanical unloading reverses transverse tubule remodelling and normalizes local Ca^{2+}-induced Ca^{2+} release in a rodent model of heart failure. *Eur. J. Heart Fail.* 14, 571–580. doi: 10.1093/eurjhf/hfs038

Ibrahim, M., Navaratnarajah, M., Kukadia, P., Rao, C., Siedlecka, U., Cartledge, J. E., et al. (2013a). Heterotopic abdominal heart transplantation in rats for functional studies of ventricular unloading. *J. Surg. Res.* 179, 31–39. doi: 10.1016/j.jss.2012.01.053

Ibrahim, M., Navaratnarajah, M., Siedlecka, U., Rao, C., Dias, P., Moshkov, A., et al. (2013b). Mechanical unloading reverses transverse tubule remodelling and normalises local calcium-induced calcium release in a rodent model of heart failure. *Lancet* 381, S54. doi: 10.1016/S0140-6736(13)60494-8

Lucia, C., de Eguchi, A., and Koch, W. J. (2018). New insights in cardiac β-adrenergic signaling during heart failure and aging. *Front. Pharmacol.* 9:904. doi: 10.3389/fphar.2018.00904

MacDougall, D. A., Agarwal, S. R., Stopford, E. A., Chu, H., Collins, J. A., Longster, A. L., et al. (2012). Caveolae compartmentalise β2-adrenoceptor signals by curtailing cAMP production and maintaining phosphatase activity in the sarcoplasmic reticulum of the adult ventricular myocyte. *J. Mol. Cell. Cardiol.* 52, 388–400. doi: 10.1016/j.yjmcc.2011.06.014

Nguyen, M.-N., Kiriazis, H., Ruggiero, D., Gao, X.-M., Su, Y., Jian, A., et al. (2015). Spontaneous ventricular tachyarrhythmias in β2-adrenoceptor transgenic mice in relation to cardiac interstitial fibrosis. *Am. J. Physiol. Circ. Physiol.* 309, H946–H957. doi: 10.1152/ajpheart.00405.2015

Nikolaev, V. O., Bünemann, M., Hein, L., Hannawacker, A., and Lohse, M. J. (2004). Novel single chain cAMP sensors for receptor-induced signal propagation. *J. Biol. Chem.* 279, 37215–37218. doi: 10.1074/jbc.C400302200

Nikolaev, V. O., Moshkov, A., Lyon, A. R., Miragoli, M., Novak, P., Paur, H., et al. (2010). β2-adrenergic receptor redistribution in heart failure changes cAMP compartmentation. *Science* 327, 1653–1657. doi: 10.1126/science.1185988

Novak, P., Li, C., Shevchuk, A. I., Stepanyan, R., Caldwell, M., Hughes, S., et al. (2009). Nanoscale live-cell imaging using hopping probe ion conductance microscopy. *Nat. Methods* 6, 279–281. doi: 10.1038/nmeth.1306

Paur, H., Wright, P. T., Sikkel, M. B., Tranter, M. H., Mansfield, C., O'Gara, P., et al. (2012). high levels of circulating epinephrine trigger apical cardiodepression in a β(2)-Adrenoceptor/Gi-dependent manner: a new model of takotsubo cardiomyopathy. *Circulation* 126, 697–706. doi: 10.1161/CIRCULATIONAHA.112.111591

Pavlović, D., McLatchie, L. M., and Shattock, M. J. (2010). The rate of loss of T-tubules in cultured adult ventricular myocytes is species dependent. *Exp. Physiol.* 95, 518–527. doi: 10.1113/expphysiol.2009.052126

Sanchez-Alonso, J. L., Bhargava, A., O'Hara, T., Glukhov, A. V., Schobesberger, S., Bhogal, N., et al. (2016). Microdomain-specific modulation of l-type calcium channels leads to triggered ventricular arrhythmia in heart failure. *Circ. Res.* 119, 944–955. doi: 10.1161/CIRCRESAHA.116.308698

Schobesberger, S., Wright, P., Tokar, S., Bhargava, A., Mansfield, C., Glukhov, A. V., et al. (2017). T-tubule remodelling disturbs localized β2-adrenergic signalling in rat ventricular myocytes during the progression of heart failure. *Cardiovasc. Res.* 113, 770–782. doi: 10.1093/cvr/cvx074

Seidel, T., Navankasattusas, S., Ahmad, A., Diakos, N. A., Xu, W. D., Tristani-Firouzi, M., et al. (2017). Sheet-like remodeling of the transverse tubular system in human heart failure impairs excitation-contraction coupling and functional recovery by mechanical unloading. *Circulation* 135, 1632–1645. doi: 10.1161/CIRCULATIONAHA.116.024470

Selzman, C. H., Madden, J. L., Healy, A. H., McKellar, S. H., Koliopoulou, A., Stehlik, J., et al. (2015). Bridge to removal: a paradigm shift for left ventricular assist device therapy. *Ann. Thorac. Surg.* 99, 360–367. doi: 10.1016/j.athoracsur.2014.07.061

Terracciano, C., Al-Masri, A., Siedlecka, U., Soppa, G. K., Navaratnarajah, M., Hadjiphilippou, S., et al. (2009). Chronic mechanical unloading of rat hearts disrupts local calcium-induced calcium release in isolated cardiomyocytes. *Eur. Heart J.* 30:176.

Watson, S. A., Perbellini, F., and Terracciano, C. M. (2016). Cardiac t-tubules: where structural plasticity meets functional adaptation. *Cardiovasc. Res.* 112, 423–425. doi: 10.1093/cvr/cvw198

Wisler, J. W., DeWire, S. M., Whalen, E. J., Violin, J. D., Drake, M. T., Ahn, S., et al. (2007). A unique mechanism of β-blocker action: carvedilol stimulates β-arrestin signaling. *Proc. Natl. Acad. Sci. U.S.A.* 104, 16657–16662. doi: 10.1073/pnas.0707936104

Wong, J., Baddeley, D., Bushong, E. A., Yu, Z., Ellisman, M. H., Hoshijima, M., et al. (2013). Nanoscale distribution of ryanodine receptors and caveolin-3 in

mouse ventricular myocytes: dilation of t-tubules near junctions. *Biophys. J.* 104, L22–L24. doi: 10.1016/j.bpj.2013.02.059

Wright, P. T., Bhogal, N. K., Diakonov, I., Pannell, L. M. K., Perera, R. K., Bork, N. I., et al. (2018). Cardiomyocyte membrane structure and cAMP compartmentation produce anatomical variation in β2AR-cAMP responsiveness in murine hearts. *Cell Rep.* 23, 459–469. doi: 10.1016/j.celrep.2018.03.053

Wright, P. T., Nikolaev, V. O., O'Hara, T., Diakonov, I., Bhargava, A., Tokar, S., et al. (2014). Caveolin-3 regulates compartmentation of cardiomyocyte beta2-adrenergic receptor-mediated cAMP signaling. *J. Mol. Cell. Cardiol.* 67, 38–48. doi: 10.1016/j.yjmcc.2013.12.003

Conflict of Interest Statement: The authors declare that the research was conducted in the absence of any commercial or financial relationships that could be construed as a potential conflict of interest.

frontiers in Physiology

ORIGINAL RESEARCH
published: 08 October 2018
doi: 10.3389/fphys.2018.01227

Axial Tubule Junctions Activate Atrial Ca^{2+} Release Across Species

*Sören Brandenburg[1], Jan Pawlowitz[1], Funsho E. Fakuade[2], Daniel Kownatzki-Danger[1], Tobias Kohl[1], Gyuzel Y. Mitronova[3], Marina Scardigli[4], Jakob Neef[5], Constanze Schmidt[6,7,8], Felix Wiedmann[6,7,8], Francesco S. Pavone[4,9], Leonardo Sacconi[4], Ingo Kutschka[10], Samuel Sossalla[1†], Tobias Moser[5], Niels Voigt[2,11] and Stephan E. Lehnart[1,11,12]**

[1] Heart Research Center Göttingen, Department of Cardiology and Pneumology, University Medical Center Göttingen, Göttingen, Germany, [2] Heart Research Center Göttingen, Institute of Pharmacology and Toxicology, University Medical Center Göttingen, Göttingen, Germany, [3] Department of NanoBiophotonics, Max Planck Institute for Biophysical Chemistry, Göttingen, Germany, [4] European Laboratory for Non-Linear Spectroscopy and National Institute of Optics (INO-CNR), Sesto Fiorentino, Italy, [5] Institute for Auditory Neuroscience and InnerEarLab, University Medical Center Göttingen, Göttingen, Germany, [6] Department of Cardiology, University Hospital Heidelberg, Heidelberg, Germany, [7] DZHK (German Centre for Cardiovascular Research) partner site Heidelberg/Mannheim, University of Heidelberg, Heidelberg, Germany, [8] Heidelberg Center for Heart Rhythm Disorders, University Hospital Heidelberg, Heidelberg, Germany, [9] Department of Physics, University of Florence, Florence, Italy, [10] Department of Cardiothoracic and Vascular Surgery, University Medical Center Göttingen, Göttingen, Germany, [11] DZHK (German Centre for Cardiovascular Research) partner site Göttingen, Göttingen, Germany, [12] BioMET, The Center for Biomedical Engineering and Technology, University of Maryland School of Medicine, Baltimore, MD, United States

OPEN ACCESS

Edited by:
Julia Gorelik,
Imperial College London,
United Kingdom

Reviewed by:
Michele Miragoli,
Università degli Studi di Parma, Italy
Andrew F. James,
University of Bristol, United Kingdom

***Correspondence:**
Stephan E. Lehnart
slehnart@med.uni-goettingen.de

†Present address:
Samuel Sossalla,
Department for Internal Medicine II, Cardiology, Pneumology, Intensive Care, University Hospital Regensburg, Regensburg, Germany

Specialty section:
This article was submitted to Cardiac Electrophysiology, a section of the journal Frontiers in Physiology

Received: 02 May 2018
Accepted: 14 August 2018
Published: 08 October 2018

Citation:
Brandenburg S, Pawlowitz J, Fakuade FE, Kownatzki-Danger D, Kohl T, Mitronova GY, Scardigli M, Neef J, Schmidt C, Wiedmann F, Pavone FS, Sacconi L, Kutschka I, Sossalla S, Moser T, Voigt N and Lehnart SE (2018) Axial Tubule Junctions Activate Atrial Ca^{2+} Release Across Species. Front. Physiol. 9:1227. doi: 10.3389/fphys.2018.01227

Rationale: Recently, abundant axial tubule (AT) membrane structures were identified deep inside atrial myocytes (AMs). Upon excitation, ATs rapidly activate intracellular Ca^{2+} release and sarcomeric contraction through extensive AT junctions, a cell-specific atrial mechanism. While AT junctions with the sarcoplasmic reticulum contain unusually large clusters of ryanodine receptor 2 (RyR2) Ca^{2+} release channels in mouse AMs, it remains unclear if similar protein networks and membrane structures exist across species, particularly those relevant for atrial disease modeling.

Objective: To examine and quantitatively analyze the architecture of AT membrane structures and associated Ca^{2+} signaling proteins across species from mouse to human.

Methods and Results: We developed superresolution microscopy (nanoscopy) strategies for intact live AMs based on a new custom-made photostable cholesterol dye *and* immunofluorescence imaging of membraneous structures and membrane proteins in fixed tissue sections from human, porcine, and rodent atria. Consistently, in mouse, rat, and rabbit AMs, intact cell-wide tubule networks continuous with the surface membrane were observed, mainly composed of ATs. Moreover, co-immunofluorescence nanoscopy showed L-type Ca^{2+} channel clusters adjacent to extensive junctional RyR2 clusters at ATs. However, only junctional RyR2 clusters were highly phosphorylated and may thus prime Ca^{2+} release at ATs, locally for rapid signal amplification. While the density of the integrated L-type Ca^{2+} current was similar in human and mouse AMs, the intracellular Ca^{2+} transient showed quantitative differences. Importantly, local intracellular Ca^{2+} release from AT junctions occurred through instantaneous action potential propagation

via transverse tubules (TTs) from the surface membrane. Hence, sparse TTs were sufficient as electrical conduits for rapid activation of Ca^{2+} release through ATs. Nanoscopy of atrial tissue sections confirmed abundant ATs as the major network component of AMs, particularly in human atrial tissue sections.

Conclusion: AT junctions represent a conserved, cell-specific membrane structure for rapid excitation-contraction coupling throughout a representative spectrum of species including human. Since ATs provide the major excitable membrane network component in AMs, a new model of atrial "super-hub" Ca^{2+} signaling may apply across biomedically relevant species, opening avenues for future investigations about atrial disease mechanisms and therapeutic targeting.

Keywords: atria, atrial myocyte, axial tubule, calcium, heart, ryanodine receptor

INTRODUCTION

As one billion individuals 65 years or older are expected by the year 2030, aging populations will be affected by a sharp increase in chronic diseases (Moslehi et al., 2012). Most frequent in elderly people, electrical and contractile dysfunction of the atria contributes to stroke, heart failure, and atrial fibrillation the latter alone predicted to increase threefold in prevalence by 2050 (Yiin et al., 2014). While atrial fibrillation is often considered a proximal cause of thrombembolic stroke, recent clinical studies question a direct relationship (Brambatti et al., 2014; Martin et al., 2015). Therefore, a broader pathophysiological concept of atrial cardiomyopathy was developed, which explicitly addresses atrial myocyte (AM) specific disease mechanisms (Goette et al., 2017). However, given that AM dysfunction represents a central cause of the disease burden, fundamental cellular mechanisms remain unclear (Brandenburg et al., 2016a; Guichard and Nattel, 2017). Recently, an emerging atrial Ca^{2+} nanodomain model, extending significantly beyond the canonical role of transverse tubule (TT) invaginations in ventricular myocytes (VMs), was proposed: super-hub Ca^{2+} signaling based on axial tubule (AT) junctions that rapidly activate Ca^{2+} release *and* atrial contraction through cell-specific molecular nanodomain mechanisms (Brandenburg et al., 2016b).

In ventricular myocytes, TTs occur periodically near sarcomeric Z-lines at a fixed density, which may unify cell-wide Ca^{2+} release (Crossman et al., 2015), and contribute to heterogeneous Ca^{2+} release in heart failure due to TT reorganization (Song et al., 2006; Wagner et al., 2012). In contrast to VMs, AMs are significantly smaller and have significantly different functions [for review (Brandenburg et al., 2016a)], which may explain why few or no cells with TTs were reported in various species including cat (McNutt and Fawcett, 1969; Huser et al., 1996), guinea pig (Forbes and van Neil, 1988), mouse (Forbes et al., 1984), rabbit (Tidball et al., 1991; Maxwell and Blatter, 2017), or rat (Brette et al., 2002; Kirk et al., 2003; Woo et al., 2005; Sheehan et al., 2006; Smyrnias et al., 2010). Notably, denser atrial TT structures were identified in large mammals including sheep (Dibb et al., 2009; Lenaerts et al., 2009), dog (Wakili et al., 2010), pig (Frisk et al., 2014; Gadeberg et al., 2016), cow, horse, and human (Richards et al., 2011). Yet, irrespective of smaller (i.e., rat) or larger (i.e., dog) species, contractile activation occurs generally faster in atrial than ventricular muscle (Lüss et al., 1999), contributing to the atrial 'kick' *in vivo*, an essential booster function for ventricular filling and stress adaptation (Brandenburg et al., 2016a).

Since few or no TTs were found in rat AMs, voltage-dependent L-type Ca^{2+} channels (LCC) were thought to function mainly at the surface sarcolemma, where adjacent ryanodine receptor (RyR2) Ca^{2+} release channels were locally activated through peripheral junctions (Thul et al., 2012). Yet in the same rat species, dense or irregular TT morphologies and LCC currents at TT orifices were recently demonstrated (Frisk et al., 2014; Glukhov et al., 2015). In addition to surface-bound locations, we directly counted LCC clusters by superresolution imaging inside mouse AMs, finding a ∼50% higher density in AT than TT components (Brandenburg et al., 2016b). While these observations were only possible through methodological developments that preserve endogenous membrane structures in live AM samples for nanoscopy studies (Wagner et al., 2012, 2014), it is important to note that intact transverse-axial tubule (TAT) networks were confirmed in 100% of isolated AMs (Brandenburg et al., 2016b). Hence, the notion that AMs from small rodent hearts are mostly devoid of excitable TAT structures warrants re-evaluation across species to identify common mechanisms of atrial excitation-contraction coupling. Here, we show in cells and tissues from mouse, rat, rabbit, pig, and human atria that ATs represent the major TAT component and activate Ca^{2+} release instantaneously in AMs. Thus, the specific TAT membrane network architecture of AMs is conserved across commonly investigated species, opening avenues for future interventions in genetically tractable hearts as well as therapeutic studies that elucidate atria-specific disease mechanisms.

RESULTS

Mouse, Rat, and Rabbit Atria Contain Cell-Wide TAT Networks

Recently, we showed that ATs contain a high density of Caveolin3 clusters (Brandenburg et al., 2016b), a bona fide cholesterol binding protein. Hence, we took advantage of a recent strategy to synthesize photostable, far-red emitting fluorescent cholesterol

analogs (Chol-PEG-KK114; see methods) for live cell imaging based on STimulated Emission Depletion (STED) nanoscopy (Kolmakov et al., 2010; Sezgin et al., 2016). Bulk labeling with 5 μM Chol-PEG-KK114 readily revealed intact TAT structures in living AMs clearly visible as membrane networks throughout the cytoplasm except the nucleus and continuous with the outer surface sarcolemma in mouse, rat, and rabbit AMs (**Figure 1A**). Notably, while few TTs were visible at the peripheral (cortical) surface membrane, numerous prominent AT components were observed deep inside AMs (**Figure 1A**, magnifications).

In addition to the heart weight (**Supplementary Figure S1A**), the dimensions of AMs vary considerably between mouse, rat, and rabbit (**Supplementary Figures S1B,C**). For example, as compared to mouse AMs, rabbit AMs were significantly longer and wider (**Supplementary Figures S1B,C**). Accordingly, the calculated cell area and heart weight were both correlated in the order mouse < rat < rabbit (**Supplementary Figures S1A,C**). Whereas AMs from the different rodent species differed significantly in their cell dimensions, remarkably, we observed similar cell-wide TAT network morphologies mainly comprised of AT components in isolated AMs.

To explore the vulnerability of TAT membranes to increased cell isolation stress, we performed the same protocol without *in vivo* heparin pre-treatment followed by isolation of rabbit AMs (**Supplementary Figure S2A**). As hypothesized, the TAT network appeared disrupted while residual AT and TT components, visualized by STED nanoscopy, showed locally demarcated membrane fragmentation events, i.e., along AT structures in rabbit AMs (**Supplementary Figure S2B**). In addition, larger aggregates of disrupted membrane components remained stably associated with residual intact membrane structures (**Supplementary Figure S2C**). These results document the vital role of heparin pre-treatment presumably to prevent blood clotting, maintain tissue perfusion, and allow for efficient extracellular matrix digestion via collagenase perfusion. In summary, live cell STED nanoscopy through visualization of individual membrane components can directly discriminate between intact *versus* disrupted individual TAT components in live AMs.

Cholesterol-Rich Nanodomains Visualized in Intact AT Membranes

While immunofluorescence imaging established that VMs express Caveolin3 throughout TTs, abundant Caveolin3 clusters were identified in AT structures recently (Brandenburg et al., 2016b). Yet we and others have previously shown in VMs that TTs rarely contain caveolae-shaped membrane structures (Wagner et al., 2012; Burton et al., 2017). To identify intact native cholesterol-rich domains in ATs, we adjusted the labeling strategy. Strikingly, a 20-fold lower Chol-PEG-KK114 dye concentration (250 nM) directly resolved individual cholesterol-rich domains deep inside AMs (**Figure 1B**, *left*). While the overall abundance of cholesterol-rich membrane domains was similar on ATs as compared to the caveolae-rich lateral AM surface membrane, STED resolved individual cholesterol domains on ATs (**Figure 1B**, *magnification*). To estimate the size of individual cholesterol domains on a given AT structure, we plotted the intensity profile through a clearly demarcated signal spot and fitted a Gaussian function, resulting in a width (FWHM) of ∼90 nm (**Figure 1B**, *right*). Thus, intact cholesterol-rich domains inside AMs are not only abundant on ATs, but their dimensions are consistent with those of signaling nanodomains.

ATs Contain Large L-type Ca^{2+} Channel Clusters at Cholesterol-Rich Domains

Depletion of membrane cholesterol was previously shown to decrease the density of caveolae as well as ion conduction through LCCs at the surface of rat AMs (Glukhov et al., 2015). To confirm the expected association between $Ca_v1.2$ channels and cholesterol-rich AT nanodomains, we used co-immunofluorescence staining and dual-color STED nanoscopy. Individual Caveolin3 positive signal areas were visualized on AT structures yet located immediately adjacent to $Ca_v1.2$ LCC clusters (**Figure 1C**, *left panels*). Since $Ca_v1.2$ and Caveolin3 clusters on AT structures were located next to each other, only a minor fraction of the signal overlapped (**Figure 1C**, *merge*). Interestingly, $Ca_v1.2$ and Caveolin3 clusters on ATs were relatively large when visualized individually through separate color channels (**Figure 1C**, *right panels*). Taken together, cluster-cluster interactions rather than co-localization of $Ca_v1.2$ and Caveolin3 protein complexes on ATs may indicate a key role of cholesterol-rich domains for local LCC regulation of $Ca_v1.2$ channel clusters.

In addition, functional expression of the $Ca_v1.3$ LCC isoform has been demonstrated in mouse atria previously (Zhang et al., 2005). As the physiological role of atrial membrane invaginations was unclear at that time, we wondered if the $Ca_v1.3$ isoform is also expressed in AT membranes. Indeed, STED co-immunofluorescence labeling of mouse AMs showed that Caveolin3 clusters in AT structures are located close to $Ca_v1.3$ clusters (**Figure 2A**). Interestingly, in immunohistological confocal sections of inner hair cells (IHCs) from the inner ear the same antibody identified $Ca_v1.3$ clusters associated with the scaffolding protein bassoon (**Figure 2B**, *left*). STED imaging confirmed the close association between presynaptic bassoon and linearly arranged synaptic $Ca_v1.3$ channels at the active zone as described previously (**Figure 2B**, *right*) (Frank et al., 2010; Neef et al., 2018). Thus, while both $Ca_v1.2$ and $Ca_v1.3$ LCCs are expressed in ATs, only the latter isoform is predominantly found in atrial as compared to ventricular myocytes (Zhang et al., 2005). Due to significantly different biophysical properties and more restricted expression, $Ca_v1.3$ LCCs may contribute to the unique cell-specific (patho)physiology of AMs and IHCs (see also discussion).

TAT Network Analysis Reveals Abundant Axial Tubules Across Species

Corresponding with **Figure 1A**, live cell images of bulk cholesterol-stained mouse, rat, and rabbit AMs were used for component-specific TAT analysis. For this, the orientation of intact membrane components was analyzed via binarized

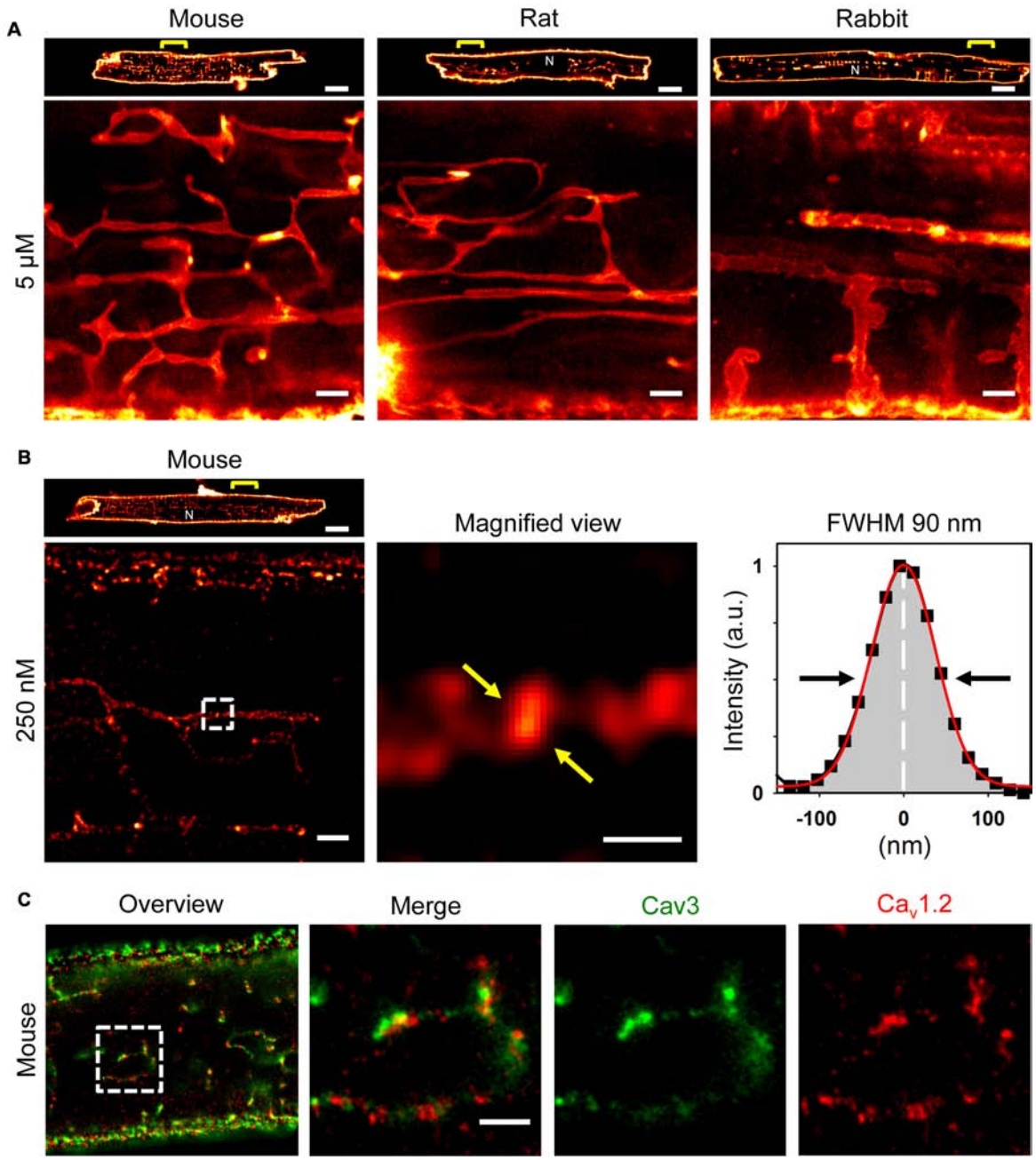

FIGURE 1 | Atrial myocytes from mouse, rat, and rabbit show cell-wide TAT networks composed of abundant axial tubules. **(A)** Live cell imaging of TAT membranes in isolated AMs using Chol-PEG-KK114 as bulk label (5 µM) for STED nanoscopy. Note, abundant axial tubules (ATs) but sparse transverse tubules (TTs) connected with the lateral surface membrane. Examples are representative for three independent AM isolations from three hearts of each species. Scale bars 10 µm (top row) or 1 µm (bottom row). **(B)** Here, the Chol-PEG-KK114 marker concentration was reduced 20-fold (250 nM). Note the clearly delimited cholesterol domains visualized live inside TAT membranes of a mouse AM. The signal intensity distribution of one cholesterol domain (black squares indicate individual data points) was fitted by a Gaussian (red curve) to determine the FWHM ~90 nm (arrows). Scale bars: top 10 µm; bottom: overview 1 µm; magnified view 200 nm. **(C)** Co-immunofluorescence STED images show Caveolin3 and $Ca_v1.2$ clusters in a mouse AM. Scale bar 1 µm. N, nucleus. Yellow brackets and dashed boxes indicate magnified regions.

TAT skeletons oriented according to the major cell axis (**Figure 3A**). Intriguingly, despite the variance in AM and cardiac dimensions between species, orientation-specific TAT network analysis showed similar frequencies of the AT, oblique tubule (OT), and TT components (**Figure 3B**). Importantly, the frequency of the major AT components did not significantly differ between mouse, rat, and rabbit (**Figure 3C**, *left*). For the minor components, only in rat AMs, OTs were more frequent at the cost of TTs (**Figure 3C**, *left*). In contrast, the absolute component densities were significantly different

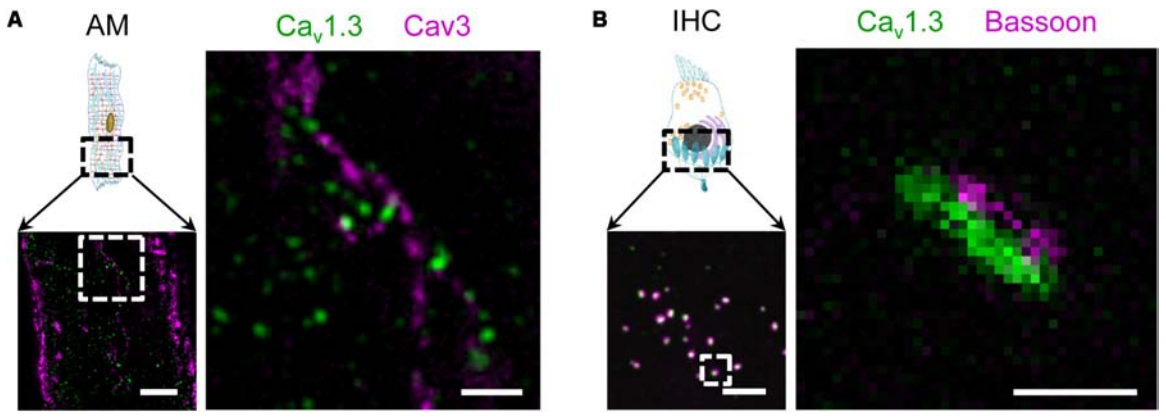

FIGURE 2 | Surface expression of the LCC channel isoform $Ca_v1.3$ in AT structures of AMs and at the basal pole of inner hair cells (IHC). **(A)** Co-immunofluorescence STED imaging of $Ca_v1.3$ and Caveolin3 (Cav3) in an isolated mouse AM. *Right*: the magnified region (dashed box) shows $Ca_v1.3$ next to Cav3 clusters, the latter indicating AT membrane structures. Scale bars: *left* 2 μm; *right* 500 nm (magnification). **(B)** *Left:* Confocal immunohistochemical imaging of $Ca_v1.3$ and the presynaptic scaffold protein bassoon showing a representative section of the IHC basal pole. *Right:* A magnified active zone obtained at higher resolution by STED microscopy. In synapses of IHCs, $Ca_v1.3$ channels are typically arranged in linear clusters and juxtaposed with bassoon. Scale bars: *left* 2 μm; *right* 200 nm (magnification).

between the species. For example, AT and TT components occurred at a significantly higher density in mouse compared to rat and rabbit AMs (**Figure 3C**, *right*), suggesting an inverse correlation with the calculated cell area (**Supplementary Figure S1C**). While the TAT network density (**Figure 3D**, *left*) and network junctions (**Figure 3D**, *center*) were ranked in the order mouse > rat > rabbit, the mean component branch length was not different between species (**Figure 3D**, *right*). Interestingly, the differences in network density were inversely correlated with atrial cell size (**Supplementary Figure S1C**), and previously correlated with the basal heart rate between different species (Milani-Nejad and Janssen, 2014). Taken together, while mouse, rat, and rabbit AMs showed significant differences in their absolute component and network junction densities, the orientation-specific frequency and absolute density was always dominated by abundant ATs across all rodent species investigated.

Axial Tubules Have Unique Dimensions

In living AMs stained with 5 μM Chol-PEG-KK114, STED nanoscopy resolved the membrane boundaries of individual membrane tubules in the image plane. For analysis, the signal intensity distribution across individual TT components was fitted by a 2-peak Gaussian function, which showed major differences between exemplar mouse, rat, and rabbit tubules (**Figure 4A**). In addition, intensity profiles of AT structures fitted by Gaussian confirmed similar species differences (**Figure 4B**). Importantly, we quantified significantly larger AT than TT widths in mouse and rat AMs (**Figure 4C**), both confirming and extending previous results based on di-8-ANEPPS (Brandenburg et al., 2016b). For example, as compared to TTs, the width of AT components was 18% larger in mouse and 26% larger in rat AMs. In contrast, while the width of AT and TT components was similar in rabbit AMs, it was approximately twice as large compared to mouse and rat AMs (**Figure 4C**). Hence, mouse and rat AMs express significantly larger AT than TT structures.

Axial Tubule Junctions Contain Extensive, Highly Phosphorylated RyR2 Clusters

As previously shown by confocal imaging and electron tomography in mouse AMs, ATs form contact junctions of μm extent with the SR, where LCCs can rapidly activate Ca^{2+} induced Ca^{2+} release (CICR) through a less than 15 nm wide subspace (Brandenburg et al., 2016b). Here, immunofluorescence labeling and STED nanoscopy of Caveolin3 and RyR2 in mouse AMs showed RyR2 clusters alternating with Caveolin3 clusters on AT structures (**Figure 5A**). Notably, the majority of RyR2 clusters organized transversally in striations near Z-lines were not associated with any Caveolin3-labeled membrane structures (**Figure 5A**). Additionally, co-immunostaining of RyR2 clusters for RyR2-pS2808 phosphorylation identified highly phosphorylated and axially aligned RyR2 clusters, which intersect the transversally aligned yet minimally Protein Kinase A (PKA) phosphorylated RyR2 clusters (**Figure 5B**, *top*). Indeed, phospho-epitope specific antibody labeling showed that PKA phosphorylated RyR2-pS2808 clusters occurred at AT junctions (**Figure 5C**, *top and bottom*). Confirming earlier confocal studies, the new STED imaging data show specific RyR2 cluster associations and phosphorylation states in AMs, junctional versus non-junctional, where only the former are associated with AT structures.

Importantly, STED nanoscopy further revealed that highly phosphorylated RyR2 clusters appear to be significantly larger compared to less phosphorylated clusters (**Figure 5B**, *bottom*). Moreover, phosphoepitope-specific RyR2-pS2808 labeling was confirmed in PKA-phosphorylation incompetent AMs from $Ryr2^{S2808A/S2808A}$ knockin mice through completely

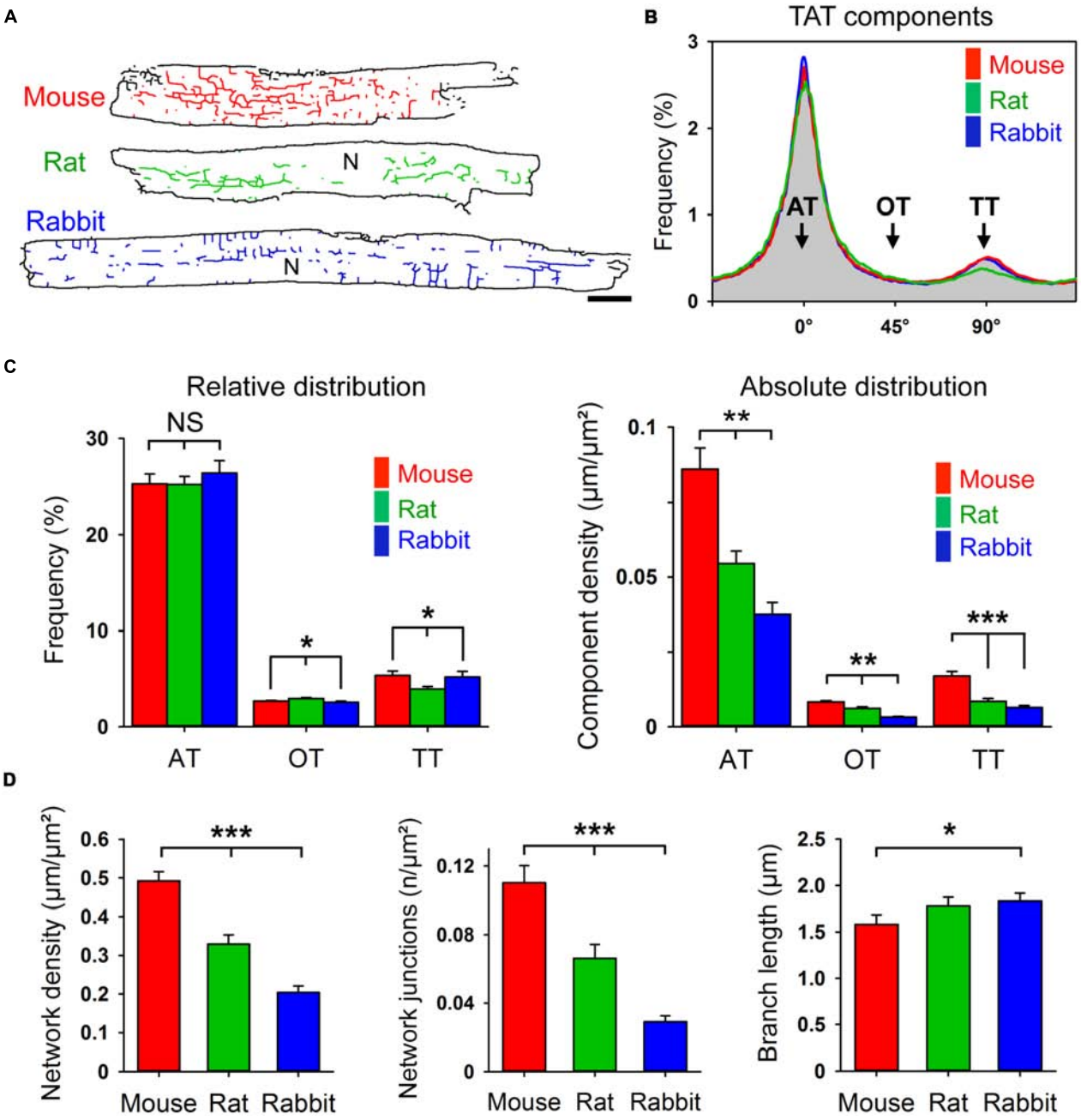

FIGURE 3 | Component-specific TAT analysis in mouse, rat, and rabbit AMs. **(A)** Corresponding TAT live cell images in **Figure 1A** were converted into binarized skeletons for quantitative network analysis. N, nucleus. Scale bar 10 µm. **(B)** The histogram shows the bimodal distribution of specific TAT network components. Major peak: ATs (0°); minor peak: TTs (90°); interim: OTs (oblique tubules, 45°); binning ± 5°. **(C)** Bar graphs comparing the relative and absolute distribution of the three main TAT components. While the relative distribution of TAT components does not differ much between the indicated species, the absolute component density differs significantly between mouse, rat and rabbit AMs. **(D)** The network density, the number of network junctions, and the mean branch length were compared between mouse, rat, and rabbit AM. Cell numbers: 30 mouse, 34 rat, and 23 rabbit AMs, each from 3 individual cell isolations and hearts per species. Student's *t*-test $^{*}P < 0.05$, $^{**}P < 0.01$, $^{***}P < 0.001$.

ablated RyR2-pS2808 phospho-epitope specific cluster signals (**Figure 5D**). Extending further to rat, again highly phosphorylated RyR2 clusters appear axially aligned, indicating the functional relevance of differential RyR2 cluster phosphorylation in AMs (**Figure 5E**). Finally, rabbit AMs showed axially aligned Caveolin3 and RyR2 clusters (**Figure 5F**), again highly phosphorylated *in situ* at the RyR2-pS2808 residue (**Figure 5G**). In line with the co-immunostaining STED images in mouse, Caveolin3 and RyR2 cluster signals were aligned axially (i.e., with axial tubules), where the clusters alternate

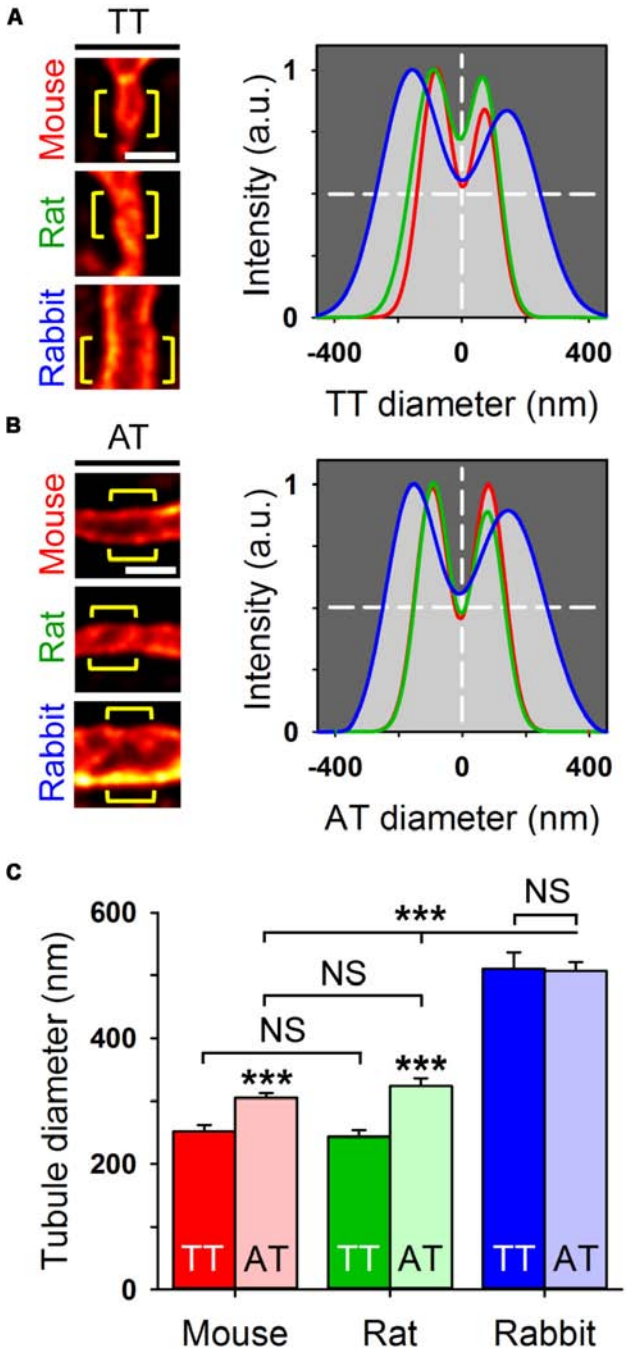

FIGURE 4 | Live cell STED nanoscopy resolves individual tubule dimensions. Representative TT **(A)** and AT **(B)** images from mouse, rat, and rabbit AMs. Bulk staining with Chol-PEG-KK114 (5 μM) and STED nanoscopy resolved the individual tubule membrane structures. Regional intensity profiles from ideally oriented tubule regions (yellow brackets) were used for intensity profiling and Gaussian fitting to estimate tubule width (FWHM) as indicated by horizontal dashed lines. Scale bars in **(A,B)** 500 nm. **(C)** Bar graph comparing TT versus AT diameters (FWHM). In mouse and rat AMs, AT components are significantly larger compared to TT components. In rabbit AMs, AT and TT dimensions far exceed the size of the analogous components in mouse and rat AMs. Component numbers: mouse AM 84 ATs/37 TTs; rat AM 53 ATs/18 TTs; rabbit AM 47 ATs/18 TTs. Data are representative for 3 individual cell isolations and hearts for each species. Student's *t*-test $^{***}P < 0.001$.

spatially but do not co-localize in rabbit AMs. Apparently, and only in rabbit AMs, RyR2 clusters show a much wider lateral separation across AT structures in agreement with our live cell quantification of unusually large AT diameters in rabbit AMs (**Figure 4C**). Hence, across species AMs are characterized by highly phosphorylated RyR2 clusters at AT junctions, in contrast to minimally phosphorylated mostly non-junctional transversal RyR2 clusters near Z-lines.

A Comparison of Ca^{2+} Currents and Ca^{2+} Transients in Mouse and Human AMs

To compare systolic CICR mechanisms between mouse and human AMs, we simultaneously recorded the L-type Ca^{2+} current ($I_{Ca,L}$) and steady-state intracellular Ca^{2+} transients using previously established protocols (Voigt et al., 2013, 2014). Specifically, mouse and human AMs were patch-clamped using the same extracellular Ca^{2+} concentration (1 mM). Despite potential differences in cell size, measurements of the membrane capacitance of isolated mouse and human AMs showed no significant difference (77.07 ± 6.13 pF, n = 8; 106.45 ± 15.85 pF, n = 11, respectively). $I_{Ca,L}$ current traces indicated apparent differences between mouse and human AMs (**Figures 6A** vs. **6B**, *top*). When we calculated the density of $I_{Ca,L}$ (**Figure 6C**), the current amplitude normalized to capacitance was significantly smaller in human AMs (*top*) while the integrated $I_{Ca,L}$ density showed only a non-significant trend toward lower currents in human AMs (*bottom*). Furthermore, combined Ca^{2+} imaging showed a non-significant decrease of the Ca^{2+} transient amplitude in human compared to mouse AMs (**Figure 6D**).

As membrane capacitance depends both on the outer surface and inner TAT sarcolemma, we explored the state of the TAT membranes in human AMs isolated from relatively small tissue samples of patients (**Supplementary Table S1**). It is important to note that the human AM isolation technique differs significantly from that used for rodent AM isolation in two points: (1) initial mechanical tissue dissection is necessary to provide substrate access for (2) collagenase digestion in sufficiently small tissue pieces in suspension, in contrast to tissue perfusion used in Langendorff hearts (Voigt et al., 2013, 2014). Following isolation via mechanical dissection, the intact state of human AMs stained with 5 μM Chol-PEG-KK114 was documented by bright field and confocal microscopy (**Supplementary Figure S3A**). In addition, STED nanoscopy showed residual AT and TT fragments as well as abnormal membrane aggregates (**Supplementary Figure S3B**). These results confirm that intact human AMs were successfully isolated, while their TAT structures appeared at least partly disrupted. Therefore, we decided to develop an additional tissue-based strategy for structural analysis of the TAT network in human AMs (see further below).

In summary, while these results indicate that membrane capacitance may have been underestimated in human AMs (please refer to the methods section for details) due to partial TAT fragmentation, the integrated $I_{Ca,L}$ current and the Ca^{2+} release amplitude in isolated human and mouse AMs were of similar magnitude.

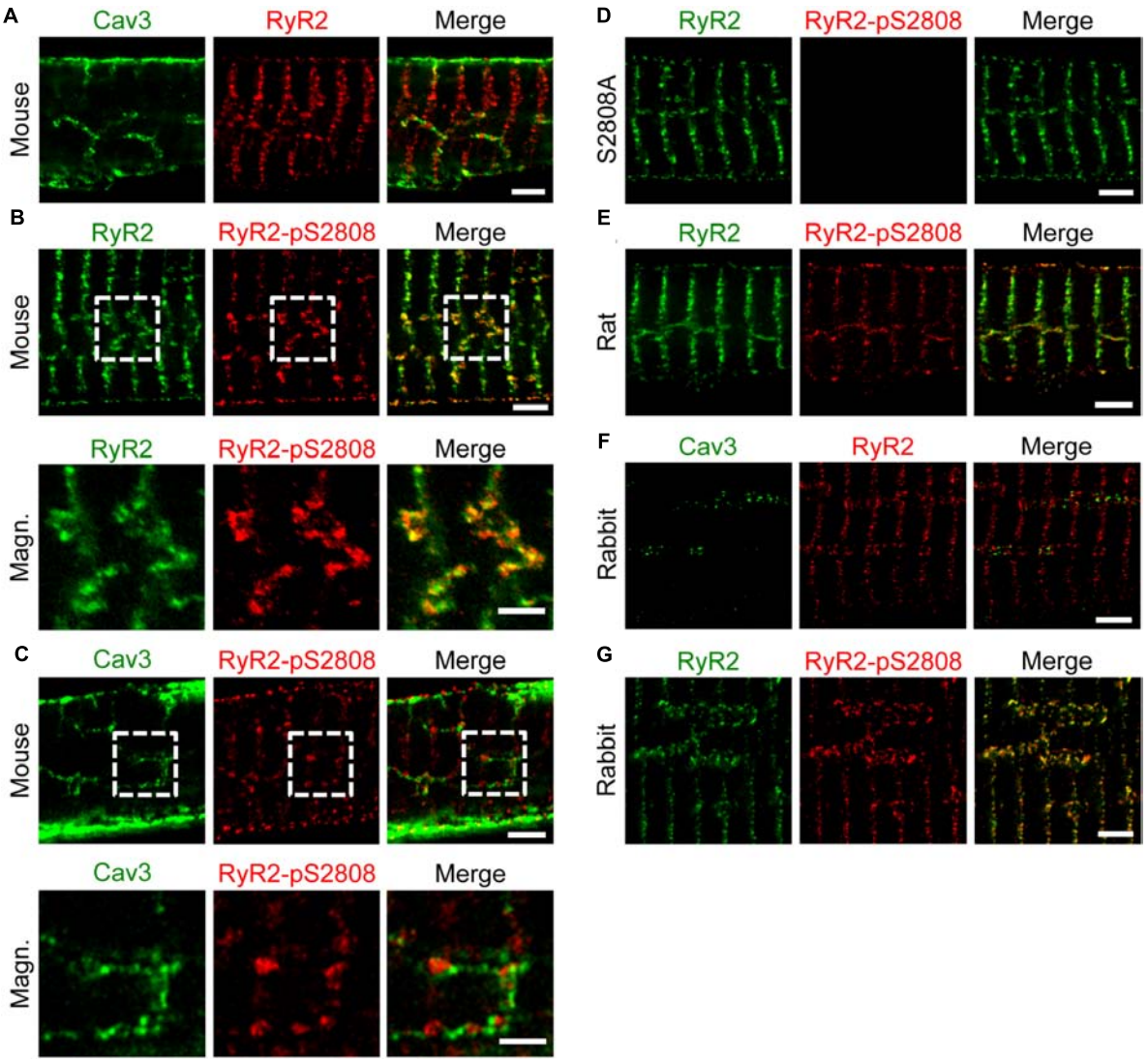

FIGURE 5 | Axial tubules are associated with large, highly phosphorylated RyR2 clusters. STED images show representative AM sections from mouse, rat and rabbit. Co-immunolabeling with primary antibodies against Caveolin3, RyR2 and the phospho-specific epitope RyR2-pS2808 as indicated. **(A)** Caveolin3 labeling is used as a specific marker for the TAT components. Junctional RyR2 clusters are associated with AT structures in contrast to non-junctional RyR2 clusters. **(B)** Through RyR2 and RyR2-pS2808 labeling, large highly phosphorylated RyR2 clusters can be distinguished from low phosphorylated RyR2 clusters. **(C)** The RyR2-pS2808 phospho-epitope specific labeling shows increased PKA phosphorylation of AT-associated junctional RyR2 clusters in contrast to non-junctional RyR2 clusters. **(D)** AM from *Ryr2*$^{S2808A/S2808A}$ knockin mice were used as epitope specific negative control. **(E)** Similar axially aligned RyR2-pS2808 clusters were confirmed in rat AM. **(F)** In rabbit AM, larger AT structures align with RyR2 clusters, which **(G)** show increased PKA phosphorylation evidenced by RyR2-pS2808 labeling. Dashed boxes indicate the magnified regions shown below. All scale bars 2 μm, except for magnified regions 1 μm **(B,C)**.

Next, we sought to determine the relative contributions by SERCA and NCX to extrusion of Ca^{2+} from the cytosol during the systolic Ca^{2+} transient. For this, we used experimental protocols that determine the effect of each Ca^{2+} sink individually on the rate of decay (k) of $[Ca^{2+}]_i$ by fitting systolic and caffeine-evoked Ca^{2+} transients with a single exponential function (O'Neill et al., 1991). **Figure 6E** summarizes the mean data: (*left*) the rate of decay of $[Ca^{2+}]_i$ during the systolic Ca^{2+} transient was significantly faster in mouse compared to human AMs; (*middle*) while the rate of decay of the caffeine transient was not significantly different ($k_{caff:}$ 0.68 ± 0.10 s^{-1} in mouse and 0.80 ± 0.10 $s^{-}1$ in human AMs), the SERCA-dependent rate of cytosolic Ca^{2+} extrusion (k_{SERCA}, *right*) was significantly higher in mouse compared to human AMs (n = 8 mouse and 11 human cells). Assuming that NCX functions as the predominant Ca^{2+} extrusion pathway, from this analysis the relative contribution to systolic Ca^{2+} extrusion, each by SERCA- and NCX-dependent transport, can be obtained. Whereas the fraction of Ca^{2+} extruded by SERCA was significantly larger in mouse AMs, the fraction extruded by non-SERCA dependent pathways (i.e., NCX) was significantly larger in human AMs (**Figure 6F**).

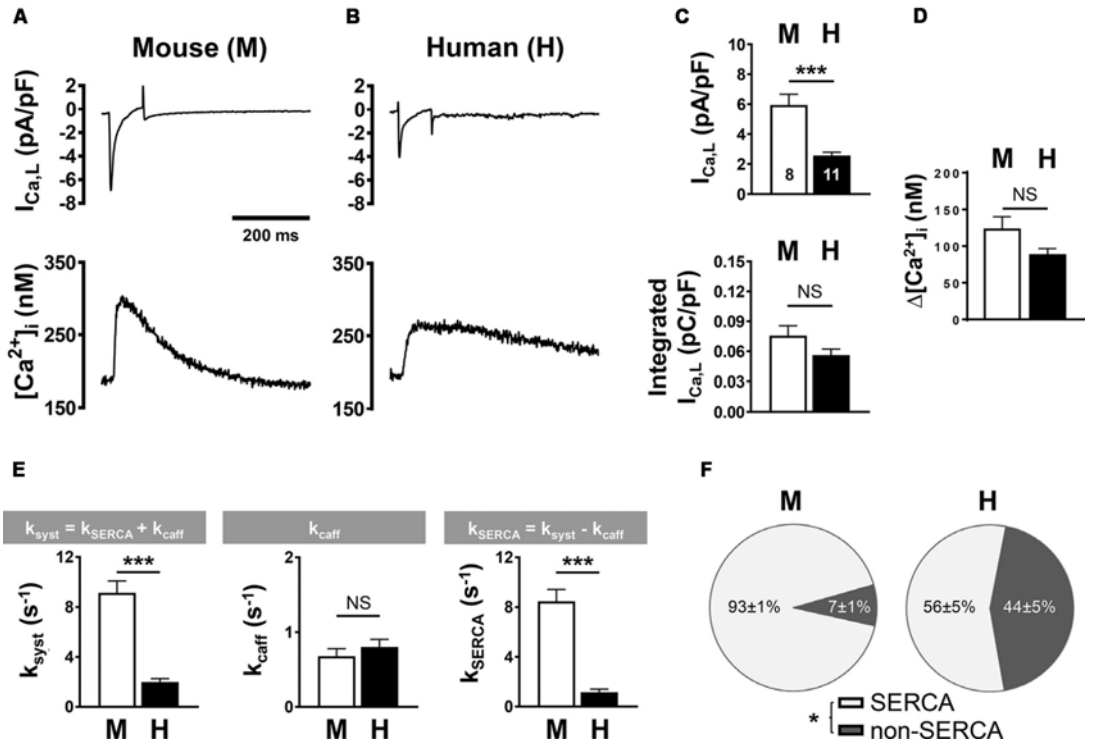

FIGURE 6 | L-type Ca^{2+} current ($I_{Ca,L}$) density and Ca^{2+} transient amplitude in mouse (M) and human (H) atrial myocytes. (**A,B**, *top*) Voltage-clamp was used to depolarize and repolarize the membrane potential at a rate of 0.5 Hz for combined recording of $I_{Ca,L}$ and steady-state intracellular Ca^{2+} transients. Representative mouse **(A)** and human **(B)** traces from individual AM recordings are shown. Bar graphs comparing **(C)** the peak (*top*) and the integrated (*lower*) $I_{Ca,L}$ density normalized to cell capacitance and **(D)** the systolic Ca^{2+} transient amplitude. **(E)** Bar graphs summarizing the indicated rate constants determined by mono-exponential fitting of systolic Ca^{2+} (k_{syst}) and caffeine-induced (k_{caff}) Ca^{2+} transients; and the calculated SERCA-dependent rate of decay. **(F)** Pie plots comparing fractional contributions to Ca^{2+} extrusion by SERCA and non-SERCA flux components (NCX, PMCA, and mitochondria) in mouse and human AMs. AMs were isolated from five mouse hearts and six human heart samples. $^*P < 0.05$, $^{***}P < 0.001$. Numbers of cells shown in **(C)** apply to all panels. Please refer to **Supplementary Table S1** for clinical information about the human samples.

Atrial Expression of Ca^{2+} Handling Proteins

Previous studies of rat hearts showed that phospholamban (PLN), a physiological inhibitor of the SR Ca^{2+} (SERCA2) pump released by PKA phosphorylation of PLN-S16, is expressed at significantly lower levels in atria compared to ventricles (Walden et al., 2009). In addition, atrial versus ventricular SERCA2 expression was found to be approximately 2-times higher in mouse, rat, and dog (Lüss et al., 1999; Walden et al., 2009; Brandenburg et al., 2016b). Comparing samples from five species (rodents, pig, and human), we analyzed the expression level of the Na^+/Ca^{2+}-exchanger (NCX), the Na^+/K^+-ATPase α-subunit (Na,K-ATPase), and SERCA2 by immunoblotting (**Figure 7A**; the full blots are shown in **Supplementary Figure S4**). While human atrial NCX protein levels were not significantly different from mouse and rat, we found significantly higher Na,K-ATPase and SERCA2 levels in mouse atria, gradually decreasing in line with different species-dimensions with the lowest significant levels found in human atria (**Figure 7B**). In addition, expression of the cardiac ryanodine receptor (RyR2) and phospholemman (PLM) was significantly higher in mouse compared to human atria (**Figure 7B**). Importantly, while PLN levels varied across species, in mouse and human atria PLN expression was not significantly different (**Figure 7B**).

As expected for human compared to mouse atria (Lüss et al., 1999; Walden et al., 2009; Brandenburg et al., 2016b), the capacity to extrude Ca^{2+} to the extracellular space versus Ca^{2+} uptake by the SR was significantly higher as indicated by the NCX/SERCA2 ratio (**Figure 7C**). Furthermore, the PLM/Na,K-ATPase ratio tended to be higher in human atria relative to any other species (**Figure 7C**). Finally, the PLN/SERCA2 ratio was significantly smaller in mouse and rat compared to larger species (**Figure 7C**). These differences in protein expression support a higher versus lower dependence on SERCA2 in mouse as compared to human AMs, respectively. In agreement with the protein expression data, in human AMs we found a significantly lower SERCA-dependent rate of Ca^{2+} removal and a greater fraction of Ca^{2+} extrusion by NCX (**Figures 6E,F**).

Excitation and Ca^{2+} Release at Axial Junctions Occur Instantaneously

Since relatively large LCC clusters are expressed in AT membranes (**Figure 1C**) and AT-localized clusters occur at

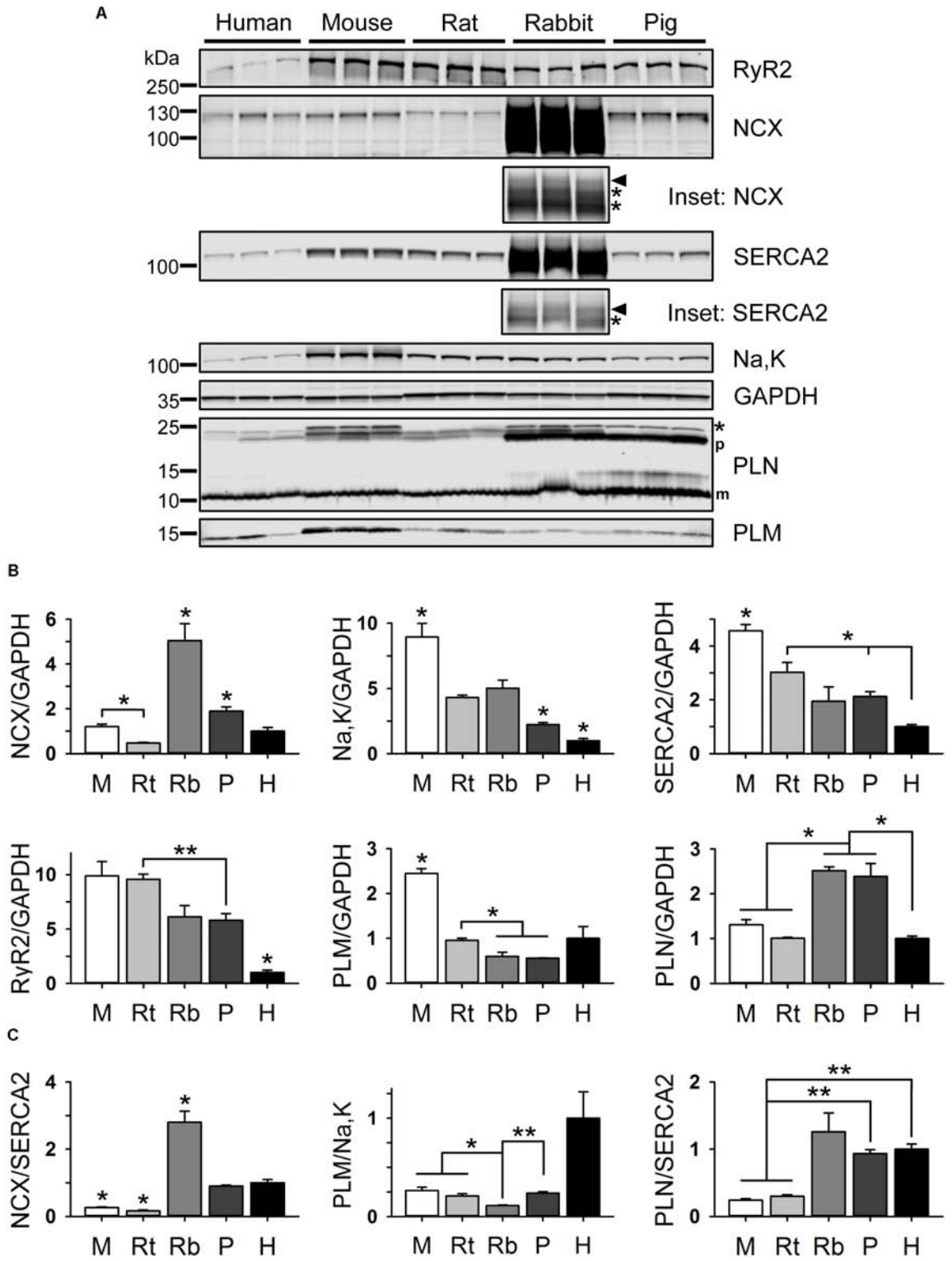

FIGURE 7 | Atrial expression of Ca^{2+} handling proteins in different rodent species, pig, and human. **(A)** Immunoblots comparing the expression of ryanodine receptor 2 (RyR2), sodium-calcium exchanger 1 (NCX), SR Ca^{2+}-ATPase 2 (SERCA2), sodium-potassium ATPase α1 subunit (Na,K), glyceraldehyde 3-phosphate dehydrogenase (GAPDH), phospholamban (PLN), and phospholemman (PLM). Insets document the intensity-corrected rabbit NCX and SERCA2 as used for quantification (arrowheads) and additional rabbit-specific antibody cross-reactions (asterisks). Also, the PLN pentameric (p) and monomeric (m) bands are indicated. See **Supplementary Figure S4** for full blots and **Supplementary Table S1** for clinical patient information. Immunoblot/GAPDH signals **(B)** and relative protein ratios **(C)** each normalized to human. M, mouse; Rt, rat; Rb, rabbit; P, pig; H, human. Student's *t*-test $*P < 0.05$, $**P < 0.01$.

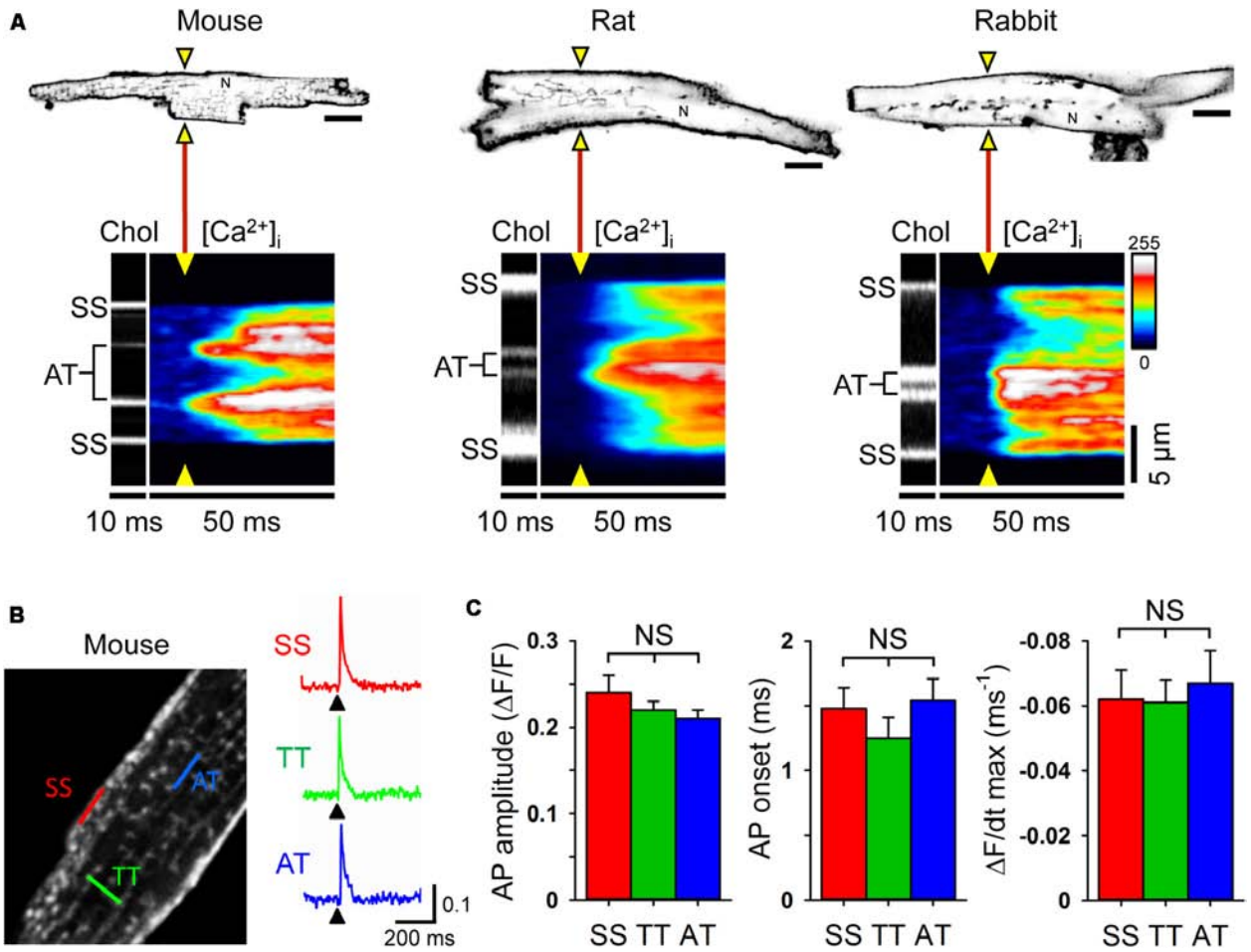

FIGURE 8 | Rapid intracellular Ca^{2+} release at ATs triggered by instantaneous action potential propagation. **(A)** Combined confocal imaging of AT membranes via Chol-PEG-KK114 and $[Ca^{2+}]_i$ via Fluo-4 in mouse, rat and rabbit AM during 0.5 Hz electrical field stimulation. *Top row:* AM imaging plane and position of the laser line (yellow triangles) used to detect intracellular Ca^{2+} release at AT structures (see also section "Materials and Methods"). *Bottom row:* Transversal line scans showing two ATs localized by Chol-PEG-KK114 (Chol) between the surface sarcolemma (SS) boundaries in representative AMs from each species. Note the earliest local Ca^{2+} transient onset and amplitude dynamics upon electrical field excitation (yellow triangles). N, nucleus. Scale bars top row 10 µm. **(B)** *Left:* Exemplar 2-photon recording from a mouse AM. TAT components were labeled with the voltage-sensitive dye di-4-ANE(F)PTEA (2 µM). *Right:* Normalized fluorescence traces ($\Delta F/F_0$) recorded from representative scan regions indicated in color. Simultaneous action potential activation upon stimulation (black arrowheads) is clearly visible in TT and AT structures. **(C)** Grouped bar graphs show no significant differences between AT and other membrane locations for AP amplitude ($\Delta F/F$), AP onset (the time interval between the end of the stimulus and the rise of the fluorescence signal above a threshold of 4% $\Delta F/F$), and maximum slope (ΔF/dt). Sample numbers: n = 13 SS, 44 TT, and 8 AT from 13 AMs and 4 mouse hearts.

a high local density (Brandenburg et al., 2016b), upon electrical excitation CICR may rapidly activate directly adjacent, highly phosphorylated RyR2 clusters through AT junctions (**Figures 5B,C**). To visualize CICR locally at AT junctions, we applied transverse line scanning for combined AT membrane localization and high-resolution intracellular Ca^{2+} imaging in mouse, rat, and rabbit AMs using fluo-4 AM and Chol-PEG-KK114 (1 µM) as membrane stain (**Figure 8A**). Visualization of AT structures during electrical excitation showed rapid yet highly heterogeneous Ca^{2+} release, apparently earlier at AT membranes relative to membrane-free non-junctional sites. In addition, while Ca^{2+} release at the surface sarcolemma appeared to be fast, a delay relative to the more rapid signal activation via CICR at AT sites was apparent in mouse, rat, and rabbit AMs (**Figure 8A**, $[Ca^{2+}]_i$ *transients*). Taken together, excitation rapidly triggers Ca^{2+} release at AT junctions likely through extensive junctional RyR2 clusters that are highly phosphorylated and, thus, more sensitive to activation through CICR.

While ATs represent the most distant network components relative to the outer surface sarcolemma, action potentials are thought to be conducted initially through TTs to downstream membrane network structures. Thus, we wondered if and how action potentials propagate to AT components. To directly visualize the membrane depolarization of AT components, we recorded the local fluorescence signal of the voltage-sensitive dye di-4-ANE(F)PTEA by random access multi-photon microscopy (RAMP). RAMP measurements

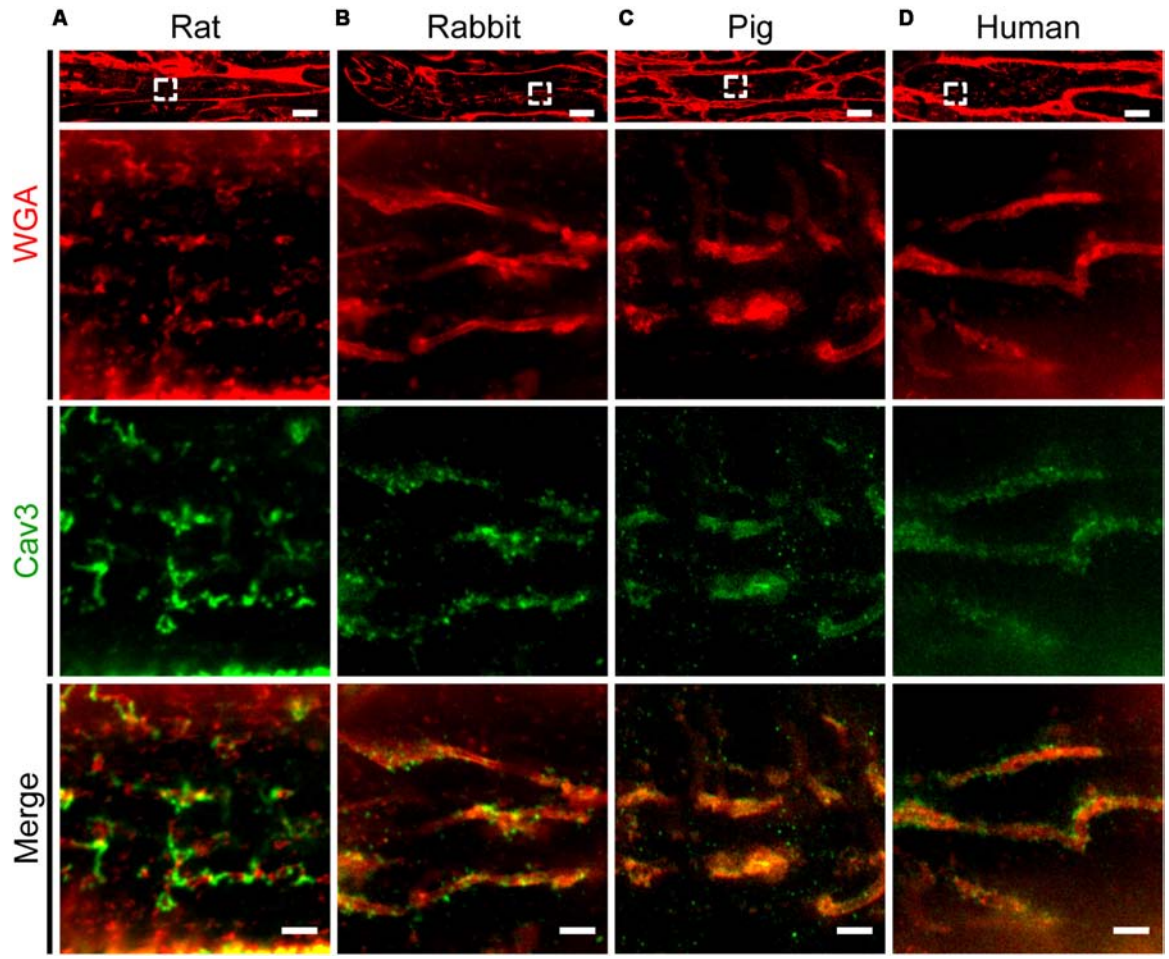

FIGURE 9 | Comparison of TAT structures in rat, rabbit, porcine, and human atrial tissue sections. STED imaging was used to identify individual AMs in **(A)** rat, **(B)** rabbit, **(C)** pig, and **(D)** human atrial tissue co-stained by WGA and Caveolin3 antibody (see methods for details). The magnified regions (dashed boxes) highlight local subcellular structures: WGA signals staining the intraluminal surface of ATs (red), in contrast with punctate Caveolin3 patterns at the abluminal cytosolic AT surface (green). Images are representative of immuno-histological stainings from three animals or patients each. Please see **Supplementary Table S1** for clinical patient information. Scale bars: top 10 μm; magnifications, 1 μm.

allowed to record robust fluorescence signals during steady-state electrical field stimulation at 0.34 Hz throughout the surface sarcolemma at distinct TAT structures in mouse AMs (**Figure 8B**). Apparently, upon field stimulation, action potential depolarization occurred simultaneously at ATs relative to other membrane sites (**Figure 8B**). Analysis of the action potential amplitude, AP onset (the time interval between the end of the stimulus and the rise of the fluorescence signal above a threshold of 4% $\Delta F/F$), and maximal slope did not reveal any significant differences between AT, TT or surface sarcolemmal locations consistent with instantaneous electrical propagation and voltage-dependent activation of CICR throughout AT components (**Figure 8C**). These results underline the tight electrical coupling between the AM surface and its membrane invaginations through a continuous, intact sarcolemmal system and, furthermore, suggest a space constant of the TAT membrane network larger than the cellular dimensions in line with previous findings in ventricular cardiomyocytes (Kong et al., 2017; Scardigli et al., 2017).

Abundant AT Structures in Human, Porcine and Rodent Atrial Tissues

Previous studies established protocols to stain TAT components by wheat germ agglutinin (WGA) in histological sections of larger species including human (Richards et al., 2011). Specifically, WGA labels *N*-acetylglucosamine, neuraminic, and sialic acid side chains on the extracellular membrane surface of cardiomyocytes (Arakel et al., 2014). Here, we adapted the WGA staining for paraffin-embedded atrial tissue sections from rat, rabbit, pig, and human atrial samples for STED imaging. In rat atrial tissue sections we observed discrete intracellular WGA signal spots, alternating with Caveolin3 positive domains on TAT structures (**Figure 9A**). In contrast to rat, atrial tissue sections from rabbit and pig showed a more extensive pattern of WGA

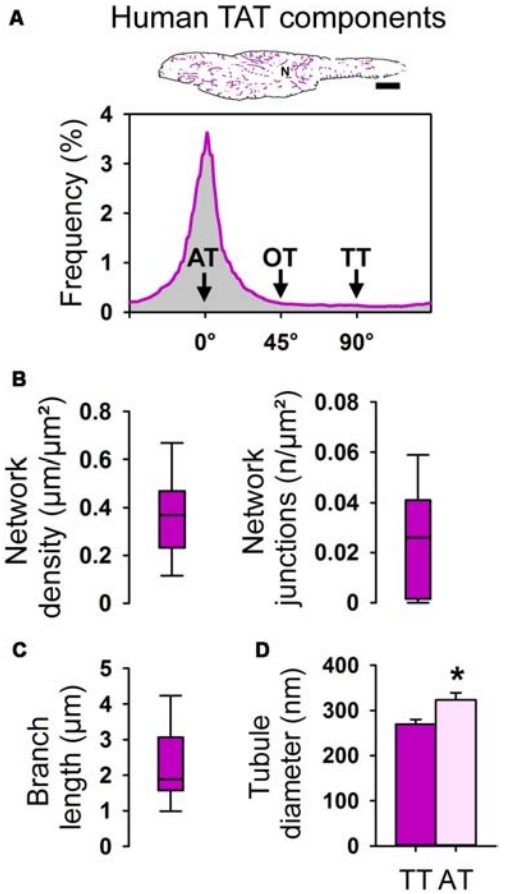

FIGURE 10 | Component-specific TAT analysis of atrial myocytes in human tissue samples. **(A)** Skeleton representation (pink) of the WGA stained human AM from **Figure 9D**. Histogram analysis showing the frequency distribution of individual TAT components. The major peak represents abundant ATs (0°). N, nucleus. Scale bar 10 µm. **(B)** Box plots summarizing the TAT network density and the number of network junctions. **(C)** Box plot showing the branch length in human AM. Boxes represent the median, lower and upper quartiles, and whiskers the 5th and the 95th percentiles. $n = 21$ AMs in histological tissue sections from three patients. **(D)** Bar graph summarizing the AT and TT diameter (FWHM) as determined in WGA stained AMs in human tissue sections. $n = 35$ ATs and 17 TTs from 22 human AMs in tissue sections. Please see **Supplementary Table S1** for clinical patient information. Student's *t*-test $^*P < 0.05$.

labeling inside the lumen of AT structures, tightly surrounded by punctate Caveolin3 signals on the abluminal cytosolic surface (**Figures 9B,C**). Importantly, similar to the pattern in rabbit and pig, we identified extensively WGA-labeled AT components in human right atrial tissue sections (**Figure 9D**, *WGA*). Similar to rabbit and pig, discrete abluminal Caveolin3 signals were tightly associated with the AT structures in human atrial sections (**Figures 9B–D**, *merge*).

Next, the WGA-labeled TAT network signals, visualized by STED in individual human AMs in tissue sections, were extracted as skeleton information and analyzed as follows. First, screening of human atrial tissue samples for individual AMs with the major longitudinal cell axis in the imaging plane through the central nucleus was used to visualize TAT skeletons (**Figure 10A**, *top*). Second, the skeletonized image information was analyzed to determine the orientation and frequency of individual TAT network components (**Figure 10A**, *bottom*). The frequency histogram clearly shows a major peak confirming abundant AT structures in human AMs of atrial tissue sections. We note that the expected minor peak at 90° due to TT components, as shown in isolated live rodent AMs (**Figure 3B**), was lost, which can be attributed to an increased 3D variability of AM orientations in atrial tissue. Consequently, we studied the nature of individual TT components in transversally cut AMs in atrial tissue sections. Interestingly, while occasional TT invaginations were clearly identified in AM cross-sections in atrial tissue, the path of TTs from the lateral surface membrane was often oblique, indicating additional limitations for the TT specific component analysis in atrial tissue sections (**Supplementary Figure S5**).

In human atrial tissue sections we determined an average TAT network density of 0.368 $\mu m/\mu m^2$ (median 0.369 $\mu m/\mu m^2$) and 0.023/μm^2 (median 0.026 $n/\mu m^2$) for the number of network junctions (**Figure 10B**). The average branch length amounted to 2.29 µm (median 1.88 µm) in human AMs in tissue sections (**Figure 10C**). Finally, *in situ* STED nanoscopy was used to measure the cross-sectional diameters of individual AT and TT components. Strikingly, the width (FWHM) of ATs was significantly larger compared to TTs in human AMs in WGA-stained tissue sections (**Figure 10D**). In summary, human AMs contain TAT networks that consist mainly of voluminous AT structures consistent in width with intact AT structures observed in isolated mouse and rat AMs.

DISCUSSION

Across five species, from mouse to human, we identify continuous intracellular tubule networks in AMs characterized by: (1) abundant AT structures oriented along the main cell axis and (2) connected to the AM surface through sparse TT components. During electrical stimulation, (3) AP depolarization at ATs was instantaneous relative to the surface sarcolemma and contributed to (4) rapid CICR activation at ATs. In line with a previously proposed model of atrial super-hub Ca^{2+} signaling, we confirmed that (5) AT structures exhibit significantly larger diameters compared with TTs in most species except rabbit; (6) ATs are spatially associated with unusually large RyR2 clusters, and (7) junctional RyR2 clusters are constitutively highly phosphorylated. While these observations present a robust basis to explain AT-dependent, rapid intracellular Ca^{2+} signaling in AMs, they were only possible through membrane-preserving isolation and staining protocols, here visualized through a photostable fluorescent cholesterol dye and live cell STED nanoscopy. Importantly, the concept of AT-dominated TAT networks as atria-specific mechanism of excitation-contraction coupling appears to be conserved throughout the species investigated. In line with the recently discovered physiological significance of ATs for graded intracellular CICR regulation (Brandenburg et al., 2016b), we propose that super-hub Ca^{2+} signaling represents a structurally

conserved atrial mechanism that may fundamentally change our perspectives about atrial function through specific subcellular contractile activation mechanisms in health and disease.

In contrast, earlier *and* recent studies could not identify any TAT components in isolated rat, rabbit, or cat AMs (Huser et al., 1996; Brette et al., 2002; Thul et al., 2012; Greiser et al., 2014; Maxwell and Blatter, 2017). Accordingly, the TAT volume ratio quantified in rabbit atrial as compared to ventricular thin sections by electron microscopy was over ∼10-fold lower (Tidball et al., 1991). Together, such imaging data led to influential theories about physiological and disease mechanisms, for example how intracellular Ca^{2+} signaling is altered due to atrial fibrillation or rapid pacing, usually based on models devoid of TTs with slow inward propagated Ca^{2+} transients as reviewed in detail (Bootman et al., 2011; Greiser et al., 2011; Schotten et al., 2011; Heijman et al., 2016; Goette et al., 2017; Greiser, 2017). However, confocal imaging studies also showed clear evidence of TAT networks yet only in fractions of isolated rat AMs, generally attributed to a larger cell width (Kirk et al., 2003; Smyrnias et al., 2010; Johnsen et al., 2013; Glukhov et al., 2015). Furthermore, both AT and TT components were described in atrial EM sections of the mouse and rat (Forssmann and Girardier, 1970; Forbes et al., 1984). Accordingly, dense TAT structures were shown in isolated mouse AMs (Greiser et al., 2014). Finally, atrial TT structures were documented in larger mammalian species including dog (Wakili et al., 2010), sheep (Dibb et al., 2009; Lenaerts et al., 2009), pig (Frisk et al., 2014; Gadeberg et al., 2016), cow, and horse (Richards et al., 2011). Of note, TTs were either absent in isolated human AMs (Greiser et al., 2014) or present in human atrial tissue sections (Richards et al., 2011). While Richards et al. developed a WGA-based protocol for human AMs to assess the TT density, they did not analyze the different tubule components, particularly not ATs in histological tissue sections with longitudinally aligned AMs. Taken together, the nature of the atrial sample (i.e., isolated cell or tissue section), cell isolation or tissue dissection protocols, imaging techniques to identify TAT structures in isolated AMs or atrial tissue, and other factors can contribute significantly to the outcome of quantitative TAT imaging studies.

Here, we developed new strategies for high-resolution imaging of TAT networks in isolated AMs and tissue sections. A bright and photostable fluorophore (i.e., KK114) was linked by a large extracellular PEG domain to cholesterol to prevent dye internalization and stably label the extracellular membrane leaflet. While bulk membrane labeling at higher concentrations (5 μM) showed continuous TAT network structures throughout different species except human, live cell STED nanoscopy using significantly lower concentrations (250 nM) directly resolved cholesterol nanodomains in AT structures (**Figure 1**). Importantly, while continuous tubule signals are generally interpreted as healthy intact membrane structures in confocal images, STED nanoscopy clearly showed local membrane fragmentation events, directly documenting membrane disruptions due to on-purpose suboptimal rabbit AM isolation (**Supplementary Figure S2**). Here, global and local AT fragmentation and membrane aggregation were evidenced in rabbit AMs due to absent heparin pre-treatment. Furthermore, human AMs isolated by mechanical tissue dissection showed only residual AT and TT fragments (**Supplementary Figure S3**), whereas continuous cell-wide TAT components were identified in AMs visualized individually in human tissue sections (**Figure 10A**). Notably, a confocal live imaging study found no TAT structures in isolated human AMs previously (Greiser et al., 2014). Thus, for detailed subcellular TAT studies in AMs, labeling of intact TAT membranes combined with live cell nanoscopy provides a powerful strategy to directly identify intact tubule structures.

Cholesterol accounts for 25–50% of the total lipid content in eukaryotic membranes (Bloch, 1989). Although cholesterol is an abundant membrane component, it is concentrated in cholesterol-rich domains, also known as membrane rafts (Simons and Ikonen, 1997). In VMs cholesterol-rich domains were established in caveolae, where Caveolin3 binds cholesterol with high affinity (Parton and Simons, 2007). Importantly, in AMs we observed AT structures densely populated by cholesterol-rich nanodomains (**Figure 1B**) and frequent Caveolin3 clusters (**Figure 1C**). However, in the TTs of VMs few caveolae-like structures exist (Wagner et al., 2012; Burton et al., 2017) and AT membranes in AMs are also devoid of classic caveolae (Brandenburg et al., 2016b). Moreover, cholesterol-rich domains interact functionally with $Ca_v1.2$ LCCs in VMs (Balijepalli et al., 2006) and AMs (Glukhov et al., 2015). Chemical depletion of cholesterol in AMs decreased LCC function in caveolae but not at TT orifices (Glukhov et al., 2015) and altered TTs structurally (Carozzi et al., 2000). Interestingly, while $Ca_v1.2$ and Caveolin3 clusters were closely associated, STED nanoscopy showed no major co-localization (**Figure 1C**), which may indicate a modular organization of two directly adjacent nanodomains. Interestingly, in skeletal muscle cells, the highest density of LCCs was determined in TAT membranes (Almers et al., 1981; Jorgensen et al., 1989). Future studies may elucidate the impact of cholesterol-rich nanodomains in AT membranes on local nanodomain functions.

High-resolution scanning of LCC ion conductance (SICM) at the lateral membrane of AMs has shown two major, equally distributed functional surface locations: the membrane crest and TT orifices (Glukhov et al., 2015). While LCCs that contain the pore-forming $Ca_v1.2(\alpha1C)$ subunit are commonly expressed in cardiomyocytes, expression of the $Ca_v1.3(\alpha1D)$ isoform is highly selective, for example restricted to AMs and the sinoatrial node (Zhang et al., 2005). In this context, a unique electrophysiological and molecular identity of AMs was uncovered through knockout of the pore-forming $Ca_v1.3(\alpha1D)$ subunit, which revealed a lower activation threshold compared to $Ca_v1.2(\alpha1C)$ (Zhang et al., 2005). Interestingly, the SANDD syndrome, diagnosed in patients with sinoatrial node dysfunction and deafness, is caused by genetic defects of the $Ca_v1.3(\alpha1D)$ isoform (Baig et al., 2011). Previously we showed in mouse AMs that ATs contain a significantly higher number and density of $Ca_v1.2$ clusters compared to TTs, suggesting important structural and functional roles of AT junctions during CICR (Brandenburg et al., 2016b). Here, we identified both large $Ca_v1.2$ and $Ca_v1.3$ LCC clusters on AT structures (**Figures 1C**, **2A**) and adjacent highly phosphorylated RyR2 clusters using STED nanoscopy (**Figure 5**).

Finally, the same antibody showed presynaptic $Ca_v1.3$ clusters in IHCs isolated from the inner ear of mice (**Figure 2B**). Given that $Ca_v1.3(\alpha1D)$ knockout in mice is viable (Platzer et al., 2000; Zhang et al., 2005) and reproduces key aspects of the SANDD syndrome, future studies will need to characterize the yet unknown role of $Ca_v1.3$ LCCs in ATs and how AM function might be affected by knockout or SANDD mutations.

In addition to voltage-dependent LCC activation, ATs are functionally coupled to unusually large RyR2 clusters in axial couplons, extensive junctional nanodomains that allow for rapid CICR onset (Brandenburg et al., 2016b) and characteristically shape atrial Ca^{2+} transients (**Figure 8A**). STED nanoscopy confirmed extensive RyR2 clusters at AT membranes that were highly phosphorylated by PKA *in situ*, and hence functionally different from directly neighboring minimally phosphorylated non-junctional RyR2 clusters (**Figure 5**). The AM-specific PKA phosphorylation pattern correlated not only with substantially earlier Ca^{2+} release from AT-associated RyR2 clusters (**Figure 8A**), but also with faster central sarcomere shortening as shown previously (Brandenburg et al., 2016b). While RyR2 clusters have been studied extensively in VMs, the distinct morphology of atrial RyR2 clusters and their organization in AT junctions warrants further investigation. Moreover, ultrastructural and close-to-native data about individual RyR2 clusters can inform direct structure-function analysis of individual clusters, for instance, how 3D spatial cluster arrangements control local Ca^{2+} release events as shown by mathematical modeling (Walker et al., 2014). Of note, a recent quantitative mathematical model of highly as well as minimally phosphorylated RyR2 clusters has reproduced AT-associated Ca^{2+} mega-sparks similar to biological Ca^{2+} signals observed in isolated AMs, and in line with the super-hub Ca^{2+} signaling concept (Brandenburg et al., 2016b). Future studies might employ the recently established STED Ca^{2+} imaging (Neef et al., 2018) to gain further experimental insight into the nanoscale Ca^{2+} signals at super-hub junctions at ATs.

In summary, live cell imaging by STED nanoscopy combined with customized membrane-preserving workflows and cholesterol-based staining has enabled direct visualization of AT structures throughout AMs. Furthermore, AM-specific TAT network structures were confirmed in atrial tissue sections of the rodent, porcine and human heart. Interestingly, based on collagenase perfusion, we consistently identified cell-wide TAT membrane networks in isolated AMs from mouse, rat, and rabbit hearts. Moreover, direct visualization of individual TAT components by STED nanoscopy showed abundant cholesterol nanodomains in AT membranes as well as local AT fragmentations in the absence of heparin pre-treatment. While AT membrane structures are abundant in AMs, they contain large LCC clusters and interact with extensive junctional RyR2 clusters. The nature of this complex super-hub protein-membrane assembly may support essential functions, in particular maintain and adapt atrial excitation-contraction coupling. Importantly, our finding of extensive junctional highphos RyR2 clusters will be instrumental to elucidate the differential nanodomain physiology and pharmacology of associated G protein-coupled receptors and ion channels associated with ATs. Notably, in samples from patients with chronic atrial fibrillation both LCC loss-of-function and RyR2 gain-of-function are now commonly observed (Vest et al., 2005; Schotten et al., 2011). In particular, RyR2 channel dysfunction was originally identified in the atria of elderly patients with chronic atrial fibrillation (Vest et al., 2005) and more recently after short-term tachypacing in rabbit atria (Greiser et al., 2014). Within this context, the causal relation between AT structures and highly phosphorylated junctional RyR2 clusters significantly strengthens recent rationales to identify early atria-specific disease mechanisms that may underlie atrial cardiomyopathies (Goette et al., 2017), and, ultimately, facilitate the development of new therapeutic rationales.

MATERIALS AND METHODS

Mouse, Rat, and Rabbit Samples

Unless indicated otherwise, experiments were based on isolated AMs or atrial tissue from the hearts of different species: (a) 12–16 weeks old female mice in the C57BL/6N background; (b) 16–20 weeks old female Wistar rats; (c) female New Zealand White rabbits 17 weeks old with a body weight of 3.0 to 3.5 kg; and (d) 3-month-old healthy German landrace pigs of either gender with body weights of 40–45 kg. Mice and rats were euthanized by cervical dislocation under 1.5–2% isoflurane anesthesia; rabbits by pentobarbital (400 mg/kg). The generation of $Ryr2^{S2808A/S2808A}$ knockin mice was described previously (Lehnart et al., 2005); for genotyping we used the following primer pairs: F 5′-ATCCCGAGGTAATCAGGTTTCT-3′, R 5′-AGTTGGGTTCAAAGTTCTAGGC-3′; and PCR product digestion by *Fsp I* restriction enzyme (New England Biolabs). This study was carried out according to guidelines for the care and use of laboratory animals following directive 2010/63/EU of the European Parliament and the Council of the European Union, Strasbourg, France, and in keeping with NIH guidelines. After mouse, rat, or rabbit euthanasia, the heart was rapidly extracted for atrial myocyte isolation (see below). All animal procedures followed institutional rules (Tötungsanzeige) as reviewed by the IACUC and the Veterinarian State Authority (LAVES, Oldenburg, Germany).

Porcine Atrial Tissue Samples

Left atrial tissue was obtained from 3-month-old healthy German landrace pigs of either gender (n = 3, body weight 40–45 kg). Anesthesia was performed using azaperone, midazolam and propofol and isoflurane as reported (Schmidt et al., 2014). Pigs were sacrificed with intracardiac injection of KCl 7.45% and hearts were removed quickly. This study was performed in accordance with the Guide for the Care and Use of Laboratory Animals as adopted and promulgated by the United States National Institutes of Health (NIH publication No. 86-23, revised 1985), and the current version of the German Law on the Protection of Animals was followed (approval number G296/14).

Human Atrial Samples

Human atrial tissue samples were obtained from the right atrial appendage of patients in sinus rhythm and a negative history for atrial fibrillation, undergoing open heart surgery for bypass grafting or valve replacement, respectively. Please see **Supplementary Table S1** for detailed clinical patient information. All patients gave written informed consent. The protocol to use human atrial samples was reviewed and approved by the ethics committee of the University Medical Center Göttingen (No. 14/9/11).

Chol-PEG-KK114 Synthesis

The fluorescent Cholesterol analog Chol-PEG-KK114 was prepared by coupling the fluorescent dye KK114 (Kolmakov et al., 2010) to a Cholesterol-Polyethylene Glycol (Chol-PEG) derivative as follows. 4 mg (4 mM) of the dye-NHS ester were dissolved in dry *N*,*N*-dimethylformamide (DMF, 0.1 mL). A solution of 16 mg (6 μM) of Chol-PEG-NH2 (PG2-AMCS, NANOCS Inc., United States) in dry DMF (0.2 mL) and 5 μL (36 μM) trimethylamine were added and the reaction mixture was stirred for 40 min at room temperature. Then the reaction mixture was warmed up to 36°C and stirred for an additional 15 min. The reaction was controlled by thin-layer chromatography (TLC). After the volatile components were removed *in vacuo*, the product was isolated by flash column chromatography on SiO_2 using Biotage Isolera flash purification system (Biotage SNAP Ultra 10 g cartridge; isocratic elution with 25% methanol and 5% water in chloroform). This yielded 5 mg (22%) of blue solid product. Analytical TLC was performed on ready-to-use silica gel 60 (F_{254}) aluminum plates (Merck). Liquid chromatography (HPLC) was performed using a Knauer Smartline liquid chromatography system consisting of: two pumps (1000), a UV-detector 2500, a column thermostat 4000, a mixing chamber and injection valve with a 20 μL loop for the analytical column Eurospher 100 C18 (10 μm, 150 mm × 4 mm), and a 6-port-3-channel switching valve. A: acetonitrile + 0.1% v/v TFA, solvent B: H_2O + 0.1% v/v TFA; temperature 25°C. HPLC: t_R = 9.2 min (A/B: 30/70 – 100/0 in 15 min, 1.2 ml/min, 254 nm). Mass spectra were recorded on a MICROTOF spectrometer (Bruker) equipped with an ESI ion source (Apollo) and a direct injector with the LC autosampler Agilent RR 1200. ESI-MS, negative mode: *m/z* (rel. int., %) = 1742.5 (40) ± n × 22 $[M-3H+Na]^{2-}$, where n = 0–8 is the number of repeating ethylene oxide units OCH_2CH_2. The polydispersity of the copolymer reflects that of the PEG used in the synthesis.

Atrial Myocyte Isolation From Mouse, Rat, and Rabbit Hearts

The AM isolation protocol used a modified Langendorff setup and cardiac perfusion starting with a nominally Ca^{2+} free buffer (in mM: NaCl 120.4, KCl 14.7, KH_2PO_4 0.6, Na_2HPO_4 0.6, $MgSO_4$ 1.2, HEPES 10, $NaHCO_3$ 4.6, taurine 30, 2,3-butanedione-monoxime 10, glucose 5.5, pH 7.4 with NaOH) followed by collagenase type II containing buffer for digestion of the extracellular matrix as previously described (Wagner et al., 2014; Brandenburg et al., 2016b). For mouse, rat, or rabbit hearts, 21 G, 17 G, or 14 G cannulas were used for aortic cannulation and perfusion at 4, 8, or 16 ml/min, respectively.

Live Cell STED Nanoscopy

For superresolution imaging of TAT structures, isolated AMs were plated on laminin-coated coverslips and incubated for 10 min in perfusion buffer containing 5 μM Chol-PEG-KK114 for bulk membrane labeling. In addition, AMs were incubated for 15 min with 250 nM Chol-PEG-KK114 to visualize individual cholesterol-rich domains inside TAT structures. Following incubation, isolated AMs were washed three times in perfusion buffer and imaged at room temperature (20°C). A Ca^{2+} free perfusion buffer and 2,3-butanedione-monoxime were used to inhibit AM contractions. For imaging we used a Leica TCS SP8 STED system with a HC PL APO C2S 100×/1.40 oil objective. Microscope parameters were optimized for KK114: pixel size 16.23 nm × 16.23 nm, pixel dwell time of 400 ns, scanning speed 600 Hz, 32× line averaging, excitation using a white light laser at 635 nm, a STED depletion laser at 775 nm, and fluorescence detection at 650–700 nm. The STED laser power was adjusted to maximize resolution. In parallel, confocal imaging was applied for cell-wide TAT analysis at a pixel size of 114 nm × 114 nm with 16× line averaging. Raw images were processed in ImageJ/Fiji[1]. ROIs from 30 mouse AMs used for TAT network analysis in **Figure 3** are available for download through the online link: https://hdl.handle.net/21.11101/0000-0007-C9D2-9; doi: 10.5281/zenodo.1311573. Furthermore, images in **Figures 1B**, **4A,B** were deconvolved with Huygens Professional 17.10 software for visualization (Scientific Volume Imaging, Netherlands[2]). The fluorescence intensity plot profile of the cholesterol-rich nanodomain in **Figure 1B** was fitted by a 2D Gaussian function using OriginPro 8.5G followed by FWHM computation.

TAT Network Analysis

2D skeletons were extracted from confocal live cell images of TAT structures stained with Chol-PEG-KK114 using ImageJ/Fiji as previously described (Brandenburg et al., 2016b). Cells were aligned and ROIs were selected excluding the surface membrane and nuclei. After background subtraction and smoothing, ROIs were binarized using a predefined threshold and consecutively skeletonized. Network length and the number of network junctions were calculated in ImageJ/Fiji using the plugin Analyze Skeleton (2D/3D). TAT network component orientations were analyzed via the plugin Directionality.

Tubule Diameter Measurements

Chol-PEG-KK114 stained STED images of ATs and TTs were aligned. ROIs of 50 pixels × 30 pixels (pixel size 16.23 nm × 16.23 nm) were manually selected and used for fluorescence intensity plot profiling. AT and TT signal profiles were fitted by a 2-peak Gaussian function using OriginPro 8.5G to calculate FWHM as a measure of tubule width.

[1] http://imagej.nih.gov/ij/

[2] http://svi.nl

Histology of Atrial Tissue

For immunofluorescence labeling, atrial tissues from rat, rabbit, pig, and human were fixed in 4% PFA over night, embebbed in paraffin, cut into 4 μm thick histological sections, deparaffinized, rehydrated, and the antigen unmasked with 10 mM sodium-citrate buffer prior to WGA or antibody incubation.

Immunofluorescence STED Nanoscopy

Isolated cardiomyocytes were plated on laminin-coated coverslips and fixed in 4% PFA for 5 min followed by three PBS washing steps. Next, isolated myocytes or unmasked histological tissue sections were incubated in blocking/permeabilization buffer over night (10% bovine calf serum, 0.2% Triton in PBS). Primary antibodies were diluted in blocking buffer and incubated over night at 4°C as follows: RyR2 1:500 (HPA020028, Sigma-Aldrich); RyR2 1:500 (MA3-916, Thermo Fisher Scientific); RyR2-pS2808 1:250 (A010-30, Badrilla Ltd.); Caveolin3 1:500 (610421, BD Biosciences); $Ca_v1.2$ 1:250 (ACC-003, Alomone labs); $Ca_v1.3$ 1:100 (ACC-005, Alomone labs). For histological sections, the Caveolin3 antibody was used at a dilution of 1:250. Subsequently, samples were washed three times in blocking buffer and incubated with secondary antibodies diluted 1:1000 for cells or 1:300 for tissue sections for 2 h at room temperature: anti-rabbit (STAR 635P, Abberior) and anti-mouse (STAR 580, Abberior). Unconjugated WGA (VEC-L-1020-10, Biozol) was labeled by NHS ester (STAR 635P, Abberior; 07679, Sigma-Aldrich) and incubated at a concentration of ≈10 μM with samples in blocking buffer for 2 h in combination with the secondary anti-mouse antibody (STAR 580, Abberior). After washing, samples were embedded in mounting medium (ProLong Gold antifade reagent, Thermo Fisher Scientific). A Leica TCS SP8 STED microscope was used for superresolution imaging using the parameters stated above. STAR 635P and STAR 580 fluorophore emission was detected between 650–700 nm and 600–630 nm, respectively. Raw images were processed in ImageJ/Fiji.

Immunohistochemistry of Inner Hair Cells

Apical cochlear turns were fixed in methanol for 20 min at −20°C immediately after dissection. The tissue was then washed three times for 10 min in PBS and incubated for 1 h in goat serum dilution buffer (GSDB) (16% normal goat serum, 450 mM NaCl, 0.3 Triton X-100, 20 mM phosphate buffer, pH 7.4) in a wet chamber at room temperature. Primary antibodies (mouse anti-Sap7f407 to bassoon, 1:600, Abcam ab82958, and rabbit anti-$Ca_v1.3$, 1:75, Alomone Labs ACC-005) were diluted in GSDB and applied overnight at 4°C in a wet chamber. After washing three times for 10 min (wash buffer: 450 mM NaCl, 20 mM phosphate buffer, and 0.3% Triton X-100), the tissue was incubated with secondary antibodies [STAR 580-tagged goat-anti-rabbit or goat-anti-mouse (1:200, Abberior 2-0002-005-1 or 2-0012-005-8)], and STAR 635P-tagged goat-anti-mouse or goat-anti-rabbit (1:200, Abberior 2-0002-007-5 or 2-0012-007-2) in GSDB in a wet light-protected chamber for 1 h at room temperature. The preparations were then washed three times for 10 min in wash buffer and one time for 10 min in 5 mM phosphate buffer, placed onto glass microscope slides with a drop of fluorescence mounting medium (Mowiol), and covered with thin glass coverslips. Images were acquired on an Abberior Instruments Expert Line 775 nm 2-color STED microscope, with excitation lasers at 561 and 633 nm and a STED laser at 775 nm, 1.2 W, using a 1.4 NA 100× oil immersion objective, with pixel sizes of 20 nm × 20 nm.

Random Access Multi-Photon Microscopy (RAMP)

Isolated cardiomyocytes were loaded in Tyrode's solution with 10 μM of blebbistatin and 4 μM of cytochalasin D both dissolved in DMSO. 2 μg/mL of di-4-AN(F)EPPTEA (Yan et al., 2012) dissolved in ethanol were added for 15 min, and then cells were resuspended in fresh Tyrode's buffer containing blebbistatin and cytochalasin D. Loaded AM preparations were used for RAMP experiments within 30 min. The staining and imaging sessions were performed at room temperature. The RAMP imaging system has been described previously in detail (Sacconi et al., 2012; Crocini et al., 2014, 2016). Briefly, a 1064 nm fiber laser provides the excitation light. The scanning head is provided through two orthogonally oriented acousto-optic deflectors (AODs) and the excitation light is focused onto the specimen by the objective lens (60 × 1.4 NA). The two-photon fluorescence signal is collected forward and backward by an oil immersion condenser (1.4 NA) and the objective, respectively. Fluorescence signals are detected by two photomultiplier tubes (H7422, Hamamatsu) using an emission filter of 655 ± 20 nm. Measurements are performed during steady-state stimulation (0.34 Hz). Cells are field-stimulated using two parallel platinum wires (250 μm in diameter) placed at a distance of 6.3 mm. Square pulses of 10–20 V and duration of 3 ms were used to reach action potential threshold. In a typical measurement, we sampled 5–6 different sarcolemmal sites through 10 subsequent trials. The length of the scanned lines ranges from 2 to 10 μm with an integration time per membrane pass of ∼100–200 μs, leading to a temporal resolution of 0.5–1.5 ms.

Combined Imaging of TAT Membranes and Intracellular Ca^{2+}

Transverse line scan imaging of AMs plated on laminin-coated coverslips was performed with a Zeiss LSM 880 confocal microscope and a Plan-Apochromat 63×/1.40 oil objective. The membrane dye Chol-PEG-KK114 (10 min incubation of the cells at 1 μM) and the Ca^{2+} indicator Fluo-4 AM (30 min incubation of the cells at 10 μM; Thermo Fisher Scientific) signals were recorded as previously described (Brandenburg et al., 2016b) at room temperature in Tyrode's solution (in mM: NaCl 140, KCl 5.4, $MgCl_2$ 1.2, HEPES 10, Na_2HPO_4 0.33, $CaCl_2$ 1, glucose 10; pH 7,4 with NaOH). Chol-PEG-KK114 was excited at 633 nm and detected between 650 and 700 nm. AMs were field-stimulated at 0.5 Hz using 3 ms steps to 23 V. Transverse lines of 20 μm (100 pixels) were scanned at 650 Hz. ImageJ/Fiji was used for image processing.

Combined Patch-Clamp and Intracellular [Ca^{2+}] Measurements

Human AMs were isolated from right atrial tissue samples using protocols established previously (Voigt et al., 2013, 2014). Please see **Supplementary Table S1** for clinical patient information. Membrane currents were measured at 37°C in whole-cell ruptured-patch configuration using voltage-clamp with simultaneous intracellular [Ca^{2+}] measurements. pClamp-Software (V10.7, Molecular Devices, Sunnyvale, CA, United States) was used for data acquisition and analysis. Intracellular [Ca^{2+}] was quantified using 10 μM of the Fluo-3-acetoxymethyl ester (Fluo-3 AM; Invitrogen, Carlsbad, CA, United States) with 10 min loading and 30 min de-esterification (Grynkiewicz et al., 1985). In addition, Fluo-3 was included into the electrode solution containing (in mM): EGTA 0.02, Fluo-3 0.1 (Invitrogen), GTP-Tris 0.1, HEPES 10, K-aspartate 92, KCl 48, Mg-ATP 1, Na_2-ATP 4; pH7.2. Borosilicate glass microelectrodes had tip resistances of 2–4 MΩ when filled with the pipette solution. Seal-resistances were 4–8 GΩ. For voltage-clamp experiments, the series resistance and cell capacitance were compensated. AMs were superfused at 37°C with a bath solution containing (in mM): $CaCl_2$ 1, glucose 10, HEPES 10, KCl 4, $MgCl_2$ 1, NaCl 140, probenecid 2, pH7.4. K^+ currents were blocked by 4-aminopyridine (5 mM) and $BaCl_2$ (0.1 mM) in the bath solution. L-type Ca^{2+}-current ($I_{Ca,L}$) and corresponding $[Ca^{2+}]_i$ transients were recorded simultaneously, using a holding potential of −80 mV and ramp pulse depolarization to −40 mV for 500 ms in mouse AMs or 100 ms in human AMs to inactivate the fast Na^+-current followed by a 100 ms test pulse to +10 mV at 0.5 Hz. Membrane current amplitude and integrated membrane current were normalized to cell capacitance as a measure of the cell surface area for atrial myocytes from different species. The sarcoplasmic reticulum (SR) Ca^{2+} content was determined by the application of 10 mM caffeine at a holding potential of −80 mV, with the resulting NCX current integrated and normalized to capacitance measurements from cells. Corresponding diastolic calcium removal mechanisms, i.e., SERCA and non-SERCA flux components (NCX, PMCA, and mitochondria) were mathematically interpolated from caffeine induced $[Ca^{2+}]_i$ transients and systolic $[Ca^{2+}]_i$ transients as described.

Protein Analysis

For protein analysis, mouse and rat samples were selected sex-mixed. Atrial tissue was directly frozen in liquid nitrogen and stored at −80°C. Then, atrial tissues were homogenized in ice-cold homogenization buffer [HEPES 10 mM, sucrose 300 mM, NaCl 150 mM, EGTA 1 mM, $CaCl_2$ 2 mM, Triton X-100 0.5% (v/v), protease and phosphatase inhibitor mix (Roche), pH 7.4] using a Miccra D-1 homogenizer. The homogenized tissues were solubilized for 30 min at 4°C by rotation and subsequently centrifuged at 8000 × *g* for 10 min at 4°C to obtain the post-nuclear fraction. Protein concentrations were determined with the Pierce BCA protein Assay Kit (Thermo Fisher Scientific). For Western blots 20 μg of protein per lane were resolved by SDS-PAGE using 4–20% Tris-HCl protein gels (3450033, Bio-Rad). Proteins were transferred onto PVDF membranes (0.45 μm, Immobilon-FL, Merck Millipore) using the Bio-Rad criterion blotter (plate electrodes). Membranes were blocked for 1 h in 5% (w/v) non-fat milk in Tris-buffered saline with 0.05% (v/v) Tween 20, and incubated with the primary antibodies overnight at 4°C as follows: RyR2 1:2500 (HPA020028, Sigma-Aldrich); NCX 1:1000 (11-13, Swant); SERCA2 1:2000 (A010-20, Badrilla); Na,K-ATPase α1 subunit 1:500 (sc-21712, Santa-Cruz); GAPDH 1:160,000 (5G4 Mab 6C5, HyTest); PLN 1:2500 (ab2865, Abcam); PLM 1:1000 (13721-1-AP, Proteintech). After washing, blots were incubated with fluorescence-labeled anti-rabbit or anti-mouse secondary antibodies at a dilution of 1:10,000 for a minimum period of 1 h at room temperature (LI-COR, P/N 926-32212, P/N 926-68072, P/N 926-32213, P/N 926-68073). Membranes were developed with the Odyssey CLx imaging system (LI-COR). Band densitometry analysis was performed using Image Studio Lite Version 5.2 and normalized to GAPDH.

Statistics

Statistical analyses were performed with Microsoft Excel 2010, GraphPad Prism 7.03, and SigmaPlot 12.3. All data are normally distributed and presented as the mean ± the standard error of the mean (SEM). *P*-values < 0.05 were accepted to indicate statistical differences.

DATA AVAILABILITY

ROIs from 30 mouse AMs analyzed for TAT network analysis in **Figure 3** are available for download via online link: https://hdl.handle.net/21.11101/0000-0007-C9D2-9; doi: 10.5281/zenodo.1311573. Raw data supporting the conclusions of this manuscript will be made available by the authors, without undue reservation, to any qualified researcher.

AUTHOR CONTRIBUTIONS

SB and SEL were responsible for the central hypothesis, design and implementation of the study, collection and analysis of experimental data, and for preparing the manuscript. CS, DK-D, FF, FP, FW, IK, JN, JP, LS, MS, NV, SB, SEL, SS, and TK performed experiments, analyzed data, and contributed to the manuscript. IK, NV, and SS provided expertise about human heart samples and data analysis, and contributed to the manuscript. GM contributed expertise for customized synthesis and quality control of fluorescent lipid markers and contributed to the manuscript. TM provided critical comments, data, and analysis for the manuscript.

FUNDING

SB received financial support through the clinician scientist program "Translational Medicine" of the University Medical

Center Göttingen. This work was supported by grants from the Deutsche Forschungsgemeinschaft to SEL (SFB1002 project A09 and service project S02, and SFB1190 project P03), to NV (VO 1568/3-1, IRTG1816, and SFB1002 project A13), to CS (SCHM 3358/1-1), and to TM (SFB889 project A02); by the Else-Kröner-Fresenius Foundation to NV (EKFS 2016_A20), and by DZHK (German Centre for Cardiovascular Research) to SEL (DZHK GOE MD3) and CS (Excellence Grant). CS was supported in part by research grants from the University of Heidelberg, Faculty of Medicine (Rahel Goitein-Straus Scholarship and Olympia-Morata Scholarship), and from the Ministry of Science, Research and the Arts Baden-Württemberg (Sonderlinie Medizin to CS). FW was supported by the German Cardiac Society (Fellowship and Otto-Hess-Scholarship).

ACKNOWLEDGMENTS

We are grateful for the excellent technical assistance by Birgit Schumann and Brigitte Korff; for human AM isolation by Ines Müller; and to the patients who provided atrial samples based on informed consent and approved protocols by the ethics committee of the University Medical Center Göttingen (No. 14/9/11).

SUPPLEMENTARY MATERIAL

The Supplementary Material for this article can be found online at: https://www.frontiersin.org/articles/10.3389/fphys.2018.01227/full#supplementary-material

REFERENCES

Almers, W., Fink, R., and Palade, P. T. (1981). Calcium depletion in frog muscle tubules: the decline of calcium current under maintained depolarization. *J. Physiol.* 312, 177–207. doi: 10.1113/jphysiol.1981.sp013623

Arakel, E. C., Brandenburg, S., Uchida, K., Zhang, H., Lin, Y. W., Kohl, T., et al. (2014). Tuning the electrical properties of the heart by differential trafficking of KATP ion channel complexes. *J. Cell Sci.* 127, 2106–2119. doi: 10.1242/jcs.141440

Baig, S. M., Koschak, A., Lieb, A., Gebhart, M., Dafinger, C., Nurnberg, G., et al. (2011). Loss of Ca (V)1.3 (CACNA1D) function in a human channelopathy with bradycardia and congenital deafness. *Nat. Neurosci.* 14, 77–84. doi: 10.1038/nn.2694

Balijepalli, R. C., Foell, J. D., Hall, D. D., Hell, J. W., and Kamp, T. J. (2006). Localization of cardiac L-type Ca(2+) channels to a caveolar macromolecular signaling complex is required for beta(2)-adrenergic regulation. *Proc. Natl. Acad. Sci. U.S.A.* 103, 7500–7505. doi: 10.1073/pnas.0503465103

Bloch, K. (1989). Sterol structure and function. *Steroids* 53, 261–270. doi: 10.1016/0039-128X(89)90014-7

Bootman, M. D., Smyrnias, I., Thul, R., Coombes, S., and Roderick, H. L. (2011). Atrial cardiomyocyte calcium signalling. *Biochim. Biophys. Acta* 1813, 922–934. doi: 10.1016/j.bbamcr.2011.01.030

Brambatti, M., Connolly, S. J., Gold, M. R., Morillo, C. A., Capucci, A., Muto, C., et al. (2014). Temporal relationship between subclinical atrial fibrillation and embolic events. *Circulation* 129, 2094–2099. doi: 10.1161/CIRCULATIONAHA.113.007825

Brandenburg, S., Arakel, E. C., Schwappach, B., and Lehnart, S. E. (2016a). The molecular and functional identities of atrial cardiomyocytes in health and disease. *Biochim. Biophys. Acta* 1863, 1882–1893. doi: 10.1016/j.bbamcr.2015.11.025

Brandenburg, S., Kohl, T., Williams, G. S., Gusev, K., Wagner, E., Rog-Zielinska, E. A., et al. (2016b). Axial tubule junctions control rapid calcium signaling in atria. *J. Clin. Invest.* 126, 3999–4015. doi: 10.1172/JCI88241

Brette, F., Komukai, K., and Orchard, C. H. (2002). Validation of formamide as a detubulation agent in isolated rat cardiac cells. *Am. J. Physiol. Heart Circ. Physiol.* 283, H1720–H1728. doi: 10.1152/ajpheart.00347.2002

Burton, R. A. B., Rog-Zielinska, E. A., Corbett, A. D., Peyronnet, R., Bodi, I., Fink, M., et al. (2017). Caveolae in rabbit ventricular myocytes: distribution and dynamic diminution after cell isolation. *Biophys. J.* 113, 1047–1059. doi: 10.1016/j.bpj.2017.07.026

Carozzi, A. J., Ikonen, E., Lindsay, M. R., and Parton, R. G. (2000). Role of cholesterol in developing t-tubules: analogous mechanisms for T-tubule and caveolae biogenesis. *Traffic* 1, 326–341. doi: 10.1034/j.1600-0854.2000.010406.x

Crocini, C., Coppini, R., Ferrantini, C., Yan, P., Loew, L. M., Tesi, C., et al. (2014). Defects in T-tubular electrical activity underlie local alterations of calcium release in heart failure. *Proc. Natl. Acad. Sci. U.S.A.* 111, 15196–15201. doi: 10.1073/pnas.1411557111

Crocini, C., Ferrantini, C., Scardigli, M., Coppini, R., Mazzoni, L., Lazzeri, E., et al. (2016). Novel insights on the relationship between T-tubular defects and contractile dysfunction in a mouse model of hypertrophic cardiomyopathy. *J. Mol. Cell. Cardiol.* 91, 42–51. doi: 10.1016/j.yjmcc.2015.12.013

Crossman, D. J., Young, A. A., Ruygrok, P. N., Nason, G. P., Baddelely, D., Soeller, C., et al. (2015). T-tubule disease: relationship between T-tubule organization and regional contractile performance in human dilated cardiomyopathy. *J. Mol. Cell. Cardiol.* 84, 170–178. doi: 10.1016/j.yjmcc.2015.04.022

Dibb, K. M., Clarke, J. D., Horn, M. A., Richards, M. A., Graham, H. K., Eisner, D. A., et al. (2009). Characterization of an extensive transverse tubular network in sheep atrial myocytes and its depletion in heart failure. *Circ. Heart Fail.* 2, 482–489. doi: 10.1161/CIRCHEARTFAILURE.109.852228

Forbes, M. S., Hawkey, L. A., and Sperelakis, N. (1984). The transverse-axial tubular system (Tats) of mouse myocardium: its morphology in the developing and adult animal. *Am. J. Anat.* 170, 143–162. doi: 10.1002/aja.1001700203

Forbes, M. S., and van Neil, E. E. (1988). Membrane systems of guinea pig myocardium: ultrastructure and morphometric studies. *Anat. Rec.* 222, 362–379. doi: 10.1002/ar.1092220409

Forssmann, W. G., and Girardier, L. (1970). A study of the t system in rat heart. *J. Cell Biol.* 44, 1–19. doi: 10.1083/jcb.44.1.1

Frank, T., Rutherford, M. A., Strenzke, N., Neef, A., Pangrsic, T., Khimich, D., et al. (2010). Bassoon and the synaptic ribbon organize Ca(2)+ channels and vesicles to add release sites and promote refilling. *Neuron* 68, 724–738. doi: 10.1016/j.neuron.2010.10.027

Frisk, M., Koivumaki, J. T., Norseng, P. A., Maleckar, M. M., Sejersted, O. M., and Louch, W. E. (2014). Variable T-tubule organization and Ca2+ homeostasis across the atria. *Am. J. Physiol. Heart Circ. Physiol.* 307, H609–H620. doi: 10.1152/ajpheart.00295.2014

Gadeberg, H. C., Bond, R. C., Kong, C. H., Chanoit, G. P., Ascione, R., Cannell, M. B., et al. (2016). Heterogeneity of T-tubules in pig hearts. *PLoS One* 11:E0156862. doi: 10.1371/journal.pone.0156862

Glukhov, A. V., Balycheva, M., Sanchez-Alonso, J. L., Ilkan, Z., Alvarez-Laviada, A., Bhogal, N., et al. (2015). Direct evidence for microdomain-specific localization and remodeling of functional L-type calcium channels in rat and human atrial myocytes. *Circulation* 132, 2372–2384. doi: 10.1161/CIRCULATIONAHA.115.018131

Goette, A., Kalman, J. M., Aguinaga, L., Akar, J., Cabrera, J. A., Chen, S. A., et al. (2017). Ehra/Hrs/Aphrs/Solaece expert consensus on atrial cardiomyopathies: definition, characterization, and clinical implication. *Heart Rhythm* 14, E3–E40. doi: 10.1016/j.hrthm.2016.05.028

Greiser, M. (2017). Calcium signalling silencing in atrial fibrillation. *J. Physiol.* 595, 4009–4017. doi: 10.1113/JP273045

Greiser, M., Kerfant, B. G., Williams, G. S., Voigt, N., Harks, E., Dibb, K. M., et al. (2014). Tachycardia-induced silencing of subcellular Ca2+ signaling in atrial myocytes. *J. Clin. Invest.* 124, 4759–4772. doi: 10.1172/JCI70102

Greiser, M., Lederer, W. J., and Schotten, U. (2011). Alterations of atrial Ca(2+) handling as cause and consequence of atrial fibrillation. *Cardiovasc. Res.* 89, 722–733. doi: 10.1093/cvr/cvq389

Grynkiewicz, G., Poenie, M., and Tsien, R. Y. (1985). A new generation of Ca2+ indicators with greatly improved fluorescence properties. *J. Biol. Chem.* 260, 3440–3450.

Guichard, J. B., and Nattel, S. (2017). Atrial cardiomyopathy: a useful notion in cardiac disease management or a passing fad? *J. Am. Coll. Cardiol.* 70, 756–765. doi: 10.1016/j.jacc.2017.06.033

Heijman, J., Erfanian Abdoust, P., Voigt, N., Nattel, S., and Dobrev, D. (2016). Computational models of atrial cellular electrophysiology and calcium handling, and their role in atrial fibrillation. *J. Physiol.* 594, 537–553. doi: 10.1113/JP271404

Huser, J., Lipsius, S. L., and Blatter, L. A. (1996). Calcium gradients during excitation-contraction coupling in cat atrial myocytes. *J. Physiol.* 494(Pt 3), 641–651. doi: 10.1113/jphysiol.1996.sp021521

Johnsen, A. B., Rolim, N. P., Stolen, T., Alves, M., Sousa, M. M., Slupphaug, G., et al. (2013). Atrial myocyte function and Ca2+ handling is associated with inborn aerobic capacity. *PLoS One* 8:E76568. doi: 10.1371/journal.pone.0076568

Jorgensen, A. O., Shen, A. C., Arnold, W., Leung, A. T., and Campbell, K. P. (1989). Subcellular distribution of the 1,4-dihydropyridine receptor in rabbit skeletal muscle in situ: an immunofluorescence and immunocolloidal gold-labeling study. *J. Cell Biol.* 109, 135–147. doi: 10.1083/jcb.109.1.135

Kirk, M. M., Izu, L. T., Chen-Izu, Y., Mcculle, S. L., Wier, W. G., Balke, C. W., et al. (2003). Role of the transverse-axial tubule system in generating calcium sparks and calcium transients in rat atrial myocytes. *J. Physiol.* 547, 441–451. doi: 10.1113/jphysiol.2002.034355

Kolmakov, K., Belov, V. N., Bierwagen, J., Ringemann, C., Muller, V., Eggeling, C., et al. (2010). Red-emitting rhodamine dyes for fluorescence microscopy and nanoscopy. *Chemistry* 16, 158–166. doi: 10.1002/chem.200902309

Kong, C. H. T., Rog-Zielinska, E. A., Orchard, C. H., Kohl, P., and Cannell, M. B. (2017). Sub-microscopic analysis of T-tubule geometry in living cardiac ventricular myocytes using a shape-based analysis method. *J. Mol. Cell. Cardiol.* 108, 1–7. doi: 10.1016/j.yjmcc.2017.05.003

Lehnart, S. E., Wehrens, X. H., Reiken, S., Warrier, S., Belevych, A. E., Harvey, R. D., et al. (2005). Phosphodiesterase 4d deficiency in the ryanodine-receptor complex promotes heart failure and arrhythmias. *Cell* 123, 25–35. doi: 10.1016/j.cell.2005.07.030

Lenaerts, I., Bito, V., Heinzel, F. R., Driesen, R. B., Holemans, P., D'hooge, J., et al. (2009). Ultrastructural and functional remodeling of the coupling between Ca2+ influx and sarcoplasmic reticulum Ca2+ release in right atrial myocytes from experimental persistent atrial fibrillation. *Circ. Res.* 105, 876–885. doi: 10.1161/CIRCRESAHA.109.206276

Lüss, I., Boknik, P., Jones, L. R., Kirchhefer, U., Knapp, J., Linck, B., et al. (1999). Expression of cardiac calcium regulatory proteins in atrium V ventricle in different species. *J. Mol. Cell. Cardiol.* 31, 1299–1314. doi: 10.1006/jmcc.1999.0962

Martin, D. T., Bersohn, M. M., Waldo, A. L., Wathen, M. S., Choucair, W. K., Lip, G. Y., et al. (2015). Randomized trial of atrial arrhythmia monitoring to guide anticoagulation in patients with implanted defibrillator and cardiac resynchronization devices. *Eur. Heart J.* 36, 1660–1668. doi: 10.1093/eurheartj/ehv115

Maxwell, J. T., and Blatter, L. A. (2017). A novel mechanism of tandem activation of ryanodine receptors by cytosolic and Sr luminal Ca(2+) during excitation-contraction coupling in atrial myocytes. *J. Physiol.* 595, 3835–3845. doi: 10.1113/JP273611

McNutt, N. S., and Fawcett, D. W. (1969). The ultrastructure of the cat myocardium. II. Atrial muscle. *J. Cell Biol.* 42, 46–67.

Milani-Nejad, N., and Janssen, P. M. (2014). Small and large animal models in cardiac contraction research: advantages and disadvantages. *Pharmacol. Ther.* 141, 235–249. doi: 10.1016/j.pharmthera.2013.10.007

Moslehi, J., Depinho, R. A., and Sahin, E. (2012). Telomeres and mitochondria in the aging heart. *Circ. Res.* 110, 1226–1237. doi: 10.1161/CIRCRESAHA.111.246868

Neef, J., Urban, N. T., Ohn, T. L., Frank, T., Jean, P., Hell, S. W., et al. (2018). Quantitative optical nanophysiology of Ca(2+) signaling at inner hair cell active zones. *Nat. Commun.* 9:290. doi: 10.1038/s41467-017-02612-y

O'Neill, S. C., Valdeolmillos, M., Lamont, C., Donoso, P., and Eisner, D. A. (1991). The contribution of Na-Ca exchange to relaxation in mammalian cardiac muscle. *Ann. N. Y. Acad. Sci.* 639, 444–452. doi: 10.1111/j.1749-6632.1991.tb17331.x

Parton, R. G., and Simons, K. (2007). The multiple faces of caveolae. *Nat. Rev. Mol. Cell Biol.* 8, 185–194. doi: 10.1038/nrm2122

Platzer, J., Engel, J., Schrott-Fischer, A., Stephan, K., Bova, S., Chen, H., et al. (2000). Congenital deafness and sinoatrial node dysfunction in mice lacking class D L-type Ca2+ channels. *Cell* 102, 89–97. doi: 10.1016/S0092-8674(00)00013-1

Richards, M. A., Clarke, J. D., Saravanan, P., Voigt, N., Dobrev, D., Eisner, D. A., et al. (2011). Transverse tubules are a common feature in large mammalian atrial myocytes including human. *Am. J. Physiol. Heart Circ. Physiol.* 301, H1996–H2005. doi: 10.1152/ajpheart.00284.2011

Sacconi, L., Ferrantini, C., Lotti, J., Coppini, R., Yan, P., Loew, L. M., et al. (2012). Action potential propagation in transverse-axial tubular system is impaired in heart failure. *Proc. Natl. Acad. Sci. U.S.A.* 109, 5815–5819. doi: 10.1073/pnas.1120188109

Scardigli, M., Crocini, C., Ferrantini, C., Gabbrielli, T., Silvestri, L., Coppini, R., et al. (2017). Quantitative assessment of passive electrical properties of the cardiac t-tubular system by frap microscopy. *Proc. Natl. Acad. Sci. U.S.A.* 114, 5737–5742. doi: 10.1073/pnas.1702188114

Schmidt, C., Wiedmann, F., Langer, C., Tristram, F., Anand, P., Wenzel, W., et al. (2014). Cloning, functional characterization, and remodeling of K2P3.1 (Task-1) potassium channels in a porcine model of atrial fibrillation and heart failure. *Heart Rhythm* 11, 1798–1805. doi: 10.1016/j.hrthm.2014.06.020

Schotten, U., Verheule, S., Kirchhof, P., and Goette, A. (2011). Pathophysiological mechanisms of atrial fibrillation: a translational appraisal. *Physiol. Rev.* 91, 265–325. doi: 10.1152/physrev.00031.2009

Sezgin, E., Can, F. B., Schneider, F., Clausen, M. P., Galiani, S., Stanly, T. A., et al. (2016). A comparative study on fluorescent cholesterol analogs as versatile cellular reporters. *J. Lipid Res.* 57, 299–309. doi: 10.1194/jlr.M065326

Sheehan, K. A., Zima, A. V., and Blatter, L. A. (2006). Regional differences in spontaneous Ca2+ spark activity and regulation in cat atrial myocytes. *J. Physiol.* 572, 799–809. doi: 10.1113/jphysiol.2005.103267

Simons, K., and Ikonen, E. (1997). Functional rafts in cell membranes. *Nature* 387, 569–572. doi: 10.1038/42408

Smyrnias, I., Mair, W., Harzheim, D., Walker, S. A., Roderick, H. L., and Bootman, M. D. (2010). Comparison of the T-tubule system in adult rat ventricular and atrial myocytes, and its role in excitation-contraction coupling and inotropic stimulation. *Cell Calcium* 47, 210–223. doi: 10.1016/j.ceca.2009.10.001

Song, L. S., Sobie, E. A., Mcculle, S., Lederer, W. J., Balke, C. W., and Cheng, H. (2006). Orphaned ryanodine receptors in the failing heart. *Proc. Natl. Acad. Sci. U.S.A.* 103, 4305–4310. doi: 10.1073/pnas.0509324103

Thul, R., Coombes, S., Roderick, H. L., and Bootman, M. D. (2012). Subcellular calcium dynamics in a whole-cell model of an atrial myocyte. *Proc. Natl. Acad. Sci. U.S.A.* 109, 2150–2155. doi: 10.1073/pnas.1115855109

Tidball, J. G., Cederdahl, J. E., and Bers, D. M. (1991). Quantitative analysis of regional variability in the distribution of transverse tubules in rabbit myocardium. *Cell Tissue Res.* 264, 293–298. doi: 10.1007/BF00313966

Vest, J. A., Wehrens, X. H., Reiken, S. R., Lehnart, S. E., Dobrev, D., Chandra, P., et al. (2005). Defective cardiac ryanodine receptor regulation during atrial fibrillation. *Circulation* 111, 2025–2032. doi: 10.1161/01.CIR.0000162461.67140.4C

Voigt, N., Heijman, J., Wang, Q., Chiang, D. Y., Li, N., Karck, M., et al. (2014). Cellular and molecular mechanisms of atrial arrhythmogenesis in patients with paroxysmal atrial fibrillation. *Circulation* 129, 145–156. doi: 10.1161/CIRCULATIONAHA.113.006641

Voigt, N., Zhou, X. B., and Dobrev, D. (2013). Isolation of human atrial myocytes for simultaneous measurements of Ca2+ transients and membrane currents. *J. Vis. Exp.* 77:E50235. doi: 10.3791/50235

Wagner, E., Brandenburg, S., Kohl, T., and Lehnart, S. E. (2014). Analysis of tubular membrane networks in cardiac myocytes from atria and ventricles. *J. Vis. Exp.* 92:E51823. doi: 10.3791/51823

Wagner, E., Lauterbach, M. A., Kohl, T., Westphal, V., Williams, G. S., Steinbrecher, J. H., et al. (2012). Stimulated emission depletion live-cell super-resolution imaging shows proliferative remodeling of T-tubule membrane structures after myocardial infarction. *Circ. Res.* 111, 402–414. doi: 10.1161/CIRCRESAHA.112.274530

Wakili, R., Yeh, Y. H., Yan Qi, X., Greiser, M., Chartier, D., Nishida, K., et al. (2010). Multiple potential molecular contributors to atrial hypocontractility caused by atrial tachycardia remodeling in dogs. *Circ. Arrhythm. Electrophysiol.* 3, 530–541. doi: 10.1161/CIRCEP.109.933036

Walden, A. P., Dibb, K. M., and Trafford, A. W. (2009). Differences in intracellular calcium homeostasis between atrial and ventricular myocytes. *J. Mol. Cell. Cardiol.* 46, 463–473. doi: 10.1016/j.yjmcc.2008.11.003

Walker, M. A., Williams, G. S., Kohl, T., Lehnart, S. E., Jafri, M. S., Greenstein, J. L., et al. (2014). Superresolution modeling of calcium release in the heart. *Biophys. J.* 107, 3018–3029. doi: 10.1016/j.bpj.2014.11.003

Woo, S. H., Cleemann, L., and Morad, M. (2005). Diversity of atrial local $Ca2^{+}$ signalling: evidence from 2-D confocal imaging in $Ca2^{+}$-buffered rat atrial myocytes. *J. Physiol.* 567, 905–921. doi: 10.1113/jphysiol.2005.092270

Yan, P., Acker, C. D., Zhou, W. L., Lee, P., Bollensdorff, C., Negrean, A., et al. (2012). Palette of fluorinated voltage-sensitive hemicyanine dyes. *Proc. Natl. Acad. Sci. U.S.A.* 109, 20443–20448. doi: 10.1073/pnas.1214850109

Yiin, G. S., Howard, D. P., Paul, N. L., Li, L., Luengo-Fernandez, R., Bull, L. M., et al. (2014). Age-specific incidence, outcome, cost, and projected future burden of atrial fibrillation-related embolic vascular events: a population-based study. *Circulation* 130, 1236–1244. doi: 10.1161/CIRCULATIONAHA.114.010942

Zhang, Z., He, Y., Tuteja, D., Xu, D., Timofeyev, V., Zhang, Q., et al. (2005). Functional roles of Cav1.3(Alpha1d) calcium channels in atria: insights gained from gene-targeted null mutant mice. *Circulation* 112, 1936–1944. doi: 10.1161/CIRCULATIONAHA.105.540070

Conflict of Interest Statement: The authors declare that the research was conducted in the absence of any commercial or financial relationships that could be construed as a potential conflict of interest.

frontiers in Physiology

MINI REVIEW
published: 09 October 2018
doi: 10.3389/fphys.2018.01301

Dual Activation of Phosphodiesterases 3 and 4 Regulates Basal Spontaneous Beating Rate of Cardiac Pacemaker Cells: Role of Compartmentalization?

Tatiana M. Vinogradova, Evgeny Kobrinsky and Edward G. Lakatta*

Laboratory of Cardiovascular Science, Intramural Research Program, NIA, NIH, Baltimore, MD, United States

Spontaneous firing of sinoatrial (SA) node cells (SANCs) is regulated by cyclic adenosine monophosphate (cAMP)-mediated, protein kinase A (PKA)-dependent (cAMP/PKA) local subsarcolemmal Ca^{2+} releases (LCRs) from ryanodine receptors (RyR). The LCRs occur during diastolic depolarization (DD) and activate an inward Na^{+}/Ca^{2+} exchange current that accelerates the DD rate prompting the next action potential (AP). Basal phosphodiesterases (PDEs) activation degrades cAMP, reduces basal cAMP/PKA-dependent phosphorylation, and suppresses normal spontaneous firing of SANCs. The cAMP-degrading PDE1, PDE3, and PDE4 represent major PDE activities in rabbit SANC, and PDE inhibition by 3-isobutyl-1-methylxanthine (IBMX) increases spontaneous firing of SANC by ∼50%. Though inhibition of single PDE1–PDE4 only moderately increases spontaneous SANC firing, dual PDE3 + PDE4 inhibition produces a synergistic effect hastening the spontaneous SANC beating rate by ∼50%. Here, we describe the expression and distribution of different PDE subtypes within rabbit SANCs, several specific targets (L-type Ca^{2+} channels and phospholamban) regulated by basal concurrent PDE3 + PDE4 activation, and critical importance of RyR Ca^{2+} releases for PDE-dependent regulation of spontaneous SANC firing. Colocalization of PDE3 and PDE4 beneath sarcolemma or in striated patterns inside SANCs strongly suggests that PDE-dependent regulation of cAMP/PKA signaling might be executed at the local level; this idea, however, requires further verification.

Keywords: sinoatrial node cells, phosphodiesterases, PKA phosphorylation, L-type Ca^{2+} channel, sarcoplasmic reticulum, sarco(endo)plasmic reticulum calcium ATPase

OPEN ACCESS

Edited by:
Alexey V. Glukhov, University of Wisconsin System, United States

Reviewed by:
Stefano Morotti, University of California, Davis, United States
Robert Alan Rose, University of Calgary, Canada

****Correspondence:***
Tatiana M. Vinogradova
vinogradovat@grc.nia.nih.gov

Specialty section:
This article was submitted to Cardiac Electrophysiology, a section of the journal Frontiers in Physiology

Received: *14 June 2018*
Accepted: *29 August 2018*
Published: *09 October 2018*

Citation:
Vinogradova TM, Kobrinsky E and Lakatta EG (2018) Dual Activation of Phosphodiesterases 3 and 4 Regulates Basal Spontaneous Beating Rate of Cardiac Pacemaker Cells: Role of Compartmentalization? Front. Physiol. 9:1301. doi: 10.3389/fphys.2018.01301

INTRODUCTION

The sinoatrial (SA) node, the primary physiological pacemaker of the heart, drives more than 3 billion heartbeats during a human life span. The SA node automaticity is generated within the SA node pacemaker cells (SANCs), which fire spontaneous action potentials (APs) because of gradual depolarization of the membrane potential called diastolic depolarization (DD) linked to complex interactions of 'coupled clock' mechanisms. The 'membrane clock' refers

to multiple voltage-gated ion channels and transporters in the cell membrane, including hyperpolarization-activated "funny" current I_f, L-type and T-type Ca^{2+} currents ($I_{Ca,L}$ and $I_{Ca,T}$), delayed rectifier potassium current (I_K), Na^+/Ca^{2+} exchange current (I_{NCX}), Na^+/K^+ exchange current (I_{NaK}), etc. (**Figures 1A,B**; Irisawa et al., 1993; Mangoni and Nargeot, 2008).

Like other cardiac cells, SANCs have the sarcoplasmic reticulum (SR) and are equipped to cycle Ca^{2+} via sarco/endoplasmic reticulum Ca^{2+}-ATPase (SERCA2) and Ca^{2+} release channels, ryanodine receptors (RyRs). The SANCs can generate spontaneous local Ca^{2+} releases (LCRs) from RyR in the subsarcolemmal space during late DD before the AP upstroke (**Figures 1A,B**; Bogdanov et al., 2001). Numerous studies have confirmed the presence of rhythmic LCRs under normal physiological conditions in SANCs of different species (Huser et al., 2000; Lipsius et al., 2001; Vinogradova et al., 2004; Joung et al., 2009; Wu et al., 2009; Sirenko et al., 2017). The LCRs activate an inward I_{NCX}, which exponentially accelerates the rate of DD, prompting the "Membrane clock" to generate the next AP (Bogdanov et al., 2001; Sanders et al., 2006; Lakatta et al., 2010). Colocalization of Na^+/Ca^{2+} exchanger (NCX) and RyRs in rabbit SANC (Lyashkov et al., 2007) permits a quick conversion of LCRs beneath the sarcolemma into changes in the inward current that depolarizes the membrane potential. The SR-generated LCRs can occur independent of concurrent changes in the membrane potential; they persist during the voltage clamp of the cell membrane or in permeabilized SANCs (Vinogradova et al., 2004; Lakatta et al., 2010), manifesting the intracellular SR Ca^{2+} cycling "Ca^{2+} clock" in the absence of the "Membrane clock." The dynamic interaction of the "Ca^{2+} clock" and "Membrane clock" permits a high level of mutual entrainment between two individual clocks on a beat-to-beat basis (**Figures 1A,B**). This clock entrainment provides an additional degree of flexibility and robustness to the generation of spontaneous APs by the cardiac pacemaker cells (Lakatta et al., 2010; Yaniv et al., 2015).

The cyclic adenosine monophosphate (cAMP) is a ubiquitous secondary messenger that modulates multiple cell processes, e.g., cAMP-mediated protein kinase A (PKA)-dependent protein phosphorylation. Basal level of cAMP in rabbit SANCs is substantially higher than in ventricular myocytes (VM) (Vinogradova et al., 2006; Younes et al., 2008; Lakatta et al., 2010) due to constitutive activation of adenylyl cyclases (ACs). This basal AC activity is independent of constitutive β-adrenergic receptor (β-AR) activation, since neither the β1-AR antagonist, CGP-20712A, nor the β2-AR inverse agonist, ICI 118,551 affect the spontaneous SANCs beating rate (Vinogradova et al., 2006; Lakatta et al., 2010). Both the "Membrane clock" and "Ca^{2+} clock" are regulated by cAMP and cAMP-mediated PKA-dependent phosphorylation. Funny current is directly activated by cAMP (DiFrancesco and Tortora, 1991; St Clair et al., 2013). Several ion currents in SANCs are targets of the PKA-dependent phosphorylation including $I_{Ca,L}$, I_K, I_f, etc. (Irisawa et al., 1993; Mangoni and Nargeot, 2008; Liao et al., 2010). Proteins involved in the intracellular SR Ca^{2+} cycling in SANC [i.e., phospholamban (PLB), RyR, and SERCA] are also regulated by PKA-dependent phosphorylation (Vinogradova et al., 2006; Lakatta et al., 2010). The generation of rhythmic spontaneous LCRs and basal spontaneous firing of SANCs require a high basal level of cAMP and cAMP-mediated PKA-dependent phosphorylation (Vinogradova et al., 2006; Lakatta et al., 2010).

The cell cAMP level is the result of a balance between cAMP production by ACs and its degradation into 5′-AMP by cyclic nucleotide phosphodiesterases (PDEs), the only known mechanism to degrade cAMP (Beavo and Brunton, 2002). The PDE superfamily contains 11 distinct gene families (PDEs 1–11), and at least four PDE families (PDE1-PDE4) can hydrolyze cAMP in the heart. Specifically, PDE1 is activated by Ca^{2+}/calmodulin, PDE2 is stimulated by cGMP, PDE3 is inhibited by cGMP, and PDE4 is specific for cAMP. The PDE3 and PDE4 represent the major cAMP PDE activities in cardiac myocytes (Takahashi et al., 2002; Wechsler et al., 2002; Mongillo et al., 2004).

The normal AP firing of rabbit SANC is regulated by basal PDE activation, and its inhibition by broad-spectrum PDE inhibitor, 3-isobutyl-1-methylxanthine (IBMX), markedly increases the level of cAMP and concurrently increases the spontaneous SANC firing rate by ∼50%, which surpasses the positive chronotropic effect of the β-AR agonist isoproterenol (Vinogradova et al., 2008; **Figure 1C**). Combined activities of PDE3 and PDE4 represent the major basal PDE activities in the rabbit SA node, accounting for ∼50% in cytosolic and ∼90% in SR fractions (**Figure 1D**; Shakur et al., 2002). A synergistic relationship between PDE3 and PDE4 inhibition has been noted in different cell types, including vascular smooth muscle cells (Palmer et al., 1998), brown adipose tissue (Kraynik et al., 2013), and rat VM (Mika et al., 2013). Normal automaticity of rabbit SANC is regulated by dual PDE3 + PDE4 activation apparently operating in a synergistic manner (Vinogradova et al., 2018).

This mini-review is focused upon how cAMP-degrading PDEs regulate the normal spontaneous beating rate of SANCs, including expression and distribution of different PDE subtypes within SANCs, specific targets, and mechanisms of PDE-dependent regulation of spontaneous SANC firing. Evidence for compartmentalization of cAMP signaling in cardiac pacemaker cells under basal conditions is also discussed.

BASAL PDE ACTIVITY CONTROLS NORMAL SPONTANEOUS FIRING OF CARDIAC PACEMAKER CELLS

Suppression of PDE activity in isolated SA node produces an increase in cAMP level (Shahid and Rodger, 1989), acceleration of DD rate, and increase in the spontaneous SA node beating rate of different species (Kodama et al., 1983; Orito et al., 1996; Liu et al., 2011; Sharpe et al., 2017). The PDE3 is the most abundant PDE isoenzyme in the myocardial tissue of most mammalian species (Osadchii, 2007). Although PDE3 can hydrolyze both cAMP and cGMP, the catalytic rates for cAMP are 5–10-fold higher, than for cGMP, which makes PDE3 very efficient in degrading cAMP (Bender and Beavo, 2006; Osadchii, 2007).

The PDE3 inhibition increases the spontaneous beating rate of the SA node in guinea pigs (Orito et al., 1996), rabbits

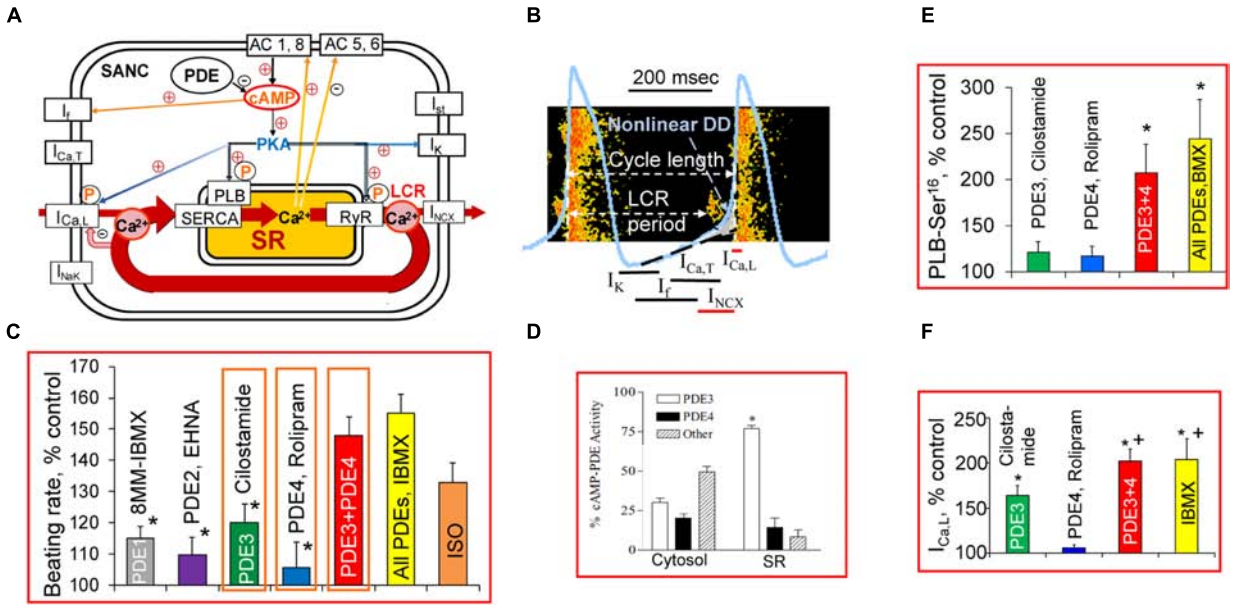

FIGURE 1 | A schematic illustration of regulation of the basal cardiac pacemaker function by PDEs and PKA-dependent phosphorylation in intact SANC. **(A)** The coupled-clock pacemaker system. Intracellular SR Ca^{2+} cycling (in red) operates in conjunction with the ensemble of membrane ion channels on a beat-to-beat basis. Note that L-type Ca^{2+} channel and I_{NCX} current are both Ca^{2+} cycling proteins and surface membrane currents. Constitutive activation of the basal AC activity results in an elevated level of cAMP and cAMP/PKA-dependent phosphorylation, which is kept in check by a high basal PDE activity. The PKA-dependent phosphorylation modulates function of Ca^{2+} cycling proteins (PLB, RyR, L-type Ca^{2+} channel, NCX current). **(B)** Schematic illustration of spontaneous SANC APs, Ca^{2+} transients, LCRs, and several major ion currents involved in generation of the DD. The LCR-induced increase in local $[Ca^{2+}]$ beneath the sarcolemma activates an inward NCX current creating exponential increase in the DD rate (Non-linear DD). See text for additional details. **(C)** Comparison of relative changes in the spontaneous SANC beating rate produced by selective inhibitors of PDE1-PDE4 alone or in combination and expressed as % of control. One-way ANOVA with Tukey *post hoc* test, $^*P < 0.05$ vs. PDE3 + PDE4 or All PDEs inhibition. **(D)** Distribution of PDE3 and PDE4 activities in SR-enriched and cytosolic fractions in rabbit SA node [modified from Shakur et al. (2002)]. **(E)** Average changes in PLB phosphorylation at Ser^{16} site in rabbit SANC by cilostamide (0.3 μmol/L) or rolipram (2 μmol/L) alone, combination of cilostamide + rolipram or 100 μmol/L IBMX expressed as % of control (n = 7–9 rabbits). One-way ANOVA with Tukey *post hoc* test, $^*P < 0.05$ vs. cilostamide or rolipram alone. **(F)** Regulation of L-type Ca^{2+} current amplitude by dual PDE3 + PDE4 activation; average increases in $I_{Ca,L}$ amplitude during inhibition of PDE3 or PDE4 alone, concurrent PDE3 + PDE4 inhibition, or IBMX presented as % of control (n = 5–7 SANC). One-way ANOVA with Bonferroni *post hoc* test $^*P < 0.01$ vs. rolipram alone; $^+P < 0.01$ vs. cilostamide alone. **(C,E,F)** Modified from Vinogradova et al. (2008, 2018).

(Kaumann et al., 2009), dogs (Sato et al., 1986), and humans (Jaski et al., 1985). In the murine heart, PDE4 is the major PDE isoform and accounts for∼60% of the total cAMP hydrolyzing activity (Osadchii, 2007). Inhibition of either PDE3 or PDE4 increases the spontaneous beating of the mouse SANCs (Hua et al., 2012) or rat SA node (Kaumann et al., 2009).

The PDE1 is an abundant cytosolic PDE isoenzyme in human ventricular myocardium (Wallis et al., 1999) or VM (Johnson et al., 2012). Targets of PDE1-dependent regulation in VM, however, remain obscure, since inhibition of PDE1 activity produces a decrease rather than increase in contraction amplitude of human VM (Johnson et al., 2012). Nimodipine-sensitive activity of PDE1, measured in lysates of isolated rabbit SANCs, accounted for ∼40% of total PDE activity (Lukyanenko et al., 2016), but PDE1 inhibition increased spontaneous firing of rabbit SANCs by ∼15% (**Figure 1C**). The PDE1 activity might have a greater impact at higher cAMP levels; indeed, stimulation of ACs with forskolin markedly increases both cAMP level and PDE1 activity in paced mouse VM (Sprenger et al., 2016).

Although average increases in the basal spontaneous beating rate of rabbit SANCs by inhibition of single cAMP-degrading PDEs (PDE1–PDE4) are relatively small (**Figure 1C**), concurrent inhibition of PDE3 + PDE4 increases the spontaneous SANC beating rate by ∼48% (Vinogradova et al., 2018), creating an effect comparable with that of IBMX (**Figure 1C**). An acceleration of spontaneous SANC firing by concomitant PDE3 + PDE4 inhibition by ∼twofold exceeds the summed increases in the spontaneous firing produced by inhibition of PDE3 (∼20%) and PDE4 (∼5%) alone (Vinogradova et al., 2018), indicating that the dual PDE3 + PDE4 activation operates synergistically to suppress basal spontaneous firing of rabbit SANCs (Vinogradova et al., 2018).

EFFECTS OF PDE INHIBITION ON PROTEIN PHOSPHORYLATION IN SANC

An increase in cAMP-mediated PKA-dependent phosphorylation of multiple proteins in cardiac cells occurs in response to PDE inhibition. Among Ca^{2+} cycling proteins phosphorylated in the basal state in rabbit SANC are PLB (Vinogradova et al., 2006; Lakatta et al., 2010), RyRs (Li et al., 2016), and likely L-type Ca^{2+} channels (Petit-Jacques et al., 1993). PLB modulates kinetics of SR Ca^{2+} pumping: in unphosphorylated state PLB

colocalizes with SERCA2 to inhibit its function to pump Ca^{2+} into SR (MacLennan and Kranias, 2003). Phosphorylation of PLB by PKA at Ser^{16} site in VM relieves this inhibition elevating SERCA activity by ∼2–3-fold (MacLennan and Kranias, 2003). Phosphorylation status of PLB at Ser^{16} site is a useful marker of PKA-dependent protein phosphorylation in SANC. Inhibition of either PDE3 or PDE4 alone produces only minor (∼20%, $P > 0.05$) increase in PLB phosphorylation at Ser^{16} site in SANC, but dual PDE3 + PDE4 inhibition increases PLB phosphorylation by ∼110%, an effect comparable to that of IBMX (**Figure 1E**). Therefore, basal PLB phosphorylation at Ser^{16} site in SANC appeared to be regulated by synergism of concurrent PDE3 + PDE4 activation (Vinogradova et al., 2018). This boost in basal PKA-dependent phosphorylation, produced by dual PDE3 + PDE4 inhibition and reflected in PLB phosphorylation, might also affect multiple other proteins involved in the regulation of cardiac pacemaker function which require further investigation.

EFFECTS OF PDE INHIBITION ON IONIC CURRENTS AND SR Ca^{2+} CYCLING IN SANC

The L-type Ca^{2+} channels are a well-known target of cAMP-mediated PKA-dependent pathway regulated by PDE activation. Comparable increases in basal $I_{Ca,L}$ amplitude by ∼60 and ∼72% occur when PDE3 or PDE4 are inhibited in mouse SANC (Hua et al., 2012), consistent with an important role of basal PDE3 and PDE4 activity in the murine heart (Osadchii, 2007). Synergistic effect of dual PDE3 + PDE4 inhibition on $I_{Ca,L}$ amplitude was observed both in human and rabbit atrial myocytes, creating effect comparable to that of IBMX. In contrast, PDE4 inhibition alone is without effect and PDE3 inhibition only moderately increases $I_{Ca,L}$ amplitude in human and rabbit atrial myocytes (Kajimoto et al., 1997). The PDE4 inhibition in rabbit SANC, as in human atrial myocytes, has no effect on $I_{Ca,L}$ amplitude, while inhibition of PDE3 increases $I_{Ca,L}$ by ∼60% (**Figure 1F**). Dual PDE3 + PDE4 inhibition increases $I_{Ca,L}$ in rabbit SANC by ∼100%, markedly exceeding combined effects of separate PDE3 or PDE4 inhibition and creating effect comparable with that of IBMX (**Figure 1F**). Therefore, dual PDE3 + PDE4 activation regulates basal $I_{Ca,L}$ amplitude in rabbit SANC in a synergistic manner (Vinogradova et al., 2018).

Other ionic currents involved in the generation of DD are also regulated by PDEs, e.g., inhibition of PDE3 in rabbit SANC increases I_K and shifts voltage dependence of I_f activation to more positive potentials (DiFrancesco and Tortora, 1991; Hata et al., 1998; Vinogradova et al., 2008). In mouse SANC, inhibition of PDE activity by IBMX or PDE4 activity by rolopram shifts voltage dependence of I_f current to more positive potentials (St Clair et al., 2017). The PDE3 inhibitor, milrinone, significantly increases I_f current amplitude by ∼20% (Springer et al., 2012) without shift of the voltage dependence of I_f current (St Clair et al., 2017).

The LCRs are also regulated by basal PDE activation both in intact and permeabilized rabbit SANCs (Vinogradova et al., 2008, 2018; Lakatta et al., 2010). During each spontaneous cycle, AP-induced Ca^{2+} influx through L-type Ca^{2+} channels triggers global Ca^{2+} transient, depleting SR Ca^{2+}, resetting the "Ca^{2+} clock," and leading to LCR termination. When the SR Ca^{2+} content is refilled by SERCA, LCRs start to occur, and the time from AP-induced Ca^{2+} transient to the onset of LCRs is the LCR period (**Figure 1B**). An increase in cAMP-mediated PKA-dependent phosphorylation of Ca^{2+} cycling proteins concurrently elevates amount of Ca^{2+} (influx via I_{CaL}) available for pumping into SR, accelerates the SR Ca^{2+} refilling (PLB), and likely alters the threshold for spontaneous Ca^{2+} releases (RyR), creating conditions required to boost spontaneous LCRs and speed up their appearance.

In intact rabbit, SANCs inhibition of PDE3 markedly increases the LCR size and number per each spontaneous cycle by ∼20% each ($P < 0.05$) and decreases the LCR period by ∼15% ($P < 0.05$), while changes in these parameters by rolipram are relatively small. Dual PDE3 + PDE4 inhibition, however, produces a synergistic effect and augments both the LCR size and number by ∼45% ($P < 0.01$) each, as RyR activation becomes more synchronized via RyR recruitment and decreases the LCR period by ∼40% ($P < 0.01$). An amplification of local RyR Ca^{2+} release activates augmented I_{NCX} at earlier times leading to an increase in the DD rate and spontaneous SANC beating rate (Vinogradova et al., 2018).

The contribution of "funny" current in the acceleration of spontaneous SANC beating rate by dual PDE3 + PDE4 inhibition was assessed in the presence or absence of I_f current inhibitors. Suppression of I_f current by either ivabradine or Cs^+ markedly decreased the spontaneous SANC beating rate. The positive chronotropic effect of dual PDE3 + PDE4 inhibition or IBMX, however, remained preserved even in the absence of I_f current (Vinogradova et al., 2018), indicating that the I_f current was not indispensable for the positive chronotropic effect of dual PDE3 + PDE4 inhibition. This might be related to specific locations of I_f channels within lipid raft domains of rabbit SANC (Barbuti et al., 2004), which could provide spatial barriers shielding I_f channels from cAMP elevation produced by dual PDE3 + PDE4 inhibition.

In contrast, when RyR function is disabled by ryanodine, dual PDE3 + PDE4 inhibition failed to accelerate the DD rate or increase the spontaneous SANC beating rate (Vinogradova et al., 2018), despite preserved increase of $I_{Ca,L}$ and I_K amplitudes (Vinogradova et al., 2008), indicating requirement of intact RyR function. Therefore, effects of PDE inhibition to increase function of ionic currents alone are not sufficient to increase the basal spontaneous SANC beating rate, which requires a link between PDE inhibition-induced increases in ionic currents and SR Ca^{2+} cycling within the coupled clock system (**Figures 1A,B**).

Though L-type Ca^{2+} channels or PLB and likely others are regulated by concurrent PDE3 + PDE4 activation in a synergistic manner (**Figure 1**), changes in global intracellular cAMP in SANC did not follow this pattern. Specifically, dual PDE3 + PDE4 inhibition in SANC lysates increases cAMP level by only ∼90% less than the effect produced by IBMX (∼160%)

or the sum of cAMP elevations created by inhibition of either PDE3 (∼45%) or PDE4 (∼56%) alone (Lukyanenko, unpublished data). Therefore, an increase in the spontaneous SANC beating rate by dual PDE3 + PDE4 inhibition (**Figure 1C**) is not created by changes in global cAMP, but likely by changes in local cAMP levels produced in the vicinity of PLB or L-type Ca^{2+} channels (scheme in **Figure 2**) or RyR etc.

Rabbit SANC lack t-tubular system, but they have considerable number of caveolae, flask-like invaginated lipid rafts containing caveolin, which could provide abundant physical boundaries for localized cAMP signaling. In rabbit SANCs, caveolae increase the surface plasma membrane by ∼115 and ∼30% in VM (Masson-Pevet et al., 1980). A variety of signaling molecules could be targeted to caveolae, including GPCRs, ACs, and PKA (Rybin et al., 2000; Younes et al., 2008; Bhogal et al., 2018). The subpopulation of L-type Ca^{2+} channels and HCN4 channels are also localized to caveolae (Barbuti et al., 2004; Glukhov et al., 2015). Caveolae have been identified as membrane subdomains that compartmentalize β-adrenergic receptor signaling and as negative regulators of cAMP accumulation in cardiac myocytes (Rybin et al., 2000; Bhogal et al., 2018). Though activity of PDE3 and PDE4 in rabbit SA node has been measured (**Figure 1D**), there is no information on how much of that activity might be inside or outside of caveolae.

EVIDENCE FOR COMPARTMENTALIZED cAMP-PKA SIGNALING IN VM

In VM, intracellular cAMP concentration in the basal conditions is close to 1 μmol/L, and this value is ∼10-fold higher during hormone or neurotransmitter activation (Iancu et al., 2008; Borner et al., 2011; Koschinski and Zaccolo, 2017). Multiple PDEs are expressed in each cell, with different affinities for cAMP: PDE3 in the range of 10–100 nmol/L (Manganiello et al., 1995), PDE4 in the range of 2–8 μmol/L (Salanova et al., 1998), while affinity of PDE1A or PDE2 exceeds 10 μmol/L (Bender and Beavo, 2006). Thus, cAMP is degraded over a wide range of concentrations and cells can maintain cAMP level at the physiological range both in the basal state or during hormone and neurotransmitter stimulation.

Because affinity of endogenous PKA for cAMP is in the range 100–300 nmol/L (Mongillo et al., 2004) and free diffusion of cAMP within the cell is relatively fast (∼200 $\mu m^2/s$) (Saucerman et al., 2014), cAMP would rapidly spread, PKA would be fully activated under basal conditions, and hormones would not be able to produce any cAMP-mediated PKA-dependent functional responses. This controversy led to a hypothesis that PKA is compartmentalized in special domains with significantly lower basal cAMP level compared with that of the global cytosol (Iancu et al., 2007). Therefore, intracellular pools of cAMP in the cell, their signaling pathways, and functional responses are spatially and functionally compartmentalized by PDEs, which rapidly degrade cAMP, providing functional barriers to cAMP diffusion (Bender and Beavo, 2006; Houslay, 2010; Francis et al., 2011; Keravis and Lugnier, 2012; Conti et al., 2014). The PDEs might create local pools "microdomains" with high or low cAMP levels; in the latter case, PDEs act like "black holes" converting cAMP into 5′-AMP and thus, protecting specific compartments from cAMP influx and PKA activation (Conti et al., 2014; Maurice et al., 2014).

Genetic manipulations of mice showed that both PDE3 and PDE4 may reside in the same localized compartments associated with either L-type Ca^{2+} channels or SR in VM. Indeed, PDE3A is colocalized with SERCA2-PLB-AKAP18 multiprotein complex or "signalosome" that regulates refilling of SR through modulation of PLB phosphorylation both in mouse and human VM (Ahmad et al., 2015). In the mouse heart, PDE4B is a part of the L-type Ca^{2+} channel complex and represents the major PDE isoform modulating $I_{Ca,L}$ amplitude during β-AR stimulation (Leroy et al., 2011). The PDE4D is incorporated in the SERCA2-PLB signaling complex in mouse VM (Kerfant et al., 2007), while PDE4D3 was integrated into SR-associated RyR2 complex (Lehnart et al., 2005).

RNA ABUNDANCE, PROTEIN EXPRESSION, AND DISTRIBUTION OF DIFFERENT PDE SUBTYPES IN SANC

At the messenger RNA level, PDE3A, PDE4A, PDE4B, and PDE4D are the major cAMP-degrading PDE subtypes expressed in both rabbit SANC and VM (Vinogradova et al., 2018). Expressions of PDE3A and PDE4B mRNA in rabbit SANC are comparable and exceed expression of other PDE subtypes (**Figure 2A**). Compared with PDE3 or PDE4, PDE1 mRNA in rabbit SANC is relatively low, but PDE1A transcript abundance in SANC surpasses that in VM by fourfold (Lukyanenko et al., 2016). Interestingly, mRNA transcripts for PDE2A, PDE3A, PDE4A, PDE4B, and PDE4D are comparably expressed in the mouse SA node (**Figure 2B**; Hua et al., 2012). Expression of PDE3A and PDE4A protein was less abundant in the rabbit SA node compared with the left ventricle; expression of PDE4B protein was similar in both tissues, while expression of PDE4D (Vinogradova et al., 2018) and PDE1A protein (Lukyanenko et al., 2016) was significantly higher in the rabbit SA node than in ventricle (**Figure 2C**).

Very little is known about the distribution of major PDE subtypes within SANC. Recent studies established that PDE1A, PDE3A, and PDE4B are localized beneath the sarcolemma of rabbit SANC (**Figure 2**; Lukyanenko et al., 2016; Vinogradova et al., 2018). Colocalization of PDE3A and PDE4B beneath the sarcolemma of rabbit SANC (**Figure 2D**) suggests that, like in the mouse heart, these PDE subtypes could work together limiting Ca^{2+} influx through L-type Ca^{2+} channels in a synergistic manner (**Figure 1F**). The PDE3A is also detected in a striated pattern and colocalizes with the *Z*-line associated protein α-actinin in rabbit SANC. Similar to human or mouse VM (Ahmad et al., 2015), PDE3A is colocalized with SERCA, PLB, and PDE4D in striated patterns inside SANCs (Vinogradova et al., 2018; **Figure 2**). Colocalization of PDE3A and PDE4D with SERCA and PLB suggests that these PDE isoforms could likely regulate cAMP-mediated PKA-dependent phosphorylation of major SR proteins in SANC (**Figure 2**).

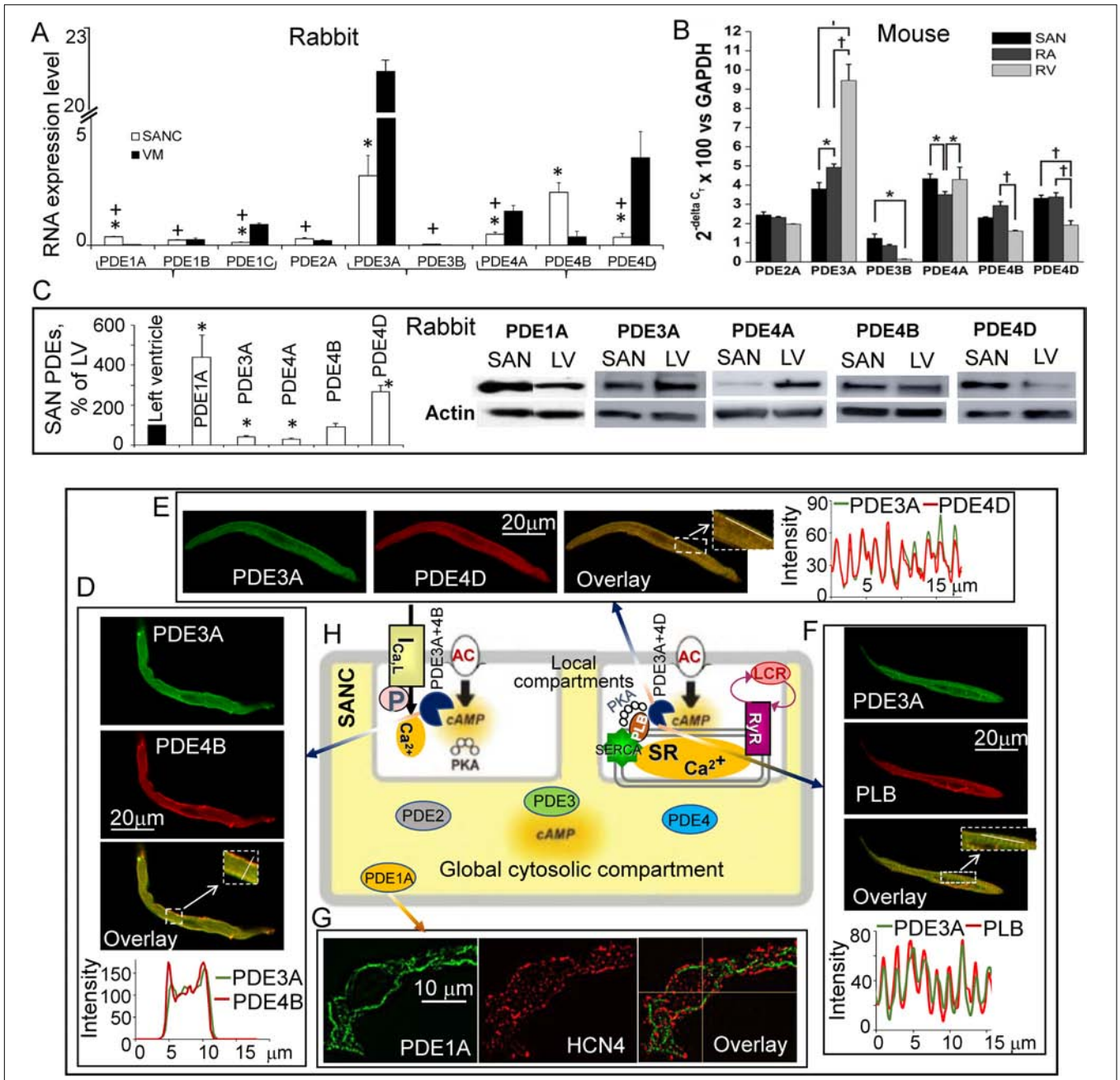

FIGURE 2 | Expression of cAMP-degrading PDEs at RNA and protein levels in the cardiac pacemaker and ventricle. Possible organization of PDE1A and major PDE3 and PDE4 subtypes within compartments in single rabbit SANC. **(A)** Relative expression of PDE-coding transcripts (mean ± SEM) in rabbit SANCs and VM; (n = 4–9); 1-way ANOVA with Tukey *post hoc* test, adjusted $^*P < 0.05$ (SANC vs. VM for each PDE subtype); $^+P < 0.05$ (PDE subtypes in SANC vs. PDE3A or PDE4B); **(B)** Quantitative mRNA expression of PDE 2, 3, and 4 subtypes in mouse SA node, right atrium (RA) and right ventricle (RV). Expression of PDE2A, PDE3A, PDE3B, PDE4A, PDE4B, and PDE4D are shown relative to GAPDH as (mean ± SEM); n = 5 SA node trials, 5 RA trials, and 3 RV trials; $^*P < 0.05$; $^+P < 0.001$ by two way ANOVA with Tukey's *post hoc* test [modified from Hua et al. (2012)]. **(C)** (left) average data (n = 8) of PDE1A, PDE3A, PDE4A, PDE4B, and PDE4D protein expression in the rabbit SA node compared with the left ventricle (LV = 100%), column statistics $^*P < 0.05$; (right) representative Western blots of major PDE subtypes in the rabbit SA node and left ventricle. **(D)** Double immunostaining for PDE3A, PDE4B, and superimposed images (inset shows magnification of the rectangular area in overlay); intensity plots (taken along the line in inset) show overlapping distribution of PDE3A with PDE4B beneath sarcolemma of SANC. **(E)** Double immunostaining for PDE3A, PDE4D, and merged images (inset shows magnification of the rectangular area in overlay); intensity plots (taken along the line in inset) display overlapping distribution of PDE3A with PDE4D along Z-lines in SANC. **(F)** Double immunostaining for PDE3A, PLB, and merged images (inset shows magnification of the rectangular area in overlay); intensity plots (taken along the line in inset) display overlapping distribution of PDE3A and PLB. **(G)** Double immunostaining for PDE1A, HCN4, and merged images. **(H)** A schematic of possible organization of compartmentalized signaling in rabbit SANC associated with L-type Ca^{2+} channels or PLB-dependent regulation of SR Ca^{2+} cycling. **(A,C–G)** modified from Vinogradova et al. (2018) and Lukyanenko et al. (2016).

SYNERGISTIC EFFECTS OF DUAL PDE3 + PDE4 INHIBITION IN SANC ARE LIKELY EXECUTED AT THE LOCAL LEVEL

Though dual PDE3 and PDE4 inhibition could interact synergistically to modulate functional effects mediated by cAMP in multiple cell types, the mechanisms underlying these synergistic effects remain unclear. This synergistic effect could be based on colocalization and interaction of different PDE3 and PDE4 subtypes (**Figure 2**). Since PDE3 affinity is ∼10–100 nmol/L, it is likely that PDE3 is active and degrades cAMP in the basal state, while PDE4 remains dormant. An increase in local cAMP level by inhibition of PDE3 alone may increase cAMP to a range required for PDE4 activation, concurrently elevating PKA-dependent phosphorylation of PDE4, which is associated with 2–6-fold increase in PDE4 activity (Sette and Conti, 1996). Activation of PDE4 would lead to a more efficient degradation of cAMP, creating a PKA-mediated feedback loop to promote local cAMP degradation. Therefore, PDE3- and PDE4-dependent modulation of spontaneous beating of SANC can be self-adaptive, i.e., the full functional effect being achieved only when both PDE3 and PDE4 are concurrently inhibited, elevating local level of cAMP and PKA-dependent phosphorylation to their highest levels and leading to a full-sized synergistic functional response. Coordinated regulation of several targets (L-type Ca^{2+} channels, PLB, etc.) by synergistic dual PDE3 + PDE4 activation could be energetically beneficial, since slight variations in local cAMP levels at multiple locations could lead to substantial functional effects.

Recent studies demonstrated that physiologically relevant cAMP signals operate within the nanometer range, creating local cAMP nanodomains, while 'global cAMP' is less involved in functional responses (Surdo et al., 2017). Computational models of cAMP signaling help to understand changes in cAMP activity at the local level in the subcellular compartments of cardiac cells. Models predict that low basal [cAMP] in caveolae is critically dependent on restricted cAMP diffusion between membrane compartments and cytosol (Iancu et al., 2007). The cAMP gradients might be also shaped by enhanced PDE activity (Saucerman et al., 2014), as e.g., in rabbit SANC. Future numerical models might explain how specific patterns of different PDE3 and PDE4 subtype protein expressions in rabbit SANC could impact local and global cAMP levels and affect numerous players involved in generation of the cardiac pacemaker function.

FUTURE DIRECTIONS IN MEASUREMENTS OF LOCAL cAMP-PKA SIGNALING IN SANC

Though it is helpful to directly measure PDE activity using classical biochemical assays, this experimental approach lacks spatial resolution. Local degradation of cAMP produced by PDEs creates cAMP gradients and forms nanodomain organization of cellular signaling (Lohse et al., 2017). Real-time imaging of changes in [cAMP] dynamics using fluorescence resonance energy transfer (FRET)-based reporters is a powerful tool to study local intracellular signaling events linked to PDE activity. Multiple FRET sensors have been constructed to image local changes in cAMP in living cells based mostly on interaction between pairs of green (GFP) and yellow (YFP) fluorescent proteins. Upon cAMP binding, the conformation of FRET sensor protein changes, leading to displacement of fluorophores and alteration of FRET signal. Though FRET imaging has enhanced our understanding of compartmentalized cAMP signaling in different cell types, i.e., cardiomyocytes, pancreatic-β cells, neuron, and cancer cells (Henderson et al., 2014; Larsen et al., 2016; Maiellaro et al., 2016; Beltejar et al., 2017; Elliott et al., 2017), employment of FRET in the cardiac pacemaking field has only recently begun to emerge (Yaniv et al., 2015). Exploration of local signaling in cardiac pacemaker cells using FRET sensors, however, is a challenging task, because expression of detectable level of FRET sensors requires a culture of SANC. Even a short-term culture markedly changes basal characteristics of rabbit SANC via significant decrease in the level of type 2 regulator of G-protein signaling (RGS2) that facilitates activation of the AC/cAMP/PKA pathway via G_i inhibition, leading to a diminished level of cAMP/PKA-dependent phosphorylation accompanied by a ∼50% decrease in spontaneous SANC firing rate (Yang et al., 2012). Furthermore, cultured SANCs lose their spindle shape and became spherical or spread out with more than three projections (Yang et al., 2012). Changes in the cell shape alter the surface-to-volume ratio and modify the local balance of cAMP synthesis and degradation (Saucerman et al., 2014). Because of substantial differences in the shape and basal cAMP-PKA signaling, changes in local cAMP levels recorded with FRET sensors in cultured SANCs might be different from those in freshly isolated SANC. Moreover, because cAMP levels in the vicinity of individual PDEs could be relatively low (∼100 nmol/L), it might be beyond detection by currently available FRET sensors (Koschinski and Zaccolo, 2017). Recently developed AKAP79–CUTie FRET, however, shows some promise in this regard, and detects statistically significant changes of cAMP in the range of 100 $nmol/L^{-1}$ μmol/L (Koschinski and Zaccolo, 2017). In short, future studies that utilize advanced methods of local cAMP measurements are required to understand specific mechanisms of compartmentalized PDE-regulated signaling and synergism of dual PDE3 + PDE4 inhibition in cardiac pacemaker cells.

AUTHOR CONTRIBUTIONS

TV made substantial contributions to conception, design and writing of the manuscript, and approved the last version for publication. EK helped to draft the manuscript, revised its content, and approved the last version for publication. EL helped to draft the manuscript, critically reviewed its content, and approved the last version for publication.

FUNDING

This work was supported by the Intramural Research Program of the National Institute on Aging and National Institutes of Health.

ACKNOWLEDGMENTS

The authors are deeply grateful to Dr. Yevgeniya O. Lukyanenko for her valuable comments and help with the manuscript and references.

REFERENCES

Ahmad, F., Shen, W., Vandeput, F., Szabo-Fresnais, N., Krall, J., Degerman, E., et al. (2015). Regulation of sarcoplasmic reticulum Ca2 + ATPase 2 (SERCA2) activity by phosphodiesterase 3A (PDE3A) in human myocardium: phosphorylation-dependent interaction of PDE3A1 with SERCA2. *J. Biol. Chem.* 290, 6763–6776. doi: 10.1074/jbc.M115.638585

Barbuti, A., Gravante, B., Riolfo, M., Milanesi, R., Terragni, B., and DiFrancesco, D. (2004). Localization of pacemaker channels in lipid rafts regulates channel kinetics. *Circ. Res.* 94, 1325–1331. doi: 10.1161/01.RES.0000127621.54132.AE

Beavo, J. A., and Brunton, L. L. (2002). Cyclic nucleotide research – still expanding after half a century. *Nat. Rev.* 3, 710–718. doi: 10.1038/nrm911

Beltejar, M. G., Lau, H. T., Golkowski, M. G., Ong, S. E., and Beavo, J. A. (2017). Analyses of PDE-regulated phosphoproteomes reveal unique and specific cAMP-signaling modules in T cells. *Proc. Natl. Acad. Sci. U.S.A.* 114, E6240–E6249. doi: 10.1073/pnas.1703939114

Bender, A. T., and Beavo, J. A. (2006). Cyclic nucleotide phosphodiesterases: molecular regulation to clinical use. *Pharmacol. Rev.* 58, 488–520. doi: 10.1124/pr.58.3.5

Bhogal, N. K., Hasan, A., and Gorelik, J. (2018). The Development of compartmentation of cAMP signaling in cardiomyocytes: the role of t-tubules and caveolae microdomains. *J. Cardiovasc. Dev. Dis.* 5, E25. doi: 10.3390/jcdd5020025

Bogdanov, K. Y., Vinogradova, T. M., and Lakatta, E. G. (2001). Sinoatrial nodal cell ryanodine receptor and Na(+)-Ca(2 +) exchanger: molecular partners in pacemaker regulation. *Circ. Res.* 88, 1254–1258. doi: 10.1161/hh1201.092095

Borner, S., Schwede, F., Schlipp, A., Berisha, F., Calebiro, D., Lohse, M. J., et al. (2011). FRET measurements of intracellular cAMP concentrations and cAMP analog permeability in intact cells. *Nat. Protoc.* 6, 427–438. doi: 10.1038/nprot.2010.198

Conti, M., Mika, D., and Richter, W. (2014). Cyclic AMP compartments and signaling specificity: role of cyclic nucleotide phosphodiesterases. *J. Gen. Physiol.* 143, 29–38. doi: 10.1085/jgp.201311083

DiFrancesco, D., and Tortora, P. (1991). Direct activation of cardiac pacemaker channels by intracellular cyclic AMP. *Nature* 351, 145–147. doi: 10.1038/351145a0

Elliott, A. D., Bedard, N., Ustione, A., Baird, M. A., Davidson, M. W., Tkaczyk, T., et al. (2017). Hyperspectral imaging for simultaneous measurements of two FRET biosensors in pancreatic beta-cells. *PLoS One* 12:e0188789. doi: 10.1371/journal.pone.0188789

Francis, S. H., Blount, M. A., and Corbin, J. D. (2011). Mammalian cyclic nucleotide phosphodiesterases: molecular mechanisms and physiological functions. *Physiol. Rev.* 91, 651–690. doi: 10.1152/physrev.00030.2010

Glukhov, A. V., Balycheva, M., Sanchez-Alonso, J. L., Ilkan, Z., Alvarez-Laviada, A., Bhogal, N., et al. (2015). Direct evidence for microdomain-specific localization and remodeling of functional l-type calcium channels in rat and human atrial myocytes. *Circulation* 132, 2372–2384. doi: 10.1161/CIRCULATIONAHA.115.018131

Hata, T., Nishimura, M., Ogino, K., Uchiyama, H., and Watanabe, Y. (1998). Electrophysiological effects of amrinone on the automaticity and membrane current system of the rabbit sinoatrial node cells. *Heart Vessels* 13, 114–121. doi: 10.1007/BF01747828

Henderson, D. J., Byrne, A., Dulla, K., Jenster, G., Hoffmann, R., Baillie, G. S., et al. (2014). The cAMP phosphodiesterase-4D7 (PDE4D7) is downregulated in androgen-independent prostate cancer cells and mediates proliferation by compartmentalising cAMP at the plasma membrane of VCaP prostate cancer cells. *Br. J. Cancer* 110, 1278–1287. doi: 10.1038/bjc.2014.22

Houslay, M. D. (2010). Underpinning compartmentalised cAMP signalling through targeted cAMP breakdown. *Trends Biochem. Sci.* 35, 91–100. doi: 10.1016/j.tibs.2009.09.007

Hua, R., Adamczyk, A., Robbins, C., Ray, G., and Rose, R. A. (2012). Distinct patterns of constitutive phosphodiesterase activity in mouse sinoatrial node and atrial myocardium. *PLoS One* 7:e47652. doi: 10.1371/journal.pone.0047652

Huser, J., Blatter, L. A., and Lipsius, S. L. (2000). Intracellular Ca2 + release contributes to automaticity in cat atrial pacemaker cells. *J. Physiol.* 524(Pt 2), 415–422.

Iancu, R. V., Jones, S. W., and Harvey, R. D. (2007). Compartmentation of cAMP signaling in cardiac myocytes: a computational study. *Biophys. J.* 92, 3317–3331. doi: 10.1529/biophysj.106.095356

Iancu, R. V., Ramamurthy, G., Warrier, S., Nikolaev, V. O., Lohse, M. J., Jones, S. W., et al. (2008). Cytoplasmic cAMP concentrations in intact cardiac myocytes. *Am. J. Physiol. Cell Physiol.* 295, C414–C422. doi: 10.1152/ajpcell.00038.2008

Irisawa, H., Brown, H. F., and Giles, W. (1993). Cardiac pacemaking in the sinoatrial node. *Physiol. Rev.* 73, 197–227. doi: 10.1152/physrev.1993.73.1.197

Jaski, B. E., Fifer, M. A., Wright, R. F., Braunwald, E., and Colucci, W. S. (1985). Positive inotropic and vasodilator actions of milrinone in patients with severe congestive heart failure. Dose-response relationships and comparison to nitroprusside. *J. Clin. Investig.* 75, 643–649. doi: 10.1172/JCI111742

Johnson, W. B., Katugampola, S., Able, S., Napier, C., and Harding, S. E. (2012). Profiling of cAMP and cGMP phosphodiesterases in isolated ventricular cardiomyocytes from human hearts: comparison with rat and guinea pig. *Life Sci.* 90, 328–336. doi: 10.1016/j.lfs.2011.11.016

Joung, B., Tang, L., Maruyama, M., Han, S., Chen, Z., Stucky, M., et al. (2009). Intracellular calcium dynamics and acceleration of sinus rhythm by beta-adrenergic stimulation. *Circulation* 119, 788–796. doi: 10.1161/CIRCULATIONAHA.108.817379

Kajimoto, K., Hagiwara, N., Kasanuki, H., and Hosoda, S. (1997). Contribution of phosphodiesterase isozymes to the regulation of the L-type calcium current in human cardiac myocytes. *Br. J. Pharmacol.* 121, 1549–1556. doi: 10.1038/sj.bjp.0701297

Kaumann, A. J., Galindo-Tovar, A., Escudero, E., and Vargas, M. L. (2009). Phosphodiesterases do not limit beta1-adrenoceptor-mediated sinoatrial tachycardia: evidence with PDE3 and PDE4 in rabbits and PDE1-5 in rats. *Naunyn Schmiedebergs Arch. Pharmacol.* 380, 421–430. doi: 10.1007/s00210-009-0445-5

Keravis, T., and Lugnier, C. (2012). Cyclic nucleotide phosphodiesterase (PDE) isozymes as targets of the intracellular signalling network: benefits of PDE inhibitors in various diseases and perspectives for future therapeutic developments. *Br. J. Pharmacol.* 165, 1288–1305. doi: 10.1111/j.1476-5381.2011.01729.x

Kerfant, B. G., Zhao, D., Lorenzen-Schmidt, I., Wilson, L. S., Cai, S., Chen, S. R., et al. (2007). PI3Kgamma is required for PDE4, not PDE3, activity in subcellular microdomains containing the sarcoplasmic reticular calcium ATPase in cardiomyocytes. *Circ. Res.* 101, 400–408. doi: 10.1161/CIRCRESAHA.107.156422

Kodama, I., Kondo, N., and Shibata, S. (1983). Effects of amrinone on the transmembrane action potential of rabbit sinus node pacemaker cells. *Br. J. Pharmacol.* 80, 511–517. doi: 10.1111/j.1476-5381.1983.tb10723.x

Koschinski, A., and Zaccolo, M. (2017). Activation of PKA in cell requires higher concentration of cAMP than *in vitro*: implications for compartmentalization of cAMP signalling. *Sci. Rep.* 7:14090. doi: 10.1038/s41598-017-13021-y

Kraynik, S. M., Miyaoka, R. S., and Beavo, J. A. (2013). PDE3 and PDE4 isozyme-selective inhibitors are both required for synergistic activation of brown adipose tissue. *Mol. Pharmacol.* 83, 1155–1165. doi: 10.1124/mol.112.084145

Lakatta, E. G., Maltsev, V. A., and Vinogradova, T. M. (2010). A coupled SYSTEM of intracellular Ca2 + clocks and surface membrane voltage clocks controls the timekeeping mechanism of the heart's pacemaker. *Circ. Res.* 106, 659–673. doi: 10.1161/CIRCRESAHA.109.206078

Larsen, H. E., Bardsley, E. N., Lefkimmiatis, K., and Paterson, D. J. (2016). Dysregulation of neuronal Ca2 + channel linked to heightened sympathetic phenotype in prohypertensive States. *J. Neurosci.* 36, 8562–8573. doi: 10.1523/JNEUROSCI.1059-16.2016

Lehnart, S. E., Wehrens, X. H., Reiken, S., Warrier, S., Belevych, A. E., Harvey, R. D., et al. (2005). Phosphodiesterase 4D deficiency in the ryanodine-receptor complex promotes heart failure and arrhythmias. *Cell* 123, 25–35. doi: 10.1016/j.cell.2005.07.030

Leroy, J., Richter, W., Mika, D., Castro, L. R., Abi-Gerges, A., Xie, M., et al. (2011). Phosphodiesterase 4B in the cardiac L-type Ca(2)(+) channel complex regulates Ca(2)(+) current and protects against ventricular arrhythmias in mice. *J. Clin. Invest.* 121, 2651–2661. doi: 10.1172/JCI44747

Li, Y., Sirenko, S., Riordon, D. R., Yang, D., Spurgeon, H., Lakatta, E. G., et al. (2016). CaMKII-dependent phosphorylation regulates basal cardiac pacemaker function via modulation of local Ca2 + releases. *Am. J. Physiol.* 311, H532–H544. doi: 10.1152/ajpheart.00765.2015

Liao, Z., Lockhead, D., Larson, E. D., and Proenza, C. (2010). Phosphorylation and modulation of hyperpolarization-activated HCN4 channels by protein kinase A in the mouse sinoatrial node. *J. Gen. Physiol.* 136, 247–258. doi: 10.1085/jgp.201010488

Lipsius, S. L., Huser, J., and Blatter, L. A. (2001). Intracellular Ca2 + release sparks atrial pacemaker activity. *News Physiol. Sci.* 16, 101–106.

Liu, J., Sirenko, S., Juhaszova, M., Ziman, B., Shetty, V., Rain, S., et al. (2011). A full range of mouse sinoatrial node AP firing rates requires protein kinase A-dependent calcium signaling. *J. Mol. Cell Cardiol.* 51, 730–739. doi: 10.1016/j.yjmcc.2011.07.028

Lohse, C., Bock, A., Maiellaro, I., Hannawacker, A., Schad, L. R., Lohse, M. J., et al. (2017). Experimental and mathematical analysis of cAMP nanodomains. *PLoS One* 12:e0174856. doi: 10.1371/journal.pone.0174856

Lukyanenko, Y. O., Younes, A., Lyashkov, A. E., Tarasov, K. V., Riordon, D. R., Lee, J., et al. (2016). Ca(2 +)/calmodulin-activated phosphodiesterase 1A is highly expressed in rabbit cardiac sinoatrial nodal cells and regulates pacemaker function. *J. Mol. Cell Cardiol.* 98, 73–82. doi: 10.1016/j.yjmcc.2016.06.064

Lyashkov, A. E., Juhaszova, M., Dobrzynski, H., Vinogradova, T. M., Maltsev, V. A., Juhasz, O., et al. (2007). Calcium cycling protein density and functional importance to automaticity of isolated sinoatrial nodal cells are independent of cell size. *Circ. Res.* 100, 1723–1731. doi: 10.1161/CIRCRESAHA.107.153676

MacLennan, D. H., and Kranias, E. G. (2003). Phospholamban: a crucial regulator of cardiac contractility. *Nat. Rev.* 4, 566–577. doi: 10.1038/nrm1151

Maiellaro, I., Lohse, M. J., Kittel, R. J., and Calebiro, D. (2016). cAMP signals in drosophila motor neurons are confined to single synaptic boutons. *Cell Rep.* 17, 1238–1246. doi: 10.1016/j.celrep.2016.09.090

Manganiello, V. C., Taira, M., Degerman, E., and Belfrage, P. (1995). Type III cGMP-inhibited cyclic nucleotide phosphodiesterases (PDE3 gene family). *Cell. Signal.* 7, 445–455. doi: 10.1016/0898-6568(95)00017-J

Mangoni, M. E., and Nargeot, J. (2008). Genesis and regulation of the heart automaticity. *Physiol. Rev.* 88, 919–982. doi: 10.1152/physrev.00018.2007

Masson-Pevet, M., Gros, D., and Besselsen, E. (1980). The caveolae in rabbit sinus node and atrium. *Cell Tissue Res.* 208, 183–196. doi: 10.1007/BF00234869

Maurice, D. H., Ke, H., Ahmad, F., Wang, Y., Chung, J., and Manganiello, V. C. (2014). Advances in targeting cyclic nucleotide phosphodiesterases. *Nat. Rev. Drug Discov.* 13, 290–314. doi: 10.1038/nrd4228

Mika, D., Bobin, P., Pomerance, M., Lechene, P., Westenbroek, R. E., Catterall, W. A., et al. (2013). Differential regulation of cardiac excitation-contraction coupling by cAMP phosphodiesterase subtypes. *Cardiovasc. Res.* 100, 336–346. doi: 10.1093/cvr/cvt193

Mongillo, M., McSorley, T., Evellin, S., Sood, A., Lissandron, V., Terrin, A., et al. (2004). Fluorescence resonance energy transfer-based analysis of cAMP dynamics in live neonatal rat cardiac myocytes reveals distinct functions of compartmentalized phosphodiesterases. *Circ. Res.* 95, 67–75. doi: 10.1161/01.RES.0000134629.84732.11

Orito, K., Takase, H., Fujiki, H., and Mori, T. (1996). Effects of toborinone (OPC-18790), a new positive inotropic agent, on action potential in guinea pig sinoatrial node: compared with milrinone and E-4031. *Jpn. J. Pharmacol.* 72, 79–82. doi: 10.1254/jjp.72.79

Osadchii, O. E. (2007). Myocardial phosphodiesterases and regulation of cardiac contractility in health and cardiac disease. *Cardiovasc. Drugs Ther.* 21, 171–194. doi: 10.1007/s10557-007-6014-6

Palmer, D., Tsoi, K., and Maurice, D. H. (1998). Synergistic inhibition of vascular smooth muscle cell migration by phosphodiesterase 3 and phosphodiesterase 4 inhibitors. *Circ. Res.* 82, 852–861. doi: 10.1161/01.RES.82.8.852

Petit-Jacques, J., Bois, P., Bescond, J., and Lenfant, J. (1993). Mechanism of muscarinic control of the high-threshold calcium current in rabbit sino-atrial node myocytes. *Pflugers Arch.* 423, 21–27. doi: 10.1007/BF00374956

Rybin, V. O., Xu, X., Lisanti, M. P., and Steinberg, S. F. (2000). Differential targeting of beta -adrenergic receptor subtypes and adenylyl cyclase to cardiomyocyte caveolae. A mechanism to functionally regulate the cAMP signaling pathway. *J. Biol. Chem.* 275, 41447–41457. doi: 10.1074/jbc.M006951200

Salanova, M., Jin, S. C., and Conti, M. (1998). Heterologous expression and purification of recombinant rolipram-sensitive cyclic AMP-specific phosphodiesterases. *Methods* 14, 55–64. doi: 10.1006/meth.1997.0565

Sanders, L., Rakovic, S., Lowe, M., Mattick, P. A., and Terrar, D. A. (2006). Fundamental importance of Na + -Ca2 + exchange for the pacemaking mechanism in guinea-pig sino-atrial node. *J. Physiol.* 571(Pt 3), 639–649.

Sato, Y., Wada, Y., and Taira, N. (1986). Comparative study of cardiovascular profiles of milrinone and amrinone by use of isolated, blood-perfused dog heart preparations. *Heart Vessels* 2, 213–220. doi: 10.1007/BF02059971

Saucerman, J. J., Greenwald, E. C., and Polanowska-Grabowska, R. (2014). Mechanisms of cyclic AMP compartmentation revealed by computational models. *J. Gen. Physiol.* 143, 39–48. doi: 10.1085/jgp.201311044

Sette, C., and Conti, M. (1996). Phosphorylation and activation of a cAMP-specific phosphodiesterase by the cAMP-dependent protein kinase. Involvement of serine 54 in the enzyme activation. *J. Biol. Chem.* 271, 16526–16534. doi: 10.1074/jbc.271.28.16526

Shahid, M., and Rodger, I. W. (1989). Chronotropic and inotropic actions of amrinone, carbazeran and isobutylmethyl xanthine: role of phosphodiesterase inhibition. *Br. J. Pharmacol.* 98, 291–301. doi: 10.1111/j.1476-5381.1989.tb16894.x

Shakur, Y., Fong, M., Hensley, J., Cone, J., Movsesian, M. A., Kambayashi, J., et al. (2002). Comparison of the effects of cilostazol and milrinone on cAMP-PDE activity, intracellular cAMP and calcium in the heart. *Cardiovasc. Drugs Ther.* 16, 417–427. doi: 10.1023/A:1022186402442

Sharpe, E. J., Larson, E. D., and Proenza, C. (2017). Cyclic AMP reverses the effects of aging on pacemaker activity and If in sinoatrial node myocytes. *J. Gen. Physiol.* 149, 237–247. doi: 10.1085/jgp.201611674

Sirenko, S. G., Yang, D., Maltseva, L. A., Kim, M. S., Lakatta, E. G., and Maltsev, V. A. (2017). Spontaneous, local diastolic subsarcolemmal calcium releases in single, isolated guinea-pig sinoatrial nodal cells. *PLoS One* 12:e0185222. doi: 10.1371/journal.pone.0185222

Sprenger, J. U., Bork, N. I., Herting, J., Fischer, T. H., and Nikolaev, V. O. (2016). Interactions of calcium fluctuations during cardiomyocyte contraction with real-time camp dynamics detected by FRET. *PLoS One* 11:e0167974. doi: 10.1371/journal.pone.0167974

Springer, J., Azer, J., Hua, R., Robbins, C., Adamczyk, A., McBoyle, S., et al. (2012). The natriuretic peptides BNP and CNP increase heart rate and electrical conduction by stimulating ionic currents in the sinoatrial node and atrial myocardium following activation of guanylyl cyclase-linked natriuretic peptide receptors. *J. Mol. Cell Cardiol.* 52, 1122–1134. doi: 10.1016/j.yjmcc.2012.01.018

St Clair, J. R., Larson, E. D., Sharpe, E. J., Liao, Z., and Proenza, C. (2017). Phosphodiesterases 3 and 4 differentially regulate the funny current, if, in mouse sinoatrial node myocytes. *J. Cardiovasc. Dev. Dis.* 4:10. doi: 10.3390/jcdd4030010

St Clair, J. R., Liao, Z., Larson, E. D., and Proenza, C. (2013). PKA-independent activation of I(f) by cAMP in mouse sinoatrial myocytes. *Channels* 7, 318–321. doi: 10.4161/chan.25293

Surdo, N. C., Berrera, M., Koschinski, A., Brescia, M., Machado, M. R., Carr, C., et al. (2017). FRET biosensor uncovers cAMP nano-domains at beta-adrenergic targets that dictate precise tuning of cardiac contractility. *Nat. Commun.* 8:15031. doi: 10.1038/ncomms15031

Takahashi, K., Osanai, T., Nakano, T., Wakui, M., and Okumura, K. (2002). Enhanced activities and gene expression of phosphodiesterase types 3 and 4 in pressure-induced congestive heart failure. *Heart Vessels* 16, 249–256. doi: 10.1007/s003800200032

Vinogradova, T. M., Lyashkov, A. E., Zhu, W., Ruknudin, A. M., Sirenko, S., Yang, D., et al. (2006). High basal protein kinase A-dependent phosphorylation drives rhythmic internal Ca2 + store oscillations and spontaneous beating

of cardiac pacemaker cells. *Circ. Res.* 98, 505–514. doi: 10.1161/01.RES.0000204575.94040.d1

Vinogradova, T. M., Sirenko, S., Lukyanenko, Y. O., Yang, D., Tarasov, K. V., Lyashkov, A. E., et al. (2018). Basal spontaneous firing of rabbit sinoatrial node cells is regulated by dual activation of PDEs (Phosphodiesterases) 3 and 4. *Circ. Arrhythm. Electrophysiol.* 11:e005896. doi: 10.1161/CIRCEP.117.005896

Vinogradova, T. M., Sirenko, S., Lyashkov, A. E., Younes, A., Li, Y., Zhu, W., et al. (2008). Constitutive phosphodiesterase activity restricts spontaneous beating rate of cardiac pacemaker cells by suppressing local Ca2 + releases. *Circ. Res.* 102, 761–769. doi: 10.1161/CIRCRESAHA.107.161679

Vinogradova, T. M., Zhou, Y. Y., Maltsev, V., Lyashkov, A., Stern, M., and Lakatta, E. G. (2004). Rhythmic ryanodine receptor Ca2 + releases during diastolic depolarization of sinoatrial pacemaker cells do not require membrane depolarization. *Circ. Res.* 94, 802–809. doi: 10.1161/01.RES.0000122045.55331.0F

Wallis, R. M., Corbin, J. D., Francis, S. H., and Ellis, P. (1999). Tissue distribution of phosphodiesterase families and the effects of sildenafil on tissue cyclic nucleotides, platelet function, and the contractile responses of trabeculae carneae and aortic rings in vitro. *Am. J. Cardiol.* 83, 3C–12C.

Wechsler, J., Choi, Y. H., Krall, J., Ahmad, F., Manganiello, V. C., and Movsesian, M. A. (2002). Isoforms of cyclic nucleotide phosphodiesterase PDE3A in cardiac myocytes. *J. Biol. Chem.* 277, 38072–38078. doi: 10.1074/jbc.M203647200

Wu, Y., Gao, Z., Chen, B., Koval, O. M., Singh, M. V., Guan, X., et al. (2009). Calmodulin kinase II is required for fight or flight sinoatrial node physiology. *Proc. Natl. Acad. Sci. U.S.A.* 106, 5972–5977. doi: 10.1073/pnas.0806422106

Yang, D., Lyashkov, A. E., Li, Y., Ziman, B. D., and Lakatta, E. G. (2012). RGS2 overexpression or G(i) inhibition rescues the impaired PKA signaling and slow AP firing of cultured adult rabbit pacemaker cells. *J. Mol. Cell Cardiol.* 53, 687–694. doi: 10.1016/j.yjmcc.2012.08.007

Yaniv, Y., Tsutsui, K., and Lakatta, E. G. (2015). Potential effects of intrinsic heart pacemaker cell mechanisms on dysrhythmic cardiac action potential firing. *Front. Physiol.* 6:47. doi: 10.3389/fphys.2015.00047

Younes, A., Lyashkov, A. E., Graham, D., Sheydina, A., Volkova, M. V., Mitsak, M., et al. (2008). Ca(2 +) -stimulated basal adenylyl cyclase activity localization in membrane lipid microdomains of cardiac sinoatrial nodal pacemaker cells. *J. Biol. Chem.* 283, 14461–14468. doi: 10.1074/jbc.M707540200

Conflict of Interest Statement: The authors declare that the research was conducted in the absence of any commercial or financial relationships that could be construed as a potential conflict of interest.

frontiers in Physiology

REVIEW
published: 22 October 2018
doi: 10.3389/fphys.2018.01472

Shining New Light on the Structural Determinants of Cardiac Couplon Function: Insights From Ten Years of Nanoscale Microscopy

Izzy Jayasinghe[1], Alexander H. Clowsley[2], Oscar de Langen[3], Sonali S. Sali[4], David J. Crossman[3] and Christian Soeller[2]*

[1] Faculty of Biological Sciences, University of Leeds, Leeds, United Kingdom, [2] Living Systems Institute, University of Exeter, Exeter, United Kingdom, [3] Faculty of Medical and Health Sciences, University of Auckland, Auckland, New Zealand, [4] Department of Biosciences and Bioengineering, Indian Institute of Technology Bombay, Mumbai, India

Remodelling of the membranes and protein clustering patterns during the pathogenesis of cardiomyopathies has renewed the interest in spatial visualisation of these structures in cardiomyocytes. Coincidental emergence of single molecule (super-resolution) imaging and tomographic electron microscopy tools in the last decade have led to a number of new observations on the structural features of the couplons, the primary sites of excitation-contraction coupling in the heart. In particular, super-resolution and tomographic electron micrographs have revised and refined the classical views of the nanoscale geometries of couplons, t-tubules and the organisation of the principal calcium handling proteins in both healthy and failing hearts. These methods have also allowed the visualisation of some features which were too small to be detected with conventional microscopy tools. With new analytical capabilities such as single-protein mapping, *in situ* protein quantification, correlative and live cell imaging we are now observing an unprecedented interest in adapting these research tools across the cardiac biophysical research discipline. In this article, we review the depth of the new insights that have been enabled by these tools toward understanding the structure and function of the cardiac couplon. We outline the major challenges that remain in these experiments and emerging avenues of research which will be enabled by these technologies.

Keywords: cardiac muscle, couplons, super-resolution, localization microscopy, ryanodine receptors

OPEN ACCESS

Edited by:
Di Lang,
University of Wisconsin–Madison,
United States

Reviewed by:
Gudrun Antoons,
Maastricht University, Netherlands
Rob Gourdie,
Medical University of South Carolina,
United States

****Correspondence:***
Izzy Jayasinghe
i.jayasinghe@leeds.ac.uk

Specialty section:
This article was submitted to Cardiac Electrophysiology, a section of the journal Frontiers in Physiology

Received: *25 July 2018*
Accepted: *28 September 2018*
Published: *22 October 2018*

Citation:
Jayasinghe I, Clowsley AH, de Langen O, Sali SS, Crossman DJ and Soeller C (2018) Shining New Light on the Structural Determinants of Cardiac Couplon Function: Insights From Ten Years of Nanoscale Microscopy. Front. Physiol. 9:1472. doi: 10.3389/fphys.2018.01472

BACKGROUND

Historically coined as a name for the focal contacts between the sarcolemma and the sarcoplasmic reticulum (SR) of skeletal muscle (Stern et al., 1997), the term 'couplon' in the present day relates more broadly to the nanodomains which encompass the fast calcium (Ca^{2+}) signalling mechanisms in striated muscle cells. In cardiac muscle, voltage-dependent inward Ca^{2+} currents (I_{Ca}) via L-type Ca^{2+} channels (LCC) at the couplons activate arrays of the giant (>2 MDa) type-2 ryanodine receptor Ca^{2+} channels (RyR2, Cannell et al., 1987) in a Ca^{2+} dependent manner (the mechanism called Ca^{2+}-induced Ca^{2+} release or CICR; Fabiato, 1983). Ca^{2+} released from RyRs is the principal activator of cardiomyocyte contraction and is the primary intracellular second messenger in the myocardial excitation-contraction (EC) coupling (see review by Bers, 2002). The large size

of cardiac myocytes means that diffusion of the Ca^{2+} released at the cell surface cannot be relied upon for the fast and forceful muscle contraction throughout the cell thickness (Hill, 1949). This problem is circumvented by the tubular invaginations of the sarcolemma which allow couplons to be strategically placed, in a morphology described as 'dyads,' mirroring the sarcomeric periodicity of the intracellular organisation of organelles and proteins. Crucial for the cell's contractile function, this allows highly synchronised cell-wide Ca^{2+} release (Ca^{2+} transient) following an action potential (Cannell et al., 1987). The identification of localised Ca^{2+} release events (Ca^{2+} sparks) (Cheng et al., 1993) as the elementary events of SR Ca^{2+} release consolidated the couplons as the likely structural units of EC coupling. The models of 'local control' accounting for the geometrical constraint of the narrow couplon clefts predict the steep dependence of local Ca^{2+} transients on I_{Ca} (Cannell et al., 1995) better than a well-stirred cytoplasm. They emphasise the importance of the couplon architecture, particularly the narrow cytoplasmic cleft space (Soeller and Cannell, 1997), as crucial to its role in EC coupling (Stern, 1992). Adding credence to this point, today, we have a more comprehensive view of the couplon as the hub for the principal Ca^{2+} handling proteins including LCC, RyR and Na^{+}/Ca^{2+} exchanger (NCX) as well as numerous regulatory proteins such as calcium/calmodulin-dependent protein kinase II (CaMKII), junctophilin-2 and FK506 binding protein (FKBP). Much of this biophysical understanding comes from microscopy studies spanning over a century, detailing the fine ultrastructure and the mutual arrangement of EC coupling proteins. See the historic account by Franzini-Armstrong (2018a,b) on how this understanding was developed in previous decades.

IMPRESSIONS OF COUPLON STRUCTURE FROM CONVENTIONAL MICROSCOPIES

A decade ago, our view of the cardiac muscle ultrastructure, particularly relating to cardiac couplons, was primarily defined by high quality thin-section (transmission electron microscopy; TEM) and scanning electron microscopy (SEM). The regularly spaced 'feet' morphologies in TEM (Flucher and Franzini-Armstrong, 1996; Franzini-Armstrong et al., 1999) and the freeze fractures of sarcolemmal membranes (Sun et al., 1995) were the primary view of couplons. From skeletal muscle EMs, 'feet' were quickly identified as individual RyRs (Ferguson et al., 1984); particles and membrane indentations on freeze-fracture SEM images were deduced to be LCCs and the imprints of RyRs (Sun et al., 1995). However, translating the microscopy data of couplons toward understanding the biophysics of Ca^{2+} signalling at the couplon has required a quantitative approach to their imaging and spatial analysis. Capturing the couplon's three-dimensional (3D) architecture from early EM data involved extensive imaging experience and certain assumptions on the geometries of the cellular compartments. For example, counting RyRs within couplons required awareness of the overall orientation of t-tubules and approximation of couplon circularity and symmetry (Franzini-Armstrong et al., 1999). As discussed by Franzini-Armstrong (2010), detection of 'feet' may require alignment of the RyR rows with the microscope axis in TEM. Complementing the EM data, a number of optical (predominantly confocal and widefield) experiments coupled with advanced image analysis (e.g., deconvolution) defined the working model of the couplon structure by the end of the first decade of the 2000s (Scriven et al., 2000; Scriven et al., 2005; Chen-Izu et al., 2006; Soeller et al., 2007; Jayasinghe et al., 2009). From these data, RyR2 clusters associated with cardiac couplons were estimated to typically contain $\geq$ 100 receptors (Franzini-Armstrong et al., 1999; Soeller et al., 2007). Some co-localisation analyses from immunofluorescence micrographs had demonstrated a very high mutual spatial association between the LCC and RyR consistently in normal cardiomyocytes (Sun et al., 1995; Scriven et al., 2000). These studies reinforced the idea of close mutual alignment between these two complexes, hypothesised based on freeze-fracture SEMs (Sun et al., 1995). Despite some disagreement (Scriven et al., 2000), a moderately strong co-localisation of NCX with the couplon (Jayasinghe et al., 2009) had been confirmed by electrophysiological and *in silico* studies (Lines et al., 2006). However, it is important to note that differences remain between the findings by different research groups that may be attributable to differences in methodology (e.g., fixation, antibody probes, image analysis protocols). This is discussed further in section 9.

Three-dimensional (3D) confocal and multiphoton imaging had revealed the t-tubules to be a dense network with interconnectivity both transversely and longitudinally (Soeller and Cannell, 1999; Jayasinghe et al., 2009) (**Figure 1A**). An optimised approach to confocal imaging (Chen-Izu et al., 2006), had further revealed couplons, reported by clustered RyR were organised throughout the entire transverse aspect of the Z-discs, much closer to each other (∼600–700 nm) than the previously assumed sarcomeric spacings (∼1.8 μm; Chen-Izu et al., 2006; Soeller et al., 2007; **Figures 1B,C**). These observations, together with the demonstration of non-planar arrangement of the z-lines at the transverse plane of cardiomyocytes (Soeller et al., 2009; Jayasinghe et al., 2010) led to a series of geometrically realistic simulations of spontaneous propagating Ca^{2+} release (Ca^{2+} waves) throughout the volumes of myocytes (Izu et al., 2006; Soeller et al., 2009; Li et al., 2010). These simulations reinforced the idea that the spatial organisation of couplons plays a vital role in the cell wide Ca^{2+} release properties and emphasised the need to develop models of myocyte EC coupling based on experimentally determined geometries rather than stylised volumes. However, not all of the RyR clusters were found to be associated with 'couplons' with the expected co-localisation with the t-tubules. Approximately 15% of RyR clusters in rat ventricular myocytes (Jayasinghe et al., 2009) (**Figure 1C**) and a larger proportion in rabbit (Sachse et al., 2009) and human (Jayasinghe I. et al., 2012) ventricular myocytes were found to be non-junctional, based on high-resolution 3D confocal image data.

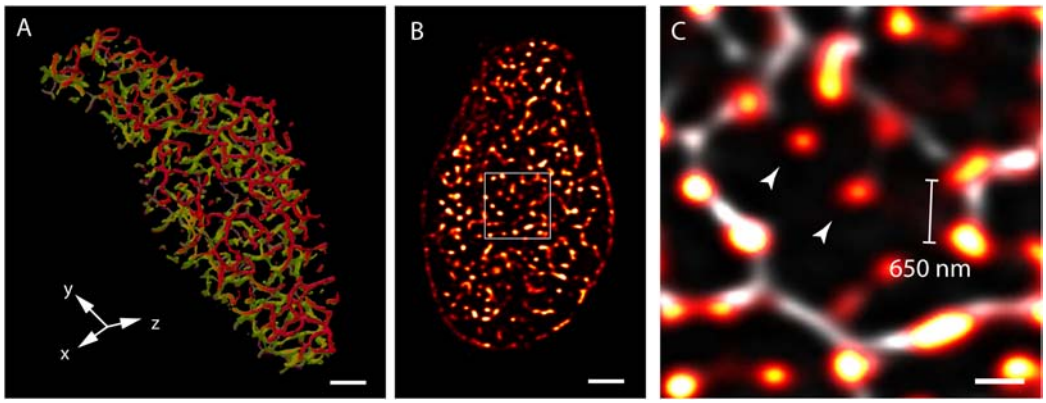

FIGURE 1 | View of the t-system and couplons of rat ventricular myocytes. **(A)** An isosurface reconstruction of the t-tubular network in a myocyte imaged with confocal microscopy in transverse orientation. The regions coloured in red and green respectively are tubules at two adjacent Z-discs; tubules extending between the Z-discs are coloured in purple. **(B)** A transverse view of punctate RyR staining in a myocyte visualised with high resolution confocal imaging; **(C)** Magnified view of the RyR clusters (red hot) of the region demarcated in **(B)**, overlaid with the corresponding t-tubule staining (grey). The typical distance between neighbouring clusters detected with this method was ∼650 nm. Examples of 'non-junctional' clusters which did not align with the t-tubules are noted with arrowheads. Scale bars, **(A,B)**: 2 μm, **(C)**: 500 nm. All data re-rendered from Jayasinghe et al. (2009).

RESURGENCE IN ULTRASTRUCTURAL ANALYSIS OF FAILING MYOCYTES

Confocal microscopy, in particular, played a central role in the pioneering observations of the correlation between dysfunctional intracellular Ca^{2+} release and remodelling of the t-tubules in both animal and human heart pathologies (Gomez et al., 1997; Balijepalli et al., 2003; Louch et al., 2004). The types of remodelling commonly observed through fluorescence imaging included loss of t-tubules in large cytoplasmic regions (Balijepalli et al., 2003; Louch et al., 2004; Crossman et al., 2011), relative increase in the longitudinal t-tubules compared to transverse tubules (Song et al., 2006; Wei et al., 2010), oblique tubules which departed from the z-line locations (Cannell et al., 2006; Crossman et al., 2011, 2015b), increase in the frequency of highly dilated tubules (Crossman et al., 2017) or sheet-like t-tubules (Seidel et al., 2017) (also see section 6 below) in animal and human cardiomyopathies. In the initial confocal-based studies, Song et al. (2006) reported the surprising observation that the highly periodic sarcomeric organisation of RyR clusters appeared undisturbed in confocal micrographs of failing cardiomyocytes from spontaneously hypertensive rats (SHRs), whilst the t-tubule network appeared aberrant and heterogeneous. These observations were the basis of the view that the ensuing loss of local control of these 'orphaned' RyR clusters was, at least in part, responsible for the lack of synchrony of Ca^{2+} release throughout the cells [analogous to that seen in ventricular myocytes following osmotically induced detubulation (Brette et al., 2002)]. Any changes to the SR or RyR clusters were not apparent in confocal studies. There was, however, a striking change in the co-localisation between LCCs and RyR as well as structural proteins of the couplon (e.g., junctophilin-2; JPH2) in the cells exhibiting t-tubule remodelling, examined with confocal microscopy (Song et al., 2006; van Oort et al., 2011; Crossman et al., 2015b).

LIMITATIONS IN DIFFRACTION-LIMITED IMAGING AND RESURGING INTEREST IN COUPLON STRUCTURE

Despite these advances in confocal and similar microscopies, the spatial sensitivity (i.e., resolution) achievable in visualising fine structure of couplons remained limited, by the diffraction of light, to approximately half of the wavelength (i.e., ∼250 nm in optimal imaging conditions) (Abbe, 1873). The typical sizes of cardiac couplons observed in EMs were close to this so-called 'diffraction limit in resolution'; hence, analysis and interpretation of such optical data were far from straightforward. RyR labelling in putative single couplons often appeared as smooth punctate labelling densities with variable intensities (Soeller et al., 2007) (**Figures 1C**, **2A**). In confocal and total internal reflection fluorescence (TIRF) micrographs, some clusters appeared elongated (Jayasinghe et al., 2009) (see example in **Figure 2A**). These observations were, at the time, strong indicators that couplons are likely to be of diverse shapes and sizes which could be better studied with an imaging modality with superior resolution. This lack of resolution in existing techniques also posed uncertainty in segmenting images for cluster size and co-localisation analyses (Scriven et al., 2000; Jayasinghe et al., 2009), and could lead to an over-estimation of the spatial overlap of proteins such as LCC and RyR (Scriven et al., 2010; Manfra et al., 2018), raising some concern over contrasting measurements made by independent laboratories. The approach of imaging cardiomyocytes in vertical orientation (achieved by embedding cells in agarose gels; Chen-Izu et al., 2006) offered a modest improvement in the achieved resolution to this end (Jayasinghe et al., 2009; Scriven et al., 2010). Despite this improvement, optical techniques such as confocal microscopy always involved a sensitivity limit such that only t-tubules, couplons or other structures which exceeded a critical size and/or fluorescence labelling density were detectable

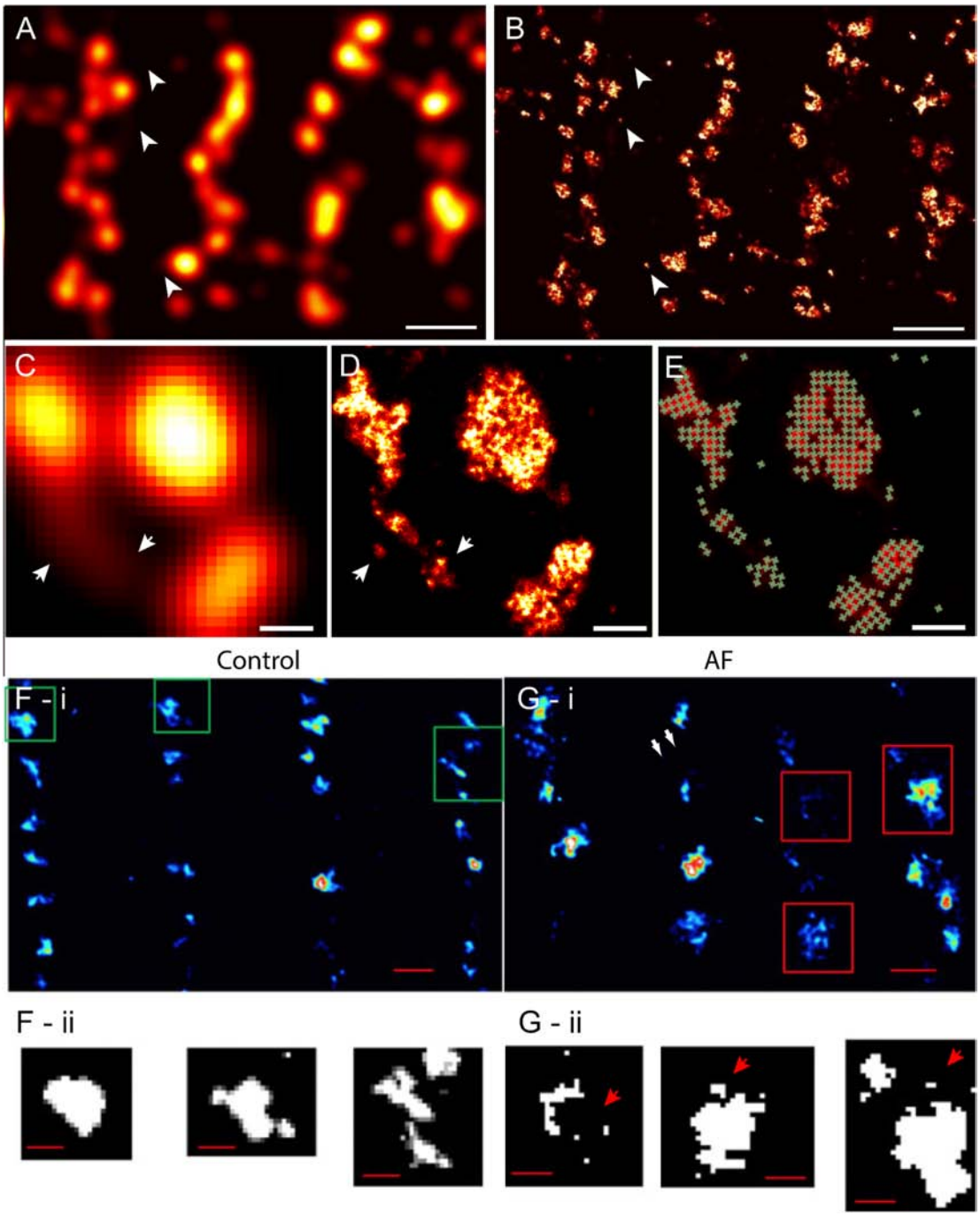

FIGURE 2 | Improved visualisation and analysis of clustered RyR organisation in peripheral couplons of rat ventricular myocytes with dSTORM super-resolution. **(A)** RyR labelling near the surface of a myocyte in diffraction-limited view of RyR clusters, many of which are oblong or elongated in shape. **(B)** The dSTORM image corresponding to the region shown in **(A)**. **(C,D)** Magnified views of matching diffraction-limited and dSTORM images from a few peripheral couplons. Note the small clusters and likely unitary RyRs [indicated in **(A–D)** by arrowheads] are undetectable in the diffraction-limited data. **(E)** To quantify cluster sizes (in RyRs/cluster), quasi-crystalline 30 × 30 nm assembly of RyRs in the regions of labelling was assumed. **(F-i)** Macquaide et al. (2015) compared deconvolved STED images of RyR labelling of healthy sheep atrial myocytes (control) with **(G-i)** RyR labelling in atrial myocytes of a sheep model of atrial fibrillation (AF). Compared to control **(F-ii),** the AF myocytes **(G-ii)** consisted of a higher frequency of smaller RyR cluster (arrows) and a smaller inter-cluster spacings, as illustrated by the magnified views of the clusters outlined in **(F,G-i)**. Scale bars, **(A,B)**: 1 μm, **(C–E)**: 150 nm, **(F,G-i)**: 500 nm, **(F,G-ii)**: 200 nm. **(F,G)** Adapted with permission from Macquaide et al. (2015).

above background noise (Soeller et al., 2007; Hou et al., 2015).

ADVENT OF SUPER-RESOLUTION OPTICAL MICROSCOPY AND A FRESH LOOK AT THE COUPLON

With the demonstration of photoactivated localisation microscopy (PALM, Betzig et al., 2006; Hess et al., 2006) and stochastic optical reconstruction microscopy (STORM, Rust et al., 2006), which are collectively known as 'single molecule localisation microscopy (SMLM),' a path was opened for imaging sub-cellular components which were, in size, below the 'diffraction-limited' conventional confocal resolution. New and exciting images that were enabled by SMLM included optically resolved focal adhesions (Betzig et al., 2006), mitochondria, endoplasmic reticulum (Shim et al., 2012), caveolae (Gambin et al., 2013), cytoskeletal microtubules (Ries et al., 2012), and actin (Xu et al., 2013). Encouragingly, it also showed great promise in resolving small assemblies of proteins such as the nuclear pore complexes (Loschberger et al., 2012), cell surface receptors, their mobility and clusters (Williamson et al., 2011). All of these spatial features were well beyond the sensitivity and resolution of the conventional optical microscopes.

SMLM, as a principle, relies on the detection and nanometre-scale localisation of fluorescent dye molecules within sample, a subset at a time, until a near-complete map of the dye molecule distribution has been obtained. In common approaches such as PALM or STORM, this is achieved by photoactivating and photo-chemical switching of the fluorescent dye molecules within the sample respectively. The latter particularly relies on the redox chemistry of the microenvironment of the fluorophores to stochastically switch the fluorophores between fluorescent and dark states to observe spatially isolated fluorescent molecules (see detailed review by Sauer and Heilemann, 2017). Long (>30 min) time series of image frame data are recorded and often analysed live to determine the centroid of each fluorescent event corresponding to a single photoactivated/switched fluorescent molecule. Maps of the fluorophore positions compiled over such an image series or density-encoded greyscale images from this type of experiments regularly offer spatial resolution of ∼ 30–50 nm. This near10-fold improvement in the achievable optical resolution was unprecedented and can be anecdotally likened to the difference between being legally blind and gaining twenty-twenty vision[1]. Along with the large improvement in the achievable resolution, SMLM image data also offered an unprecedented detection sensitivity, under suitable conditions approaching single antibodies or marker molecules. With suitably specific markers carefully acquired SMLM images generally involve minimal background signal or noise which has made image analysis, particularly segmentation, much more straightforward than in conventional optical image data.

An important catalyst for the successful uptake of SMLM for studying cardiac cell structure was that it built on existing labelling technologies (e.g., immunofluorescence or fluorescent fusion proteins), therefore sample preparation was, in comparison to EM, still very convenient. Another highly desirable feature is the extremely high sensitivity in detecting marker molecules to the structures of interest (e.g., microtubules stained with nanobody markers by Mikhaylova et al. (2015) compared to marker detection in immuno-gold EMs which are lower in contrast). These unique features provide SMLM a niche in the repertoire of the cardiac cell biophysicist.

In more recent years, we and others have demonstrated that the SMLM image data, particularly the densities of the marker molecules within a sample and the temporal patterns of localisation, encode the underpinning protein target density, independent of the resolution achieved in the final image (Jungmann et al., 2016; Munro et al., 2016). As a result of this, quantification of fluorescence image data is no longer limited to proportional co-localisation analyses. We are now able to detect changes in the protein density within nanoscale cellular domains (Jayasinghe et al., 2014; Munro et al., 2016), count the absolute number of protein targets within a structure of interest (Jungmann et al., 2016) and even estimate the local stoichiometry of protein association (Jayasinghe et al., 2018). These capabilities can make SMLM a more user-friendly and more sensitive approach to quantifying *local* protein changes in cardiomyocytes compared to traditional *in vitro* techniques of measuring protein levels such as calibrated Western Blots of fractionated myocardial tissues or cell suspensions.

The versatility of earlier versions of SMLM were enhanced by the use of the Highly Inclined and Laminated Optical sheet (HILO) illumination approach (Tokunaga et al., 2008) which allows SMLM to be performed in optically thick samples (e.g., thicker than 10 μm). This is particularly relevant to super-resolution imaging of cardiomyocytes which are among the largest cell types in animals. Combining SMLM and HILO has therefore allowed us and others to examine dyads and t-tubules in both isolated cardiomyocytes (Wong et al., 2013; Fu et al., 2016) and hydrated tissue sections (Hou et al., 2014; Crossman et al., 2015a). Despite being a comparatively low-throughput imaging technique in terms of cell numbers (a typical 2D image requiring 10–60 min of acquisition time), dSTORM image data have traditionally allowed the visualisation of large regions in optically thick samples compared to EM ultra-thin sections that are typically 50–60 nm thin (Franzini-Armstrong, 2010). This meant that SMLM offered the researcher the capacity to perform larger-scale spatial statistics [e.g., 1000s of couplons (Jayasinghe et al., 2018)] with relative ease. The typical fields of view in earlier SMLM experiments were limited primarily by the array sizes of the electron multiplying charge coupled device (EMCCD) cameras which were essential for single molecule detection. Within those constraints, a standard dSTORM experiment allowed the super-resolution mapping of a ∼20 × 20 μm 2D area.

[1]We refer to visual acuity which is a measure of the sharpness or clarity of vision. Based on the Hermann Snellen charts, visual acuity measurement of 20/20 relates to matching the resolution of 'normal' human vision (i.e. the ability to resolve contours which are 1.75 mm apart from a distance of 20 ft) from 20 ft away. In North America and parts of Europe, the limit for legal blindness is 20/200 which corresponds to a 10-fold reduction in the visual acuity, broadly similar in proportion to the resolution difference between diffraction-limited techniques and SMLM.

More recent development of flatfield illumination techniques coupled with large array cameras now expand the field of view to the millimetre range (Douglass et al., 2016). Applications such as these offer the potential to map EC coupling proteins in whole (or multiple) cells conveniently. To date, the majority of the SMLM studies of cardiac myocytes have come from laboratories using custom-built systems, underscoring its robustness as a relatively inexpensive nanoscale imaging technique.

Early Visualisation of the Nanoscale RyR Organisation

With the earliest application of SMLM (dSTORM, with an estimated resolution of 30–50 nm) to examine cardiac muscle, we were able to resolve more complex shapes and sizes of peripheral couplons, as reported by the clustering of RyRs near the cell surface (Baddeley et al., 2009) (**Figures 2A,B**). Subsequently, tissue dSTORM images of transversely sectioned myocytes allowed us to resolve and characterise the RyR clusters throughout the entire transverse depth of the cell (Hou et al., 2015). These two investigations, in tandem, demonstrated that dyadic RyR clusters, located deep within the cell interior, were $\sim$ 4 times larger than the sub-sarcolemmal clusters. This is a distinction which was not clearly made in previous optical or EM data. The single molecule detection approach maps dye molecules within the sample independently of each other. This departure from the reliance from dense immunofluorescence labelling for optical detection allowed the visualisation of solitary (i.e., non-clustered) RyRs for the first time in cardiac muscle (Baddeley et al., 2009; Hou et al., 2015). The vast majority of regions with RyR labelling, in fact, corresponded to solitary RyRs or small clusters (**Figures 2A,B**). Comparing the super-resolution images with the diffraction-limited images revealed that many of the smaller RyR clusters were virtually undetectable in the latter (**Figures 2C,D**). The resolved RyR cluster regions enabled us (Baddeley et al., 2009) and others (Macquaide et al., 2015) to estimate upper bounds of the number of receptors within them. For these estimates, it was hypothesised that *in situ* RyR cluster self-assembly reflected the quasi-crystalline patterns at $\sim$ 30 nm RyR centre-to-centre positioning seen in *in vitro* studies (Yin et al., 2005) (schematically illustrated in **Figures 2D,E**). In this analysis, an exponential distribution was observed in the cluster sizes, with a high proportion of clusters consisting of <5 receptors. Strikingly, >80% of the cells' RyRs appeared to reside within a small minority of clusters, each with a size > 100 receptors. (Hou et al., 2015). As a result of the improved sensitivity in detecting RyR clusters, the observable cluster density had doubled from $\sim$1 μm^{-3} in confocal data (Soeller et al., 2007) to 2.2 μm^{-3} in dSTORM (Hou et al., 2015). In agreement with this observation, the edge-to-edge distances between RyR clusters, in both sub-sarcolemmal and dyadic couplons, were significantly smaller (mean of 140 nm in dSTORM data of interior RyR clusters compared to $\sim$670 nm with confocal). These were significant revisions to the existing models of RyR distribution within cardiomyocytes and a proposal of a new unifying model of the couplon function (Xie et al., 2010). Given predictions that $[Ca^{2+}]_i$ within a radial distance of 100 nm outside of the couplon is likely to be elevated to micromolar concentrations (Soeller and Cannell, 1997; Sobie et al., 2006), it was hypothesised that RyR clusters located within a similar edge-to-edge distance are likely to co-activate as a 'functional super-cluster.' It meant that 2–6 neighbouring clusters (mean of $\sim$3.4) within a 'super-cluster,' even if not coupled individually to the sarcolemmal triggers, could be recruited rapidly in a 'triggered saltatory' fashion. Whether the super-clusters are likely components of the same dyad structure, is yet unresolved. This is due to the lack of markers which allow reliable and independent visualisation of the SR membranes with SMLM. However, the visual analysis performed by Hou et al. (2015) showed that all sub-clusters within super-cluster groupings in the cell interior commonly aligned strongly with the same segment of t-tubule membrane. This supported the idea that an underpinning structural template (e.g., a shared SR terminus) may determine the high mutual proximities between these RyR arrays making up a super-cluster. Whilst this is yet to be confirmed, such an arrangement would have significant ramifications to the way parts of the super-cluster are recruited, the levels of luminal SR $[Ca^{2+}]$ seen by each of them and how they may participate in propagating (Izu et al., 2006) or late (Fowler et al., 2018) Ca^{2+} release events. Sub-clusters which are readily recruited by other sub-clusters belonging to the same super-cluster could also create greater redundancy in the LCC/RyR coupling required for optimal Ca^{2+} release synchronisation and maintain the Ca^{2+} contributions from RyR clusters which are seemingly uncoupled from LCC.

Super-Resolution Insights Into t-Tubule Structure and Accessory Proteins

With renewed focus over the last two decades on t-tubule remodelling coinciding with pathology, SMLM has presented an imaging modality that is superior to conventional optical microscopies for probing the nanometre-scale events which may underpin it. Common t-tubule labelling methods which included antibodies, membrane impermeable dextrans (reporting tubule volume) and membrane dyes used for confocal imaging were broadly compatible with SMLM and other super-resolution techniques. This encouraged a number of groups to promptly adapt super-resolution imaging for t-tubule visualisation. Wagner et al. (2012) used a non-SMLM super-resolution technique known as Stimulated Emission Depletion (STED) microscopy to visualise the topology of the t-tubular membrane in living ventricular myocytes stained with a lipophilic membrane dye. More recently, we characterised the morphological differences between the t-tubular systems in a range of mammalian species (Jayasinghe et al., 2015). We demonstrated that differences in the diameters and the degree of tubule branching was clearly observable between the species. Brandenburg et al. (2016) have used super-resolution STED to reveal the intricate features of a poorly ordered tubular system in human and mouse atrial myocytes which form a series of axial couplons deep in the cell interiors. In the absence of a highly organised t-tubular systems, the combined STED and confocal data led them to propose that these axial couplons in

atrial myocytes containing hyperphosphorylated RyR clusters can act as 'super-hubs' which relay excitation to the majority of the surrounding RyR cluster which are non-junctional. Among the notable features of t-tubule structures first to be characterised with SMLM, is the tubule dilatations which were observed in two-colour dSTORM images of murine t-tubules (stained for caveolin-3) and RyR (Wong et al., 2013). These tubule dilatations were then confirmed with 3D EM tomograms of mice in the same study and reported later as a feature which may be lost during t-tubule remodelling and the loss of BIN-1 from the couplon coinciding with pathology such as arrhythmia (Hong et al., 2014). Local variations in the t-tubule diameters were likely to be underestimated in confocal and TEM data but were demonstrated well in dSTORM images of small mammal t-tubules and tomographic EMs of rat ventricular myocytes (Pinali et al., 2013).

SMLM has played a major role in revealing the localisation of key structural and functional regulators of couplons. One such protein is Junctophillin-2 (JPH2), which is essential for the formation of cardiac couplons (Takeshima et al., 2000) including the maintenance of the local coupling between the SR and sarcolemmal membranes as well as stabilising the RyR openings (van Oort et al., 2011). The dual-colour mapping of the RyR and JPH2, with super-resolution dSTORM was the first visual demonstration of how accessory proteins (e.g., JPH2) were tightly co-clustered within the couplon (Jayasinghe I.D. et al., 2012). The background-free nature of rendered dSTORM images also allowed robust segmentation of couplon images and estimation of protein co-localisation at an accuracy that was not afforded by previous diffraction-limited imaging data (e.g., Scriven et al., 2000; Jayasinghe et al., 2009). Further to this, dSTORM was instrumental in elucidating the dual structural and regulatory roles of JPH2. The examination of a mouse model overexpressing JPH2 with quantitative dSTORM revealed a larger and rounder RyR cluster morphology but paradoxically resulted in little change in the Ca^{2+} spark properties. Furthermore, only a modest increase in apparent co-localisation between RyR and JPH2 was observed (Munro et al., 2016). A carefully controlled analysis of the relative *densities* of localised RyR and JPH2 markers within each cluster revealed that (i) the larger RyR cluster size was the likely result of a higher local JPH2 density and (ii) despite the approximately unchanged number of RyRs in the clusters, the lower spontaneous Ca^{2+} spark frequency observed in the transgenic animals is the likely result of the additional inhibitory effect imparted on the RyRs by the additional JPH2s.

UTILITY OF NANOSCALE RESOLUTION FOR STUDYING COUPLON REMODELLING

Pathological remodelling of ventricular myocytes was observed over a decade before the development of super-resolution techniques. In a large majority of the studies examining cellular structure in disease, t-tubule remodelling is a dominant feature [see Guo et al. (2013) for a comprehensive list of studies]. Super-resolution microscopy and other nanoscale imaging methods have been useful tools for characterising the finer features of cellular remodelling and probing possible mechanisms. For example, where confocal microscopy was unable to detect any changes in the SR structure, tomographic EM has demonstrated widespread remodelling of the SR in step with local remodelling of t-tubules and mitochondria (Pinali et al., 2013) in heart failure. Despite the previous confocal studies reporting unaltered RyR arrays, deconvolved STED microscopy super-resolution images examining these in atrial myocytes from a sheep model of atrial fibrillation has shown a fragmentation, a reduction of the average cluster-to-cluster distances and greater longitudinal extents of the clusters (Macquaide et al., 2015) (**Figures 2F,G**). Their computational models predict that these redistributions and remodelling features could explain higher spontaneous Ca^{2+} spark rates and easier propagation of Ca^{2+} waves.

Super-resolution has also been useful for characterising finer features of t-tubule and couplon remodelling as well as probing the underpinning mechanisms. STED image data showing the local *changes* of t-tubule diameter (in the order of 10–25 nm) and orientations in living ventricular myocytes following myocardial infarction (Wagner et al., 2012) were the first to report nanometre-scale remodelling as a feature of this pathology in rat hearts. A number of mechanisms of t-tubule remodelling during pathology that are intrinsic to the myocytes have been characterised. These include the downregulation or cleavage of JPH2 (see review Beavers et al., 2014) and loss of expression of proteins involved in t-tubule biogenesis and maintenance such as bridging integrator-1 (BIN1) (Lyon et al., 2012) and Mitsugumin-29 (MG29) (Correll et al., 2017). In two studies based on a BIN1 deletion mutant mouse model, the authors used tomographic EM and STORM images to suggest that BIN1 expression was essential to developing a complex (folded) membrane topology and functional coupling between LCC and RyR (Hong et al., 2014; Fu et al., 2016). They hypothesised that the loss of this topology, in step with the downregulation of BIN1 expression during failure, leads to a widening of the couplon cleft and diminishing local control of EC coupling. The nanoscale 3D resolution offered by tomographic EM was pivotal to this report. Whilst their analysis consisted of a limited number of example datasets and the folded membrane topology has not been reported elsewhere, it is possible that this t-tubule morphology is either related or equivalent to the junctional dilatation of t-tubules observed previously with dSTORM and EM tomography (Wong et al., 2013). In the cases of JPH2, BIN1 and MG29, visual analysis of t-tubules and couplons in murine models with altered expression of these proteins has been a major strategy of studying mechanisms. In each case, compensatory overexpression of the protein has shown encouraging results in restoring t-tubule structure, or at least function. In each of these avenues, the nanoscale resolution achieved with super-resolution or modern tomographic EM has been essential.

In addition to the above features, a handful of new observations of couplon and cellular remodelling now call for further investigation with the use of nanoscale imaging methods. Among the more recently observed phenomena of t-tubule remodelling, we underscore the 't-sheets,' flattened invaginations of the sarcolemma which form longitudinal compartments

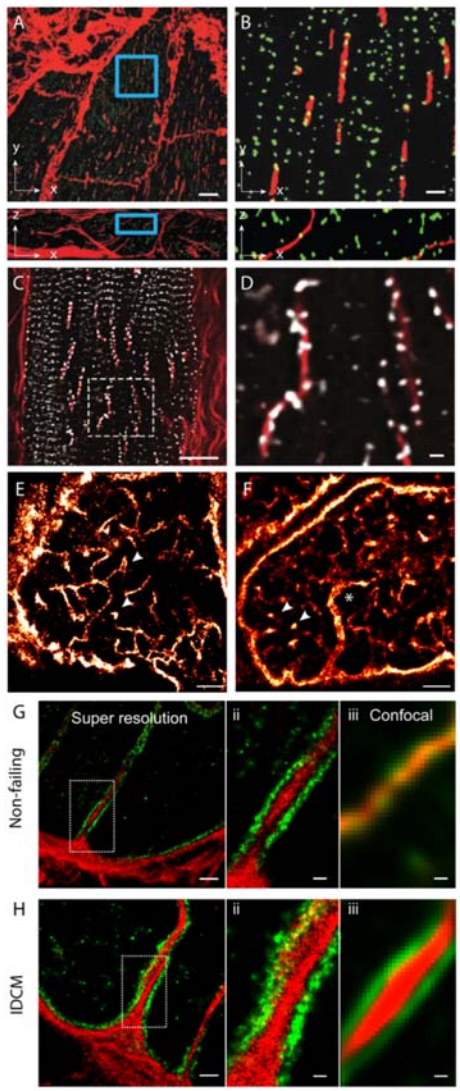

FIGURE 3 | Dilatation of t-tubules in disease and ageing. **(A)** Dilated sheet-like tubules (red) were observed in x-y (upper) and x-z view (lower) by Seidel et al. (2017) in ventricular tissues of patients with chronic heart failure. **(B)** Magnified views illustrate how a subset of RyR clusters (green) appeared to align with these sheet-like tubules (red). **(C)** Similar sheet-like tubules were observed by us in confocal micrographs of ventricular muscle tissue from a human patient with end-stage idiopathic dilated cardiomyopathy (IDCM). **(D)** Magnified view illustrates how a majority of local RyR clusters (grey) are re-arranged along the sheet-like tubules (extending longitudinally, shown in red) instead of maintaining the sarcomeric pattern (transverse). **(E,F)** Compared, are dSTORM images from transverse tissue sections of ventricular cells of young adult (9-weeks old) and aged (100 weeks) stained for t-tubule marker Caveolin-3, respectively. Whilst local dilatations or pockets were observed in the t-tubules in both age groups (arrowheads), macro-tubules (typically > 300 nm in diameter; asterisk in **D**) were observable. **(G,H-i)** Super resolution of both normal and IDCM t-tubules revealed Collagen-VI (red) encased within the tubule lumina whilst dystrophin (green) lined the tubules (magnified view shown in **G,H-ii**). **(G,H-iii)** Illustrate how the limited resolution in the equivalent confocal data fail to reveal this spatial feature in non-dilated t-tubules (in the non failing myocardium). Scale bars: **(A)**: 10 μm, **(B)**: 2 μm, **(C):** 15 μm, **(D):** 2 μm, **(E,F)**: 2 μm. **(G-i,Hi)**: 1 μm, **(G-ii,iii,H-ii,iii)**: 250 nm. **(A,B)** Adapted from Seidel et al. (2017) with permission; **(E,F)** from Crossman et al. (2017) with permission.

spanning many sarcomeres. Seidel et al. (2017) have observed such 't-sheets' in ventricular tissues of patients with chronic heart failure. These structures, visualised with 3D confocal microscopy, coincided with an apparent physical and functional reorganisation of a subset of nearby RyR clusters (**Figures 3A,B**). In tissues that we have examined from human patients with idiopathic dilated cardiomyopathy, we see that a larger proportion of RyR clusters are re-arranged to align with the sheet-like tubules whilst their z-line localisation is lost in the nearby regions of the cytoplasm (**Figures 3C,D**). This point of difference between our observations and those reported Seidel et al. (2017) at the very least, may underscore different severities of the cellular remodelling pathology associated with heart failure. Alternatively, it could indicate different aetiologies which have not been understood yet. Pinali et al. (2015) have observed 'super-tubules' in confocal micrographs and EM tomograms of ischemic border zone tissues following myocardial infarction. In dSTORM tissue imaging, we have observed analogous macro-tubules in a small subset of ventricular myocytes in aged (70–110 week old) mice which display normal cardiac function (**Figures 3E,F**). Whilst computer modelling has predicted that such structures are the likely result of fused t-tubules, the molecular mechanisms, the time course and the consequences to the nanoscale structure of couplons is yet to be investigated. Our recent work which utilised multicolour dSTORM was able to shed light onto one of the likely mechanisms underpinning t-tubule remodelling, particularly dilatation in heart failure (idiopathic dilated cardiomyopathies; IDCM; **Figures 3G,H**). It appeared that the excessive deposition of collagen VI within the lumina of t-tubules driven by local fibroblasts and the direct interactions between collagen VI and dystrophin-associated glycoprotein complexes resident on the remodelling t-tubular membrane can impart t-tubule membrane remodelling observed in IDCM. It is noteworthy that confocal data of the same samples lacked the resolution to identify the organisation of the intra-tubular collagen VI, particularly in the non-failing heart. This underscores how the added resolution of dSTORM was instrumental for this mechanistic observation of t-tubule remodelling.

MODELS OF COUPLON FUNCTION INFORMED BY RECENT NANOSCALE MICROSCOPY

The wide ranging RyR cluster sizes observed by Baddeley et al. (2009) with dSTORM were captured in their Monte Carlo model of unconstrained spontaneous cluster assembly to demonstrate how their variable size and shapes can be simulated. Based on simulated and STED-based RyR image data, Walker et al simulated the excitability of the RyRs, given the cluster size, shape and the position of the receptor within the cluster (Walker et al., 2015). By approximating the RyR arrays in each cluster to a well-filled crystalline array, they demonstrated a higher spark fidelity (i.e., probability of evoking a Ca^{2+} spark, given the opening of an LCC) in larger, well-filled RyR clusters. In a supporting simulation, they predicted that a poorly filled RyR cluster would show diminished spark fidelity. However,

neither STED nor conventional SMLM techniques offered any insights into variations in the RyR-RyR assembly patterns *within* the clusters. A series of simulations of the effects of fragmented RyR clusters seen in atrial fibrillation build on the hypotheses that smaller clusters may lack allosteric inter-RyR coupling and may be prone to greater Ca^{2+} leak compared to larger clusters in the healthy atrial myocytes (Macquaide et al., 2015). In their model, these two attributes provide possible explanations for the greater spontaneous Ca^{2+} spark and wave probabilities observed in the myocytes from tissues showing atrial fibrillation. Beyond these studies, the number of computational models which capture the nanoscale features of couplons are limited. Whilst tomographic EM data have been exploited to good effect to simulate myoplasmic Ca^{2+} dynamics in the sub-micron scale (Rajagopal et al., 2015; Colman et al., 2017), these models do not directly utilise experimentally determined shapes and sizes of couplons or the positions of RyRs within the couplons. Rather, the couplons are simplified as point sources of Ca^{2+}. However, because EM tomograms used thus far have lacked information on the molecular configuration of couplons (e.g., RyR positions), such models have tended to approximate couplons as unitary structures, lacking information on variabilities in cluster sizes, shapes and spacings.

ADVANCING THE RESOLUTION AND QUANTITATIVE UTILITY OF SMLM

Limitations in Contemporary Nanoscale Imaging Techniques

Approaching a decade since the first application of SMLM to study couplons, we have learnt that the resolution achievable with techniques like dSTORM transformed our view of the shapes and mutual positions of RyR clusters. However, with resolution limited to ∼30–50 nm, dSTORM failed to resolve the receptor arrangement pattern within the individual couplon architecture. In particular, it has become clear that the pattern of signal across the extent of RyR clusters observed with dSTORM (see, for example, the enlarged cluster in **Figure 1D**) results almost exclusively from stochastic dye switching and exhibits little correlation with the distribution of receptors across the cluster [see simulation in Supplementary Figure 2A in Jayasinghe et al. (2018)]. 'Counting' of the number of RyRs in each cluster was therefore based rigidly on the assumption that RyR arrays were well-filled quasi-crystalline arrays with receptor assembly with a centre-to-centre distance of ∼30 nm. This approximation was supported by the regularity of the 'feet' spacing in early thin-section TEMs of cardiac couplons and the SEMs of RyR *in vitro* self-assembly observed by Yin and Lai (2000) and Yin et al. (2005). The emerging tomographic EM data from mouse and rat ventricular myocytes in 2009 argued, however, that RyR arrays are unlikely to be uniformly filled (Asghari et al., 2009; Hayashi et al., 2009). It was also not clear whether the area occupied by RyR labelling in dSTORM images was an accurate representation of the couplon geometry, due to the lack of an independent marker for the SR, particularly terminal SR, membranes. EM tomography data appeared to argue that the couplons were a larger structure than reported by the positions of RyRs (Asghari et al., 2009; Hayashi et al., 2009). However, this observation was subject to the manual segmentation approaches that were necessary for reconstructing RyR arrays in the image data which, at the time, lacked an RyR-specific contrast mechanism. Tilt-EM tomograms of RyR in rat ventricular couplons published more recently revealed more convincingly that receptor arrangement can be non-uniform and that they can acutely re-organise into a quasi-crystalline pattern upon altered receptor phosphorylation and changes in free $[Mg^{2+}]_i$ (Asghari et al., 2014). However, detection of couplons with this method was essentially manual and therefore favours larger couplons (e.g., ∼21 RyRs within a single cluster) where an obvious RyR array pattern is visible. There is to date no demonstrated evidence suggesting that the current state of tomographic EM can faithfully detect and segment smaller RyR clusters or solitary RyRs. Whether a free $[Mg^{2+}]_i$ -dependent re-arrangement of RyRs is present similarly in small RyR clusters (e.g., <9) is therefore not known.

DNA-PAINT as a Tool to Visualising Couplons at the True Molecular Scale

An alternative SMLM technique, DNA-PAINT was described in Jungmann et al. (2014). The authors demonstrated its capacity to offer superior resolution in imaging intracellular structures (<10 nm) and greater versatility in multiplexed imaging compared to dSTORM. These two benefits were largely the product of its departure from the photochemical principle which underpinned existing SMLM methods such as dSTORM. The single molecule localisation precision in dSTORM, one of the crucial determinants of resolution, intrinsically depended on the photons which were detectable from each fluorophore photoswitching event (Mortensen et al., 2010) which, in turn, was a function of the redox microenvironment of the sample (Bates et al., 2007). Over the last decade many laboratories around the world, including us, have found it challenging to control or maximise the photon yield to obtain sub-10 nm localisation precision. DNA-PAINT achieves this by complete departure from photochemical switching of fluorophores. The markers in DNA-PAINT are localised by the thermally driven reversible hybridisation of complementary strands of DNA oligonucleotides that leads to transient immobilisation of dye molecules on markers as summarised in **Figure 4A**. As a result, brighter and longer single molecule events are achieved enabling higher photon yield and hence improved signal-to-noise ratio and marker localisation precision. We have recently used this method for mapping RyRs in peripheral couplons of myocytes at resolution of ∼10–15 nm (Jayasinghe et al., 2018).

At a magnified view, the DNA-PAINT images of RyR distribution reported highly distinctive and highly reproducible 'punctate' labelling densities within the cluster area, which were not observed in the dSTORM images (**Figures 4B–D**). Utilising correlative dSTORM imaging experiments and a target

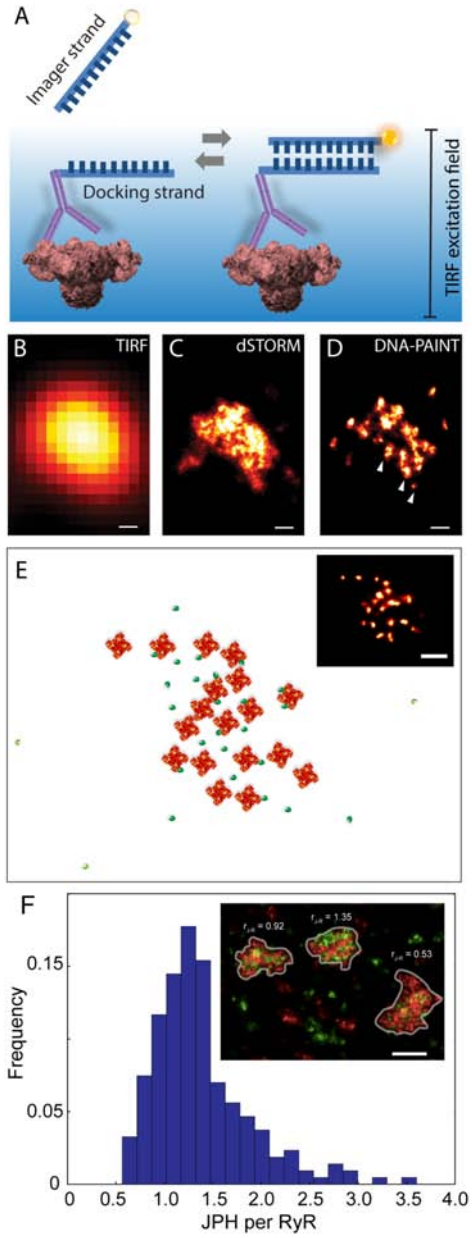

FIGURE 4 | Adaptation of DNA-PAINT to mapping RyR in peripheral couplons of rat cardiomyocytes. **(A)** DNA-PAINT relies on the thermally driven stochastic and reversible binding between a fluorescently labelled 'imager' DNA oligo and a 'docking' DNA oligo which in this scenario is linked to the anti-RyR antibody. Markers near the cell surface are illuminated with a TIRF excitation field. Shown, is a comparison of **(B)** conventional TIRF, **(C)** dSTORM and **(D)** DNA-PAINT images of an RyR cluster, highlighting the detection of finer punctate labelling densities which are unique to the latter (arrowheads). **(E)** Example of an approximate reconstruction of individual RyR arrangement (red) and hypothesised accessory proteins such as JPH2 (green) based on the RyR positions reported by an experimental DNA-PAINT image of a peripheral couplon (inset). **(F)** Histogram illustrating the distribution of JPH2 to RyR ratios [mean 1.38, mode at 1.25 and a width of 0.5 (standard deviation), $n = 250$ clusters (containing ≥ 15 RyRs)]. Inset illustrates examples of three adjacent couplons exhibiting JPH2/RyR ratios ranging between 0.53 and 1.35 (RyR shown in red and JPH2 in green). Scale bars: **(B–D)**: 50 nm, **(E)**: 100 nm, **(F)**: 250 nm. All panels adapted from Jayasinghe et al. (2018).

counting algorithm called qPAINT (Jungmann et al., 2016), we were able to confirm that these puncta corresponded to individual RyRs within clusters which were first resolved nearly a decade ago with dSTORM. Their individual positions offered a more realistic view of the *in situ* positioning of RyRs and accessory proteins such as JPH2 in the intact couplon (see **Figure 4E** for an approximate reconstruction). Exploiting the novel ability to visualise large areas of the cell with sub-10-nanometre resolution, we sampled large numbers (>1000) of RyR clusters to robustly observe that peripheral RyR clusters, on average, contained ∼9 RyRs – a number that is approximately half of that estimated a decade ago with dSTORM (Baddeley et al., 2009). Consistent with the tomographic EM analysis (Asghari et al., 2014), the DNA-PAINT maps of RyR revealed an irregular receptor arrangement which was not consistent with the crystalline array structures observed previously *in vitro* (Yin and Lai, 2000; Yin et al., 2005). However, this may be compatible with the more stochastic RyR-RyR associations (called 'branched arrays') predicted by computational modelling based on *in vitro* interactions observed between adjacent receptors (Cabra et al., 2016). Large (>50 nm) gaps which were observed within the RyR clusters in DNA-PAINT image data may be a manifestation of this type of *in situ* cluster assembly. With the superior resolution and robust detection of the RyR positions, DNA-PAINT provided an opportunity to visualise JPH2 co-clustering at the couplons. Based on spatial and target counting analyses, multiplexed DNA-PAINT data revealed that JPH2 is, on average, localised within 50 nm of the centre of RyR channels in a likely bound configuration. It was also observed that the stoichiometry of JPH2:RyR co-clustering varied significantly (between 0.5 and 2.5) in the couplons of the same cell (**Figure 4F**). Noting that the density of local JPH2 regulates the excitability of RyRs (van Oort et al., 2011; Munro et al., 2016), it has allowed us to propose that the variable co-clustering of regulatory proteins such as JPH2 in couplons could represent a previously unseen mechanism of regulating Ca^{2+} release function in a given cytoplasmic locality.

CURRENT UNDERSTANDING OF COUPLON STRUCTURE-FUNCTION RELATIONSHIP AND FUTURE CHALLENGES

With the new molecular-scale visualisations, both with the latest SMLM and the advancing tomographic EM technologies, it is our observation that couplon structure appears to be less stereotypic than previously assumed (i.e., RyR arrays are less crystalline and less well filled; **Figures 5A,B**). However, it is important to note that quasi-crystalline RyR array patterns [i.e., side-by-side or diagonal/'checkerboard' arrangement of neighbouring RyRs, observed by Asghari et al. (2009)] are still compatible with the receptor positions mapped by DNA-PAINT (see **Figure 5B** inset). Assessing the DNA-PAINT data, it is unlikely to be orchestrated by direct

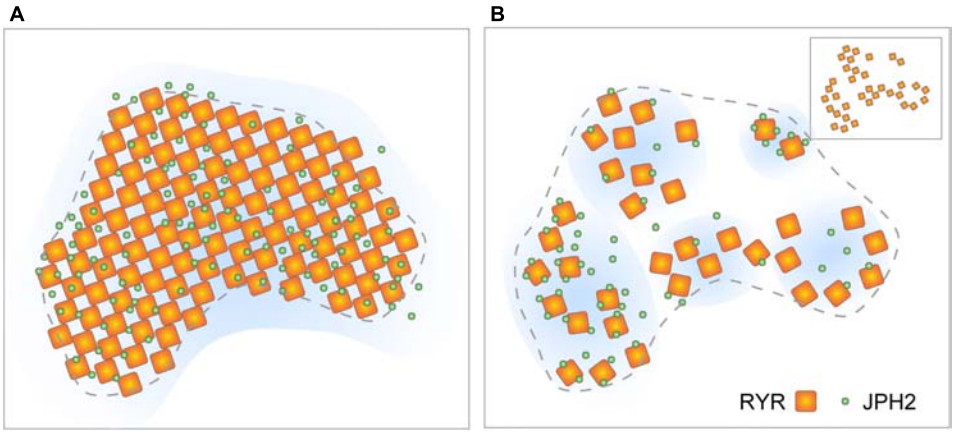

FIGURE 5 | Evolving view of RyR arrangement within couplons. **(A)** The classic model of quasi-crystalline arrangement of RyR and near-uniform co-clustering with JPH2 within well-filled couplon sections. **(B)** Revised model based on tomographic EM and DNA-PAINT data proposing looser arrangement of RyRs and variable co-clustering with JPH. Inset illustrates the scenario where a diagonal ('checkerboard') arrangement of RyRs could be achieved even in the loosely arranged clusters. Adapted from Jayasinghe et al. (2018).

RyR-RyR contact via the SPRY1/P1 domain interactions. The fact that the patterns are sensitive to $[Mg^{2+}]_i$ and phosphorylation state (Asghari et al., 2009) could support the idea that the RyR array patterns are organised by accessory proteins resident within the couplon. These features, in fact, reveal new dynamic aspects of the couplon structure. More recent reports based on live cell confocal imaging of myocytes expressing RyR-GFP fusion proteins (Hiess et al., 2018) demonstrate that large RyR clusters located at the cell periphery might be subject to acute turnover or mobilisation. Both the simulations based on STED analyses (Walker et al., 2014; Wang et al., 2014) and the JPH2/RyR co-clustering analysis from DNA-PAINT (Wang et al., 2014; Jayasinghe et al., 2018) suggest that couplons are likely to possess heterogeneous excitabilities. They may also possess different likelihoods of Ca^{2+} release termination, depending on the RyR-spacings and the couplon cleft spaces resulting from variable RyR arrangement; however, the current computer models need to explore the RyR array morphologies within their spatial models (Gillespie and Fill, 2013; Laver et al., 2013). Variability in the couplon structure and/or composition may also underly mechanisms giving rise to the spontaneous late Ca^{2+} sparks characterised recently by Fowler et al. (2018) as a potentially arrhythmogenic phenomenon.

Limitations of the Current Nanoscale Couplon Imaging Experiments

Despite the rapid uptake of SMLM by hundreds of research groups worldwide, the number of groups which have comfortably incorporated this technology into investigations on myocyte, particularly couplon, structure remains limited. This may be because SMLM represents either a considerable financial investment (in off-the-shelf instrumentation) or, alternatively, a skill investment of specialist researchers to harness the open source software tools which are essential for it. However, nearly a decade on from our first experiments, SMLM, particularly DNA-PAINT, remains a robust approach to achieving single-protein level of resolution in imaging couplons. With the demonstration of various applications of DNA-PAINT, particularly in imaging optically thick samples (Auer et al., 2017; Lutz et al., 2018) in 3D imaging protocols (Schueder et al., 2017), it is set to extend our view of the couplon structure well beyond the sub-sarcolemmal nanodomains resolved recently (Jayasinghe et al., 2018). However, it needs to be emphasised that the accuracy of the super-resolution imaging extends only as far as the reliability and availability of probes, particularly antibodies. Whilst a number of studies have used well-characterised antibodies against RyR2, the access to a reliable LCC antibody remains limited to a handful of research groups. Repeated (and mostly unpublished) immunolabelling data of LCC by a number of other groups underscores the currently limited opportunity to visualise the local couplings of RyR2 and LCC at the single-protein level of resolution that is now available. In our view, this challenge calls for a multi-partisan approach to comparing antibody (or alternative specific) probes and tissue/cell preparation protocols. From the data that has been published thus far, DNA-PAINT analyses appear to strongly complement the tomographic EM approaches that have been used to visualise the arrangement of single RyRs (Asghari et al., 2009, 2014). Correlative SMLM/EM protocols (e.g., Löschberger et al., 2014), as laborious and time consuming as they are, may capture the best of both nanoscale approaches. Incorporation of these spatial features into geometrically realistic computer models will continue to provide crucial insights into how this nanostructure can determine function. However, these models would benefit from live cell-super resolution microscopy measurements. Transgenic mice expressing fluorescent protein-fused RyRs that have recently been made (Hiess et al., 2018; Hou et al., 2018) could provide a unique

opportunity to visualise these proteins at the nanoscale in the living cell.

ETHICS STATEMENT

Figures 3C,D includes original images recorded from a human cardiac tissue sample of a failing heart, obtained from the Auckland City Hospital transplant program. All human tissue was obtained with written and informed consent from transplant recipients or families of organ donors in accordance to the declaration of Helsinki, institutional guidelines as approved by the Health and Disability Ethics Committee of New Zealand (NTY/05/08/050/AM05). **Figures 3E,F** include original images acquired from heart tissue of C57BL/6 mice. These experiments were done according to a protocol approved by the Animal Ethics Approval Committee of the University of Exeter (reference: EMPS-2014-1). All other data are re-productions of data that were published previously, as per citations.

AUTHOR CONTRIBUTIONS

IJ, DC, and CS conceived the idea. IJ, AC, OdL, and SS acquired or re-analysed the data. IJ, DC, and CS wrote the paper.

ACKNOWLEDGMENTS

The authors thank the Wellcome Trust (Grant # 207684/Z/17/Z to IJ), Engineering and Physical Sciences Research Council of the UK (Grant # EP/N008235/1 to CS) and the Auckland Medical Research Foundation of New Zealand (Grant # 1111009 to DC) for funding supporting the work presented in this manuscript.

REFERENCES

Abbe, E. (1873). Beiträge zur theorie des mikroskops und der mikroskopischen wahrnehmung. *Arch. Mikrosk. Anat.* 9, 413–418. doi: 10.1007/BF02956173

Asghari, P., Schulson, M., Scriven, D. R., Martens, G., and Moore, E. D. (2009). Axial tubules of rat ventricular myocytes form multiple junctions with the sarcoplasmic reticulum. *Biophys. J.* 96, 4651–4660. doi: 10.1016/j.bpj.2009.02.058

Asghari, P., Scriven, D. R., Sanatani, S., Gandhi, S. K., Campbell, A. I., and Moore, E. D. (2014). Nonuniform and variable arrangements of ryanodine receptors within mammalian ventricular couplons. *Circ. Res.* 115, 252–262. doi: 10.1161/CIRCRESAHA.115.303897

Auer, A., Strauss, M. T., Schlichthaerle, T., and Jungmann, R. (2017). Fast, background-free DNA-PAINT imaging using FRET-based probes. *Nano Lett.* 17, 6428–6434. doi: 10.1021/acs.nanolett.7b03425

Baddeley, D., Jayasinghe, I. D., Lam, L., Rossberger, S., Cannell, M. B., and Soeller, C. (2009). Optical single-channel resolution imaging of the ryanodine receptor distribution in rat cardiac myocytes. *Proc. Natl. Acad. Sci. U.S.A.* 106, 22275–22280. doi: 10.1073/pnas.0908971106

Balijepalli, R. C., Lokuta, A. J., Maertz, N. A., Buck, J. M., Haworth, R. A., Valdivia, H. H., et al. (2003). Depletion of T-tubules and specific subcellular changes in sarcolemmal proteins in tachycardia-induced heart failure. *Cardiovasc. Res.* 59, 67–77. doi: 10.1016/S0008-6363(03)00325-0

Bates, M., Huang, B., Dempsey, G. T., and Zhuang, X. (2007). Multicolor super-resolution imaging with photo-switchable fluorescent probes. *Science* 317, 1749–1753. doi: 10.1126/science.1146598

Beavers, D. L., Landstrom, A. P., Chiang, D. Y., and Wehrens, X. H. (2014). Emerging roles of junctophilin-2 in the heart and implications for cardiac diseases. *Cardiovasc. Res.* 103, 198–205. doi: 10.1093/cvr/cvu151

Bers, D. M. (2002). Cardiac excitation-contraction coupling. *Nature* 415, 198–205. doi: 10.1038/415198a

Betzig, E., Patterson, G. H., Sougrat, R., Lindwasser, O. W., Olenych, S., Bonifacino, J. S., et al. (2006). Imaging intracellular fluorescent proteins at nanometer resolution. *Science* 313, 1642–1645. doi: 10.1126/science.1127344

Brandenburg, S., Kohl, T., Williams, G. S., Gusev, K., Wagner, E., Rog-Zielinska, E. A., et al. (2016). Axial tubule junctions control rapid calcium signaling in atria. *J. Clin. Invest.* 126, 3999–4015. doi: 10.1172/JCI88241

Brette, F., Komukai, K., and Orchard, C. H. (2002). Validation of formamide as a detubulation agent in isolated rat cardiac cells. *Am. J. Physiol. Heart Circ. Physiol.* 283, H1720–H1728. doi: 10.1152/ajpheart.00347.2002

Cabra, V., Murayama, T., and Samso, M. (2016). Ultrastructural analysis of self-associated RyR2s. *Biophys. J.* 110, 2651–2662. doi: 10.1016/j.bpj.2016.05.013

Cannell, M. B., Berlin, J. R., and Lederer, W. J. (1987). Effect of membrane potential changes on the calcium transient in single rat cardiac muscle cells. *Science* 238, 1419–1423. doi: 10.1126/science.2446391

Cannell, M. B., Cheng, H., and Lederer, W. J. (1995). The control of calcium release in heart muscle. *Science* 268, 1045–1049. doi: 10.1126/science.7754384

Cannell, M. B., Crossman, D. J., and Soeller, C. (2006). Effect of changes in action potential spike configuration, junctional sarcoplasmic reticulum micro-architecture and altered t-tubule structure in human heart failure. *J. Muscle Res. Cell Motil.* 27, 297–306. doi: 10.1007/s10974-006-9089-y

Cheng, H., Lederer, W. J., and Cannell, M. B. (1993). Calcium sparks: elementary events underlying excitation-contraction coupling in heart muscle. *Science* 262, 740–744. doi: 10.1126/science.8235594

Chen-Izu, Y., Mcculle, S. L., Ward, C. W., Soeller, C., Allen, B. M., Rabang, C., et al. (2006). Three-dimensional distribution of ryanodine receptor clusters in cardiac myocytes. *Biophys. J.* 91, 1–13. doi: 10.1529/biophysj.105.077180

Colman, M. A., Pinali, C., Trafford, A. W., Zhang, H., and Kitmitto, A. (2017). A computational model of spatio-temporal cardiac intracellular calcium handling with realistic structure and spatial flux distribution from sarcoplasmic reticulum and t-tubule reconstructions. *PLoS Comput. Biol.* 13:e1005714. doi: 10.1371/journal.pcbi.1005714

Correll, R. N., Lynch, J. M., Schips, T. G., Prasad, V., York, A. J., Sargent, M. A., et al. (2017). Mitsugumin 29 regulates t-tubule architecture in the failing heart. *Sci. Rep.* 7:5328. doi: 10.1038/s41598-017-05284-2

Crossman, D. J., Hou, Y., Jayasinghe, I., Baddeley, D., and Soeller, C. (2015a). Combining confocal and single molecule localisation microscopy: a correlative approach to multi-scale tissue imaging. *Methods* 88, 98–108. doi: 10.1016/j.ymeth.2015.03.011

Crossman, D. J., Young, A. A., Ruygrok, P. N., Nason, G. P., Baddelely, D., Soeller, C., et al. (2015b). T-tubule disease: relationship between t-tubule organization and regional contractile performance in human dilated cardiomyopathy. *J. Mol. Cell Cardiol.* 84, 170–178. doi: 10.1016/j.yjmcc.2015.04.022

Crossman, D. J., Ruygrok, P. N., Soeller, C., and Cannell, M. B. (2011). Changes in the organization of excitation-contraction coupling structures in failing human heart. *PLoS One* 6:e17901. doi: 10.1371/journal.pone.0017901

Crossman, D. J., Shen, X., Jullig, M., Munro, M., Hou, Y., Middleditch, M., et al. (2017). Increased collagen within the transverse tubules in human heart failure. *Cardiovasc. Res.* 113, 879–891. doi: 10.1093/cvr/cvx055

Douglass, K. M., Sieben, C., Archetti, A., Lambert, A., and Manley, S. (2016). Super-resolution imaging of multiple cells by optimised flat-field epi-illumination. *Nat. Photonics* 10, 705–708. doi: 10.1038/nphoton.2016.200

Fabiato, A. (1983). Calcium-induced release of calcium from the cardiac sarcoplasmic reticulum. *Am. J. Physiol.* 245, C1–C14.

Ferguson, D. G., Schwartz, H. W., and Franzini-Armstrong, C. (1984). Subunit structure of junctional feet in triads of skeletal muscle: a freeze-drying, rotary-shadowing study. *J. Cell Biol.* 99, 1735–1742. doi: 10.1083/jcb.99.5.1735

Flucher, B. E., and Franzini-Armstrong, C. (1996). Formation of junctions involved in excitation-contraction coupling in skeletal and cardiac muscle. *Proc. Natl. Acad. Sci. U.S.A.* 93, 8101–8106. doi: 10.1073/pnas.93.15.8101

Fowler, E. D., Kong, C. H. T., Hancox, J. C., and Cannell, M. B. (2018). Late $Ca(2^+)$ sparks and ripples during the systolic $Ca(2^+)$ transient in heart muscle cells. *Circ. Res.* 122, 473–478. doi: 10.1161/CIRCRESAHA.117.312257

Franzini-Armstrong, C. (2010). RyRs: their disposition, frequency, and relationships with other proteins of calcium release units. *Curr. Top. Membr.* 66, 3–26. doi: 10.1016/S1063-5823(10)66001-2

Franzini-Armstrong, C. (2018a). Correction: the relationship between form and function throughout the history of excitation-contraction coupling. *J. Gen. Physiol.* 150:369. doi: 10.1085/jgp.20171188901162018c

Franzini-Armstrong, C. (2018b). The relationship between form and function throughout the history of excitation-contraction coupling. *J. Gen. Physiol.* 150, 189–210. doi: 10.1085/jgp.201711889

Franzini-Armstrong, C., Protasi, F., and Ramesh, V. (1999). Shape, size, and distribution of $Ca(2^+)$ release units and couplons in skeletal and cardiac muscles. *Biophys. J.* 77, 1528–1539. doi: 10.1016/S0006-3495(99)77000-1

Fu, Y., Shaw, S. A., Naami, R., Vuong, C. L., Basheer, W. A., Guo, X., et al. (2016). Isoproterenol promotes rapid ryanodine receptor movement to bridging integrator 1 (BIN1)-organized dyads. *Circulation* 133, 388–397. doi: 10.1161/CIRCULATIONAHA.115.018535

Gambin, Y., Ariotti, N., Mcmahon, K. A., Bastiani, M., Sierecki, E., Kovtun, O., et al. (2013). Single-molecule analysis reveals self assembly and nanoscale segregation of two distinct cavin subcomplexes on caveolae. *eLife* 3:e01434. doi: 10.7554/eLife.01434

Gillespie, D., and Fill, M. (2013). Pernicious attrition and inter-RyR2 CICR current control in cardiac muscle. *J. Mol. Cell Cardiol.* 58, 53–58. doi: 10.1016/j.yjmcc.2013.01.011

Gomez, A. M., Valdivia, H. H., Cheng, H., Lederer, M. R., Santana, L. F., Cannell, M. B., et al. (1997). Defective excitation-contraction coupling in experimental cardiac hypertrophy and heart failure. *Science* 276, 800–806. doi: 10.1126/science.276.5313.800

Guo, A., Zhang, C., Wei, S., Chen, B., and Song, L. S. (2013). Emerging mechanisms of T-tubule remodelling in heart failure. *Cardiovasc. Res.* 98, 204–215. doi: 10.1093/cvr/cvt020

Hayashi, T., Martone, M. E., Yu, Z., Thor, A., Doi, M., Holst, M. J., et al. (2009). Three-dimensional electron microscopy reveals new details of membrane systems for $Ca2^+$ signaling in the heart. *J. Cell Sci.* 122, 1005–1013. doi: 10.1242/jcs.028175

Hess, S. T., Girirajan, T. P. K., and Mason, M. D. (2006). Ultra-high resolution imaging by fluorescence photoactivation localization microscopy. *Biophys. J.* 91, 4258–4272. doi: 10.1529/biophysj.106.091116

Hiess, F., Detampel, P., Nolla-Colomer, C., Vallmitjana, A., Ganguly, A., Amrein, M., et al. (2018). Dynamic and irregular distribution of RyR2 clusters in the periphery of live ventricular myocytes. *Biophys. J.* 114, 343–354. doi: 10.1016/j.bpj.2017.11.026

Hill, A. V. (1949). The onset of contraction. *Proc. R. Soc. Lond. B Biol. Sci.* 136, 242–254. doi: 10.1098/rspb.1949.0023

Hong, T., Yang, H., Zhang, S. S., Cho, H. C., Kalashnikova, M., Sun, B., et al. (2014). Cardiac BIN1 folds T-tubule membrane, controlling ion flux and limiting arrhythmia. *Nat. Med.* 20, 624–632. doi: 10.1038/nm.3543

Hou, Y., Crossman, D. J., Rajagopal, V., Baddeley, D., Jayasinghe, I., and Soeller, C. (2014). Super-resolution fluorescence imaging to study cardiac biophysics: alpha-actinin distribution and Z-disk topologies in optically thick cardiac tissue slices. *Prog. Biophys. Mol. Biol.* 115, 328–339. doi: 10.1016/j.pbiomolbio.2014.07.003

Hou, Y., Jayasinghe, I., Crossman, D. J., Baddeley, D., and Soeller, C. (2015). Nanoscale analysis of ryanodine receptor clusters in dyadic couplings of rat cardiac myocytes. *J. Mol. Cell Cardiol.* 80, 45–55. doi: 10.1016/j.yjmcc.2014.12.013

Hou, Y., Manfra, O., Li, J., Shen, X., and Louch, W. E. (2018). Live cell palm techniques for super resolution imaging of murine cardiac myocytes. *Biophys. J.* 113:549a. doi: 10.1016/j.bpj.2017.11.3000

Izu, L. T., Means, S. A., Shadid, J. N., Chen-Izu, Y., and Balke, C. W. (2006). Interplay of ryanodine receptor distribution and calcium dynamics. *Biophys. J.* 91, 95–112. doi: 10.1529/biophysj.105.077214

Jayasinghe, I., Clowsley, A. H., Lin, R., Lutz, T., Harrison, C., Green, E., et al. (2018). True molecular scale visualization of variable clustering properties of ryanodine receptors. *Cell Rep.* 22, 557–567. doi: 10.1016/j.celrep.2017.12.045

Jayasinghe, I., Crossman, D., Soeller, C., and Cannell, M. (2012). Comparison of the organization of T-tubules, sarcoplasmic reticulum and ryanodine receptors in rat and human ventricular myocardium. *Clin. Exp. Pharmacol. Physiol.* 39, 469–476. doi: 10.1111/j.1440-1681.2011.05578.x

Jayasinghe, I. D., Baddeley, D., Kong, C. H., Wehrens, X. H., Cannell, M. B., and Soeller, C. (2012). Nanoscale organization of junctophilin-2 and ryanodine receptors within peripheral couplings of rat ventricular cardiomyocytes. *Biophys. J.* 102, L19–L21. doi: 10.1016/j.bpj.2012.01.034

Jayasinghe, I. D., Cannell, M. B., and Soeller, C. (2009). Organization of ryanodine receptors, transverse tubules, and sodium-calcium exchanger in rat myocytes. *Biophys. J.* 97, 2664–2673. doi: 10.1016/j.bpj.2009.08.036

Jayasinghe, I. D., Clowsley, A. H., Munro, M., Hou, Y., Crossman, D. J., and Soeller, C. (2015). Revealing T-tubules in striated muscle with new optical super-resolution microscopy techniquess. *Eur. J. Transl. Myol.* 25:4747. doi: 10.4081/ejtm.2015.4747

Jayasinghe, I. D., Crossman, D. J., Soeller, C., and Cannell, M. B. (2010). A new twist in cardiac muscle: dislocated and helicoid arrangements of myofibrillar z-disks in mammalian ventricular myocytes. *J. Mol. Cell Cardiol.* 48, 964–971. doi: 10.1016/j.yjmcc.2009.12.012

Jayasinghe, I. D., Munro, M., Baddeley, D., Launikonis, B. S., and Soeller, C. (2014). Observation of the molecular organization of calcium release sites in fast- and slow-twitch skeletal muscle with nanoscale imaging. *J. R. Soc. Interface* 11:20140570. doi: 10.1098/rsif.2014.0570

Jungmann, R., Avendaño, M. S., Dai, M., Woehrstein, J. B., Agasti, S. S., Feiger, Z., et al. (2016). Quantitative super-resolution imaging with qPAINT. *Nat. Methods* 13, 439–442. doi: 10.1038/nmeth.3804

Jungmann, R., Avendano, M. S., Woehrstein, J. B., Dai, M., Shih, W. M., and Yin, P. (2014). Multiplexed 3D cellular super-resolution imaging with DNA-PAINT and Exchange-PAINT. *Nat. Methods* 11, 313–318. doi: 10.1038/nmeth.2835

Laver, D. R., Kong, C. H., Imtiaz, M. S., and Cannell, M. B. (2013). Termination of calcium-induced calcium release by induction decay: an emergent property of stochastic channel gating and molecular scale architecture. *J. Mol. Cell Cardiol.* 54, 98–100. doi: 10.1016/j.yjmcc.2012.10.009

Li, P., Wei, W., Cai, X., Soeller, C., Cannell, M. B., and Holden, A. V. (2010). Computational modelling of the initiation and development of spontaneous intracellular $Ca2^+$ waves in ventricular myocytes. *Philos. Trans. A Math. Phys. Eng. Sci.* 368, 3953–3965. doi: 10.1098/rsta.2010.0146

Lines, G. T., Sande, J. B., Louch, W. E., Mork, H. K., Grottum, P., and Sejersted, O. M. (2006). Contribution of the $Na^+/Ca2^+$ exchanger to rapid $Ca2^+$ release in cardiomyocytes. *Biophys. J.* 91, 779–792. doi: 10.1529/biophysj.105.072447

Löschberger, A., Franke, C., Krohne, G., Van De Linde, S., and Sauer, M. (2014). Correlative super-resolution fluorescence and electron microscopy of the nuclear pore complex with molecular resolution. *J. Cell Sci.* 127, 4351–4355. doi: 10.1242/jcs.156620

Loschberger, A., Van De Linde, S., Dabauvalle, M. C., Rieger, B., Heilemann, M., Krohne, G., et al. (2012). Super-resolution imaging visualizes the eightfold symmetry of gp210 proteins around the nuclear pore complex and resolves the central channel with nanometer resolution. *J. Cell Sci.* 125, 570–575. doi: 10.1242/jcs.098822

Louch, W. E., Bito, V., Heinzel, F. R., Macianskiene, R., Vanhaecke, J., Flameng, W., et al. (2004). Reduced synchrony of $Ca2^+$ release with loss of T-tubules-a comparison to $Ca2^+$ release in human failing cardiomyocytes. *Cardiovasc. Res.* 62, 63–73. doi: 10.1016/j.cardiores.2003.12.031

Lutz, T., Clowsley, A. H., Lin, R., Pagliara, S., Di Michele, L., and Soeller, C. (2018). Versatile multiplexed super-resolution imaging of nanostructures by Quencher-Exchange-PAINT. *Nano Res.* 114:349a. doi: 10.1007/s12274-018-1971-6

Lyon, A. R., Nikolaev, V. O., Miragoli, M., Sikkel, M. B., Paur, H., Benard, L., et al. (2012). Plasticity of surface structures and beta(2)-adrenergic receptor localization in failing ventricular cardiomyocytes during recovery from heart

failure. *Circ. Heart Fail.* 5, 357–365. doi: 10.1161/CIRCHEARTFAILURE.111.964692

Macquaide, N., Tuan, H. T., Hotta, J., Sempels, W., Lenaerts, I., Holemans, P., et al. (2015). Ryanodine receptor cluster fragmentation and redistribution in persistent atrial fibrillation enhance calcium release. *Cardiovasc. Res.* 108, 387–398. doi: 10.1093/cvr/cvv231

Manfra, O., Shen, X., Hell, J. W., and Edward Louch, W. (2018). Super-resolution (dSTORM) imaging of calcium handling proteins in cardiomyocytes. *Biophys. J.* 114:620a. doi: 10.1016/j.bpj.2017.11.3356

Mikhaylova, M., Cloin, B. M., Finan, K., Van Den Berg, R., Teeuw, J., Kijanka, M. M., et al. (2015). Resolving bundled microtubules using anti-tubulin nanobodies. *Nat. Commun.* 6:7933. doi: 10.1038/ncomms8933

Mortensen, K. I., Churchman, L. S., Spudich, J. A., and Flyvbjerg, H. (2010). Optimized localization analysis for single-molecule tracking and super-resolution microscopy. *Nat. Methods* 7, 377–381. doi: 10.1038/nmeth.1447

Munro, M. L., Jayasinghe, I. D., Wang, Q., Quick, A., Wang, W., Baddeley, D., et al. (2016). Junctophilin-2 in the nanoscale organisation and functional signalling of ryanodine receptor clusters in cardiomyocytes. *J. Cell Sci.* 129, 4388–4398. doi: 10.1242/jcs.196873

Pinali, C., Bennett, H., Davenport, J. B., Trafford, A. W., and Kitmitto, A. (2013). Three-dimensional reconstruction of cardiac sarcoplasmic reticulum reveals a continuous network linking transverse-tubules: this organization is perturbed in heart failure. *Circ. Res.* 113, 1219–1230. doi: 10.1161/CIRCRESAHA.113.301348

Pinali, C., Holt, C. M., Bennett, H. J., Davenport, J. B., Walker, R., Murfitt, L., et al. (2015). 166 T-tubule remodelling and formation of super-tubules in the border zone of cardiac myocytes in the infarcted pig heart. *Heart* 101, A94–A94. doi: 10.1136/heartjnl-2015-308066.166

Rajagopal, V., Bass, G., Walker, C. G., Crossman, D. J., Petzer, A., Hickey, A., et al. (2015). Examination of the effects of heterogeneous organization of RyR clusters, myofibrils and mitochondria on $Ca2^+$ release patterns in cardiomyocytes. *PLoS Comput. Biol.* 11:e1004417. doi: 10.1371/journal.pcbi.1004417

Ries, J., Kaplan, C., Platonova, E., Eghlidi, H., and Ewers, H. (2012). A simple, versatile method for GFP-based super-resolution microscopy via nanobodies. *Nat. Methods* 9, 582–584. doi: 10.1038/nmeth.1991

Rust, M. J., Bates, M., and Zhuang, X. (2006). Sub-diffraction-limit imaging by stochastic optical reconstruction microscopy (STORM). *Nat. Methods* 3, 793–795. doi: 10.1038/nmeth929

Sachse, F. B., Savio-Galimberti, E., Goldhaber, J. I., and Bridge, J. H. (2009). Towards computational modeling of excitation-contraction coupling in cardiac myocytes: reconstruction of structures and proteins from confocal imaging. *Pac. Symp. Biocomput.* 2009, 328–339.

Sauer, M., and Heilemann, M. (2017). Single-molecule localization microscopy in eukaryotes. *Chem. Rev.* 117, 7478–7509. doi: 10.1021/acs.chemrev.6b00667

Schueder, F., Lara-Gutiérrez, J., Beliveau, B. J., Saka, S. K., Sasaki, H. M., Woehrstein, J. B., et al. (2017). Multiplexed 3D super-resolution imaging of whole cells using spinning disk confocal microscopy and DNA-PAINT. *Nat. Commun.* 8:2090. doi: 10.1038/s41467-017-02028-8

Scriven, D. R., Asghari, P., Schulson, M. N., and Moore, E. D. (2010). Analysis of Cav1.2 and ryanodine receptor clusters in rat ventricular myocytes. *Biophys. J.* 99, 3923–3929. doi: 10.1016/j.bpj.2010.11.008

Scriven, D. R., Dan, P., and Moore, E. D. (2000). Distribution of proteins implicated in excitation-contraction coupling in rat ventricular myocytes. *Biophys. J.* 79, 2682–2691. doi: 10.1016/S0006-3495(00)76506-4

Scriven, D. R., Klimek, A., Asghari, P., Bellve, K., and Moore, E. D. (2005). Caveolin-3 is adjacent to a group of extradyadic ryanodine receptors. *Biophys. J.* 89, 1893–1901. doi: 10.1529/biophysj.105.064212

Seidel, T., Navankasattusas, S., Ahmad, A., Diakos, N. A., Xu, W. D., Tristani-Firouzi, M., et al. (2017). Sheet-like remodeling of the transverse tubular system in human heart failure impairs excitation-contraction coupling and functional recovery by mechanical unloading. *Circulation* 135, 1632–1645. doi: 10.1161/CIRCULATIONAHA.116.024470

Shim, S. H., Xia, C., Zhong, G., Babcock, H. P., Vaughan, J. C., Huang, B., et al. (2012). Super-resolution fluorescence imaging of organelles in live cells with photoswitchable membrane probes. *Proc. Natl. Acad. Sci. U.S.A.* 109, 13978–13983. doi: 10.1073/pnas.1201882109

Sobie, E. A., Guatimosim, S., Gomez-Viquez, L., Song, L. S., Hartmann, H., Saleet Jafri, M., et al. (2006). The Ca 2^+ leak paradox and rogue ryanodine receptors: SR Ca 2^+ efflux theory and practice. *Prog. Biophys. Mol. Biol.* 90, 172–185. doi: 10.1016/j.pbiomolbio.2005.06.010

Soeller, C., and Cannell, M. B. (1997). Numerical simulation of local calcium movements during L-type calcium channel gating in the cardiac diad. *Biophys. J.* 73, 97–111. doi: 10.1016/S0006-3495(97)78051-2

Soeller, C., and Cannell, M. B. (1999). Examination of the transverse tubular system in living cardiac rat myocytes by 2-photon microscopy and digital image–processing techniques. *Circ. Res.* 84, 266–275. doi: 10.1161/01.RES.84.3.266

Soeller, C., Crossman, D., Gilbert, R., and Cannell, M. B. (2007). Analysis of ryanodine receptor clusters in rat and human cardiac myocytes. *Proc. Natl. Acad. Sci. U.S.A.* 104, 14958–14963. doi: 10.1073/pnas.0703016104

Soeller, C., Jayasinghe, I. D., Li, P., Holden, A. V., and Cannell, M. B. (2009). Three-dimensional high-resolution imaging of cardiac proteins to construct models of intracellular $Ca2^+$ signalling in rat ventricular myocytes. *Exp. Physiol.* 94, 496–508. doi: 10.1113/expphysiol.2008.043976

Song, L. S., Sobie, E. A., Mcculle, S., Lederer, W. J., Balke, C. W., and Cheng, H. (2006). Orphaned ryanodine receptors in the failing heart. *Proc. Natl. Acad. Sci. U.S.A.* 103, 4305–4310. doi: 10.1073/pnas.0509324103

Stern, M. D. (1992). Theory of excitation-contraction coupling in cardiac muscle. *Biophys. J.* 63, 497–517. doi: 10.1016/S0006-3495(92)81615-6

Stern, M. D., Pizarro, G., and Rios, E. (1997). Local control model of excitation-contraction coupling in skeletal muscle. *J. Gen. Physiol.* 110, 415–440. doi: 10.1085/jgp.110.4.415

Sun, X. H., Protasi, F., Takahashi, M., Takeshima, H., Ferguson, D. G., and Franzini-Armstrong, C. (1995). Molecular architecture of membranes involved in excitation-contraction coupling of cardiac muscle. *J. Cell Biol.* 129, 659–671. doi: 10.1083/jcb.129.3.659

Takeshima, H., Komazaki, S., Nishi, M., Iino, M., and Kangawa, K. (2000). Junctophilins: a novel family of junctional membrane complex proteins. *Mol. Cell.* 6, 11–22.

Tokunaga, M., Imamoto, N., and Sakata-Sogawa, K. (2008). Highly inclined thin illumination enables clear single-molecule imaging in cells. *Nat. Methods* 5, 159–161. doi: 10.1038/nmeth1171

van Oort, R. J., Garbino, A., Wang, W., Dixit, S. S., Landstrom, A. P., Gaur, N., et al. (2011). Disrupted junctional membrane complexes and hyperactive ryanodine receptors after acute junctophilin knockdown in mice. *Circulation* 123, 979–988. doi: 10.1161/CIRCULATIONAHA.110.006437

Wagner, E., Lauterbach, M. A., Kohl, T., Westphal, V., Williams, G. S., Steinbrecher, J. H., et al. (2012). Stimulated emission depletion live-cell super-resolution imaging shows proliferative remodeling of T-tubule membrane structures after myocardial infarction. *Circ. Res.* 111, 402–414. doi: 10.1161/CIRCRESAHA.112.274530

Walker, M. A., Kohl, T., Lehnart, S. E., Greenstein, J. L., Lederer, W. J., and Winslow, R. L. (2015). On the adjacency matrix of RyR2 cluster structures. *PLoS Comput. Biol.* 11:e1004521. doi: 10.1371/journal.pcbi.1004521

Walker, M. A., Williams, G. S., Kohl, T., Lehnart, S. E., Jafri, M. S., Greenstein, J. L., et al. (2014). Superresolution modeling of calcium release in the heart. *Biophys. J.* 107, 3018–3029. doi: 10.1016/j.bpj.2014.11.003

Wang, W., Landstrom, A. P., Wang, Q., Munro, M. L., Beavers, D., Ackerman, M. J., et al. (2014). Reduced junctional $Na^+/Ca2^+$-exchanger activity contributes to sarcoplasmic reticulum $Ca2^+$ leak in junctophilin-2-deficient mice. *Am. J. Physiol. Heart Circ. Physiol.* 307, H1317–H1326. doi: 10.1152/ajpheart.00413.2014

Wei, S., Guo, A., Chen, B., Kutschke, W., Xie, Y. P., Zimmerman, K., et al. (2010). T-tubule remodeling during transition from hypertrophy to heart failure. *Circ. Res.* 107, 520–531. doi: 10.1161/CIRCRESAHA.109.212324

Williamson, D. J., Owen, D. M., Rossy, J., Magenau, A., Wehrmann, M., Gooding, J. J., et al. (2011). Pre-existing clusters of the adaptor Lat do not participate in early T cell signaling events. *Nat. Immunol.* 12, 655–662. doi: 10.1038/ni.2049

Wong, J., Baddeley, D., Bushong, E. A., Yu, Z., Ellisman, M. H., Hoshijima, M., et al. (2013). Nanoscale distribution of ryanodine receptors and caveolin-3 in mouse ventricular myocytes: dilation of t-tubules near junctions. *Biophys. J.* 104, L22–L24. doi: 10.1016/j.bpj.2013.02.059

Xie, W., Brochet, D. X., Wei, S., Wang, X., and Cheng, H. (2010). Deciphering ryanodine receptor array operation in cardiac

myocytes. *J. Gen. Physiol.* 136, 129–133. doi: 10.1085/jgp.201010416

Xu, K., Zhong, G., and Zhuang, X. (2013). Actin, spectrin, and associated proteins form a periodic cytoskeletal structure in axons. *Science* 339, 452–456. doi: 10.1126/science.1232251

Yin, C.-C., Han, H., Wei, R., and Lai, F. A. (2005). Two-dimensional crystallization of the ryanodine receptor $Ca2^{+}$ release channel on lipid membranes. *J. Struct. Biol.* 149, 219–224. doi: 10.1016/j.jsb.2004.10.008

Yin, C.-C., and Lai, F. A. (2000). Intrinsic lattice formation by the ryanodine receptor calcium-release channel. *Nat. Cell Biol.* 2, 669–671. doi: 10.1038/35023625

Conflict of Interest Statement: The authors declare that the research was conducted in the absence of any commercial or financial relationships that could be construed as a potential conflict of interest.

frontiers in Physiology

MINI REVIEW
published: 09 November 2018
doi: 10.3389/fphys.2018.01548

Caveolin-3 Microdomain: Arrhythmia Implications for Potassium Inward Rectifier and Cardiac Sodium Channel

*Ravi Vaidyanathan, Louise Reilly and Lee L. Eckhardt**

Cellular and Molecular Arrhythmia Research Program, University of Wisconsin-Madison, Madison, WI, United States

In human cardiac ventricular myocytes, caveolin-3 functions as a scaffolding and regulatory protein for signaling molecules and compartmentalizes ion channels. Our lab has recently explored this sub-cellular microdomain and found that potassium inward rectifier Kir2.x is found in association with caveolin-3. The three cardiac Kir2.x isoforms (Kir2.1, Kir2.2, and Kir2.3) are the molecular correlates of I_{K1} in the heart, of which Kir2.1 is the dominant isoform in the ventricle. Kir2.1 channels assemble with Kir2.2 and Kir2.3 forming hetero-tetramers that modulate I_{K1}. I_{K1} sets the resting membrane potential and assists with terminal phase 3 ventricular repolarization. In our studies using native human ventricular tissue, Kir2.x co-localizes with caveolin-3 and significance of the association between Kir2.x and caveolin-3 is emphasized in relation to mutations in the gene which encodes caveolin-3, *CAV3*, associated with Long QT Syndrome 9 (LQT9). LQT9-associated *CAV3* mutations cause decreased current density in Kir2.1 and Kir2.2 as homomeric and heteromeric channels, which affects repolarization and membrane potential stability. A portion of Kir2.1 cardiac localization parallels that of the cardiac sodium channel (Nav1.5). This may have implications for Long QT9 in which *CAV3* mutations cause an increase in the late current of Nav1.5 (I_{Na-L}) via nNOS mediated nitrosylation of Nav1.5. In iPS-CMs, expression of LQT9 *CAV3* mutations resulted in action potential duration (APD) prolongation and early-after depolarizations (EADs), supporting the arrhythmogenicity of LQT9. To evaluate the combined effect of the *CAV3* mutants on I_{Na-L} and I_{K1}, we studied both ventricular and Purkinje myocyte mathematical modeling. Interestingly, mathematical ventricular myocytes, similar to iPS-CMs, demonstrated EADs but no sustained arrhythmia. In contrast, Purkinje modeling demonstrated delayed-after depolarizations (DADs) driven mechanism for sustained arrhythmia, dependent on the combined loss of I_{K1} and gain of I_{Na-L}. This finding changes the overall assumed arrhythmia phenotype for LQT9. In future studies, we are exploring caveolar micro-domain disruption in heart failure and how this effects Kir2.x and Nav1.5. Here we review the caveolae cardiac microdomain of Kir2.x and Nav1.5 and explore some of the downstream effects of caveolin-3 and caveolae disruption in specific clinical scenarios.

Keywords: potassium channel, potassium channel (inward-rectifier, outward-rectifier), Cav3, microdomain, sodium channel

OPEN ACCESS

Edited by:
Sarah Calaghan,
University of Leeds, United Kingdom

Reviewed by:
Przemyslaw Radwanski,
The Ohio State University, United States
David Sedmera,
Charles University, Czechia

***Correspondence:**
Lee L. Eckhardt
lle@medicine.wisc.edu

Specialty section:
This article was submitted to Cardiac Electrophysiology, a section of the journal Frontiers in Physiology

Received: *02 August 2018*
Accepted: *16 October 2018*
Published: *09 November 2018*

Citation:
Vaidyanathan R, Reilly L and Eckhardt LL (2018) Caveolin-3 Microdomain: Arrhythmia Implications for Potassium Inward Rectifier and Cardiac Sodium Channel. Front. Physiol. 9:1548. doi: 10.3389/fphys.2018.01548

CAVEOLIN AND ION CHANNEL MICRODOMAINS

Caveolae (Latin for 'little caves') are small (50–100 nm) structural invaginations in the lipid bilayer enriched in sphingolipids, cholesterol, and created by oligiomerized scafolding protein caveolin (Bastiani and Parton, 2010). The caveolin family of proteins is encoded by 3 genes (*CAV1*, *CAV2,* and *CAV3*) and consists of six known caveolin subtypes: caveolin-1a and 1b, caveolin-2α, 2β and 2γ, and caveolin-3 (Cav3) (Balijepalli and Kamp, 2008). Cav3 is specifically expressed in muscle tissue including the heart, where it functions as a scaffolding protein and assembles signaling complexes that can regulate the function of ion channels in caveolae. Caveolae have been shown to be present in atria, ventricle and nodal cells in the heart (Balijepalli and Kamp, 2008). Multiple ion channels and transporters expressed in the heart such as the L-Type calcium channel (Cav1.2) (Balijepalli et al., 2006), T-type calcium channel (Cav3.1) (Markandeya et al., 2011), sodium channel (Nav1.5) (Yarbrough et al., 2002), potassium channels including the inward rectifier potassium channel (Kir2.x) (Vaidyanathan et al., 2013), pacemaker channel (HCN4) (Ye et al., 2008), the sodium/calcium exchanger (NCX1) (Bossuyt et al., 2002) and others have been shown to localize to caveolae. Mutations in Cav3 disrupt these signaling and coordinating microdomains and can cause structural cardiac and arrhythmic disease such as long QT syndrome (LQT9), sudden infant death syndrome, and hypertrophic cardiomyopathy (Hayashi et al., 2004; Vatta et al., 2006; Cronk et al., 2007).

This review will focus on the importance of this microdomain and how it determines cardiac excitability. Recent publications by us and other groups have reported that the ion channels that regulate cardiac excitability form membrane bound macromolecular complexes (Milstein et al., 2012; Vaidyanathan et al., 2013, 2018). Additionally, we will discuss the downstream effects of Cav3 mutations on cardiac excitability as a cause for ventricular arrhythmias in inherited arrhythmia syndromes.

ION CHANNELS INVOLVED IN CARDIAC EXCITABILITY

The cardiac action potential is determined by an interplay of *trans*-membrane ionic currents in myocardial cells. Depolarization of cellular membranes in atrial, ventricular and Purkinje cells is dominated by cardiac sodium (Na^+) current (I_{Na}) through voltage-gated sodium channels, Nav1.5. Depolarization from −80 to −70 mV to peak voltages of +30 to +40 mV allows for activation of the L-type calcium (Ca^{2+}) channels and induction of calcium-induced-calcium-release to facilitate excitation-contraction coupling. Repolarization is a complex process governed by the gradual activation of outward potassium (K^+) currents and inactivation of depolarizing inward currents (Na^+ and L-type Ca^{2+} channels). The terminal phases of cellular repolarization to the resting membrane current depends on the inward rectifying K^+ current (I_{K1}) and the molecular correlates of I_{K1} are the Kir2.x family (Kir2.1, Kir2.2, and Kir2.3) of ion channels. For the next action potential to be initiated, channels carrying depolarizing current (usually Na^+ channels) must recover to a closed state before they can reopen for the next action potential. Na^+ channel recovery occurs when the cell is polarized by I_{K1}. Thus, by controlling the resting membrane potential, I_{K1} modifies sodium channel availability and therefore I_{Na}, cell excitability, action potential duration, and velocity of impulse propagation.

ASSOCIATION OF Kir2.x AND Nav1.5 IN CAVEOLAR COMPLEXES

We were the first to identify that Kir2.x channels associate with Cav3 in the heart (Vaidyanathan et al., 2013, 2018). This novel interaction was inspired by the presence of prominent U-waves on electrocardiograms (ECG) from an LQT patient with a *CAV3* mutation. This ECG feature is found in patients with low K^+ or in genetic conditions with loss of Kir2.1 function, such as Andersen-Tawil Syndrome (Tristani-Firouzi et al., 2002), thus, suggesting that LQT9 associated *CAV3* mutations could possibly affect the function of Kir2.1. We used multiple molecular techniques including immunostaining, co-immunoprecipitation, and fluorescent resonant energy transfer (FRET) to demonstrate the association between Cav3 and Kir2.1 (directly or indirectly). We also identified residues/domains on each protein required for this association. Other cardiac Kir2.x isoforms, Kir2.2 and Kir2.3, associate with Cav3 and the residues of Kir2.x that are crucial for the association with Cav3 appear to be a conserved N-terminal sequence containing a caveolin-binding motif (CBM) composed of a specific sequence of aromatic amino acids including QxQxxxxQ where "Q" is an aromatic amino acid residue (tyrosine, Y; tryptophan, W; and phenylalanine F) and a "x" represents any other residue (Raab-Graham et al., 1994; Couet et al., 1997; Han et al., 2014). We found that the Kir2.x CBM is required for co-immunoprecipitation as deletion of this results in no association of Cav3 and Kir2.x (Vaidyanathan et al., 2018). This finding should be taken into context, because CBM sequences as evidence for a Cav3 interaction site has been questioned, largely related to the relationship of CBM and accessibility based on protein 3D structure (Byrne et al., 2012; Collins et al., 2012). We suspect that the Kir2.x N-terminal CBM (amino acids 81–92) is accessible based on both our findings as well as its close proximity to amino acids which interact with other cytoplasmic regulatory molecules including phosphatidylinositol biphosphate and nitric oxide (Donaldson et al., 2003; Gomez et al., 2009). Cav3 has 4 domains: N-terminal (NT; aa 1–54), scaffolding (aa 55–73), membrane-associated (aa 74–106), and C-terminal (CT; aa 107–151). We also determined that only the scaffolding and membrane domains associate with Kir2.x. The implications of this are that disruption of the Kir2.x CBM sequence or scaffolding or membrane Cav3 domains may affect the presence of Kir2.x channels in caveolar microdomains.

The association of Cav3 and Nav1.5 has been demonstrated by several investigators (Vatta et al., 2006; Cronk et al., 2007; Cheng et al., 2013). $Na_V1.5$ localizes to caveolin-rich membrane domains, demonstrated by co-immunoprecipitation in heterologous cells (HEK293 cells) but also in rat ventricular tissue (Yarbrough et al., 2002; Vatta et al., 2006). It is currently unclear if the interaction of Cav3 with Nav1.5 is direct or indirect. However, in rat ventricular myocytes these proteins appear to be part of a macromolecular complex composed of syntrophin alpha-1, neuronal nitric oxide synthase (nNOS), Cav3, and Nav1.5 (Cheng et al., 2013).

We previously investigated and reported the association of Kir2.x and Cav3 in human ventricular cardiomyocytes (Vaidyanathan et al., 2018). We demonstrated by employing stimulated emission depletion (STED) microscopy, a super-resolution microscopy technique, Kir2.1 localized to the T-tubules, lateral membrane and intercalated disk in cardiomyocytes. Others have reported that Kir2.1 and Nav1.5 channels are not only part of the same macromolecular complex in cardiac myocytes (Milstein et al., 2012; Matamoros et al., 2016) but also traffic together (Ponce-Balbuena et al., 2018). As shown in **Figure 1**, Nav1.5, Kir2.1, and Cav3 co-localize to similar sub-cellular locations suggesting that they are part of the same macromolecular complex (Vaidyanathan et al., 2018). Kir2.x isoforms localize to different regions: Kir2.1 localizes to the sarcolemma, T-tubules and intercalated disk, Kir2.2 preferentially is found at the T-tubules, and Kir2.3 localizes to the intercalated disk. However, Kir2.1 and Nav1.5 immunolocalize with Cav3 with a Pearson's correlation coefficient >0.5, suggesting close localization of Kir2.1 with Cav3 and Nav1.5 with Cav3.

ARRHYTHMIA PATHOLOGY RELATED TO ABNORMAL Cav3

Mutations in *CAV3* cause several types of muscle related clinical diseases including muscular dystrophy, hypertrophic cardiomyopathy and the arrhythmia syndrome of Long QT syndrome (LQTS) (Balijepalli and Kamp, 2008). From a cohort of patients referred for genetic testing for LQTS, several *CAV3* mutations were identified from individuals who were gene negative for other known LQTS genes [*KCNQ1* (LQT1), *KCNH2* (LQT2), *SCN5A* (LQT3), *KCNE1* (LQT5), *KCNE2* (LQT6), and *KCNJ2* (ATS1) and targeted analysis of *ANK2* (LQT4) and *RyR2* (CPVT1)] (Vatta et al., 2006). To determine how these *CAV3* mutations cause LQTS, constructs of the mutations were expressed in cells with ion channels known to associate with Cav3. When co-expressed with Nav1.5, LQT-associated *CAV3* mutations did not affect the peak current density of I_{Na} compared to wild type (WT). However, F97C-Cav3 and S141R-Cav3 increased late I_{Na} ($I_{Na\text{-}L}$) by ∼2-3 fold compared to vector and WT-Cav3. In the complex containing Nav1.5, Cav3, alpha-1-syntrophin, and nNOS, Cav3 inhibits nNOS mediated nitrosylation of Nav1.5 (Cheng et al., 2013). However, LQT9 associated mutation F97C-Cav3 remains in the complex but has lost the ability to suppress nNOS mediated nitrosylation of Nav1.5. Thus, it appeared that $I_{Na\text{-}L}$ increases due to nitrosylation of Nav1.5 when LQT9 mutations are present.

We observed that one patient with LQT9 also had prominent U-waves (Vatta et al., 2006), which is an electrocardiographic feature seen in patients with loss of function mutations in the Kir2.1 related to Andersen-Tawil Syndrome (ATS1) (Tristani-Firouzi et al., 2002). For these reasons, we investigated

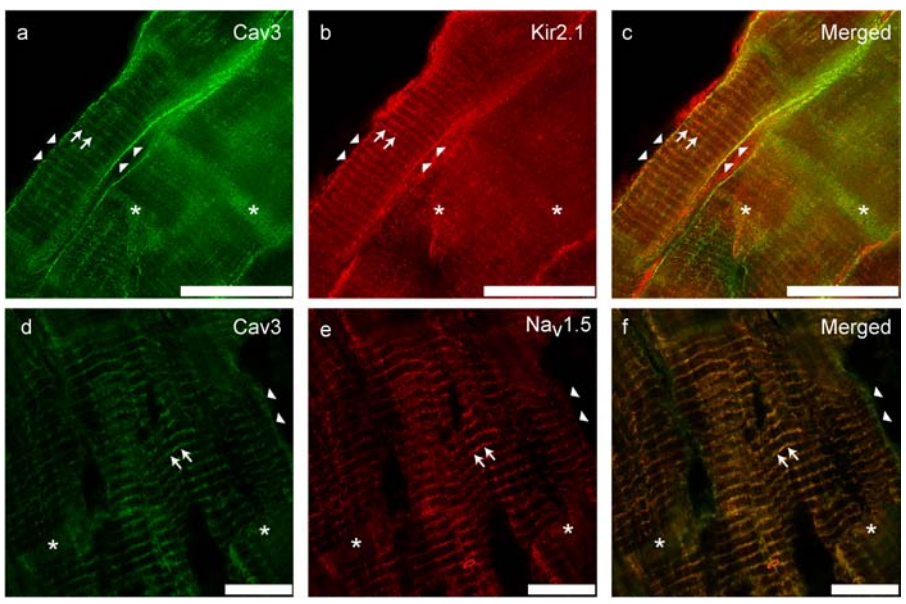

FIGURE 1 | Immuno-colocalization of Kir2.1 **(b)** and Nav1.5 **(e)** with Cav3 **(a,d)** in human ventricular tissue (adapted from Vaidyanathan et al., 2018). **(c,f)** Represent merged images; yellow color indicates areas of overlap. Scale bar = 25 μm.

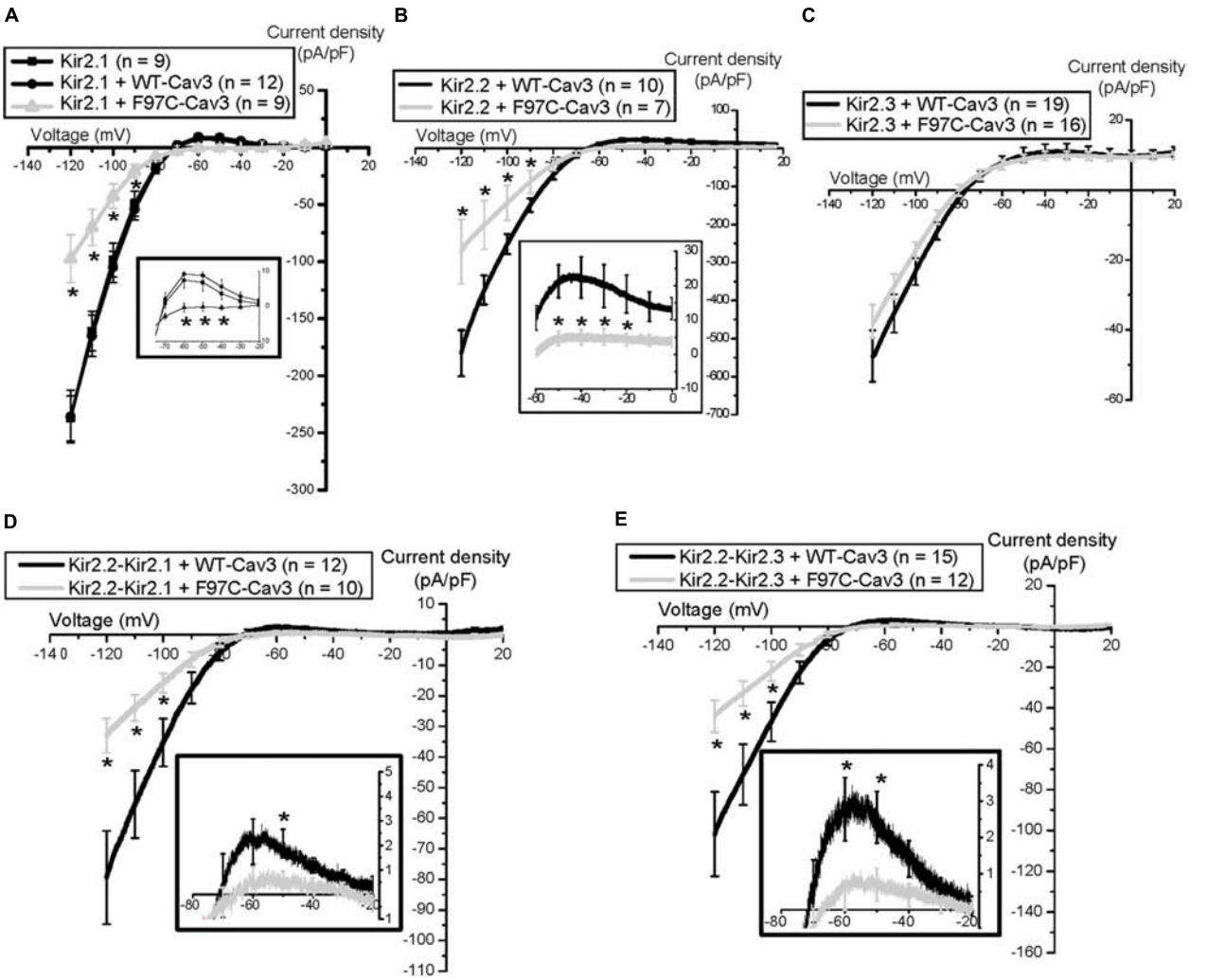

FIGURE 2 | Electrophysiological properties of Nav1.5 channels and Kir2.x homomeric and heteromeric channels with F97C-Cav3 (Vaidyanathan et al., 2018). *$p < 0.05$.

the effect of LQT9 mutations on Kir2.x channels by co-expressing homomeric Kir2.1 or Kir2.2 or Kir2.3 with WT-Cav3 or LQT9-associated F97C-Cav3 (Vaidyanathan et al., 2013, 2018). Interestingly, F97C-Cav3 decreased peak inward and outward current density of homomeric Kir2.1 (**Figure 2A**) and homomeric Kir2.2 (**Figure 2B**) by ∼ 50–60% but not homomeric Kir2.3 (**Figure 2C**) compared to WT-Cav3. Since Kir2.x channels can be present as heteromeric channels in cardiomyocytes and given the differential effect of F97C-Cav3 on Kir2.x channels, we created heteromeric vectors of Kir2.2-P2A-Kir2.1 and Kir2.2-P2A-Kir2.3 (P2A is a self-cleaving peptide). When heteromeric channels are co-expressed with F97C-Cav3, peak inward and outward current density decreased compared to WT-Cav3 (**Figures 2D,E**). Interestingly, even though F97C-Cav3 had no effect on Kir2.3 homomeric channels, there is decreased peak inward and outward current of the Kir2.2-Kir2.3 heteromeric channels compared to WT-Cav3, suggesting that Cav3 is able to regulate Kir2.3 when expressed with Kir2.2. Perhaps this is related to channel assembly leading to lack of membrane expression as we determined that the F97C-Cav3 mutation caused a 50% reduction in membrane trafficking of Kir2.1 and Kir2.2 channels (Vaidyanathan et al., 2013, 2018). Immunostaining experiments suggested that Kir2.1 channels are localized to the Golgi when co-expressed with F97C-Cav3, which is the site for channel tetrameric assembly. Thus, it is possible that the F97C-Cav3 prohibits heteromeric channels from leaving the Golgi and decreases current density, decreasing I_{K1} and membrane repolarization.

DUAL CELLULAR MOLECULAR MECHANISM of *CAV3* MUTATIONS CAUSING LQT

The initial studies demonstrating the major effects of LQT9 mutations left significant questions as there are two distinct

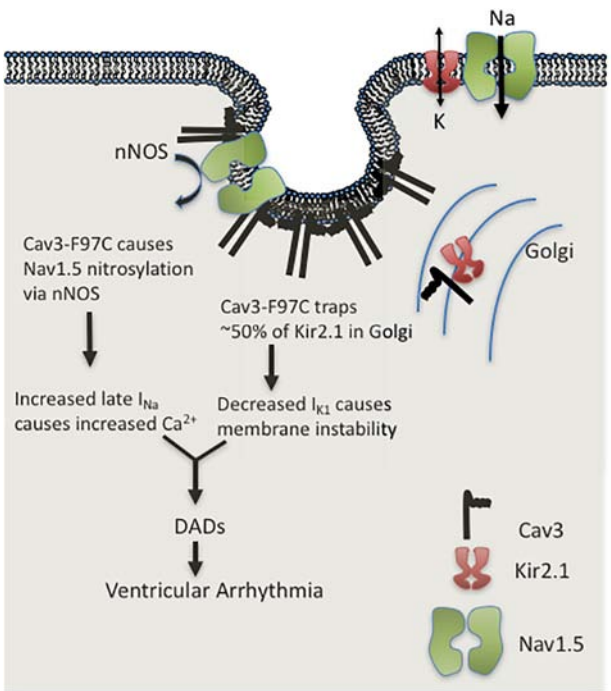

FIGURE 3 | Cartoon illustration of LQT9 arrhythmia mechanism.

cellular mechanisms causing ionic current abnormalities: gain of $I_{Na\text{-}L}$ due to sodium channel nitrosylation and inhibition of Kir2.1 and Kir2.2 channel membrane trafficking causing loss of I_{K1}. How and by what mechanism do LQT9 Cav3 mutations cause a clinical ventricular arrhythmia? Cheng et. al. demonstrated in rat ventricular myocytes in culture, over-expression of WT-Cav3 or F97C-Cav3 caused significant prolongation of action potential duration (APD) at 90% repolarization in cells expressing F97C-Cav3 as compared to cells expressing WT-Cav3. This effect was reversed by the addition of L-NMMA (an nNOS inhibitor). We also demonstrated that in human iPS cardiomyocytes a similar prolongation of APD at 50, 70, and 90% repolarization occurred in cells with F97C-Cav3 compared to WT-Cav3 at 0.5 and 1 Hz pacing frequency (Vaidyanathan et al., 2016). At lower pacing frequency (0.33 Hz) we recorded early after depolarization's (EADs). EADs are the triggered activity required in congenital or drug-induced LQTS to induce a specific type of polymorphic ventricular tachycardia called torsade de pointes (Vaidyanathan et al., 2016). Thus, we hypothesized that with action potential prolongation due to $I_{Na\text{-}L}$ and decreased I_{K1}, EAD triggered activity is the arrhythmia mechanism in LQT9. To test this, we ran mathematical simulation on a human ventricular cell model (Grandi et al., 2010; O'Hara et al., 2011) in our recent report (Vaidyanathan et al., 2018). In the human ventricular cell model by either decreasing I_{K1} or increasing $I_{Na\text{-}L}$, the APD prolonged and increased $I_{Na\text{-}L}$ induced EADs at low pacing frequency. Unexpectedly, when both, increased $I_{Na\text{-}L}$ and decreased I_{K1} was simulated in the model, EADs were prevented because of resting membrane potential depolarization that decreasing total I_{Na} and thus $I_{Na\text{-}L}$. We then tested same ionic current changes found experimentally in LQT9 using the Li-Rudy canine Purkinje cell model (Li and Rudy, 2011). In contrast to ventricular myocyte model, the Purkinje cell model with increased $I_{Na\text{-}L}$ and decreased I_{K1} demonstrated delayed after depolarizations (DADs), prominent at both low (0.25 Hz) and high (3.33 Hz) pacing frequencies (Vaidyanathan et al., 2018). At these frequencies, the mechanism involved calcium loading due to increased $I_{Na\text{-}L}$, and unstable resting membrane potential due to decreased I_{K1} density. As depicted in **Figure 3**, this increased cellular calcium load combined with reduced repolarization reserve decreased the DAD threshold leading to sustained arrhythmia. Although the cellular ventricular myocytes show APD prolongation and EADs, sustained arrhythmia is triggered from DADs in the Purkinje cells. This finding changes the overall assumed arrhythmia mechanism for LQT9.

LQT9 VS. "CLASSICAL" LQTS ARRHYTHMIA MECHANISMS

The cellular mechanism for LQTS is related to gain or loss of ion channel function directly or indirectly by mutations which reduce ion channel surface membrane expression or by ion channel accessory/regulatory proteins which can exert a direct or indirect effect. While there are currently 17 different LQTS types based on the gene implicated, the most common three LQTS are: LQT1 involving mutations in the *KCNQ1* gene (30–35% of patients), LQT2 involves mutations in the *KCNH2* gene (25–30% of patients) and LQT3 involves mutations in the *SCN5a* gene (10% of patients) (Cerrone et al., 2012; Priori et al., 2013). LQT4-17 are more rare, including LQT9 and based on our work and others, the mechanism of arrhythmia initiation may be dissimilar to classically described LQTS (Koenig and Mohler, 2017; Vaidyanathan et al., 2018). The signature arrhythmia in LQTS is torsade de pointes, resulting from decreased repolarization reserve and susceptibility for EADs (Marban et al., 1986). EADs occur when the action potential duration is prolonged, which permits more time for the time- and voltage-dependent recovery and reopening of L-type Ca^{2+} channels at plateau voltages to carry added depolarizing current (January et al., 1988). In LQT9, we did not find that EAD initiation led to sustained arrhythmia, but rather purkinje cell DADs causes sustained arrhythmia (Vaidyanathan et al., 2018). DADs and EADs are different mechanistically. DADs result from the overloading of cells with Ca^{2+}, which then overloads the sarcoplasmic reticulum (SR) with Ca^{2+}. The SR releases Ca^{2+} during an action potential and under conditions of Ca^{2+} overload is transiently re-released into the myoplasm. These transient rises in myoplasmic Ca^{2+} activate Ca^{2+}–dependent depolarizing membrane current, mostly through the Na^{+} – Ca^{2+} exchange causing voltage oscillations or a DADs (Ter Keurs and Boyden, 2007; Fink et al., 2011). DADs that reach voltage threshold can initiate a

subsequent action potential. These divergent mechanisms for triggered activity are not only distinct experimentally, they are approached differently clinically, as DADs are enhanced by rapid stimulation, whereas EADs occur at slow stimulation rates where action potential duration is longest and are usually abolished at higher stimulation rates. Our model of LQT9 is speculative but is akin to Purkinje-dependent DAD perpetuation in EAD-susceptible myocytes in heart failure (Myles et al., 2012). This highlights the overall impact of our investigation and the importance of ongoing studies to optimize treatment approaches for these arrhythmia syndromes.

Cav3 IN HEART FAILURE AND DOWNSTREAM MICRODOMAIN DYSREGULATION

Beyond more rare *CAV3* mutations, Cav3 is also down regulated in the ventricle of animal models of heart failure and in human heart failure (Feiner et al., 2011). Multiple murine models of heart failure such as pressure overload induced by transverse aortic constriction (TAC) (Feiner et al., 2011), transgenic mice with constitutive overexpression of A1-adenosine receptor and angiotensin-II infusion (Markandeya et al., 2015), report that there is significant loss of Cav3 and caveolae at the sarcolemma in ventricular myocytes. Woodman et. al. report that Cav3 knockout (KO) mice develop progressive cardiomyopathy at 4 months of age marked by significant hypertrophy, dilation, and reduced fractional shortening (Woodman et al., 2002). Interestingly, over-expression (OE) of Cav3 in mice attenuates hypertrophy phenotype (Horikawa et al., 2011). When Cav3 OE mice are exposed to TAC, they had increased survival, reduced cardiac hypertrophy and preservation of cardiac function as compared to control mice (Horikawa et al., 2011).

Ion channel remodeling occurs in animal models of heart failure. L-type calcium channel current ($I_{Ca\text{-}L}$) is decreased in heart failure has in part been attributed to loss of Cav3 (Bryant et al., 2018a,b). Bryant et al. (2018a) report that in TAC exposed mice, there was T-tubule disruption, decreased expression of Junctophilin 2 and Cav3, impairment of calcium release at the T-tubules and decreased $I_{Ca\text{-}L}$ at the T-tubule with no change in $I_{Ca\text{-}L}$ at the sarcolemma. These results suggest that Cav3 microdomains play a key role in maintaining normal physiology and perturbations of caveolae can cause pathology.

In systolic heart failure it has been reported that I_{K1} and I_{Na} are downregulated (Beuckelmann et al., 1993; Li et al., 2004; Valdivia et al., 2005), however, it is not yet understood if this is related to the loss of caveolae, as with L-type calcium channel. We are currently investigating if decreased I_{K1} and I_{Na} in heart failure is related to loss of caveolae or Cav3 regulation. Due to the complexity we have observed of cell type (modeling experiments) and the differences in effects by *CAV3* mutations on I_{K1} and I_{Na}, we anticipate that there may also be a complex effect in heart failure on Kir2.x and Nav1.5 remodeling. We hope that answering these questions of caveolar microdomain disruption in various forms of heart failure will lead to improved clarity of ionic channel remodeling in heart failure.

CONCLUSION

Cav3 microdomain containing Kir2.x and Nav1.5 in cardiomyocytes are an essential part of normal cardiac physiology. Mutations in *CAV3* cause increased I_{Na-L} and decreased I_{K1} resulting in membrane instability and mathematical modeling suggests this causes calcium loading leading to DAD-dependent arrhythmia. The importance of Cav3 changes in HF and downstream microdomain dysregulation may have important implications for arrhythmia generation.

AUTHOR CONTRIBUTIONS

RV contributed to writing, figure production, and editing. LR contributed to manuscript writing and editing. LE contributed to project conceptualization, writing, figure production, and editing.

FUNDING

This study was supported by NIH R01 HL128598-01 (LE).

REFERENCES

Balijepalli, R. C., Foell, J. D., Hall, D. D., Hell, J. W., and Kamp, T. J. (2006). Localization of cardiac L-type Ca(2 +) channels to a caveolar macromolecular signaling complex is required for beta(2)-adrenergic regulation. *Proc. Natl. Acad. Sci. U.S.A.* 103, 7500–7505. doi: 10.1073/pnas.0503465103

Balijepalli, R. C., and Kamp, T. J. (2008). Caveolae, ion channels and cardiac arrhythmias. *Prog. Biophys. Mol. Biol.* 98, 149–160. doi: 10.1016/j.pbiomolbio.2009.01.012

Bastiani, M., and Parton, R. G. (2010). Caveolae at a glance. *J. Cell Sci.* 123(Pt 22), 3831–3836. doi: 10.1242/jcs.070102

Beuckelmann, D. J., Näbauer, M., and Erdmann, E. (1993). Alterations of K + currents in isolated human ventricular myocytes from patients with terminal heart failure. *Circ. Res.* 73, 379–385. doi: 10.1161/01.RES.73.2.379

Bossuyt, J., Taylor, B. E., James-Kracke, M., and Hale, C. C. (2002). The cardiac sodium-calcium exchanger associates with caveolin-3. *Ann. N. Y. Acad. Sci.* 976, 197–204. doi: 10.1111/j.1749-6632.2002.tb04741.x

Bryant, S. M., Kong, C. H. T., Watson, J. J., Gadeberg, H. C., James, A. F., Cannell, M. B., et al. (2018a). Caveolin 3-dependent loss of t-tubular I. *Exp. Physiol.* 103, 652–665. doi: 10.1113/EP086731

Bryant, S. M., Kong, C. H. T., Watson, J. J., Gadeberg, H. C., Roth, D. M., Patel, H. H., et al. (2018b). CAVEOLIN-3 KO disrupts T-tubule structure and decreases T-TUBULAR I. *Am. J. Physiol. Heart Circ. Physiol.* 315, H1101–H1111. doi: 10.1152/ajpheart.00209.2018

Byrne, D. P., Dart, C., and Rigden, D. J. (2012). Evaluating caveolin interactions: do proteins interact with the caveolin scaffolding domain through a widespread aromatic residue-rich motif? *PLoS One* 7:e44879. doi: 10.1371/journal.pone.0044879

Cerrone, M., Napolitano, C., and Priori, S. G. (2012). Genetics of ion-channel disorders. *Curr. Opin. Cardiol.* 27, 242–252. doi: 10.1097/HCO.0b013e328352429d

Cheng, J., Valdivia, C. R., Vaidyanathan, R., Balijepalli, R. C., Ackerman, M. J., and Makielski, J. C. (2013). Caveolin-3 suppresses late sodium current by inhibiting nNOS-dependent S-nitrosylation of SCN5A. *J. Mol. Cell Cardiol.* 61, 102–110. doi: 10.1016/j.yjmcc.2013.03.013

Collins, B. M., Davis, M. J., Hancock, J. F., and Parton, R. G. (2012). Structure-based reassessment of the caveolin signaling model: do caveolae regulate signaling through caveolin-protein interactions? *Dev. Cell* 23, 11–20. doi: 10.1016/j.devcel.2012.06.012

Couet, J., Li, S., Okamoto, T., Ikezu, T., and Lisanti, M. P. (1997). Identification of peptide and protein ligands for the caveolin-scaffolding domain. Implications for the interaction of caveolin with caveolae-associated proteins. *J. Biol. Chem.* 272, 6525–6533. doi: 10.1074/jbc.272.10.6525

Cronk, L. B., Ye, B., Kaku, T., Tester, D. J., Vatta, M., Makielski, J. C., et al. (2007). Novel mechanism for sudden infant death syndrome: persistent late sodium current secondary to mutations in caveolin-3. *Heart Rhythm.* 4, 161–166. doi: 10.1016/j.hrthm.2006.11.030

Donaldson, M. R., Jensen, J. L., Tristani-Firouzi, M., Tawil, R., Bendahhou, S., Suarez, W. A., et al. (2003). PIP2 binding residues of Kir2.1 are common targets of mutations causing Andersen syndrome. *Neurology* 60, 1811–1816. doi: 10.1212/01.WNL.0000072261.14060.47

Feiner, E. C., Chung, P., Jasmin, J. F., Zhang, J., Whitaker-Menezes, D., Myers, V., et al. (2011). Left ventricular dysfunction in murine models of heart failure and in failing human heart is associated with a selective decrease in the expression of caveolin-3. *J. Card. Fail.* 17, 253–263. doi: 10.1016/j.cardfail.2010.10.008

Fink, M., Noble, P. J., and Noble, D. (2011). Ca(2)(+)-induced delayed afterdepolarizations are triggered by dyadic subspace Ca2(2)(+) affirming that increasing SERCA reduces aftercontractions. *Am. J. Physiol. Heart Circ. Physiol.* 301, H921–H935. doi: 10.1152/ajpheart.01055.2010

Gomez, R., Caballero, R., Barana, A., Amoros, I., Calvo, E., Lopez, J. A., et al. (2009). Nitric oxide increases cardiac IK1 by nitrosylation of cysteine 76 of Kir2.1 channels. *Circ. Res.* 105, 383–392. doi: 10.1161/CIRCRESAHA.109.197558

Grandi, E., Pasqualini, F. S., and Bers, D. M. (2010). A novel computational model of the human ventricular action potential and Ca transient. *J. Mol. Cell Cardiol.* 48, 112–121. doi: 10.1016/j.yjmcc.2009.09.019

Han, H., Rosenhouse-Dantsker, A., Gnanasambandam, R., Epshtein, Y., Chen, Z., Sachs, F., et al. (2014). Silencing of Kir2 channels by caveolin-1: cross-talk with cholesterol. *J. Physiol.* 592, 4025–4038. doi: 10.1113/jphysiol.2014.273177

Hayashi, T., Arimura, T., Ueda, K., Shibata, H., Hohda, S., Takahashi, M., et al. (2004). Identification and functional analysis of a caveolin-3 mutation associated with familial hypertrophic cardiomyopathy. *Biochem. Biophys. Res. Commun.* 313, 178–184. doi: 10.1016/j.bbrc.2003.11.101

Horikawa, Y. T., Panneerselvam, M., Kawaraguchi, Y., Tsutsumi, Y. M., Ali, S. S., Balijepalli, R. C., et al. (2011). Cardiac-specific overexpression of caveolin-3 attenuates cardiac hypertrophy and increases natriuretic peptide expression and signaling. *J. Am. Coll. Cardiol.* 57, 2273–2283. doi: 10.1016/j.jacc.2010.12.032

January, C. T., Riddle, J. M., and Salata, J. J. (1988). A model for early afterdepolarizations: induction with the Ca2 + channel agonist Bay K 8644. *Circ. Res.* 62, 563–571. doi: 10.1161/01.RES.62.3.563

Koenig, S. N., and Mohler, P. J. (2017). The evolving role of ankyrin-B in cardiovascular disease. *Heart Rhythm.* 14, 1884–1889. doi: 10.1016/j.hrthm.2017.07.032

Li, G. R., Lau, C. P., Leung, T. K., and Nattel, S. (2004). Ionic current abnormalities associated with prolonged action potentials in cardiomyocytes from diseased human right ventricles. *Heart Rhythm.* 1, 460–468. doi: 10.1016/j.hrthm.2004.06.003

Li, P., and Rudy, Y. (2011). A model of canine purkinje cell electrophysiology and Ca(2 +) cycling: rate dependence, triggered activity, and comparison to ventricular myocytes. *Circ. Res.* 109, 71–79. doi: 10.1161/CIRCRESAHA.111.246512

Marban, E., Robinson, S. W., and Wier, W. G. (1986). Mechanisms of arrhythmogenic delayed and early afterdepolarizations in ferret ventricular muscle. *J. Clin. Invest.* 78, 1185–1192. doi: 10.1172/JCI112701

Markandeya, Y. S., Fahey, J. M., Pluteanu, F., Cribbs, L. L., and Balijepalli, R. C. (2011). Caveolin-3 regulates protein kinase A modulation of the Ca(V)3.2 (alpha1H) T-type Ca2 + channels. *J. Biol. Chem.* 286, 2433–2444. doi: 10.1074/jbc.M110.182550

Markandeya, Y. S., Phelan, L. J., Woon, M. T., Keefe, A. M., Reynolds, C. R., August, B. K., et al. (2015). Caveolin-3 overexpression attenuates cardiac hypertrophy via inhibition of T-type Ca2 + current modulated by protein kinase Cα in cardiomyocytes. *J. Biol. Chem.* 290, 22085–22100. doi: 10.1074/jbc.M115.674945

Matamoros, M., Perez-Hernandez, M., Guerrero-Serna, G., Amoros, I., Barana, A., Nunez, M., et al. (2016). Nav1.5 N-terminal domain binding to alpha1-syntrophin increases membrane density of human Kir2.1, Kir2.2 and Nav1.5 channels. *Cardiovasc. Res.* 110, 279–290. doi: 10.1093/cvr/cvw009

Milstein, M. L., Musa, H., Balbuena, D. P., Anumonwo, J. M., Auerbach, D. S., Furspan, P. B., et al. (2012). Dynamic reciprocity of sodium and potassium channel expression in a macromolecular complex controls cardiac excitability and arrhythmia. *Proc. Natl. Acad. Sci. U.S.A.* 109, E2134–E2143. doi: 10.1073/pnas.1109370109

Myles, R. C., Wang, L., Kang, C., Bers, D. M., and Ripplinger, C. M. (2012). Local beta-adrenergic stimulation overcomes source-sink mismatch to generate focal arrhythmia. *Circ. Res.* 110, 1454–1464. doi: 10.1161/CIRCRESAHA.111.262345

O'Hara, T., Virag, L., Varro, A., and Rudy, Y. (2011). Simulation of the undiseased human cardiac ventricular action potential: model formulation and experimental validation. *PLoS Comput. Biol.* 7:e1002061. doi: 10.1371/journal.pcbi.1002061

Ponce-Balbuena, D., Guerrero-Serna, G., Valdivia, C. R., Caballero, R., Diez-Guerra, F. J., Jimenez-Vazquez, E. N., et al. (2018). Cardiac Kir2.1 and NaV1.5 channels traffic together to the sarcolemma to control excitability. *Circ. Res.* 122, 1501–1516. doi: 10.1161/CIRCRESAHA.117.311872

Priori, S. G., Wilde, A. A., Horie, M., Cho, Y., Behr, E. R., Berul, C., et al. (2013). Executive summary: HRS/EHRA/APHRS expert consensus statement on the diagnosis and management of patients with inherited primary arrhythmia syndromes. *Europace* 10, e85–e108. doi: 10.1093/europace/eut272

Raab-Graham, K. F., Radeke, C. M., and Vandenberg, C. A. (1994). Molecular cloning and expression of a human heart inward rectifier potassium channel. *Neuroreport* 5, 2501–2505. doi: 10.1097/00001756-199412000-00024

Ter Keurs, H. E., and Boyden, P. A. (2007). Calcium and arrhythmogenesis. *Physiol. Rev.* 87, 457–506. doi: 10.1152/physrev.00011.2006

Tristani-Firouzi, M., Jensen, J. L., Donaldson, M. R., Sansone, V., Meola, G., Hahn, A., et al. (2002). Functional and clinical characterization of KCNJ2 mutations associated with LQT7 (Andersen syndrome). *J. Clin. Invest.* 110, 381–388. doi: 10.1172/JCI15183

Vaidyanathan, R., Markandeya, Y. S., Kamp, T. J., Makielski, J. C., January, C. T., and Eckhardt, L. L. (2016). IK1-enhanced human-induced pluripotent stem cell-derived cardiomyocytes: an improved cardiomyocyte model to investigate inherited arrhythmia syndromes. *Am. J. Physiol. Heart Circ. Physiol.* 310, H1611–H1621. doi: 10.1152/ajpheart.00481.2015

Vaidyanathan, R., Van Ert, H., Haq, K. T., Morotti, S., Esch, S., McCune, E. C., et al. (2018). Inward rectifier potassium channels (Kir2.x) and Caveolin-3 domain-specific interaction: implications for purkinje cell-dependent ventricular arrhythmias. *Circ. Arrhythm. Electrophysiol.* 11:e005800. doi: 10.1161/CIRCEP.117.005800

Vaidyanathan, R., Vega, A. L., Song, C., Zhou, Q., Tan, B. H., Tan, B., et al. (2013). The interaction of caveolin 3 protein with the potassium inward rectifier channel Kir2.1: physiology and pathology related to long qt syndrome 9 (LQT9). *J. Biol. Chem.* 288, 17472–17480. doi: 10.1074/jbc.M112.435370

Valdivia, C. R., Chu, W. W., Pu, J., Foell, J. D., Haworth, R. A., Wolff, M. R., et al. (2005). Increased late sodium current in myocytes from a canine heart failure model and from failing human heart. *J. Mol. Cell Cardiol.* 38, 475–483. doi: 10.1016/j.yjmcc.2004.12.012

Vatta, M., Ackerman, M. J., Ye, B., Makielski, J. C., Ughanze, E. E., Taylor, E. W., et al. (2006). Mutant caveolin-3 induces persistent late sodium current and is associated with long-QT syndrome. *Circulation* 114, 2104–2112. doi: 10.1161/CIRCULATIONAHA.106.635268

Woodman, S. E., Park, D. S., Cohen, A. W., Cheung, M. W., Chandra, M., Shirani, J., et al. (2002). Caveolin-3 knock-out mice develop a progressive cardiomyopathy and show hyperactivation of the p42/44 MAPK cascade. *J. Biol. Chem.* 277, 38988–38997. doi: 10.1074/jbc.M205511200

Yarbrough, T. L., Lu, T., Lee, H. C., and Shibata, E. F. (2002). Localization of cardiac sodium channels in caveolin-rich membrane domains: regulation of sodium current amplitude. *Circ. Res.* 90, 443–449. doi: 10.1161/hh0402.105177

Ye, B., Balijepalli, R. C., Foell, J. D., Kroboth, S., Ye, Q., Luo, Y. H., et al. (2008). Caveolin-3 associates with and affects the function of hyperpolarization-activated cyclic nucleotide-gated channel 4. *Biochemistry* 47, 12312–12318. doi: 10.1021/bi8009295

Conflict of Interest Statement: The authors declare that the research was conducted in the absence of any commercial or financial relationships that could be construed as a potential conflict of interest.

frontiers in Physiology

ORIGINAL RESEARCH
published: 12 November 2018
doi: 10.3389/fphys.2018.01516

Cholesterol Protects Against Acute Stress-Induced T-Tubule Remodeling in Mouse Ventricular Myocytes

*Azadeh Nikouee†, Keita Uchida†, Ian Moench and Anatoli N. Lopatin**

Department of Molecular and Integrative Physiology, University of Michigan, Ann Arbor, MI, United States

Efficient excitation-contraction coupling in ventricular myocytes depends critically on the presence of the t-tubular network. It has been recently demonstrated that cholesterol, a major component of the lipid bilayer, plays an important role in long-term maintenance of the integrity of t-tubular system although mechanistic understanding of underlying processes is essentially lacking. Accordingly, in this study we investigated the contribution of membrane cholesterol to t-tubule remodeling in response to acute hyposmotic stress. Experiments were performed using isolated left ventricular cardiomyocytes from adult mice. Depletion and restoration of membrane cholesterol was achieved by applying methyl-β-cyclodextrin (MβCD) and water soluble cholesterol (WSC), respectively, and t-tubule remodeling in response to acute hyposmotic stress was assessed using fluorescent dextran trapping assay and by measuring t-tubule dependent I_{K1} tail current ($I_{K1,\,tail}$). The amount of dextran trapped in t-tubules sealed in response to stress was significantly increased when compared to control cells, and reintroduction of cholesterol to cells treated with MβCD restored the amount of trapped dextran to control values. Alternatively, application of WSC to normal cells significantly reduced the amount of trapped dextran further suggesting the protective effect of cholesterol. Importantly, modulation of membrane cholesterol (without osmotic stress) led to significant changes in various parameters of $I_{K1,\,tail}$ strongly suggesting significant but essentially hidden remodeling of t-tubules prior to osmotic stress. Results of this study demonstrate that modulation of the level of membrane cholesterol has significant effects on the susceptibility of cardiac t-tubules to acute hyposmotic stress.

Keywords: mouse ventricular myocytes, t-tubule, cholesterol, osmotic stress, potassium currents

OPEN ACCESS

Edited by:
Alexey V. Glukhov,
University of Wisconsin System, United States

Reviewed by:
Andrew F. James,
University of Bristol, United Kingdom
TingTing Hong,
Cedars-Sinai Medical Center, United States

***Correspondence:**
Anatoli N. Lopatin
alopatin@umich.edu

† These authors have contributed equally to this work

Specialty section:
This article was submitted to Cardiac Electrophysiology, a section of the journal Frontiers in Physiology

Received: *30 May 2018*
Accepted: *09 October 2018*
Published: *12 November 2018*

Citation:
Nikouee A, Uchida K, Moench I and Lopatin AN (2018) Cholesterol Protects Against Acute Stress-Induced T-Tubule Remodeling in Mouse Ventricular Myocytes. Front. Physiol. 9:1516. doi: 10.3389/fphys.2018.01516

INTRODUCTION

Transverse-axial t-tubular system (TATS) is a complex network of invaginations of the surface membrane necessary for efficient excitation-contraction coupling in cardiac and skeletal muscle cells. In particular, a dense TATS is present in adult ventricular myocytes of likely all mammalian hearts. The TATS becomes significantly remodeled in response to a variety of experimental

challenges [e.g., osmotic stress (Kawai et al., 1999; Moench et al., 2013)] and in clinically relevant stress conditions (e.g., heart failure; Guo et al., 2013, for review). It has been well established that a number of t-tubular structural proteins are involved in the maintenance and remodeling of TATS (Kline and Mohler, 2013 for review). However, it is less clear how other membrane components affect TATS structure and remodeling.

T-tubular system membranes are highly enriched in cholesterol (Sumnicht and Sabbadini, 1982) and are stiffer than other biological membranes (Hidalgo, 1985). Cholesterol is an important player in the formation of membrane rafts including caveolae (Simionescu et al., 1983; Rothberg et al., 1990), which can also be found in cardiac t-tubules (Page, 1978). Changes in cellular cholesterol has also been suggested to contribute to electrical remodeling in cardiomyocytes and may have pro- or anti-arrhythmic effects (Coronel, 2017). However, it remains unknown whether in cardiac t-tubules cholesterol exerts its effects through its numerous molecular targets or it can affect their structural stability. Interestingly, patients undergoing statin therapy sometimes experience myalgia associated with skeletal muscle t-tubular dilation and vacuolation (Mohaupt et al., 2009). These skeletal muscle t-tubular defects could be recapitulated *in vitro* in isolated human and mouse muscle fibers by extracting cholesterol using methyl-β-cyclodextrin (MβCD) (Draeger et al., 2006). Recent work has shown that modification of cholesterol content in cardiomyocytes affects cardiac TATS structure (Zhu et al., 2016) although another report has contradicted this initial finding (Gadeberg et al., 2017). One potential underlying reason contributing to this controversy is that these studies, whether using whole animal or isolated cell models, are focused on the analysis of the final result of long term remodeling of TATS and thus may miss the immediate and largely hidden changes in the TATS properties.

Given the important structural role that cholesterol plays in TATS, we hypothesize that one of the likely early consequences of membrane cholesterol modification could be a change in the susceptibility of TATS to various stresses. In this study we show that manipulation of membrane cholesterol leads to significant changes in the susceptibility of TATS to hyposmotic challenge while having no significant changes in the overall appearance of TATS. Furthermore, cholesterol modulation causes significant changes in the electrophysiological properties of cardiomyocytes reflecting diffusional accessibility of TATS that may indicate changes in the underlying t-tubular structure.

MATERIALS AND METHODS

Animals

This study was carried out in accordance with the recommendations provided in the Guide for the Care and Use of Laboratory Animals (8th edition; The National Academic Press, Washington, DC, United States). The protocol was approved by the veterinary staff of the University Committee on Use and Care of Animals at the University of Michigan.

Two- to six-months old male and female C57BL/6 mice were included in this study.

Solutions (mM)

All solutions were filtered using a 0.22 μm filter and pH adjusted to 7.35 with NaOH. Osmolarity was measured in previous study (Uchida et al., 2016) using a Vapro 5520 osmometer (Wescor, France; mean ± standard deviation; sample size = 3).

Modified Tyrode's solution (Tyr; 281 ± 4 mOsm/l): 137 NaCl, 5.4 KCl, 0.5 $MgCl_2$, 0.3 $CaCl_2$, 0.16 NaH_2PO_4, 3 $NaHCO_3$, 5 HEPES, 10 glucose.

Myocyte storage solution (C solution; 290 ± 3 mOsm/l): 122 NaCl, 5.4 KCl, 4 $MgCl_2$, 0.16 NaH_2PO_4, 3 $NaHCO_3$, 15 HEPES, 10 glucose, 5 mg/mL of bovine serum albumin, 1.38 mg/mL taurine.

Hyposmotic Tyrode's solution (0.6 Na; 186 ± 3 mOsm/l): prepared as Tyr but with 60% of NaCl.

Hyposmotic (0.7 Na; 211 ± 2 mOsm/l) solution: prepared by mixing 0.6 Na and Tyr solution in a 3:1 ratio.

Chemicals

HEPES (Calbiochem, United States); KCl, $NaHCO_3$, NaH_2PO_4 (Mallinckrodt Chemicals, United States); 3 kDa tetramethylrhodamine dextrans in anionic, lysine fixable form (Thermo Fisher Scientific Inc., Waltham, MA, United States). Collagenase (Type 2) (Worthington Biochemical Corp., Lakewood, NJ, United States). Methyl-β-cyclodextrin (MβCD; C4555), Water Soluble Cholesterol (WSC; C4951), Filipin (F9765) and all other chemicals and reagents were purchased from Sigma, St. Louis, MO, United States.

Isolation of Ventricular Myocytes

Myocytes were isolated from the hearts essentially as described in the study by Moench and Lopatin (2014) and used for experiments within 1–8 h post-isolation.

Cholesterol Modulation

Methyl-β-cyclodextrin was dissolved in C solution at concentrations of 4, 8, and 12 mg/mL, corresponding to approximate concentrations of 3, 6, and 9 mM. WSC was dissolved in C solution at 5 mg/mL, corresponding to approximately 50 μM cholesterol. All experiments, unless specifically noted, were carried out at room temperature (RT, ≈19–22°C). One of the main reasons for using RT vs. 37°C was to minimize damaging effects of stronger and faster cholesterol depletion at higher temperatures, as well as to reduce general stress on cardiomyocytes.

Filipin Staining

Quantification of membrane cholesterol was performed using staining with filipin with all procedures carried out at RT. Cardiomyocytes were fixed for 20 min using 2% paraformaldehyde, washed with paraformaldehyde-free solution and incubated with 65 μg/mL filipin for 20 min. After washing out filipin cardiomyocytes were imaged on Nikon TE 20000 microscope using 60× oil immersion objective (NA = 1.4) and CoolSnapEZ camera (Photometrix, Tucson, AZ, United States). Filipin was excited at 340 nm and the emission was collected using 400 nm dichroic mirror and no emission filter in the light

path. The data from individual images were corrected for system background, average fluorescence of filipin-free cardiomyocytes (<1–3% of the useful signal) and time-dependent decline in filipin fluorescence due to its washout from the cells (∼30% per hour).

Electrophysiological Measurements

Ionic currents were recorded in the whole-cell configuration essentially as described in a previous study (Uchida et al., 2016). In brief (**Figures 2A,B**), accumulation of K^+ in TATS was induced by applying 400 ms depolarizing step to +50 mV in order to activate voltage-dependent K^+ currents. Repolarization back to the holding potential of −75 mV leads to appearance of inward-going I_{K1} current, known as $I_{K1,\,tail}$, originating due to transiently increased concentration of K^+ in TATS. The density of I_{K1} itself was quantified by measuring the peak of I_{K1} in response to 400 ms voltage step to −120 mV prior to the following voltage ramp (**Figure 2A**). The ramp data were not used for any analysis and are presented here just for illustration purpose. Initial fast decline of I_{K1} from its peak value (black dot in **Figure 2A**) is due to depletion of t-tubular K^+ but not due to change in membrane potential which follows later as a ramp. In order to minimize the variation of various parameters due to the highly variable size of cardiomyocytes the data were normalized to the cell size (cross-sectional, XY, area).

Patched cardiomyocytes were imaged with a MD500 microscope eyepiece camera and the AmScope 3.7 software (AmScope, Irvine, CA, United States). The cross-sectional area was calculated by manually outlining the cell border using *ImageJ*[1].

Time Lapse Cell Width Measurements

Control and MβCD treated (4 mg/mL in C solution for 1 h) cardiomyocytes were plated onto a RC-20 perfusion chamber (Warner Instruments, Hamden, CT, United States). Only cells that settled in the center of the perfusion lane were imaged. Images were obtained at 10 s intervals. After a short (∼5 min) period of washout of C solution with Tyr, the perfusion was switched to 0.6 Na solution for 7 min.

The kinetics of solution exchange in the center of the perfusion chamber was measured by recording the change in fluorescence when switching from distilled water to distilled water containing 1:200 diluted 3 kDa dextran. After switching solutions, there is a delay of 3–5 s depending on the location in the bath chamber. The time course of fluorescence change was characterized by a time constant of <500 ms when fit with a single exponential function.

In response to hyposmotic stress, cardiomyocytes behave as nearly perfect osmometers and increase intracellular volume by expanding in width rather than in length (Drewnowska and Baumgarten, 1991). Furthermore, the cell depth to cell width ratio remains constant during hyposmotic swelling (Ogura et al., 2002), indicating that changes in the cell width serve as a good measure of cell volume changes. Experimentally, cardiomyocyte cell width was calculated from time-lapse image stacks using a combination of custom *ImageJ* and *MATLAB* scripts.

Di-8-ANEPPS Labeling of Cardiomyocytes

Stock solution of di-8-ANEPPS was prepared in DMSO at a concentration of 8.4 mM. The stock di-8-ANEPPS was mixed with 20% pluronic acid in 1:1 ratio and the resulting mixture was diluted (1:600) in C solution to prepare the working solution as previously described (Moench et al., 2013). Right before imaging, cardiomyocytes were incubated in the working solution for 15 min followed by washout with C solution without di-8-ANEPPS.

Dextran Trapping Assay

Dextran trapping assay was performed essentially as described in earlier publications (Moench et al., 2013; Uchida et al., 2016). In brief, 3 kDa dextran was added to a suspension of isolated ventricular myocytes during the swelling phase in hyposmotic 0.6 Na solution in order to fill t-tubules with this fluorescent marker. Cells were then returned to Tyr solution, still containing dextran, and finally extracellular dextran was washed out using normal Tyr. The cells were further washed and stored in C solution on ice prior to confocal imaging. Control myocytes were treated identically except that they were exposed to Tyr solution instead of 0.6 Na solution.

Confocal Imaging

Confocal imaging was performed in Microscopy and Image Analysis Laboratory (University of Michigan, Ann Arbor, MI, United States) on an Olympus FV-500 microscope using 60× 1.4 NA oil objective. Images of myocytes were manually outlined and mean intracellular fluorescence of trapped dextran per unit area calculated using *ImageJ*. Further data analysis, e.g., correction for background fluorescence, was performed in Microsoft Excel.

Skeletonization of TATS

Skeletonization of TATS was performed using approach similar to that described in the paper by Guo and Song (2014). Cardiomyocytes were labeled with di-8-ANEPPS and imaged on confocal microscope using 60× 1.4 NA oil objective and 68 nm pixel size. Image analysis was performed using *ImageJ* and custom macro to automate various steps in the procedure. Images were rotated to bring cardiomyocytes to the same (horizontal) orientation, smoothed using 1 pixel Gaussian Blur. Application of "Auto Threshold" using Huang method followed by "Analyze Particles" to exclude all objects smaller than the size of cardiomyocyte produces the outline of the cell. The outlined cell is then filled with black color and the resulting object uniformly reduced in size using "Erode" function thus creating a mask of cell interior (i.e., cell border excluded). Application of cell interior mask to the original smoothed image followed by "Auto Local Threshold" using Otsu method with radius = 20 provides a binary image of TATS. The images were then skeletonized using Skeletonize (2D/3D) plug-in. Separation of axial ant transverse t-tubules

[1]https://imagej.nih.gov

was carried out by application of appropriate morphological filters using MorphoLibJ plug-ins. Specifically, radial and axial t-tubule segments were isolated using 3 pixels long lines (structural element) at 90 and 45 degrees (for radial) and 0 and 135 degrees (for axial), respectively. The use of 45 and 135 degrees lines allows for assigning slanted t-tubular segments to either radial or axial group, and because of left/right symmetry of the cell the effects of application of asymmetrical lines (45 vs. 135 degrees) cancel out. It should be noted that segments smaller than 3 pixels will be lost during the above procedure but this does not affect the ratio of radial vs. axial t-tubules. The density of TATS was calculated as the % of t-tubule pixels relative to the total number of pixels in the cell mask.

Statistics

The data (mean ± standard error) in each experimental series are from at least two heart preparations. Statistical significance was determined using a one-way ANOVA with Bonferroni correction or two-sample *t*-test assuming equal or unequal variances (whichever is appropriate) and considered significant if $p < 0.05$. With some data one-way ANOVA could not be applied (e.g., due to large disparity in variance) and the data were then analyzed using two-sample *t*-tests. In figures, *, **, *** and #, ##, ### correspond to ANOVA or *t*-test with *p*-values of 0.05, 0.01, and 0.001, respectively.

RESULTS

Effects of Membrane Cholesterol Modulation on the Overall Organization of TATS

We first tested the tolerance of cardiomyocytes to various concentrations of MβCD at room temperature (**Supplementary Figure 1**). There were no easily observable changes in TATS appearance at 3 or 6 mM MβCD but at 9 mM MβCD cells displayed clear deterioration of TATS and increased death rate.

In particular, we also found that the treatment of cardiomyocytes with 1 mM MβCD at 37°C (one of the commonly used conditions) is more damaging than that performed with 3 mM MβCD at room temperature (same exposure time; 1 h). Importantly, with 1 mM MβCD at 37°C only few cardiomyocytes survived the following standard hyposmotic detubulation while cells treated with 1 or 3 mM MβCD at room temperature did not show any overt changes in mortality following detubulation.

Accordingly, the following experiments were performed using 3 mM MβCD to minimize the detrimental consequences of cholesterol depletion in order to help unmask the underlying reasons behind its action.

As expected, the data in **Figures 1A–C** show that application of either 3 mM MβCD or WSC (5 mg/mL) has little effect on the overall appearance of TATS. In particular, the regularity of TATS estimated as the amplitude of the first harmonic of fluorescence spectra of membrane bound di-8-ANEPPS dye was not affected by MβCD and WSC (**Figures 1B,C**). However,

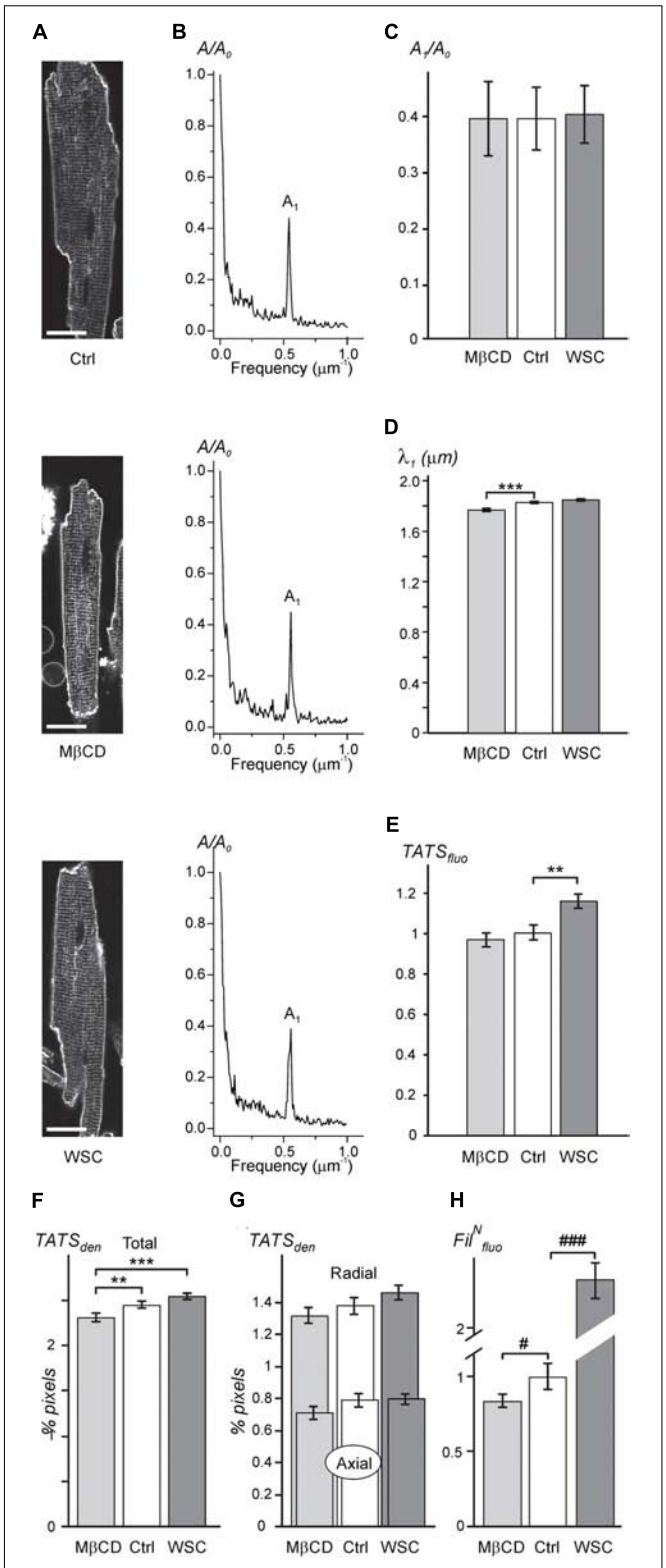

FIGURE 1 | Effects of MβCD and WSC on TATS appearance (**A**; left column). Representative confocal images of control (Ctrl), 3 mM MβCD- and 5 mg/mL WSC-treated ventricular myocytes stained with di-8-ANEPPS. Scale bars: 20 μm. (**B**; middle column). Corresponding amplitude spectra of fluorescence

(Continued)

FIGURE 1 | Continued
normalized to the amplitude of zero order component (A_0). **(C)** Normalized amplitude (A_1) and **(D)** wavelength (λ_1) of the first harmonic of fluorescence. **(E)** Density of t-tubular fluorescence ($TATS_{fluo}$) normalized to that in Ctrl myocytes. **(F,G)** Densities of various components of TATS derived from skeletonization of confocal images of cardiomyocytes labeled with di-8-ANEPPS. The density is calculated as percentage of pixels belonging to TATS skeleton. n = 20, 20, and 20 for Ctrl, MβCD- and WSC-treated cells, respectively. **(H)** Effects of MβCD and WSC on the intensity of filipin (cholesterol specific agent) staining. The data are normalized to that obtained in control cardiomyocytes. n = 67, 44 and 59 for Ctrl, MβCD- and WSC-treated cells, respectively.

quite small (∼3.4%) but statistically significant reduction in the wavelength of the first harmonic corresponding to the sarcomeric length of cardiomyocytes was observed in MβCD-treated cells (**Figure 1D**). TATS density was estimated in two different ways. First, **Figure 1E** shows that the intensity of intracellular (t-tubular) fluorescence of di-8-ANEPPS was not affected by MβCD but was increased by ∼16% in cardiomyocytes treated with WSC. Second, skeletonization of the TATS shows no significant effects of the drugs relative to control, although small, but statistically significant difference, can be observed when one would compare the effects of MβCD and WSC (**Figure 1F**). Additional analysis also shows that the balance between radial and axial t-tubules is not affected as well (**Figure 1G**). Consistent with relatively low effective concentration of MβCD the fluorescence of filipin, a cholesterol specific agent, was reduced only by ∼12% compared to that in control cardiomyocytes (see section "Discussion" and **Supplementary Figure 2** on limitations of filipin-based assay). Importantly, the magnitude of reduction in filipin fluorescence observed with treatment using 3 mM MβCD for 1 h at RT (∼12% reduction; **Figure 1H**) is significantly smaller than the reduction observed with 1 mM MβCD for 1 h at 37°C (∼50% reduction; **Supplementary Figure 2**), suggesting that cholesterol extraction treatment in our study is milder than that used in similar studies (e.g., Gadeberg et al., 2017).

Overall, the general appearance of the TATS network remains largely unchanged following cholesterol depletion or supplementation at the indicated concentrations of cholesterol modifying agents.

Electrophysiological Characterization of the Effects of Membrane Cholesterol Modulation

Many ionic currents originate from ion channels concentrated in TATS. However, the $I_{K1,\,tail}$ current ($I_{K1,\,tail}$) is a unique current that is in large degree dependent on the lumenal K^+ within TATS (Clark et al., 2001; Cheng et al., 2011), which in turn are dependent on their fine geometrical structure (Uchida and Lopatin, 2018). **Figures 2A–C** explains the origin of $I_{K1,\,tail}$ and highlights some important features of this current related to TATS structure. In brief, during a prolonged depolarization, outward potassium currents cause potassium ions to flow into the t-tubular lumen and accumulate due to restricted diffusion to the extracellular space (**Figure 2C**, top). Upon repolarization, the accumulated potassium depletes by (1) flowing into the cell through I_{K1} channels manifesting as the $I_{K1,\,tail}$ and by (2) diffusing out of the t-tubule lumen to the extracellular space (**Figure 2C**, bottom). It has been shown that under conditions similar to that used in our experiments (e.g., holding membrane potential −75 mV) depletion of accumulated potassium by diffusion constitutes a large portion of total efflux and thus $I_{K1,\,tail}$ can serve as a quantitative measure of diffusional component of TATS (Clark et al., 2001).

We first assessed the effects of cholesterol modulation on membrane capacitance. The averaged values of membrane capacitance (177.1 ± 9.3 pF, 168.2 ± 7.7 pF, and 173.5 ± 9.9 pF) and cell size (cross-sectional area; 3821.4 ± 153.6 μm^2, 4005.1 ± 164.0 μm^2, and 3388.5 ± 159.1 μm^2) were not different (p = NS by ANOVA) between Ctrl, MβCD, and WSC groups, respectively. In order to better estimate potential changes in specific membrane capacitance, cell size should be taken into account. As shown in **Figure 2D**, treatment with MβCD significantly decreases normalized (to cell cross-sectional area) membrane capacitance. Conversely, treatment with WSC leads to an increase in normalized membrane capacitance although with no statistical significance (p = 0.06). Since cholesterol modulation significantly affects specific membrane capacitance, membrane currents were normalized to cell cross sectional area. Importantly, we found that I_{K1} is unaffected by cholesterol modulation (**Figure 2E**). In contrast, the outward potassium current at the end of the depolarizing pulse ($I_{K,\,end}$) was significantly increased by MβCD treatment compared to that in control cells. Somewhat surprisingly, $I_{K,\,end}$ in WSC treated cells was essentially unchanged (**Figure 2F**).

Since the magnitude of potassium accumulation in TATS is dependent on the magnitude of outward potassium current, $I_{K1,\,tail}$ were normalized to $I_{K,\,end}$ (Cheng et al., 2011). Consistent with the data in **Figure 1**, which shows that the overall appearance of TATS is essentially unaffected by cholesterol modulation, no significant differences in the amplitude of the normalized $I_{K1,\,tail}$ were observed as well (**Figure 2G**). However, the kinetics of $I_{K1,\,tail}$ decline, which primarily reflects the rate of potassium diffusion out of the t-tubule lumen, was significantly affected (**Figures 2H,I**). Specifically, cells treated with MβCD display $I_{K1,\,tail}$ that decline faster than in control cells as both τ_1 and τ_2 of the two-exponential fit were decreased. Conversely, WSC treated cells display a slower decline in $I_{K1,\,tail}$ with both τ_1 and τ_2 significantly increased. This data suggests significant changes in fine (sub-microscopic) geometrical structure of TATS which may occur due to modulation of membrane cholesterol.

Effects of Modulation of Membrane Cholesterol on the Magnitude of Detubulation

Despite there being no or minor observable effects of cholesterol modifying agents on the overall architecture of TATS (**Figure 1**) the electrophysiological data above show significant, largely

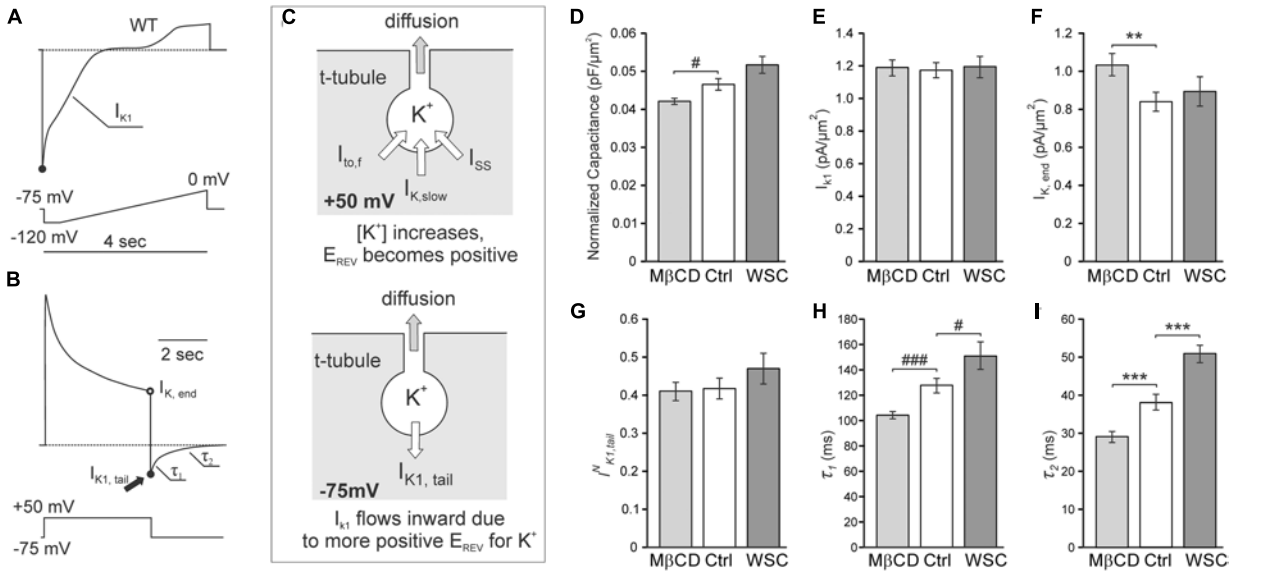

FIGURE 2 | Electrophysiological properties of cholesterol depleted and supplemented cardiomyocytes. **(A)** Cartoon trace of I_{K1} current in response to a slow ramp protocol. **(B)** Cartoon trace of outward K^+ currents in response to a 400 ms step depolarization to +50 mV and inward $I_{K1, tail}$ in response to a step repolarization back to –75 mV. The amplitude of $I_{K1, tail}$ and its kinetics (characterized by time constants τ_1 and τ_2) are measures of diffusional properties of TATS. **(C)** Cartoon diagram depicting the origin of the $I_{K1, tail}$. Top: outward potassium currents cause the accumulation of potassium within the t-tubular lumen during depolarization. Bottom: upon repolarization, the accumulated potassium can either flow into the cell through I_{K1} channels producing the $I_{K1, tail}$ or diffuse out of the t-tubular lumen to the extracellular space. **(D–G)** Quantification of the membrane capacitance normalized to the cell cross-sectional area **(D)**, peak I_{K1} current normalized to the cell cross-sectional area **(E)**, steady-state $I_{K, end}$ **(F)**, and $I_{K1, tail}$ amplitude normalized to the steady-state $I_{K, end}$ current. n = 35 control, 40 MβCD, and 16 WSC-treated cells. **(H,I)** Quantification of the slow **(H)** and fast **(I)** time constants of $I_{K1, tail}$ decline. n = 37 control, 39 MβCD-, and 16 WSC-treated cells.

hidden but likely important changes in TATS structure strongly suggesting that there might be other consequences of cholesterol modulation. Specifically, we tested whether susceptibility of TATS to osmotic challenge, known to strongly affect the integrity of TATS (Moench et al., 2013), is affected by MβCD or WSC. In this regard, the magnitude of stress-induced sealing of TATS measured by the amount of trapped extracellular dextran serves as a useful and quantitative measure of TATS stability (Moench et al., 2013). Hyposmotic detubulation with 0.6 Na stress, however, leads to nearly complete detubulation in control cardiomyocytes. In order to maximize the putative observable effect, a milder osmotic stress (0.7 Na) was used to expand the dynamic range of dextran trapping. The data in **Figures 3A,B**, along with that in **Supplementary Figures 3**, **4**, highlight one of the central findings of this work: depletion of cholesterol by MβCD significantly compromises the resistance of TATS to sealing in response to hyposmotic shock. Importantly, the effect is fully reversible by re-introducing cholesterol with WSC. Significant (>twofold) protective effect of membrane cholesterol is also confirmed in experiments using "full strength" hyposmotic shock with 0.6 Na solution where WSC is applied to normal cardiomyocytes (not previously treated with MβCD; **Figures 3C,D**).

The data in **Supplementary Figure 3** show that cardiomyocytes treated with 1 mM MβCD at 37°C display significantly greater dextran trapping than cardiomyocytes treated with 1 or 3 mM MβCD at room temperature for the same duration. It also follows from the data in **Supplementary Figure 3** that treatment with 3 mM MβCD followed by detubulation with 0.7 Na solution places the response in a "dynamic" range allowing for observation of both increases and decreases in dextran trapping.

Notably, the magnitude of dextran trapping in MβCD treated cells inversely correlates with the remaining filipin fluorescence (**Supplementary Figure 4**), consistent with the notion that membrane cholesterol plays a critical role in TATS susceptibility to osmotic stress.

Consistent with the above findings, the magnitude of reduction in both normalized membrane capacitance and normalized $I_{K1, tail}$ amplitude (due to sealing of TATS) in response to 0.7 Na hyposmotic stress is more pronounced in MβCD treated cells compared to that in control cells (**Figure 4**). Overall, the above results suggest that MβCD treated cells are more susceptible to t-tubular remodeling in response to hyposmotic stress.

Cell Swelling Is Unaffected by Cholesterol Depletion

Previous work suggested that cholesterol depletion may accelerate cardiomyocyte swelling in response to osmotic stress (Kozera et al., 2009) and thus may affect the magnitude of changes in TATS following osmotic detubulation. Accordingly,

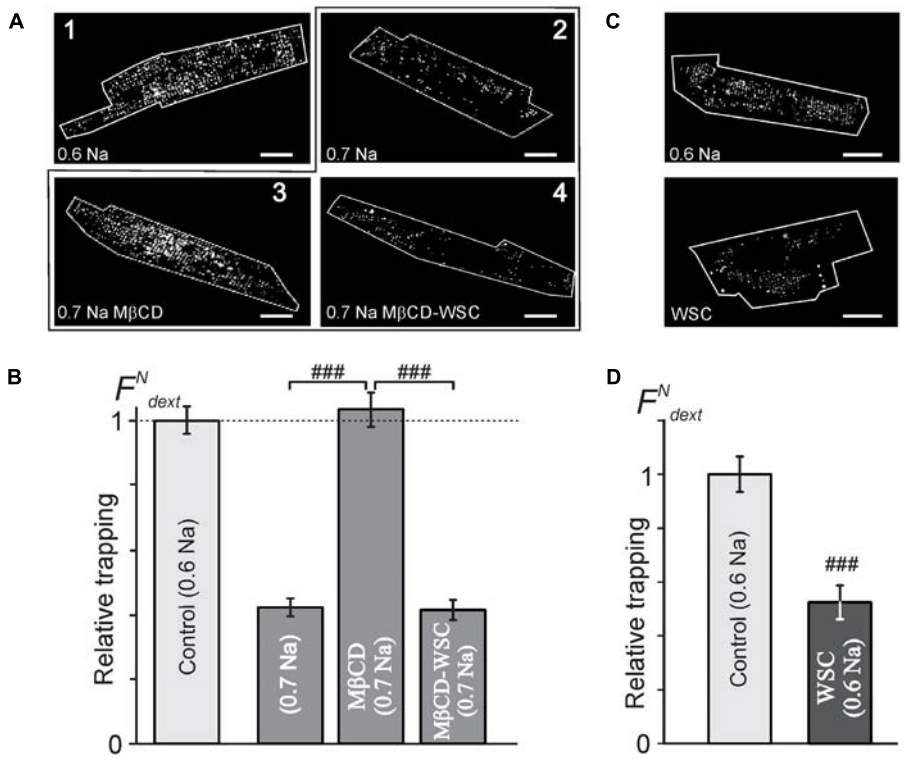

FIGURE 3 | Effects of MβCD and WSC on the amount of dextran trapped in sealed t-tubules. **(A)** Representative confocal images of ventricular myocytes (cell border zone indicated by white outline) highlighting the magnitude of t-tubular sealing in response to hyposmotic shock under various conditions. Detubulation with 0.6 Na solution (1) served as a reference, (2) no treatment, (3) MβCD for 1 h at RT, and (4) 3 mM MβCD for 1 h at RT followed by washout and application of 5 mg/mL WSC for 45 min at RT, all in response to shock using 0.7 Na solution. Scale bar: 20 μm. **(B)** Quantification of the data in panel **(A)**. *n* = 68, 58, 55, and 40 cells, respectively. **(C)** Representative confocal images of control (top) and WSC-treated (5 mg/mL for 45 min) ventricular myocytes detubulated with standard 0.6 Na. **(D)** Quantification of dextran trapping of the data in pane **(C)**. *n* = 35 cells each.

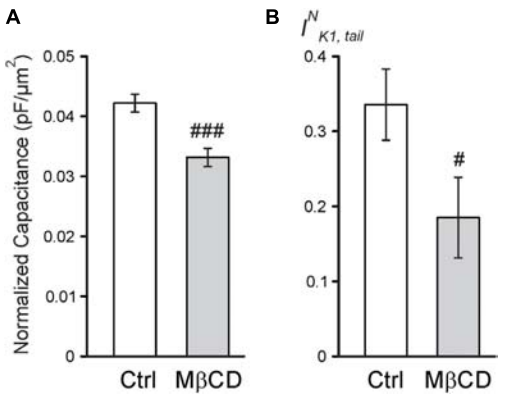

FIGURE 4 | Electrophysiological effects of MβCD after 0.7 Na detubulation. **(A)** Quantification of cell area normalized membrane capacitance of control and MβCD treated cells after detubulation with 0.7 Na. *n* = 13 cells each. **(B)** Quantification of normalized $I_{K1, tail}$ in control and MβCD treated cells after detubulation with 0.7 Na. *n* = 12 and 11 cells, respectively.

the kinetics of cell swelling in 0.6 Na solution was measured in control and MβCD treated cardiomyocytes. As shown in **Figure 5**, in both control and MβCD treated cardiomyocytes cell width increases in a nearly identical manner upon perfusion with 0.6 Na solution. The change in cell width can be fitted with a single exponential function and the time constant characterizing the kinetics of cell swelling is not significantly different between those measured in control and MβCD treated cells. Furthermore, there is no significant difference in the magnitude of cell swelling in 0.6 Na solution. These data suggest that cholesterol depletion has no effect on hyposmotic swelling and argues against an osmotic effect underlying the differences in dextran trapping between control and MβCD treated cells.

DISCUSSION

Role of Cholesterol in T-Tubular Membranes

The importance of cholesterol in t-tubular membranes is highlighted in recent papers. In particular, cholesterol depletion using MβCD was shown to affect TATS integrity in a concentration and time-dependent manner (Zhu et al., 2016). This effect of MβCD seems controversial as more recent work demonstrated that cholesterol depletion does not appear to

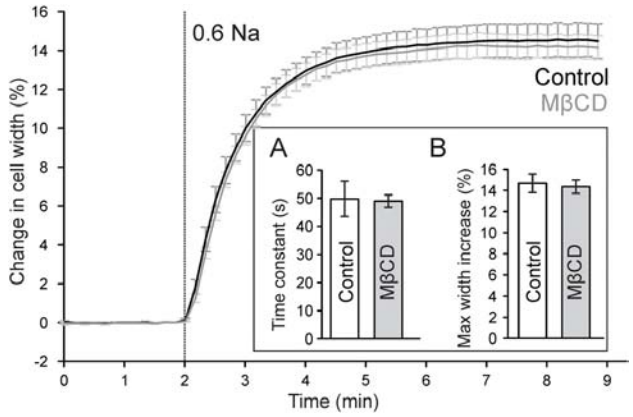

FIGURE 5 | Effect of MβCD treatment on hyposmotic cell swelling. Traces of average changes in relative cell width of control (black) and MβCD treated (gray) cardiomyocytes as a function of time. Vertical line denotes the start of perfusion with hyposmotic 0.6 Na solution. Inset: **(A)** Quantification of the kinetics of cell swelling. A single exponential function was fitted to the time course of cell width during 0.6 Na perfusion and the time constant was averaged for each group (n = 7 and 9 for control and MβCD treated cells, respectively). **(B)** Quantification of the maximum change in cell width.

disrupt TATS organization (Gadeberg et al., 2017). However, a closer look at the specific experimental conditions in the mentioned studies can reconcile the findings. Specifically, in the study by Gadeberg et al. (2017) threefold lower concentration of MβCD was used compared to the lowest concentration employed in the study by Zhu et al (1 mM vs. 3 mM) (Zhu et al., 2016). The data in our study confirm this view and essentially eliminate that formal discrepancy. Although we performed experiments at RT (vs. 37°C in mentioned papers) a different range of MβCD concentrations was tested.

The data in **Figure 1** and **Supplementary Figure 1** show that, indeed, at RT and 3 mM MβCD concentration essentially no or only minor changes in the overall structure of TATS can be observed while at 6 mM and higher concentrations the disruptive effect of cholesterol depletion becomes apparent. It should be noted here, that the amount of membrane cholesterol measured using filipin approach is likely overestimated, and thus the effect of MβCD on membrane cholesterol is underestimated (**Figure 1H**), likely due to membrane permeability of filipin leading to staining intracellular pools of cholesterol (see **Supplementary Figure 2** for further detail). Alternatively, the amount of membrane cholesterol may be overestimated in WSC-treated cardiomyocytes likely due to membrane binding of WSC aggregates or micelles.

The two parameters which we found to be affected by modulation of membrane cholesterol were sarcomeric length (**Figure 1D**; ∼3.4%; MβCD vs. control) and the density of TATS estimated using either di-8-ANEPPS labeling (**Figure 1E**; ∼19%; control vs. WSC) or skeletonizing algorithm (**Figure 1F**; ∼10%; MβCD vs. WSC). The change in the sarcomeric length is very small, and the observation became possible in part due to relatively high precision of the measurements employing Fourier transformation. The effect is likely linked to changes in the concentration of resting intracellular Ca^{2+}, however, it was impractical to proceed with further investigation of this phenomenon keeping in mind the magnitude of the changes. Measurements of TATS density using di-8-ANEPPS can be significantly confounded by unpredictable effects of cholesterol modulation on the binding of the dye (likely more than due to minor changes in the resting membrane potential of cardiomyocytes), and therefore the data should be interpreted with caution. In contrast, skeletonization approach using local thresholding algorithms is not sensitive to the variation in the intensity of di-8-ANEPPS. Changes in TATS density measured with this approach are very small and could only be reliably detected by comparing two extreme treatments (MβCD vs. WSC). We speculate that the observed effects are not due to true changes in TATS density but are rather apparent (i.e., algorithm dependent) changes due to submicroscopic transformations in the morphology of individual t-tubules. Overall, quantitative data show that the appearance of TATS is essentially unaffected by treatment with MβCD and WSC.

Importantly, however, one has to make a clear distinction between the overall TATS *integrity* and its *stability*. In this regard, one of the central findings of our study is that although the TATS *integrity* appears essentially unaffected following cholesterol modulation with 3 mM MβCD, the *stability* of the TATS in response to stress is greatly compromised. In particular, the data in **Figure 3** demonstrate that cholesterol depletion promotes dextran trapping following hyposmotic detubulation, while cholesterol supplementation protects against osmotic detubulation. These data suggest that cholesterol plays a significant role in stabilizing t-tubules against osmotic stress. Importantly, as shown in **Figure 5**, modulation of membrane cholesterol did not affect the magnitude and kinetics of osmotic swelling suggesting that the observed results cannot be simply explained by changes in mechanical forces caused by osmotic stress. Furthermore, this data may suggest that Zhu et al. observed the combined effects of MβCD treatment and long-term culture, a condition known to cause t-tubule loss (Louch et al., 2004; Zhu et al., 2016; Guo et al., 2018).

Effects of Cholesterol Modulation on Electrophysiological Properties of Cardiomyocytes

It is commonly expected that cholesterol modulation would have significant effects on membrane capacitance. However, the available data are quite controversial, even in studies using artificial membranes. For example, Ohki (1969) found that capacitance of phosphatidylcholine bilayers increases with addition of cholesterol while in other studies an opposite effect was observed (Naumowicz et al., 2005; Budvytyte et al., 2013), and the effect of cholesterol on membrane

capacitance may even show biphasic relationship in lipid monolayers (Pasek et al., 2008). Assuming that increasing membrane cholesterol monotonically decreases membrane capacitance and that cholesterol modulation does not alter the total membrane surface area, one would expect that treatment with MβCD would result in increased membrane capacitance. In contrast, Gadeberg et al. (2017) have recently found that in mouse cardiomyocytes depletion of membrane cholesterol does not alter the membrane capacitance. In even greater contrast, we observe the opposite effect of cholesterol on membrane capacitance (**Figure 2**). As mentioned earlier, differences in experimental conditions may underlie quantitative differences between the studies. In particular, we used higher concentration of MβCD but lower (RT) temperature which altogether likely led to a stronger modulation of membrane cholesterol. Overall, the data highlight the complexity of cholesterol action on membrane capacitance, which likely involves cholesterol-dependent caveolae that contribute significantly to membrane area (Levin and Page, 1980). In this regard, EM images of cardiomyocytes treated with MβCD display significantly fewer caveolae than control cells (Kozera et al., 2009). However, it remains unknown whether these caveolae are internalized thus decreasing total membrane area or whether the proteins supporting the caveolae structure merely disassemble thus retaining the lipids in the surface membrane. If these caveolae are removed from the total surface membrane, then the membrane capacitance would be expected to decrease, consistent with our findings. Unfortunately, the effect of cholesterol supplementation on the number of caveolae remains unknown and, therefore, it is unclear whether additional cholesterol increases the total surface membrane area as suggested by the membrane capacitance measurements. It should be noted that direct correlation between the intensity of di-8-ANEPPS fluorescence and membrane area cannot be made since di-8-ANEPPS fluorescence is strongly dependent on the presence of membrane cholesterol (Gross et al., 1994).

In contrast to none or relatively small effects of cholesterol modulation on membrane capacitance, there are numerous reports on significant roles of this lipid in the activity of various ion channels (Dart, 2010). In this study we focused on two types of potassium currents highly useful in determining the diffusional properties of TATS: cardiac outward rectifier and inward rectifier potassium currents (**Figure 2**). We have previously shown that the magnitude of K^+ accumulation in TATS maximizes at about 400 ms after membrane depolarization and is primarily determined by $I_{K,\,end}$ which is, in turn, is carried primarily by several members of Kv1 and Kv2 subfamilies of voltage-gated K^+ channels underlying $I_{K,\,slow}$ (Nerbonne, 2000). Consistent with previous reports we find that depletion of membrane cholesterol leads to significant increase in late $I_{K,\,end}$ (Balse et al., 2009), although cholesterol enrichment with WSC did not have any significant effect (**Figure 2**). Accordingly, because of sensitivity of $I_{K,\,end}$ to changes in membrane cholesterol, for a meaningful interpretation of the data the magnitude of $I_{K1,\,tail}$ should be normalized to the magnitude of $I_{K,\,end}$ (leading to $I^N_{K1,\,tail}$; **Figure 2**).

As mentioned in **Figure 2**, $I_{K1,\,tail}$ dissipates due to two fluxes: movement of potassium into the cell through I_{K1} channels carried by Kir2 subfamily (Anumonwo and Lopatin, 2010) and diffusion of potassium out of t-tubular lumen. Surprisingly, we found that in mouse cardiomyocytes I_{K1} is essentially insensitive to cholesterol modulation (**Figure 2E**). This is different from the effects observed in endothelial cells endogenously expressing inward-rectifier K^+ channels (Romanenko et al., 2002) or in cells exogenously expressing Kir2.1 channels (Romanenko et al., 2004) where treatment with MβCD or cholesterol loaded MβCD causes robust changes in the current density. Due to insensitivity of cardiac I_{K1} to membrane cholesterol there was no need to further normalize the $I^N_{K1,\,tail}$ to I_{K1} amplitude.

Consistent with no effects of cholesterol modulation on the overall structure of TATS we found no significant changes in the amplitude of $I^N_{K1,\,tail}$ upon treatment with MβCD or WSC (**Figure 2**). It should be noted, however, that the interpretation of the $I^N_{K1,\,tail}$ amplitude with regard to TATS structure is not that straightforward, in particular, because it depends on both the density of outward K^+ current and t-tubular diffusion. In contrast, kinetics of $I_{K1,\,tail}$ (**Figure 2C**) depends in a large degree on the diffusional properties of TATS (Clark et al., 2001). In this regard, we recently demonstrated that t-tubular dilations and constrictions, which generally can be viewed as submicroscopic irregularities of t-tubular lumen shape, have a significant impact on the diffusion of molecules within TATS (Uchida and Lopatin, 2018). T-tubule dilations are common features of normal cardiac TATS (Savio-Galimberti et al., 2008; Pinali et al., 2013) and a recent study has reported that t-tubular dilations are associated with regions where Cav3 and RyR2 colocalize (Wong et al., 2013). The loss of these sub-microscopic structures resulting in more uniformly shaped t-tubules would be expected to accelerate the diffusion rate while introduction of more constrictions/dilations will restrict diffusion and slow diffusion rate. The data in **Figures 2H,I** show that modulation of membrane cholesterol leads to significant changes in diffusional properties of TATS, consistent with the notion that disruption of cholesterol domains [e.g., t-tubular caveolae (Levin and Page, 1980; Burton et al., 2017)] by MβCD results in reduced irregularity of t-tubule diameters and thus faster diffusion of potassium while supplementation with additional cholesterol by WSC does the opposite. An alternative mechanism may involve the effect of cholesterol on t-tubular cBIN1-microfolds which were suggested to contribute significantly to diffusional properties of TATS (Hong et al., 2014). Quantitative analysis of the changes in cBIN1-microfolds, however, would require optical super-resolution or electron microscopy imaging in future projects.

Overall, the results of this study show that in mouse ventricular myocytes modulation of membrane cholesterol leads to significant changes in susceptibility of TATS to acute hyposmotic stress. These findings suggest that long term effects of membrane cholesterol on the integrity of TATS

may be explained, at least in part, by its effects of the stability of TATS.

AUTHOR CONTRIBUTIONS

AN, KU, and AL designed the research, performed the experiments, analyzed the data, and wrote the manuscript. IM performed the experiments and analyzed the data. All the authors contributed to the final version of the manuscript.

FUNDING

This work was supported by the National Institutes of Health National Heart, Lung, and Blood Institute (Grant HL127023; AL) and AHA Predoctoral Fellowship (17PRE33350049; KU).

ACKNOWLEDGMENTS

The authors would like to thank Yasmine Elghoul for assistance with isolation of cardiomyocytes.

SUPPLEMENTARY MATERIAL

The Supplementary Material for this article can be found online at: https://www.frontiersin.org/articles/10.3389/fphys.2018.01516/full#supplementary-material

REFERENCES

Anumonwo, J. M., and Lopatin, A. N. (2010). Cardiac strong inward rectifier potassium channels. *J. Mol. Cell. Cardiol.* 48, 45–54. doi: 10.1016/j.yjmcc.2009.08.013

Balse, E., El-Haou, S., Dillanian, G., Dauphin, A., Eldstrom, J., Fedida, D., et al. (2009). Cholesterol modulates the recruitment of Kv1.5 channels from Rab11-associated recycling endosome in native atrial myocytes. *Proc. Natl. Acad. Sci. U.S.A.* 106, 14681–14686. doi: 10.1073/pnas.0902809106

Budvytyte, R., Mickevicius, M., Vanderah, D. J., Heinrich, F., and Valincius, G. (2013). Modification of tethered bilayers by phospholipid exchange with vesicles. *Langmuir* 29, 4320–4327. doi: 10.1021/la304613a

Burton, R. A. B., Rog-Zielinska, E. A., Corbett, A. D., Peyronnet, R., Bodi, I., Fink, M., et al. (2017). Caveolae in rabbit ventricular myocytes: distribution and dynamic diminution after cell isolation. *Biophys. J.* 113, 1047–1059. doi: 10.1016/j.bpj.2017.07.026

Cheng, L., Wang, F., and Lopatin, A. N. (2011). Metabolic stress in isolated mouse ventricular myocytes leads to remodeling of t-tubules. *Am. J. Physiol. Heart Circ. Physiol.* 301, H1984–H1995. doi: 10.1152/ajpheart.00304.2011

Clark, R. B., Tremblay, A., Melnyk, P., Allen, B. G., Giles, W. R., and Fiset, C. (2001). T-tubule localization of the inward-rectifier K(+) channel in mouse ventricular myocytes: a role in K(+) accumulation. *J. Physiol.* 537, 979–992. doi: 10.1111/j.1469-7793.2001.00979.x

Coronel, R. (2017). The pro- or antiarrhythmic actions of polyunsaturated fatty acids and of cholesterol. *Pharmacol. Ther.* 176, 40–47. doi: 10.1016/j.pharmthera.2017.02.004

Dart, C. (2010). Lipid microdomains and the regulation of ion channel function. *J. Physiol.* 588, 3169–3178. doi: 10.1113/jphysiol.2010.191585

Draeger, A., Monastyrskaya, K., Mohaupt, M., Hoppeler, H., Savolainen, H., Allemann, C., et al. (2006). Statin therapy induces ultrastructural damage in skeletal muscle in patients without myalgia. *J. Pathol.* 210, 94–102. doi: 10.1002/path.2018

Drewnowska, K., and Baumgarten, C. M. (1991). Regulation of cellular volume in rabbit ventricular myocytes: bumetanide, chlorothiazide, and ouabain. *Am. J. Physiol.* 260, C122–C131. doi: 10.1152/ajpcell.1991.260.1.C122

Gadeberg, H. C., Kong, C. H. T., Bryant, S. M., James, A. F., and Orchard, C. H. (2017). Cholesterol depletion does not alter the capacitance or Ca handling of the surface or t-tubule membranes in mouse ventricular myocytes. *Physiol. Rep.* 5:e13500. doi: 10.14814/phy2.13500

Gross, E., Bedlack, R. S. Jr., and Loew, L. M. (1994). Dual-wavelength ratiometric fluorescence measurement of the membrane dipole potential. *Biophys. J.* 67, 208–216. doi: 10.1016/S0006-3495(94)80471-0

Guo, A., Chen, R., Wang, Y., Huang, C. K., Chen, B., Kutschke, W., et al. (2018). Transient activation of PKC results in long-lasting detrimental effects on systolic [Ca(2 +)]i in cardiomyocytes by altering actin cytoskeletal dynamics and T-tubule integrity. *J. Mol. Cell. Cardiol.* 115, 104–114. doi: 10.1016/j.yjmcc.2018.01.003

Guo, A., and Song, L. S. (2014). AutoTT: automated detection and analysis of t-tubule architecture in cardiomyocytes. *Biophys. J.* 106, 2729–2736. doi: 10.1016/j.bpj.2014.05.013

Guo, A., Zhang, C., Wei, S., Chen, B., and Song, L. S. (2013). Emerging mechanisms of T-tubule remodelling in heart failure. *Cardiovasc. Res.* 98, 204–215. doi: 10.1093/cvr/cvt020

Hidalgo, C. (1985). Lipid phase of transverse tubule membranes from skeletal muscle. an electron paramagnetic resonance study. *Biophys. J.* 47, 757–764. doi: 10.1016/S0006-3495(85)83978-3

Hong, T., Yang, H., Zhang, S. S., Cho, H. C., Kalashnikova, M., Sun, B., et al. (2014). Cardiac BIN1 folds T-tubule membrane, controlling ion flux and limiting arrhythmia. *Nat. Med.* 20, 624–632. doi: 10.1038/nm.3543

Kawai, M., Hussain, M., and Orchard, C. H. (1999). Excitation-contraction coupling in rat ventricular myocytes after formamide-induced detubulation. *Am. J. Physiol.* 277, H603–H609. doi: 10.1152/ajpheart.1999.277.2.H603

Kline, C. F., and Mohler, P. J. (2013). Evolving form to fit function: cardiomyocyte intercalated disc and transverse-tubule membranes. *Curr. Top. Membr.* 72, 121–158. doi: 10.1016/B978-0-12-417027-8.00004-0

Kozera, L., White, E., and Calaghan, S. (2009). Caveolae act as membrane reserves which limit mechanosensitive I(Cl,swell) channel activation during swelling in the rat ventricular myocyte. *PLoS One* 4:e8312. doi: 10.1371/journal.pone.0008312

Levin, K. R., and Page, E. (1980). Quantitative studies on plasmalemmal folds and caveolae of rabbit ventricular myocardial cells. *Circ. Res.* 46, 244–255. doi: 10.1161/01.RES.46.2.244

Louch, W. E., Bito, V., Heinzel, F. R., Macianskiene, R., Vanhaecke, J., Flameng, W., et al. (2004). Reduced synchrony of Ca2 + release with loss of T-tubules-a comparison to Ca2 + release in human failing cardiomyocytes. *Cardiovasc. Res.* 62, 63–73. doi: 10.1016/j.cardiores.2003.12.031

Moench, I., and Lopatin, A. N. (2014). Ca homeostasis in sealed t-tubules of mouse ventricular myocytes. *J. Mol. Cell. Cardiol.* 72, 374–383. doi: 10.1016/j.yjmcc.2014.04.011

Moench, I., Meekhof, K. E., Cheng, L. F., and Lopatin, A. N. (2013). Resolution of hypo-osmotic stress in isolated mouse ventricular myocytes causes sealing of t-tubules. *Exp. Physiol.* 98, 1164–1177. doi: 10.1113/expphysiol.2013.072470

Mohaupt, M. G., Karas, R. H., Babiychuk, E. B., Sanchez-Freire, V., Monastyrskaya, K., Iyer, L., et al. (2009). Association between statin-associated myopathy and skeletal muscle damage. *CMAJ* 181, E11–E18. doi: 10.1503/cmaj.081785

Naumowicz, M., Petelska, A. D., and Figaszewski, Z. A. (2005). Impedance analysis of phosphatidylcholine-cholesterol system in bilayer lipid membranes. *Electrochim. Acta* 50, 2155–2161. doi: 10.1016/j.electacta.2004.09.023

Nerbonne, J. M. (2000). Molecular basis of functional voltage-gated K + channel diversity in the mammalian myocardium. *J. Physiol.* 525, 285–298. doi: 10.1111/j.1469-7793.2000.t01-1-00285.x

Ogura, T., Imanishi, S., and Shibamoto, T. (2002). Osmometric and water-transporting properties of guinea pig cardiac myocytes. *Jpn. J. Physiol.* 52, 333–342. doi: 10.2170/jjphysiol.52.333

Ohki, S. (1969). The electrical capacitance of phospholipid membranes. *Biophys. J.* 9, 1195–1205. doi: 10.1016/S0006-3495(69)86445-3

Page, E. (1978). Quantitative ultrastructural analysis in cardiac membrane physiology. *Am. J. Physiol.* 235, C147–C158. doi: 10.1152/ajpcell.1978.235.5.C147

Pasek, M., Brette, F., Nelson, A., Pearce, C., Qaiser, A., Christe, G., et al. (2008). Quantification of t-tubule area and protein distribution in rat cardiac ventricular myocytes. *Prog. Biophys. Mol. Biol.* 96, 244–257. doi: 10.1016/j.pbiomolbio.2007.07.016

Pinali, C., Bennett, H., Davenport, J. B., Trafford, A. W., and Kitmitto, A. (2013). 3-D reconstruction of the cardiac sarcoplasmic reticulum reveals a continuous network linking t-tubules: this organization is perturbed in heart failure. *Circ. Res.* 113, 1219–1230. doi: 10.1161/CIRCRESAHA.113.301348

Romanenko, V., Fang, Y., Byfield, F., Travis, A. J., Vandenberg, C., Rothblat, G. H., et al. (2004). Cholesterol sensitivity and lipid raft targeting of kir 2.1 channels. *Biophys. J.* 87, 3850–3861. doi: 10.1529/biophysj.104.043273

Romanenko, V. G., Rothblat, G. H., and Levitan, I. (2002). Modulation of endothelial inward-rectifier K + current by optical isomers of cholesterol. *Biophys. J.* 83, 3211–3222. doi: 10.1016/S0006-3495(02)75323-X

Rothberg, K. G., Ying, Y. S., Kamen, B. A., and Anderson, R. G. (1990). Cholesterol controls the clustering of the glycophospholipid-anchored membrane receptor for 5-methyltetrahydrofolate. *J. Cell Biol.* 111, 2931–2938. doi: 10.1083/jcb.111.6.2931

Savio-Galimberti, E., Frank, J., Inoue, M., Goldhaber, J. I., Cannell, M. B., Bridge, J. H., et al. (2008). Novel features of the rabbit transverse tubular system revealed by quantitative analysis of three-dimensional reconstructions from confocal images. *Biophys. J.* 95, 2053–2062. doi: 10.1529/biophysj.108.130617

Simionescu, N., Lupu, F., and Simionescu, M. (1983). Rings of membrane sterols surround the openings of vesicles and fenestrae, in capillary endothelium. *J. Cell Biol.* 97, 1592–1600. doi: 10.1083/jcb.97.5.1592

Sumnicht, G. E., and Sabbadini, R. A. (1982). Lipid composition of transverse tubular membranes from normal and dystrophic skeletal muscle. *Arch. Biochem. Biophys.* 215, 628–637. doi: 10.1016/0003-9861(82)90124-2

Uchida, K., and Lopatin, A. N. (2018). Diffusional and electrical properties of t-tubules are governed by their constrictions and dilations. *Biophys. J.* 114, 437–449. doi: 10.1016/j.bpj.2017.11.3742

Uchida, K., Moench, I., Tamkus, G., and Lopatin, A. N. (2016). Small membrane permeable molecules protect against osmotically induced sealing of t-tubules in mouse ventricular myocytes. *Am. J. Physiol. Heart Circ. Physiol.* 311, H229–H238. doi: 10.1152/ajpheart.00836.2015

Wong, J., Baddeley, D., Bushong, E. A., Yu, Z., Ellisman, M. H., Hoshijima, M., et al. (2013). Nanoscale distribution of ryanodine receptors and caveolin-3 in mouse ventricular myocytes: dilation of T-tubules near junctions. *Biophys. J.* 104, L22–L24. doi: 10.1016/j.bpj.2013.02.059

Zhu, Y., Zhang, C., Chen, B., Chen, R., Guo, A., Hong, J., et al. (2016). Cholesterol is required for maintaining T-tubule integrity and intercellular connections at intercalated discs in cardiomyocytes. *J. Mol. Cell. Cardiol.* 97, 204–212. doi: 10.1016/j.yjmcc.2016.05.013

Conflict of Interest Statement: The authors declare that the research was conducted in the absence of any commercial or financial relationships that could be construed as a potential conflict of interest.

frontiers in Physiology

REVIEW
published: 27 November 2018
doi: 10.3389/fphys.2018.01686

Functional Microdomains in Heart's Pacemaker: A Step Beyond Classical Electrophysiology and Remodeling

*Di Lang and Alexey V. Glukhov**

Department of Medicine, School of Medicine and Public Health, University of Wisconsin-Madison, Madison, WI, United States

Spontaneous beating of the sinoatrial node (SAN), the primary pacemaker of the heart, is initiated, sustained, and regulated by a complex system that integrates ion channels and transporters on the cell membrane surface (often referred to as "membrane clock") with subcellular calcium handling machinery (by parity of reasoning referred to as an intracellular "Ca^{2+} clock"). Stable, rhythmic beating of the SAN is ensured by a rigorous synchronization between these two clocks highlighted in the coupled-clock system concept of SAN timekeeping. The emerging results demonstrate that such synchronization of the complex pacemaking machinery at the cellular level depends on tightly regulated spatiotemporal signals which are restricted to precise subcellular microdomains and associated with discrete clusters of different ion channels, transporters, and regulatory receptors. It has recently become evident that within the microdomains, various proteins form an interacting network and work together as a part of a macromolecular signaling complex. These protein–protein interactions are tightly controlled and regulated by a variety of neurohormonal signaling pathways and the diversity of cellular responses achieved with a limited pool of second messengers is made possible through the organization of essential signal components in particular microdomains. In this review, we highlight the emerging understanding of the functionality of distinct subcellular microdomains in SAN myocytes and their functional role in the accumulation and neurohormonal regulation of proteins involved in cardiac pacemaking. We also demonstrate how changes in scaffolding proteins may lead to microdomain-targeted remodeling and regulation of pacemaker proteins contributing to SAN dysfunction.

Keywords: sinoatrial node, pacemaker, microdomain, ion channel, remodeling, signaling complex

OPEN ACCESS

Edited by:
Bas J. Boukens, University of Amsterdam, Netherlands

Reviewed by:
Arun V. Holden, University of Leeds, United Kingdom
Vadim V. Fedorov, The Ohio State University, United States

***Correspondence:**
Alexey V. Glukhov
aglukhov@medicine.wisc.edu

Specialty section:
This article was submitted to Cardiac Electrophysiology, a section of the journal Frontiers in Physiology

Received: *31 July 2018*
Accepted: *09 November 2018*
Published: *27 November 2018*

Citation:
Lang D and Glukhov AV (2018) Functional Microdomains in Heart's Pacemaker: A Step Beyond Classical Electrophysiology and Remodeling. Front. Physiol. 9:1686. doi: 10.3389/fphys.2018.01686

INTRODUCTION

The sinoatrial node (SAN) is the primary pacemaker of the heart. Spontaneous beating of the SAN is initiated, sustained, and regulated by a complex system that integrates ion channels and transporters located on the cell membrane surface (often referred to as "membrane clock") with subcellular calcium handling machinery (by parity of reasoning referred to as an intracellular "Ca-Clock") (Lakatta and DiFrancesco, 2009; Lakatta et al., 2010). Stable, rhythmic beating of the SAN is ensured by a rigorous synchronization between these two clocks highlighted in

the coupled-clock system concept of SAN timekeeping. Following achievement of the maximal diastolic potential, K^+ current (a combination of a rapidly recovering transient outward current I_{to}, and a rapidly, I_{Kr}, and slowly, I_{Ks}, activating delayed rectifier currents) conductance decreases which unmasks several inward background currents. Together with hyperpolarization-activated current (I_f) and low-voltage activated T-type Ca^{2+} current ($I_{Ca,T}$), these start gradual changes of the membrane potential (V_m) (early diastolic depolarization). Then, spontaneous and rhythmic submembrane local Ca^{2+} releases (LCR) from ryanodine receptors (RyRs) occur and activate an inward Na^+/Ca^{2+} exchange (NCX) current (I_{NCX}) to boost diastolic depolarization rate and fire an action potential (AP) via activation of L-type Ca^{2+} current ($I_{Ca,L}$).

Until recently, the prevailing concept of cardiac electrophysiology has been that ion channels and receptors are freely mobile in the plasma membrane providing uniform activity through the sarcolemma. Though such simplification was beneficial for computational modeling and enabled the development of relatively straightforward biophysical models based on non-linear dynamics and oscillatory theory, it recently became evident that this simple "random collision model" is inadequate to explain the emerging experimental results which highlight microdomain-specific regulation of cardiomyocyte physiology (reviewed in details elsewhere, Zaccolo and Pozzan, 2002; Warrier et al., 2007; Best and Kamp, 2012; Balycheva et al., 2015; Vinogradova et al., 2018). In the SAN, these include findings on a complex spatial-temporal coupling between the membrane- and Ca^{2+} clocks confirmed in various species, including human (Kim et al., 2018; Tsutsui et al., 2018), synchronization of spontaneous LCRs between discrete RyR clusters (Stern et al., 2014; Torrente et al., 2016), compartmentalized autonomic regulation of pacemaker ion channels which relies on tightly confined cAMP signaling (Barbuti et al., 2004; St Clair et al., 2017; Vinogradova et al., 2018), as well as microdomain-specific remodeling of ion channels secondary to structural alterations including changes in scaffolding proteins (Le Scouarnec et al., 2008; Alcalay et al., 2013; Bryant et al., 2018). The emerging results demonstrate that the functioning of the complex pacemaking machinery at the cellular level depends on tightly regulated spatiotemporal signals which are restricted to precise subcellular microdomains and associated with discrete clusters of different ion channels, transporters and regulatory receptors. Within different subcellular compartments, various proteins form an interacting network and work together as a part of a macromolecular signaling complex. These protein–protein interactions are tightly controlled and regulated by a variety of neurohumoral signaling pathways, and the diversity of cellular responses achieved with a limited pool of second messengers is made possible through the organization of essential signal components in particular microdomains. Importantly, on a tissue level, these are manifested by a dynamic pattern of beat-to-beat migration of leading pacemaker location within the SAN at baseline and during autonomic stimulation, a complex interaction between discrete pacemaker clusters, and the development of SAN arrhythmias associated with pathological remodeling which could not be described in simplified oscillatory models of cardiac pacemaking.

In this review, we highlight the emerging understanding of the functionality of distinct subcellular microdomains in SAN cardiomyocytes (SANCs) (**Figure 1**) and their role in autonomic regulation of cardiac pacemaking. We also demonstrate how changes in scaffolding proteins may lead to microdomain-targeted remodeling and regulation of pacemaker proteins and contribute to SAN dysfunction (SND).

FUNCTIONAL MACRO- AND MICRO-ARCHITECTURE OF THE SAN

The SAN has a highly complex and heterogeneous structure (reviewed in detail elsewhere, Boyett et al., 2000; Fedorov et al., 2012; Csepe et al., 2016). It was shown in humans (Boineau et al., 1988; Li et al., 2017) and dogs (Glukhov et al., 2013) that the SAN consist of several intranodal pacemaker clusters which have different electrophysiological properties, including automaticity robustness and varying response to autonomic stimulation. These were thought to underlie the dynamic pattern of a beat-to-beat shift of the leading pacemaker location within the SAN pacemaker complex during heart rate change under various conditions (Boyett et al., 2000), the development of intranodal conduction blocks, temporally unexcitable areas, SAN micro-reentry and exit block (Glukhov et al., 2013; Li et al., 2017). On the cellular level, the difference between intranodal pacemaker clusters was linked to distinct pacemaker protein expression profiles as well as cellular microarchitecture (Boyett et al., 2000). The latter is critical for pacemaker proteins' distribution as well as their communication with each other and with subcellular Ca^{2+} clock. Transmission electron microscopy studies by Ayettey and Navaratnam demonstrated that specialized transversal (T)-tubular system is either absent or far less developed in rat SAN than atrial or ventricular myocytes (Ayettey and Navaratnam, 1978). The authors found that in primary SANCs, T-tubules are represented by short and narrow (about 60 nm in diameter versus 105 and 130 nm in atrial and ventricular myocytes, respectively) invaginations of the sarcolemma, which do not usually penetrate sufficiently far to contact the myofibrillae. Instead, SANCs are highly rich with caveolae structures, i.e., muscle-specific caveolin-3 (Cav-3) scaffolding protein containing a subpopulation of lipid rafts, representing small (50–100 nm in diameter) invaginations of the plasma membrane (**Figure 1**, '*caveolae*' microdomain). Caveolae density in rabbit SANCs is 2-times higher than in atrial and 4 to 5-times higher than in ventricular myocytes as estimated from electron microscopy photographs (Masson-Pevet et al., 1980). Through binding to caveolin-scaffolding domain, Cav-3 compartmentalizes and concentrates various proteins, including ion channels, transporters, G-protein subunits, kinases, endothelial nitric oxide synthase (eNOS), and others, many of which contribute to SAN pacemaking.

Through, it is quite difficult to localize the center SAN in electron microscopy studies without functional characterization of the leading pacemaker localization, Ayettey and Navaratnam highlighted the presence of some transitional cells within the

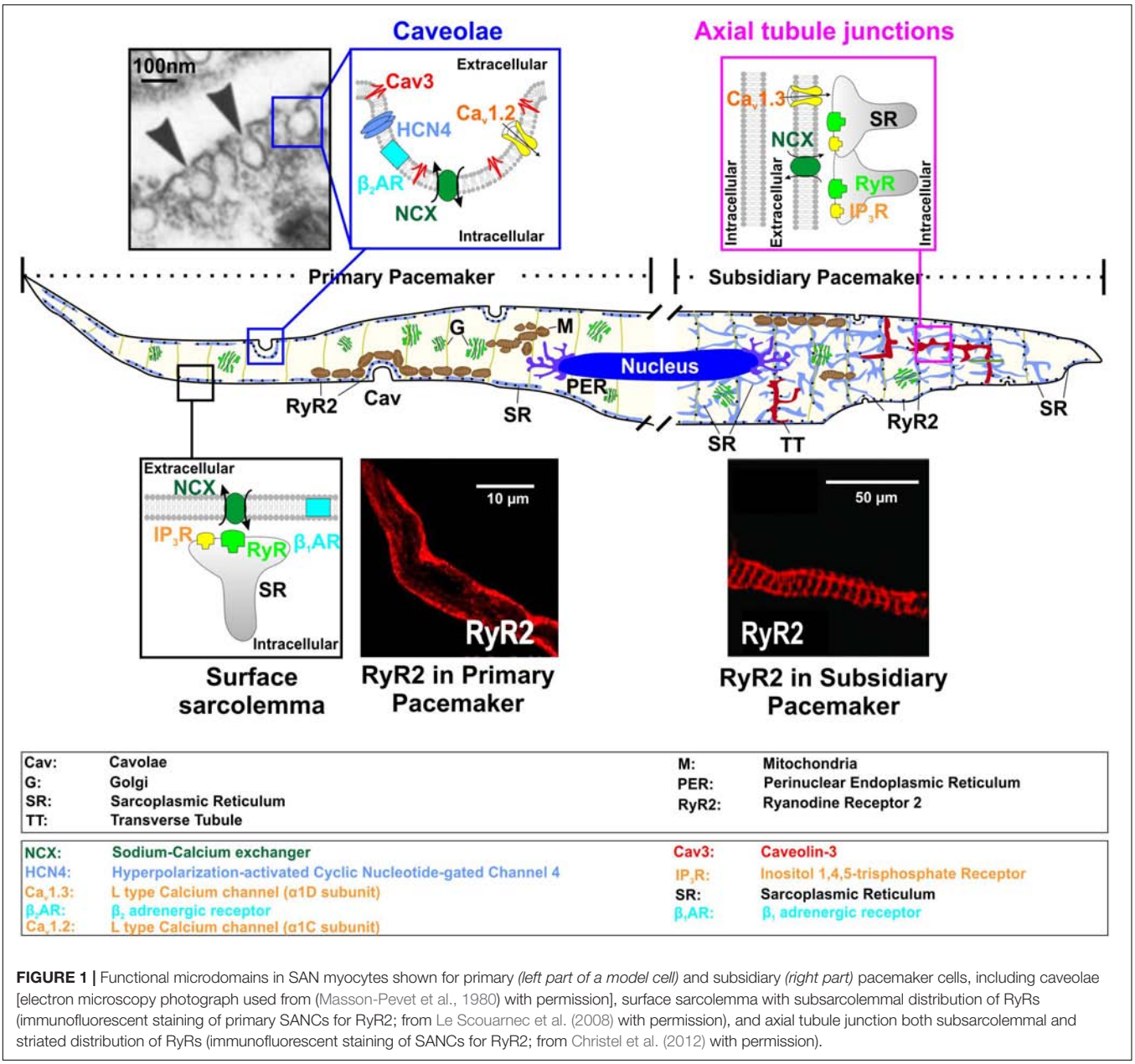

FIGURE 1 | Functional microdomains in SAN myocytes shown for primary *(left part of a model cell)* and subsidiary *(right part)* pacemaker cells, including caveolae [electron microscopy photograph used from (Masson-Pevet et al., 1980) with permission], surface sarcolemma with subsarcolemmal distribution of RyRs (immunofluorescent staining of primary SANCs for RyR2; from Le Scouarnec et al. (2008) with permission), and axial tubule junction both subsarcolemmal and striated distribution of RyRs (immunofluorescent staining of SANCs for RyR2; from Christel et al. (2012) with permission).

SAN region. These transitional myocytes resemble nodal cells in diminutiveness of size and lack of atrial granules and also possess a sparse and disorganized T-tubule system (Ayettey and Navaratnam, 1978). It appears that a sparse tubular system in SANCs is likely different from that in working ventricular myocytes, and may rather represent a 'super-hub' of Ca^{2+} signaling associated with axial tubule junctions that rapidly activate Ca^{2+} release through cell-specific molecular microdomain mechanisms and was recently proposed for atrial myocytes by the Lehnart's group (Brandenburg et al., 2016, 2018). The authors demonstrated that axial tubule junctions in atrial myocytes are highly enriched by cholesterol-rich nanodomains visualized by the fluorescent cholesterol analog dye Chol-PEG-KK114 in live cells (**Figure 1**, '*axial tubule junctions*'), in contrast to ventricular myocytes where T-tubules rarely contain caveolae-shaped membrane structures. Axial tubule junctions form contact junctions with the sarcoplasmic reticulum (SR) and are associated with highly phosphorylated RyRs (Brandenburg et al., 2016) which may play an important role in SANC pacemaking as discussed below (see section "Ca Clock"). Axial tubule junctions and their role in atrial Ca^{2+} signaling have been shown in mouse, rat, rabbit, pig, and human myocytes (Brandenburg et al., 2018).

Such intrinsic structural heterogeneity of the SAN has been recently confirmed on the functional level as well. By performing consecutively measurement of I_f and $I_{Ca,L}$ from the rabbit pacemaker cells isolated from the intercaval region, including the SAN, Monfredi et al. (2018) found their significantly diverse

range. Importantly, I_f, but not $I_{Ca,L}$ current density was positively related to baseline beating rate. These data correlate well with the distribution of transversal-axial tubule system within the SAN: primary pacemakers with the fastest spontaneous beating rate do not have T-tubules, express the smallest $I_{Ca,L}$ which predominantly rely on extratubular LTCCs, and have the highest pacemaker current I_f, while subsidiary SAN pacemakers possess a rudimentary T-tubule network which results in a significant increase of $I_{Ca,L}$ and decrease in I_f. Subsequently, two recent reports from Lakatta's group demonstrated in guinea pig (Kim et al., 2018) and human SANCs (Tsutsui et al., 2018) several populations of cells which show rhythmic pacemaking activity, dysrhythmic firing, and no spontaneous activity (i.e., 'dormant' cells). Dysrhythmic and dormant SANCs have smaller and desynchronized LCR activity than rhythmic SANCs; however, in response to sympathetic stimulation, all dysrhythmic cells and a third of dormant SANCs increased their LCR activity and developed automaticity resulting in spontaneous electrical beating (Kim et al., 2018). Whether or not these cells are associated with different pacemaker clusters and responsible for certain ranges of heart rate, remains open to question. These, however, may provide mechanistic basis for dynamic pacemaker location shift within the SAN as it was observed experimentally in intact optically mapped mouse, canine, and human SAN preparations (Fedorov et al., 2010; Glukhov et al., 2010, 2013, 2015b; Li et al., 2017).

In the following sections, we describe microdomain-specific distribution, functioning, and remodeling of the main components of both membrane and Ca^{2+} clocks. Specifically, we focus on how the changes in scaffolding proteins affect functional pacemaker microdomains and results in SND. Though most of these changes are studied in transgenic mouse models, emerging evidence from SND patients harboring similar mutations, which are summarized in the review for available proteins, support the observed results and highlight microdomain-targeted remodeling as a new dimension to cardiovascular disease.

MEMBRANE CLOCK

Pacemaker Channels

The hyperpolarization-activated, cyclic nucleotide-gated (HCN) ion channels are responsible for generating the pacemaker current (funny current, I_f) which is the inward current that contributes to the early stage diastolic depolarization in the SAN (DiFrancesco, 1993). At diastolic potentials, I_f is predominantly carried by Na^+ (DiFrancesco, 1993). I_f is activated by hyperpolarizing voltage steps, with the threshold potential varies from −40 to −60 mV. The voltage dependence of the I_f activation is influenced by intracellular cyclic adenosine monophosphate (cAMP); a direct binding of cAMP to this channel increases the open probability via a depolarizing shift in the midpoint activation voltage ($V_{1/2}$) (DiFrancesco and Tortora, 1991).

While HCN4 is the most predominant isoform expressed in rodent SANCs (Marionneau et al., 2005), recent reports showed that all three cardiac HCN isoforms (HCN1, HCN2, and HCN4) are highly expressed in the human SAN (Li et al., 2015). Several studies demonstrated that HCN channels localize to caveolae based on the presence of HCN4 in low-density membrane fractions along with Cav-3 as well as the specific interaction of HCN4 with Cav-3 (Barbuti et al., 2007; Ye et al., 2008). Barbuti et al. (2012) reported that all HCN isoforms have a conserved caveolin-binding domain which impact both channel function and trafficking. Disruption of caveolae by reducing membrane cholesterol using methyl-β-cyclodextrin (MβCD) or by expression of dominant negative caveolin mutants alters the gating of HCN channels by shifting the voltage dependence of the activation by approximately 10 mV in the positive direction (Ye et al., 2008). In addition, β_2-adrenergic receptor (β_2AR) modulation of HCN4 channel is lost when caveolae are disrupted, which is supported by co-localization of β_2ARs and HCN4 channels in caveolae (Barbuti et al., 2007).

Recent studies indicate that caveolae-associated β_2AR-dependent stimulation of HCN4 channels relies on subcellular compartmentalization of cAMP signaling. First, it was found that HCN4 can be phosphorylated by cAMP-dependent protein kinase A (PKA) at the distal C-terminus, in addition to the well-studied cAMP binding to a conserved cyclic nucleotide binding domain in the proximal C-terminus (Liao et al., 2010). Moreover, PKA activity is necessary for cAMP-dependent signaling between β_2ARs and HCN channels in SANCs; inhibition of PKA with an inhibitory peptide, PKI, significantly reduced the shift in $V_{1/2}$ produced by β_2ARs stimulation while does not affect a direct stimulation of the channels by exogenous cAMP and Rp-cAMP (an analog than cannot activate PKA) (St Clair et al., 2013). St Clair and colleagues showed that PKA modulation of HCN4 channels depends on distinct cAMP signaling domains created by subcellular localization of cyclic nucleotide phosphodiesterases 3 and 4 (PDE3 and 4) which are responsible for cAMP degradation in the SANCs. The authors demonstrated that PDE4 inhibition in mouse SANCs produced a PKA-independent depolarizing shift in the $V_{1/2}$ of I_f at rest, likely via a direct binding of elevated cAMP to the channel, but did not remove the requirement for PKA in β_2AR-to-HCN signaling. In contrast, PDE3 inhibition produced PKA-dependent changes in I_f both at rest and in response to β_2AR stimulation (St Clair et al., 2017). Microdomain-specific localization and activity of PDEs in SANCs have been recently reviewed by Vinogradova et al. (2018) and highlight functional importance of local cAMP microdomains with high and low cAMP levels which are involved in local regulation of coupled-clock system components.

L-Type Ca^{2+} Channels

In the center of the SAN, where the AP upstroke is slow, and little or no Na^+ current is expressed, $I_{Ca,L}$ is principally responsible for the upstroke. Though $Ca_v1.2$ represents the major isoform of the L-type Ca^{2+} channel (LTCC) central pore subunit expressed in the heart, SANCs also express $Ca_v1.3$ isoform (Zhang et al., 2002). In comparison to $Ca_v1.2$ channels which are activated at −40 mV and mainly contribute to AP upstroke, channels formed by $Ca_v1.3$ are activated ∼20 mV more negatively than $Ca_v1.2$ and thus play an important role in the generation of diastolic depolarization. Knockout of $Ca_v1.3$ in mice decreased

$I_{Ca,L}$ density by 69% and resulted in severe bradycardia and highly erratic pacing rate in the SAN (Mangoni et al., 2003).

A number of important $Ca_v1.2$ subpopulations have been identified in cardiomyocytes that associate with unique macromolecular signaling complexes and scaffolding proteins (**Figures 1**, **2**) (Best and Kamp, 2012). These include channels localized to dyadic junctions (i.e., T-tubules) as well as extradyadic channels that reside in biochemically distinct regions of surface membrane, including caveolae, lipid rafts, and plasmalemma. Most of the studies performed on isolated mouse SANCs (Le Scouarnec et al., 2008; Christel et al., 2012) demonstrated a predominant plasma membrane localization of $Ca_v1.2$ channels; however, a ratio between caveolar and non-caveolar LTCCs in SANCs is unknown and requires additional studies. In contrast, immunofluorescence analysis of mouse SANCs showed $Ca_v1.3$ channels localized both on the plasma membrane (Le Scouarnec et al., 2008) and in sarcomeric structures (presumably, within a sparse T-tubule network observed in subsidiary pacemakers (Ayettey and Navaratnam, 1978) where they co-localize with RyRs (Christel et al., 2012). STimulated Emission Depletion (STED) co-immunofluorescence labeling of mouse atrial myocytes showed that $Ca_v1.3$ clusters are located close to Cav-3 clusters in axial tubule junctions where highly PKA phosphorylated clusters of RyR-pS2808 are identified (Brandenburg et al., 2018). Such highly phosphorylated, both at PKA- (P-Ser^{2809}) and Ca^{2+}/calmodulin-dependent protein kinase II (CaMKII)-dependent (P-Ser^{2815}), clusters of RyRs have been found in rabbit SAN and proposed to contribute to spontaneous LCRs. Along with a heterogeneous distribution of T-tubules in the SAN (compare primary vs. subsidiary pacemakers in **Figure 1**), this may indicate a variable contribution of $Ca_v1.3$ to $I_{Ca,L}$ in different SAN pacemaker clusters, their functional interaction with RyRs and thus their impact on heart rate. Indeed, Christel and colleagues demonstrated a significantly stronger inactivation of $Ca_v1.2$ versus $Ca_v1.3$ channels measured in mouse SANCs during strong (+80 mV) depolarization. The authors used a numerical model of mouse SAN automaticity and found that $Ca_v1.3$ voltage-dependent facilitation enhanced recovery of pacemaker activity after pauses and positively regulated pacemaking during slow heart rate (Christel et al., 2012). In a subsequent study from the same group, Torrente et al. (2016) showed that $Ca_v1.3$ deficiency strongly impaired $[Ca^{2+}]_i$ dynamics, reducing the frequency of local $[Ca^{2+}]_i$ release events and preventing their synchronization. These data highlight an importance of microdomain-specific localization of $Ca_v1.3$ channels in calcium-voltage clock coupling and in opposing abnormal slowing of heart rate.

Along with distinct functional roles that LTCCs play in cellular microdomains, emerging evidence indicate that subpopulations of LTCCs may possess different biophysical properties resulted from the difference in channel's structure and/or subcellular microenvironment influence, and therefore experience diverse pathological remodeling. For example, extratubular LTCCs measured in rat and human atrial myocytes, which express both $Ca_v1.2$ and $Ca_v1.3$, demonstrate low single channel activity (Glukhov et al., 2015a) indicating either a different LTCC structure (both on pore-forming $Ca_v1.2$ and $Ca_v1.3$ or regulatory $Ca_v\beta_{1-4}$ and $\alpha_2\delta$ (Foell et al., 2004) subunits) or microdomain-specific regulation, including the association with various scaffolding proteins. β-subunits enhance channel trafficking to the distinct plasma membrane microdomains, increase the channel's open probability, cause a hyperpolarization shift in the voltage-dependence of activation, and affect voltage-dependent inactivation (Foell et al., 2004). Though $Ca_v\beta_2$ is the most abundant β subunit expressed in the heart, both $Ca_v\beta_1$ and $Ca_v\beta_3$ mRNA expression have been found in mouse (Marionneau et al., 2005) and rat (Yanni et al., 2011) SAN, and their mRNA levels were higher than those measured in atrial and ventricular myocardium. Similar to $Ca_v\beta$, $\alpha_2\delta$ subunits are also involved in channel's trafficking via interactions with other proteins, such as extracellular matrix and other membrane proteins involved in cell adhesion (Whittaker and Hynes, 2002).

Along with spatial compartmentalization, LTCCs show a microdomain-specific cAMP- mediated and PKA-dependent regulation, both at baseline and during autonomic stimulation [reviewed in details elsewhere (Best and Kamp, 2012; Vinogradova et al., 2018) and discussed below in 'Ca^{2+} clock' section]. The specificity of cAMP signaling is modulated by the binding of PKA to A kinase-anchoring proteins (AKAPs) (**Figure 2**), which target the kinase to specific intracellular locations and LTCC pools, and provide spatiotemporal control over cAMP signaling events. Various AKAPs serve as a scaffold to assemble proteins involved in Ca^{2+} signaling regulation via microdomain-specific phosphorylation of different subpopulations of LTCCs thus adding another level of complexity to $I_{Ca,L}$ and Ca^{2+} signaling regulation (see section "SND and Scaffolding Proteins").

T-Type Ca^{2+} Channels

Hagiwara et al. (1988) reported the existence of both long-lasing ($I_{Ca,L}$) and transient ($I_{Ca,T}$) Ca^{2+} currents in isolated rabbit SANCs. The authors described their distinct biophysical properties, including voltage dependencies for activation/inactivation and pharmacology. Threshold for activation of $I_{Ca,T}$ was around −60 mV, and $I_{Ca,T}$ was fully activated at about −10 mV. Because activation range of $I_{Ca,T}$ overlapped the pacemaker potential of SAN, the potential involvement of $I_{Ca,T}$ in the generation of the diastolic depolarization in SANCs was proposed. Indeed, selective inhibition of $I_{Ca,T}$ by Ni^{2+} (Hagiwara et al., 1988) or mibefradil (Protas and Robinson, 2000) resulted in significant slowing of spontaneous activity of isolated rabbit SANCs by selective suppression of the later phase of pacemaker depolarization in a concentration-dependent manner, with no effects on AP amplitude and duration.

Two out of three T-type Ca^{2+} channel α-subunits, namely $Ca_v3.1$ (α_{1H}) and $Ca_v3.2$ (α_{1I}), were detected in the heart. In contrast to Ca_v1, Ca_v3 channels produce large currents in the absence of co-expressed accessory β or $\alpha_2\delta$ subunits, and therefore these proteins are not obligate auxiliary subunits for Ca_v3 channels. Genetic inactivation of $Ca_v3.1$ channels significantly slowed the intrinsic *in vivo* heart rate, prolonged the SAN recovery time, and slowed pacemaker activity of

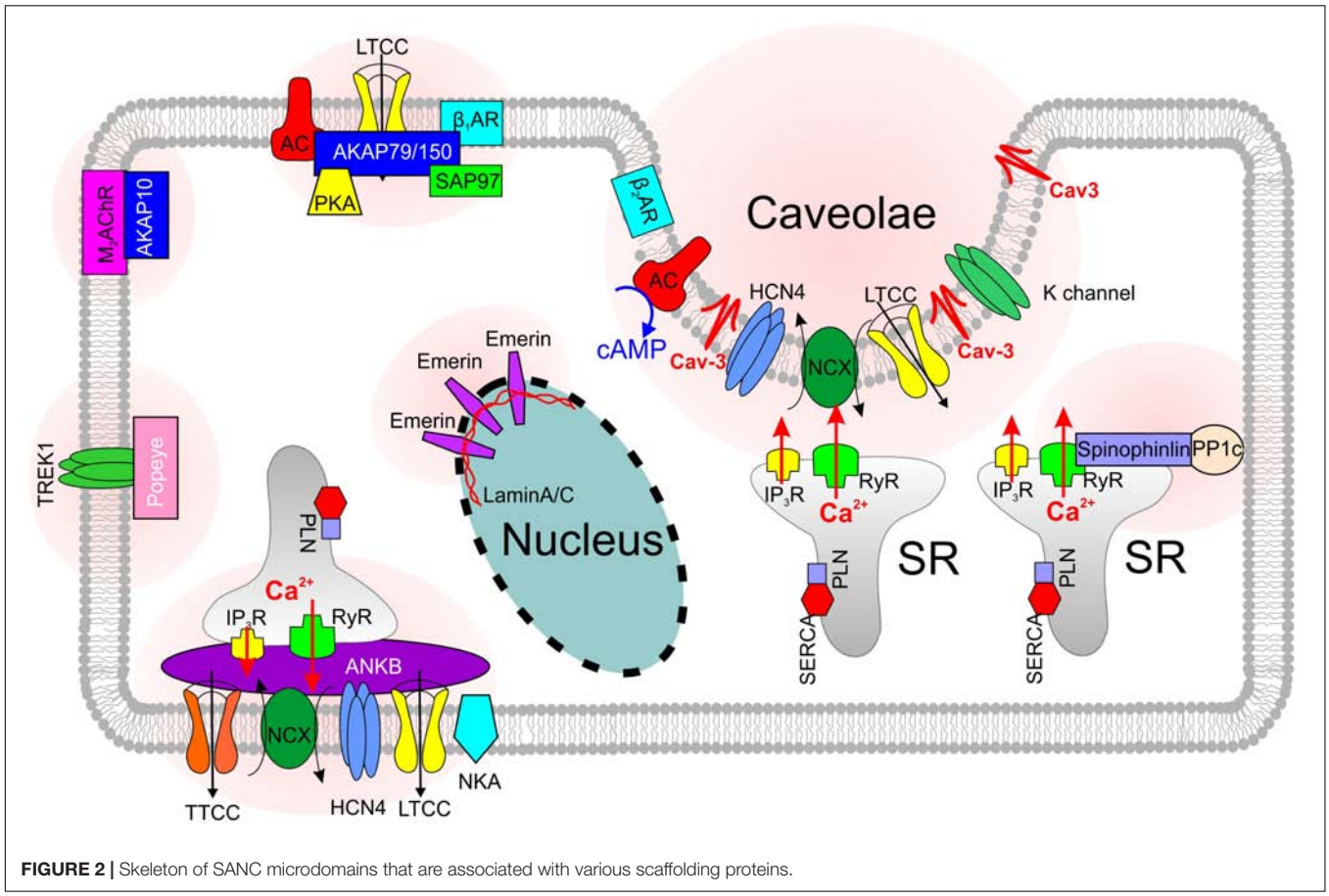

FIGURE 2 | Skeleton of SANC microdomains that are associated with various scaffolding proteins.

mouse SANCs through a reduction of the slope of the diastolic depolarization (Mangoni et al., 2006). In contrast, $Ca_v3.2$-deficient mice displayed normal sinus rhythm without arrhythmias (Chen et al., 2003).

To date, experimental data on T-type Ca^{2+} channels subcellular distribution, including SAN, is limited. In mice with cardiac-specific, conditional expression of the $Ca_v3.1$ channels, immunocytochemical labeling revealed their presence primarily on the surface sarcolemma of ventricular myocytes, with less staining within the T-tubules (Jaleel et al., 2008). Osmotic shock, which selectively eliminates T-tubules, induced a greater reduction in L- versus T-type Ca^{2+} currents. Ca^{2+} influx through T-type Ca^{2+} channels also did not induce normal SR Ca^{2+} release which suggests that T- and L-type Ca^{2+} channels are located in different portions of the sarcolemma (Jaleel et al., 2008). Similarly, in wild type mouse atrial myocytes, Curran et al. (2015) showed both $Ca_v3.1$ and $Ca_v3.2$ expressed on the plasma membrane and, surprisingly, over the atrial Z-line while their association with T-tubules is questionable. Co-immunoprecipitation analysis suggested an association of $Ca_v3.1$ and $Ca_v3.2$ channel isoforms with caveolae scaffolding protein Cav-3 in neonatal mouse ventricular myocytes (Markandeya et al., 2011). Interestingly, co-expression of Cav-3 significantly decreased the peak $Ca_v3.2$ current density in HEK293 cells, whereas co-expression of Cav-3 did not alter peak $Ca_v3.1$ current density. It is possible that $Ca_v3.1$ and $Ca_v3.2$ channels are located on the surface sarcolemma, in association with different structural microdomains (**Figure 1**).

Na^+/Ca^{2+} Exchanger

NCX plays a critical role in SAN pacemaking by producing a depolarizing current and boosting depolarization rate in late diastole when local Ca^{2+} released by RyRs beneath the cell surface membrane (**Figure 1**, *primary pacemaker*) (Lakatta et al., 2010). NCX1 is the predominant isoform expressed in the heart. Atrial-specific NCX knock-out in mice resulted in severe pacemaker abnormalities manifested by "tachy-brady" arrhythmias and associated with quiescent isolated SANCs where, however, copious intracellular Ca^{2+} waves were present but failed to trigger APs (Torrente et al., 2015). These highlight a key role of NCX in synchronizing Ca^{2+} and membrane clocks.

Though data on NCX distribution in SANCs is limited, studies on atrial and ventricular myocytes indicate that NCX membrane localization might be associated with different targeting components. Immunohistological evidence from rabbit SANCs indicate significant submembrane co-localization of NCX1 and RyRs which exceeds that measured in atrial and ventricular myocytes (Lyashkov et al., 2007) where NCX1 labeling is present throughout the cell (attribute to an extensive T-tubular network) (compare '*caveolae*' vs. '*axial tubule junction*' compartments in **Figure 1**). Such localization allows

crosstalk between RyR LCRs and NCX (**Figure 1**, '*surface sarcolemma*' compartment). Several groups have identified NCX associated with Cav-3 by both co-immunoprecipitation and immunolabeling (Scriven et al., 2005; Camors et al., 2006) with the latter finding those complexes enriched on the cell surface and little in the T-tubules (Scriven et al., 2005). It was also reported that NCX1 has several caveolin binding motifs and that the NCX1 protein associates with Cav-3 (Bossuyt et al., 2002). Others, using the same techniques, have found little, if any, association (Cavalli et al., 2007).

Other Channels

Besides the ion channels discussed above, there are other ion channels that participate in the SAN pacemaking. These include (1) ion channels involved in store-operated Ca^{2+} entry (SOCE); (2) SR-Ca^{2+} activated non-selective Na^+ transient receptor potential melastatin 4 (TRPM4) ion channel; (3) sodium channels $Na_v1.5$ which are likely expressed the periphery but not in the center of the SAN; and (4) chloride channels. All these channels provide an additional inward current during spontaneous diastolic depolarization and thus may contribute to SAN pacemaking. Though these channels may not play a prominent role in SAN activity, the mutations of the genes that encode them are reported to associate with SND observed clinically, suggesting their contributions to the SAN pacemaking. Importantly, most of those channels are associated with different structural proteins and have been linked to distinct microdomains, including caveolae/lipid rafts, intercalated disks, luminal SR, etc., and thus may require a precise spatial arrangement to support their functional coupling and integrity. Disruption in one of the protein localization could affect other proteins involved in a complex protein–protein interaction and thus disturb pacemaker automaticity. Finally, potassium ion channels, including a rapidly recovering transient outward current I_{to} ($K_v4.2$), a rapidly, I_{Kr} (ERG), and slowly activating, I_{Ks} (K_vLQT1), delayed rectifier currents, acetylcholine-activated K^+ current $I_{K,ACh}$ ($K_{ir}3.1$ and $K_{ir}3.4$), and ATP-sensitive K^+ current $I_{K,ATP}$ ($K_{ir}6.2$), are expressed in the SAN and also demonstrate microdomain-specific distribution and regulation, as reviewed in details elsewhere (Balycheva et al., 2015).

Ca-CLOCK

Besides ion channels that depolarize SAN V_m during diastole, spontaneous Ca^{2+} oscillations also play a critical role in pacemaking (Lakatta et al., 2010). Attributed to the 'Ca-clock' component of the pacemaking system, this $[Ca^{2+}]_i$ cycling activity is comprised of spontaneous local Ca^{2+} releases from the RyRs (i.e., AP-independent Ca^{2+} releases, or LCRs, in contrast to AP-triggered SR Ca^{2+} releases, or Ca^{2+} transients, CaT) and Ca^{2+} reuptake back to the SR via SERCA. Emerging evidence shows that disruption of LCR activity leads to dramatic changes in SAN pacemaking (Vinogradova and Lakatta, 2009; Gao et al., 2010). LCRs occur during the late phase of the diastolic depolarization. They generate small increments in the local $[Ca^{2+}]_i$ which activates NCX to pump Ca^{2+} out of the cell in exchange for Na^+ ions at the ratio of 1 Ca^{2+}: 3 Na^+, therefore leading to a net positive charge influx and a subsequent depolarization of the V_m to the threshold of the next beat. Unlike AP-triggered CaT, LCRs are V_m-independent, rhythmic activities that are localized near the sarcolemmal membrane (Vinogradova et al., 2004). Such highly localized LCR patterns are associated with a unique distribution of RyR found in SANCs. In contrast to atrial and ventricular myocytes, immunofluorescent staining studies performed on SANCs demonstrated that RyRs are exclusively expressed beneath the sarcolemma in rabbit (Musa et al., 2002), guinea-pig (Rigg et al., 2000) and mouse (Le Scouarnec et al., 2008) SANC from a central SAN area. Internal labeling of RyRs that followed a striation pattern was also observed by other groups in mouse and guinea-pig SANs (Rigg et al., 2000; Christel et al., 2012) as well as in rabbit myocytes isolated from a peripheral SAN area (Musa et al., 2002) (compare immunofluorescent staining images for RyR2 distribution in primary and subsidiary pacemakers in **Figure 1**).

Molecular mechanisms that underlie the generation and regulation of LCR activity, are still incompletely understood. Multiple factors have been proposed to contribute to these spontaneous SR Ca^{2+} releases including an elevated SR Ca^{2+} load (i.e., $[Ca^{2+}]_{SR}$) as well as hyperactivity of RyRs due to their hyperphosphorylation or hypersensitization via IP_3R-mediated Ca^{2+} release.

SR Ca^{2+} release depends on the level of $[Ca^{2+}]_{SR}$ which affects the sensitivity of RyR2 (Bassani et al., 1995). Though no accurate $[Ca^{2+}]_{SR}$ was reported in SANCs, atrial myocytes possess a threefold higher SR Ca^{2+} load compared to ventricular myocytes (Walden et al., 2009). Though amplitude of caffeine-evoked CaT in rabbit central SANCs is ∼50% lower than that in atrial myocytes (Jones et al., 2008), SANCs have a dramatically smaller size than atrial myocytes and thus a higher single SR Ca^{2+} load might be expected in SANCs. Such "Ca^{2+} overload" may lead to spontaneous Ca^{2+} releases such as LCRs. "Ca^{2+} overload" then gets restored after Ca^{2+} is replenished by SERCA from AP-induced CaT, thus the next leak follows and rhythmic LCRs are generated.

SR Ca^{2+} load is tightly associated with a SR protein calsequestrin (Casq2). Casq2 is a low-affinity, high-capacity Ca^{2+} binding protein expressed in cardiomyocytes (Knollmann et al., 2006). Overexpression of Casq2 in transgenic mice (Jones et al., 1998) causes a significant increase in the SR Ca^{2+} load and SR Ca^{2+} release. With such increase, a higher heart rate was indeed observed in mice overexpressing *Casq2* (Jones et al., 1998). Accordingly, bradycardia was reported in *Casq2* knockout mice (Glukhov et al., 2015b).

IP_3Rs may also contribute to the LCR generation via hypersensitization of RyRs. IP_3Rs are another type of SR Ca^{2+} releasing channels which are activated by IP_3 through the hydrolysis of phosphatidylinositol-(4,5)-bisphosphate by phospholipase C. Recent studies demonstrated that this process might be confined within different microdomains including lipid rafts (Delos Santos et al., 2015) and dorsal ruffles

(Gu and Neel, 2003). Stimulation of IP_3Rs was found to accelerate a spontaneous beating rate of mouse SANCs likely through regulation of Ca^{2+} spark parameters and RyR open probability (Ju et al., 2011). In heart failure rabbit atrial myocytes, upregulation of IP_3R-induced Ca^{2+} releases was detected and linked to the enhanced spontaneous SR Ca^{2+} releases (Hohendanner et al., 2015). Unlike RyRs, IP_3Rs seem to express both beneath the sarcolemma membrane and inside SANCs (**Figure 1**), with the ones near membrane found partially co-localized with HCN4, RyR, and SERCA (Ju et al., 2011). In canine ventricular myocytes, a direct interplay between IP_3-mediated G_q protein coupled receptor signaling pathway and Cav-3 has been demonstrated (Guo et al., 2011), linking IP_3-dependent non-junctional Ca^{2+} activities to subsarcolemmal caveolae. Significant decrease in the occurrence of spontaneous Ca^{2+} sparks was reported in rat and human atrial myocytes treated with MβCD, which depletes cholesterol and destroys caveolae structures (Glukhov et al., 2015a). Stimulation of IP_3Rs through sphingosine kinase 1 is shown to control the Ca^{2+} release in caveolar microdomains (Pulli et al., 2015). IP_3Rs were also associated with structural protein AnkB: their expression and membrane targeting were found to be significantly reduced in $AnkB^{+/-}$ mice (Le Scouarnec et al., 2008).

Phosphorylation of RyRs, SERCA and phospholamban (PLN), are also suggested to regulate LCRs. cAMP-mediated, PKA- (Vinogradova et al., 2006) and CaMKII-dependent phosphorylation (Vinogradova et al., 2000; Li et al., 2016) of RyRs have been reported to affect the size and rhythm of LCRs in rabbit SANCs. At the same time, knock-in alanine replacement of RyR phosphorylation sites PKA (S2808) or CaMKII (S2814) did not affect heart rate responses to isoproterenol *in vivo* or in isolated SANCs in mice (Wu et al., 2016). Furthermore, Wu et al. (2016) demonstrated that selective mutations of PLN phosphorylation sites PKA (S16) or CaMKII (T17) in mice also did not affect heart rate. Therefore, although phosphorylation of SR Ca^{2+} proteins may contribute in SAN LCRs, they appear to not affect heart rate by one single target site governing SR Ca^{2+} uptake or release. Recent studies found that RyR phosphorylation follows a highly localized pattern and was linked to specific subcellular microdomains including lipid rafts (Younes et al., 2008; Lukyanenko et al., 2016).

With a progress in the development of biosensor techniques, different pools of cAMP activities between the plasma membrane and the bulk cytoplasmic compartment have been observed. Recent studies unveiled that cAMP activity may be more compartmentalized within discrete subcellular microdomains, including lipid rafts and caveolae (Younes et al., 2008). It was shown that activities of some ACs (Younes et al., 2008) and PDEs (Senzaki et al., 2001) that are responsible for cAMP synthesis and degradation, respectively, are restricted to lipid rafts in SANCs. In the SAN, high basal PDE activity (Vinogradova et al., 2008; Hua et al., 2012) is one of the control checkpoints. Inhibition of basal PDEs in SANCs markedly elevates cAMP-mediated phosphorylation of membrane and Ca-clocks' proteins, resulting in an acceleration of spontaneous AP firing rate in the rabbit SAN (Vinogradova et al., 2008). PDE2-4 are the most abundant in the mouse SAN (Hua et al., 2012) where they regulate the beating rate of atrial preparations (Galindo-Tovar and Kaumann, 2008), AP firing rate, and I_{Ca} in SANCs (Hua et al., 2012). In rat ventricular myocytes, inhibition of PDE4, similar to MβCD treatment, results in loss of confined βAR-mediated cAMP signaling, resulting in a cell-wide cAMP signal propagation patterns (Nikolaev et al., 2010). In SANCs, caveolae may localize cAMP signaling to confined subsarcolemmal microdomains, similar to that observed in ventricular myocytes, and thus participate in compartmentalized regulation of both clocks. Downregulation of caveolae scaffolding protein Cav-3 in failing ventricular myocytes (Nikolaev et al., 2010) as well as expression of the dominant negative Cav-3 mutant (Wright et al., 2014), or disruption of caveolae by MβCD (Calaghan et al., 2008), converts the sarcolemmal-confined cAMP signal to a global signal that targets proteins of the SR and myofilaments, increasing cell contractility and CaT amplitude. This was not linked to the modulation of $I_{Ca,L}$, but instead to a discrete PKA-mediated phosphorylation of PLN (Macdougall et al., 2012). Recently, by using a PLN-linked cAMP biosensor, Sprenger et al. (2015) uncovered the existence of compartmentalized SERCA phosphorylation mediated by cAMP in adult mouse ventricular myocytes. Because SERCA activity is critical in the regulation of $[Ca^{2+}]_i$ balance and SR Ca^{2+} cycling in SANCs (Logantha et al., 2016), one could expect that this compartmentalized phosphorylation may be important for the determination of distribution and size of LCRs in the regulation of the Ca-clock.

cAMP

Although cardiac pacemaking, at rest and during the sympathetic fight-or-flight response, was shown to depend on cAMP signaling in SAN myocytes, cAMP does not directly regulate Ca-clock and SR Ca^{2+} cycling (Lakatta et al., 2010). Instead, it regulates the membrane clock functioning via a direct binding to HCN4 channels. In addition, cAMP modulates the Ca-clock via the regulation of PKA-dependent phosphorylation of SR proteins including RyR, SERCA and PLN. SANCs have a high basal level of cAMP due to a high constitutive activation of adenylyl cyclase (AC), the enzyme that converts adenosine triphosphate to cAMP (Vinogradova et al., 2006). Such high basal level of cAMP may facilitate the periodical LCR activities in the SAN.

CaMKII

Ca^{2+}/calmodulin-dependent protein kinase II (CaMKII) is another important component regulating the coupled-clock system. CaMKII is involved in the regulation of both clocks and participates in both physiological (Vinogradova et al., 2000; Li et al., 2016) and pathological (Luo et al., 2013) activities of the SAN. CaMKII is a Ser/Thr protein kinase and is known as one of the major downstream targets of Ca^{2+} signaling. In SANCs, CaMKII senses subcellular Ca^{2+} changes and is activated via binding to Ca^{2+}-calmodulin (CaM) complex at the CaM regulatory domain (Wu and Anderson, 2014). Activated CaMKII

catalyzes phosphorylation of both L- and T-type Ca^{2+} channels, PLN (Grimm and Brown, 2010) and RyRs (Wehrens et al., 2004).

Recent studies suggested that CaMKII activity may be confined to some specific membrane microdomains. Caveolae-specific activation of CaMKII was also detected in cardiomyocytes and linked to caveolae-localized phosphorylation of LTCCs (Tonegawa et al., 2017). In ventricular myocytes, a local Ca^{2+}/reactive oxygen species (ROS) function microdomain was reported, where a cluster of RyRs directly couples to CaMKII and ROS and thus gets a direct modulation from local CaMKII activity (Dries et al., 2013). In such localized microdomains, CaMKII is found to translocate to specific target compartments, and spatial barriers to CaMKII phosphorylation could be overcome by its translocation and anchoring to the substrate itself or to nearby target protein within the localized compartments (Tsui et al., 2005).

These findings highlight a critical role of localized CaMKII-mediated regulation of Ca^{2+} handling proteins and suggest a potential role of microdomain-specific activity of CaMKII in the regulation of SAN pacemaking. Furthermore, CaMKII- and cAMP-mediated regulation are reported to share microdomain location in SAN myocytes where a cross talk between CaMKII and PDE1 is found (Lukyanenko et al., 2016). Deciphering the disruptions of such localized regulation in SAN may create a new direction for SND treatment in the future.

COMPARTMENTALIZED AUTONOMIC REGULATION IN SANCs

Compartmentalized β-Adrenergic Receptors

β_1- and β_2ARs are the primary sympathetic receptors in the heart and play different roles in the regulation of cardiac rhythm. In early 2000s, researchers already found that both ARs show a compartmentalized distribution in cardiomyocytes: β_2ARs are predominantly concentrated in T-tubules and caveolar structures, whereas β_1ARs are mainly localized in the non-caveolar membrane and non-lipid raft heavy fractions of plasma membrane (Rybin et al., 2000) (**Figure 1**). Distinct functional domains then were found in cardiomyocytes to conduct β_1- and β_2-adrenergic signaling (Shcherbakova et al., 2007). The cardiomyocyte membrane was reported to develop into specialized zones associated with scaffold proteins SAP97 and AKAP79/150, where β_1ARs are found enriched, whereas, β_2ARs are excluded from such microdomains (Shcherbakova et al., 2007) (**Figure 2**). Disrupted compartmentalized pattern of βARs was shown to be involved in ventricular myocyte remodeling associated with heart failure (Nikolaev et al., 2010).

In SAN myocytes, β_2/β_1 expression ratio is higher comparing to atrial and ventricular myocytes (Brodde et al., 1982), and a higher efficiency of β_2ARs was observed (Brodde et al., 2001). Co-immunoprecipitation and immunocytochemistry studies found in rabbit SANCs that β_2ARs co-localized with HCN4 channels in the caveolar microdomain (**Figure 1**), and their disruption via cholesterol depletion by MβCD completely abolished the effect of β_2-adrenergic stimulation, while the effect of β_1-adrenergic stimulation still maintained (Barbuti et al., 2007). Altogether, these suggest that the β-adrenergic stimulation in the SAN is presented in a compartmentalized pattern, in which, β_1- and β_2ARs localize and function in distinct microdomains.

Compartmentalized Muscarinic Receptors

M_2 muscarinic receptors are the primary type of muscarinic receptors expressed in cardiac myocytes. It was shown that M_2 receptors are located outside of caveolar fractions of plasma membrane (Feron et al., 1997). Upon parasympathetic stimulation, the translocation of M_2 receptors to caveolar fractions was detected using a PKA FRET-based biosensor (Warrier et al., 2005). It is reported that the M_2 receptor-mediated cAMP response is associated with distinct AC isoforms expressed in different membrane microdomains (Iancu et al., 2007).

SND AND SCAFFOLDING PROTEINS

Etiology of SND may include both intrinsic and extrinsic reasons. Prevailing intrinsic factors leading to SND are associated with mutations or dysfunctions of key components in the coupled clock systems including HCN4 channel, potassium channel (*KCNQ1*), sodium channel (*SCN5A*), RyR and others. Emerging evidence has shown that dysfunction of structural or scaffolding proteins could also result in SND (**Table 1**). Below, we summarize several scaffolding proteins which dysfunctions could lead to SND.

Ankyrin-B

Ankyrin-B (AnkB) is an important multifunctional scaffolding protein that is essential for membrane structure organization as well as trafficking and localization of various pacemaker proteins. AnkB syndrome, i.e., a type 4 long QT syndrome, is a rare cardiac arrhythmia syndrome, which is associated with a loss-of-function mutation of AnkB in the heart (Mohler et al., 2004). Dysfunctions in AnkB result in SND in human (Le Scouarnec et al., 2008) and mice (Le Scouarnec et al., 2008; Glukhov et al., 2010) and are associated with atrial fibrillation (Le Scouarnec et al., 2008; Cunha et al., 2011).

Heterozygous knocking out AnkB in mice results in significantly reduced expression of NCX, NKA and IP_3Rs in the SAN (**Figure 2**); furthermore, $AnkB^{+/-}$ SANCs show abnormal localization of $Ca_v1.3$ and NCX proteins. In contrast to the homogenous membrane distribution of $Ca_v1.3$ channels in wild type SANCs, $Ca_v1.3$ expression in $AnkB^{+/-}$ cells was limited to an internal perinuclear distribution (Le Scouarnec et al., 2008). This was associated with a concomitant decrease in a whole-cell $I_{Ca,L}$ density. Cunha et al. (2011) demonstrated that AnkB directly associates with $Ca_v1.3$, and this interaction is regulated by a short, highly-conserved motif on the C4 region of the C-terminus of $Ca_v1.3$. Importantly, no changes in $Ca_v1.2$ expression and localization were found in $AnkB^{+/-}$ SAN and atrial myocytes. Similar, $AnkB^{+/-}$ mice showed significant

TABLE 1 | SAN pacemaking abnormalities linked to mutations in scaffolding proteins and associated remodeling of the coupled-clock pacemaking system.

Protein	Gene	Species	Condition	Dysfunction	Associated pacemaking component remodeling		Reference
					Membrane clock	Calcium clock	
AKAP10	*AKAP10*	Human	646V	Fast HR; low HRV	AChR-mediated targets	AChR-mediated targets	Tingley et al., 2007
		Mouse	Global I646V	Bradycardia; sinus pauses	AChR-mediated targets	AChR-mediated targets	Tingley et al., 2007
Ankyrin-B	*ANK2*	Human	E1425G	Bradycardia; AF	NCX; NKA	IP_3R	Mohler et al., 2003; Le Scouarnec et al., 2008
		Mouse	Global AnkB$^{+/-}$	Bradycardia; high HRV	NCX($\downarrow I_{NCX}$); NKA; Cav1.3 ($\downarrow\downarrow I_{CaL}$)	IP_3R	Le Scouarnec et al., 2008
Caveolin-3	*CAV3*	Human	T78M	Bradycardia; tarchycardia; AF	Kv1.5; HCN4	cAMP signaling	Campostrini et al., 2017
Emerin	*EMD*	Human	Lys37del	Bradycardia; AF	?	?	Karst et al., 2008
Lamin A/C	*LMNA*	Human	A331G	Bradycardia; AF	?	?	Hoorntje et al., 2017
MHC-α	*MYH6*	Human	A721T	Sick sinus syndrome	?	?	Holm et al., 2011
Popeye	*POPDC1.2*	Mouse	Global Popdd, 2$^{-/-}$	Bradycardia; sinus pauses	I_K, I_{Na}		Froese et al., 2012
Spinophilin /neurabin	*PPP1R9B*	Mouse	Global Sp$^{-/-}$	Enhanced bradycardiac response to a-adrenergic stimulation	cAMP-mediated targets	RyR; cAMP signaling	Lu et al., 2010; Chiang et al., 2014

HR: Heart Rate; HRV: Heart Rate Variability

reduction of I_{NCX} current density in SANCs (Le Scouarnec et al., 2008). Altogether, these resulted in SAN pacemaking abnormalities observed both in single SANCs (Le Scouarnec et al., 2008) and isolated SAN preparations (Glukhov et al., 2010).

Caveolin-3

Cav-3, the integral membrane protein that is essential in formation of caveolae (**Figures 1**, **2**), is also linked with SND (Lang et al., 2016; Campostrini et al., 2017). As discussed in the previous sections, Cav-3 is involved in the regulation of multiple ion channels and transporters, including those involved in pacemaking. Cav-3 F97C and S141R mutations have been linked to the long QT type 9 inherited arrhythmia syndrome (LQT9) causing AP duration prolongation which had been attributed to an increase in late Na^+ current (Vatta et al., 2006). In spontaneously beating neonatal cardiomyocytes, the expression of the T78M mutation in *CAV3* gene significantly increased AP peak-to-peak variability without altering neither the mean rate nor the maximum diastolic potential (Campostrini et al., 2017) and was associated with a positive shift of activation of HCN4 channels, in a dominant way. The authors also identified a small cohort of patients with supraventricular arrhythmias including sinus tachycardia, bradycardia, and atrial fibrillation where the T78M Cav-3 variant is more frequent than in the general population. Recent preliminary findings from out laboratory indicate that cardiac-specific conditional knock-out of Cav-3 in mice results in significant beat-to-beat heart rate lability linked with suppressed SAN function, enhanced atrial ectopy and paroxysms of alternating periods of tachycardia-bradycardia rhythm (Lang et al., 2016). These results highlight the importance of Cav-3 in supporting functional integrity of the SAN pacemaker complex.

Spinophilin

Another scaffolding protein involved in the SAN pacemaking and dysfunction is spinophilin. Spinophilin is ubiquitously expressed (**Figure 2**) and interacts with a variety of target proteins essential for Ca^{2+} homeostasis and cellular contraction in adult ventricular myocytes (Petzhold et al., 2011). Spinophilin mediates the targeting of protein phosphatase 1 to RyR (Ragusa et al., 2010). Single RyR channel's open probability was observed to increase in spinophilin knockout mice (Chiang et al., 2014). A recent study reported a bradycardic response to α_2-adrenergic stimulation found in spinophilin null mice; however, no significant heart rate changes comparing to wild type mice were observed at baseline condition (Lu et al., 2010).

Popdc Protein

The Popeye domain containing (Popdc, *POPDC1-3*) gene family displays preferential expression in skeletal muscle and the heart, and encode membrane proteins harboring an evolutionarily conserved Popeye domain, which functions as a binding domain for cAMP. Popdc proteins are abundantly present in intercalated disks, lateral membranes and T-tubules (**Figure 2**). In the heart, atrial expression of Popdc1 is higher than in the ventricle, and the entire cardiac conduction system, including the SAN, displays the most intense expression levels (Froese et al., 2012). Null mutations of members of the Popdc gene family in mice are associated with a stress-induced sinus bradycardia and prominent sinus pauses. Moreover, the phenotype develops in an age-dependent manner, being absent in the young animal and becoming increasingly severe, as the animals grow older. In addition to cAMP binding site, Popeye domain of POPDC1 has the binding sites of KCNK2 (TREK-1, a member of two-pore K^+ channels family) (Froese et al., 2012) and Cav-3 (Alcalay et al., 2013) proteins. It was found that TREK-1 current was

increased twofold in the presence of Popdc1-3 proteins. Along with a prevalent SAN phenotype characterized by bradycardia with frequent episodes of sinus pause following stress in cardiac-specific TREK-1-deficient mice (Unudurthi et al., 2016), this may contribute to SND observed in Popdc-null mice. Finally, Popdc1-null cardiomyocytes showed a statistically significant 70% reduction in caveolae number (Alcalay et al., 2013) which can additionally contribute to SND phenotype via modulation of various pacemaker ion channels in transporters discussed in previous sections.

A-Kinase Anchor Proteins

Another scaffolding protein family linked to SND, is AKAPs. AKAPs localize PKA to a different subcellular compartment, permitting a higher degree of selectivity and specificity of phosphorylation for different downstream PKA substrates. More than 14 different AKAPs have been shown to be expressed in both rodent and human heart tissue including: AKAP5 (AKAP150/79), AKAP7 (AKAP 15/18), gravin (AKAP12), AKAP9 (yotiao) and mAKAP. Though AKAPs' function in the SAN is not clear, those proteins are critically important for $[Ca^{2+}]_i$ regulation and thus may contribute to Ca-clock regulation and SAN pacemaking.

Throughout all AKAPs, AKAP150/79 (AKAP5) is probably the most studied in the heart. AKAP150/79 targets PKA and phosphatases to regions near $Ca_v1.2$ (**Figure 2**) increasing the probability of long openings and coupled gating events between channels. Enzymes known to associate with AKAP150/79 include PKA, protein kinase C, CaM, AC5/6, and PP2B. Sympathetic stimulation of adult cardiomyocytes requires association of AKAP150/79 with a subpopulation of LTCCs coupled with Cav-3 (Nichols et al., 2010). Ablation of AKAP150 in mice with long QT syndrome 8 (LQT8), a disease also known as Timothy syndrome characterized by sinus bradycardia, prolonged QT interval and lethal arrhythmias, restores normal gating in $Ca_v1.2$-LQT8 channels and protects the heart from arrhythmias (Cheng et al., 2011). Dysfunction in AKAP10 has been associated with SAN pacemaking and SND in both mice and humans by effecting vagal regulation of the heart (Tingley et al., 2007).

Other Structural Proteins

A rare variant in MYH6, which encodes protein myosin heavy chain α isoform (MHC-α) is also reported associated with high risk of sick sinus syndrome (Holm et al., 2011). There are also some nuclear structural proteins that have been reported to be involved in the SND. A type II integral membrane protein that anchored to the inner nuclear membrane, emerin (**Figure 2**), whose mutation is known to develop Emery-Dreifuss Muscular Dystrophy (Emery and Dreifuss, 1966), is reported to associate with SND with underlying mechanism yet to illustrate (Karst et al., 2008). Mutations in the lamin A/C gene LMNA are reported to cause a variety of heart diseases including SND (**Figure 2**) (Hoorntje et al., 2017). Though the direct mechanisms of nucleus-associated scaffolding protein-induced modulation of SAN activity are unknown, it might be linked to pacemaker protein expression and/or trafficking.

SUMMARY

Contemporary evidence clearly demonstrates an emerging role of compartmentalized, i.e., associated with distinct, spatially-confined microdomains, organization of pacemaker signaling complexes in the SANCs. Disruption in subcellular targeting of pacemaker proteins and associated signaling molecules upon structural remodeling of the SAN, may affect their biophysical properties and neurohormonal regulation as well as protein–protein interactions within the pacemaker signaling complex disturbing rhythmic generation of APs and thus contributing to the pathophysiology of the SND. These are clear from patients and animal models with genetic defects of scaffolding proteins which are closely associated with SND via the indirect changes of key components in the coupled-clock systems in terms of protein expression, functioning and membrane localization. This extends beyond the classical concept of electrical remodeling, according to which dysfunction can be explained by straightforward increases or decreases in protein expression alone, and adds a new dimension to cardiovascular disease. It thus introduces a novel framework for therapeutic approaches for pacemaker dysfunction treatment targeted at preventing the degradation of cardiac cytoarchitecture.

AUTHOR CONTRIBUTIONS

AG and DL substantially contributed to the conception and design of the work; the acquisition, analysis or interpretation of the data and literature; drafting the work critically for important intellectual content; provide approval for publication of the content; agree to be accountable for all aspects of the work in ensuring that questions related to the accuracy or integrity of any part of the work are appropriately investigated and resolved.

FUNDING

This work was supported by NIH 1R01HL141214-01 and AHA 16SDG29120011 to AG and AHA Fellowship 17POST33370089 to DL.

REFERENCES

Alcalay, Y., Hochhauser, E., Kliminski, V., Dick, J., Zahalka, M. A., Parnes, D., et al. (2013). Popeye domain containing 1 (Popdc1/Bves) is a caveolae-associated protein involved in ischemia tolerance. *PLoS One* 8:e71100. doi: 10.1371/journal.pone.0071100

Ayettey, A. S., and Navaratnam, V. (1978). The T-tubule system in the specialized and general myocardium of the rat. *J. Anat.* 127(Pt 1), 125–140.

Balycheva, M., Faggian, G., Glukhov, A. V., and Gorelik, J. (2015). Microdomain-specific localization of functional ion channels in cardiomyocytes: an emerging concept of local regulation and remodelling. *Biophys. Rev.* 7, 43–62. doi: 10.1007/s12551-014-0159-x

Barbuti, A., Gravante, B., Riolfo, M., Milanesi, R., Terragni, B., and DiFrancesco, D. (2004). Localization of pacemaker channels in lipid rafts regulates channel kinetics. *Circ. Res.* 94, 1325–1331. doi: 10.1161/01.RES.0000127621.54132.AE

Barbuti, A., Scavone, A., Mazzocchi, N., Terragni, B., Baruscotti, M., and Difrancesco, D. (2012). A caveolin-binding domain in the HCN4 channels mediates functional interaction with caveolin proteins. *J. Mol. Cell. Cardiol.* 53, 187–195. doi: 10.1016/j.yjmcc.2012.05.013

Barbuti, A., Terragni, B., Brioschi, C., and DiFrancesco, D. (2007). Localization of f-channels to caveolae mediates specific beta2-adrenergic receptor modulation of rate in sinoatrial myocytes. *J. Mol. Cell. Cardiol.* 42, 71–78. doi: 10.1016/j.yjmcc.2006.09.018

Bassani, J. W., Yuan, W., and Bers, D. M. (1995). Fractional SR Ca release is regulated by trigger Ca and SR Ca content in cardiac myocytes. *Am. J. Physiol.* 268(5 Pt 1), C1313–C1319. doi: 10.1152/ajpcell.1995.268.5.C1313

Best, J. M., and Kamp, T. J. (2012). Different subcellular populations of L-type Ca^{2+} channels exhibit unique regulation and functional roles in cardiomyocytes. *J. Mol. Cell. Cardiol.* 52, 376–387. doi: 10.1016/j.yjmcc.2011.08.014

Boineau, J. P., Canavan, T. E., Schuessler, R. B., Cain, M. E., Corr, P. B., and Cox, J. L. (1988). Demonstration of a widely distributed atrial pacemaker complex in the human heart. *Circulation* 77, 1221–1237. doi: 10.1161/01.CIR.77.6.1221

Bossuyt, J., Taylor, B. E., James-Kracke, M., and Hale, C. C. (2002). The cardiac sodium-calcium exchanger associates with caveolin-3. *Ann. N. Y. Acad. Sci.* 976, 197–204. doi: 10.1111/j.1749-6632.2002.tb04741.x

Boyett, M. R., Honjo, H., and Kodama, I. (2000). The sinoatrial node, a heterogeneous pacemaker structure. *Cardiovasc. Res.* 47, 658–687. doi: 10.1016/S0008-6363(00)00135-8

Brandenburg, S., Kohl, T., Williams, G. S., Gusev, K., Wagner, E., Rog-Zielinska, E. A., et al. (2016). Axial tubule junctions control rapid calcium signaling in atria. *J. Clin. Invest.* 126, 3999–4015. doi: 10.1172/JCI88241

Brandenburg, S., Pawlowitz, J., Fakuade, F. E., Kownatzki-Danger, D., Kohl, T., Mitronova, G., et al. (2018). Axial tubule junctions activate atrial Ca^{2+} release across species. *Front. Physiol.* 9:1227. doi: 10.3389/fphys.2018.01227

Brodde, O. E., Bruck, H., Leineweber, K., and Seyfarth, T. (2001). Presence, distribution and physiological function of adrenergic and muscarinic receptor subtypes in the human heart. *Basic Res. Cardiol.* 96, 528–538. doi: 10.1007/s003950170003

Brodde, O. E., Leifert, F. J., and Krehl, H. J. (1982). Coexistence of beta 1- and beta 2-adrenoceptors in the rabbit heart: quantitative analysis of the regional distribution by (-)-3H-dihydroalprenolol binding. *J. Cardiovasc. Pharmacol.* 4, 34–43. doi: 10.1097/00005344-198201000-00007

Bryant, S. M., Kong, C. H. T., Watson, J. J., Gadeberg, H. C., Roth, D. M., Patel, H. H., et al. (2018). Caveolin-3 KO disrupts t-tubule structure and decreases t-tubular ICa density in mouse ventricular myocytes. *Am. J. Physiol. Heart Circ. Physiol.* 315, H1101–H1111. doi: 10.1152/ajpheart.00209.2018

Calaghan, S., Kozera, L., and White, E. (2008). Compartmentalisation of cAMP-dependent signalling by caveolae in the adult cardiac myocyte. *J. Mol. Cell. Cardiol.* 45, 88–92. doi: 10.1016/j.yjmcc.2008.04.004

Camors, E., Charue, D., Trouve, P., Monceau, V., Loyer, X., Russo-Marie, F., et al. (2006). Association of annexin A5 with Na^{+}/Ca^{2+} exchanger and caveolin-3 in non-failing and failing human heart. *J. Mol. Cell. Cardiol.* 40, 47–55. doi: 10.1016/j.yjmcc.2005.08.009

Campostrini, G., Bonzanni, M., Lissoni, A., Bazzini, C., Milanesi, R., Vezzoli, E., et al. (2017). The expression of the rare caveolin-3 variant T78M alters cardiac ion channels function and membrane excitability. *Cardiovasc. Res.* 113, 1256–1265. doi: 10.1093/cvr/cvx122

Cavalli, A., Eghbali, M., Minosyan, T. Y., Stefani, E., and Philipson, K. D. (2007). Localization of sarcolemmal proteins to lipid rafts in the myocardium. *Cell Calcium* 42, 313–322. doi: 10.1016/j.ceca.2007.01.003

Chen, C. C., Lamping, K. G., Nuno, D. W., Barresi, R., Prouty, S. J., Lavoie, J. L., et al. (2003). Abnormal coronary function in mice deficient in alpha1H T-type Ca2+ channels. *Science* 302, 1416–1418. doi: 10.1126/science.1089268

Cheng, E. P., Yuan, C., Navedo, M. F., Dixon, R. E., Nieves-Cintron, M., Scott, J. D., et al. (2011). Restoration of normal L-type Ca^{2+} channel function during Timothy syndrome by ablation of an anchoring protein. *Circ. Res.* 109, 255–261. doi: 10.1161/CIRCRESAHA.111.248252

Chiang, D. Y., Li, N., Wang, Q., Alsina, K. M., Quick, A. P., Reynolds, J. O., et al. (2014). Impaired local regulation of ryanodine receptor type 2 by protein phosphatase 1 promotes atrial fibrillation. *Cardiovasc. Res.* 103, 178–187. doi: 10.1093/cvr/cvu123

Christel, C. J., Cardona, N., Mesirca, P., Herrmann, S., Hofmann, F., Striessnig, J., et al. (2012). Distinct localization and modulation of Cav1.2 and Cav1.3 L-type Ca^{2+} channels in mouse sinoatrial node. *J. Physiol.* 590, 6327–6342. doi: 10.1113/jphysiol.2012.239954

Csepe, T. A., Zhao, J., Hansen, B. J., Li, N., Sul, L. V., Lim, P., et al. (2016). Human sinoatrial node structure: 3D microanatomy of sinoatrial conduction pathways. *Prog. Biophys. Mol. Biol.* 120, 164–178. doi: 10.1016/j.pbiomolbio.2015.12.011

Cunha, S. R., Hund, T. J., Hashemi, S., Voigt, N., Li, N., Wright, P., et al. (2011). Defects in ankyrin-based membrane protein targeting pathways underlie atrial fibrillation. *Circulation* 124, 1212–1222. doi: 10.1161/CIRCULATIONAHA.111.023986

Curran, J., Musa, H., Kline, C. F., Makara, M. A., Little, S. C., Higgins, J. D., et al. (2015). Eps15 homology domain-containing protein 3 regulates cardiac T-type Ca^{2+} channel targeting and function in the atria. *J. Biol. Chem.* 290, 12210–12221. doi: 10.1074/jbc.M115.646893

Delos Santos, R. C., Garay, C., and Antonescu, C. N. (2015). Charming neighborhoods on the cell surface: plasma membrane microdomains regulate receptor tyrosine kinase signaling. *Cell Signal.* 27, 1963–1976. doi: 10.1016/j.cellsig.2015.07.004

DiFrancesco, D. (1993). Pacemaker mechanisms in cardiac tissue. *Annu. Rev. Physiol.* 55, 455–472. doi: 10.1146/annurev.ph.55.030193.002323

DiFrancesco, D., and Tortora, P. (1991). Direct activation of cardiac pacemaker channels by intracellular cyclic AMP. *Nature* 351, 145–147. doi: 10.1038/351145a0

Dries, E., Bito, V., Lenaerts, I., Antoons, G., Sipido, K. R., and Macquaide, N. (2013). Selective modulation of coupled ryanodine receptors during microdomain activation of calcium/calmodulin-dependent kinase II in the dyadic cleft. *Circ. Res.* 113, 1242–1252. doi: 10.1161/CIRCRESAHA.113.301896

Emery, A. E., and Dreifuss, F. E. (1966). Unusual type of benign x-linked muscular dystrophy. *J. Neurol. Neurosurg. Psychiatry* 29, 338–342. doi: 10.1136/jnnp.29.4.338

Fedorov, V. V., Chang, R., Glukhov, A. V., Kostecki, G., Janks, D., Schuessler, R. B., et al. (2010). Complex interactions between the sinoatrial node and atrium during reentrant arrhythmias in the canine heart. *Circulation* 122, 782–789. doi: 10.1161/CIRCULATIONAHA.109.935288

Fedorov, V. V., Glukhov, A. V., and Chang, R. (2012). Conduction barriers and pathways of the sinoatrial pacemaker complex: their role in normal rhythm and atrial arrhythmias. *Am. J. Physiol. Heart Circ. Physiol.* 302, H1773–H1783. doi: 10.1152/ajpheart.00892.2011

Feron, O., Smith, T. W., Michel, T., and Kelly, R. A. (1997). Dynamic targeting of the agonist-stimulated m2 muscarinic acetylcholine receptor to caveolae in cardiac myocytes. *J. Biol. Chem.* 272, 17744–17748. doi: 10.1074/jbc.272.28.17744

Foell, J. D., Balijepalli, R. C., Delisle, B. P., Yunker, A. M., Robia, S. L., Walker, J. W., et al. (2004). Molecular heterogeneity of calcium channel beta-subunits in canine and human heart: evidence for differential subcellular localization. *Physiol. Genomics* 17, 183–200. doi: 10.1152/physiolgenomics.00207.2003

Froese, A., Breher, S. S., Waldeyer, C., Schindler, R. F., Nikolaev, V. O., Rinne, S., et al. (2012). Popeye domain containing proteins are essential for stress-mediated modulation of cardiac pacemaking in mice. *J. Clin. Invest.* 122, 1119–1130. doi: 10.1172/JCI59410

Galindo-Tovar, A., and Kaumann, A. J. (2008). Phosphodiesterase-4 blunts inotropism and arrhythmias but not sinoatrial tachycardia of (-)-adrenaline mediated through mouse cardiac beta(1)-adrenoceptors. *Br. J. Pharmacol.* 153, 710–720. doi: 10.1038/sj.bjp.0707631

Gao, Z., Chen, B., Mei-ling, A. J., Wu, Y., Guan, X., Koval, O. M., et al. (2010). If and SR Ca^{2+} release both contribute to pacemaker activity in canine sinoatrial node cells. *J. Mol. Cell. Cardiol.* 49, 33–40. doi: 10.1016/j.yjmcc.2010.03.019

Glukhov, A. V., Balycheva, M., Sanchez-Alonso, J. L., Ilkan, Z., Alvarez-Laviada, A., Bhogal, N., et al. (2015a). Direct evidence for microdomain-specific localization and remodeling of functional L-type calcium channels in rat and human atrial myocytes. *Circulation* 132, 2372–2384. doi: 10.1161/CIRCULATIONAHA.115.018131

Glukhov, A. V., Kalyanasundaram, A., Lou, Q., Hage, L. T., Hansen, B. J., Belevych, A. E., et al. (2015b). Calsequestrin 2 deletion causes sinoatrial node dysfunction and atrial arrhythmias associated with altered sarcoplasmic reticulum calcium

cycling and degenerative fibrosis within the mouse atrial pacemaker complex1. *Eur. Heart J.* 36, 686–697. doi: 10.1093/eurheartj/eht452

Glukhov, A. V., Fedorov, V. V., Anderson, M. E., Mohler, P. J., and Efimov, I. R. (2010). Functional anatomy of the murine sinus node: high-resolution optical mapping of ankyrin-B heterozygous mice. *Am. J. Physiol. Heart Circ. Physiol.* 299, H482–H491. doi: 10.1152/ajpheart.00756.2009

Glukhov, A. V., Hage, L. T., Hansen, B. J., Pedraza-Toscano, A., Vargas-Pinto, P., Hamlin, R. L., et al. (2013). Sinoatrial node reentry in a canine chronic left ventricular infarct model: role of intranodal fibrosis and heterogeneity of refractoriness. *Circ. Arrhythm. Electrophysiol.* 6, 984–994. doi: 10.1161/CIRCEP.113.000404

Grimm, M., and Brown, J. H. (2010). Beta-adrenergic receptor signaling in the heart: role of CaMKII. *J. Mol. Cell. Cardiol.* 48, 322–330. doi: 10.1016/j.yjmcc.2009.10.016

Gu, H., and Neel, B. G. (2003). The "Gab" in signal transduction. *Trends Cell Biol.* 13, 122–130. doi: 10.1016/S0962-8924(03)00002-3

Guo, Y., Golebiewska, U., and Scarlata, S. (2011). Modulation of Ca^{2+} activity in cardiomyocytes through caveolae-Gαq interactions. *Biophys. J.* 100, 1599–1607. doi: 10.1016/j.bpj.2011.02.013

Hagiwara, N., Irisawa, H., and Kameyama, M. (1988). Contribution of two types of calcium currents to the pacemaker potentials of rabbit sino-atrial node cells. *J. Physiol.* 395, 233–253. doi: 10.1113/jphysiol.1988.sp016916

Hohendanner, F., Walther, S., Maxwell, J. T., Kettlewell, S., Awad, S., Smith, G. L., et al. (2015). Inositol-1,4,5-trisphosphate induced Ca^{2+} release and excitation-contraction coupling in atrial myocytes from normal and failing hearts. *J. Physiol.* 593, 1459–1477. doi: 10.1113/jphysiol.2014.283226

Holm, H., Gudbjartsson, D. F., Sulem, P., Masson, G., Helgadottir, H. T., Zanon, C., et al. (2011). A rare variant in MYH6 is associated with high risk of sick sinus syndrome. *Nat. Genet.* 43, 316–320. doi: 10.1038/ng.781

Hoorntje, E. T., Bollen, I. A., Barge-Schaapveld, D. Q., van Tienen, F. H., Te Meerman, G. J., Jansweijer, J. A., et al. (2017). Lamin A/C-related cardiac disease: late onset with a variable and mild phenotype in a large cohort of patients with the lamin A/C p.(Arg331Gln) founder mutation. *Circ. Cardiovasc. Genet.* 10:e001631. doi: 10.1161/CIRCGENETICS.116.001631

Hua, R., Adamczyk, A., Robbins, C., Ray, G., and Rose, R. A. (2012). Distinct patterns of constitutive phosphodiesterase activity in mouse sinoatrial node and atrial myocardium. *PLoS One* 7:e47652. doi: 10.1371/journal.pone.0047652

Iancu, R. V., Jones, S. W., and Harvey, R. D. (2007). Compartmentation of cAMP signaling in cardiac myocytes: a computational study. *Biophys. J.* 92, 3317–3331. doi: 10.1529/biophysj.106.095356

Jaleel, N., Nakayama, H., Chen, X., Kubo, H., MacDonnell, S., Zhang, H., et al. (2008). Ca^{2+} influx through T- and L-type Ca^{2+} channels have different effects on myocyte contractility and induce unique cardiac phenotypes. *Circ. Res.* 103, 1109–1119. doi: 10.1161/CIRCRESAHA.108.185611

Jones, L. R., Suzuki, Y. J., Wang, W., Kobayashi, Y. M., Ramesh, V., Franzini-Armstrong, C., et al. (1998). Regulation of Ca^{2+} signaling in transgenic mouse cardiac myocytes overexpressing calsequestrin. *J. Clin. Invest.* 101, 1385–1393. doi: 10.1172/JCI1362

Jones, S. A., Yamamoto, M., Tellez, J. O., Billeter, R., Boyett, M. R., Honjo, H., et al. (2008). Distinguishing properties of cells from the myocardial sleeves of the pulmonary veins: a comparison of normal and abnormal pacemakers. *Circ. Arrhythm. Electrophysiol.* 1, 39–48. doi: 10.1161/CIRCEP.107.748467

Ju, Y. K., Liu, J., Lee, B. H., Lai, D., Woodcock, E. A., Lei, M., et al. (2011). Distribution and functional role of inositol 1,4,5-trisphosphate receptors in mouse sinoatrial node. *Circ. Res.* 109, 848–857. doi: 10.1161/CIRCRESAHA.111.243824

Karst, M. L., Herron, K. J., and Olson, T. M. (2008). X-linked nonsyndromic sinus node dysfunction and atrial fibrillation caused by emerin mutation. *J. Cardiovasc. Electrophysiol.* 19, 510–515. doi: 10.1111/j.1540-8167.2007.01081.x

Kim, M. S., Maltsev, A. V., Monfredi, O., Maltseva, L. A., Wirth, A., Florio, M. C., et al. (2018). Heterogeneity of calcium clock functions in dormant, dysrhythmically and rhythmically firing single pacemaker cells isolated from SA node. *Cell Calcium* 74, 168–179. doi: 10.1016/j.ceca.2018.07.002

Knollmann, B. C., Chopra, N., Hlaing, T., Akin, B., Yang, T., Ettensohn, K., et al. (2006). Casq2 deletion causes sarcoplasmic reticulum volume increase, premature Ca^{2+} release, and catecholaminergic polymorphic ventricular tachycardia. *J. Clin. Invest.* 116, 2510–2520. doi: 10.1172/JCI29128

Lakatta, E. G., and DiFrancesco, D. (2009). What keeps us ticking: a funny current, a calcium clock, or both? *J. Mol. Cell. Cardiol.* 47, 157–170. doi: 10.1016/j.yjmcc.2009.03.022

Lakatta, E. G., Maltsev, V. A., and Vinogradova, T. M. (2010). A coupled SYSTEM of intracellular Ca^{2+} clocks and surface membrane voltage clocks controls the timekeeping mechanism of the heart's pacemaker. *Circ. Res.* 106, 659–673. doi: 10.1161/CIRCRESAHA.109.206078

Lang, D., Warden, A., Balijepalli, R., Kamp, T. J., and Glukhov, A. V. (2016). Loss of caveolin-3 disrupts mouse sinoatrial node pacemaking and stimulates atrial arrhythmogenesis. *Circulation* 134(Suppl 1), A15361.

Le Scouarnec, S., Bhasin, N., Vieyres, C., Hund, T. J., Cunha, S. R., Koval, O., et al. (2008). Dysfunction in ankyrin-B-dependent ion channel and transporter targeting causes human sinus node disease. *Proc. Natl. Acad. Sci. U.S.A.* 105, 15617–15622. doi: 10.1073/pnas.0805500105

Li, N., Csepe, T. A., Hansen, B. J., Dobrzynski, H., Higgins, R. S., Kilic, A., et al. (2015). Molecular mapping of sinoatrial node HCN channel expression in the human heart. *Circ. Arrhythm. Electrophysiol.* 8, 1219–1227. doi: 10.1161/CIRCEP.115.003070

Li, N., Hansen, B. J., Csepe, T. A., Zhao, J., Ignozzi, A. J., Sul, L. V., et al. (2017). Redundant and diverse intranodal pacemakers and conduction pathways protect the human sinoatrial node from failure. *Sci. Transl. Med.* 9:eaam5607. doi: 10.1126/scitranslmed.aam5607

Li, Y., Sirenko, S., Riordon, D. R., Yang, D., Spurgeon, H., Lakatta, E. G., et al. (2016). CaMKII-dependent phosphorylation regulates basal cardiac pacemaker function via modulation of local Ca^{2+} releases. *Am. J. Physiol. Heart Circ. Physiol.* 311, H532–H544. doi: 10.1152/ajpheart.00765.2015

Liao, Z., Lockhead, D., Larson, E. D., and Proenza, C. (2010). Phosphorylation and modulation of hyperpolarization-activated HCN4 channels by protein kinase A in the mouse sinoatrial node. *J. Gen. Physiol.* 136, 247–258. doi: 10.1085/jgp.201010488

Logantha, S. J., Stokke, M. K., Atkinson, A. J., Kharche, S. R., Parveen, S., Saeed, Y., et al. (2016). Ca(2+)-clock-dependent pacemaking in the sinus node is impaired in mice with a cardiac specific reduction in SERCA2 abundance. *Front. Physiol.* 7:197. doi: 10.3389/fphys.2016.00197

Lu, R., Chen, Y., Cottingham, C., Peng, N., Jiao, K., Limbird, L. E., et al. (2010). Enhanced hypotensive, bradycardic, and hypnotic responses to alpha2-adrenergic agonists in spinophilin-null mice are accompanied by increased G protein coupling to the alpha2A-adrenergic receptor. *Mol. Pharmacol.* 78, 279–286. doi: 10.1124/mol.110.065300

Lukyanenko, Y. O., Younes, A., Lyashkov, A. E., Tarasov, K. V., Riordon, D. R., Lee, J., et al. (2016). Ca^{2+}/calmodulin-activated phosphodiesterase 1A is highly expressed in rabbit cardiac sinoatrial nodal cells and regulates pacemaker function. *J. Mol. Cell. Cardiol.* 98, 73–82. doi: 10.1016/j.yjmcc.2016.06.064

Luo, M., Guan, X., Luczak, E. D., Lang, D., Kutschke, W., Gao, Z., et al. (2013). Diabetes increases mortality after myocardial infarction by oxidizing CaMKII. *J. Clin. Invest.* 123, 1262–1274. doi: 10.1172/JCI65268

Lyashkov, A. E., Juhaszova, M., Dobrzynski, H., Vinogradova, T. M., Maltsev, V. A., Juhasz, O., et al. (2007). Calcium cycling protein density and functional importance to automaticity of isolated sinoatrial nodal cells are independent of cell size. *Circ. Res.* 100, 1723–1731. doi: 10.1161/CIRCRESAHA.107.153676

Macdougall, D. A., Agarwal, S. R., Stopford, E. A., Chu, H., Collins, J. A., Longster, A. L., et al. (2012). Caveolae compartmentalise beta2-adrenoceptor signals by curtailing cAMP production and maintaining phosphatase activity in the sarcoplasmic reticulum of the adult ventricular myocyte. *J. Mol. Cell. Cardiol.* 52, 388–400. doi: 10.1016/j.yjmcc.2011.06.014

Mangoni, M. E., Couette, B., Bourinet, E., Platzer, J., Reimer, D., Striessnig, J., et al. (2003). Functional role of L-type Cav1.3 Ca^{2+} channels in cardiac pacemaker activity. *Proc. Natl. Acad. Sci. U.S.A.* 100, 5543–5548. doi: 10.1073/pnas.0935295100

Mangoni, M. E., Traboulsie, A., Leoni, A. L., Couette, B., Marger, L., Le Quang, K., et al. (2006). Bradycardia and slowing of the atrioventricular conduction in mice lacking CaV3.1/alpha1G T-type calcium channels. *Circ. Res.* 98, 1422–1430. doi: 10.1161/01.RES.0000225862.14314.49

Marionneau, C., Couette, B., Liu, J., Li, H., Mangoni, M. E., Nargeot, J., et al. (2005). Specific pattern of ionic channel gene expression associated with pacemaker activity in the mouse heart. *J. Physiol.* 562(Pt 1), 223–234. doi: 10.1113/jphysiol.2004.074047

Markandeya, Y. S., Fahey, J. M., Pluteanu, F., Cribbs, L. L., and Balijepalli, R. C. (2011). Caveolin-3 regulates protein kinase A modulation of the Ca(V)3.2 (alpha1H) T-type Ca^{2+} channels. *J. Biol. Chem.* 286, 2433–2444. doi: 10.1074/jbc.M110.182550

Masson-Pevet, M., Gros, D., and Besselsen, E. (1980). The caveolae in rabbit sinus node and atrium. *Cell Tissue Res.* 208, 183–196. doi: 10.1007/BF00234869

Mohler, P. J., Splawski, I., Napolitano, C., Bottelli, G., Sharpe, L., Timothy, K., et al. (2004). A cardiac arrhythmia syndrome caused by loss of ankyrin-B function. *Proc. Natl. Acad. Sci. U.S.A.* 101, 9137–9142. doi: 10.1073/pnas.0402546101

Mohler, P. J., Schott, J. J., Gramolini, A. O., Dilly, K. W., Guatimosim, S., duBell, W. H., et al. (2003). Ankyrin-B mutation causes type 4 long-QT cardiac arrhythmia and sudden cardiac death. *Nature* 421, 634–639. doi: 10.1038/nature01335

Monfredi, O., Tsutsui, K., Ziman, B., Stern, M. D., Lakatta, E. G., and Maltsev, V. A. (2018). Electrophysiological heterogeneity of pacemaker cells in the rabbit intercaval region, including the SA node: insights from recording multiple ion currents in each cell. *Am. J. Physiol. Heart Circ. Physiol.* 314, H403–H414. doi: 10.1152/ajpheart.00253.2016

Musa, H., Lei, M., Honjo, H., Jones, S. A., Dobrzynski, H., Lancaster, M. K., et al. (2002). Heterogeneous expression of Ca^{2+} handling proteins in rabbit sinoatrial node. *J. Histochem. Cytochem.* 50, 311–324. doi: 10.1177/002215540205000303

Nichols, C. B., Rossow, C. F., Navedo, M. F., Westenbroek, R. E., Catterall, W. A., Santana, L. F., et al. (2010). Sympathetic stimulation of adult cardiomyocytes requires association of AKAP5 with a subpopulation of L-type calcium channels. *Circ. Res.* 107, 747–756. doi: 10.1161/CIRCRESAHA.109.216127

Nikolaev, V. O., Moshkov, A., Lyon, A. R., Miragoli, M., Novak, P., Paur, H., et al. (2010). Beta2-adrenergic receptor redistribution in heart failure changes cAMP compartmentation. *Science* 327, 1653–1657. doi: 10.1126/science.1185988

Petzhold, D., da Costa-Goncalves, A. C., Gross, V., and Morano, I. (2011). Spinophilin is required for normal morphology, Ca^{2+} homeostasis and contraction but dispensable for beta-adrenergic stimulation of adult cardiomyocytes. *J. Muscle Res. Cell Motil.* 32, 243–248. doi: 10.1007/s10974-011-9259-4

Protas, L., and Robinson, R. B. (2000). Mibefradil, an I(Ca,T) blocker, effectively blocks I(Ca,L) in rabbit sinus node cells. *Eur. J. Pharmacol.* 401, 27–30. doi: 10.1016/S0014-2999(00)00364-2

Pulli, I., Blom, T., Lof, C., Magnusson, M., Rimessi, A., Pinton, P., et al. (2015). A novel chimeric aequorin fused with caveolin-1 reveals a sphingosine kinase 1-regulated Ca^{2+} microdomain in the caveolar compartment. *Biochim. Biophys. Acta* 1853, 2173–2182. doi: 10.1016/j.bbamcr.2015.04.005

Ragusa, M. J., Dancheck, B., Critton, D. A., Nairn, A. C., Page, R., and Peti, W. (2010). Spinophilin directs protein phosphatase 1 specificity by blocking substrate binding sites. *Nat. Struct. Mol. Biol.* 17, 459–464. doi: 10.1038/nsmb.1786

Rigg, L., Heath, B. M., Cui, Y., and Terrar, D. A. (2000). Localisation and functional significance of ryanodine receptors during beta-adrenoceptor stimulation in the guinea-pig sino-atrial node. *Cardiovasc. Res.* 48, 254–264. doi: 10.1016/S0008-6363(00)00153-X

Rybin, V. O., Xu, X., Lisanti, M. P., and Steinberg, S. F. (2000). Differential targeting of beta -adrenergic receptor subtypes and adenylyl cyclase to cardiomyocyte caveolae. A mechanism to functionally regulate the cAMP signaling pathway. *J. Biol. Chem.* 275, 41447–41457. doi: 10.1074/jbc.M006951200

Scriven, D. R., Klimek, A., Asghari, P., Bellve, K., and Moore, E. D. (2005). Caveolin-3 is adjacent to a group of extradyadic ryanodine receptors. *Biophys. J.* 89, 1893–1901. doi: 10.1529/biophysj.105.064212

Senzaki, H., Smith, C. J., Juang, G. J., Isoda, T., Mayer, S. P., Ohler, A., et al. (2001). Cardiac phosphodiesterase 5 (cGMP-specific) modulates beta-adrenergic signaling in vivo and is down-regulated in heart failure. *FASEB J.* 15, 1718–1726. doi: 10.1096/fj.00-0538com

Shcherbakova, O. G., Hurt, C. M., Xiang, Y., Dell'Acqua, M. L., Zhang, Q., Tsien, R. W., et al. (2007). Organization of beta-adrenoceptor signaling compartments by sympathetic innervation of cardiac myocytes. *J. Cell Biol.* 176, 521–533. doi: 10.1083/jcb.200604167

Sprenger, J. U., Perera, R. K., Steinbrecher, J. H., Lehnart, S. E., Maier, L. S., Hasenfuss, G., et al. (2015). In vivo model with targeted cAMP biosensor reveals changes in receptor-microdomain communication in cardiac disease. *Nat. Commun.* 6:6965. doi: 10.1038/ncomms7965

St Clair, J. R., Larson, E. D., Sharpe, E. J., Liao, Z., and Proenza, C. (2017). Phosphodiesterases 3 and 4 differentially regulate the funny current, if, in mouse sinoatrial node myocytes. *J. Cardiovasc. Dev. Dis.* 4:10. doi: 10.3390/jcdd4030010

St Clair, J. R., Liao, Z., Larson, E. D., and Proenza, C. (2013). PKA-independent activation of I(f) by cAMP in mouse sinoatrial myocytes. *Channels* 7, 318–321. doi: 10.4161/chan.25293

Stern, M. D., Maltseva, L. A., Juhaszova, M., Sollott, S. J., Lakatta, E. G., and Maltsev, V. A. (2014). Hierarchical clustering of ryanodine receptors enables emergence of a calcium clock in sinoatrial node cells. *J. Gen. Physiol.* 143, 577–604. doi: 10.1085/jgp.201311123

Tingley, W. G., Pawlikowska, L., Zaroff, J. G., Kim, T., Nguyen, T., Young, S. G., et al. (2007). Gene-trapped mouse embryonic stem cell-derived cardiac myocytes and human genetics implicate AKAP10 in heart rhythm regulation. *Proc. Natl. Acad. Sci. U.S.A.* 104, 8461–8466. doi: 10.1073/pnas.0610393104

Tonegawa, K., Otsuka, W., Kumagai, S., Matsunami, S., Hayamizu, N., Tanaka, S., et al. (2017). Caveolae-specific activation loop between CaMKII and L-type Ca^{2+} channel aggravates cardiac hypertrophy in alpha1-adrenergic stimulation. *Am. J. Physiol. Heart Circ. Physiol.* 312, H501–H514. doi: 10.1152/ajpheart.00601.2016

Torrente, A. G., Mesirca, P., Neco, P., Rizzetto, R., Dubel, S., Barrere, C., et al. (2016). L-type Cav1.3 channels regulate ryanodine receptor-dependent Ca^{2+} release during sino-atrial node pacemaker activity. *Cardiovasc. Res.* 109, 451–461. doi: 10.1093/cvr/cvw006

Torrente, A. G., Zhang, R., Zaini, A., Giani, J. F., Kang, J., Lamp, S. T., et al. (2015). Burst pacemaker activity of the sinoatrial node in sodium-calcium exchanger knockout mice. *Proc. Natl. Acad. Sci. U.S.A.* 112, 9769–9774. doi: 10.1073/pnas.1505670112

Tsui, J., Inagaki, M., and Schulman, H. (2005). Calcium/calmodulin-dependent protein kinase II (CaMKII) localization acts in concert with substrate targeting to create spatial restriction for phosphorylation. *J. Biol. Chem.* 280, 9210–9216. doi: 10.1074/jbc.M407653200

Tsutsui, K., Monfredi, O. J., Sirenko-Tagirova, S. G., Maltseva, L. A., Bychkov, R., Kim, M. S., et al. (2018). A coupled-clock system drives the automaticity of human sinoatrial nodal pacemaker cells. *Sci. Signal.* 11:eaa7608. doi: 10.1126/scisignal.aap7608

Unudurthi, S. D., Wu, X., Qian, L., Amari, F., Onal, B., Li, N., et al. (2016). Two-pore K^+ channel TREK-1 regulates sinoatrial node membrane excitability. *J. Am. Heart Assoc.* 5:e002865. doi: 10.1161/JAHA.115.002865

Vatta, M., Ackerman, M. J., Ye, B., Makielski, J. C., Ughanze, E. E., Taylor, E. W., et al. (2006). Mutant caveolin-3 induces persistent late sodium current and is associated with long-QT syndrome. *Circulation* 114, 2104–2112. doi: 10.1161/CIRCULATIONAHA.106.635268

Vinogradova, T. M., Kobrinsky, E., and Lakatta, E. G. (2018). Dual activation of phosphodiesterases 3 and 4 regulates basal spontaneous beating rate of cardiac pacemaker cells: role of compartmentalization? *Front. Physiol.* 9:1301. doi: 10.3389/fphys.2018.01301

Vinogradova, T. M., and Lakatta, E. G. (2009). Regulation of basal and reserve cardiac pacemaker function by interactions of cAMP-mediated PKA-dependent Ca^{2+} cycling with surface membrane channels. *J. Mol. Cell. Cardiol.* 47, 456–474. doi: 10.1016/j.yjmcc.2009.06.014

Vinogradova, T. M., Lyashkov, A. E., Zhu, W., Ruknudin, A. M., Sirenko, S., Yang, D., et al. (2006). High basal protein kinase A-dependent phosphorylation drives rhythmic internal Ca^{2+} store oscillations and spontaneous beating of cardiac pacemaker cells. *Circ. Res.* 98, 505–514. doi: 10.1161/01.RES.0000204575.94040.d1

Vinogradova, T. M., Sirenko, S., Lyashkov, A. E., Younes, A., Li, Y., Zhu, W., et al. (2008). Constitutive phosphodiesterase activity restricts spontaneous beating rate of cardiac pacemaker cells by suppressing local Ca^{2+} releases. *Circ. Res.* 102, 761–769. doi: 10.1161/CIRCRESAHA.107.161679

Vinogradova, T. M., Zhou, Y. Y., Bogdanov, K. Y., Yang, D., Kuschel, M., Cheng, H., et al. (2000). Sinoatrial node pacemaker activity requires Ca^{2+}/calmodulin-dependent protein kinase II activation. *Circ. Res.* 87, 760–767. doi: 10.1161/01.RES.87.9.760

Vinogradova, T. M., Zhou, Y. Y., Maltsev, V., Lyashkov, A., Stern, M., and Lakatta, E. G. (2004). Rhythmic ryanodine receptor Ca^{2+} releases during diastolic depolarization of sinoatrial pacemaker cells do not require membrane

depolarization. *Circ. Res.* 94, 802–809. doi: 10.1161/01.RES.0000122045.55331.0F

Walden, A. P., Dibb, K. M., and Trafford, A. W. (2009). Differences in intracellular calcium homeostasis between atrial and ventricular myocytes. *J. Mol. Cell. Cardiol.* 46, 463–473. doi: 10.1016/j.yjmcc.2008.11.003

Warrier, S., Belevych, A. E., Ruse, M., Eckert, R. L., Zaccolo, M., Pozzan, T., et al. (2005). Beta-adrenergic- and muscarinic receptor-induced changes in cAMP activity in adult cardiac myocytes detected with FRET-based biosensor. *Am. J. Physiol. Cell Physiol.* 289, C455–C461. doi: 10.1152/ajpcell.00058.2005

Warrier, S., Ramamurthy, G., Eckert, R. L., Nikolaev, V. O., Lohse, M. J., and Harvey, R. D. (2007). cAMP microdomains and L-type Ca^{2+} channel regulation in guinea-pig ventricular myocytes. *J. Physiol.* 580(Pt 3), 765–776. doi: 10.1113/jphysiol.2006.124891

Wehrens, X. H., Lehnart, S. E., Reiken, S. R., and Marks, A. R. (2004). Ca^{2+}/calmodulin-dependent protein kinase II phosphorylation regulates the cardiac ryanodine receptor. *Circ. Res.* 94, e61–e70. doi: 10.1161/01.RES.0000125626.33738.E2

Whittaker, C. A., and Hynes, R. O. (2002). Distribution and evolution of von Willebrand/integrin A domains: widely dispersed domains with roles in cell adhesion and elsewhere. *Mol. Biol. Cell* 13, 3369–3387. doi: 10.1091/mbc.e02-05-0259

Wright, P. T., Nikolaev, V. O., O'Hara, T., Diakonov, I., Bhargava, A., Tokar, S., et al. (2014). Caveolin-3 regulates compartmentation of cardiomyocyte beta2-adrenergic receptor-mediated cAMP signaling. *J. Mol. Cell. Cardiol.* 67, 38–48. doi: 10.1016/j.yjmcc.2013.12.003

Wu, Y., and Anderson, M. E. (2014). CaMKII in sinoatrial node physiology and dysfunction. *Front. Pharmacol.* 5:48. doi: 10.3389/fphar.2014.00048

Wu, Y., Valdivia, H. H., Wehrens, X. H., and Anderson, M. E. (2016). A single protein kinase A or calmodulin kinase II site does not control the cardiac pacemaker Ca^{2+} clock. *Circ. Arrhythm. Electrophysiol.* 9:e003180. doi: 10.1161/CIRCEP.115.003180

Yanni, J., Tellez, J. O., Maczewski, M., Mackiewicz, U., Beresewicz, A., Billeter, R., et al. (2011). Changes in ion channel gene expression underlying heart failure-induced sinoatrial node dysfunction. *Circ. Heart Fail.* 4, 496–508. doi: 10.1161/CIRCHEARTFAILURE.110.957647

Ye, B., Balijepalli, R. C., Foell, J. D., Kroboth, S., Ye, Q., Luo, Y. H., et al. (2008). Caveolin-3 associates with and affects the function of hyperpolarization-activated cyclic nucleotide-gated channel 4. *Biochemistry* 47, 12312–12318. doi: 10.1021/bi8009295

Younes, A., Lyashkov, A. E., Graham, D., Sheydina, A., Volkova, M. V., Mitsak, M., et al. (2008). Ca^{2+}-stimulated basal adenylyl cyclase activity localization in membrane lipid microdomains of cardiac sinoatrial nodal pacemaker cells. *J. Biol. Chem.* 283, 14461–14468. doi: 10.1074/jbc.M707540200

Zaccolo, M., and Pozzan, T. (2002). Discrete microdomains with high concentration of cAMP in stimulated rat neonatal cardiac myocytes. *Science* 295, 1711–1715. doi: 10.1126/science.1069982

Zhang, Z., Xu, Y., Song, H., Rodriguez, J., Tuteja, D., Namkung, Y., et al. (2002). Functional roles of Ca(v)1.3 (alpha(1D)) calcium channel in sinoatrial nodes: insight gained using gene-targeted null mutant mice. *Circ. Res.* 90, 981–987. doi: 10.1161/01.RES.0000018003.14304.E2

Conflict of Interest Statement: The authors declare that the research was conducted in the absence of any commercial or financial relationships that could be construed as a potential conflict of interest.

frontiers in Physiology

ORIGINAL RESEARCH
published: 04 December 2018
doi: 10.3389/fphys.2018.01737

Degradation of T-Tubular Microdomains and Altered cAMP Compartmentation Lead to Emergence of Arrhythmogenic Triggers in Heart Failure Myocytes: An *in silico* Study

*Alexandra D. Loucks, Thomas O'Hara and Natalia A. Trayanova**

Institute for Computational Medicine and Department of Biomedical Engineering at Johns Hopkins University, Baltimore, MD, United States

OPEN ACCESS

Edited by:
Sarah Calaghan,
University of Leeds, United Kingdom

Reviewed by:
Andrew F. James,
University of Bristol, United Kingdom
Alexey V. Glukhov,
University of Wisconsin System, United States

***Correspondence:**
Natalia A. Trayanova
ntrayan1@jhu.edu;
ntrayanova@jhu.edu

Specialty section:
This article was submitted to Cardiac Electrophysiology, a section of the journal Frontiers in Physiology

Received: *31 May 2018*
Accepted: *16 November 2018*
Published: *04 December 2018*

Citation:
Loucks AD, O'Hara T and Trayanova NA (2018) Degradation of T-Tubular Microdomains and Altered cAMP Compartmentation Lead to Emergence of Arrhythmogenic Triggers in Heart Failure Myocytes: An in silico Study. Front. Physiol. 9:1737. doi: 10.3389/fphys.2018.01737

Heart failure (HF) is one of the most common causes of morbidity and mortality worldwide. Although many patients suffering from HF die from sudden cardiac death caused by arrhythmias, the mechanism linking HF remodeling to an increased arrhythmogenic propensity remains incomplete. HF is typically characterized by a progressive loss of transverse tubule (T-tubule) domains, which leads to an altered distribution of L-type calcium channels (LTCCs). Microdomain degradation also causes the disruption of the β_2 adrenergic receptor (β_2AR) and phosphodiesterase (PDE) signaling localization, normally confined to the dyadic space. The goal of this study was to analyze how these subcellular changes affect the function of LTCCs and lead to the emergence of ventricular cell-level triggers of arrhythmias. To accomplish this, we developed a novel computational model of a human ventricular HF myocyte in which LTCCs were divided into six different populations, based on their location and signaling environment they experience. To do so, we included T-tubular microdomain remodeling which led to a subset of LTCCs to be redistributed from the T-tubular to the surface membrane and allowed for different levels of phosphorylation of LTCCs by PKA, based on the presence of β_2ARs and PDEs. The model was used to study the behavior of the LTCC current (I_{CaL}) under basal and sympathetic stimulation and its effect on cellular action potential. Our results showed that channels redistributed from the T-tubular membrane to the bulk of the sarcolemma displayed an altered function in their new, non-native signaling domain. Incomplete calcium dependent inactivation, which resulted in a longer-lasting and larger-in-magnitude LTCC current, was observed when we decoupled LTCCs from ryanodine receptors and removed them from the dyadic space. The magnitude of the LTCC current, especially in the surface sarcolemma, was also increased via phosphorylation by the redistributed β_2ARs and PDEs. These

changes in LTCC current led to the development of early afterdepolarizations. Thus, our study shows that altered LTCC function is a potential cause for the emergence of cell-level triggers of arrhythmia, and that β_2ARs and PDEs present useful therapeutic targets for treatment of HF and prevention of sudden cardiac death.

Keywords: heart failure, computational modeling, early afterdepolarizations, arrhythmia, microdomain degradation

INTRODUCTION

The occurrence of heart failure (HF), a disease currently affecting about 5.7 million Americans, is expected to rise by 46% from 2012 to 2030 as the population ages (Mozaffarian et al., 2016). HF patients are 6 to 9 times more likely to die from sudden cardiac death due to lethal arrhythmias than healthy individuals (Tomaselli and Zipes, 2004). Despite these troubling statistics, the mechanism linking pathophysiological remodeling to arrhythmogenesis in HF patients remains poorly understood. This has resulted in ineffective pharmacological therapy for preventing sudden arrhythmic death and in unsuccessful approaches to arrhythmia risk stratification of HF patients (Stevenson, 2003; Fishman et al., 2010).

Heart failure causes the heart to undergo remodeling across multiple scales (Tomaselli and Marbán, 1999). However, studies have shown that nearly all arrhythmias in non-ischemic HF and approximately 50% of those in ischemic HF develop due to abnormal automaticity or triggered activity such as early afterdepolarizations (EADs) and delayed afterdepolarizations (Rubart and Zipes, 2005).

Previous research has also shown that remodeling at cellular and subcellular levels characteristic of HF can lead to action potential (AP) prolongation and delayed repolarization, which could be important causes of EAD formation. In turn, these changes could be linked to the modification in ion channel behavior, especially the L-type calcium channels (LTCC) whose activity is highly regulated via cAMP by various molecules co-localized in the T-tubular region, and the disruption of intracellular calcium (Ca^{+2}) handling also observed in unhealthy myocytes (Tomaselli and Marbán, 1999; Lyon et al., 2009; Zima et al., 2014). These subcellular changes are often exacerbated by sympathetic stimulation which increases the levels of cAMP and can cause an increase in inward current, particularly through LTCCs. This, in turn, can destabilize the labile plateau phase of APs (Tomaselli and Zipes, 2004). However, the exact mechanism linking changes in T-tubule organization and in cAMP compartmentation to abnormal LTCC function and the development of arrhythmogenic triggers remains unknown.

L-type calcium channels play an important role in excitation–contraction coupling and influence the electrical and mechanical functioning of cardiac muscle (Bryant et al., 2015). In ventricular myocytes, under normal conditions, LTCCs are clustered in the transverse tubules (T-tubules). Gradual T-tubule loss, a known effect of HF, forces LTCCs to be redistributed to the surface membrane where they maintain their function but experience a different environment than that of the dyadic space (Sanchez-Alonso et al., 2016).

Within the T-tubules, LTCCs are usually associated with a number of specific macromolecular signaling complexes and scaffolding proteins which allow for precise control of Ca^{+2} signaling (Bers, 2008; Timofeyev et al., 2013). One such signaling complex is the β_2AR, responsible for mediating the functional effects of cathecolamines in the heart, and more specifically, inside T-tubules, where they are confined. Selective sympathetic stimulation of the two receptor subtypes, β_1AR and β_2AR, lead to distinct physiological responses, based on their different localization and kinetics (Nikolaev et al., 2010). β_1ARs stimulate the cAMP-dependent PKA-mediated phosphorylation of phospholamban and cardiac contractile proteins. Sympathetic stimulation of the β_2AR, on the other hand, activates the G-protein/adenylyl cyclase (AC)/cAMP/PKA pathway which leads to the phosphorylation of several substrates, including LTCCs. In failing cardiomyocytes β_2ARs are redistributed from the T-tubular membrane to the non-T-tubular membrane areas where stimulation of the receptor induces far reaching cAMP signals, similar to those elicited by β_1AR stimulation (Nikolaev et al., 2010; Wright et al., 2014).

Apart from the molecules mentioned above, PDEs, which cleave cAMP into adenosine monophosphate (AMP) and protein phosphatases that dephosphorylate LTCCs also have an effect on the phosphorylation state of LTCCs. Furthermore, PDE molecules also show a high localization to the T-tubule membrane in healthy cells and along with AC and PKA play a key role in controlling the compartmentation of cAMP (Heijman et al., 2011). Activation of PKA by cAMP leads to PDE phosphorylation, increasing its activity, which in turn removes phosphorylation from other molecules. Thus, PDEs provide a negative feedback-loop for cAMP level control. Disrupting the localized PDE expression could lead to increased levels of cellular cAMP and inhibition of the PDE hydrolyzing effect (Wright et al., 2014).

The goal of this study was to uncover the mechanism by which HF-induced changes in cAMP compartmentation combines with the LTCCs T-tubule-to-surface-membrane redistribution to cause an abnormal LTCC current which promotes the development of EADs in human ventricular myocytes. To this end, we developed a novel model, using the O'Hara-Rudy human cardiac ventricular AP formulation (O'Hara et al., 2011) combined with the Heijman and colleagues β-adrenergic signaling simulations (Heijman et al., 2011) as our cornerstone. As the specific aim of this study was to dissect the effects

of β_2AR signaling localization loss and PDE-dependent cAMP level control impairment on the electrophysiological function of the cell, our single-cell model brought together various aspects of microdomain remodeling characteristic to HF, such as LTCC redistribution presented by Sanchez-Alonso et al. (2016), and modified cAMP compartmentation observed experimentally by Nikolaev et al. (2010). Our results show valuable insight into the pathophysiological changes that favor the development of cellular arrhythmogenic triggers in HF patients.

MATERIALS AND METHODS

Overview of the Modeling Approach to Simulate the Behavior of Human HF Ventricular Myocyte

As a baseline model representing the healthy human ventricular myocyte, we used the O'Hara-Rudy human ventricular AP model (O'Hara et al., 2011) combined with the Heijman and coleagues β-adrenergic signaling model (Heijman et al., 2011), as described previously (O'Hara and Rudy, 2012). Within this model, the behavior of the LTCCs is described using a Hodgkin–Huxley formulation, and LTCC calcium dependent inactivation (CDI) depends on the concentration of Ca^{+2} the channels sense. To simulate a human HF ventricular myocyte, we incorporated various changes into the baseline model, reproducing ionic and structural remodeling observed *in vitro*, and described in detail in the sections below.

First, similar to a previous study (Sanchez-Alonso et al., 2016), we introduced T-tubular microdomain loss, resulting in LTCCs and Na^+/Ca^{+2} exchangers (NCXs) being redistributed from the T-tubular membrane to the bulk of the sarcolemma and in RyRs decoupling from LTCCs. However, instead of creating a single model of an HF ventricular myocyte as in the Sanchez-Alonso and colleagues study, we permitted the amount of microdomain loss to vary and thus created a family of HF myocyte models that allowed us to analyze different stages of the disease. The progression of the disease was also modeled by letting the phosphorylation level of the channels to vary based on the presence of β_2ARs and PDEs in both the T-tubular space and in the bulk of the cytoplasm or sarcolemma. The more advanced the stage of the disease was, the more PDE molecules were redistributed from the dyadic space to the bulk of the cytoplasm, and the more β_2ARs were shifted from the T-tubular to the surface membrane. Since LTCCs would display a different behavior based on their location and the signaling domain they experience, we divided LTCCs within a myocyte into six different subgroups (subgroups A–F) based on their position in the T-tubular or surface membrane and their signaling environment, where they may or may not experience the phosphorylating effect of PKA and the hydrolyzing effect of PDEs (**Figure 1**, subgroups A–F). The resulting models containing all LTCC populations were utilized to carry out computer simulations uncovering the mechanisms responsible for the generation of EADs in human HF myocytes under adrenergic stimulation.

Introducing T-Tubular Mirodomain Degradation in HF

The combined O'Hara-Rudy and Heijman model contained LTCCs exclusively in the T-tubular membrane (O'Hara and Rudy, 2012). We used a similar approach to that in Sanchez-Alonso et al. (2016), and allowed for LTCCs to be redistributed to the surface membrane. Thus, in addition to the already defined dyadic volume, we included a sub-sarcolemmal volume which allowed for Ca^{+2} accumulation near the intracellular mouth of LTCCs in the surface membrane. We described fluxes from and into this volume in the O'Hara-Rudy myocyte model (O'Hara et al., 2011) based on the work of Shannon et al. (2004) and Grandi et al. (2010). Similar to Sanchez-Alonso and colleagues, we modeled the relocation of LTCCs to the surface membrane by allowing the redistributed channels to contribute to and sense the Ca^{+2} concentration from the sub-sarcolemmal volume as opposed to that from the dyadic volume for those remaining in the T-tubular membrane. However, to study the progression of the disease, we created multiple models in which T-tubule microdomains were gradually lost. In order to account for this HF-induced T-tubular degradation, we introduced the parameter f_TT in the model and used it to encode T-tubule integrity. The value of this parameter was allowed to range from fully intact (f_TT = 1.0, 0% T-tubule loss) to completely degraded (f_TT = 0.0, 100% T-tubule loss) in increments of 0.1. We then set the fraction of LTCCs that were redistributed from the T-tubule to the surface membrane to be directly proportional to the loss of T-tubules. Thus, when the T-tubular membrane was intact (f_TT = 1.0), all LTCCs were confined to it. In contrast, when the microdomain was completely disrupted (f_TT = 0.0), all LTCCs were redistributed to the surface membrane.

Modeling the Effect of T-Tubular Loss on the Na^+/Ca^{+2} Exchanger and RyRs

Two other molecules affected by the loss of T-tubular domains are the NCX molecules and RyRs. In the original O'Hara-Rudy model, RyRs are always associated with LTCCs from the T-tubular membrane and only a fifth of the NCX are located in the surface membrane, while the rest reside in the T-tubular subspace (O'Hara et al., 2011). We used the same approach as in Sanchez-Alonso and colleagues, and redistributed a fraction of NCXs proportional to the amount of de-tubulation from the T-tubular sites to the sarcolemma based on observations made by Gadeberg et al. (2016). The same fraction, but this time of RyRs, was also decoupled from LTCCs (Sanchez-Alonso et al., 2016).

Representing the Effect of β_2ARs and PDEs Presence on LTCCs

Activation of the β_2AR leads to an increase in adenylyl cyclase (AC) activity which, in turn, increases the levels of cAMP. Next, cAMP binds to the regulatory subunits of PKA, enabling the catalytic subunits to phosphorylate their substrates at specific serine or threonine residues. This signaling cascade is counterbalanced by the hydrolyzing activity of PDEs that degrades cAMP (Heijman et al., 2011). Because there is only one detectable phosphorylation site

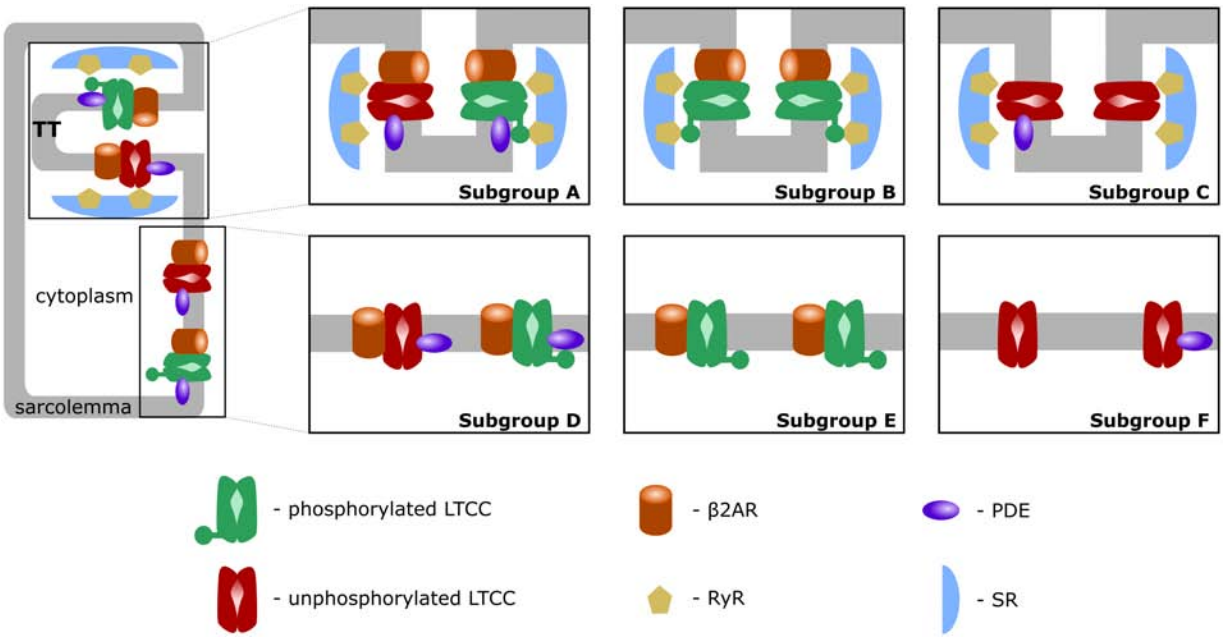

FIGURE 1 | Schematic representation of LTCC subgroups A–F. LTCCs are located either in the T-tubular membrane (subgroups A–C) or in the bulk of the sarcolemma (subgroups D–F). LTCCs were either associated with both β_2ARs and PDEs (subgroups A, D), solely with β_2ARs (subgroups B, E), or not associated with β_2ARs at all (subgroups C, F). The channels were either phosphorylated (red) or unphosphorylated (green).

that allows PKA to regulate LTCCs (Kamp and Hell, 2000), an LTCC can be characterized by one of two conditions: phosphorylated or not phosphorylated. In other words, an LTCC cannot be partially phosphorylated, and phosphorylation can be modeled as a binary process. Based on these observations, we divided all LTCCs within a myocyte into two different populations, phosphorylated and not phosphorylated.

We also introduced two new parameters, f_PDE and f_B2AR to quantify the fractions of LTCCs that experience phosphorylation due to the activation of the β_2AR/G-protein/AC/cAMP/PKA signaling cascade and dephosphorylation due to PDE activity. In other words, localized upregulation of I_{CaL} due to β_2AR stimulation was encoded to affect only a certain proportion of LTCCs, which varied from all LTCCs (f_B2AR = 1.0) to none (f_B2AR = 0.0) in increments of 0.1. Similarly, the hydrolyzing activity of PDEs was allowed to range from affecting no LTCC (f_PDE = 0.0), to affecting all LTCCs (f_PDE = 1.0) in steps of 0.1.

Allowing LTCCs to Function in Different Locations and Signaling Domains

A comprehensive population-based approach in which LTCCs were distributed between the six different subgroups mentioned in the overview and described below was then used to integrate the effects of T-tubule loss and the disruption of β_2AR and PDE signaling localization on the LTCC current in HF myocytes. The Hodgkin–Huxley formulation of LTCC current combines together the number of LTCCs and their conductance in order to obtain a current density for the whole cell. Empirically, no significant changes in LTCC current density have been observed in failing human cardiac myocytes (Piacentino et al., 2003; Chen et al., 2008), which may be due to HF myocytes showing a decrease in LTCC number, paired with an increase of the channel's activity (Bryant et al., 2014). However, in our myocyte model the total number of LTCCs and their conductance were kept constant, each LTCC being assigned a current (I_{CaL}) equal to unity. This assumption was made in order to limit the degrees of freedom of our model, to be able to draw mechanistic insights from the data obtained. If an LTCC was phosphorylated by PKA, the amplitude of the current through that channel was increased by a factor of 2.5 (Heijman et al., 2011). Subgroup A, depicted in **Figure 1**, subgroup A, contains channels identical to the LTCCs found in healthy myocytes: they are located in the T-tubular membrane and experience cAMP levels regulated by both PKA and PDE. In the second group – subgroup B (**Figure 1**, subgroup B), LTCCs located in the T-tubular membrane do not experience the hydrolyzing activity of PDE, so they are assumed to always be phosphorylated. In contrast, the subgroup C of LTCCs (**Figure 1**, subgroup C), which experience the activity of PDE, are assumed to never be phosphorylated as they lack association with β_2ARs. Based on this logic, another subgroup could be defined as the channels lacking both PDE and β_2AR in the T-tubular membrane, but physiologically, these would be indistinguishable from the channels in subgroups C as they would never be phosphorylated. Therefore, we assumed they are also part of subgroup C. The other three groups (subgroups D–F) are similar to the ones just mentioned but are located in the surface cellular membrane as opposed to the T-tubular membrane. The total LTCC current for

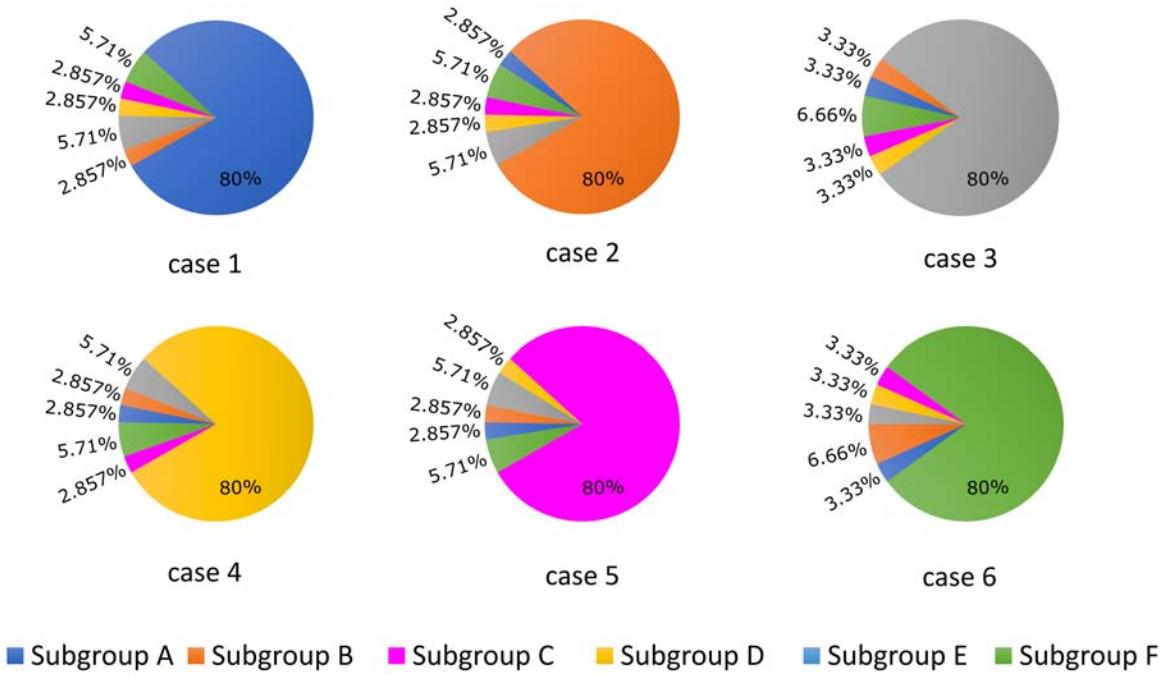

FIGURE 2 | Schematic representation of the LTCC distribution between the six different subgroups (A–F) for each case analyzed (1–6). The total number of LTCCs in the cells from each case was kept constant, but the channels were divided into the six subgroups in the ratios displayed. In case 1, 80% of the channels are located inside the T-tubular membrane, while the remaining ones were distributed to the remaining subgroups based on their probability to be associated with PDEs and β_2ARs. In case 2, the dominant channel population was represented by channels located in T-tubules, lacking PDE association, while in case 3, the majority of channels were also located in the T-tubular membrane, but were not associated with β_2ARs. Cases 4, 5, and 6 are similar to cases 1, 2, and 3, but their dominant channel populations are located in the surface sarcolemma.

a cell was calculated as the sum of the currents passing through each channel population.

The Effects of Phosphorylation on Other Molecules

A similar population-based approach was used to represent the degree of PKA phosphorylation, in the presence or absence of β_2AR stimulation, of seven different targets: RyR, Phospholamban (PLB), Slow Delayed Rectifier K^+ Current (I_{Ks}), Fast Na^+ Current (I_{Na}), Na^+/K^+ATPase Current (I_{NaK}), rapidly activating K^+ current (I_{Kur}) and Troponin I (TnI).

Assuming that channel gating has no effect on phosphorylation, the molecules mentioned above can have only two distinct conformations (phosphorylated and non-phosphorylated). Therefore, each of the seven phosphorylation targets were divided into two subgroups: phosphorylated and not phosphorylated. The effect of phosphorylation on each target, as described by Heijman et al. (2011), was included in the model. Basal conditions were modeled to account for the phosphorylation of 25% of targets while β_2AR stimulation led to the phosphorylation of 75% of each substrate population. These values were chosen in order to obtain LTCC current traces in the healthy myocytes similar to those experimentally recorded and presented by Bryant et al. (2014). In order to be as physiologically accurate as possible, the model also accounted for CaMKII-dependent phosphorylation of I_{CaL}, I_{Na} and late I_{Na} ($I_{Na,L}$) based on recently published data (Sanchez-Alonso et al., 2016). For each of these molecules it was assumed that PKA and CaMKII phosphorylation are independent processes. Therefore, the targets were divided into four populations. At each time step, the currents through the LTCCs and I_{Na} channels were computed for both (phosphorylated and non-phosphorylated) populations. The total current was obtained by adding together the currents through each population and thus integrating the β_2AR and CaMKII cascades. While the level of PKA phosphorylation varied for the purpose of this study, the CaMKII phosphorylation level was kept constant.

I_{CaL} and Action Potential Duration (APD) Analysis Protocol

APD_{90} was computed as the time point of 90% repolarization of the membrane potential minus the time point of maximal upstroke velocity $(dV/dt)_{max}$. For the first part of the study, we established six different cases (cases 1–6) in which 80% of LTCCs within a cell were assigned to one of each of the six subgroups described above and in **Figure 1**, and for each case the remaining channels were distributed between the other five subgroups (**Figure 2**). This allowed us to observe and analyze separately the effects of LTCC redistribution, loss of β_2AR signaling localization, and PDE's impaired control of cAMP on the LTCC current and APD_{90}. The model myocyte was first allowed to reach steady state under a voltage clamp of −96.7 mV. To determine the effect

of each parameter (f_TT, f_B2AR, and f_PDE) on the LTCC current, the membrane voltage was then stepped up from −96.7 to −6.7 mV, clamped again, and the LTCC current was recorded. In order to analyze the effect of the same parameters on APD_{90}, the myocyte was paced at near resting pacing rates (1000 ms, 60 bpm) until steady state was reached; the following three beats were recorded.

Protocol for Evaluating EADs in the Human Ventricular AP Model

The same protocol used to analyze APD_{90}, was also used to investigate how the model variables drive the emergence of EADs. The myocyte was again paced at near resting pacing rates (1000 ms, 60 bpm) until steady state was reached and the following 15 beats were recorded. For this part of the study, LTCCs were distributed into the six different subgroups represented in **Figure 1** by varying the model variables f_TT, f_B2AR, and f_PDE. The probability that an LTCC was corresponding to one of the subgroups was computed by multiplying these state variables. The procedure was repeated for values of f_TT and f_PDE uniformly covering the range of possible values from 0.0 to 1.0 in increments of 0.1, and for values of the f_B2AR ranging from 0.0 to 1.0 in increments of 0.25. The APs generated both in the presence and absence of adrenergic stimulation were analyzed.

RESULTS

HF Remodeling Leads to a Higher Amplitude, Longer Lasting LTCC Current

The LTCC current traces from the cases outlined in **Figure 2** are plotted in **Figure 3** under both basal and adrenergic stimulation conditions. The control case (**Figure 3**, case 1 – black) was represented by the LTCC current in the healthy myocyte with intact tubulation as well as localization of β_2AR and PDE activity. LTCC current decay was rapid, especially in the T-tubules (τ_1 = 18.7 ms, τ_2 = 318.3 ms), due to the strong CDI caused by the accumulation of Ca^{+2} in the dyadic volume of the model. β_2AR stimulation in the control case led to an increase in the magnitude of LTCC current and a faster decay rate (τ_1 = 18.3 ms, τ_2 = 257 ms), as compared to the basal conditions (**Figure 3**, case 1 – red). The effect of PDE on controlling cAMP levels and thus LTCCs level of phosphorylation was evaluated by removing PDE from the model (**Figure 3**, case 2). Although this change had little to no effect for the case with basal PKA phosphorylation (black), it considerably increased LTCC current peak when adrenergic stimulation was applied (red). This showed that PDE has a protective role that helps lower inward LTCC current, as PKA activity was not inhibited at all by the hydrolyzing activity of PDE on cAMP. Removing all β_2ARs led to smaller currents as PKA did not phosphorylate any channel (**Figure 3**, case 3). In the control case, when tubulation was removed and LTCCs shifted to the surface membrane (**Figure 3**, case 4), Ca^{+2} was not able to accumulate in significant amounts in the proximity of the LTCCs. Thus CDI was delayed, peak current was elevated, and I_{CaL} inactivation rate was lower (τ_1 = 29.0 ms, τ_2 = 3392 ms). Applying β_2AR stimulation in this case led to an even larger in magnitude and slower current (**Figure 3**, case 4 – red), and removing PDE further exacerbated this effect (**Figure 3**, case 5). Removing T-tubules when β_2ARs were absent (**Figure 3**, case 6) led to a slower decaying current, of similar magnitude to that in fully tubulated cells. Overall, subcellular changes associated with the HF phenotype, such as de-tubulation, LTCC redistribution to the surface membrane, and loss of β_2AR and PDE signaling localization, led to an increase of the LTCC peak current and a delay in the channels' inactivation.

HF Remodeling Leads to Altered SR Ca Release and Ca Transient

For each of the cases described above, the Ca^{+2} flux from the SR into the cytoplasm through RyRs is plotted in **Figure 4** and the Ca^{+2} concentration inside the cytoplasm in **Figure 5**. When adrenergic stimulation is applied, the β_2AR/G-protein/AC/cAMP/PKA signaling cascade is triggered, which leads to the phosphorylation of RyRs along with LTCCs. Thus, not only do RyRs experience a higher Ca^{+2} concentration in the dyadic space due to the phosphorylation of LTCCs, but their activity is also enhanced by direct PKA phosphorylation, leading to a higher Ca^{+2} flux from the SR into the cytoplasm (**Figure 4**). However, due to the higher Ca^{+2} concentration inside the dyadic space, RyRs deactivate faster under adrenergic conditions, and the Ca^{+2} concentration inside the cytoplasm does not differ greatly between baseline and adrenergic stimulation conditions in intact myocytes (**Figure 5**). The β_2AR enhancing effect on Ca^{+2} release appears stronger when the microdomain is degraded. By removing T-tubules, we disrupt the association between LTCCs and RyRs within the dyadic space. Removing T-tubules and relocating LTCCs from the dyadic space to the surface of the membrane leads to a lower Ca^{+2} concentration within the dyadic volume, and a weaker release of Ca^{+2} from the SR into the cytoplasm. While completely removing β_2AR molecules in the intact HF myocyte model leads to a lower amount of Ca^{+2} being released via RyRs in, it has the opposite effect in de-tubulated cells (**Figure 4**). This is explained by the fact that LTCCs in the surface membrane experience CaMKII phosphorylation, while those in the T-tubular membrane do not (Sanchez-Alonso et al., 2016). Overall, the Ca^{+2} concentration inside intact myocytes is higher than that in de-tubulated cells due to higher LTCC current through T-tubular channels, and an increase in the flux of Ca from the SR into the cytoplasm.

Changes in I_{CaL} and RyR Function Impact the NCX Current

The NCX (INaCa) current traces from the cases outlined in **Figure 2** are plotted in **Figure 6** under both basal and adrenergic stimulation conditions. Similar to the re-distributed LTCCs, NCX molecules which shifted to the surface membrane experience the Ca^{+2} concentration from the sub-sarcolemmal volume. Under baseline conditions, microdomain loss lead to a small decrease in I_{NaCa} corresponding to a lower SR Ca release and an overall lower Ca^{+2} transient. However, similar to

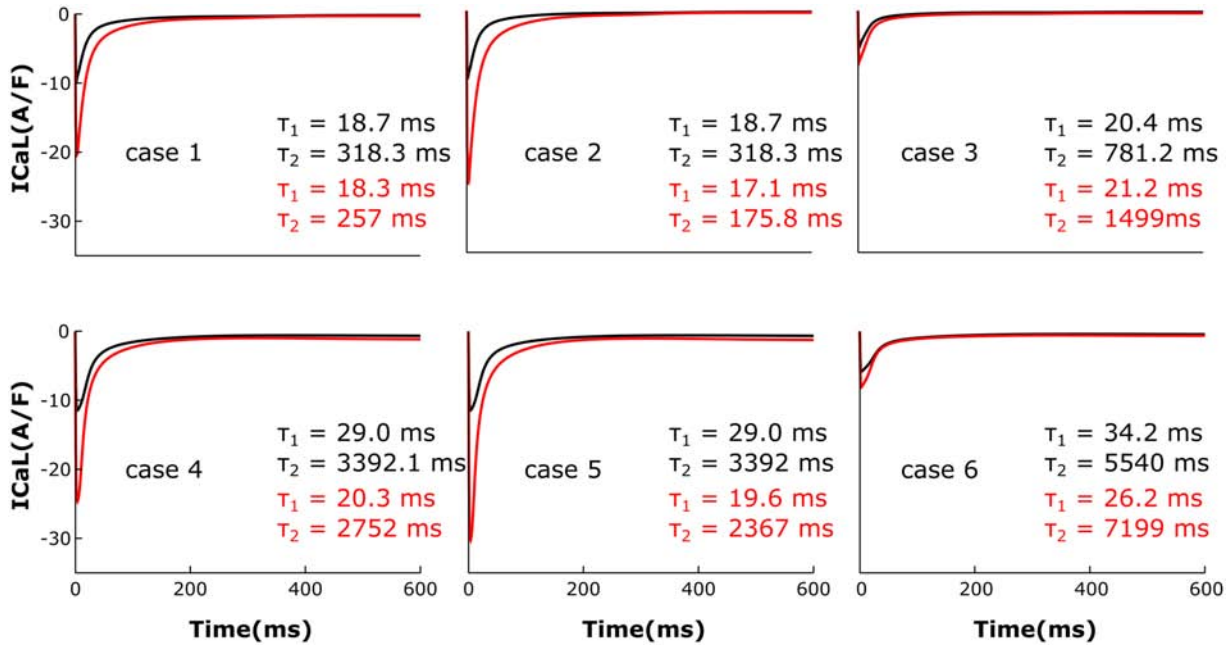

FIGURE 3 | The effect of microstructure remodeling on LTCC current. Total LTCC current was plotted over time from cells corresponding to cases 1–6 described in methods, under both basal (black) and sympathetic stimulation (red) conditions. The decay time constants for the current through the channels in the T-tubules and the ones in the bulk of the sarcolemma were displayed as τ_1 and τ_2.

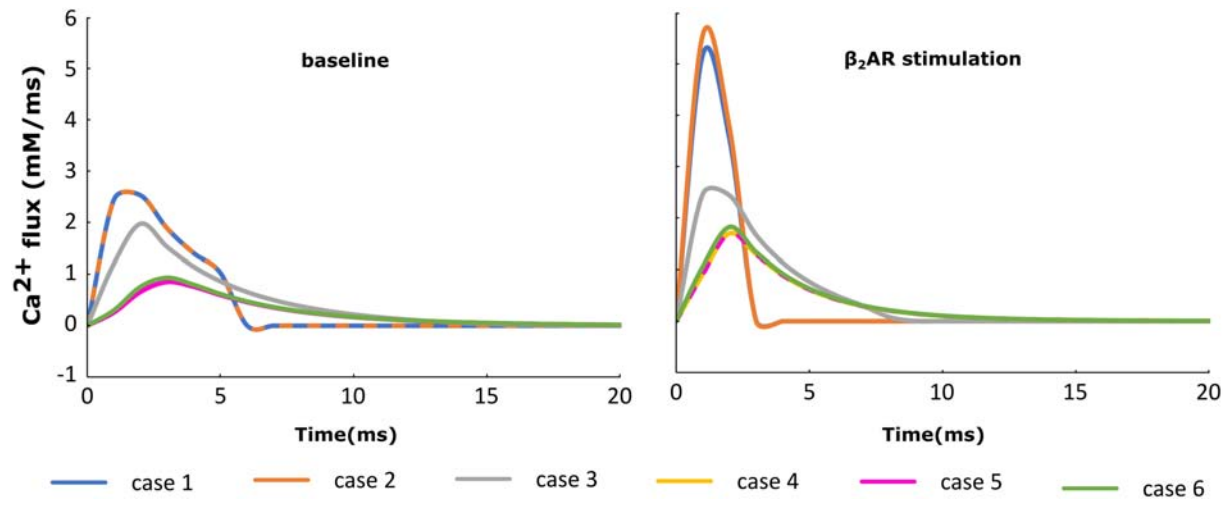

FIGURE 4 | The effect of microstructure remodeling on SR Ca^{+2} release. The Ca^{+2} flux from the SR into the cytoplasm via RyRs was plotted over time from cells corresponding to cases 1–6, under both basal **(left)** and sympathetic stimulation **(right)** conditions.

I_{CaL}, under adrenergic stimulation I_{NaCa} displayed an increase in amplitude when the myocyte underwent de-tubulation, but not a slowdown in decay rate. These results can be explained based on the observations we made before on RyR and LTCC function. NCX is an antiport driven by the concentration gradients of Ca^{+2} and Sodium. A high amplitude I_{CaL} within a de-tubulated cell leads to a high concentration of Ca inside the sub-sarcolemmal volume which in turn causes a steep gradient between the inside and outside of the cell. Thus, we observe a high amplitude I_{NaCa} under adrenergic stimulation in the HF myocyte, which in theory should lead to APD shortening.

Abnormal LTCC Current Affects APD_{90}

We then analyzed the effect of varying the parameters encoding for T-tubule integrity, β_2AR and PDE on AP shape and duration. The membrane potential corresponding to the six cases described above was plotted in **Figure 7**. For the control case under

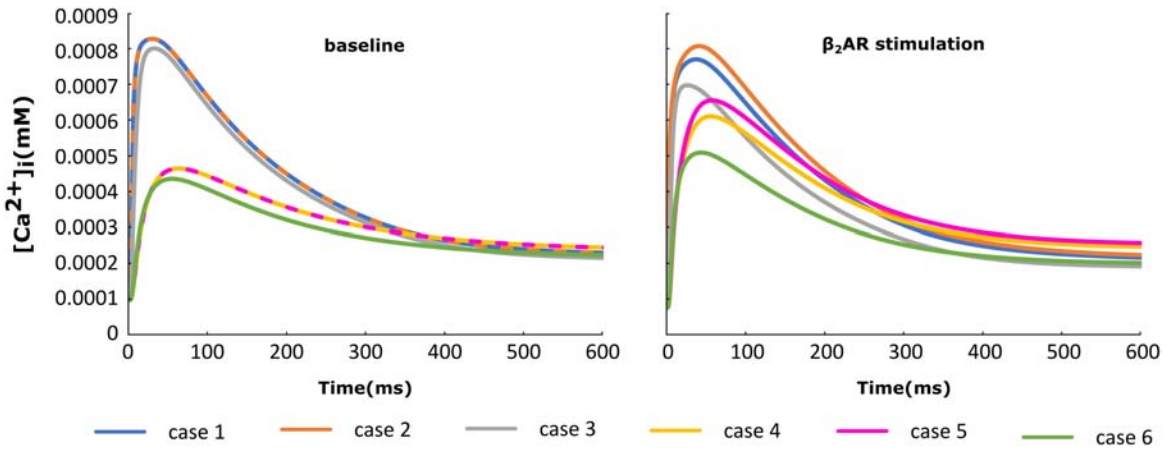

FIGURE 5 | The effect of microstructure remodeling on Ca^{+2} transient. The Ca^{+2} concentration inside the cytoplasm was plotted over time from cells corresponding to cases 1–6 described in methods, under both basal **(left)** and sympathetic stimulation **(right)** conditions.

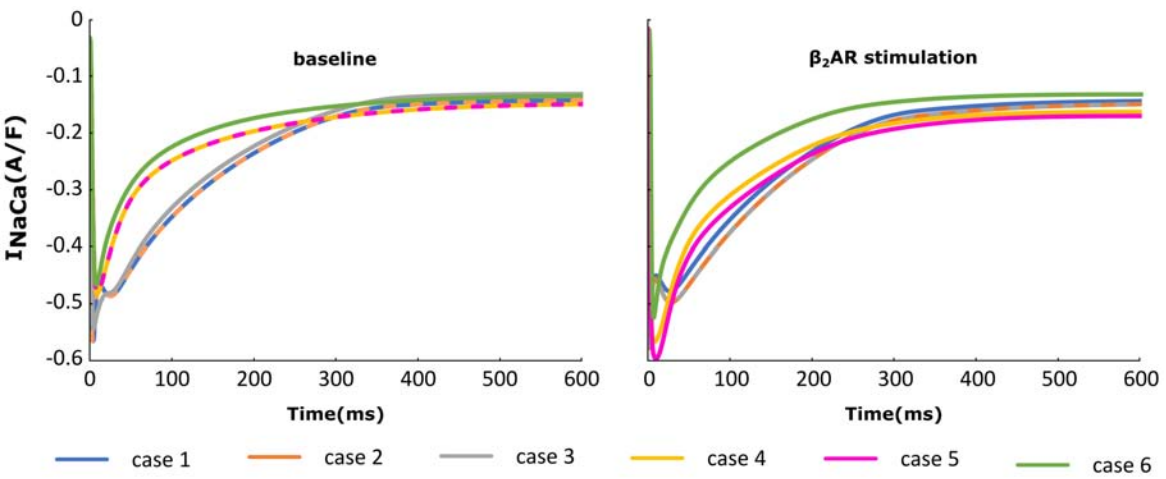

FIGURE 6 | The effect of microstructure remodeling on I_{NaCa} current. The I_{NaCa} current was plotted over time from cells corresponding to cases 1–6, under both basal **(left)** and sympathetic stimulation **(right)** conditions.

no adrenergic stimulation, an APD_{90} of 281 ms was recorded. Adding β_2AR stimulation lead to an increase and slower decay rate in the LTCC current, which caused a slight prolongation of APD_{90} to 308 ms (**Figure 7**, case 1). Removing PDEs from the model and applying β_2AR stimulation caused the emergence of single EADs in intact myocytes (**Figure 7**, case 2). Removing all β_2ARs from the model, on the other hand, had the opposite effect, preventing EADs and causing APD_{90} to shorten (**Figure 7**, case 3). When tubulation was removed from the control case, and no adrenergic stimulation applied, the observed increase in LTCC current led to a corresponding 44 ms APD_{90} prolongation.

The effect of β_2-stimulaton was significantly stronger in the absence of T-tubules resulting in an APD_{90} of 517/668 ms and the development of multiple EADs (**Figure 7**, case 4). However, in de-tubulated myocytes, applying adrenergic stimulation while lacking PDE led to an oscillatory state in which the cells did not repolarize before the next stimulus was applied (**Figure 7**, case 5). Removing all β_2ARs from the de-tubulated model prevented EAD formation (**Figure 7**, case 6).

Effects of De-tubulation and β_2AR Loss on APD_{90}

Lastly, we analyzed how gradual changes in the amount of de-tubulation as well as β_2AR and PDE signaling localization affect APD_{90} and EAD development. The heatmaps in **Figure 8** were plotted in order to quantify how each of these variables impacts APD_{90} and EAD formation. The results demonstrate that EADs occurred only under adrenergic stimulation. Moreover, the loss of PDE control of cAMP in the dyadic space also contributed to the emergence of EADs.

No EADs formed when only 25% of the β_2ARs were present. When 50% of the β_2ARs were present EADs emerged either in fully de-tubulated cells, or in cells that lacked more than

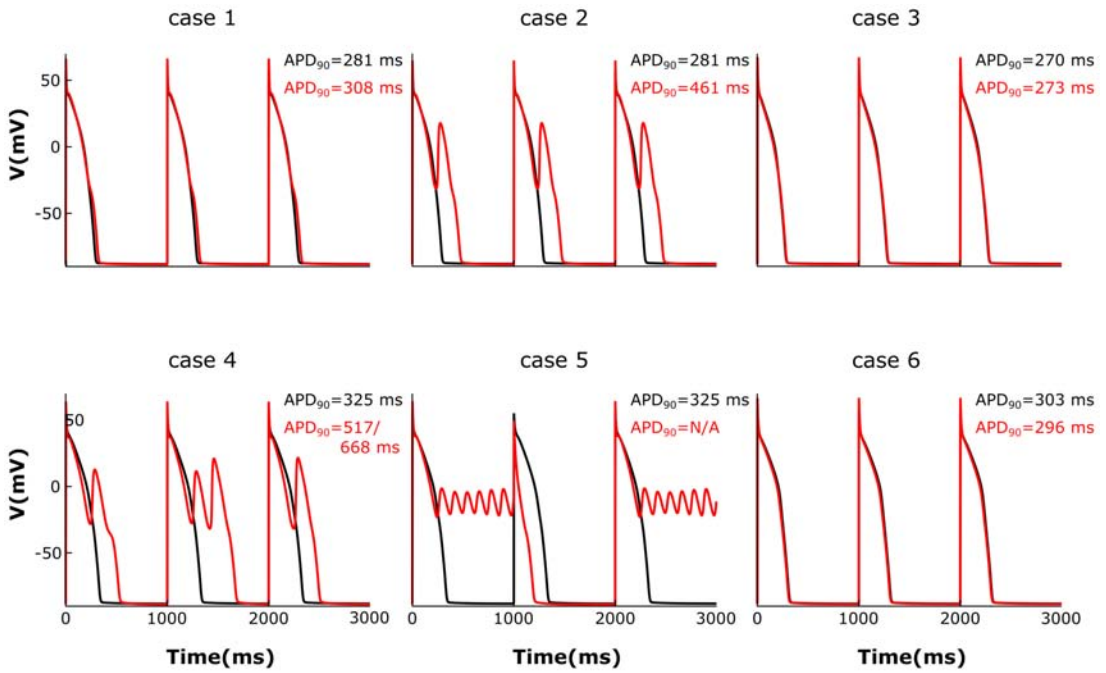

FIGURE 7 | The effect of microstructure remodeling on membrane voltage and APs. The membrane potential of cells from cases 1–6 is plotted over time under both basal (black) and sympathetic stimulation (red) conditions. EADs emerged only under sympathetic stimulation in the cells where most LTCCs were either located in the T-tubules and lacking PDEs **(case 2)**, or they were in the surface membrane and experienced the effect of both β_2ARs and PDEs **(case 4)**. When most LTCCs were located in the bulk of the sarcolemma and were not associated with PDEs **(case 5)**, the cells were not able to repolarize and remained in an oscillatory state until the next stimulus was applied.

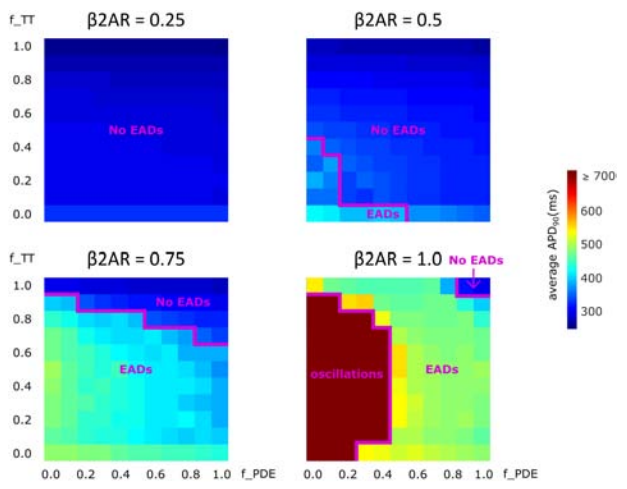

FIGURE 8 | The effect of microstructure remodeling on APD_{90} and EAD emergence. Heatmaps of the average APD_{90} under sympathetic stimulation for four fixed values of the f_B2AR parameter. The cells range from intact (f_TT = 1.0) to fully de-tubulated (f_TT = 0.0), and PDEs range from present and fully functional (f_PDE = 1.0) to completely absent (f_PDE = 0.0). EAD occurrence and oscillation behavior were also represented.

20% of their PDE. In all the other cells, APDs appeared to increase proportionally to PDE and tubulation loss but no arrhythmogenic triggers were observed. The same trend was detected when the amount of functional β_2AR molecules was increased to 75%. In this case, we observed more frequent EAD emergence, while the presence of intact tubulation and PDE had a protective effect. When all β_2ARs were present and functional, the model generated membrane potential oscillations for most cells that were lacking more than 60% of their initial T-tubules. EADs were obtained in almost all other cases, except the one in which tubulation was intact and at least 90% of PDEs were present. Thus, the presence of PDE molecules had a protecting effect, opposing APD_{90} prolongation and in some cases inhibiting EAD development.

DISCUSSION

Findings and Significance

Because HF electrophysiological remodeling is such a complex phenomenon (Tomaselli and Marbán, 1999), for the purpose of this computational study we used simulations to model and integrate only the structural changes described above. There are multiple other aspects described in Limitations that could be introduced in subsequent studies. Thus, the goal of this project was to elucidate the mechanisms by which subcellular changes in cardiac myocytes lead, via altered LTCC function, and under adrenergic stimulation, to the generation of cellular-level triggers of arrhythmia in human HF. To accomplish this goal, we developed a new

ventricular myocyte computational approach that integrated various known characteristics of HF and allowed us to vary their severity. The model included the effects of microdomain remodeling on LTCC as in Sanchez-Alonso et al. (2016), as well as novel developments incorporating β_2AR stimulation, and arrhythmogenic remodeling of β_2 adrenergic signaling, as well as impaired control of cAMP levels due to altered PDE localization. We found that redistribution of the LTCCs combined with an enhanced phosphorylation of the channel due to abnormally high cAMP levels caused increases in LTCC current magnitude and duration. This resulted in AP prolongation and the development of single EADs, multiple EADs, or oscillations, depending on the amount of remodeling present.

Transverse Tubules Loss in HF

The T-tubule system plays a vital role in normal ventricular cell function. Its structure and distribution are responsible for the rapid electric excitation, and the initiation and synchronous triggering of Ca^{+2} release from the sarcoplasmic reticulum (SR). The increase in Ca^{+2} levels throughout the cytoplasm leads to the coordinated contraction of all contractile units inside a cell (Wei et al., 2010). Scanning ion conductance microscopy (SICM) and fluorescence staining experiments have shown that ventricular myocytes obtained from HF patients are characterized by a decrease in T-tubule density (Lyon et al., 2009; Wei et al., 2010). This change in surface topography has been shown to take place gradually as the cardiac muscle transitions from hypertrophy to HF and to have a negative impact of excitation–contraction coupling (Wei et al., 2010). Song and colleagues proposed that this deleterious effect is due to the reorganization of subcellular microdomains, which force RyRs to decouple from their partner LTCC and become orphaned. Thus Ca^{+2} ions flowing through the LTCCs fail to bind to RyRs and do not cause further Ca^{+2} release from the SR (Song et al., 2006). Other studies have shown that in HF, the loss of T-tubule microdomains is usually complemented by a spatial redistribution of LTCCs from the T-tubule membrane to the bulk of the sarcolemma, where they experience a different signaling environment (Sanchez-Alonso et al., 2016). Finally, work by Kawai et al. (1999) and Bryant et al. (2014) showed that complete myocyte de-tubulation is associated with reduction in I_{CaL} and shortening of APD. Taken together, the findings of these previous experimental studies suggest that altered LTCC function is a likely candidate for the mechanism linking T-tubule microdomain loss to the emergence of arrhythmogenic triggers in ventricular HF myocytes.

A novel aspect of our simulation approach lies in the fact that instead of creating a single model, by varying the amount of remodeling we obtained a family of models which allowed us to get an accurate depiction of the implications of T-tubule and cAMP compartmentalization loss in HF. By using this approach, we were able to analyze the effects of T-tubular loss alone, as well as in conjunction with a few other pathophysiological changes previously observed in HF in a setting that resembled the progression of the disease. Because our study showed an increase in I_{CaL} and APD due to de-tubulation, it appears that our results are at odds with the results by Kawai et al. (1999) and Bryant et al. (2015). However, that is not the case. The difference in our results comes mainly from the way we define de-tubulation and the exact distribution of channels between the T-tubular and the bulk of the sarcolemma. In our study, we view T-tubular microdomain disruption as a gradual process which slowly advances as HF progresses, similar to the changes that the myocytes from the above-mentioned studies undergo after coronary artery ligation (CAL). We are not trying to reproduce the data from a specific phase of the disease, as that would be impossible without introducing all the aspects of HF electrophysiological remodeling, but rather analyze the specific changes caused by gradual de-tubulation and cAMP re-distribution. If we compare one of our myocyte models constructed using the same ratio of channels in the T-tubular membrane vs. the bulk of the sarcolemma as in the CAL myocytes from the Bryant and colleagues, with what would be the equivalent of a healthy human myocyte in the Sanchez-Alonso and colleagues study (Sanchez-Alonso et al., 2016), we get similar whole cell I_{CaL} current density (data not shown). However, because in their study de-tubulation is defined as a fast, chemical process which completely removes all T-tubular microdomain, and in our model de-tubulation is a slow process which allows the channels to relocate to the surface membrane, our results are different when we analyze de-tubulation. We could partially replicate their results if we completely eliminated the T-tubular component of I_{CaL}.

Furthermore, even though our results show an increase in I_{CaL} density due to HF when there are no experimental studies in humans showing that, we have to keep in mind that I_{CaL} peak and density seem to vary in HF from study to study (Tomaselli and Marbán, 1999), and *in-silico* studies don't always match the experimental ones (Elshrif et al., 2015) when it comes to this issue. However, our results do reflect the most common change in I_{CaL} morphology caused by HF which is a slowing of the decay of the whole-cell current. Thus, our findings are consistent with the findings described above. They reproduce the change in I_{CaL} shape, add new insight about different stages of the disease, and highlight the existence of a threshold of T-tubule integrity that can predict the development of cellular level triggers of arrhythmia, as seen in **Figure 8**.

The Role of β_2AR and PDE Signaling Localization Loss in EAD Development

Another hallmark of HF is βAR desensitization. Wright and colleagues showed, by combining a nanoscale SICM with a fluorescence resonance energy transfer (FRET) approach, that in healthy ventricular myocytes β_2AR-induced cAMP signals were highly localized within the T-tubular domain (Wright et al., 2014). Heijman and colleagues used a computational model to describe in great detail the quantitative contribution of various molecules, including LTCCs, and the effects of the above mentioned signaling localization in adrenergic stimulation (Heijman et al., 2011). In HF myocytes, sympathetic

stimulation of β_2AR appears to result in diffused, far reaching cAMP signals, which resembled those obtained via β_1AR stimulation. This suggests that similar to LTCCs, β_2ARs also change location from the T-tubular membrane to the surface membrane when tubulation is lost (Nikolaev et al., 2010). In addition, Lang and colleagues demonstrated that during end-stage HF, β_2AR stimulation leads to heterogeneities in APD and arrhythmogenic activity (Lang et al., 2015). In our study, we were able to control the degree of both PDE and β_2AR loss of function and redistribution and to analyze how it influences the electrophysiological functioning of the myocytes in HF, and specifically, LTCC function. Completely blocking β_2AR function in the model did not lead to abnormal LTCC current, nor to EAD occurrence. This is consistent with the fact that ligand binding failed to trigger a signaling cascade, and LTCCs were never phosphorylated (βAR desensitization). It also explains why adrenergic blockers work well as antiarrhythmic agents. When the β_2AR molecules were allowed to maintain partial functionality, but lost their localization, significant increases in LTCC current magnitude and APD_{90} as well as EAD development were observed. Moreover, when all β_2AR molecules were present, instead of EADs, the cells displayed an oscillatory behavior in which the membrane potential did not return to its baseline value. This is a biological phenomenon also recorded in isoprenaline perfused rabbit ventricular cardiomyocytes affected by long QT syndrome and thought to lead to sudden cardiac death (Liu et al., 2012). These changes were opposed by the presence of PDE, which appears to have a protective, anti-arrhythmogenic effect. The new mechanistic insights presented here show that the binding of the ligand to functional, redistributed β_2ARs causes a cAMP signal propagation and amplification throughout the cell, which leads to the phosphorylation of multiple LTCCs across the cell membrane. Phosphorylated LTCCs have a higher open probability, which leads to a higher magnitude LTCC current, causing APD_{90} prolongation and EAD development.

CONCLUSION

Altered LTCC current is a major factor in the process linking microstructural remodeling to the increased risk of cellular arrhythmia triggers development in HF patients. Our results show that the disruption of subcellular microdomains and the redistribution of LTCCs, PDEs, and β_2ARs cause a higher-magnitude and longer-lasting LTCC current, which delays cellular repolarization. APs are thus prolonged and upon sympathetic stimulation, EADs may arise. These findings provide important insight into the mechanism underlying the development of cellular level triggers of arrhythmia in human HF and suggest β_2ARs and PDEs as possible targets for future therapies and preventive treatments of ventricular arrhythmia.

Limitations

Our study has several limitations. HF remodeling is a very complex process with many unknowns. Our model thus had various assumptions. First, in the lack of experimental evidence otherwise, we assumed that the LTCCs remaining in the T-tubular membrane in HF are fully functional; even super-resolution scanning patch clamp studies such as the one presented by Sanchez-Alonso et al. (2016) cannot measure LTCC activity deep inside the T-tubule system. Secondly, in order to be able to draw mechanistic insight, we limited the degrees of freedom of our model by keeping both the number of LTCCs as well as their conductance constant. This may be at odds with observations by Bryant and colleagues which suggest that in HF, myocytes show a decrease in the number of LTCCs and an increase in their activity (Bryant et al., 2014). Also, our model focused exclusively on the activity of LTCC channels in HF, and did not include changes in other currents such as $I_{Na,L}$, I_{Ks}, and I_{Kr} which are also affected by HF remodeling. Due to limited data on PKA-mediated phosphorylation of LTCCs in HF, we had to make approximations regarding the fraction of channels phosphorylated under baseline conditions and under adrenergic stimulation. Moreover, our study focuses exclusively on the effect of microdomain loss on β_2AR, based on previous studies showing that HF leads to the re-distribution of these receptors which in turn affects the activity of LTCCs (Nikolaev et al., 2010), although β_1AR stimulation is the major receptor mediating the effects of sympathetic stimulation of the heart. This could be explored in greater depth in future work. CaMKII-dependent phosphorylation of different channels was also included in the model, but as our study focused solely on the effect of sympathetic stimulation and PKA-dependent phosphorylation of LTCCs, CaMKII remodeling was not implemented. Since PDE acts as a negative feedback-loop for cAMP level control, the model assumed that PDE-mediated cAMP degradation is a process activated by PKA and thus PDE should only be active under sympathetic stimulation when PKA levels are increased. Lastly, the present study focused on single cell behavior; thus, it is possible that the results can be modulated by the effect of cell coupling on the susceptibility of cells to form EADs, as described by Xie et al. (2010).

AUTHOR CONTRIBUTIONS

AL helped design the experiments, performed the simulations, and wrote the manuscript. TO guided the design of the experiments. NT supervised the project and edited the manuscript.

FUNDING

This work was supported by grants from the National Institutes of Health (HL126802) and the Fondation Leducq to NAT, and the Gakenheimer fellowship to ABL.

REFERENCES

Bers, D. M. (2008). Calcium cycling and signaling in cardiac myocytes. *Annu. Rev. Physiol.* 70, 23–49. doi: 10.1146/annurev.physiol.70.113006.100455

Bryant, S., Kimura, T. E., Kong, C. H. T., Watson, J. J., Chase, A., Suleiman, M. S., et al. (2014). Stimulation of ICa by basal PKA activity is facilitated by caveolin-3 in cardiac ventricular myocytes. *J. Mol. Cell. Cardiol.* 68, 47–55. doi: 10.1016/j.yjmcc.2013.12.026

Bryant, S. M., Kong, C. H. T., Watson, J., Cannell, M. B., James, A. F., and Orchard, C. H. (2015). Altered distribution of ICa impairs Ca release at the t-tubules of ventricular myocytes from failing hearts. *J. Mol. Cell. Cardiol.* 86, 23–31. doi: 10.1016/j.yjmcc.2015.06.012

Chen, X., Zhang, X., Harris, D. M., Piacentino, V., Berretta, R. M., Margulies, K. B., et al. (2008). Reduced effects of BAY K 8644 on L-type calcium current in failing human cardiac myocytes are related to abnormal adrenergic regulation. *Am. J. Physiol. Heart Circ. Physiol.* 294, H2257–H2267. doi: 10.1152/ajpheart.01335.2007

Elshrif, M. M., Shi, P., and Cherry, E. M. (2015). Representing variability and transmural differences in a model of human heart failure. *IEEE J. Biomed. Health Inform.* 19, 1308–1320. doi: 10.1109/jbhi.2015.2442833

Fishman, G. I., Chugh, S. S., Dimarco, J. P., Albert, C. M., Anderson, M. E., Bonow, R. O., et al. (2010). Sudden cardiac death prediction and prevention: report from a national heart, lung, and blood institute and heart rhythm society workshop. *Circulation* 122, 2335–2348. doi: 10.1161/CIRCULATIONAHA.110.976092

Gadeberg, H. C., Bryant, S. M., James, A. F., and Orchard, C. H. (2016). Altered Na/Ca exchange distribution in ventricular myocytes from failing hearts. *Am. J. Physiol. Heart Circ. Physiol.* 310, H262–H268. doi: 10.1152/ajpheart.00597.2015

Grandi, E., Pasqualini, F. S., and Bers, D. M. (2010). A novel computational model of the human ventricular action potential and ca transient. *J. Mol. Cell. Cardiol.* 48:112. doi: 10.1016/j.yjmcc.2009.09.019

Heijman, J., Volders, P. G. A., Westra, R. L., and Rudy, Y. (2011). Local control of β-adrenergic stimulation: effects on ventricular myocyte electrophysiology and Ca +2-transient. *J. Mol. Cell. Cardiol.* 50, 863–871. doi: 10.1016/j.yjmcc.2011.02.007

Kamp, T. J., and Hell, J. W. (2000). Regulation of cardiac L-type calcium channels by protein kinase a and protein kinase c. *Circ. Res.* 87, 1095–1102. doi: 10.1161/01.RES.87.12.1095

Kawai, M., Hussain, M., and Orchard, C. H. (1999). Excitation-contraction coupling in rat ventricular myocytes after formamide-induced detubulation. *Am. J. Physiol.* 277, H603–H609. doi: 10.1152/ajpheart.1999.277.2.h603

Lang, D., Holzem, K., Kang, C., Xiao, M., Jin, H., Ewald, G. A., et al. (2015). Arrhythmogenic remodeling of β2 versus β1 adrenergic signaling in the human failing heart. *Circ. Arrhythm. Electrophysiol.* 8, 409–419. doi: 10.1161/CIRCEP.114.002065.Arrhythmogenic

Liu, G. X., Choi, B. R., Ziv, O., Li, W., de Lange, E., Qu, Z., et al. (2012). Differential conditions for early after-depolarizations and triggered activity in cardiomyocytes derived from transgenic LQT1 and LQT2 rabbits. *J. Physiol.* 590, 1171–1180. doi: 10.1113/jphysiol.2011.218164

Lyon, A. R., Macleod, K. T., Zhang, Y., Garcia, E., Kanda, G. K., Lab, M. J., et al. (2009). Loss of T-tubules and other changes to surface topography in ventricular myocytes from failing human and rat heart. *Proc. Natl. Acad. Sci. U.S.A.* 106, 6854–6859. doi: 10.1073/pnas.0809777106

Mozaffarian, D., Benjamin, E. J., Go, A. S., Arnett, D. K., Blaha, M. J., Cushman, M., et al. (2016). Heart disease and stroke statistics-2016 update:a report from the american heart association. *Circulation* 133:e38–360. doi: 10.1161/CIR.0000000000000350

Nikolaev, V. O., Moshkov, A., Lyon, A. R., Miragoli, M., Novak, P., Paur, H., et al. (2010). B2-adrenergic receptor redistribution in heart failure changes cAMP compartmentation. *Science* 327, 1653–1657. doi: 10.1126/science.1185988

O'Hara, T., and Rudy, Y. (2012). Arrhythmia formation in subclinical ("silent") long QT syndrome requires multiple insults: quantitative mechanistic study using the KCNQ1 mutation Q357R as example. *Heart Rhythm* 9, 275–282. doi: 10.1016/j.hrthm.2011.09.066

O'Hara, T., Virág, L., Varró, A., and Rudy, Y. (2011). Simulation of the undiseased human cardiac ventricular action potential: model formulation and experimental validation. *PLoS Comput. Biol.* 7:e1002061. doi: 10.1371/journal.pcbi.1002061

Piacentino, V. III., Weber, C. R., Chen, X., Weisser-Thomas, J., Margulies, K. B., Bers, D. M., et al. (2003). Cellular basis of abnormal calcium transients of failing human ventricular myocytes. *Circ. Res.* 92, 651–658. doi: 10.1161/01.res.0000062469.83985.9b

Rubart, M., and Zipes, D. P. (2005). Mechanisms of sudden cardiac death. *J. Cllin. Invest.* 115, 2305–2315. doi: 10.1172/JCI26381

Sanchez-Alonso, J. L., Bhargava, A., O'Hara, T., Glukhov, A. V., Schobesberger, S., Bhogal, N. K., et al. (2016). Microdomain-specific modulation of L-type calcium channels leads to triggered ventricular arrhythmia in heart failure. *Circ. Res.* 119, 944–955. doi: 10.1161/CIRCRESAHA.116.308698

Shannon, T. R., Wang, F., Puglisi, J., Weber, C., and Bers, D. M. (2004). A mathematical treatment of integrated ca dynamics within the ventricular myocyte. *Biophys. J.* 87, 3351–3371. doi: 10.1529/biophysj.104.047449

Song, L.-S., Sobie, E. A., Mcculle, S., Lederer, W. J., Balke, W., Cheng, H., et al. (2006). Orphaned ryanodine receptors in the failing heart. *Proc. Natl. Acad. Sci. U.S.A.* 103, 4305–4310. doi: 10.1073/pnas.0509324103

Stevenson, W. G. (2003). Predicting sudden death risk for heart failure patients in the implantable cardioverter-defibrillator age. *Circulation* 107, 514–516. doi: 10.1161/01.CIR.0000053944.35059

Timofeyev, V., Myers, R. E., Kim, H. J., Woltz, R. L., Sirish, P., Heiserman, J. P., et al. (2013). Adenylyl cyclase subtype-specific compartmentalization: differential regulation of l-type calcium current in ventricular myocytes. *Circ. Res.* 112, 1567–1576. doi: 10.1161/CIRCRESAHA.112.300370

Tomaselli, G. F., and Marbán, E. (1999). Electrophysiological remodeling in hypertrophy and heart failure. *Cardiovasc. Res.* 42, 270–283. doi: 10.1016/S0008-6363(99)00017-6

Tomaselli, G. F., and Zipes, D. P. (2004). What causes sudden death in heart failure? *Circ. Res.* 95, 754–763. doi: 10.1161/01.RES.0000145047.14691

Wei, S., Guo, A., Chen, B., Kutschke, W., Xie, Y. P., Zimmerman, K., et al. (2010). T-tubule remodeling during transition from hypertrophy to heart failure. *Circ. Res.* 107, 520–531. doi: 10.1161/CIRCRESAHA.109.212324

Wright, P. T., Nikolaev, V. O., O'Hara, T., Diakonov, I., Bhargava, A., Tokar, S., et al. (2014). Caveolin-3 regulates compartmentation of cardiomyocyte beta2-adrenergic receptor-mediated cAMP signaling. *J. Mol. Cell. Cardiol.* 67, 38–48. doi: 10.1016/j.yjmcc.2013.12.003

Xie, Y., Sato, D., Garfinkel, A., Qu, Z., and Weiss, J. N. (2010). So little source, so much sink: requirements for afterdepolarizations to propagate in tissue. *Biophys. J.* 99, 1408–1415. doi: 10.1016/j.bpj.2010.06.042

Zima, A. V., Bovo, E., Mazurek, S. R., Rochira, J. A., Li, W., and Terentyev, D. (2014). Ca handling during excitation-contraction coupling in heart failure. *Pflugers. Arch.* 466, 1129–1137. doi: 10.1007/s00424-014-1469-3

Conflict of Interest Statement: The authors declare that the research was conducted in the absence of any commercial or financial relationships that could be construed as a potential conflict of interest.

The handling Editor and reviewer AG declared their involvement as co-editors in the Research Topic, and confirm the absence of any other collaboration.

frontiers in Physiology

REVIEW
published: 11 December 2018
doi: 10.3389/fphys.2018.01773

Dyadic Plasticity in Cardiomyocytes

Peter P. Jones[1,2], *Niall MacQuaide*[3,4] *and William E. Louch*[5,6]*

[1] Department of Physiology, School of Biomedical Sciences, University of Otago, Dunedin, New Zealand, [2] HeartOtago, University of Otago, Dunedin, New Zealand, [3] Institute of Cardiovascular Sciences, University of Glasgow, Glasgow, United Kingdom, [4] Clyde Biosciences, Glasgow, United Kingdom, [5] Institute for Experimental Medical Research, Oslo University Hospital, University of Oslo, Oslo, Norway, [6] KG Jebsen Center for Cardiac Research, University of Oslo, Oslo, Norway

Contraction of cardiomyocytes is dependent on sub-cellular structures called dyads, where invaginations of the surface membrane (t-tubules) form functional junctions with the sarcoplasmic reticulum (SR). Within each dyad, Ca^{2+} entry through t-tubular L-type Ca^{2+} channels (LTCCs) elicits Ca^{2+} release from closely apposed Ryanodine Receptors (RyRs) in the SR membrane. The efficiency of this process is dependent on the density and macroscale arrangement of dyads, but also on the nanoscale organization of LTCCs and RyRs within them. We presently review accumulating data demonstrating the remarkable plasticity of these structures. Dyads are known to form gradually during development, with progressive assembly of both t-tubules and junctional SR terminals, and precise trafficking of LTCCs and RyRs. While dyads can exhibit compensatory remodeling when required, dyadic degradation is believed to promote impaired contractility and arrythmogenesis in cardiac disease. Recent data indicate that this plasticity of dyadic structure/function is dependent on the regulatory proteins junctophilin-2, amphiphysin-2 (BIN1), and caveolin-3, which critically arrange dyadic membranes while stabilizing the position and activity of LTCCs and RyRs. Indeed, emerging evidence indicates that clustering of both channels enables "coupled gating", implying that nanoscale localization and function are intimately linked, and may allow fine-tuning of LTCC-RyR crosstalk. We anticipate that improved understanding of dyadic plasticity will provide greater insight into the processes of cardiac compensation and decompensation, and new opportunities to target the basic mechanisms underlying heart disease.

Keywords: dyad, t-tubule, sarcoplasmic reticulum, calcium homeostasis, development, disease

OPEN ACCESS

Edited by:
Antonius Baartscheer, University of Amsterdam, Netherlands

Reviewed by:
Jin O-Uchi, University of Minnesota Twin Cities, United States
Toon Van Veen, Utrecht University, Netherlands

***Correspondence:**
William E. Louch
w.e.louch@medisin.uio.no

Specialty section:
This article was submitted to Cardiac Electrophysiology, a section of the journal Frontiers in Physiology

Received: *13 August 2018*
Accepted: *23 November 2018*
Published: *11 December 2018*

Citation:
Jones PP, MacQuaide N and Louch WE (2018) Dyadic Plasticity in Cardiomyocytes. Front. Physiol. 9:1773. doi: 10.3389/fphys.2018.01773

INTRODUCTION: DYADIC ORGANIZATION AT THE MACROSCALE AND NANOSCALE

In mammalian cardiac myocytes, contraction of the cell is elicited by a process known as excitation-contraction coupling. This process is initiated by electrical excitation during the cardiac action potential, which triggers the opening of voltage-gated L-type Ca^{2+} channels (LTCCs) present in both the surface membrane and within membrane invaginations called the transverse-axial tubule system (*t-tubules*). Ca^{2+} influx through LTCCs triggers release of Ca^{2+} from ryanodine receptors (RyRs) in the sarcoplasmic reticulum (SR), and contraction as this released Ca^{2+} binds to the myofilaments. Tight control of contractility thus requires efficient crosstalk between LTCCs and

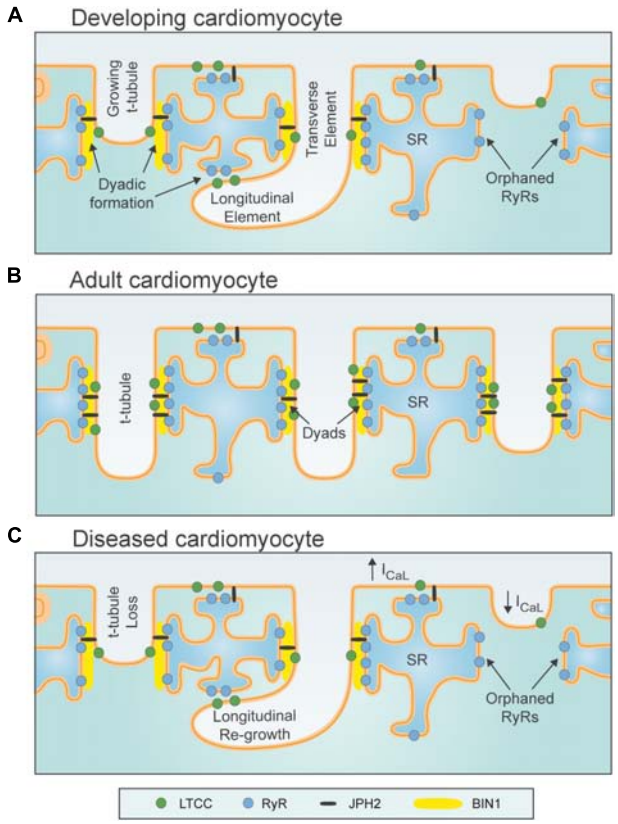

FIGURE 1 | Plasticity of dyadic structure in ventricular cardiomyocytes. **(A)** Dyads form gradually in developing ventricular cardiomyocytes, as growing t-tubules extend the surface sarcolemma into the cell interior, initially in a largely longitudinal orientation. Rudimentary junctional SR terminals and contained ryanodine receptors (RyRs) are present in advance of t-tubule arrival. Formation of dyadic junctions between L-type Ca^{2+} channels (LTCCs) and RyRs requires the anchoring protein Junctophilin (JPH2), and the membrane sensing and bending protein BIN1. **(B)** Dyadic density increases toward adulthood, and assumes a predominantly transverse orientation. **(C)** During diseases such as heart failure, levels of JPH2 and BIN1 decline, and ventricular cardiomyocytes exhibit loss of t-tubules and SR. However, new dyads in the longitudinal orientation reappear, in resemblance to developing cells. T-tubule function also declines during heart failure, as L-type Ca^{2+} current (I_{CaL}) is shifted to the surface sarcolemma.

RyRs, which is afforded by close apposition of the sarcolemmal and SR membranes at junctions called *dyads* (**Figure 1**; Sun et al., 1995; Bers, 2001).

Adult ventricular cardiomyocytes generally have a well-organized network of dyads, with *transverse* elements predominantly arranged along z-lines at the ends of each sarcomere (Fawcett and McNutt, 1969; Brette and Orchard, 2003; Song et al., 2005; Louch et al., 2010). However, *longitudinal* or *axial* dyads are also present at the level of the A-band (between z-lines), where they are oriented along the long axis of the cell (Asghari et al., 2009; Swift et al., 2012; Pinali et al., 2013). Smaller mammalian species with high heart rates such as mice and rats exhibit high densities of dyads in both orientations, while a less dense dyadic network with fewer longitudinal tubules is present in ventricular cardiomyocytes from larger species (Brette and Orchard, 2003; Song et al., 2005; Louch et al., 2010). Atrial cardiomyocytes generally exhibit a lower dyadic density than ventricular cells, although dyadic organization varies across the atria (Lenaerts et al., 2009; Smyrnias et al., 2010; Richards et al., 2011; Dibb et al., 2013; Frisk et al., 2014; Glukhov et al., 2015; Gadeberg et al., 2016; Arora et al., 2017).

Dyadic density and organization have considerable functional implications. A high density of dyads ensures that Ca^{2+} release occurs evenly across the cell, resulting in a rapid and co-ordinated rise in intracellular Ca^{2+} concentration ($[Ca^{2+}]_i$) and rapid contraction. Of note, findings from a range of species indicate that RyR organization has greater regularity than the t-tubule network, resulting in the presence of "orphaned" or non-junctional RyRs along z-lines which do not have colocalized t-tubules (Louch et al., 2006; Song et al., 2006; Heinzel et al., 2008). Ca^{2+} release at these orphaned RyRs is delayed, as it is dependent on the diffusion of Ca^{2+} released from nearby RyRs. Thus, greater dyssynchrony and slowing of Ca^{2+} release is promoted by conditions which trigger loss of t-tubules (and dyads) including hyperosmotic shock (Brette et al., 2004, 2005), cell culture (Lipp et al., 1996; Louch et al., 2004), and diseases such as heart failure (Louch et al., 2006; Song et al., 2006; Heinzel et al., 2008).

Beyond macroscale considerations of the local presence or absence of dyads, the nanoscale arrangement of proteins *within* dyads is also of key importance. Recent studies employing electron microscopy (EM) and super-resolution imaging have indicated that dyads are not completely filled with RyRs, but often contain multiple, smaller RyR clusters (Baddeley et al., 2009; Hayashi et al., 2009; Jayasinghe et al., 2018; Kolstad et al., 2018). These considerations are essential for understanding Ca^{2+} sparks, the fundamental units of Ca^{2+} release in cardiomyocytes (Cheng et al., 1993). On the t-tubule side of the dyad, LTCCs are arranged opposite from RyR clusters. Interestingly, recent data suggest that neighboring LTCCs may be clustered and functionally paired (Dixon et al., 2012, 2015), in a manner somewhat reminiscent of groupings of neighboring RyRs (Marx et al., 2001; Sobie et al., 2006; Cabra et al., 2016). The precise mechanisms by which individual or grouped LTCCs may be anchored and apposed from RyRs is unclear, although the dyadic anchor junctophilin-2 (JPH2) has been shown to interact with both proteins (Jiang et al., 2016; Munro et al., 2016; Reynolds et al., 2016). More clear is the role that JPH2 plays in setting a consistent and remarkably narrow dyadic cleft (12–15 nm) (Sun et al., 1995; Takeshima et al., 2000) required for efficient LTCC-RyR crosstalk.

The above discussion has illustrated that considerable progress has been made into understanding dyadic organization and function in healthy adult cardiomyocytes. However, accumulating data indicate that these structures also exhibit remarkable plasticity. Indeed, dyads are known to form gradually during development (Ziman et al., 2010; Louch et al., 2015), and to exhibit compensatory remodeling when required (Kemi et al., 2011; Swift et al., 2012). In contrast, dyadic degradation is widely described during cardiac disease, where it is believed to contribute to impaired contractility and arrythmogenesis (Guo et al., 2013; Orchard et al., 2013; Manfra et al., 2017). In the

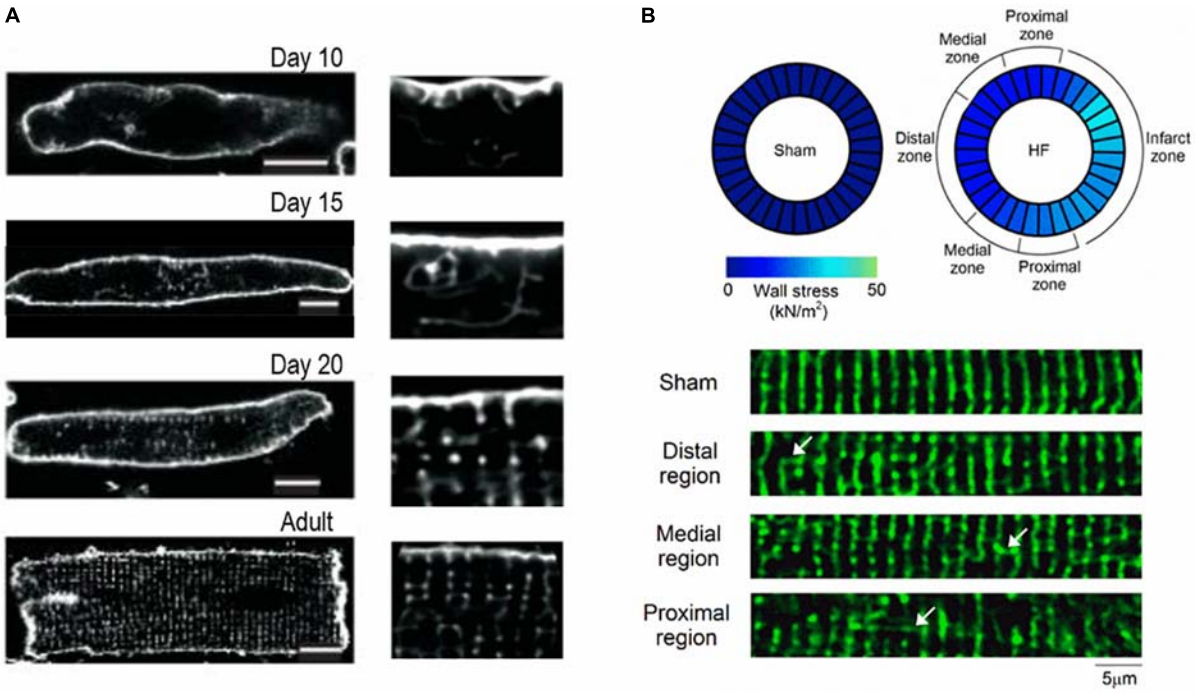

FIGURE 2 | T-tubule plasticity during development and heart failure. **(A)** Confocal imaging of rat cardiomyocytes isolated at a range of post-natal time points reveals progressive t-tubule growth. T-tubules initially appear as a sparse network which is largely oriented in the longitudinal orientation, before the dense, predominantly transverse network is established in adulthood (whole cell images at left, with enlargements at right; adapted from Ziman et al. (2010); scale bar = 10 μm, copyright permission to reproduce the figure). **(B)** Typical t-tubule remodeling during heart failure exhibits a return to an immature phenotype, with loss of transverse elements and re-appearance of longitudinal elements (arrows). In a post-infarction rat model of heart failure, it was observed that remodeling is most marked proximal to the infarction scar, where *in vivo* wall stress is particularly elevated (adapted from Frisk et al. (2016), copyright permission to reproduce the figure). These data contribute to a growing understanding that high workload/wall stress signals t-tubule remodeling in this condition (reviewed in Ibrahim and Terracciano, 2013; Manfra et al., 2017).

remainder of this review, we will summarize how such plasticity of dyadic structure/function is attained, with focus on macroscale changes in t-tubule and SR structure, as well as nanoscale regulation of LTCCs and RyRs. Particular attention will be given to an emerging understanding of the drivers of dyadic plasticity, and their potential targeting for novel therapies.

Macroscale Plasticity

T-Tubules During Development and Disease

In small rodents such as mice and rats, t-tubules form after birth, growing from the cell surface into the interior of the ventricular myocyte (Ziman et al., 2010; Louch et al., 2015; Mackova et al., 2017). Initially, this developing t-tubule network is rather disorganized in appearance, and oriented largely along the longitudinal axis of the cell (**Figures 1A**, **2A**). With further maturation, t-tubule density increases and the network becomes predominantly transversely organized along z-lines; a process that continues until surprisingly late periods of adulthood (Ziman et al., 2010; Øyehaug et al., 2013; Louch et al., 2015; Mackova et al., 2017). Recent data indicate that sheep myocytes already exhibit t-tubules *in utero* (Munro and Soeller, 2016), supporting species-dependent differences in the time course of ventricular myocyte development. In either case, prenatal or postnatal t-tubule maturation coincides with expression of JPH2 (Ziman et al., 2010; Munro and Soeller, 2016), which critically forms dyads by anchoring MORN motifs in the t-tubular membrane to the junctional SR (Takeshima et al., 2000). Indeed, when JPH2 levels are reduced in mice, t-tubules either don't appear or remain in an immature longitudinal configuration (Chen et al., 2013; Reynolds et al., 2013). Full knockout of JPH2 in mice results in *embryonic* mortality, consistent with a requirement of the protein to form dyads at the surface of the cell, in advance of t-tubule development (Takeshima et al., 2000; Franzini-Armstrong et al., 2005). The membrane sensing and bending protein Amphyphisin-2 (BIN1) is also reported to play a key role in t-tubule growth (Lee et al., 2002), and the intricate folding of the tubule inner membrane (Hong et al., 2014). Hong *et al* noted a particularly important role of a cardiac-specific isoform of BIN1 (isoform 13+17) which is capable of initiating t-tubule growth even in non-muscle cells (Hong et al., 2014). Assuming that BIN1 is essential for t-tubule development across a range of species, it is anticipated that this role is prominent at earlier stages in larger mammals which exhibit t-tubule development *in utero*.

Evidence of t-tubule plasticity is further supported by examinations of cardiac disease. A large number of studies have reported remodeling of t-tubules in left ventricular cardiomyocytes during heart failure with an array of etiologies, spanning myocardial infarction (Louch et al., 2006; Swift et al.,

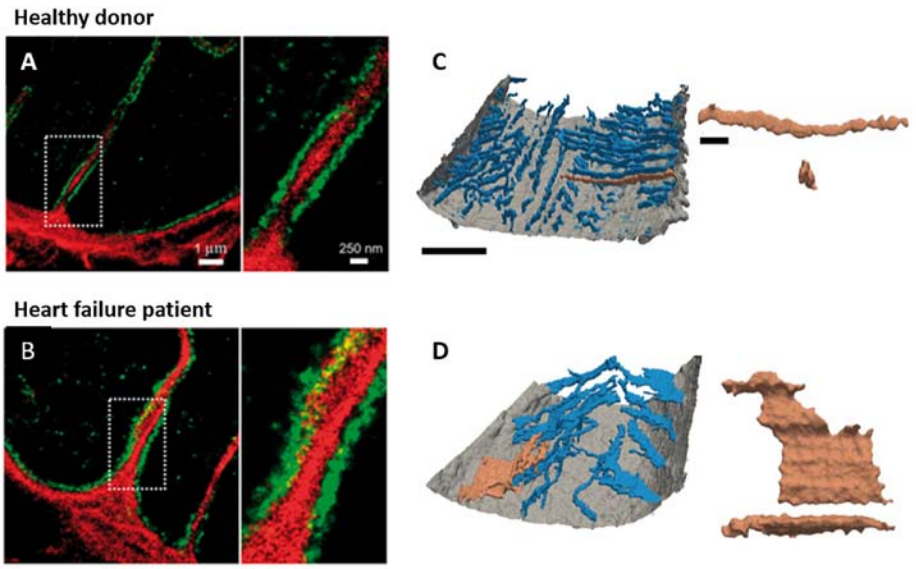

FIGURE 3 | New insights into t-tubule remodeling during human heart failure. In comparison with ventricular tissue obtained from healthy donor hearts **(A)** tissue from heart failure patients undergoing transplant **(B)** revealed dilation of t-tubules associated with collagen deposition within the t-tubule lumen. Images were obtained with dSTORM super-resolution microscopy with staining for collagen VI (red) and dystrophin (green); enlargements of the indicated regions are shown at right (adapted from Crossman et al., 2017, copyright permission to reproduce the figure). Other recent work has indicated that in addition to t-tubule loss, cardiomyocytes in heart failure patients exhibit fusion of neighboring t-tubules into sheet-like structures (donor example in **C**, heart failure patient in **D)**. 3D reconstructions illustrate the surface sarcolemma (gray) and t-tubules (blue), with the indicated tubule enlarged at right (longitudinal and transverse views; left scale bar = 10 μm, right scale bar = 2 μm; adapted from Seidel et al., 2017a, copyright permission to reproduce the figure).

2008; Lyon et al., 2009; Biesmans et al., 2011; Chen et al., 2012; Wagner et al., 2012; Øyehaug et al., 2013; Frisk et al., 2016; Sanchez-Alonso et al., 2016; **Figure 2B**), aortic stenosis (Wei et al., 2010; Ibrahim et al., 2013; Pinali et al., 2013), tachycardia (He et al., 2001; Balijepalli et al., 2003), hypertension (Song et al., 2006; Singh et al., 2017), chronic ischemia (Heinzel et al., 2008), and diabetes (Stølen et al., 2009; Ward and Crossman, 2014). Despite the range of species and disease models employed in these studies, there is general agreement that overall t-tubule density is reduced, and commonly accompanied by a re-emergence of longitudinally-oriented tubules (**Figures 1C**, **2B**). More detailed analyses have revealed t-tubular swelling in failing myocytes (Wagner et al., 2012; Pinali et al., 2013, 2017; Crossman et al., 2017; **Figures 3A,B**) and the appearance of abnormal t-tubule "sheets" which may result from fusion of neighboring tubules (Seidel et al., 2017a; **Figures 3C,D**). Similar changes in t-tubule organization have been observed during right ventricular failure (Xie et al., 2012; Caldwell et al., 2014) and in the atria during heart failure (Dibb et al., 2009) and atrial fibrillation (Lenaerts et al., 2009), suggesting that t-tubular remodeling may be endemic to a variety of cardiac pathologies across the chambers of the heart.

Structural similarities between diseased and developing ventricular myocytes (**Figure 1**) have implied that pathological t-tubule remodeling may result from re-expression of fetal genes and/or suppression of adult genes in these conditions (Louch et al., 2015). Although the details of these mechanisms are still being elucidated, existing studies have already linked t-tubule remodeling in failing cells to declining expression of JPH2 (Minamisawa et al., 2004; Wei et al., 2010; Landstrom et al., 2011; Frisk et al., 2016), which is reminiscent of developing cells. An important role of JPH2 reduction in disease pathophysiology is supported by the observation that overexpression of this dyadic anchor protects against t-tubule degradation and heart failure development (Guo et al., 2014). Xu et al reported that JPH2 expression may be suppressed during disease by upregulation of microRNA-24 (miR-24), and showed that a miR-24 antagomir protected against changes in t-tubular architecture (Xu et al., 2012). Others have reported that JPH2 may be mislocalized in the failing heart, due to reorganization of microtubules necessary for its delivery to dyads (Zhang et al., 2014; Prins et al., 2016). JPH2 may also be degraded during heart failure by calpain cleavage. Guo et al. (2015) identified four distinct cut sites on JPH2 which resulted in functionally inactive fragments and disrupted dyadic junctions. Finally, recent data have suggested that JPH2's functionality is dependent on its phosphorylation status. Quick et al. (2017) showed that JPH2 is phosphorylated by Striated Muscle Preferentially Expressed Protein Kinase (SPEG) and that this phosphorylation is reduced in heart failure, with knockout of SPEG also resulting in t-tubule disarray. These findings suggest that there may be several mechanisms which underlie loss of JPH2 expression and/or function during disease leading to pathologic disruption of t-tubule structure. Thus, JPH2 is an exciting potential candidate for future therapies aimed at preserving t-tubule integrity (Røe et al., 2015; Manfra et al., 2017).

BIN1 is another regulator of t-tubule structure which plays key roles in the developing and diseased heart. Indeed, just as BIN1 is believed crucial for the formation of t-tubules during development, so too has t-tubule loss and disarray during disease

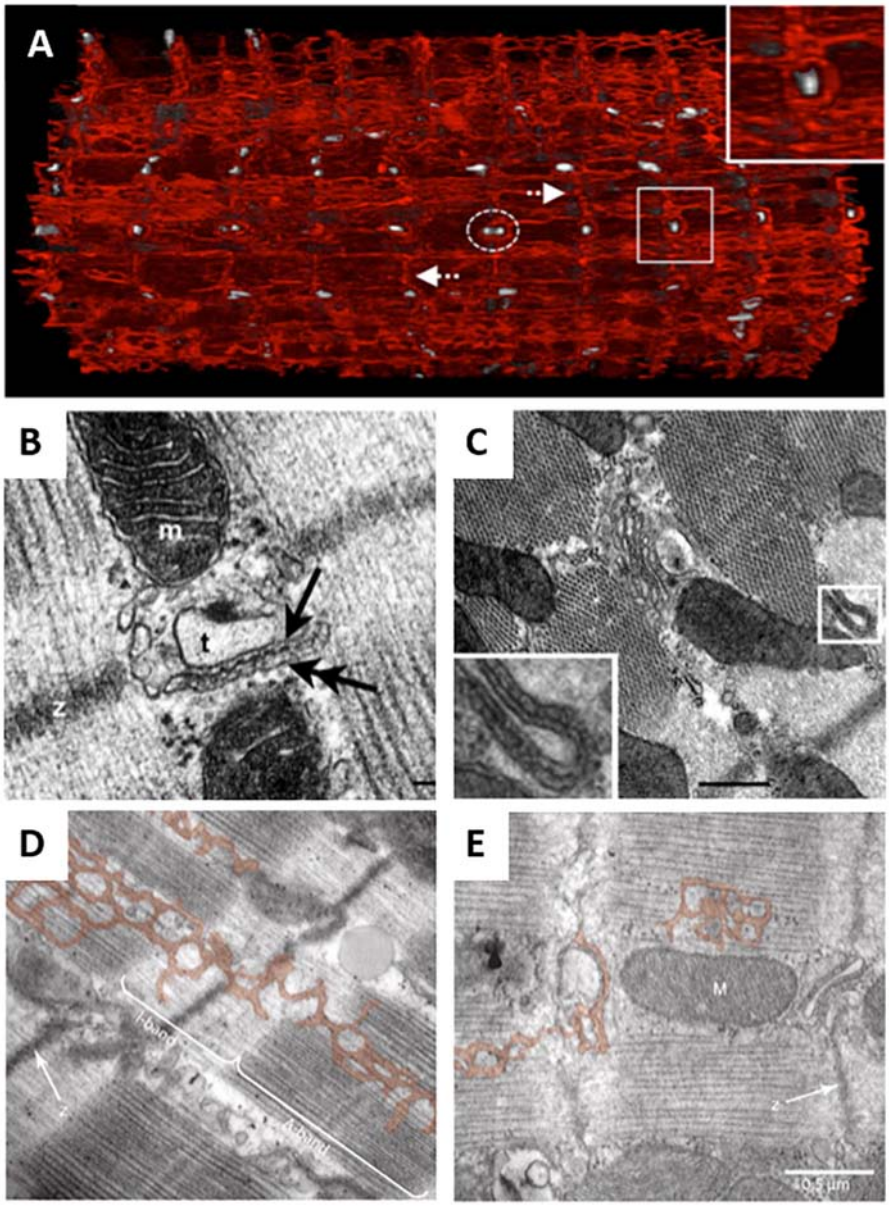

FIGURE 4 | EM imaging of dyadic structure. **(A)** Block-face scanning EM performed on a sheep cardiomyocyte illustrates the complex, mesh-like nature of 3D SR structure (red), and it's interrelationship with t-tubules (gray). Both longitudinal and perpendicular elements (arrows) are readily apparent, which converge to engulf t-tubules (enlarged region). Occasional twinning of t-tubules was observed with surrounding junctional SR (dashed elipsoid) (adapted from Pinali et al., 2013, copyright permission to reproduce the figure). Transmission EM imaging of transversely **(B)** and longitudinally-oriented dyads **(C)** revealed similar geometries, suggesting similar functionality of these structures (t, t-tubule; m, mitochondrion; double arrow, SR; scale bar in C = 100 nm). Ryanodine receptor heads are readily apparent (single arrow, adapted from Asghari et al., 2009, copyright permission to reproduce the figure). SR degradation during heart failure (Pinali et al., 2013) is suggested to be linked to reduction in SERCA levels, based on observations in the conditional SERCA knockout mouse (**D**, control cardiomyocyte; **E**, following SERCA knockout, with SR pseudo-colored; adapted from Swift et al., 2012, copyright permission was not required to reproduce the figure).

been linked to its downregulation (Lee et al., 2002; Caldwell et al., 2014; Hong et al., 2014). While the precise role of BIN1 in t-tubule growth and maintenance is unclear, it has been shown to group phosphoinositides allowing dynamin-2 polymerization; steps essential in tubulogenesis (Lee et al., 2002; Picas et al., 2014). Declining BIN1 levels in heart failure are reported to promote not only overall t-tubule loss (Caldwell et al., 2014), but also decreased t-tubule folding (Hong et al., 2014). Based on mathematical modeling studies, Hong et al. (2014) predicted that such loss of fine structure augments ion diffusion within the t-tubule, predisposing for cardiac arrhythmia. These authors have further proposed that continuous turnover of BIN1 from dyads in healthy patients maintains high levels in blood, explaining why decreased BIN1 plasma levels are linked to heart failure in

patients and predict- future arrhythmia (Hong et al., 2012). These exciting data suggest that BIN1 may serve as both a biomarker and therapeutic target in heart failure patients.

While new molecular regulators such as JPH2 and BIN1 are emerging, recent work has also linked control of t-tubule structure to upstream mechanical signals. Experiments pioneered by the Terracciano group first indicated that t-tubule loss during heart failure may be directly triggered by the elevated ventricular workload in this condition. They observed that unloading failing hearts by heterotopic transplantation into healthy animals rescued t-tubule structure (Ibrahim et al., 2012a,b). Indeed, other strategies that unload the failing heart either pharmacologically (Chen et al., 2012; Xie et al., 2012; Huang et al., 2016) or via resynchronization therapy (Lichter et al., 2014), are similarly, protective. More recent work by our group indicated that elevated ventricular wall stress, which occurs in the dilated, thin-walled ventricle of the failing heart, may be the specific mechanical signal underlying t-tubule degradation (Frisk et al., 2016; **Figure 2B**).

How does mechanical overload lead to t-tubule degradation? While the precise mechanisms are unclear, it is important to consider that elevated workload and wall stress regulate not only cardiomyocyte remodeling but also promote changes in the extracellular matrix, including significant fibrosis. An exciting new study by Crossman et al., 2017; has shown striking localization of fibroblast filopodia and collagen within the t-tubular lumen in failing ventricular cardiomyocytes (**Figures 3A,B**). The authors suggested that such collagen deposition may directly drive t-tubular dilation in this condition, although it may also stiffen the t-tubule membrane, and impair normal mechanosignaling (McNary et al., 2012). Perhaps such changes mark a t-tubule for degradation (Louch and Nattel, 2017). In support of this view, regions of the failing heart with the most pronounced fibrosis, such as those proximal to an infarction, exhibit the most marked t-tubule loss (Frisk et al., 2016; Seidel et al., 2017b; **Figure 2B**). The Terracciano group has proposed that the stretch-sensitive protein titin cap (TCap) may play a key role in integrating these mechanical signals (Ibrahim and Terracciano, 2013; Ibrahim et al., 2013). With established binding proteins in the t-tubule membrane as well as partners in the cytoskeleton, TCap certainly appears to be well-positioned to serve such a function. Direct manipulation of the cytoskeleton has also been shown to regulate t-tubule structure, as cytoskeletal disruptors inhibit t-tubule loss during culture (Tian et al., 2012; Hodne et al., 2017). Recent data from the Song laboratory have further implicated protein kinase C activation as a critical determinant of cytoskeletal reorganization and t-tubule degradation (Guo et al., 2018). Taken together, these data raise the intriguing possibility that, by sensing local load, the t-tubule can regulate its own structure via signals transmitted from the extracellular matrix to the cytoskeleton.

Not all changes in t-tubule structure appear to be detrimental. At early stages of heart failure, longitudinal tubules appear before transverse elements have disappeared (Louch et al., 2006); changes which are suggested to be compensatory since additional Ca^{2+} influx at these sites supports the Ca^{2+} transient (Swift et al., 2012). However, a full understanding of the consequences of t-tubule dynamics for cardiomyocyte function requires detailed knowledge of SR structure, as well as the regulation of LTCCs and RyRs within these membranes. These topics are discussed in the following sections.

Plasticity of SR Structure

In comparison with t-tubule structure, SR structure has, in general, been less extensively studied. This is in part due to the fact that t-tubule structure is rather easily assessed by simple membrane staining and confocal microscopy; techniques which can be extended to 3D with relative ease. Direct staining and fluorescence imaging has not proven to effectively reveal SR structure, although junctional SR localization has been inferred from confocal immunostaining of RyRs (Bootman et al., 2006; Song et al., 2006; Swift et al., 2012) or calsequestrin (Terentyev et al., 2003). Greater detail has been provided by studies employing transmission EM, which revealed that the SR consists of a complex, branching network (Franzini-Armstrong, 1980). 3D structure has more recently been unveiled by serial block-face imaging with scanning EM, showing that the SR network is in fact contiguous between each t-tubule, is in regular contact with the surface membrane, and is variable between species (Pinali et al., 2013; **Figure 4A**). Importantly, the junctional SR forms dyads not only with the surface sarcolemma and along transversely-oriented t-tubules at z-lines, but also with longitudinally-oriented tubules within the A-band. EM studies have reported that these longitudinal dyads have similar dimensions to their transversely-oriented counterparts, suggesting that the two types of dyads may have similar functionality (Asghari et al., 2009; Pinali et al., 2013; **Figures 4B,C**).

Accumulating data suggest that, like t-tubules, SR structure is also malleable. Transmission EM imaging of developing hearts has shown that the junctional SR forms dyads with the surface sarcolemma from early stages of embryonic ventricular development (Franzini-Armstrong et al., 2005). However, rudimentary junctional SR terminals (cisternae) appear at internal sites along z-lines during the late embryonic stage (Korhonen et al., 2010), and remain present during the neonatal period prior to the arrival of growing t-tubules (Ziman et al., 2010). Thus, wavelike Ca^{2+} release patterns are observed, traveling from the cell membrane toward the cell interior, as Ca^{2+} release propagates between as yet "orphaned" RyRs. The subsequent arrival of t-tubules and formation of internal dyads synchronizes Ca^{2+} release across the cell, and has been linked to the presence of the dyadic anchoring protein JPH2, as described above (Chen et al., 2013; Reynolds et al., 2013).

Restructuring of the SR is also apparent during disease. Pinali et al. (2013) reported an overall loss of SR in sheep following tachypacing-induced heart failure, with local patchiness and disorder of SR observed near sites of abnormal mitochondrial clustering. The implications of such remodeling are unclear but imply that there may be disruption of Ca^{2+} fluxes within the network SR in diseased cells. Results from the SERCA knockout mouse suggest that SR degradation may be driven directly by SERCA loss during heart failure (Swift et al., 2012; **Figures 4D,E**). However, despite evidence of overall SR loss during heart failure, most report that the junctional SR and associated RyRs remain present along z-lines, at least in a rudimentary arrangement (Song

et al., 2006; Swift et al., 2008; Pinali et al., 2013; Frisk et al., 2016). Thus, there is an increased presence of orphaned RyRs in diseased cells reminiscent of the developing heart (Louch et al., 2015). With fewer RyR clusters served by a t-tubule, Ca^{2+} release becomes desynchronized, as uncoupled CRUs are recruited by diffusion (Louch et al., 2004, 2006; Song et al., 2006; Heinzel et al., 2008). The resulting overall slowing and reduced amplitude of systolic Ca^{2+} release has been linked to reduced cardiac output in this condition (Bøkenes et al., 2008; Mørk et al., 2009; Guo et al., 2013; Røe et al., 2015). At sites where the junctional SR remains coupled to t-tubules, Wu et al. (2012) reported that there is shortening of the interface in failing cells as the SR terminals are shortened. This implies that there is less available space for LTCCs and RyRs within the dyad, which may impair triggering of Ca^{2+} release beyond effects associated with loss of t-tubules and reduced Ca^{2+} release synchrony. Importantly, while there may be some loss of SR structure along z-lines, there appears to be growth or at least specialization of SR within the A-band, allowing the formation of dyads with newly-grown longitudinal t-tubules (Song et al., 2006; Swift et al., 2012). It is hypothesized that these new dyads somewhat counterbalance those lost along z-lines, at least at early stages of disease, to help maintain Ca^{2+} release (Swift et al., 2012).

The above discussion has illustrated that t-tubule and SR structure exhibit considerable plasticity, which enables a malleable arrangement of dyads important for controlling the synchrony of Ca^{2+} homeostasis. In the following section we will describe emerging data indicating that there is also impressive plasticity of LTCCs and RyRs *within* dyads, consistent with nanoscale control of dyadic function.

NANOSCALE PLASTICITY

Plasticity of LTCC Localization and Function

Whilst much is known of how the LTCC localizes to the triad in skeletal muscle, targeting of LTCCs to the cardiac dyad is more poorly understood. In skeletal muscle, LTCC positioning appears to be stabilized by both the presence of STAC3 (Nelson et al., 2013; Polster et al., 2016; Campiglio and Flucher, 2017) and direct physical interaction between the II-III loop of the channel and the skeletal muscle ryanodine receptor (RyR1) (Lu et al., 1994; El-Hayek et al., 1995). These interactions enable the formation of a distinctive tetrad arrangement, with 4 LTCCs apposed from 4 RyRs (Franzini-Armstrong et al., 1998; Takekura et al., 2004). However, cardiac muscle does not express STAC3 or a homologous protein nor does the cardiac isoform of the LTCC have a physical interaction with RyR (c.f. Dulhunty et al., 2005), leading to the question of how the channel is targeted.

At both the surface of cardiomyocytes and within t-tubules, LTCCs are found resident within caveolae. The bulk of channel delivery to these caveloae appears to be dependent on BIN1, which couples the channels to microtubules (Hong et al., 2010). However, the actin filament cytoskeleton is also proposed to play a role in LTCC trafficking, at least in neurons and recombinant cell lines (Hall et al., 2013; Ghosh et al., 2018). Once delivered, LTCCs are maintained within the dyad via links between the caveolae and cytoskeleton (Head et al., 2006; Balijepalli and Kamp, 2008). Interestingly, BIN1 may also help maintain LTCC positioning, as BIN1-induced microfolds within the t-tubule membrane are suggested to prevent lateral movement of the caveolae (Basheer and Shaw, 2016). Further evidence of the importance of BIN1 for LTCC maintenance is provided by Hong et al. (2012), who showed that in human heart failure there is no change in LTCC expression but a significant reduction in dyadic channels. Such loss of dyadic LTCCs correlates well with a reduction in the expression of BIN1, both in failing patients (Hong et al., 2012) and sheep (Caldwell et al., 2014). Finally, evidence from skeletal muscle indicates that JPH2 may also play a role in maintaining LTCCs as part of a dyadic protein complex (Golini et al., 2011), suggesting that JPH2 reduction during heart failure could have complex effects on both LTCC localization and overall dyadic structure. The mechanism by which un-anchored LTCCs are degraded is presently unclear, although indirect evidence showing that dynasore increases surface LTCC expression indicates that channel internalization may occur via dynamin-dependent endocytosis (Hong et al., 2010).

While the above discussion has highlighted an important role of caveolae in clustering LTCCs within dyads, accumulating data suggest that these structural arrangements also critically regulate channel function. Recent studies have shown that Caveolin-3 (Cav-3), which is known to play an important role in the formation of caveolae and t-tubules (Parton et al., 1997), interacts with both LTCCs and protein-kinase A (PKA) to enable PKA-mediated phosphorylation of the channel and augmentation of L-type current (Kamp and Hell, 2000). Indeed, using peptide mimics of the scaffolding domain of Cav-3 to disrupt this interaction, Bryant et al. (2014) observed reduction in both basal L-type function and its response to β-adrenergic stimulation. More recently the same group has gone on to show that in heart failure the loss of t-tubular Cav-3 reduces t-tubular L-type current, despite the continued presence of L-type channels (Bryant et al., 2015, 2018; **Figure 1C**). Thus, while loss of t-tubules promotes dyssynchronous release in failing ventricular cardiomyocytes, as discussed above, it seems that there is also an important Cav-3-dependent loss of functionality in remaining tubules which further compromises Ca^{2+} release in this condition. Interestingly, the loss of t-tubular L-type current appears to be paralleled by increased current on the cell surface (Bryant et al., 2015; Sanchez-Alonso et al., 2016), likely explaining why many groups have reported unchanged overall current density in heart failure (Gomez et al., 1997; Benitah et al., 2002; Kamp and He, 2002; Mørk et al., 2009). The Gorelik group has proposed that increased LTCC activity on the surface sarcolemma results from physical movement of channels out of dyads and onto the membrane crests present between Z-grooves (Sanchez-Alonso et al., 2016). They further suggest that the delocalization-induced increase in channel activity promotes instability of myocyte membrane potential and a concomitant increase in arrhythmias often associated with heart failure (Sanchez-Alonso et al., 2016). These findings raise the possibility that nanoscale LTCC localization might be therapeutically targeted in disease.

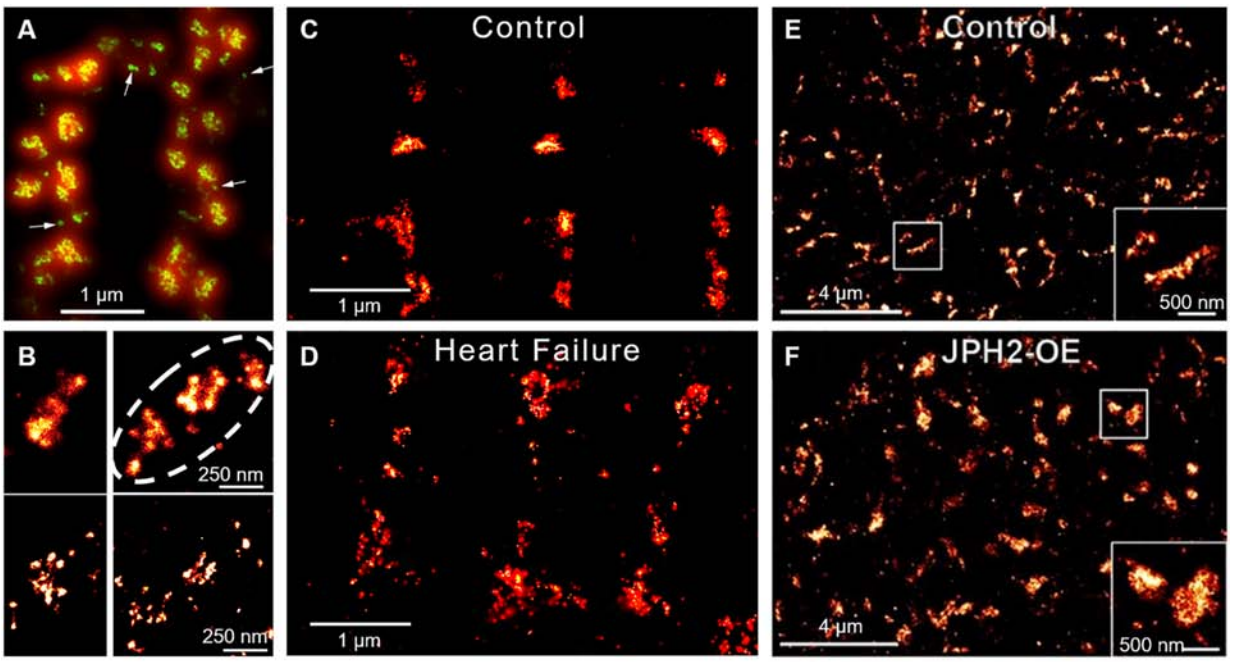

FIGURE 5 | Super-resolution imaging of RyR clusters and plasticity. **(A)** RyRs on the cell surface of ventricular cardiomyocytes form clusters primarily along either side of the z-lines (double rows of RyRs). The limited resolution of conventional confocal imaging (shown red) is markedly improved using the dSTORM technique (green), which reveals the range of size and morphologies of RyR clusters. dSTORM also allows the visualization of smaller clusters and single RyRs (arrows, from Baddeley et al., 2009, copyright permission was not required to reproduce the figure). **(B)** Neighboring clusters can form superclusters or Ca^{2+} release units (CRUs) (dotted line; upper panel). DNA-PAINT reveals that RyRs within clusters are found in various orientations and groupings (lower panel, from Jayasinghe et al., 2018, copyright permission to reproduce the figure). **(C,D)** During heart failure, RyR clusters are broken apart, resulting in dispersed CRUs (from Kolstad et al., 2018, copyright permission was not required to reproduce the figure). **(E,F)** In contrast, RyR cluster size is increased in response to JPH2 overexpression (from Munro et al., 2016, copyright permission to reproduce the figure).

Finally, exciting recent data indicate that LTCC activity is also critically regulated by the physical clustering of the channels themselves. Using single channel electrophysiology and optical channel recordings in neonatal myocytes, Navedo et al. (2010) found that clustered LTCCs open together more frequently than stochastic opening would predict. The same group went on to show in ventricular myocytes that this functional coupling of LTCCs occurs through the physical interaction of their C-terminal tails (Dixon et al., 2012, 2015). It is likely that such coupling ensures that Ca^{2+} influx is rapid and large enough to drive efficient RyR opening during Ca^{2+}-induced Ca^{2+} release. In light of findings described above, it seems plausible that loss of t-tubular L-type current during heart failure (Bryant et al., 2015; Sanchez-Alonso et al., 2016) may, at least in part, result from loss of channel clustering due to downregulation of Cav-3, BIN1, and/or JPH2.

Plasticity of RyR Organization

Inter-Cluster RyR Dynamics

While it was traditionally believed that dyads in ventricular myocytes are uniformly packed with RyRs, more recent super-resolution microscopy studies have indicated that dyads are in fact composed of sub-clusters (Baddeley et al., 2009; Hayashi et al., 2009; Jayasinghe et al., 2018; Kolstad et al., 2018; **Figures 5A,B**). Neighboring RyR clusters with sufficiently short distances between them (<100 nm in Sobie et al., 2006; <150 nm in Macquaide et al., 2015) are suggested to concertively generate Ca^{2+} sparks, as released Ca^{2+} can effectively jump from one cluster to the next. These functional groupings have thus been termed "superclusters" or Ca^{2+} release units (CRUs) (Baddeley et al., 2009), and may provide opportunities to fine tune spark dynamics (Walker et al., 2014). EM data suggest that RyR clusters, and presumably CRUs, are assembled gradually during development, first at the cell surface and then within the cell interior (Franzini-Armstrong et al., 2005). This process may be reversed during disease, as emerging data from our laboratories indicate that RyR clusters are broken apart (Macquaide et al., 2015; Kolstad et al., 2018; Shen et al., 2018; **Figures 5C,D**, 6). We have specifically linked dispersion of RyR clusters and CRUs during post-infarction heart failure to slowing of Ca^{2+} spark kinetics, due to the time lag inherent as multiple clusters are sequentially activated (Louch et al., 2013; Kolstad et al., 2018; Shen et al., 2018). Slowing of Ca^{2+} sparks in these cells was additionally linked to de-synchronization and slowing of the overall Ca^{2+} transient (Louch et al., 2013; Kolstad et al., 2018). We observed similar fragmentation of RyR clusters and slowing of Ca^{2+} spark kinetics during atrial fibrillation (Macquaide et al., 2015). An associated increased fraction of RyRs located between Z-lines was further predicted to augment propagation of pro-arrhythmic Ca^{2+} waves. Thus, accumulating data indicate that

RyR clusters exhibit marked plasticity of their organization and function, and that this malleability has important implications for pathophysiology.

What is the timescale of RyR cluster dynamics? Some insight has been provided by a recent study employing direct visualization of RyR clusters using GFP-labeled RyR in live cells (Hiess et al., 2018). The authors observed that clusters close to the periphery of cells can undergo movement either laterally along the cell surface or down toward the interior. This movement altered cluster size as both cluster fusion and fission were observed. Remarkably, over a 12 min period movements of up to 1 μm occurred, which was sufficient for clusters to traverse half a sarcomere. Importantly, not all neighboring clusters repositioned, suggesting that cluster rearrangement was not an artifact due to SR movement (Hiess et al., 2018).

Importantly, inter-cluster dynamics appear to be controlled by external stimuli. Stimulatory conditions such as high Ca^{2+} were found to promote movement whereas conditions known to suppress RyR function such as low Ca^{2+} and tetracaine retarded their movement (Hiess *et al.,* 2018). This raises the possibility that hyperactivity of the RyR, a hallmark of diseased cardiomyocytes (Bers, 2014; Dries et al., 2018), directly promotes its migration. However, it has been suggested that RyR localization is also dependent on associated dyadic proteins. BIN1 is reported to traffic RyRs to the t-tubule during β-adrenergic stimulation (Fu et al., 2016), with a time scale that appears to be consistent with the rate of RyR cluster movements reported by Hiess et al. (2018). JPH2 may also play a role in RyR arrangement, as overexpression of the protein was observed to augment RyR cluster size (Munro et al., 2016; **Figures 5E,F**). Interestingly, in these larger clusters JPH2 expression appears to stabilize RyR activity (van Oort et al., 2011; Beavers et al., 2013; Reynolds et al., 2016). These observations suggest that both dispersion of RyRs and increased channel activity during heart failure and atrial fibrillation could be linked to downregulation of BIN1 and JPH2 in these conditions.

Intra-Cluster RyR Dynamics

Although super-resolution imaging techniques such as dSTORM have yielded a wealth of information about RyR cluster size and distribution, their ability to examine intra-cluster architecture is limited. A recent breakthrough by the Soeller group employed the DNA-paint technique, which yielded <10 nm resolution (Jayasinghe et al., 2018). These measurements allowed the first visualization of single channels using optical means. Jayasinghe et al found that most clusters contained largely disordered channels with a relatively low packing density (Jayasinghe et al., 2018). This finding disagrees with historical assumptions of ventricular cardiomyocyte RyR packing based on EM descriptions of skeletal muscle, which showed a crystalline checkerboard arrangement of RyR1 (Ferguson et al., 1984; Franzini-Armstrong et al., 1999). More recent EM studies have suggested a *somewhat* structured arrangement with cardiac RyRs predominantly organized in a checkerboard pattern (∼50% of channels) but with many channels present in side-by-side or disordered arrangements (Asghari et al., 2014; **Figure 6**). Strikingly, as with clusters themselves, the orientation of channels within a cluster appears highly plastic. For example, exposure of cells to high Mg^{2+} conditions was observed to drive clusters into a side-by-side orientation, whereas low Mg^{2+} favored checkerboard. Most dramatically, however, was the finding that phosphorylated channels appeared almost exclusively in a checkerboard orientation (Asghari et al., 2014) (**Figure 6**). These findings suggest that the crystalline array favors greater RyR activity. More recently, the same group has refined their model with data indicating that it is phosphorylation of RyR at S2030 and S2814 that drives the change in cluster orientation (Asghari et al., 2017). Whether other established post-translational modifications of RyR such as oxidation (Waddell et al., 2016) or agonists such as caffeine (Jones et al., 2008) also result in similar changes in orientation remains unknown.

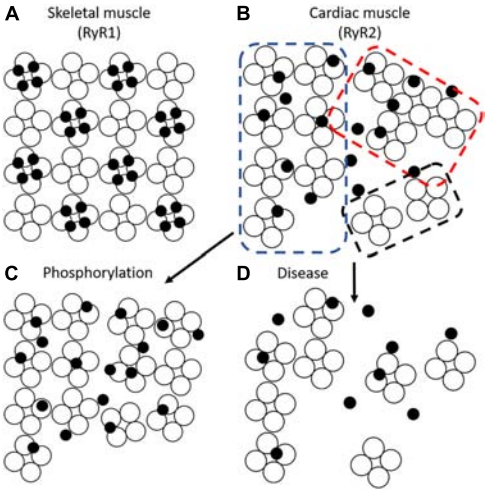

FIGURE 6 | RyR cluster conformations. **(A)** Skeletal muscle RyRs (RyR1) form a regular crystalline array with 4 four LTCCs (filled circles) apposing alternate RyRs (open circles) to form tetrads. **(B)** Cardiac muscle RyRs (RyR2) interact in several conformations including crystalline array (blue dotted box), side-by-side (red dotted box), and disordered arrangements (black dotted box). Different stimuli modify the predominant conformation; phosphorylation promotes a crystalline array which may enhance the apposition of LTCCs and RyRs **(C)**. Pathological conditions are reported to promote RyR cluster dispersion (Louch et al., 2013; Macquaide et al., 2015; Kolstad et al., 2018) and mislocalize t-tubules, thus, decreasing the coupling between LTCCs and RyRs **(D)**.

Given that the clamp region of RyR is thought to enable assembly of the crystalline array, and that this region undergoes substantial movement during the transition of a channel to an open state, it is plausible that re-arrangement into the checkerboard pattern enhances coupled gating of channels (Cabra et al., 2016). Coupled gating has been previously proposed based on recordings of RyRs in bilayers, and implies that neighboring RyRs within a cluster exhibit synchronization of their opening and closing (Marx et al., 2001; Sobie et al., 2006). This mechanism has been suggested to be facilitated by FK506-binding protein (FKBP12.6), however, a role for this accessory protein in controlling RyR function remains controversial (Marx et al., 2000, 2001; Zhang et al., 2016; Gonano and Jones, 2017). Regardless of mechanism, an increase in coupled gating

during transition to the checkerboard arrangement appears essential, as Walker et al. (2015) suggest that the increased intra-channel spacing in this configuration would otherwise *reduce* the likelihood of spark occurrence. However, the concept of coupled gating remains contentious as direct evidence linking cluster orientation and single channel activity is lacking (Williams et al., 2018).

In support of the work of the Moore group (Asghari et al., 2014), Samso and co-workers employed an alternative approach to examine RyR cluster formation, namely self-association in solution (Cabra et al., 2016). They found that akin to the patterns observed in cardiac muscle, *in vitro* RyRs adopt two major arrangements, namely side-by-side (further classified as center to side and adjoining) and checkerboard (further classified as oblique and center-to-corner). At low Ca^{2+} concentrations the channels were found to be relatively evenly distributed between the two conformations but, consistent with Asghari et al., stimulatory conditions (high Ca^{2+}) favored an oblique and center-to-corner conformation, the basis of the crystalline array (Cabra et al., 2016). Given that stimulatory conditions such as high Ca^{2+} levels or phosphorylation appear to also increase both intra- and inter-cluster mobility, it would be of interest to examine the relative mobility of checkerboard and side-by-side orientated clusters in future studies.

PLASTICITY OF LTCC-RYR COUPLING

The preceding sections have illustrated that there is remarkable plasticity of not only the membranes of the dyad, but also their contained LTCCs and RyRs. The malleable activity of these proteins is mediated through direct changes to single channel function but also through the coordinated movement and organization of the channels which provides another layer of control. However, our knowledge of these phenomena is largely limited to LTCCs and RyRs individually; whether plasticity of the two proteins is coordinated, or indeed if the molecular stimuli are shared, remains less clear. The dynamic clustering observed in response to β-adrenergic stimulation of both channels might not only increase each channel's activity but also hints at more effective coupling through optimization of LTCC and RyR apposition. Perhaps the phosphorylation-induced transition of RyR to a checkerboard conformation might, similarly, position LTCCs into an arrangement more similar to that found in skeletal muscle. Similarly, it is plausible that the loss of dyadic channels in disease not only reduces their own function but, due to an altered nano-structural arrangement, also results in a further reduction in Ca^{2+} coupling between the remaining channels. Since molecular players such as JPH2, BIN1, and Cav-3 control the localization of both LTCCs and RyRs, perhaps downregulation of these regulators critically reduces channel alignment in diseased cardiomyocytes. More indirect effects might also be important, as changes to the t-tubule architecture such as dilation or swelling (Wagner et al., 2012; Pinali et al., 2013, 2017; Crossman et al., 2017) could also "misalign" or otherwise disrupt the functional coupling between the channels. This form of remodeling has been hypothesized for more than 20 years, based on an observed reduction in the "gain" of Ca^{2+}-induced Ca^{2+} release (Gomez et al., 1997; Litwin et al., 2000). However, it is only now with the host of recent technological advances, that we might examine this concept experimentally, by combining gain measurements with live-cell imaging of LTCCs and RyRs.

CONCLUSION

This review has presented a growing body of evidence illustrating that the concept of a static dyad severely underestimates the complexity of the structure. Rather, it is now fully apparent that there is remarkable plasticity of both t-tubule and SR structure, which enables dynamic dyad formation and degradation. Furthermore, it appears that within these structures there is likely continual regulation of both the positioning and activity of LTCCs and RyRs. This plasticity is postulated to augment dyadic Ca^{2+} cycling when required, but also to underlie impaired Ca^{2+} cycling during disease. Thus, greater understanding of dyadic plasticity holds considerable therapeutic potential.

AUTHOR CONTRIBUTIONS

All authors contributed to the conceptualization, drafting, and editing of the manuscript.

FUNDING

This work was supported by the European Union's Horizon 2020 Research and Innovation Programme (Consolidator grant, WEL) under grant agreement No. 647714. Additional support for WEL was provided by The South-Eastern Norway Regional Health Authority, Anders Jahre's Fund for the Promotion of Science, The Norwegian Institute of Public Health, Oslo University Hospital Ullevål, and the University of Oslo. PPJ was supported by the Marsden Fund administered by the Royal Society of New Zealand (UOO1501) and the Health Research Council of New Zealand (18-232).

REFERENCES

Arora, R., Aistrup, G. L., Supple, S., Frank, C., Singh, J., Tai, S., et al. (2017). Regional distribution of T-tubule density in left and right atria in dogs. *Heart Rhythm* 14, 273–281. doi: 10.1016/j.hrthm.2016.09.022

Asghari, P., Schulson, M., Scriven, D. R., Martens, G., and Moore, E. D. (2009). Axial tubules of rat ventricular myocytes form multiple junctions with the sarcoplasmic reticulum. *Biophys. J.* 96, 4651–4660. doi: 10.1016/j.bpj.2009.02.058

Asghari, P., Scriven, D. R., Sanatani, S., Gandhi, S. K., Campbell, A. I., and Moore, E. D. (2014). Nonuniform and variable arrangements of ryanodine receptors within mammalian ventricular couplons. *Circ. Res.* 115, 252–262. doi: 10.1161/CIRCRESAHA.115.303897

Asghari, P., Scriven, D. R., Zhao, Y., Mondragon, R. R., Valdivia, H., Wehrens, X. H., et al. (2017). RyR2 tetramer distributions in ventricular myocytes from phosphomutant mice. *Biophys. J.* 112:161a. doi: 10.1016/j.bpj.2016.11.886

Baddeley, D., Jayasinghe, I. D., Lam, L., Rossberger, S., Cannell, M. B., and Soeller, C. (2009). Optical single-channel resolution imaging of the ryanodine receptor distribution in rat cardiac myocytes. *Proc. Natl. Acad. Sci. U.S.A.* 106, 22275–22280. doi: 10.1073/pnas.0908971106

Balijepalli, R. C., and Kamp, T. J. (2008). Caveolae, ion channels and cardiac arrhythmias. *Prog. Biophys. Mol. Biol.* 98, 149–160. doi: 10.1016/j.pbiomolbio.2009.01.012

Balijepalli, R. C., Lokuta, A. J., Maertz, N. A., Buck, J. M., Haworth, R. A., Valdivia, H. H., et al. (2003). Depletion of T-tubules and specific subcellular changes in sarcolemmal proteins in tachycardia-induced heart failure. *Cardiovasc. Res.* 59, 67–77. doi: 10.1016/S0008-6363(03)00325-0

Basheer, W. A., and Shaw, R. M. (2016). Connexin 43 and CaV1.2 ion channel trafficking in healthy and diseased myocardium. *Circ. Arrhythm. Electrophysiol.* 9:e001357. doi: 10.1161/CIRCEP.115.001357

Beavers, D. L., Wang, W., Ather, S., Voigt, N., Garbino, A., Dixit, S. S., et al. (2013). Mutation E169K in junctophilin-2 causes atrial fibrillation due to impaired RyR2 stabilization. *J. Am. Coll. Cardiol.* 62, 2010–2019. doi: 10.1016/j.jacc.2013.06.052

Benitah, J. P., Kerfant, B. G., Vassort, G., Richard, S., and Gomez, A. M. (2002). Altered communication between L-type calcium channels and ryanodine receptors in heart failure. *Front. Biosci.* 7, e263–e275. doi: 10.2741/A922

Bers, D. M. (2001). *Excitation-Contraction Coupling and Cardiac Contractile Force*, 2nd Edn. Dordrecht: Springer. doi: 10.1007/978-94-010-0658-3

Bers, D. M. (2014). Cardiac sarcoplasmic reticulum calcium leak: basis and roles in cardiac dysfunction. *Annu. Rev. Physiol.* 76, 107–127. doi: 10.1146/annurev-physiol-020911-153308

Biesmans, L., Macquaide, N., Heinzel, F. R., Bito, V., Smith, G. L., and Sipido, K. R. (2011). Subcellular heterogeneity of ryanodine receptor properties in ventricular myocytes with low T-tubule density. *PLoS One* 6:e25100. doi: 10.1371/journal.pone.0025100

Bøkenes, J., Aronsen, J. M., Birkeland, J. A., Henriksen, U. L., Louch, W. E., Sjaastad, I., et al. (2008). Slow contractions characterize failing rat hearts. *Basic Res. Cardiol.* 103, 328–344. doi: 10.1007/s00395-008-0719-y

Bootman, M. D., Higazi, D. R., Coombes, S., and Roderick, H. L. (2006). Calcium signalling during excitation-contraction coupling in mammalian atrial myocytes. *J. Cell Sci.* 119, 3915–3925. doi: 10.1242/jcs.03223

Brette, F., Despa, S., Bers, D. M., and Orchard, C. H. (2005). Spatiotemporal characteristics of SR Ca^{2+} uptake and release in detubulated rat ventricular myocytes. *J. Mol. Cell. Cardiol.* 39, 804–812. doi: 10.1016/j.yjmcc.2005.08.005

Brette, F., and Orchard, C. (2003). T-tubule function in mammalian cardiac myocytes. *Circ. Res.* 92, 1182–1192. doi: 10.1161/01.RES.0000074908.17214.FD

Brette, F., Rodriguez, P., Komukai, K., Colyer, J., and Orchard, C. H. (2004). beta-adrenergic stimulation restores the Ca transient of ventricular myocytes lacking t-tubules. *J. Mol. Cell. Cardiol.* 36, 265–275. doi: 10.1016/j.yjmcc.2003.11.002

Bryant, S., Kimura, T. E., Kong, C. H., Watson, J. J., Chase, A., Suleiman, M. S., et al. (2014). Stimulation of ICa by basal PKA activity is facilitated by caveolin-3 in cardiac ventricular myocytes. *J. Mol. Cell. Cardiol.* 68, 47–55. doi: 10.1016/j.yjmcc.2013.12.026

Bryant, S. M., Kong, C. H., Watson, J., Cannell, M. B., James, A. F., and Orchard, C. H. (2015). Altered distribution of ICa impairs Ca release at the t-tubules of ventricular myocytes from failing hearts. *J. Mol. Cell. Cardiol.* 86, 23–31. doi: 10.1016/j.yjmcc.2015.06.012

Bryant, S. M., Kong, C. H. T., Cannell, M. B., Orchard, C. H., and James, A. F. (2018). Loss of caveolin-3-dependent regulation of ICa in rat ventricular myocytes in heart failure. *Am. J. Physiol. Heart Circ. Physiol.* 314, H521–H529. doi: 10.1152/ajpheart.00458.2017

Cabra, V., Murayama, T., and Samso, M. (2016). Ultrastructural analysis of self-associated RyR2s. *Biophys. J.* 110, 2651–2662. doi: 10.1016/j.bpj.2016.05.013

Caldwell, J. L., Smith, C. E., Taylor, R. F., Kitmitto, A., Eisner, D. A., Dibb, K. M., et al. (2014). Dependence of cardiac transverse tubules on the BAR domain protein amphiphysin II (BIN-1). *Circ. Res.* 115, 986–996. doi: 10.1161/CIRCRESAHA.116.303448

Campiglio, M., and Flucher, B. E. (2017). STAC3 stably interacts through its C1 domain with CaV1.1 in skeletal muscle triads. *Sci. Rep.* 7:41003. doi: 10.1038/srep41003

Chen, B., Guo, A., Zhang, C., Chen, R., Zhu, Y., Hong, J., et al. (2013). Critical roles of junctophilin-2 in T-tubule and excitation-contraction coupling maturation during postnatal development. *Cardiovasc. Res.* 100, 54–62. doi: 10.1093/cvr/cvt180

Chen, B., Li, Y., Jiang, S., Xie, Y. P., Guo, A., Kutschke, W., et al. (2012). beta-Adrenergic receptor antagonists ameliorate myocyte T-tubule remodeling following myocardial infarction. *FASEB J.* 26, 2531–2537. doi: 10.1096/fj.11-199505

Cheng, H., Lederer, W. J., and Cannell, M. B. (1993). Calcium sparks: elementary events underlying excitation-contraction coupling in heart muscle. *Science* 262, 740–744. doi: 10.1126/science.8235594

Crossman, D. J., Shen, X., Jullig, M., Munro, M., Hou, Y., Middleditch, M., et al. (2017). Increased collagen within the transverse tubules in human heart failure. *Cardiovasc. Res.* 113, 879–891. doi: 10.1093/cvr/cvx055

Dibb, K. M., Clarke, J. D., Eisner, D. A., Richards, M. A., and Trafford, A. W. (2013). A functional role for transverse (t-) tubules in the atria. *J. Mol. Cell. Cardiol.* 58, 84–91. doi: 10.1016/j.yjmcc.2012.11.001

Dibb, K. M., Clarke, J. D., Horn, M. A., Richards, M. A., Graham, H. K., Eisner, D. A., et al. (2009). Characterization of an extensive transverse tubular network in sheep atrial myocytes and its depletion in heart failure. *Circ. Heart Fail.* 2, 482–489. doi: 10.1161/CIRCHEARTFAILURE.109.852228

Dixon, R. E., Moreno, C. M., Yuan, C., Opitz-Araya, X., Binder, M. D., Navedo, M. F., et al. (2015). Graded Ca^{2+}/calmodulin-dependent coupling of voltage-gated CaV1.2 channels. *eLife* 4:e05608. doi: 10.7554/eLife.05608

Dixon, R. E., Yuan, C., Cheng, E. P., Navedo, M. F., and Santana, L. F. (2012). Ca^{2+} signaling amplification by oligomerization of L-type Cav1.2 channels. *Proc. Natl. Acad. Sci. U.S.A.* 109, 1749–1754. doi: 10.1073/pnas.1116731109

Dries, E., Santiago, D. J., Gilbert, G., Lenaerts, I., Vandenberk, B., Nagaraju, C. K., et al. (2018). Hyperactive ryanodine receptors in human heart failure and ischemic cardiomyopathy reside outside of couplons. *Cardiovasc. Res.* 114, 1512–1524. doi: 10.1093/cvr/cvy088

Dulhunty, A. F., Karunasekara, Y., Curtis, S. M., Harvey, P. J., Board, P. G., and Casarotto, M. G. (2005). The recombinant dihydropyridine receptor II-III loop and partly structured 'C' region peptides modify cardiac ryanodine receptor activity. *Biochem. J.* 385, 803–813. doi: 10.1042/BJ20041152

El-Hayek, R., Antoniu, B., Wang, J., Hamilton, S. L., and Ikemoto, N. (1995). Identification of calcium release-triggering and blocking regions of the II-III loop of the skeletal muscle dihydropyridine receptor. *J. Biol. Chem.* 270, 22116–22118. doi: 10.1074/jbc.270.38.22116

Fawcett, D. W., and McNutt, N. S. (1969). The ultrastructure of the cat myocardium. I. Ventricular papillary muscle. *J. Cell Biol.* 42, 1–45. doi: 10.1083/jcb.42.1.1

Ferguson, D. G., Schwartz, H. W., and Franzini-Armstrong, C. (1984). Subunit structure of junctional feet in triads of skeletal muscle: a freeze-drying, rotary-shadowing study. *J. Cell Biol.* 99, 1735–1742. doi: 10.1083/jcb.99.5.1735

Franzini-Armstrong, C. (1980). Structure of sarcoplasmic reticulum. *Fed. Proc.* 39, 2403–2409.

Franzini-Armstrong, C., Protasi, F., and Ramesh, V. (1998). Comparative ultrastructure of Ca^{2+} release units in skeletal and cardiac muscle. *Ann. N. Y. Acad. Sci.* 853, 20–30. doi: 10.1111/j.1749-6632.1998.tb08253.x

Franzini-Armstrong, C., Protasi, F., and Ramesh, V. (1999). Shape, size, and distribution of Ca^{2+} release units and couplons in skeletal and cardiac muscles. *Biophys. J.* 77, 1528–1539. doi: 10.1016/S0006-3495(99)77000-1

Franzini-Armstrong, C., Protasi, F., and Tijskens, P. (2005). The assembly of calcium release units in cardiac muscle. *Ann. N. Y. Acad. Sci.* 1047, 76–85. doi: 10.1196/annals.1341.007

Frisk, M., Koivumaki, J. T., Norseng, P. A., Maleckar, M. M., Sejersted, O. M., and Louch, W. E. (2014). Variable t-tubule organization and Ca^{2+} homeostasis across the atria. *Am. J. Physiol. Heart Circ. Physiol.* 307, H609–H620. doi: 10.1152/ajpheart.00295.2014

Frisk, M., Ruud, M., Espe, E. K., Aronsen, J. M., Røe, A. T., Zhang, L., et al. (2016). Elevated ventricular wall stress disrupts cardiomyocyte t-tubule structure and calcium homeostasis. *Cardiovasc. Res.* 112, 443–451. doi: 10.1093/cvr/cvw111

Fu, Y., Shaw, S. A., Naami, R., Vuong, C. L., Basheer, W. A., Guo, X., et al. (2016). Isoproterenol promotes rapid ryanodine receptor movement to bridging integrator 1 (BIN1)-organized dyads. *Circulation* 133, 388–397. doi: 10.1161/CIRCULATIONAHA.115.018535

Gadeberg, H. C., Bond, R. C., Kong, C. H., Chanoit, G. P., Ascione, R., Cannell, M. B., et al. (2016). Heterogeneity of T-tubules in pig hearts. *PLoS One* 11:e0156862. doi: 10.1371/journal.pone.0156862

Ghosh, D., Nieves-Cintron, M., Tajada, S., Brust-Mascher, I., Horne, M. C., Hell, J. W., et al. (2018). Dynamic L-type CaV1.2 channel trafficking facilitates CaV1.2 clustering and cooperative gating. *Biochim. Biophys. Acta* 1865, 1341–1355. doi: 10.1016/j.bbamcr.2018.06.013

Glukhov, A. V., Balycheva, M., Sanchez-Alonso, J. L., Ilkan, Z., Alvarez-Laviada, A., Bhogal, N., et al. (2015). Direct evidence for microdomain-specific localization and remodeling of functional L-type calcium channels in rat and human atrial myocytes. *Circulation* 132, 2372–2384. doi: 10.1161/CIRCULATIONAHA.115.018131

Golini, L., Chouabe, C., Berthier, C., Cusimano, V., Fornaro, M., Bonvallet, R., et al. (2011). Junctophilin 1 and 2 proteins interact with the L-type Ca^{2+} channel dihydropyridine receptors (DHPRs) in skeletal muscle. *J. Biol. Chem.* 286, 43717–43725. doi: 10.1074/jbc.M111.292755

Gomez, A. M., Valdivia, H. H., Cheng, H., Lederer, M. R., Santana, L. F., Cannell, M. B., et al. (1997). Defective excitation-contraction coupling in experimental cardiac hypertrophy and heart failure. *Science* 276, 800–806. doi: 10.1126/science.276.5313.800

Gonano, L. A., and Jones, P. P. (2017). FK506-binding proteins 12 and 12.6 (FKBPs) as regulators of cardiac Ryanodine Receptors: insights from new functional and structural knowledge. *Channels* 11, 415–425. doi: 10.1080/19336950.2017.1344799

Guo, A., Chen, R., Wang, Y., Huang, C. K., Chen, B., Kutschke, W., et al. (2018). Transient activation of PKC results in long-lasting detrimental effects on systolic $Ca^{2+}{}_i$ in cardiomyocytes by altering actin cytoskeletal dynamics and T-tubule integrity. *J. Mol. Cell. Cardiol.* 115, 104–114. doi: 10.1016/j.yjmcc.2018.01.003

Guo, A., Hall, D., Zhang, C., Peng, T., Miller, J. D., Kutschke, W., et al. (2015). Molecular determinants of calpain-dependent cleavage of junctophilin-2 protein in cardiomyocytes. *J. Biol. Chem.* 290, 17946–17955. doi: 10.1074/jbc.M115.652396

Guo, A., Zhang, C., Wei, S., Chen, B., and Song, L. S. (2013). Emerging mechanisms of T-tubule remodelling in heart failure. *Cardiovasc. Res.* 98, 204–215. doi: 10.1093/cvr/cvt020

Guo, A., Zhang, X., Iyer, V. R., Chen, B., Zhang, C., Kutschke, W. J., et al. (2014). Overexpression of junctophilin-2 does not enhance baseline function but attenuates heart failure development after cardiac stress. *Proc. Natl. Acad. Sci. U.S.A.* 111, 12240–12245. doi: 10.1073/pnas.1412729111

Hall, D. D., Dai, S., Tseng, P. Y., Malik, Z., Nguyen, M., Matt, L., et al. (2013). Competition between alpha-actinin and Ca^{2+}-calmodulin controls surface retention of the L-type Ca^{2+} channel Ca(V)1.2. *Neuron* 78, 483–497. doi: 10.1016/j.neuron.2013.02.032

Hayashi, T., Martone, M. E., Yu, Z., Thor, A., Doi, M., Holst, M. J., et al. (2009). Three-dimensional electron microscopy reveals new details of membrane systems for Ca^{2+} signaling in the heart. *J. Cell Sci.* 122, 1005–1013. doi: 10.1242/jcs.028175

He, J., Conklin, M. W., Foell, J. D., Wolff, M. R., Haworth, R. A., Coronado, R., et al. (2001). Reduction in density of transverse tubules and L-type Ca^{2+} channels in canine tachycardia-induced heart failure. *Cardiovasc. Res.* 49, 298–307. doi: 10.1016/S0008-6363(00)00256-X

Head, B. P., Patel, H. H., Roth, D. M., Murray, F., Swaney, J. S., Niesman, I. R., et al. (2006). Microtubules and actin microfilaments regulate lipid raft/caveolae localization of adenylyl cyclase signaling components. *J. Biol. Chem.* 281, 26391–26399. doi: 10.1074/jbc.M602577200

Heinzel, F. R., Bito, V., Biesmans, L., Wu, M., Detre, E., von, W. F., et al. (2008). Remodeling of T-tubules and reduced synchrony of Ca^{2+} release in myocytes from chronically ischemic myocardium. *Circ. Res.* 102, 338–346. doi: 10.1161/CIRCRESAHA.107.160085

Hiess, F., Detampel, P., Nolla-Colomer, C., Vallmitjana, A., Ganguly, A., Amrein, M., et al. (2018). Dynamic and irregular distribution of RyR2 clusters in the periphery of live ventricular myocytes. *Biophys. J.* 114, 343–354. doi: 10.1016/j.bpj.2017.11.026

Hodne, K., Lipsett, D. B., and Louch, W. E. (2017). Gene transfer in isolated adult cardiomyocytes. *Methods Mol. Biol.* 1521, 169–182. doi: 10.1007/978-1-4939-6588-5_11

Hong, T., Yang, H., Zhang, S. S., Cho, H. C., Kalashnikova, M., Sun, B., et al. (2014). Cardiac BIN1 folds T-tubule membrane, controlling ion flux and limiting arrhythmia. *Nat. Med.* 20, 624–632. doi: 10.1038/nm.3543

Hong, T. T., Cogswell, R., James, C. A., Kang, G., Pullinger, C. R., Malloy, M. J., et al. (2012). Plasma BIN1 correlates with heart failure and predicts arrhythmia in patients with arrhythmogenic right ventricular cardiomyopathy. *Heart Rhythm* 9, 961–967. doi: 10.1016/j.hrthm.2012.01.024

Hong, T. T., Smyth, J. W., Gao, D., Chu, K. Y., Vogan, J. M., Fong, T. S., et al. (2010). BIN1 localizes the L-type calcium channel to cardiac T-tubules. *PLoS Biol.* 8:e1000312. doi: 10.1371/journal.pbio.1000312

Huang, C. K., Chen, B. Y., Guo, A., Chen, R., Zhu, Y. Q., Kutschke, W., et al. (2016). Sildenafil ameliorates left ventricular T-tubule remodeling in a pressure overload-induced murine heart failure model. *Acta Pharmacol. Sin.* 37, 473–482. doi: 10.1038/aps.2016.13

Ibrahim, M., Kukadia, P., Siedlecka, U., Cartledge, J. E., Navaratnarajah, M., and Tokar, S. (2012a). Cardiomyocyte Ca^{2+} handling and structure is regulated by degree and duration of mechanical load variation. *J. Cell. Mol. Med.* 16, 2910–2918. doi: 10.1111/j.1582-4934.2012.01611.x

Ibrahim, M., Navaratnarajah, M., Siedlecka, U., Rao, C., Dias, P., Moshkov, A. V., et al. (2012b). Mechanical unloading reverses transverse tubule remodelling and normalizes local Ca^{2+}-induced Ca^{2+}release in a rodent model of heart failure. *Eur. J. Heart Fail.* 14, 571–580. doi: 10.1093/eurjhf/hfs038

Ibrahim, M., Siedlecka, U., Buyandelger, B., Harada, M., Rao, C., Moshkov, A., et al. (2013). A critical role for Telethonin in regulating t-tubule structure and function in the mammalian heart. *Hum. Mol. Genet.* 22, 372–383. doi: 10.1093/hmg/dds434

Ibrahim, M., and Terracciano, C. M. (2013). Reversibility of T-tubule remodelling in heart failure: mechanical load as a dynamic regulator of the T-tubules. *Cardiovasc. Res.* 98, 225–232. doi: 10.1093/cvr/cvt016

Jayasinghe, I., Clowsley, A. H., Lin, R., Lutz, T., Harrison, C., Green, E., et al. (2018). True molecular scale visualization of variable clustering properties of ryanodine receptors. *Cell Rep.* 22, 557–567. doi: 10.1016/j.celrep.2017.12.045

Jiang, M., Zhang, M., Howren, M., Wang, Y., Tan, A., Balijepalli, R. C., et al. (2016). JPH-2 interacts with $Ca^{2+}{}_i$-handling proteins and ion channels in dyads: contribution to premature ventricular contraction-induced cardiomyopathy. *Heart Rhythm* 13, 743–752. doi: 10.1016/j.hrthm.2015.10.037

Jones, P. P., Meng, X., Xiao, B., Cai, S., Bolstad, J., Wagenknecht, T., et al. (2008). Localization of PKA phosphorylation site, Ser (2030), in the three-dimensional structure of cardiac ryanodine receptor. *Biochem. J.* 410, 261–270. doi: 10.1042/BJ20071257

Kamp, T. J., and He, J. Q. (2002). L-type Ca^{2+} channels gaining respect in heart failure. *Circ. Res.* 91, 451–453. doi: 10.1161/01.RES.0000035346.21625.4A

Kamp, T. J., and Hell, J. W. (2000). Regulation of cardiac L-type calcium channels by protein kinase A and protein kinase C. *Circ. Res.* 87, 1095–1102. doi: 10.1161/01.RES.87.12.1095

Kemi, O. J., Høydal, M. A., Macquaide, N., Haram, P. M., Koch, L. G., Britton, S. L., et al. (2011). The effect of exercise training on transverse tubules in normal, remodeled, and reverse remodeled hearts. *J. Cell. Physiol.* 226, 2235–2243. doi: 10.1002/jcp.22559

Kolstad, T. R., van den Brink, J., MacQuaide, N., Lunde, P. K., Frisk, M., Aronsen, J. M. et al. (2018). Ryanodine receptor dispersion disrupts Ca^{2+} release in failing cardiac myocytes. *eLife* 7: e39427. doi: 10.7554/eLife.39427

Korhonen, T., Rapila, R., Ronkainen, V. P., Koivumaki, J. T., and Tavi, P. (2010). Local Ca^{2+} releases enable rapid heart rates in developing cardiomyocytes. *J. Physiol.* 588, 1407–1417. doi: 10.1113/jphysiol.2009.185173

Landstrom, A. P., Kellen, C. A., Dixit, S. S., van Oort, R. J., Garbino, A., Weisleder, N., et al. (2011). Junctophilin-2 expression silencing causes cardiocyte hypertrophy and abnormal intracellular calcium-handling. *Circ. Heart Fail.* 4, 214–223. doi: 10.1161/CIRCHEARTFAILURE.110.958694

Lee, E., Marcucci, M., Daniell, L., Pypaert, M., Weisz, O. A., Ochoa, G. C., et al. (2002). Amphiphysin 2 (Bin1) and T-tubule biogenesis in muscle. *Science* 297, 1193–1196. doi: 10.1126/science.1071362

Lenaerts, I., Bito, V., Heinzel, F. R., Driesen, R. B., Holemans, P., D'hooge, J., et al. (2009). Ultrastructural and functional remodeling of the coupling between Ca^{2+} influx and sarcoplasmic reticulum Ca^{2+} release in right atrial myocytes from experimental persistent atrial fibrillation. *Circ. Res.* 105, 876–885. doi: 10.1161/CIRCRESAHA.109.206276

Lichter, J. G., Carruth, E., Mitchell, C., Barth, A. S., Aiba, T., Kass, D. A., et al. (2014). Remodeling of the sarcomeric cytoskeleton in cardiac ventricular myocytes during heart failure and after cardiac resynchronization therapy. *J. Mol. Cell. Cardiol.* 72, 186–195. doi: 10.1016/j.yjmcc.2014.03.012

Lipp, P., Huser, J., Pott, L., and Niggli, E. (1996). Spatially non-uniform Ca^{2+} signals induced by the reduction of transverse tubules in citrate-loaded guinea-pig ventricular myocytes in culture. *J. Physiol.* 497, 589–597. doi: 10.1113/jphysiol.1996.sp021792

Litwin, S. E., Zhang, D., and Bridge, J. H. (2000). Dyssynchronous Ca^{2+} sparks in myocytes from infarcted hearts. *Circ. Res.* 87, 1040–1047. doi: 10.1161/01.RES.87.11.1040

Louch, W. E., Bito, V., Heinzel, F. R., Macianskiene, R., Vanhaecke, J., Flameng, W., et al. (2004). Reduced synchrony of Ca^{2+} release with loss of T-tubules-a comparison to Ca^{2+} release in human failing cardiomyocytes. *Cardiovasc. Res.* 62, 63–73. doi: 10.1016/j.cardiores.2003.12.031

Louch, W. E., Hake, J., Mørk, H. K., Hougen, K., Skrbic, B., Ursu, D., et al. (2013). Slow Ca^{2+} sparks de-synchronize Ca^{2+} release in failing cardiomyocytes: evidence for altered configuration of Ca^{2+} release units? *J. Mol. Cell. Cardiol.* 58, 41–52. doi: 10.1016/j.yjmcc.2013.01.014

Louch, W. E., Koivumaki, J. T., and Tavi, P. (2015). Calcium signalling in developing cardiomyocytes: implications for model systems and disease. *J. Physiol.* 593, 1047–1063. doi: 10.1113/jphysiol.2014.274712

Louch, W. E., Mørk, H. K., Sexton, J., Stromme, T. A., Laake, P., Sjaastad, I., et al. (2006). T-tubule disorganization and reduced synchrony of Ca^{2+} release in murine cardiomyocytes following myocardial infarction. *J. Physiol.* 574, 519–533. doi: 10.1113/jphysiol.2006.107227

Louch, W. E., and Nattel, S. (2017). T-tubular collagen: a new player in mechanosensing and disease? *Cardiovasc. Res.* 113, 839–840. doi: 10.1093/cvr/cvx091

Louch, W. E., Sejersted, O. M., and Swift, F. (2010). There goes the neighborhood: pathological alterations in T-tubule morphology and consequences for cardiomyocyte Ca^{2+} handling. *J. Biomed. Biotechnol.* 2010:503906. doi: 10.1155/2010/503906

Lu, X., Xu, L., and Meissner, G. (1994). Activation of the skeletal muscle calcium release channel by a cytoplasmic loop of the dihydropyridine receptor. *J. Biol. Chem.* 269, 6511–6516.

Lyon, A. R., MacLeod, K. T., Zhang, Y., Garcia, E., Kanda, G. K., Lab, M. J., et al. (2009). Loss of T-tubules and other changes to surface topography in ventricular myocytes from failing human and rat heart. *Proc. Natl. Acad. Sci. U.S.A.* 106, 6854–6859. doi: 10.1073/pnas.0809777106

Mackova, K., Zahradnikova, A. Jr., Hotka, M., Hoffmannova, B., Zahradnik, I., and Zahradnikova, A. (2017). Calcium release-dependent inactivation precedes formation of the tubular system in developing rat cardiac myocytes. *Eur. Biophys. J.* 46, 691–703. doi: 10.1007/s00249-017-1249-z

Macquaide, N., Tuan, H. T., Hotta, J., Sempels, W., Lenaerts, I., Holemans, P., et al. (2015). Ryanodine receptor cluster fragmentation and redistribution in persistent atrial fibrillation enhance calcium release. *Cardiovasc. Res.* 108, 387–398. doi: 10.1093/cvr/cvv231

Manfra, O., Frisk, M., and Louch, W. E. (2017). Regulation of cardiomyocyte T-tubular structure: opportunities for therapy. *Curr. Heart Fail. Rep.* 14, 167–178. doi: 10.1007/s11897-017-0329-9

Marx, S. O., Gaburjakova, J., Gaburjakova, M., Henrikson, C., Ondrias, K., and Marks, A. R. (2001). Coupled gating between cardiac calcium release channels (ryanodine receptors). *Circ. Res.* 88, 1151–1158. doi: 10.1161/hh1101.091268

Marx, S. O., Reiken, S., Hisamatsu, Y., Jayaraman, T., Burkhoff, D., Rosemblit, N., et al. (2000). PKA phosphorylation dissociates FKBP12.6 from the calcium release channel (ryanodine receptor): defective regulation in failing hearts. *Cell* 101, 365–376. doi: 10.1016/S0092-8674(00)80847-8

McNary, T. G., Spitzer, K. W., Holloway, H., Bridge, J. H., Kohl, P., and Sachse, F. B. (2012). Mechanical modulation of the transverse tubular system of ventricular cardiomyocytes. *Prog. Biophys. Mol. Biol.* 110, 218–225. doi: 10.1016/j.pbiomolbio.2012.07.010

Minamisawa, S., Oshikawa, J., Takeshima, H., Hoshijima, M., Wang, Y., Chien, K. R., et al. (2004). Junctophilin type 2 is associated with caveolin-3 and is down-regulated in the hypertrophic and dilated cardiomyopathies. *Biochem. Biophys. Res. Commun.* 325, 852–856. doi: 10.1016/j.bbrc.2004.10.107

Mørk, H. K., Sjaastad, I., Sejersted, O. M., and Louch, W. E. (2009). Slowing of cardiomyocyte Ca^{2+} release and contraction during heart failure progression in postinfarction mice. *Am. J. Physiol. Heart Circ. Physiol.* 296, H1069–H1079. doi: 10.1152/ajpheart.01009.2008

Munro, M. L., Jayasinghe, I. D., Wang, Q., Quick, A., Wang, W., Baddeley, D., et al. (2016). Junctophilin-2 in the nanoscale organisation and functional signalling of ryanodine receptor clusters in cardiomyocytes. *J. Cell Sci.* 129, 4388–4398. doi: 10.1242/jcs.196873

Munro, M. L., and Soeller, C. (2016). Early transverse tubule development begins in utero in the sheep heart. *J. Muscle Res. Cell Motil.* 37, 195–202. doi: 10.1007/s10974-016-9462-4

Navedo, M. F., Cheng, E. P., Yuan, C., Votaw, S., Molkentin, J. D., Scott, J. D., et al. (2010). Increased coupled gating of L-type Ca^{2+} channels during hypertension and Timothy syndrome. *Circ. Res.* 106, 748–756. doi: 10.1161/CIRCRESAHA.109.213363

Nelson, B. R., Wu, F., Liu, Y., Anderson, D. M., McAnally, J., Lin, W., et al. (2013). Skeletal muscle-specific T-tubule protein STAC3 mediates voltage-induced Ca^{2+} release and contractility. *Proc. Natl. Acad. Sci. U.S.A.* 110, 11881–11886. doi: 10.1073/pnas.1310571110

Orchard, C. H., Bryant, S. M., and James, A. F. (2013). Do t-tubules play a role in arrhythmogenesis in cardiac ventricular myocytes? *J. Physiol.* 591, 4141–4147. doi: 10.1113/jphysiol.2013.254540

Øyehaug, L., Loose, K. O., Jølle, G. F., Røe, A. T., Sjaastad, I., Christensen, G., et al. (2013). Synchrony of cardiomyocyte Ca^{2+} release is controlled by t-tubule organization, SR Ca^{2+} content, and ryanodine receptor Ca^{2+} sensitivity. *Biophys. J.* 104, 1685–1697. doi: 10.1016/j.bpj.2013.03.022

Parton, R. G., Way, M., Zorzi, N., and Stang, E. (1997). Caveolin-3 associates with developing T-tubules during muscle differentiation. *J. Cell Biol.* 136, 137–154. doi: 10.1083/jcb.136.1.137

Picas, L., Viaud, J., Schauer, K., Vanni, S., Hnia, K., Fraisier, V., et al. (2014). BIN1/M-Amphiphysin2 induces clustering of phosphoinositides to recruit its downstream partner dynamin. *Nat. Commun.* 5:5647. doi: 10.1038/ncomms6647

Pinali, C., Bennett, H., Davenport, J. B., Trafford, A. W., and Kitmitto, A. (2013). Three-dimensional reconstruction of cardiac sarcoplasmic reticulum reveals a continuous network linking transverse-tubules: this organization is perturbed in heart failure. *Circ. Res.* 113, 1219–1230. doi: 10.1161/CIRCRESAHA.113.301348

Pinali, C., Malik, N., Davenport, J. B., Allan, L. J., Murfitt, L., Iqbal, M. M., et al. (2017). Post-myocardial infarction T-tubules form enlarged branched structures with dysregulation of junctophilin-2 and bridging integrator 1 (BIN-1). *J. Am. Heart Assoc.* 6:e004834. doi: 10.1161/JAHA.116.004834

Polster, A., Nelson, B. R., Olson, E. N., and Beam, K. G. (2016). Stac3 has a direct role in skeletal muscle-type excitation-contraction coupling that is disrupted by a myopathy-causing mutation. *Proc. Natl. Acad. Sci. U.S.A.* 113, 10986–10991. doi: 10.1073/pnas.1612441113

Prins, K. W., Asp, M. L., Zhang, H., Wang, W., and Metzger, J. M. (2016). Microtubule-mediated misregulation of junctophilin-2 underlies T-tubule disruptions and calcium mishandling in mdx mice. *JACC Basic Transl. Sci.* 1, 122–130. doi: 10.1016/j.jacbts.2016.02.002

Quick, A. P., Wang, Q., Philippen, L. E., Barreto-Torres, G., Chiang, D. Y., Beavers, D., et al. (2017). SPEG (Striated Muscle Preferentially Expressed Protein Kinase) is essential for cardiac function by regulating junctional membrane complex activity. *Circ. Res.* 120, 110–119. doi: 10.1161/CIRCRESAHA.116.309977

Reynolds, J. O., Chiang, D. Y., Wang, W., Beavers, D. L., Dixit, S. S., Skapura, D. G., et al. (2013). Junctophilin-2 is necessary for T-tubule maturation during mouse heart development. *Cardiovasc. Res.* 100, 44–53. doi: 10.1093/cvr/cvt133

Reynolds, J. O., Quick, A. P., Wang, Q., Beavers, D. L., Philippen, L. E., Showell, J., et al. (2016). Junctophilin-2 gene therapy rescues heart failure by normalizing RyR2-mediated Ca^{2+} release. *Int. J. Cardiol.* 225, 371–380. doi: 10.1016/j.ijcard.2016.10.021

Richards, M. A., Clarke, J. D., Saravanan, P., Voigt, N., Dobrev, D., Eisner, D. A., et al. (2011). Transverse tubules are a common feature in large mammalian atrial myocytes including human. *Am. J. Physiol. Heart Circ. Physiol.* 301, H1996–H2005. doi: 10.1152/ajpheart.00284.2011

Røe, A. T., Frisk, M., and Louch, W. E. (2015). Targeting cardiomyocyte Ca^{2+} homeostasis in heart failure. *Curr. Pharm. Des.* 21, 431–448. doi: 10.2174/1381612821041412041241 29

Sanchez-Alonso, J. L., Bhargava, A., O'Hara, T., Glukhov, A. V., Schobesberger, S., Bhogal, N., et al. (2016). Microdomain-specific modulation of l-type calcium channels leads to triggered ventricular arrhythmia in heart failure. *Circ. Res.* 119, 944–955. doi: 10.1161/CIRCRESAHA.116.308698

Seidel, T., Navankasattusas, S., Ahmad, A., Diakos, N. A., Xu, W. D., Tristani-Firouzi, M., et al. (2017a). Sheet-like remodeling of the transverse tubular system in human heart failure impairs excitation-contraction coupling and functional recovery by mechanical unloading. *Circulation* 135, 1632–1645. doi: 10.1161/CIRCULATIONAHA.116.024470

Seidel, T., Sankarankutty, A. C., and Sachse, F. B. (2017b). Remodeling of the transverse tubular system after myocardial infarction in rabbit correlates with local fibrosis: a potential role of biomechanics. *Prog. Biophys. Mol. Biol.* 130, 302–314. doi: 10.1016/j.pbiomolbio.2017.07.006

Shen, X., van den Brink, J., Kolstad, T., Norden, E., Edwards, A. G., Frisk, M., et al. (2018). 3D dSTORM imaging reveals disassembly of ryanodine receptor clusters in failing cardiomyocytes. *Biophys. J.* 114:621a. doi: 10.1016/j.bpj.2017.11.3357

Singh, J. K., Barsegyan, V., Bassi, N., Marszalec, W., Tai, S., Mothkur, S., et al. (2017). T-tubule remodeling and increased heterogeneity of calcium release during the progression to heart failure in intact rat ventricle. *Physiol. Rep.* 5:e13540. doi: 10.14814/phy2.13540

Smyrnias, I., Mair, W., Harzheim, D., Walker, S. A., Roderick, H. L., and Bootman, M. D. (2010). Comparison of the T-tubule system in adult rat ventricular and atrial myocytes, and its role in excitation-contraction coupling and inotropic stimulation. *Cell Calcium* 47, 210–223. doi: 10.1016/j.ceca.2009.10.001

Sobie, E. A., Guatimosim, S., Gomez-Viquez, L., Song, L. S., Hartmann, H., Saleet, J. M., et al. (2006). The Ca^{2+} leak paradox and rogue ryanodine receptors: SR Ca^{2+} efflux theory and practice. *Prog. Biophys. Mol. Biol.* 90, 172–185. doi: 10.1016/j.pbiomolbio.2005.06.010

Song, L. S., Guatimosim, S., Gomez-Viquez, L., Sobie, E. A., Ziman, A., Hartmann, H., et al. (2005). Calcium biology of the transverse tubules in heart. *Ann. N. Y. Acad. Sci.* 1047, 99–111. doi: 10.1196/annals.1341.009

Song, L. S., Sobie, E. A., McCulle, S., Lederer, W. J., Balke, C. W., and Cheng, H. (2006). Orphaned ryanodine receptors in the failing heart. *Proc. Natl. Acad. Sci. U.S.A.* 103, 4305–4310. doi: 10.1073/pnas.0509324103

Stølen, T. O., Høydal, M. A., Kemi, O. J., Catalucci, D., Ceci, M., Aasum, E., et al. (2009). Interval training normalizes cardiomyocyte function, diastolic Ca^{2+} control, and SR Ca^{2+} release synchronicity in a mouse model of diabetic cardiomyopathy. *Circ. Res.* 105, 527–536. doi: 10.1161/CIRCRESAHA.109.199810

Sun, X. H., Protasi, F., Takahashi, M., Takeshima, H., Ferguson, D. G., and Franzini-Armstrong, C. (1995). Molecular architecture of membranes involved in excitation-contraction coupling of cardiac muscle. *J. Cell Biol.* 129, 659–671. doi: 10.1083/jcb.129.3.659

Swift, F., Birkeland, J. A., Tovsrud, N., Enger, U. H., Aronsen, J. M., Louch, W. E., et al. (2008). Altered Na^+/Ca^{2+}-exchanger activity due to downregulation of Na^+/K^+-ATPase alpha2-isoform in heart failure. *Cardiovasc. Res.* 78, 71–78. doi: 10.1093/cvr/cvn013

Swift, F., Franzini-Armstrong, C., Øyehaug, L., Enger, U. H., Andersson, K. B., Christensen, G., et al. (2012). Extreme sarcoplasmic reticulum volume loss and compensatory T-tubule remodeling following *Serca2* knockout. *Proc. Natl. Acad. Sci. U.S.A.* 109, 3997–4001. doi: 10.1073/pnas.1120172109

Takekura, H., Paolini, C., Franzini-Armstrong, C., Kugler, G., Grabner, M., and Flucher, B. E. (2004). Differential contribution of skeletal and cardiac II-III loop sequences to the assembly of dihydropyridine-receptor arrays in skeletal muscle. *Mol. Biol. Cell* 15, 5408–5419. doi: 10.1091/mbc.e04-05-0414

Takeshima, H., Komazaki, S., Nishi, M., Iino, M., and Kangawa, K. (2000). Junctophilins: a novel family of junctional membrane complex proteins. *Mol. Cell* 6, 11–22.

Terentyev, D., Viatchenko-Karpinski, S., Gyorke, I., Volpe, P., Williams, S. C., and Gyorke, S. (2003). Calsequestrin determines the functional size and stability of cardiac intracellular calcium stores: mechanism for hereditary arrhythmia. *Proc. Natl. Acad. Sci. U.S.A.* 100, 11759–11764. doi: 10.1073/pnas.1932318100

Tian, Q., Pahlavan, S., Oleinikow, K., Jung, J., Ruppenthal, S., Scholz, A., et al. (2012). Functional and morphological preservation of adult ventricular myocytes in culture by sub-micromolar cytochalasin D supplement. *J. Mol. Cell. Cardiol.* 52, 113–124. doi: 10.1016/j.yjmcc.2011.09.001

van Oort, R. J., Garbino, A., Wang, W., Dixit, S. S., Landstrom, A. P., Gaur, N., et al. (2011). Disrupted junctional membrane complexes and hyperactive ryanodine receptors after acute junctophilin knockdown in mice. *Circulation* 123, 979–988. doi: 10.1161/CIRCULATIONAHA.110.006437

Waddell, H. M. M., Zhang, J. Z., Hoeksema, K. J., McLachlan, J. J., McLay, J. C., and Jones, P. P. (2016). Oxidation of RyR2 has a biphasic effect on the threshold for store overload-induced calcium release. *Biophys. J.* 110, 2386–2396. doi: 10.1016/j.bpj.2016.04.036

Wagner, E., Lauterbach, M. A., Kohl, T., Westphal, V., Williams, G. S., Steinbrecher, J. H., et al. (2012). Stimulated emission depletion live-cell super-resolution imaging shows proliferative remodeling of T-tubule membrane structures after myocardial infarction. *Circ. Res.* 111, 402–414. doi: 10.1161/CIRCRESAHA.112.274530

Walker, M. A., Kohl, T., Lehnart, S. E., Greenstein, J. L., Lederer, W. J., and Winslow, R. L. (2015). On the adjacency matrix of RyR2 cluster structures. *PLoS Comput. Biol.* 11:e1004521. doi: 10.1371/journal.pcbi.1004521

Walker, M. A., Williams, G. S. B., Kohl, T., Lehnart, S. E., Jafri, M. S., Greenstein, J. L., et al. (2014). Superresolution modeling of calcium release in the heart. *Biophys. J.* 107, 3018–3029. doi: 10.1016/j.bpj.2014.11.003

Ward, M. L., and Crossman, D. J. (2014). Mechanisms underlying the impaired contractility of diabetic cardiomyopathy. *World J. Cardiol.* 6, 577–584. doi: 10.4330/wjc.v6.i7.577

Wei, S., Guo, A., Chen, B., Kutschke, W., Xie, Y. P., Zimmerman, K., et al. (2010). T-tubule remodeling during transition from hypertrophy to heart failure. *Circ. Res.* 107, 520–531. doi: 10.1161/CIRCRESAHA.109.212324

Williams, A. J., Thomas, N. L., and George, C. H. (2018). The ryanodine receptor: advances in structure, and organization. *Curr. Opin. Physiol.* 1, 1–6. doi: 10.4081/ejtm.2015.4840

Wu, H. D., Xu, M., Li, R. C., Guo, L., Lai, Y. S., Xu, S. M., et al. (2012). Ultrastructural remodelling of Ca^{2+} signalling apparatus in failing heart cells. *Cardiovasc. Res.* 95, 430–438. doi: 10.1093/cvr/cvs195

Xie, Y. P., Chen, B., Sanders, P., Guo, A., Li, Y., Zimmerman, K., et al. (2012). Sildenafil prevents and reverses transverse-tubule remodeling and Ca^{2+} handling dysfunction in right ventricle failure induced by pulmonary artery hypertension. *Hypertension* 59, 355–362. doi: 10.1161/HYPERTENSIONAHA.111.180968

Xu, M., Wu, H. D., Li, R. C., Zhang, H. B., Wang, M., Tao, J., et al. (2012). Mir-24 regulates junctophilin-2 expression in cardiomyocytes. *Circ. Res.* 111, 837–841. doi: 10.1161/CIRCRESAHA.112.277418

Zhang, C., Chen, B., Guo, A., Zhu, Y., Miller, J. D., Gao, S., et al. (2014). Microtubule-mediated defects in junctophilin-2 trafficking contribute to myocyte transverse-tubule remodeling and Ca^{2+} handling dysfunction in heart failure. *Circulation* 129, 1742–1750. doi: 10.1161/CIRCULATIONAHA.113.008452

Zhang, J. Z., Waddell, H. M., Wu, E., Dholakia, J., Okolo, C. A., McLay, J. C., et al. (2016). FKBPs facilitate the termination of spontaneous Ca^{2+} release in wild-type RyR2 but not CPVT mutant RyR2. *Biochem. J.* 473, 2049–2060. doi: 10.1042/BCJ20160389

Ziman, A. P., Gomez-Viquez, N. L., Bloch, R. J., and Lederer, W. J. (2010). Excitation-contraction coupling changes during postnatal cardiac development. *J. Mol. Cell. Cardiol.* 48, 379–386. doi: 10.1016/j.yjmcc.2009.09.016

Conflict of Interest Statement: NM was employed by Clyde Biosciences (Glasgow, United Kingdom).

The remaining authors declare that the research was conducted in the absence of any commercial or financial relationships that could be construed as a potential conflict of interest.

frontiers in Physiology

ORIGINAL RESEARCH
published: 13 December 2018
doi: 10.3389/fphys.2018.01785

Potential Arrhythmogenic Role of TRPC Channels and Store-Operated Calcium Entry Mechanism in Mouse Ventricular Myocytes

*Hairuo Wen[1,2], Zhenghang Zhao[3], Nadezhda Fefelova[1] and Lai-Hua Xie[1]**

[1] Department of Cell Biology and Molecular Medicine, Rutgers New Jersey Medical School, Newark, NJ, United States, [2] Key Laboratory of Beijing for Nonclinical Safety Evaluation Research of Drugs, National Center for Safety Evaluation of Drugs, National Institutes for Food and Drug Control, Beijing, China, [3] Department of Pharmacology, School of Basic Medical Sciences, Xi'an Jiaotong University, Xi'an, China

OPEN ACCESS

Edited by:
Di Lang,
University of Wisconsin–Madison, United States

Reviewed by:
Jianxin Sun,
Thomas Jefferson University, United States
Peter Backx,
University of Toronto, Canada

***Correspondence:**
Lai-Hua Xie
xiela@njms.rutgers.edu;
laihuaxie@yahoo.com

Specialty section:
This article was submitted to Cardiac Electrophysiology, a section of the journal Frontiers in Physiology

Received: *27 July 2018*
Accepted: *28 November 2018*
Published: *13 December 2018*

Citation:
Wen H, Zhao Z, Fefelova N and Xie L-H (2018) Potential Arrhythmogenic Role of TRPC Channels and Store-Operated Calcium Entry Mechanism in Mouse Ventricular Myocytes. Front. Physiol. 9:1785. doi: 10.3389/fphys.2018.01785

Background and Purpose: Store-operated calcium entry (SOCE) is an important physiological phenomenon that extensively mediates intracellular calcium ion (Ca^{2+}) load. It has been previously found in myocytes isolated from neonatal or diseased hearts. We aimed to determine its existence, molecular nature in undiseased hearts and its potential arrhythmogenic implications under hyperactive conditions.

Experimental Approach: Ventricular myocytes isolated from adult FVB mice were studied by using Ca^{2+} imaging and whole-cell perforated patch-clamp recording. In addition, lead II ECGs were recorded in isolated Langendorff-perfused mice hearts. Functional TRPC channel antibodies and inhibitors, and TRPC6 activator hyperforin were used.

Key Results: In this study, we demonstrate the existence and contribution of SOCE in normal adult mouse cardiac myocytes. For an apparent SOCE activation, complete depletion of sarcoplasmic reticulum (SR) Ca^{2+} by employing both caffeine (10 mM) and thapsigargin (1 μM) or cyclopiazonic acid (10 μM) was required. Consistent with the notion that SOCE may be mediated by heteromultimeric TRPC channels, SOCEs observed from those myocytes were significantly reduced by the pretreatment with anti-TRPC1, 3, and 6 antibodies as well as by gadolinium, a non-selective TRPC channel blocker. In addition, we showed that SOCE may regulate spontaneous SR Ca^{2+} release, Ca^{2+} waves, and triggered activities which may manifest cardiac arrhythmias. Since the spontaneous depolarization in membrane potential preceded the elevation of intracellular Ca^{2+}, an inward membrane current presumably via TRPC channels was considered as the predominant cause of cellular arrhythmias. The selective TRPC6 activator hyperforin (0.1–10 μM) significantly facilitated the SOCE, SOCE-mediated inward current, and calcium load in the ventricular myocytes. ECG recording further demonstrated the proarrhythmic effects of hyperforin in *ex vivo* mouse hearts.

Conclusion and Implications: We suggest that SOCE, which is at least partially mediated by TRPC channels, exists in adult mouse ventricular myocytes. TRPC channels and SOCE mechanism may be involved in cardiac arrhythmogenesis via promotion of spontaneous Ca^{2+} waves and triggered activities under hyperactivated conditions.

Keywords: calcium, arrhythmogenesis, TRPCs, store-operated calcium entry, hyperforin

INTRODUCTION

Intracellular/cytosolic calcium ion (Ca^{2+}) is crucial in regulating various fundamental cellular processes (Berridge, 1993; Carafoli, 2002), while dysfunction of Ca^{2+} handling leads to pathological consequences such as cardiac arrhythmias and hypertrophy (Wit and Janse, 1992). Elevation in Ca^{2+} concentration can be mediated by a process referred as SOCE in many cell types, i.e., an extracellular Ca^{2+} influx through plasma membrane channels triggered by an excessive release/depletion of Ca^{2+} from ER or SR stores (Putney, 1986; Selvaraj et al., 2010). SOCE has been identified as a major process for increasing Ca^{2+} load after the ER/SR Ca^{2+} depletion in eukaryotic cells (Parekh and Putney, 2005). Although SOCE has also been found in myocytes isolated from neonatal and diseased hearts (Uemura et al., 2002; Huang et al., 2006; Sabourin et al., 2016; Ross et al., 2017), its existence, molecular nature in undiseased hearts and its potential arrhythmogenic implications under hyperactive conditions remain elusive.

Transient receptor potential canonical (TRPC) channels are a family of non-selective cytoplasmic channels distributed throughout the cardiac myocytes, and six subtypes (TRPC1 and 3-7) have been identified in human ventricles (Venkatachalam and Montell, 2007). TRPC channels contribute to both Ca^{2+} influx and inward membrane currents, which in turn could mediate cellular signaling and Ca^{2+} homeostasis (Liao et al., 2009). The participations of TRPC channels in calcium signaling in the form of SOCE were primarily revealed in a heterogeneous expression system, in which ER/SR depletion-activated Ca^{2+} entry was significantly enhanced by the over-expression of TRPC subtypes, and reduced by pharmacological and genetic knockdown approaches (Liao et al., 2009). Recent studies have further proposed that the TRPC channels constitute SOCE by forming complex together with calcium release-activated calcium channel protein 1 (Orai1) and the STIM1 on ER/SR (Ong et al., 2007; Liao et al., 2008, 2009). Following the emptying of SR Ca^{2+} stores, STIM1 is activated and leads to the redistribution of Orai1 and TRPCs to assemble the SOCE channel complex in mediating the Ca^{2+} entry (Liao et al., 2009). Recent studies have also demonstrated TRPC channels may play important roles in the regulation of electromechanical activity of the developing heart (Sabourin et al., 2011), Ca^{2+} paradox injury (Kojima et al., 2010), as well as in pathological structural and functional remodeling after myocardial infarction (Makarewich et al., 2014). Hyperforin, an extract from the medicinal herb St. John's Wort (*Hypericum perforatum*), exhibits antidepressant properties, although the underlying mechanism is not clear yet (Chatterjee et al., 1998). It has been shown that hyperforin is a selective activator of TRPC6, and leads to a non-selective cation current (Leuner et al., 2007). Therefore, we have used hyperforin as a tool to test potential deleterious effect of TRPC channel hyperactivation.

In the present study, we demonstrate the presence of SOCE in adult mouse ventricular myocytes, and elucidate the possible roles of SOCE/TRPCs in promoting cardiac arrhythmias via facilitating the generation of inward current and calcium load. Our findings support a missing link between upregulated SOCE/TRPCs activities, especially TRPC6, to lethal arrhythmias in the heart.

Abbreviations: AP, action potential; CPA, cyclopiazonic acid; DAD, delayed afterdepolarization; EAD, early afterdepolarization; ER, endoplasmic reticulum; IP_3R, IP_3 receptor; NCX, sodium calcium exchanger; PCL, pacing cycle length; RyR, ryanodine receptor; SERCA, sarcoplasmic reticulum calcium ATPase; SOCE, store-operated calcium entry; SR, sarcoplasmic reticulum; STIM1, calcium sensor identified stromal interaction molecule 1; TAs, triggered activities; TRPC, transient receptor potential canonical.

MATERIALS AND METHODS

All animal experimental procedures were reviewed and approved by the Institutional Animal Care and Use Committee at the Rutgers New Jersey Medical School. All chemicals were purchased from Sigma Aldrich unless indicated. The functional (pore inhibitory) antibodies for TRPC1, 3 and 6 were a generous gift from Dr. Robert M. Graham (University of Sydney, and Victor Chang Cardiac Research Institute). These antibodies recognize the putative pore-forming region of mouse TRPC channels specifically, and pre-incubation with anti-TRPC6 antibody could effectively block the rise of intracellular Ca^{2+} concentration ($[Ca^{2+}]$) upon restoration of external calcium load (1.8 mM) (Mohl et al., 2011). The SERCA inhibitor thapsigargin (Tha), SOCE inhibitors ML-9, gadolinium and Pyr3, and TRPC6 activator hyperforin were dissolved in DMSO as stock solutions before diluting into the bath solution at the final concentrations. The maximum DMSO concentration was $< 0.2\%$ (vol/vol).

Cell Isolation

Ventricular myocytes were enzymatically isolated from the left ventricles of FVB mice (male, 4–6 months). Briefly, hearts were removed from mice anesthetized with overdosed isoflurane, and were perfused retrogradely at 37°C in Langendorff fashion with nominally Ca^{2+}-free Tyrode's solution containing 1.0 mg/mL collagenase (Type II; Worthington) and 0.1 mg/mL thermolysin (Sigma) for 15 min. The hearts were removed from the perfusion apparatus after

washing out the enzyme solution, the left ventricle were gently teased apart with forceps in a petri dish and the myocytes were filtered through a nylon mesh. The Ca^{2+} concentration was gradually increased to 1.0 mM, and the cells were stored at room temperature and used within 8 h (Xie and Weiss, 2009).

Ca^{2+} Measurement

Myocytes were loaded with the Ca^{2+} indicator Fluo-4 AM by incubating them for ∼30 min in bath solution containing 4 μM Fluo-4 AM (Molecular Probes), after which the cells were washed and placed in a heated chamber on an inverted microscope. Fluo-4 fluorescence was excited at ∼485 nm and the emission was measured at ∼530 nm using a Nikon Eclipse TE200 inverted microscope with a Fluor x40 oil objective lens (numerical aperture 1.3). The fluorescence signals were recorded using an Andor Ixon charge-coupled device (CCD) camera (Andor Technology) operated with Imaging Workbench software (INDEC BioSystems) at 50 frames per second with a spatial resolution of 500 × 400 pixels. Fluorescence intensity was measured as the ratio of the fluorescence (F) over the basal diastolic fluorescence (F_0). The spontaneous waves were quantified by counting the wave frequency (per minute) appeared after a 3-min perfusion of HF 0.1 μM, compared to the control state.

Electrophysiological Recording

Myocytes were patch-clamped using the whole-cell configuration of the perforated patch-clamp technique (240 μg/ml amphotericin B). Voltage or current signals were measured with a MultiClamp 700A patch-clamp amplifier controlled by a personal computer using a Digidata 1322 acquisition board driven by pCLAMP 10 software (Molecular Devices, Sunnyvale, CA, United States). For AP recordings, patch pipettes (resistance 2–5 MΩ) were filled with internal solution containing (in mM): 110 K-aspartate, 30 KCl, 5 NaCl, 10 HEPES, 0.1 EGTA, 5 MgATP, 5 Na_2-phosphocreatine, 0.05 cAMP, pH 7.2 with KOH. The cells were superfused with Tyrode's solution containing (in mM): 136 NaCl, 4.0 KCl, 0.33 Na_2PO_4, 1.0 $CaCl_2$, 1 $MgCl_2$, 10 glucose and 10 HEPES, pH 7.4 adjusted with NaOH. APs were elicited with 2-ms, 2- to 4-nA square pulses at a PCL of 6 s.

The whole-cell I–V relationship was measured by applying ramp pulses from −110 to +50 mV and the holding potential was −80 mV. K^+, L-type Ca^{2+}, Na^+-Ca^{2+} exchange currents

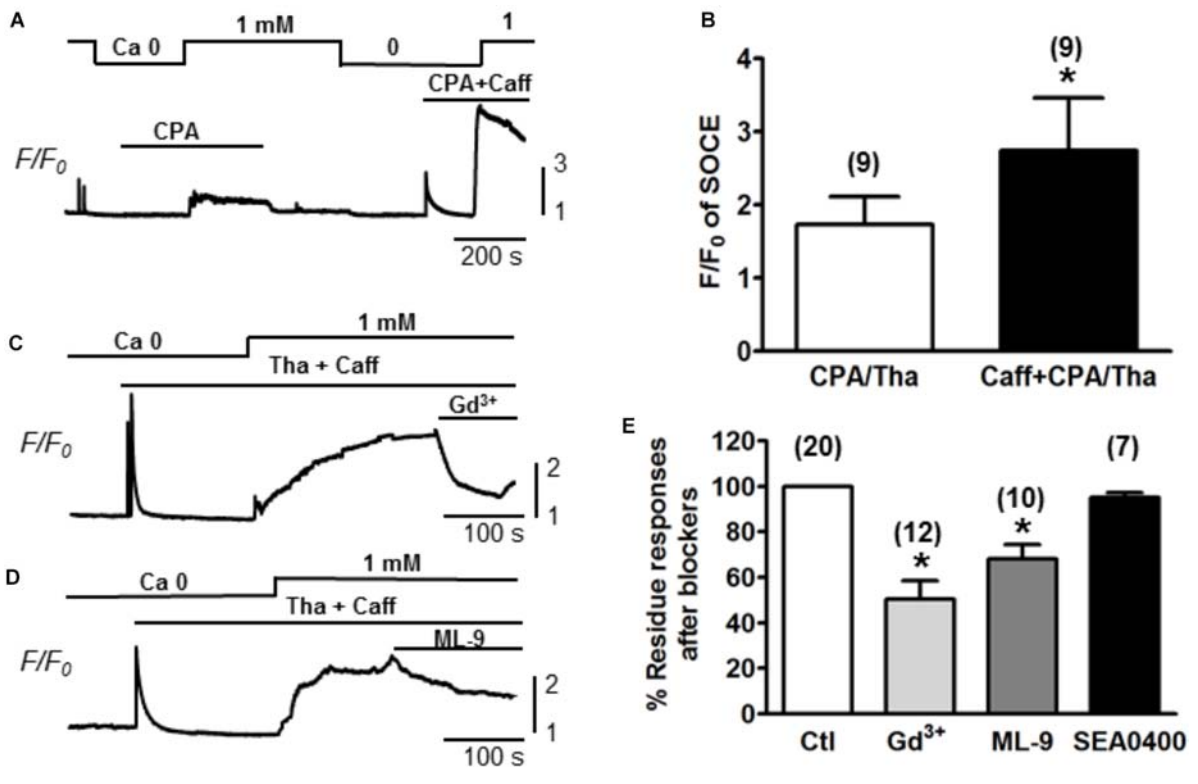

FIGURE 1 | Store-operated Ca^{2+} entry measured in adult mouse ventricular myocytes. **(A)** A representative recording of SOCE from an adult mouse ventricular myocyte. Ca^{2+} fluorescence intensity (F/F_0) in normal Tyrode's solution (1 mM Ca^{2+}) and Ca^{2+}-free (Ca^{2+}) Tyrode's solution was measured. SOCE was detected under partial SR Ca depletion by 10 μM CPA (an inhibitor of SERCA) alone or complete depletion by 10 μM CPA and 10 mM caffeine (CPA + Caff). **(B)** Summary of F/F_0 responses (SOCE) recorded in the presence of 10 μM CPA or 1 μM thapsigargin (Tha, another SERCA blocker) (CPA/Tha) alone (1.7 ± 0.4) or together with caffeine (2.7 ± 0.7, $*p < 0.05$), suggesting the complete depletion of SR Ca is required for maximal SOCE activation. **(C,D)** Representative traces of SOCE and its inhibition by TRPC or SOCE blockers (i.e., Gd^{3+} and ML-9). **(E)** Summary data demonstrating the putative SOCE was inhibited by SOCE/TRPC channel blockers (39.8 ± 4.5% inhibition by 1 mM Gd^{3+} and 31.8 ± 6.3% inhibition by 10 μM ML-9. $*p < 0.05$ compared to control, Student's t-Test) but not SEA0400 (4.9 ± 2.3%).

were previously blocked with a K^+-free extracellular solution with (in mM) 140 NaCl, 1.0 $CaCl_2$, 0.5 $MgCl_2$, 0.33 NaH_2PO_4, 5.5 glucose, 0.01 Nifedipine, 0.002 SEA400 and 5 HEPES (pH 7.4 adjusted with NaOH), and a pipette solution containing (in mM) 90 Cs-aspartate, 30 CsCl, 20 traethylammonium chloride (TEA-Cl), 2 $MgCl_2$, 5 Tris-ATP, 0.1 Li_2-GTP, 5 EGTA, 2 $CaCl_2$ and 5 HEPES (pH adjusted to 7.2 with CsOH)[17]. All patch clamp and Ca^{2+} imaging experiments were performed at 37°C.

ECG Recording and Arrhythmia Induction Testing

(Pseudo-)Lead II ECGs were recorded in isolated Langendorff-perfused hearts. A pair of Ag-AgCl electrodes were placed close to the apex of the left ventricle as well as at the right atrial appendage to obtain ECG signals at a sampling rate of 1 kHz. Two additional platinum electrodes were placed on the free wall of the right ventricle for stimulation using a stimulator (Grass) triggered by a custom-designed computer program. To induce ventricular arrhythmias, a standard S_1-S_2 arrhythmia induction protocol at twice the pacing threshold intensity was adapted from Jeron et al. (2000). Following a 20-beat train with a basic cycle length of 100 ms (S_1), 3 extra stimuli (S_2) with a coupling cycle length of 50, 40, or 30 ms, respectively, were introduced. Each of these 3 sets of stimulation were repeated 3 times. Arrhythmias will be categorized into 5 groups and assigned the following points: 0 points, no arrhythmia; 1 point, 1–3 premature ventricular complexes (PVCs); 2 points, non-sustained VT (4–10 consecutive PVCs, including bigeminal/trigeminal PVCs); 3 points, sustained VT (>10 consecutive PVCs); and 4 points, VF/SCD (Zhao et al., 2018).

Statistical Analysis

Data are presented as mean ± SEM, and at least 3 animals were used for each group. Statistical significance was assessed using paired, unpaired Student's *t*-tests or ANOVA analysis, with $P < 0.05$ considered significant.

RESULTS

SOCE Exists in Adult Cardiac Myocytes

Ventricular myocytes were isolated from adult mouse hearts and were loaded with Fluo-4 AM for measurement of Ca^{2+}. The changes of Ca^{2+} level (reflected by Fluo-4 fluorescence intensity) were measured by increasing extracellular Ca^{2+} concentration ($[Ca^{2+}]$) from 0 to 1 mM (Correll et al., 2015). SOCE was traditionally initiated by emptying SR stores with Tha or CPA (Ong et al., 2007). Both Tha and CPA are SERCA blockers, which are able to passively deplete the SR by inhibiting the SR Ca^{2+} up-taking from the cytosol. A typical protocol for inducing SOCE is demonstrated in **Figure 1A**. Following the SR depletion by

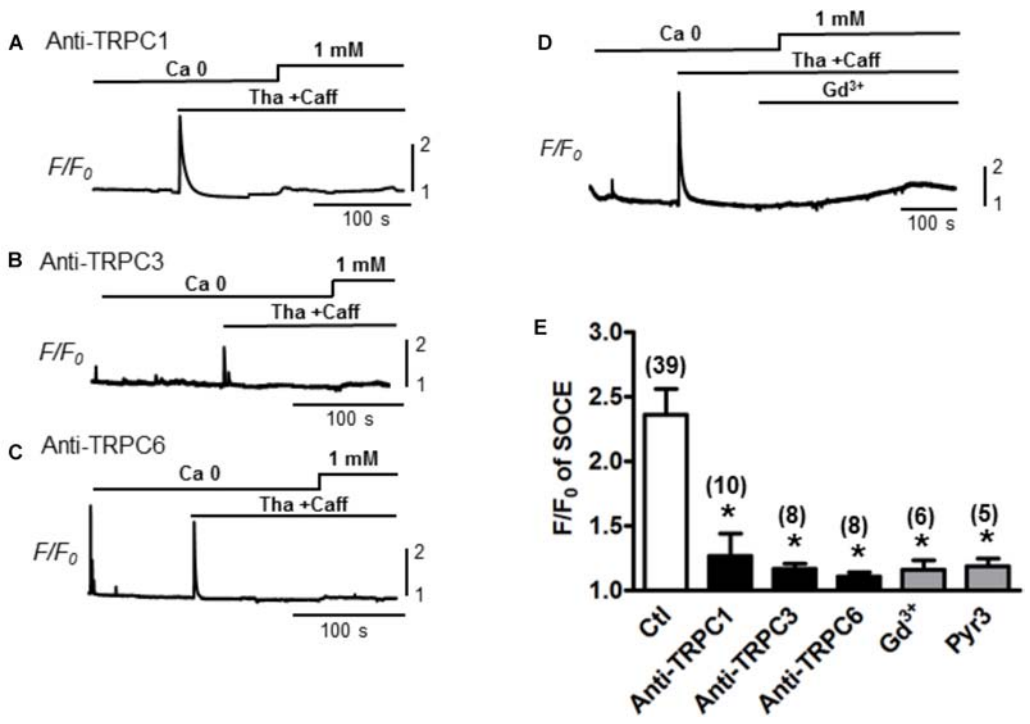

FIGURE 2 | Store-operated Ca^{2+} entry inhibition by functional antibodies or inhibitors of TRPCs. **(A–C)** Representative traces of Ca^{2+} fluorescence (F/F_0) recorded from myocytes pre-treated with TRPC channel antibodies for 30 min before recording. SOCEs were evaluated using a standard protocol (i.e., 0 Ca + Tha + Caff). **(D)** A representative trace of SOCE after pretreatment with Gd^{3+} 1 mM for 100 s. **(E)** A bar graph summarizing the effects of the TRPC antibodies and Gd^{3+} on SOCE (Ctl: 2.4 ± 0.2, TRPC1 Ab: 1.4 ± 0.2, TRPC3 Ab:1.2 ± 0.2, TRPC6 Ab: 1.1 ± 0.1 and Gd^{3+}:1.2 ± 0.1, Pyr3: 1.2 ± 0.1, Student's *t*-Test), suggesting TRPC channels account for SOCE.

using 10 μM CPA, a moderate increase of Ca^{2+} level (as showed by F/F_0 elevation) was observed when [Ca^{2+}] was changed from 0 to 1 mM. In order to maximally/completely deplete SR Ca^{2+}, in addition to CPA, we also employed 10 mM caffeine to fully open RyR. As a result, a much larger elevation of Ca^{2+} level was induced when [Ca^{2+}] was changed from 0 to 1 mM (**Figure 1A**). The same phenomena were observed when caffeine was combined with 1 mM Tha. We therefore defined the maximal SOCE amplitude to be the elevation of Ca^{2+} level after the SR Ca^{2+} was maximally depleted by using caffeine in addition to CPA or Tha (Caff + CPA/Tha). As shown in **Figure 1B**, the amplitude of SOCE obtained after caffeine (10 mM) + Tha (1 μM)/CPA (10 μM) (F/F_0 = 2.7 ± 0.7) was markedly higher than that after Tha/CPA only (F/F_0 = 1.7 ± 0.4, n = 9, $^*p < 0.05$), suggesting the existence of SOCE in adult cardiac myocytes, and a maximal SOCE activation requires the complete depletion of SR Ca^{2+}. This SOCE was effectively blocked by SOCE/TRPC blockers gadolinium (Gd^{3+}, inhibited by 39.8 ± 4.5%, n = 12, $^*p < 0.05$) and ML-9 (inhibited by 31.8 ± 6.3 %, n = 10, $^*p < 0.05$ respectively), but not by Na^+/Ca^{2+} exchanger (NCX) inhibitor SEA0400 (by 4.9 ± 2.3%, p > 0.05; n = 7, **Figures 1C,D**).

TRPC Channels Contribute to the Function of SOCE in Adult Myocytes

To determine whether the TRPC channels contribute to the modulation of SOCE in adult cardiac myocytes, functional (pore inhibitory) antibodies for TRPC1, 3 and 6 were added, respectively, to pretreat the myocytes for 30 min before SOCE was evaluated following the standard protocol with complete depletion of SR Ca^{2+} by Tha (1 μM) + caffeine (10 mM). Control myocytes without pretreatment with antibodies exhibited a peak SOCE amplitude of F/F_0 = 2.4 ± 0.2, n = 39, whereas all three TRPC1, 3 or 6 antibodies significantly inhibited the peak of SOCE to F/F_0 = 1.4 ± 0.2 (n = 10), 1.2 ± 0.2 (n = 8), 1.1 ± 0.1 (n = 8), respectively (**Figure 2**, $^*p < 0.05$). Similar inhibitory effects to 1.2 ± 0.1 (n = 5) by Gd^{3+} or to 1.2 ± 0.1 (n = 6) by the TRPC3 blocker Pyr3 pre-perfused in the bath for 10–15 min were also observed ($^*p < 0.05$, respectively) (**Figure 2**). These results suggest that various TRPC channel subtypes may account for the SOCE generation in adult myocytes.

Hyperforin Potentiates the SOCE in Adult Myocytes

Furthermore, the participation of TRPC6 in SOCE was confirmed by using various concentrations of hyperforin, a potent activator of TRPC6 (Leuner et al., 2007). As shown in **Figure 3**, SOCE was partially activated by using moderate concentration of caffeine (1 mM) + Tha (0.1 μM) (F/F_0 = 1.5 ± 0.1, n = 26). Hyperforin further potentiated the SOCE level in a concentration-dependent manner in adult mouse ventricular myocytes. The amplitudes (F/F_0) of SOCE in the presence of hyperforin at 0.1, 1, and 10 μM were, 1.9 ± 0.1 (n = 15), 2.4 ± 0.2 (n = 8) and 3.7 ± 0.4 (n = 7), respectively (**Figure 3D**, $^*p < 0.05$), which

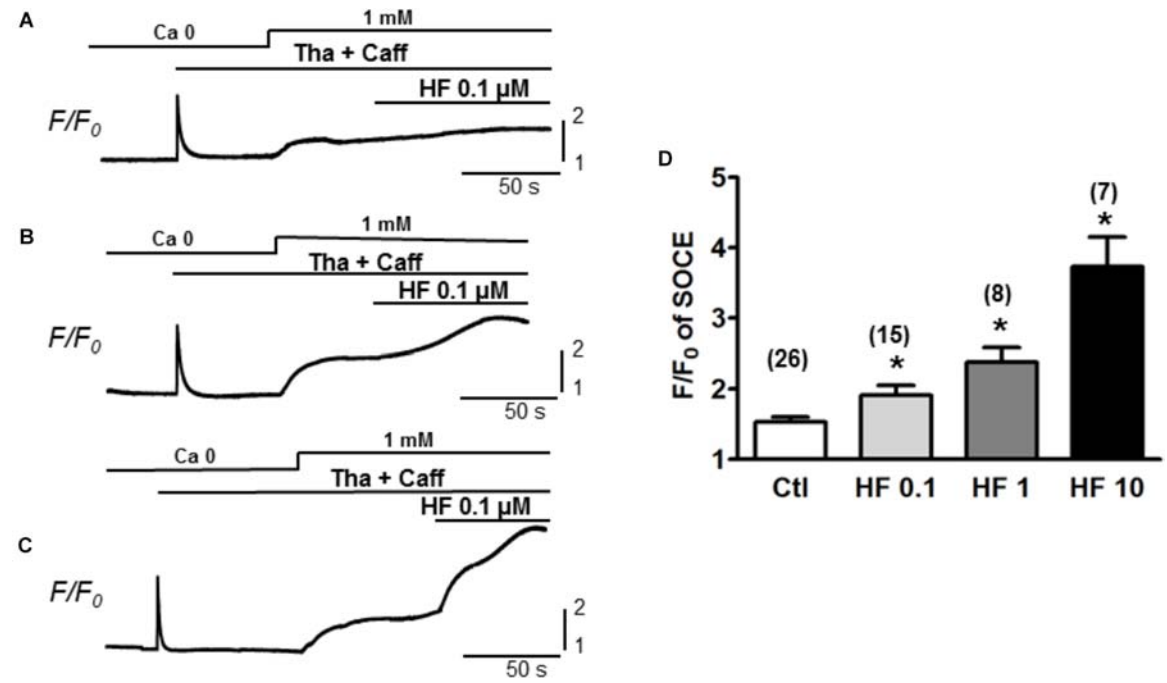

FIGURE 3 | TRPC6 activator hyperforin potentiates the SOCE in adult mouse cardiac myocytes. **(A–C)** Representative recordings of SOCE from adult mouse myocytes. Ca^{2+} fluorescence intensity (F/F_0) in normal Tyrode's solution (1 mM Ca^{2+}) and Ca^{2+}-free (0 Ca) Tyrode's solution was measured. SOCE was detected under complete depletion by 0.1 μM thapsigargin and 1 mM caffeine (Tha + Caff), and was further enhanced by hyperforin (HF) at different concentrations. **(D)** Summary of F/F_0 responses (SOCE) in the presence of 0.1, 1, and 10 μM hyperforin, which potentiated SOCE in a concentration-dependent fashion. ($^*p < 0.05$ compared to control, Student's t-Test).

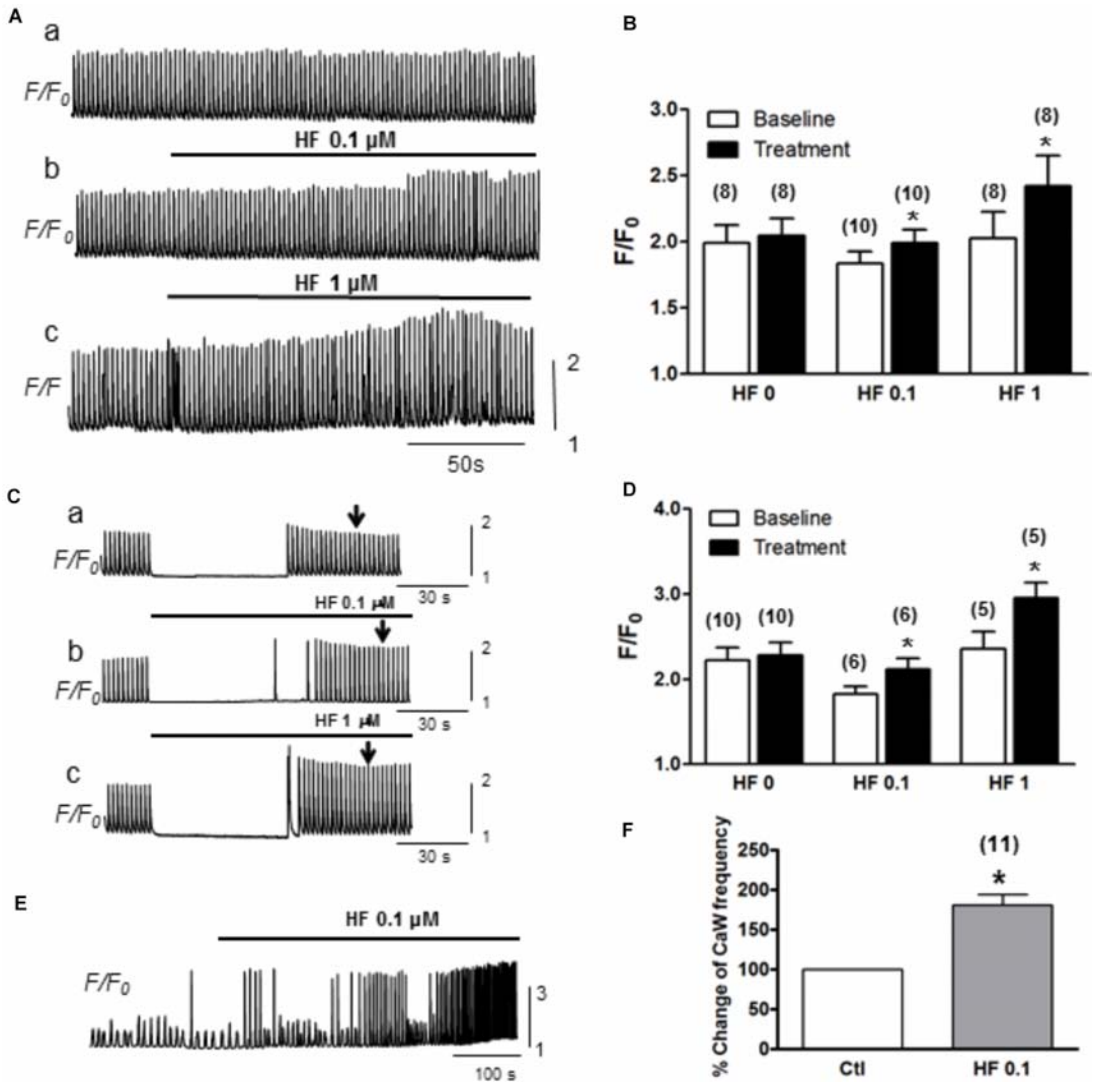

FIGURE 4 | Hyperforin enhances CaT amplitude. **(A)** A representative trace of CaTs facilitated by hyperforin (0.1 and 1 μM) when the cell was paced at a pacing cycle length (PCL) of 2 s. **(B)** Summary of the amplitudes of CaTs potentiated by hyperforin. F/F_0 increased from 1.9 ± 0.1 to 2.1 ± 0.1, n = 10 at 0.1 μM and from 2.0 ± 0.2 to 2.4 ± 0.1, n = 8 at 1 μM hyperforin, respectively (*$p < 0.05$). **(C)** Representative traces of calcium transients were measured before and after a 90s-perfusion of hyperforin (0.1 – 1 μM) while the cells were kept quiescent. **(D)** Summary of calcium transient amplitude by hyperforin perfusion. **(E)** A representative trace of Ca^{2+} waves (with $[Ca^{2+}]$ 4 mM) facilitated by hyperforin (0.1 μM). **(F)** Summary of the changes in Ca^{2+} wave frequencies caused by hyperforin, which promotes the Ca^{2+} waves by increasing the frequency to 180.5 ± 13.5% (n = 11, *$p < 0.05$ vs. control).

were all significantly higher than the control SOCE value before hyperforin application.

Activation of TRPC by Hyperforin Increases the Calcium Load in Mouse Cardiac Myocytes

Next, we evaluated how hyperforin-activated TRPC may affect Ca^{2+} transients and Ca^{2+} waves. Ca^{2+} transients were measured by pacing myocytes continuously at a PCL of 2 s. As shown in a representative trace (**Figure 4A**), the amplitudes of Ca^{2+} transients were markedly enhanced by the application of hyperforin at concentrations of 0.1 μM (**Figure 4Aa**) and 1 μM (**Figure 4Ab**). Summarized data demonstrated that F/F_0 was increased from 1.9 ± 0.1 to 2.1 ± 0.1 (*$p < 0.05$, n = 10) by 0.1 μM hyperforin, and from 2.0 ± 0.2 to 2.4 ± 0.1 (*$p < 0.05$, n = 8) by 1 μM hyperforin. To exclude the possibility that the enhancement of Ca^{2+} transients might be due to the potentiation any other voltage-gated Ca influx mechanisms, we then used a different protocol in which the cells were kept quiescent when they were perfused with hyperforin (0.1 or 1 μM) for 1 min (**Figure 4C**) (the field stimulation was terminated prior to hyperforin addition and then restarted 1 min later). To exclude any influence of post-rest potentiation and subsequent decay (i.e., negative staircase phenomenon), the amplitude of Ca^{2+} transient were measured when it reached a steady state level (∼30 s after the restart

of stimulation) as indicated by the arrow in each panel). We found that Ca^{2+} transient amplitude was enhanced by hyperforin treatment even the cells remained in resting condition. Ca^{2+} transient amplitudes increased from 1.8 ± 0.2 to 2.1 ± 0.3 (n = 6, $^*p < 0.05$) by 0.1 μM hyperforin and from 2.4 ± 0.5 to 3.0 ± 0.4 ($^*p < 0.05$, n = 5) by 1 μM hyperforin (**Figure 4D**), in comparison to the control group (no hyperforin treatment, from 2.2 ± 0.5 to 2.3 ± 0.4, n = 9). These data suggest that hyperforin promoted Ca^{2+} entry through sarcolemmal membrane and increase of cellular/SR Ca^{2+} load, unlikely via voltage-gated Ca^{2+} channels.

Next, we further assessed the effect of hyperforin on spontaneous Ca^{2+} waves. In this experiment, ventricular myocytes were perfused with Tyrode's solution containing higher [Ca^{2+}] (4 mM) without being stimulated. As shown in **Figure 4E**, spontaneous Ca^{2+} waves were observed under baseline in normal cells (Zhao et al., 2013). These spontaneous Ca^{2+} waves were significantly facilitated by hyperforin (0.1 μM) with a frequency increase from 22 ± 3/min under control condition to 38 ± 4/min after hyperforin treatment (**Figures 4E,F**, n = 11, $^*p < 0.05$). Taken together, the results shown in **Figures 3**, **4** have suggested that hyperforin is able to activate both SOCE under SR Ca^{2+} depletion condition and TRPC6 channels independent of SR Ca^{2+} depletion.

Significant Inward Currents Are Induced by SR Depletion or by Hyperforin

The inward current when SOCE occurred (i.e., SOCE current, I_{OCE}) after SR Ca^{2+} depletion was subsequently measured. As described in the Method section, K^+, Na^+, L-type Ca, and Na^+-Ca^{2+} exchange currents were pre-blocked. Whole-cell currents were recorded under the voltage clamp condition using a ramp protocol from −110 to +50 mV, and the inward current amplitudes at −110 mV were evaluated. As shown in time course and representative traces (**Figures 5A,B**), I_{OCE} was induced when [Ca^{2+}] was changed from 0 to 1 mM after SR depletion (from point a to point c). As summarized in **Figure 5C**, we observed a marked increase from −2.7 ± 0.3 to −5.6 ± 0.7 pA/pF (n = 12 each, $^*p < 0.01$) in the inward current, which was attenuated by the application of 1 mM Gd^{3+} (−1.4 ± 0.2 pA/pF, n = 10,

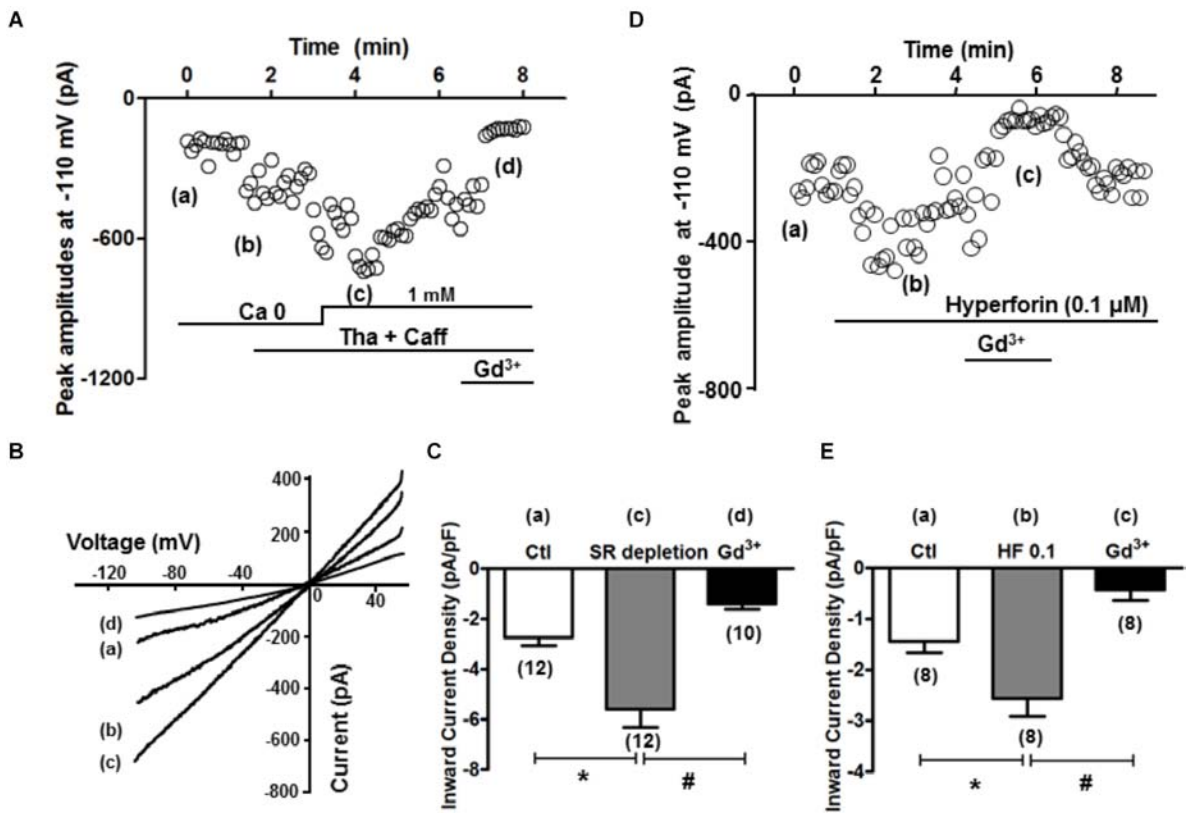

FIGURE 5 | SR depletion and the presence of hyperforin induced significant inward current. **(A)** A representative plot of currents measured at –110 mV over time. The same treatment protocol to deplete SR Ca^{2+} (Tha + Caff) was used. **(B)** I–V curves at time points a–d (control, calcium free, after SR depletion, and in the presence of Gd^{3+}, respectively) indicated in **(A)**. **(C)** Summary of the inward current densities at –110 mV measured under control and after SR depletion ($^*p < 0.05$, Student's t-Test). **(D)** A representative plot of currents measured at –110 mV over time, and the presence of hyperforin induced significant inward current entry. **(E)** Summary of the inward current densities at –110 mV measured under control and after SR depletion. Hyperforin (0.1 μM) induced a significant increase of inward current (from –1.4 ± 0.2 pA/pF to –2.6 ± 0.4 pA/pF, n = 8, $^*p < 0.05$), which was then inhibited by the SOCE blocker Gd^{3+} (1 mM) (–0.4 ± 0.2 pA/pF, n = 8, $^*p < 0.05$, Student's t-Test).

$^*p < 0.01$). The I/V relationship revealed a reversal potential around 0 mV, indicating its non-selective property, which is consistent with TRPC channels as reported by Kojima et al. (2012). As shown in **Figures 5D,E**, hyperforin (0.1 μM) also significantly enhanced the inward current from −1.4 ± 0.2 to −2.6 ± 0.4 pA/pF ($n = 8$, $^*p < 0.05$ compared to control), which was effectively blocked by 1 mM Gd^{3+} (−0.4 ± 0.2 pA/pF, $n = 8$, $\#p < 0.05$ compared to hyperforin).

Activation of SOCE or TRPC6 Contributes to Cardiac Arrhythmogenesis

The potential role of SOCE in arrhythmogenesis at cellular level was studied by simultaneous recording of whole-cell Ca^{2+} imaging and membrane potential. Normal APs were recorded when myocytes were paced at a PCL of 6 s (**Figure 6Aa**). The cell was then exposed to the standard protocol to activate SOCE. EADs, DADs and TAs, as key indicators for cellular arrhythmias, appeared after the activation of SOCE and removal of SR uptake and release inhibition (**Figures 6Ab**, **6Bc**). In order to establish a connection between membrane potential changes and corresponding changes in intracellular Ca^{2+}, we examined temporal correlation between them by comparing the onsets of spontaneous depolarizations (i.e., DAD) of membrane potential and corresponding elevation of intracellular Ca^{2+}. As shown in the expanded regions (**Figures 6C,D**) of the boxed periods in panel **Figures 6Ab,Bc**, the initiation (indicated by the dotted vertical lines) of the spontaneous depolarizations (DADs triggering APs) always preceded the elevation of intracellular Ca^{2+}, suggesting a predominant inward current, presumably via TRPC channels, contributes to the arrhythmogenic membrane depolarization. Although the SR uptake and release inhibition (Tha + Caff) had been removed in this condition when arrhythmias occurred, it seemed that Ca^{2+} release and NCX current did not play a causal role in spontaneous membrane depolarization, in which case the initiation of intracellular Ca^{2+} elevation should occur earlier than membrane potential changes. This relation has been well discussed in our previous publication (Zhao et al., 2012). The EADs, DADs and TAs were eliminated by Gd^{3+} treatment, although the action potential duration (APD) remained longer compared to control (**Figure 6Bd** vs. **Figure 6Aa**). SOCE-induced EADs, DADs and TAs were observed in 10 out of 12 cells in total. Such arrhythmic events were not seen before the cells were treated with Tha + Caff to deplete SR Ca^{2+} (**Figure 6Aa**). These data suggested the contribution of SOCE to the generation of arrhythmias at cellular level.

To examine the arrhythmogenic effect of activation of TRPC6 channel by hyperforin at the whole-heart level, hyperforin (0.1 μM) was perfused in *ex vivo* mouse hearts via a Langendorff perfusion apparatus for 20 min. Programmed stimulation

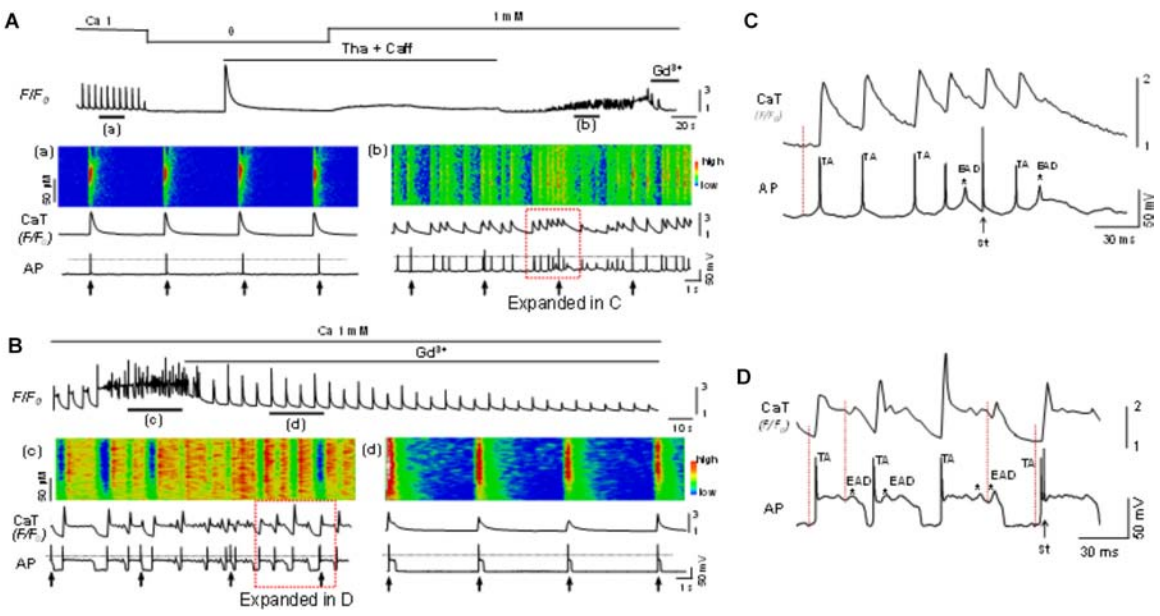

FIGURE 6 | Store-operated calcium entry contributes to cellular arrhythmogenesis. **(A)** Top panel: A Ca^{2+} fluorescence (F/F_0) recording. **(a,b)**: Simultaneous recordings of linescan image, whole-cell calcium fluorescence (F/F_0) and action potentials (AP) at the time windows a and b indicated in the top panel. The cell was paced at a pacing cycle length (PCL) of 6 s (indicated by the arrows underneath the AP trace). EADs, DADs and triggered APs appeared after SOCE was activated, indicating SOCE contributes to the generation of arrhythmias. **(B)** In another cell, the same protocol as in A was used to activate SOCE. The SOCE-induced EADs (indicated by the asterisks), DADs, and triggered APs **(c)** were eliminated by Gd^{3+} (1 mM) **(d)**. The 0 mV level is indicated by the dotted line in each panel. **(C)** Expanded region within the red box as indicated in **(Ab)**. **(D)** Expanded region within the red box as indicated in **(Bc)**. Note initiation (indicated by the dotted vertical lines) of the spontaneous depolarization phase (DADs triggering action potential) and occurrence of EADs (indicated by *) preceded the elevation of intracellular Ca^{2+}. TA, triggered action potential; St, stimulation.

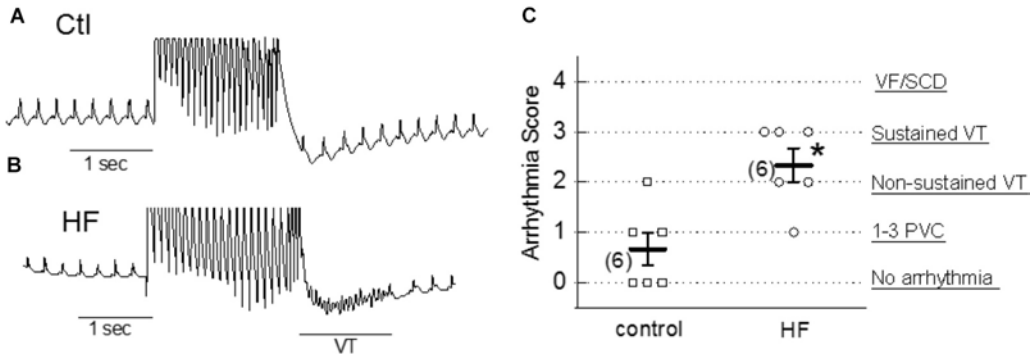

FIGURE 7 | Proarrhythmic effect of hyperforin in *ex vivo* hearts. **(A,B)** Pseudo-Lead II ECG signals recorded from control (ctl) and 20 min after perfusion with 100 nM hyperforin (HF). Programmed S1–S2 stimulations were applied to evaluate the vulnerability to arrhythmias in each case. Sustained VT was observed in HF-treated heart. **(C)** Summarized arrhythmia scores for control and hyperforin groups, $^*p < 0.05$, compared to control.

protocols (as described in Section "Materials and Methods") were used to assess the propensity to develop arrhythmias in each group. As shown in **Figures 7A–C**, hyperforin-perfused hearts were particularly susceptible to various types of arrhythmias and had an average arrhythmia score of 2.3 ± 0.3 ($n = 6$), which was significantly higher than hearts without treatment with hyperforin (0.7 ± 0.3, $n = 6$, $p < 0.05$).

DISCUSSION

SOCE Exists in Adult Cardiac Myocytes

Store-operated calcium entry has been identified as a cellular mechanism that plays a fundamental role in Ca^{2+} signaling. In addition to replenish the SR stores, its long-term and immediate physiological significances have been profoundly explored in previous studies, includes cell proliferation, apoptosis, muscle contraction and intracellular Ca^{2+} oscillations (see (Parekh and Putney, 2005) for review). Although it was primarily considered important only for non-excitable cells, growing evidence has demonstrated a crucial role of I_{OCE} in central nervous system (Baba et al., 2003), aortic myocytes (Trepakova et al., 2001) and muscle cells (Hopf et al., 1996; Kurebayashi and Ogawa, 2001; Shin et al., 2003). Due to the prevalence of distributions of L-type Ca^{2+} channel, NCX, RyR and SR Ca^{2+}-ATPase 2 (SERCA2) (Bers, 2008), the roles of SOCE in cardiomyocytes have been overlooked for balancing the Ca^{2+} loading. Until recently, capacitative calcium entry was observed in adult rat cardiomyocyte (Hunton et al., 2004), and the modulation effects of SOCE in neonatal or adult hypertrophic mice cardiomyocytes were demonstrated (Hunton et al., 2002; Voelkers et al., 2010; Wu et al., 2010).

Our present study demonstrated that SOCE and I_{OCE} exist in normal adult ventricular myocytes subsequent to a complete depletion of SR Ca^{2+} storage. SR Ca^{2+} level can be physiologically reduced following the activation of calcium-releasing signals mediated by IP3R or RyR. Whereas under our experimental condition, specific inhibitors of SR Ca^{2+} pump (i.e., Tha or CPA) are usually employed to induce SOCE, previous studies seemed to produce only moderate increase in normal adult cardiac myocytes when exposed to CPA or Tha separately (Hunton et al., 2004; Wu et al., 2010). Similarly, Kojima et al also demonstrated the SOCE activity in the mice ventricular myocytes by combining the application of angiotensin II and Tha to deplete the SR store (Kojima et al., 2012). Alternatively, caffeine as potent RyR activator has also been shown to be effective to initiate SOCE (Albert and Large, 2002; Kojima et al., 2010). In the present study, we applied caffeine together with Tha or CPA to obtain a maximum activation of SOCE, therefore, adding indisputable evidence supporting the presence of SOCE in adult mouse ventricular myocytes. As shown in the results, the combination of caffeine and SERCA inhibitors (Tha or CPA) effectively potentiated SOCE to a larger extent (F/F_0: over 2.5) compared to that induced only by SERCA inhibitor. This Ca^{2+} entry can be effectively inhibited by acute application of SOCE blockers Gd^{3+} and ML-9, but not by the NCX inhibitor SEA0400. We have noticed that neither Gd^{3+} (also blocks L-type Ca^{2+} channel and mechano-sensitive ion channel) nor ML-9 (also inhibits myosin light chain kinase) is completely selective to TRPC channels. However, our experiments using selective antibodies of TRPC channels provide more convincing evidence for the involvement of TRPC channels.

It should be pointed out that caffeine also functions as a PDE inhibitor (Rohrig et al., 2017), which increases cAMP concentration and PKA activation at cellular level. Therefore, we cannot completely exclude the possibility that caffeine-induced enhancement of SOCE may be partially attributed to SR Ca^{2+} load-independent pathway, e.g., PKA-dependent activation. This issue needs to be further elucidated.

Contribution of TRPCs to SOCE

Due to the absence of Ca^{2+} selectivity, the involvement of TRPCs in SOCE is still under debate. For example, the expression of TRPC3 has been examined in DT40 B lympohocytes by two groups individually. One group demonstrated the TRPC3 activation is triggered in response to PLC-γ or PLC-β enzymes, but independent of SR depletion (Venkatachalam

et al., 2001). Meanwhile, the other group showed substantial greater divalent cation entries by heterologous expression of hTRPCs in IP3R-knockout cells (Vazquez et al., 2001). A subsequent study revealed that these different regulation mechanisms are determined by the different expression levels of TRPC3. At low expression level, TRPC3 tend to form store-operated channels, while at higher expression level, it forms receptor-activated channels which is insensitive to Gd^{3+} (Vazquez et al., 2003). Above evidence implicated a crucial role of TRPC stoichiometry in determining its function during the subunit assembling process. It seems that low expression level of TRPCs may be insufficient to yield functional TRP complex, but may prompt the formation of a heteromeric Orai/TRPC model for SOCE. Although the participation of TRPC channels in a STIM1-stimulated Orai/TRPC model for SOCE is still under debate (Parekh and Putney, 2005; DeHaven et al., 2009), a collection of studies has indicated the roles of TRPC family in SOCE (Liao et al., 2008, 2009). Our present data provide further evidence that revealed the contribution of TRPC channels to SOCE generated in adult mouse ventricular myocytes. As shown in **Figures 1–3**, SOCE was markedly attenuated by a perfusion with TRPC blockers Gd^{3+} and Pyr3. Since Gd^{3+} and Pyr3 are considered less selective, we also used selective TRPC pore inhibitory antibodies. When the pore-blocking antibodies for TRPC 1, 3 and 6 were employed (**Figure 2**), they each resulted in partial inhibition on SOCE. In addition, the selective TRPC6 activator hyperforin enhanced SOCE level, further implicating the role of TRPC6 in mediating store-operated calcium influxes. Significant expressions of TRPC1, 3 and 6 isoforms in mouse cardiomyocytes have been reported (Katayama et al., 1990; Mohl et al., 2011). In consistence with our observations, the SOCE level is potentiated in cardiac-specific TRPC3 expressing mice (Katayama et al., 1990), and is reduced in myocytes isolated from dominant-negative TRPC3, 4 and 6 transgenic mice (Wu et al., 2010). These results imply the TRPC channels may at least partially mediate the SOCE by forming either homo- or hetero-multimers. The combination of using functional (pore inhibitory) antibodies for TRPCs and a range of different TRPC and SOCE blockers/activators, revealed that TRPC channels account for the prominent SOCE after SR depletion in adult myocytes.

Roles of SOCE/TRPCs in Arrhythmogenesis

Transient receptor potential canonical channels carry inward currents, therefore may modulate cardiac rhythm and exert potential arrhythmic effects (Hirose et al., 2011; Sabourin et al., 2011). SOCE mediated proarrhythmic effects have been suggested in different models. For example, overexpression of STIM, which is an important sensor for SOCE communicating between the sarcolemma and SR, results in leaky RyR and spontaneous Ca^{2+} transients (Correll et al., 2015). The upregulated expression of TRPC3/4 induced a proarrhythmic SOCE-like activity in adult rat ventricular cardiomyocytes (Domínguez-Rodríguez et al., 2015). A study on the developing chick heart has also demonstrated that the cardiac arrhythmias modulated by the activation of SOCE (Sabourin et al., 2011). The heart rate measured was dramatically increased by SERCA inhibitor CPA within 5 min, and this CPA-induced tachycardia was prevented by a treatment with TRPCs blocker SKF-96265 effectively. Subsequent to the SR depletion by activation of RyR with caffeine and by inhibition of SERCA with Tha, substantial Ca^{2+} current influx was measured in our experimental setting, suggesting the TRPC channels act as store-operated channels in mediating inward depolarizing Ca^{2+} current. We observed the increase of inward current and recorded EADs/DADs/TAs and Ca^{2+} waves simultaneously after SOCE activation in most cases, indicating SOCE may account for the generation of arrhythmias in the adult cardiac myocyte. Gd^{3+} is the most potent TRPC blocker that effectively eliminates arrhythmic events induced by SOCE, which implies a therapeutic potential of Gd^{3+} for the arrhythmias induced by TRPC channel activation or SOCE.

Hyperforin Exhibits Arrhythmogenic Effect

Hyperforin is known as an antidepressant compound extracted from St. John's wort (*Hypericum perforatum*), and it was reported to selectively activate TRPC6 channels. Our data clearly demonstrated that hyperforin at concentrations of 0.1 and 1 μM predominantly potentiated the SOCE and I_{OCE} in adult mouse ventricular myocytes. It also facilitated the spontaneous Ca^{2+} waves and promoted the calcium transient amplitudes. A previous study has shown that hyperforin exerts complex actions on cortical neurons. In addition to promoting TRPC6 channels in plasma membrane, hyperforin may exert protonophore-like effect, triggering the release of Ca^{2+} and Zn^{2+} from mitochondria (Tu et al., 2010). However, in mouse ventricular myocytes, we did not observe the same effect of hyperforin (at 1 or 10 μM) to depolarize the mitochondrial membrane potential (as indicated by TMRM), while the protonophore FCCP dissipated mitochondrial membrane potential (data not shown). These results exclude the possibility that hyperforin induces Ca^{2+} release from internal store (i.e., mitochondria) in the setting of our experiments, but imply that hyperforin gives rise to Ca^{2+} most likely via activation of TRPC6 in cardiac myocytes. Our results have demonstrated that although the activation of SOCE requires SR Ca^{2+} depletion, its potential composing entity, TRPC channels, are able to be activated by HF independent of SR Ca^{2+} depletion (**Figure 4**). This is possible since others have reported TRPC channels may be activated under certain conditions (e.g., myocardial infarction) when SR is not necessarily depleted (Makarewich et al., 2014). We observed that perfusion with hyperforin could increase the arrhythmia score in *ex vivo* hearts, implying a possible arrhythmogenic role of SOCE/TRPC6 in the whole heart setting. TRPC6 channel was found to be important in the pathologic cardiac remodeling as a key component of a calcium-dependent regulatory loop (Kuwahara et al., 2006). Herein, our present study provides the first evidence that links hyperforin and

TRPC6 activation to the enhanced susceptibility to arrhythmias. These data suggest an underlying mechanism for one of the side effects of St. John's wort (hyperforin), which is heart palpitations, and caution is required when treating depression in patients who also have heart diseases.

AUTHOR CONTRIBUTIONS

HW, ZZ, NF, and L-HX performed the experiments and analyzed the data. HW and L-HX conceived and designed the research, interpreted results of experiments, prepared figures, and wrote manuscript. HW, ZZ, NF, and L-HX approved final version of manuscript.

FUNDING

This work was partially supported by National Natural Science Foundation of China (81503068 to HW and 81470510 to ZZ), National Heart, Lung, and Blood Institute (R01HL97979 and R01HL133294 to L-HX), and American Heart Association (16GRNT31100022 to L-HX).

ACKNOWLEDGMENTS

We thank Dr. Robert M. Graham (University of Sydney, and Victor Chang Cardiac Research Institute) for kindly providing TRPC antibodies.

REFERENCES

Albert, A. P., and Large, W. A. (2002). A Ca2+-permeable non-selective cation channel activated by depletion of internal Ca2+ stores in single rabbit portal vein myocytes. *J. Physiol.* 538(Pt 3), 717–728. doi: 10.1113/jphysiol.2001.013101

Baba, A., Yasui, T., Fujisawa, S., Yamada, R. X., Yamada, M. K., Nishiyama, N., et al. (2003). Activity-evoked capacitative Ca2+ entry: implications in synaptic plasticity. *J. Neurosci.* 23, 7737–7741. doi: 10.1523/JNEUROSCI.23-21-07737.2003

Berridge, M. J. (1993). Inositol trisphosphate and calcium signalling. *Nature* 361, 315–325. doi: 10.1038/361315a0

Bers, D. M. (2008). Calcium cycling and signaling in cardiac myocytes. *Annu. Rev. Physiol.* 70, 23–49. doi: 10.1146/annurev.physiol.70.113006.100455

Carafoli, E. (2002). Calcium signaling: a tale for all seasons. *Proc. Natl. Acad. Sci. U.S.A.* 99, 1115–1122. doi: 10.1073/pnas.032427999

Chatterjee, S. S., Bhattacharya, S. K., Wonnemann, M., Singer, A., and Muller, W. E. (1998). Hyperforin as a possible antidepressant component of hypericum extracts. *Life Sci.* 63, 499–510. doi: 10.1016/S0024-3205(98)00299-9

Correll, R. N., Goonasekera, S. A., van Berlo, J. H., Burr, A. R., Accornero, F., Zhang, H., et al. (2015). STIM1 elevation in the heart results in aberrant Ca2 handling and cardiomyopathy. *J. Mol. Cell Cardiol.* 87, 38–47. doi: 10.1016/j.yjmcc.2015.07.032

DeHaven, W. I., Jones, B. F., Petranka, J. G., Smyth, J. T., Tomita, T., Bird, G. S., et al. (2009). TRPC channels function independently of STIM1 and Orai1. *J. Physiol.* 587(Pt 10), 2275–2298. doi: 10.1113/jphysiol.2009.170431

Domínguez-Rodríguez, A., Ruiz-Hurtado, G., Sabourin, J., Gómez, A. M., Alvarez, J. L., and Benitah, J. P. (2015). Proarrhythmic effect of sustained EPAC activation on TRPC3/4 in rat ventricular cardiomyocytes. *J. Mol. Cell Cardiol.* 87, 74–78. doi: 10.1016/j.yjmcc.2015.07.002

Hirose, M., Takeishi, Y., Niizeki, T., Nakada, T., Shimojo, H., Kashihara, T., et al. (2011). Diacylglycerol kinase zeta inhibits ventricular tachyarrhythmias in a mouse model of heart failure. *Circ. J.* 75, 2333–2342. doi: 10.1253/circj.CJ-10-1213

Hopf, F. W., Reddy, P., Hong, J., and Steinhardt, R. A. (1996). A capacitative calcium current in cultured skeletal muscle cells is mediated by the calcium-specific leak channel and inhibited by dihydropyridine compounds. *J. Biol. Chem.* 271, 22358–22367. doi: 10.1074/jbc.271.37.22358

Huang, J., van Breemen, C., Kuo, K. H., Hove-Madsen, L., and Tibbits, G. F. (2006). Store-operated Ca2+ entry modulates sarcoplasmic reticulum Ca2+ loading in neonatal rabbit cardiac ventricular myocytes. *Am. J. Physiol. Cell Physiol.* 290, C1572–C1582. doi: 10.1152/ajpcell.00226.2005

Hunton, D. L., Lucchesi, P. A., Pang, Y., Cheng, X., Dell'Italia, L. J., and Marchase, R. B. (2002). Capacitative calcium entry contributes to nuclear factor of activated T-cells nuclear translocation and hypertrophy in cardiomyocytes. *J. Biol. Chem.* 277, 14266–14273. doi: 10.1074/jbc.M107167200

Hunton, D. L., Zou, L., Pang, Y., and Marchase, R. B. (2004). Adult rat cardiomyocytes exhibit capacitative calcium entry. *Am. J. Physiol. Heart Circ. Physiol.* 286, H1124–H1132. doi: 10.1152/ajpheart.00162.2003

Jeron, A., Mitchell, G. F., Zhou, J., Murata, M., London, B., Buckett, P., et al. (2000). Inducible polymorphic ventricular tachyarrhythmias in a transgenic mouse model with a long Q-T phenotype. *Am. J. Physiol. Heart Circ. Physiol.* 278, H1891–H1898. doi: 10.1152/ajpheart.2000.278.6.H1891

Katayama, Y., Shimizu, J., Suzuki, S., Memezawa, H., Kashiwagi, F., Kamiya, T., et al. (1990). Role of arachidonic acid metabolism on ischemic brain edema and metabolism. *Adv. Neurol.* 52, 105–108.

Kojima, A., Kitagawa, H., Omatsu-Kanbe, M., Matsuura, H., and Nosaka, S. (2010). Ca2+ paradox injury mediated through TRPC channels in mouse ventricular myocytes. *Br. J. Pharmacol.* 161, 1734–1750. doi: 10.1111/j.1476-5381.2010.00986.x

Kojima, A., Kitagawa, H., Omatsu-Kanbe, M., Matsuura, H., and Nosaka, S. (2012). Presence of store-operated Ca2+ entry in C57BL/6J mouse ventricular myocytes and its suppression by sevoflurane. *Br. J. Anaesth.* 109, 352–360. doi: 10.1093/bja/aes212

Kurebayashi, N., and Ogawa, Y. (2001). Depletion of Ca2+ in the sarcoplasmic reticulum stimulates Ca2+ entry into mouse skeletal muscle fibres. *J. Physiol.* 533(Pt 1), 185–199. doi: 10.1111/j.1469-7793.2001.0185b.x

Kuwahara, K., Wang, Y., McAnally, J., Richardson, J. A., Bassel-Duby, R., Hill, J. A., et al. (2006). TRPC6 fulfills a calcineurin signaling circuit during pathologic cardiac remodeling. *J. Clin. Invest.* 116, 3114–3126. doi: 10.1172/JCI27702

Leuner, K., Kazanski, V., Muller, M., Essin, K., Henke, B., Gollasch, M., et al. (2007). Hyperforin–a key constituent of St. John's wort specifically activates TRPC6 channels. *FASEB J.* 21, 4101–4111. doi: 10.1096/fj.07-8110com

Liao, Y., Erxleben, C., Abramowitz, J., Flockerzi, V., Zhu, M. X., Armstrong, D. L., et al. (2008). Functional interactions among Orai1, TRPCs, and STIM1 suggest a STIM-regulated heteromeric Orai/TRPC model for SOCE/Icrac channels. *Proc. Natl. Acad. Sci. U.S.A.* 105, 2895–2900. doi: 10.1073/pnas.0712288105

Liao, Y., Plummer, N. W., George, M. D., Abramowitz, J., Zhu, M. X., and Birnbaumer, L. (2009). A role for orai in TRPC-mediated Ca2+ entry suggests that a TRPC:Orai complex may mediate store and receptor operated Ca2+ entry. *Proc. Natl. Acad. Sci. U.S.A.* 106, 3202–3206. doi: 10.1073/pnas.0813346106

Makarewich, C. A., Zhang, H., Davis, J., Correll, R. N., Trappanese, D. M., Hoffman, N. E., et al. (2014). Transient receptor potential channels contribute to pathological structural and functional remodeling after myocardial infarction. *Circ. Res.* 115, 567–580. doi: 10.1161/CIRCRESAHA.115.303831

Mohl, M. C., Iismaa, S. E., Xiao, X. H., Friedrich, O., Wagner, S., Nikolova-Krstevski, V., et al. (2011). Regulation of murine cardiac contractility by activation of alpha(1A)-adrenergic receptor-operated Ca(2+) entry. *Cardiovasc. Res.* 91, 310–319. doi: 10.1093/cvr/cvr081

Ong, H. L., Cheng, K. T., Liu, X., Bandyopadhyay, B. C., Paria, B. C., Soboloff, J., et al. (2007). Dynamic assembly of TRPC1-STIM1-Orai1 ternary complex is involved in store-operated calcium influx. evidence for similarities in store-operated and calcium release-activated calcium channel components. *J. Biol. Chem.* 282, 9105–9116. doi: 10.1074/jbc.M608942200

Parekh, A. B., and Putney, J. W. Jr. (2005). Store-operated calcium channels. *Physiol. Rev.* 85, 757–810. doi: 10.1152/physrev.00057.2003

Putney, J. W. Jr. (1986). A model for receptor-regulated calcium entry. *Cell Calcium* 7, 1–12. doi: 10.1016/0143-4160(86)90026-6

Rohrig, T., Pacjuk, O., Hernandez-Huguet, S., Korner, J., Scherer, K., and Richling, E. (2017). Inhibition of cyclic adenosine monophosphate-specific phosphodiesterase by various food plant-derived phytotherapeutic agents. *Medicines* 4:E80. doi: 10.3390/medicines4040080

Ross, G., Bajwa, T. J., Edwards, S., Emelyanova, L., Rizvi, F., Holmuhamedov, E., et al. (2017). Enhanced store-operated Ca2+ influx and ORAI1 expression in ventricular fibroblasts from human failing heart. *Biol. Open.* 6, 326–332. doi: 10.1242/bio.022632

Sabourin, J., Bartoli, F., Antigny, F., Gomez, A. M., and Benitah, J. P. (2016). Transient receptor potential canonical (TRPC)/orai1-dependent store-operated Ca2+ channels: new targets of aldosterone in cardiomyocytes. *J. Biol. Chem.* 291, 13394–13409. doi: 10.1074/jbc.M115.693911

Sabourin, J., Robin, E., and Raddatz, E. (2011). A key role of TRPC channels in the regulation of electromechanical activity of the developing heart. *Cardiovasc. Res.* 92, 226–236. doi: 10.1093/cvr/cvr167

Selvaraj, S., Sun, Y., and Singh, B. B. (2010). TRPC channels and their implication in neurological diseases. *CNS Neurol. Disord. Drug Targets* 9, 94–104. doi: 10.2174/187152710790966650

Shin, D. W., Pan, Z., Kim, E. K., Lee, J. M., Bhat, M. B., Parness, J., et al. (2003). A retrograde signal from calsequestrin for the regulation of store-operated Ca2+ entry in skeletal muscle. *J. Biol. Chem.* 278, 3286–3292. doi: 10.1074/jbc.M209045200

Trepakova, E. S., Gericke, M., Hirakawa, Y., Weisbrod, R. M., Cohen, R. A., and Bolotina, V. M. (2001). Properties of a native cation channel activated by Ca2+ store depletion in vascular smooth muscle cells. *J. Biol. Chem.* 276, 7782–7790. doi: 10.1074/jbc.M010104200

Tu, P., Gibon, J., and Bouron, A. (2010). The TRPC6 channel activator hyperforin induces the release of zinc and calcium from mitochondria. *J. Neurochem.* 112, 204–213. doi: 10.1111/j.1471-4159.2009.06446.x

Uemura, A., Naito, Y., and Matsubara, T. (2002). Dynamics of Ca(2+)/calmodulin-dependent protein kinase II following acute myocardial ischemia-translocation and autophosphorylation. *Biochem. Biophys. Res. Commun.* 297, 997–1002. doi: 10.1016/S0006-291X(02)02279-9

Vazquez, G., Lievremont, J. P., Bird, G. J., and Putney, J. W. Jr. (2001). Human Trp3 forms both inositol trisphosphate receptor-dependent and receptor-independent store-operated cation channels in DT40 avian B lymphocytes. *Proc. Natl. Acad. Sci. U.S.A.* 98, 11777–11782. doi: 10.1073/pnas.201238198

Vazquez, G., Wedel, B. J., Trebak, M., St John Bird, G., and Putney, J. W. Jr. (2003). Expression level of the canonical transient receptor potential 3 (TRPC3) channel determines its mechanism of activation. *J. Biol. Chem.* 278, 21649–21654. doi: 10.1074/jbc.M302162200

Venkatachalam, K., Ma, H. T., Ford, D. L., and Gill, D. L. (2001). Expression of functional receptor-coupled TRPC3 channels in DT40 triple receptor InsP3 knockout cells. *J. Biol. Chem.* 276, 33980–33985. doi: 10.1074/jbc.C100321200

Venkatachalam, K., and Montell, C. (2007). TRP channels. *Annu. Rev. Biochem.* 76, 387–417. doi: 10.1146/annurev.biochem.75.103004.142819

Voelkers, M., Salz, M., Herzog, N., Frank, D., Dolatabadi, N., Frey, N., et al. (2010). Orai1 and Stim1 regulate normal and hypertrophic growth in cardiomyocytes. *J. Mol. Cell Cardiol.* 48, 1329–1334. doi: 10.1016/j.yjmcc.2010.01.020

Wit, A. L., and Janse, M. J. (1992). Experimental models of ventricular tachycardia and fibrillation caused by ischemia and infarction. *Circulation* 1(Suppl), I32–I42.

Wu, X., Eder, P., Chang, B., and Molkentin, J. D. (2010). TRPC channels are necessary mediators of pathologic cardiac hypertrophy. *Proc. Natl. Acad. Sci. U.S.A.* 107, 7000–7005. doi: 10.1073/pnas.1001825107

Xie, L. H., and Weiss, J. N. (2009). Arrhythmogenic consequences of intracellular calcium waves. *Am. J. Physiol. Heart Circ. Physiol.* 297, H997–H1002. doi: 10.1152/ajpheart.00390.2009

Zhao, Z., Gordan, R., Wen, H., Fefelova, N., Zang, W. J., and Xie, L. H. (2013). Modulation of intracellular calcium waves and triggered activities by mitochondrial ca flux in mouse cardiomyocytes. *PLoS One* 8:e80574. doi: 10.1371/journal.pone.0080574

Zhao, Z., Kudej, R. K., Wen, H., Fefelova, N., Yan, L., Vatner, D. E., et al. (2018). Antioxidant defense and protection against cardiac arrhythmias: lessons from a mammalian hibernator (the woodchuck). *FASEB J.* 32, 4229–4240. doi: 10.1096/fj.201701516R

Zhao, Z., Wen, H., Fefelova, N., Allen, C., Baba, A., Matsuda, T., et al. (2012). Revisiting the ionic mechanisms of early afterdepolarizations in cardiomyocytes: predominant by Ca waves or Ca currents? *Am. J. Physiol. Heart Circ. Physiol.* 302, H1636–H1644. doi: 10.1152/ajpheart.00742.2011

Conflict of Interest Statement: The authors declare that the research was conducted in the absence of any commercial or financial relationships that could be construed as a potential conflict of interest.

frontiers in Physiology

MINI REVIEW
published: 26 November 2019
doi: 10.3389/fphys.2019.01406

Visualizing Cyclic Adenosine Monophosphate in Cardiac Microdomains Involved in Ion Homeostasis

*Vladimir Dikolayev[1,2], Turlybek Tuganbekov[2] and Viacheslav O. Nikolaev[1,3]**

[1]Institute of Experimental Cardiovascular Research, University Medical Center Hamburg-Eppendorf, Hamburg, Germany, [2]Department of Surgical Diseases, Astana Medical University, Nur-Sultan, Kazakhstan, [3]German Center for Cardiovascular Research (DZHK), Hamburg, Germany

3′,5′-Cyclic adenosine monophosphate (cAMP) is a key second messenger that regulates function of proteins involved in ion homeostasis and cardiac excitation-contraction coupling. Over the last decade, it has been increasingly appreciated that cAMP conveys its numerous effects by acting in discrete subcellular compartments or "microdomains." In this mini review, we describe how such localized signals can be visualized in living cardiomyocytes to better understand cardiac physiology and disease. Special focus is made on targeted biosensors that can be used to resolve second messenger signals within nanometers of cardiac ion channels and transporters. Potential directions for future research and the translational importance of cAMP compartmentalization are discussed.

Keywords: cyclic adenosine monophosphate, microdomain, imaging, cardiomyocyte, Förster resonance energy transfer biosensor

OPEN ACCESS

Edited by:
Alexey V. Glukhov, University of Wisconsin-Madison, School of Medicine and Public Health, United States

Reviewed by:
Robert Alan Rose, University of Calgary, Canada
Francisco J. Alvarado, University of Wisconsin-Madison, United States

***Correspondence:**
Viacheslav O. Nikolaev
v.nikolaev@uke.de

Specialty section:
This article was submitted to Cardiac Electrophysiology, a section of the journal Frontiers in Physiology

Received: *08 August 2019*
Accepted: *31 October 2019*
Published: *26 November 2019*

Citation:
Dikolayev V, Tuganbekov T and Nikolaev VO (2019) Visualizing Cyclic Adenosine Monophosphate in Cardiac Microdomains Involved in Ion Homeostasis. Front. Physiol. 10:1406. doi: 10.3389/fphys.2019.01406

3′,5′-Cyclic adenosine monophosphate (cAMP) is a key second messenger that serves, among many ubiquitous functions, as a critical regulator of heart performance and cardiac disease. Stimulation of G_s protein-coupled receptors on heart muscle cells (cardiomyocytes), including most notably β-adrenergic receptors (β-ARs) stimulated by catecholamines, activates adenylyl cyclase (AC) that catalyzes the generation of cAMP. In turn, cAMP will directly activate protein kinase A (PKA), Epac nucleotide exchange factors for the Rap subfamily of RAS-like small GTPases, cAMP-dependent ion channels, and Popeye domain containing proteins. Classically, cAMP was considered a freely diffusible second messenger. However, in response to adrenergic signaling during physiological fight-or-flight responses, cAMP apparently acts within discrete subcellular microdomains to fine-tune ion channel and transporter activities controlling excitation-contraction coupling. In addition, upon chronic stimulation, compartmentalized cAMP will promote cardiac hypertrophy and remodeling (Fischmeister et al., 2006; Perera and Nikolaev, 2013; Bers et al., 2019). Such microdomains, referred to by some authors as "nanodomains" or "nanocompartments" due to their apparent nanometer scale dimension, are typically organized around scaffolding proteins that bind PKA called A-kinase anchoring proteins (AKAPs). cAMP-AKAP compartments have been described for L-type calcium channels (LTCCs) important for calcium influx, ryanodine receptors (RyRs) that mediate release of Ca^{2+} from intracellular stores, and phospholamban (PLN) that mediates calcium reuptake in diastole *via* its interaction with the sarcoplasmic/endoplasmic reticulum (SR) calcium ATPase 2a (SERCA2a) pump (Bers, 2002; Lompre et al., 2010; Froese and Nikolaev, 2015). Each of these proteins is part of a multimolecular

complex containing anchored PKA molecules brought into close proximity to its substrates, specific isoforms of phosphodiesterase (PDE), which catalyze cAMP degradation to both terminate cAMP signaling and provide spatial restriction, as well as other kinases, phosphatases, and other signaling molecules that contribute to local cellular regulation. All these signaling enzymes act together in a highly localized fashion to confer specificity to the diverse physiological and pathophysiological responses triggered by the same second messenger cAMP (Buxton and Brunton, 1983; Mauban et al., 2009; Diviani et al., 2011; Scott et al., 2013). To better understand this type of regulation at the subcellular level and to modulate specific cAMP responses pharmacologically, one needs to gain much deeper insight into local microdomain-specific cAMP dynamics as currently possible only by state-of-the-art live cell imaging techniques.

CYCLIC NUCLEOTIDE BIOSENSORS ENABLE LIVE CELL IMAGING

The recently rapid development of Förster resonance energy transfer (FRET)-based biosensors has provided researchers with a versatile toolbox for real-time monitoring of cAMP in living cardiac cells (Sprenger and Nikolaev, 2013; Bers et al., 2019; Ghigo and Mika, 2019). cAMP biosensors usually have one of the following five types of design (see **Table 1**):

1. PKA holoenzyme is composed of two regulatory (R) and two catalytic (C) subunits. The first available FRET biosensor was composed of PKA holoenzyme with fluorescently labeled subunits to monitor its cAMP-dependent dissociation/re-association (Adams et al., 1991; Zaccolo and Pozzan, 2002).
2. Later, single-chain FRET biosensors were designed based on whole (Zhang et al., 2009; Herbst et al., 2011) or N-terminally truncated (DiPilato et al., 2004; Ponsioen et al., 2004) Epac1 or Epac2 sequence sandwiched between two fluorescent proteins such as enhanced cyan (CFP) and yellow (YFP) fluorescent proteins or their brighter and less pH sensitive analogues mTurquoise and circularly permuted Venus (Klarenbeek et al., 2015).
3. Fifteen years ago, we introduced a series of much more sensitive and compact CFP-YFP biosensors containing single cAMP binding domains from Epac1, Epac2, PKA, and HCN2 channels (Nikolaev et al., 2004, 2006; Norris et al., 2009). These and the aforementioned sensors have been modified to allow real time cAMP measurements in individual compartments as described below.
4. Recently, Zaccolo and colleagues have introduced a sensor called CUTie (cAMP Universal Tag for imaging experiments), which contains a single cAMP binding domain from PKA RIIβ subunit with YFP inserted into its loop 4–5 and CFP fused to the cAMP binding domain C-terminus (Surdo et al., 2017). This design allows generation of fusion proteins used as targeted biosensors with retained sensitivity and dynamic range. However, this strategy has so far been successful only for N-terminal fusions.
5. Very recently, non-FRET cAMP biosensors called Pink Flamindo and R-FlincA were developed based on the red fluorescent

TABLE 1 | Major types of design and examples of cAMP biosensors.

Design	Biosensor name	Dynamic range (%)	EC_{50} (μM)	References
1. Whole PKA heterotetramer				
a. chemically labeled with Fluorophores	FlCRhR	~20–30	0.09	Adams et al. (1991)
b. Fused to CFP and YFP	R-CFP;C-YFP	~ 20–30	0.5–0.9	Zaccolo and Pozzan (2002)
2. Whole-length or partially truncated Epac between CFP/YFP or their mutants	CFP-Epac1-YFP	~15	~50	DiPilato et al. (2004); Ponsioen et al. (2004); Zhang et al. (2009); Herbst et al. (2011); Klarenbeek et al. (2015)
	CFP-Epac2-YFP	~10–20	~15	
	CFP-(δDEP, CD)-YFP (H30)	~50	~10–50	
	ICUE1/2/3	~20–30	~10	
	Epac-S^{H188}	~100	~49,5	
	Epac-S^{H187} (Epac-S^{H188} with Q270E mutation) (H187)	~160	~4	
3. Single CNBD sandwiched between YFP and CFP	Epac1-camps	~30	2.4	Nikolaev et al. (2004, 2006); Norris et al. (2009); Mukherjee et al. (2016)
	Epac2-camps	~20	0.9	
	PKA-camps	~20	1.9	
	HCN2-camps	~15	6	
	Epac2-camps300	~20	0.3	
	mlCNBD-FRET	~30–40	0.07	
4. Single CNBD with YFP in the loop 4–5, CFP at C-terminus	CUTie	~20	7.4	Surdo et al. (2017)
5. Non-FRET	Pink Flamindo2	~400	7.2	Harada et al. (2017); Ohta et al. (2018)
	R-FlincA	~600	0.3	

Dynamic range represents a maximally measured % change in FRET/fluorescence signal in cells or in vitro. EC_{50} shows the affinity of the sensor for cAMP. CNDB, cyclic nucleotide binding domain.

protein mApple by either inserting a single cAMP binding domain from Epac1 between amino acids 150 and 151 of mApple or by using a circularly permuted version of this fluorescent protein (cp146) inserted into the PKA regulatory RIα subunit, respectively (Harada et al., 2017; Ohta et al., 2018). No targeted versions of these biosensors have been described so far.

VISUALIZING LOCAL CYCLICAMP IN THE VICINITY OF ION CHANNELS AND TRANSPORTERS USING TARGETED BIOSENSORS

To monitor cAMP dynamics specifically in various microdomains, several targeted biosensors have been developed. If expressed at appropriate levels, FRET sensors that incorporate full-length PKA or Epac (1 and 2 above) can have a subcellular distribution comparable to that of the endogenous cAMP effector proteins, permitting visualization of varying cAMP levels in multiple PKA and Epac containing compartments across a cell. However, as individual cAMP compartments can be smaller than the resolution of light microscopy, that is, nanometers in diameter, the specific targeting of cAMP sensors to individual compartments is required if cAMP signaling within individual compartments is to be imaged independently of cAMP fluxes that may be quite distinct in neighboring intracellular compartments.

The N-terminal dimerization-docking domain of the PKA regulatory subunit confers AKAP binding. As a first approach to distinguish cAMP compartments, Zaccolo and colleagues fused these sequences derived from the two types of regulatory PKA subunits (RI and RII) to the N-terminus of Epac1-camps to monitor cAMP dynamics at the subcellular sites where endogenous type I and type II PKA are localized. This experimental strategy revealed that PKA type I and II participate in signaling compartments regulated by different PDE isoforms. Type I PKA is more prone to stimulation *via* prostaglandin and glucagon receptors, whereas type II PKA is predominantly regulated by β-ARs (Di Benedetto et al., 2008). These compartments seem to mediate distinct functional responses, although it is still not completely understood which particular set of substrates is preferentially phosphorylated by the different PKA holoenzymes. Type II PKA can phosphorylate LTCC, RyR, and PLN, a small protein which regulates the activity of the SERCA2a pump, whereas PKA type I substrates are still unknown or controversial (Di Benedetto et al., 2008). Despite providing powerful biosensors to monitor local cAMP responses, targeting sensors *via* cAMP effectors has limitations. For example, several AKAPs have been shown to bind each type of PKA regulatory subunits (Diviani et al., 2011), so that each of such sensors can be expected to be simultaneously present at multiple distinct locations in the cell, confounding signals from different compartments when imaged by standard resolution light microscopy. Also, expression of such biosensors would inevitably lead to displacement of endogenous PKA molecules from the microdomains of interest, so that PKA-dependent regulation of local cAMP, PDE, and ion channel activities might be at least partially altered. If possible, these limitations should be considered when designing new targeted biosensors.

To gain further insight into microdomains around calcium handling proteins, our group has developed new versions of the cAMP biosensor Epac1-camps that are localized either to caveolin-rich plasma membrane (Perera et al., 2015) or to major SR membrane proteins SERCA2a and RyR, by fusing the sensor to PLN (Sprenger et al., 2015) or junctin (Berisha et al., 2019), respectively (see **Figure 1**). These sensors have been expressed in ventricular myocytes of transgenic mice to allow the imaging of cAMP in both normal and disease states. In experiments using myocytes isolated from mice subjected to pressure overload to induce cardiac hypertrophy and early heart failure, these biosensors uncovered a disease driven intracellular redistribution of several PDE families. For example, PDE2 was shown to switch locations between β_1- and β_2-AR-associated plasma membrane microdomains (Perera et al., 2015), while PDE3A switched isoforms from A2 and A1 and relocated from the sarcolemma to the SR (Perera et al., 2015; Berisha et al., 2019). This type of PDE redistribution had a functional impact on myocyte contractility, enhancing β_1-AR mediated inotropic increases in contractile force, especially when natriuretic peptide receptors were co-stimulated (Perera et al., 2015). However, microdomain-specific changes in PDE localization apparently occur before a measurable decrease of β_1-AR and PDE3/4 expression at the protein level associated with the onset of ventricular dilation resulting in heart failure with reduced ejection fraction (HFrEF). Therefore, PDE redistribution might contribute to the relative preservation of systolic function during early pathological cardiac remodeling induced by pressure overload, without providing protection from fatal arrhythmia. Arrhythmias in heart failure are also associated with sodium overload. We recently studied healthy and HFrEF rat ventricular myocytes using another newly developed biosensor fused to phospholemman to enable cAMP monitoring in the vicinity of the major cardiac sodium pump, the Na/K-ATPase (see **Figure 1**). We found that the phospholemman microdomain is normally regulated by β_2-AR/cAMP and PDE3, while induction of HFrEF by myocardial infarction resulted in a pronounced exchange of PDE3 with PDE2 in this microdomain (Bastug-Özel et al., 2019). The power of targeted biosensors is illustrated by the fact that most of these early pathological alterations in cAMP compartmentation cannot be detected using non-localized, cytosolic sensors or traditional biochemical techniques. Collectively, these studies suggest that each individual microdomain regulating ion homeostasis has a unique local cAMP regulation profile that might change in disease and alter cellular function. An important challenge will be to develop therapeutic strategies to target specifically these microdomains in disease, selectively promoting those cAMP-dependent processes that preserve cardiac function.

Targeted cAMP biosensors have also provided insight into the variation in cAMP signaling induced by stimulation of different cell membrane receptors. For example, in HEK293 cells, cAMP levels monitored by variants of the H30 biosensor (see **Table 1**) targeted to the cytosol, plasma membrane, and nucleus were found after prostaglandin receptor stimulation to be relatively high at the plasma membrane, significantly

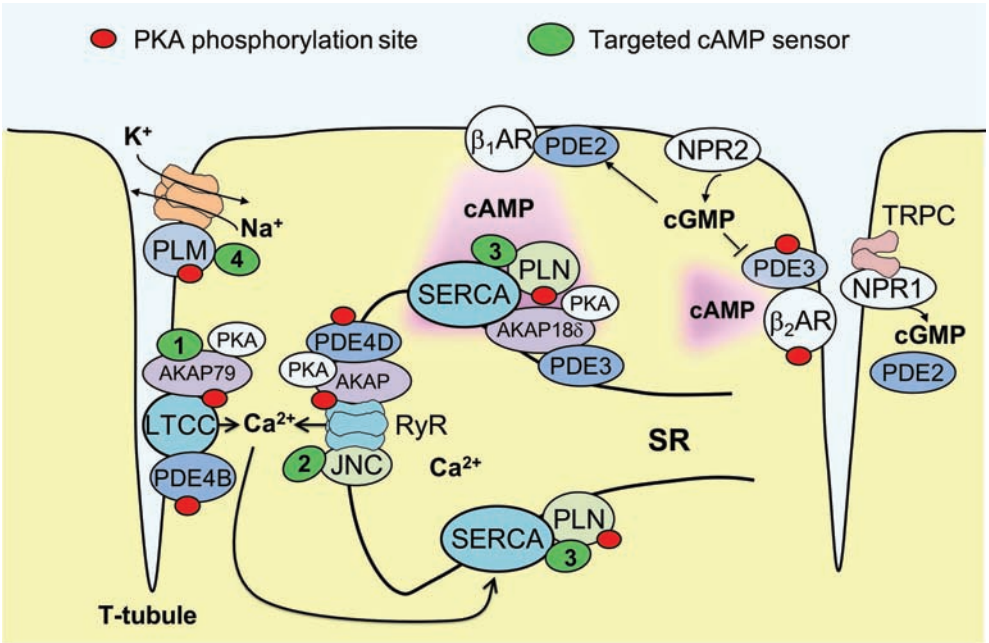

FIGURE 1 | Targeted biosensors used to visualize cAMP in the vicinity of proteins regulating cardiac ion homeostasis. Excitation-contraction coupling in ventricular cardiomyocytes is regulated by the L-type calcium channels (LTCCs) located in membrane invaginations called T-tubules, as well as by sarcoplasmic calcium release (ryanodine receptors, RyR) and reuptake (SERCA pump). Each of these locales forms a microdomain regulated by a specific set of AKAPs and associated PDEs that controls local PKA phosphorylation (marked by red dots). SERCA activity is inhibited by the small regulatory protein phospholamban (PLN); this inhibition is reduced upon PKA mediated PLN phosphorylation. Sodium homeostasis is under tight control by the Na/K-ATPase (NKA) shown in orange. This pump is inhibited by phosholemman (PLM), a regulatory protein that is less active when PKA phosphorylated. cAMP produced after stimulation of β_1-adrenergic receptors (βARs) diffuses across the cell, activating local pools of PKA in individual microdomains. cGMP can be produced by membrane guanylyl cyclases represented by natriuretic peptide receptors (NPRs) and can either activate PDE2 or inhibit PDE3. NPR1 is confined to T-tubules where it directly interacts with TRPC channels and produces a local pool of cGMP controlled by PDE2. To measure cAMP directly in the vicinities of each ion channel or transporter, targeted FRET biosensors (green) have been developed, such as AKAP79-CUTie (1, for LTCC), Epac1-JNC (2, for RyR), Epac1-PLN or AKAP18δ-CUTie (3, for SERCA) and PLM-Epac1 (4, for the NKA microdomain). See text for details. JNC – junctin, regulatory protein which forms a stable complex with RyR.

lower in the bulk cytosol and again much higher in the nucleus (Terrin et al., 2006). Likewise, β_1-AR stimulation in adult mouse ventricular cardiomyocytes led to higher cAMP levels detected at SERCA2a using Epac1-PLN sensor as compared to bulk cytosol (Sprenger et al., 2015). Also, cAMP increase measured in the vicinity of AKAP18δ (associated with SERCA2a) and AKAP79 (associated with LTCC) imaged using targeted versions of CUTie were higher than in the bulk cytosol (Surdo et al., 2017). Interestingly, this was not the case for a myofilament-associated microdomain imaged using CUTie fused to troponin I, which showed relatively low cAMP levels at submaximal β-adrenergic stimulation. This spatial heterogeneity was further accentuated under pathological conditions (Surdo et al., 2017). These studies suggest the existence of a privileged receptor/microdomain or receptor/calcium handling protein "communication." Mechanistically, this process could be mediated by the concerted action of different PDEs in different compartments (Sprenger et al., 2015). Alternatively, it has been proposed that active G protein-coupled receptors are present on intracellular membranes such as the nuclear envelope or trans-Golgi network where β-ARs, for example, can be activated by externally applied ligands that gain entry *via* organic cation transporters and activate cAMP production deep inside the cell (Irannejad et al., 2017). However, this possibility is not yet extensively studied in cardiac cells.

One way to visualize receptor/microdomain communication is to combine targeted biosensors with scanning ion conductance microscopy (SICM). SICM is a non-optical imaging technique which utilizes an electrolyte-filled glass nanopipette as a scanning probe for noncontact visualization of live cell membrane morphology (Korchev et al., 1997). The current flowing through the SICM pipette tip is decreased whenever the tip approaches the cell membrane. By clamping this drop in current at a fixed value, the distance between pipette tip and the membrane can be kept constant, so that scanning the membrane in the X-Y direction can resolve the morphological profile of the membrane with nanometer resolution. SICM as a multimodal imaging technique is useful not only for single cells but also for intact tissue structures (Miragoli et al., 2011). By combining SICM with FRET recordings of cAMP performed during local receptor stimulation *via* agonist delivery through the scanning pipette, we found that β_1-ARs were diffusely present on the surface and T-tubules of the myocyte plasma membrane, whereas β_2-AR was found exclusively in the T-tubules of healthy rat and mouse

cardiomyocytes (Nikolaev et al., 2010). Likewise, natriuretic peptide receptors NPR2 and NPR1 show a similar differential distribution pattern on the myocyte plasma membrane resulting in compartmentation of cyclic guanosine monophosphate (cGMP) signaling (Subramanian et al., 2018). Strict confinement of β_2-AR and NPR1 stimulated second messenger signals to T-tubular membrane are mediated by local PDE activities (mostly PDE4 and PDE2, respectively) and are likely to change in disease due to a redistribution of receptors and PDEs, as shown for β_2-AR and PDE2-4 (Perera et al., 2015; Sprenger et al., 2015). In the future, it would be exciting to combine SICM with targeted cAMP biosensors and with simultaneous ion channel recordings (Sanchez-Alonso et al., 2016) to directly visualize how receptors stimulated at different membrane locations regulate ion channel currents in microdomains. In this case, use of SICM allows activation of spatially resolved membrane structures, such as single T-tubules, with nanometer precision to activate a discrete pool of receptors, without affecting them at other membrane locations. When combined with localized FRET biosensor readouts in certain microdomains inside the cell, this approach provides a possibility to dissect the aforementioned receptor/microdomain communication more directly. It will be exciting to explore whether the same receptor generates different cAMP responses at different subcellular locations and if they are affected by cardiac disease.

FUTURE PERSPECTIVES

The aforementioned studies have provided an introduction into the microdomains associated with proteins regulating cardiac ion homeostasis. Beyond any doubt, this exciting field of research is still at its very beginning and much deeper insights will follow with time. We propose that future research should include the following topics for investigation:

1. Other differentially targeted biosensors with improved sensitivity and signal-to-noise should be developed and applied to imaging cAMP at ion channels and transporters involved in cardiac function and disease. For excitation-contraction coupling, targets of interest include the Nav1.5 sodium channel, the sodium-calcium exchanger and the potassium channel KCNQ1. All of them can be PKA phosphorylated, and notably KCNQ1 binds an AKAP called Yotiao, whose mutation results in long QT syndrome (Chen et al., 2007). For hypertrophy, an interesting microdomain is likely to be the vicinity of transient receptor potential C (TRPC) channels which is directly associated with NPR1 (Klaiber et al., 2011) (see **Figure 1**). When designing targeted biosensors, it is important to make sure that they do not perturb the composition and function of cAMP microdomains, for example, due to displacement of endogenous proteins or by altering microdomain regulation. For each newly developed sensor and cells expressing it, a detailed analysis of biochemical and functional properties pertaining to the microdomain of interest should be performed.
2. *In vivo* mouse models should be developed to dissect the individual contributions of specific PDE, AC, and AKAP families and subfamilies to derive insight into local cAMP signal regulation within individual microdomains. For example, at least three different PDE4 subfamilies (A, B and D) and two PDE3 subfamilies (A and B) have been implicated in local cAMP regulation in the cardiac myocyte (Conti and Beavo, 2007; Movsesian et al., 2018). PDE4B is functionally associated with LTCC and PDE4D with RyR (Lehnart et al., 2005; Leroy et al., 2011). Revisiting these studies using targeted biosensors in combination with PDE subfamily specific knockout mice should provide direct microdomain-specific readouts for individual locally acting PDEs and better link them to cardiac function and disease. Most PDE and AKAP global knockout mouse models do not allow the analysis of specific isoform contributions, for example, those of PDE4D3, PDE2A2 or AKAP18δ. There are also no specific isoform-selective pharmacological inhibitors available which could be used for this purpose. Rapid development of CRISPR/Cas9 gene editing technology should be able to overcome this limitation, providing new interesting mouse models or even specific deletions of individual isoforms in primary isolated cardiomyocytes *ex vivo*. Alternatively, for the PDE4 family in which localization is conferred by alternatively-spliced N-terminal sequences, expression of anchoring disruptor peptides may be particularly useful.
3. The aforementioned small and large animal disease models can be combined with gene therapy approaches aimed at overexpression of microdomain protein components which are downregulated in heart failure such as some PDEs, as it has been done in the pioneering work with SERCA2a (Jessup et al., 2011). Restoration of the expression of individual PDEs may restore normal local cAMP dynamics in functionally relevant microdomains and ameliorate disease-associated cardiac dysfunction. Conversely, disruption of PDE-microdomain interactions using specific peptides can be instrumental in augmenting cardioprotective cyclic nucleotide pools, as elegantly shown by Baillie and colleagues for the PDE4D3/Hps20 interaction (Sin et al., 2011). A similar approach is now under evaluation for the SERCA2a/PDE3A complex. Notably, this latter strategy has been deployed outside the cardiovascular system. For example, expression of the 4D3 N-terminal peptide has been used to disrupt mAKAPα-PDE4D3complexes in the retinal ganglion cell to confer neuroprotection (Boczek et al., 2019).
4. It will be important to transit from imaging cardiac myocytes *in vitro*, whether following culture or immediately *ex vivo* after isolation from mice, to imaging myocytes *in vivo* in the living heart. Recently, developed cAMP imaging in isolated Landgendorff perfused hearts that can be combined with electrophysiological recordings (Jungen et al., 2017) or even in open chest *in vivo* models (Tallini et al., 2006; Frankenreiter et al., 2017) are helping us achieve imaging in a physiological context. Interestingly, cAMP responses and the biochemical composition of signalosomes comprising

individual compartments can vary depending upon of the anatomical origin of the myocytes, with differences recognized between the atria and base and apex of the ventricles (Wright et al., 2018). These differences should be more carefully considered in the future studies.

5. Last but not least, it will be important to determine whether cyclic nucleotide compartmentation is conserved among mammalian species, including most importantly between rodents and humans. Most research in this field has been performed in rats and mice, given the difficulty in acquiring adult human cardiac myocytes, with the notable exception of a few studies taking advantage of atrial tissue acquired from patients with atrial fibrillation (Molina et al., 2012; Glukhov et al., 2015). Since structure of atrial and ventricular cells and their biochemical makeup including expression of receptors and PDEs are different, additional studies have to be undertaken to better compare mechanisms of cAMP compartmentation in atrial vs. ventricular myocytes. Human studies are of obvious translational importance, and the derivation of cardiac myocytes from human induced pluripotent stem cells (hiPSC-CMs) should ultimately facilitate this research. A current major limitation with using hiPSC-CMs is that current procedures for "maturing" the myocytes yield cells similar to fetal or neonatal myocytes that have significant differences in ultrastructure and excitation-contraction coupling from adult myocytes *in vivo*, an issue of obvious relevance to the study of compartmentalized signaling. Nevertheless, using a cytosolic cAMP biosensor, clear differences in β-adrenergic sensitivity and PDE function were detected using hiPSC-CM for patients with Takotsubo cardiomyopathy (Borchert et al., 2017). This landmark study should be extended using localized FRET biosensors to better understand microdomain alterations in this and other cardiac diseases. If these alterations are comparable to those happening in adult human cells, hiPSC-CMs could be useful to screening drugs for new cardiovascular therapeutics targeting cyclic nucleotide compartmentation, much as hiPSC-CMs have proven useful for diagnosis and analysis of inherited ion channel diseases such as Long QT syndrome (Sinnecker et al., 2013).

AUTHOR CONTRIBUTIONS

VD, TT, and VN discussed the concept, wrote, and edited the manuscript.

FUNDING

The work in authors' laboratory is supported by the Deutsche Forschungsgemeinschaft (grants NI 1301/3, SFB 1328, and FOR 2060), ERA-Net ERA-CVD, DZHK, and the Gertraud und Heinz Rose-Stiftung. VD was supported by a grant from DAAD.

ACKNOWLEDGMENTS

We thank Michael S. Kapiloff for critical reading of the manuscript.

REFERENCES

Adams, S. R., Harootunian, A. T., Buechler, Y. J., Taylor, S. S., and Tsien, R. Y. (1991). Fluorescence ratio imaging of cyclic AMP in single cells. *Nature* 349, 694–697. doi: 10.1038/349694a0

Bastug-Özel, Z., Wright, P. T., Kraft, A. E., Pavlovic, D., Howie, J., Froese, A., et al. (2019). Heart failure leads to altered beta2-adrenoceptor/cyclic adenosine monophosphate dynamics in the sarcolemmal phospholemman/Na, K ATPase microdomain. *Cardiovasc. Res.* 115, 546–555. doi: 10.1093/cvr/cvy221

Berisha, F., Götz, K. R., Wegener, J. W., Jungen, C., Pape, U., Kraft, A. E., et al. (2019). Direct monitoring of cAMP at the cardiac ryanodine receptor using a novel targeted fluorescence biosensor mouse. bioRxiv 623934 [Preprint]. doi: 10.1101/623934 (Accessed October 29, 2019).

Bers, D. M. (2002). Cardiac excitation-contraction coupling. *Nature* 415, 198–205. doi: 10.1038/415198a

Bers, D. M., Xiang, Y. K., and Zaccolo, M. (2019). Whole-cell cAMP and PKA activity are epiphenomena, nanodomain signaling matters. *Physiology* 34, 240–249. doi: 10.1152/physiol.00002.2019

Boczek, T., Cameron, E. G., Yu, W., Xia, X., Shah, S. H., Castillo Chabeco, B., et al. (2019). Regulation of neuronal survival and axon growth by a perinuclear cAMP compartment. *J. Neurosci.* 39, 5466–5480. doi: 10.1523/JNEUROSCI.2752-18.2019

Borchert, T., Hübscher, D., Guessoum, C. I., Lam, T. D., Ghadri, J. R., Schellinger, I. N., et al. (2017). Catecholamine-dependent beta-adrenergic signaling in a pluripotent stem cell model of Takotsubo cardiomyopathy. *J. Am. Coll. Cardiol.* 70, 975–991. doi: 10.1016/j.jacc.2017.06.061

Buxton, I. L., and Brunton, L. L. (1983). Compartments of cyclic AMP and protein kinase in mammalian cardiomyocytes. *J. Biol. Chem.* 258, 10233–10239

Chen, L., Marquardt, M. L., Tester, D. J., Sampson, K. J., Ackerman, M. J., and Kass, R. S. (2007). Mutation of an A-kinase-anchoring protein causes long-QT syndrome. *Proc. Natl. Acad. Sci. U. S. A.* 104, 20990–20995. doi: 10.1073/pnas.0710527105

Conti, M., and Beavo, J. (2007). Biochemistry and physiology of cyclic nucleotide phosphodiesterases: essential components in cyclic nucleotide signaling. *Annu. Rev. Biochem.* 76, 481–511. doi: 10.1146/annurev.biochem.76.060305.150444

Di Benedetto, G., Zoccarato, A., Lissandron, V., Terrin, A., Li, X., Houslay, M. D., et al. (2008). Protein kinase A type I and type II define distinct intracellular signaling compartments. *Circ. Res.* 103, 836–844. doi: 10.1161/CIRCRESAHA.108.174813

DiPilato, L. M., Cheng, X., and Zhang, J. (2004). Fluorescent indicators of cAMP and Epac activation reveal differential dynamics of cAMP signaling within discrete subcellular compartments. *Proc. Natl. Acad. Sci. U. S. A.* 101, 16513–16518. doi: 10.1073/pnas.0405973101

Diviani, D., Dodge-Kafka, K. L., Li, J., and Kapiloff, M. S. (2011). A-kinase anchoring proteins: scaffolding proteins in the heart. *Am. J. Physiol. Heart Circ. Physiol.* 301, H1742–H1753. doi: 10.1152/ajpheart.00569.2011

Fischmeister, R., Castro, L. R., Abi-Gerges, A., Rochais, F., Jurevicius, J., Leroy, J., et al. (2006). Compartmentation of cyclic nucleotide signaling in the heart: the role of cyclic nucleotide phosphodiesterases. *Circ. Res.* 99, 816–828. doi: 10.1161/01.RES.0000246118.98832.04

Frankenreiter, S., Bednarczyk, P., Kniess, A., Bork, N. I., Straubinger, J., Koprowski, P., et al. (2017). cGMP-elevating compounds and ischemic conditioning provide cardioprotection against ischemia and reperfusion injury via cardiomyocyte-specific BK channels. *Circulation* 136, 2337–2355. doi: 10.1161/CIRCULATIONAHA.117.028723

Froese, A., and Nikolaev, V. O. (2015). Imaging alterations of cardiomyocyte cAMP microdomains in disease. *Front. Pharmacol.* 6:172. doi: 10.3389/fphar.2015.00172

Ghigo, A., and Mika, D. (2019). cAMP/PKA signaling compartmentalization in cardiomyocytes: lessons from FRET-based biosensors. *J. Mol. Cell. Cardiol.* 131, 112–121. doi: 10.1016/j.yjmcc.2019.04.020

Glukhov, A. V., Balycheva, M., Sanchez-Alonso, J. L., Ilkan, Z., Alvarez-Laviada, A., Bhogal, N., et al. (2015). Direct evidence for microdomain-specific localization and remodeling of functional L-type calcium channels in rat and human atrial myocytes. *Circulation* 132, 2372–2384. doi: 10.1161/CIRCULATIONAHA.115.018131

Harada, K., Ito, M., Wang, X., Tanaka, M., Wongso, D., Konno, A., et al. (2017). Red fluorescent protein-based cAMP indicator applicable to optogenetics and *in vivo* imaging. *Sci. Rep.* 7:7351. doi: 10.1038/s41598-017-07820-6

Herbst, K. J., Coltharp, C., Amzel, L. M., and Zhang, J. (2011). Direct activation of Epac by sulfonylurea is isoform selective. *Chem. Biol.* 18, 243–251. doi: 10.1016/j.chembiol.2010.12.007

Irannejad, R., Pessino, V., Mika, D., Huang, B., Wedegaertner, P. B., Conti, M., et al. (2017). Functional selectivity of GPCR-directed drug action through location bias. *Nat. Chem. Biol.* 13, 799–806. doi: 10.1038/nchembio.2389

Jessup, M., Greenberg, B., Mancini, D., Cappola, T., Pauly, D. F., Jaski, B., et al. (2011). Calcium upregulation by percutaneous administration of gene therapy in cardiac disease (CUPID): a phase 2 trial of intracoronary gene therapy of sarcoplasmic reticulum Ca2+-ATPase in patients with advanced heart failure. *Circulation* 124, 304–313. doi: 10.1161/CIRCULATIONAHA.111.022889

Jungen, C., Scherschel, K., Eickholt, C., Kuklik, P., Klatt, N., Bork, N., et al. (2017). Disruption of cardiac cholinergic neurons enhances susceptibility to ventricular arrhythmias. *Nat. Commun.* 8:14155. doi: 10.1038/ncomms14155

Klaiber, M., Dankworth, B., Kruse, M., Hartmann, M., Nikolaev, V. O., Yang, R. B., et al. (2011). A cardiac pathway of cyclic GMP-independent signaling of guanylyl cyclase A, the receptor for atrial natriuretic peptide. *Proc. Natl. Acad. Sci. U. S. A.* 108, 18500–18505. doi: 10.1073/pnas.1103300108

Klarenbeek, J., Goedhart, J., van Batenburg, A., Groenewald, D., and Jalink, K. (2015). Fourth-generation epac-based FRET sensors for cAMP feature exceptional brightness, photostability and dynamic range: characterization of dedicated sensors for FLIM, for ratiometry and with high affinity. *PLoS One* 10:e0122513. doi: 10.1371/journal.pone.0122513

Korchev, Y. E., Bashford, C. L., Milovanovic, M., Vodyanoy, I., and Lab, M. J. (1997). Scanning ion conductance microscopy of living cells. *Biophys. J.* 73, 653–658. doi: 10.1016/S0006-3495(97)78100-1

Lehnart, S. E., Wehrens, X. H., Reiken, S., Warrier, S., Belevych, A. E., Harvey, R. D., et al. (2005). Phosphodiesterase 4D deficiency in the ryanodine-receptor complex promotes heart failure and arrhythmias. *Cell* 123, 25–35. doi: 10.1016/j.cell.2005.07.030

Leroy, J., Richter, W., Mika, D., Castro, L. R., Abi-Gerges, A., Xie, M., et al. (2011). Phosphodiesterase 4B in the cardiac L-type Ca(2)(+) channel complex regulates Ca(2)(+) current and protects against ventricular arrhythmias in mice. *J. Clin. Invest.* 121, 2651–2661. doi: 10.1172/JCI44747

Lompre, A. M., Hajjar, R. J., Harding, S. E., Kranias, E. G., Lohse, M. J., and Marks, A. R. (2010). Ca2+ cycling and new therapeutic approaches for heart failure. *Circulation* 121, 822–830. doi: 10.1161/CIRCULATIONAHA.109.890954

Mauban, J. R., O'Donnell, M., Warrier, S., Manni, S., and Bond, M. (2009). AKAP-scaffolding proteins and regulation of cardiac physiology. *Physiology* 24, 78–87. doi: 10.1152/physiol.00041.2008

Miragoli, M., Moshkov, A., Novak, P., Shevchuk, A., Nikolaev, V. O., El-Hamamsy, I., et al. (2011). Scanning ion conductance microscopy: a convergent high-resolution technology for multi-parametric analysis of living cardiovascular cells. *J. R. Soc. Interface* 8, 913–925. doi: 10.1098/rsif.2010.0597

Molina, C. E., Leroy, J., Richter, W., Xie, M., Scheitrum, C., Lee, I. O., et al. (2012). Cyclic adenosine monophosphate phosphodiesterase type 4 protects against atrial arrhythmias. *J. Am. Coll. Cardiol.* 59, 2182–2190. doi: 10.1016/j.jacc.2012.01.060

Movsesian, M., Ahmad, F., and Hirsch, E. (2018). Functions of PDE3 isoforms in cardiac muscle. *J. Cardiovasc. Dev. Dis.* 5:10. doi: 10.3390/jcdd5010010

Mukherjee, S., Jansen, V., Jikeli, J. F., Hamzeh, H., Alvarez, L., Dombrowski, M., et al. (2016). A novel biosensor to study cAMP dynamics in cilia and flagella. *elife* 5:e14052. doi: 10.7554/eLife.14052

Nikolaev, V. O., Bünemann, M., Hein, L., Hannawacker, A., and Lohse, M. J. (2004). Novel single chain cAMP sensors for receptor-induced signal propagation. *J. Biol. Chem.* 279, 37215–37218. doi: 10.1074/jbc.C400302200

Nikolaev, V. O., Bünemann, M., Schmitteckert, E., Lohse, M. J., and Engelhardt, S. (2006). Cyclic AMP imaging in adult cardiac myocytes reveals far-reaching beta1-adrenergic but locally confined beta2-adrenergic receptor-mediated signaling. *Circ. Res.* 99, 1084–1091. doi: 10.1161/01.RES.0000250046.69918.d5

Nikolaev, V. O., Moshkov, A., Lyon, A. R., Miragoli, M., Novak, P., Paur, H., et al. (2010). Beta2-adrenergic receptor redistribution in heart failure changes cAMP compartmentation. *Science* 327, 1653–1657. doi: 10.1126/science.1185988

Norris, R. P., Ratzan, W. J., Freudzon, M., Mehlmann, L. M., Krall, J., Movsesian, M. A., et al. (2009). Cyclic GMP from the surrounding somatic cells regulates cyclic AMP and meiosis in the mouse oocyte. *Development* 136, 1869–1878. doi: 10.1242/dev.035238

Ohta, Y., Furuta, T., Nagai, T., and Horikawa, K. (2018). Red fluorescent cAMP indicator with increased affinity and expanded dynamic range. *Sci. Rep.* 8, 1866. doi: 10.1038/s41598-018-20251-1

Perera, R. K., and Nikolaev, V. O. (2013). Compartmentation of cAMP signalling in cardiomyocytes in health and disease. *Acta Physiol.* 207, 650–662. doi: 10.1111/apha.12077

Perera, R. K., Sprenger, J. U., Steinbrecher, J. H., Hubscher, D., Lehnart, S. E., Abesser, M., et al. (2015). Microdomain switch of cGMP-regulated phosphodiesterases leads to ANP-induced augmentation of beta-adrenoceptor-stimulated contractility in early cardiac hypertrophy. *Circ. Res.* 116, 1304–1311. doi: 10.1161/CIRCRESAHA.116.306082

Ponsioen, B., Zhao, J., Riedl, J., Zwartkruis, F., van der Krogt, G., Zaccolo, M., et al. (2004). Detecting cAMP-induced Epac activation by fluorescence resonance energy transfer: Epac as a novel cAMP indicator. *EMBO Rep.* 5, 1176–1180. doi: 10.1038/sj.embor.7400290

Sanchez-Alonso, J. L., Bhargava, A., O'Hara, T., Glukhov, A. V., Schobesberger, S., Bhogal, N., et al. (2016). Microdomain-specific modulation of L-type calcium channels leads to triggered ventricular arrhythmia in heart failure. *Circ. Res.* 119, 944–955. doi: 10.1161/CIRCRESAHA.116.308698

Scott, J. D., Dessauer, C. W., and Tasken, K. (2013). Creating order from chaos: cellular regulation by kinase anchoring. *Annu. Rev. Pharmacol. Toxicol.* 53, 187–210. doi: 10.1146/annurev-pharmtox-011112-140204

Sin, Y. Y., Edwards, H. V., Li, X., Day, J. P., Christian, F., Dunlop, A. J., et al. (2011). Disruption of the cyclic AMP phosphodiesterase-4 (PDE4)-HSP20 complex attenuates the beta-agonist induced hypertrophic response in cardiac myocytes. *J. Mol. Cell. Cardiol.* 50, 872–883. doi: 10.1016/j.yjmcc.2011.02.006

Sinnecker, D., Goedel, A., Laugwitz, K. L., and Moretti, A. (2013). Induced pluripotent stem cell-derived cardiomyocytes: a versatile tool for arrhythmia research. *Circ. Res.* 112, 961–968. doi: 10.1161/CIRCRESAHA.112.268623

Sprenger, J. U., and Nikolaev, V. O. (2013). Biophysical techniques for detection of cAMP and cGMP in living cells. *Int. J. Mol. Sci.* 14, 8025–8046. doi: 10.3390/ijms14048025

Sprenger, J. U., Perera, R. K., Steinbrecher, J. H., Lehnart, S. E., Maier, L. S., Hasenfuss, G., et al. (2015). *In vivo* model with targeted cAMP biosensor reveals changes in receptor-microdomain communication in cardiac disease. *Nat. Commun.* 6:6965. doi: 10.1038/ncomms7965

Subramanian, H., Froese, A., Jonsson, P., Schmidt, H., Gorelik, J., and Nikolaev, V. O. (2018). Distinct submembrane localisation compartmentalises cardiac NPR1 and NPR2 signalling to cGMP. *Nat. Commun.* 9:2446. doi: 10.1038/s41467-018-04891-5

Surdo, N. C., Berrera, M., Koschinski, A., Brescia, M., Machado, M. R., Carr, C., et al. (2017). FRET biosensor uncovers cAMP nano-domains at beta-adrenergic targets that dictate precise tuning of cardiac contractility. *Nat. Commun.* 8:15031. doi: 10.1038/ncomms15031

Tallini, Y. N., Ohkura, M., Choi, B. R., Ji, G., Imoto, K., Doran, R., et al. (2006). Imaging cellular signals in the heart *in vivo*: cardiac expression of the high-signal Ca2+ indicator GCaMP2. *Proc. Natl. Acad. Sci. U. S. A.* 103, 4753–4758. doi: 10.1073/pnas.0509378103

Terrin, A., Di Benedetto, G., Pertegato, V., Cheung, Y. F., Baillie, G., Lynch, M. J., et al. (2006). PGE(1) stimulation of HEK293 cells generates multiple contiguous domains with different [cAMP]: role of compartmentalized phosphodiesterases. *J. Cell Biol.* 175, 441–451. doi: 10.1083/jcb.200605050

Wright, P. T., Bhogal, N. K., Diakonov, I., Pannell, L. M. K., Perera, R. K., Bork, N. I., et al. (2018). Cardiomyocyte membrane structure and cAMP compartmentation produce anatomical variation in beta2AR-cAMP responsiveness in murine hearts. *Cell Rep.* 23, 459–469. doi: 10.1016/j.celrep.2018.03.053

Zaccolo, M., and Pozzan, T. (2002). Discrete microdomains with high concentration of cAMP in stimulated rat neonatal cardiac myocytes. *Science* 295, 1711–1715. doi: 10.1126/science.1069982

Zhang, C. L., Katoh, M., Shibasaki, T., Minami, K., Sunaga, Y., Takahashi, H., et al. (2009). The cAMP sensor Epac2 is a direct target of antidiabetic sulfonylurea drugs. *Science* 325, 607–610. doi: 10.1126/science.1172256

Conflict of Interest: The authors declare that the research was conducted in the absence of any commercial or financial relationships that could be construed as a potential conflict of interest.

Advantages of publishing in Frontiers

OPEN ACCESS
Articles are free to read for greatest visibility and readership

FAST PUBLICATION
Around 90 days from submission to decision

HIGH QUALITY PEER-REVIEW
Rigorous, collaborative, and constructive peer-review

TRANSPARENT PEER-REVIEW
Editors and reviewers acknowledged by name on published articles

Frontiers
Avenue du Tribunal-Fédéral 34
1005 Lausanne | Switzerland

Visit us: www.frontiersin.org
Contact us: info@frontiersin.org | +41 21 510 17 00

REPRODUCIBILITY OF RESEARCH
Support open data and methods to enhance research reproducibility

DIGITAL PUBLISHING
Articles designed for optimal readership across devices

FOLLOW US
@frontiersin

IMPACT METRICS
Advanced article metrics track visibility across digital media

EXTENSIVE PROMOTION
Marketing and promotion of impactful research

LOOP RESEARCH NETWORK
Our network increases your article's readership